Modelling Large Scale Structure Statistics for Precision Cosmology

Dissertation
zur
Erlangung der naturwissenschaftlichen Doktorwürde
(Dr. sc. nat.)

vorgelegt der
Mathematisch-naturwissenschaftlichen Fakultät
der

Universität Zürich

von

Tobias Baldauf

aus
Deutschland

Promotionskomitee
Prof. Dr. Uroš Seljak (Vorsitz)
Prof. Dr. Philippe Jetzer
Dr. Prasenjit Saha

Zürich, 2013

Abstract

This Thesis develops and improves theoretical models for the statistical description of the galaxy and matter distribution in the Universe. These models are important, if one wants to constrain composition and history of our Universe from galaxy surveys.
The first part of this work gives an overview of the current understanding ofs the matter distribution in the Universe and bias models, which can be used to relate the matter and galaxy distribution. The second part consists of four studies. The first study describes how an accurate model of the galaxy bispectrum allows to constrain the dynamics of the early inflationary phase of the Universe through the detection of primordial non-Gaussianity. For this purpose one needs to consider the largest observable scales in the Universe, which in turn requires a general relativistic framework. This problem is considered in the second publication included in this Thesis, where we develop a general relativistic generalization of galaxy bias. The third study is again concerned with the halo bispectrum. Using N-body simulations we detect quadratic tidal tensor effects in the bias relation and show that these are in accordance with a coevolution of protohaloes and dark matter. The last part of this work discusses the power spectrum of discrete tracers of the density field. We show that corrections to the fiducial Poisson shot noise arise from non-linear biasing and exclusion effects, which are related to the finite Lagrangian size of dark matter haloes.

Zusammenfassung

In dieser Arbeit entwickeln und verbessern wir theoretische Modelle für die statistische Beschreibung der Galaxien- und Materieverteilung im Universum. Anhand dieser Modelle können ausgehend von Galaxienkatalogen Rückschlüsse auf die Zusammensetzung des Universums und seine Entstehungsgeschichte gezogen werden.
Der erste Teil der Arbeit gibt einen Überblick über theoretische Modelle der Materieverteilung im Universum und der Beziehung zwischen Materie- und Galaxienverteilung. Im zweiten Teil der Arbeit finden sich vier Studien, die auf diesen Grundlagen aufbauen. Die erste Arbeit beschäftigt sich mit der Möglichkeit anhand von nicht-Gaussschen Effekten in der Dreipunktfunktion des Galaxienfeldes Rückschlüsse auf die Dynamik der Inflation im frühen Universum zu ziehen. Dafür müssen die grössten beobachtbaren Skalen im Universum herangezogen werden, was eine Betrachtung im Rahmen der Allgemeinen Relativitätstheorie voraussetzt. Dies ist das Thema der zweiten Publikation. Im Anschluss kommen wir auf die Dreipunktfunktion von Galaxien zurück und versuchen anhand dieser, quadratische Effekte in der Relation zwischen Materie und Galaxien nachzuweisen. Der letzte Teil dieser Arbeit befasst sich mit den Effekten diskreter Dichteindikatoren im Leistungsspektrum und zeigt, dass Korrekturen zum Poisson'schen Verhalten nötig sind. Diese Korrekturen können auf die endliche Grösse der Indikatorteilchen und nicht-lineare Effekte in der Relation zwischen Materie- und Indikatorverteilung zurückgeführt werden.

Für meine Großeltern,
die immer an mich geglaubt haben.

Acknowledgements

First, I would like to thank Prof. Dr. Uroš Seljak for giving me the chance to work in his group and under his supervision.
I am very grateful to my senior collaborators Vincent Desjacques, Rachel Mandelbaum, Fabian Schmidt, Leonardo Senatore, Robert Smith, Anze Slošar, Jaiyul Yoo and Matias Zaldarriaga for their help, inspiration and motivation.
Thanks to my colleagues Donnino Anderhalden, Jonathan Blazek, Michael Busha, Andreu Font, Nico Hamaus, Lucas Lombriser, Teppei Okumura, Aurel Schneider and Zvonimir Vlah for help, discussions and a great time. Special thanks to Doug Potter for being such a nice guy and helping me with supercomputer problems.
Thanks to the Swiss Federation for funding me, for sharing her beautiful nature and for building paved roads up the mountains. I really enjoyed my time at the Institute for Theoretical Physics at the University of Zurich. Thanks to EWHA Womans University, the Lawrence Berkeley Labratory and the University of California at Berkeley for their hospitality.
Finally, I want to thank Francis, my parents and my grandparents for their continuous support and encouragement.

Zürich, January 2013

Contents

CHAPTER 1

Introduction[†]

This Chapter introduces this Thesis by discussing the historical steps that have led to the current understanding of our Universe. We furthermore describe our current understanding of the large scale distribution of luminous and dark matter and discuss where we see room for improvement.

The rest of this Thesis breaks down as follows: In Ch. 2 we discuss the physics of a homogenous expanding Universe and the relation between its dynamics and the energy content. We then proceed to discuss perturbations about this homogeneous expanding spacetime employing a Newtonian approach in Ch. 3. This Chapter also introduces the language of standard perturbation theory, a powerful technique used to describe the weakly non-linear structure formation that is heavily used throughout this Thesis. Ch. 4 introduces a general relativistic approach to perturbations about the homogenous Universe. We also give a short introduction into inflation, one of the most popular processes for the generation of the seeds for structure formation and discuss how we can possibly constrain the physics driving inflation using non-Gaussian signatures. Ch. 5 is devoted to the most non-linear objects in Large Scale Structure (LSS), dark matter haloes. We describe several theoretical approaches that can be used to estimate the abundance and distribution of these virialized objects. Readers interested in the science results should skip the introductory chapters and directly proceed to Ch. 6 on page 85, where we discuss how deviations from the simplest models of inflation imprint themselves into the bispectrum of haloes and galaxies. We will see that these imprints are dominant on the largest observable scales, where general relativistic gauge effects become important. These effects are thoroughly discussed in Ch. 7. The halo bispectrum can also be used to distinguish various models for the distribution of dark matter halos, namely Eulerian and Lagrangian bias models as we discuss in Ch. 8. The last science Chapter, Ch. 9, considers the relation between the small scale halo-halo correlation function and the halo-halo power spectrum on the largest scales. We summarize the main conclusions of this Thesis and the included publications in Ch. 10 and speculate on possible and necessary extensions of this work.

Throughout this work we will consider a flat cold dark matter cosmology with a cosmological constant as our fiducial world model and will mention explicitly whenever we consider a different world model. The matter density parameter is $\Omega_{\mathrm{m},0} = 0.25$, the density parameter of the cosmological constant is $\Omega_{\Lambda,0} = 0.75$ and the root mean square density fluctuation in spheres of radius $R = 8\ h^{-1}\mathrm{Mpc}$ is $\sigma_8 = 0.8$.

[†]Some of the basic introductory material in this Chapter is reproduced from my master's thesis [1] and standard textbooks on cosmology [2, 3, 4, 5].

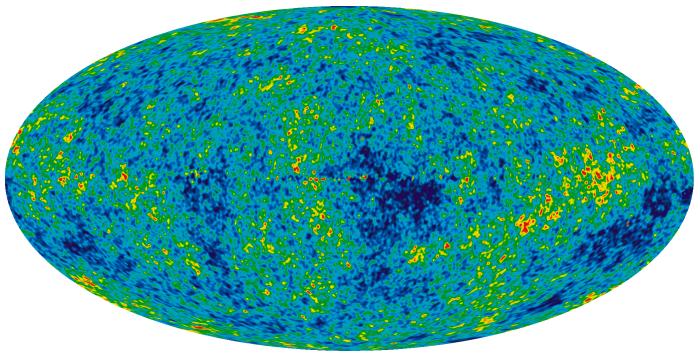

Figure 1.1.: The microwave sky as seen by WMAP 7 year data release. Credit: NASA / WMAP Science Team

1.1. Historical Account

Mankind was observing the night sky for thousands of years but it was not before the 16th and 17th century that physicists like Galileo Galilei, Johannes Kepler and Isaac Newton developed a mathematical theory of gravitation which could coherently account for the planetary orbits. This very successful theory of gravitational force turned out to be the weak field limit of general relativity, which was presented by Albert Einstein in 1916 [6]. Based on his earlier work on special relativity, he had developed a geometric theory of gravity, which abandoned the idea of gravity acting as a force and rather considered it as a property of a curved four dimensional spacetime. The core of the mathematical realisation of this theory are the Einstein field equations, relating curvature of spacetime to its energy content. The correct prediction of the excess precession of Mercury's orbit around the sun was a first confirmation for the new theory. Another validation was published in 1919, when an expedition lead by Arthur Eddington measured the light deflection by the sun during a total eclipse. Einstein himself tried to find a solution of his theory that would describe a static Universe. For this purpose he had to postulate a non-vanishing value of the cosmological constant, a step that he would later call "the biggest blunder of [his] life".
At that time astronomers also started to look beyond our local galaxy and realized that the mysterious observed nebulae were nothing but distant galaxies. Beginning with Edwin Hubble's observations in the 1920s, first quantitatively relevant measurements of the properties of the Universe became available. After a decade of observations Hubble discovered in 1929 [7], that distant galaxies are receding from us with a velocity proportional to their distance. Independently, Alexander Friedmann in 1922 [8] derived the so called Friedmann equations from the Einstein field equations, using the metric of a homogeneous and isotropic spacetime and the energy momentum tensor of a perfect fluid. The Friedmann equations could in fact predict the expansion that was observed by Hubble. The question who discovered the expansion of the Universe is debated. For a long time it was undoubtedly ascribed to Edwin Hubble. Recently it was realized [9] that Georges Lemaître had published observational evidence already in 1927 [10].
Applying the virial theorem to galaxy clusters, Fritz Zwicky [11] realized in 1933 that the luminous matter content does not suffice to make the Coma cluster gravitationally bound and postulated the existence of **dark matter**. This conclusion was later supported by Vera Rubins observations of flattened galaxy rotation curves, which could also not be supported by the observed amount of luminous matter.
Another milestone for todays understanding of the evolution of our Universe was the discovery of the **Cosmic Microwave Background** (CMB) radiation by Penzias & Wilson in 1964. This radiation, which shows an almost perfect Planckian spectrum of $T_{\mathrm{CMB}} = 2.725$ K, is a remnant from the early hot epoch of the Universe when the interstellar gas was still ionized and scattered

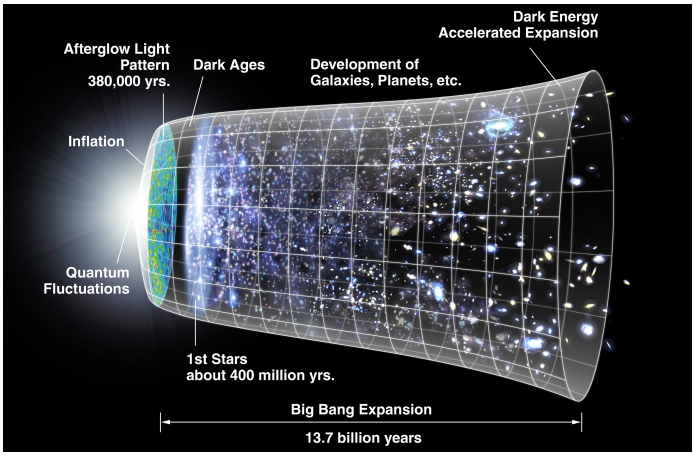

Figure 1.2.: Artist's impression of the evolution of our Universe from the early accelerated expansion during inflation to the late time non-linear structures. Credit: NASA / WMAP Science Team

photons efficiently. At a time known as **recombination** the electrons and nuclei formed neutral atoms, leading to an un-scattered propagation of the photons, which is what we detect today. The cosmic microwave background explorer (COBE) experiment, starting in 1989, measured the anisotropies of the CMB and found fluctuations in the temperature of $\Delta T/T \approx 10^{-5}$. This fluctuation pattern was consistent with the inflationary paradigm, introduced by Alan Guth in 1981 to describe the large scale homogeneity and the flatness observed today. Inflation was later refined by More accurate measurements of the temperature fluctuations were provided by the WMAP satellite mission and even tighter constraints will be possible from the Planck satellite. The temperature fluctuations measured by the WMAP satellite are depicted in Fig. 1.1.
At this point it was believed that the matter content in the flat Universe would slow down the expansion. Thus it came as a surprise, when the Supernova Cosmology Project lead by Saul Perlmutter and the High-z Supernova Search Team lead by Brian Schmidt and Adam Riess found evidence for an accelerated expansion in 1998 [12, 13].
All these observational efforts and theoretical models went hand in hand and finally led to a paradigm, which now is known as the **standard model of cosmology** and the Lambda Cold Dark Matter (ΛCDM) cosmology. Its main statements are:

- The spacetime of our Universe is globally flat.
- Approximately 25% of the total energy content of the Universe is in the form of matter, but only one sixth of the matter is of baryonic nature.
- The rest of the energy content is unknown and attributed to **dark energy**.

However, as a consequence of this model we are in the miserable situation that we are not able to observe 95% of the energy content of the Universe, since it is made up of dark ingredients. Dark energy, first introduced as a possible **cosmological constant** in the field equations by Einstein, became again popular in the last decade to account for the accelerated expansion of the Universe. It is a key question of cosmology to determine the nature of this exotic field, which comes along with negative pressure. Having said that, we furthermore have to deal with dark matter, an invisible, i.e. not electromagnetically interacting kind of matter. So far there has not been evidence for direct detection of dark matter and there have been strong theoretical efforts to invent modified versions of gravity in order to remedy the dark components.
Today we are not claiming to have a complete understanding of the processes, which govern our Universe – we are working on transient ideas and try to improve them. Cosmology has to deal with physical processes on scales of the observable Universe down to scales relevant for particle

Event	T	z	t
Now	2.73 K	0	14 Gyr
Formation of first structures	140 K	50	14 Gyr
Recombination	3000 K	1100	500000 yr
Matter-radiation equality	9500 K	3500	20000 yr
Nucleosynthesis	4×10^8 K	1×10^8	1×10^3 s
Baryogenesis	1×10^{12} K	1×10^{12}	1×10^{-5} s
Inflation ends	1×10^{27} K	1×10^{27}	1×10^{-32} s
Quantum gravity	1×10^{32} K	1×10^{32}	1×10^{-43} s

Table 1.1.: Timeline of events in the history of the Universe [3, 14]. This table is thought as an overview and quoted values should not be taken at face value.

physics, and time intervals which span the whole age of the Universe. Due to the complexity we have to adopt a lot of simplifying assumptions to make the system mathematically tractable. If we just consider the gravitational forces that form the LSS of the Universe, we soon come to a point where perturbative calculations break down and a non-linear numerical treatment has to be used. The problems become even more involved as soon as we consider the baryon physics, which leads to the formation of stars and galaxies. This complexity has lead to an intensive use of numerical simulations over all scales.

1.2. Cosmic Timeline

Table 1.1 shows a short curriculum vitae of our Universe, which is also depicted in Fig. 1.2. The Universe started with a singularity known as the **big bang**. We don't have a very detailed understanding of what happened in the first 10^{-43} s of the Universe. Most probably a theory of quantum gravity, which describes the unification of the four fundamental forces, will be needed to describe this time. However, this hot, small Universe started to expand and by doing so it cooled. At some point, the temperature decreased so much, that the quark gluon plasma underwent a phase transition to form the colour neutral baryons and mesons, a process known as **quantum chromodynamics phase transition**. A general appearance in cosmic history is that processes drop out of equilibrium, since their cross-sections decrease with decreasing cosmic temperature. This caused for instance a decoupling of the neutrinos and a freeze out of the neutron to proton ratio. Later on, these constituents started to form the lightest elements by nuclear fusion. This happened during the epoch of **nucleosynthesis**, for which predicted element abundances compare remarkably well with observations. Apart from being globally neutral, at this time locally there were still free electrons and nucleons. This era ended with **recombination** at redshift $z \approx 1100$, when the free electrons and the nucleons started to combine to form neutral atoms. At this point the photons stopped to interact effectively with the electrons and the opaque Universe became transparent for the radiation. This event is imprinted in the Universe by the **last scattering surface** or **cosmic microwave background**. The photons which were released during recombination could travel relatively undisturbed to the present time, while they were cooling to give the astonishingly homogeneous blackbody radiation field of temperature $T_{\mathrm{CMB}} = 2.75$ K. This homogeneity is an important constituent of the cosmological standard model, but there are small temperature inhomogeneities in the temperature field that are an imprint of the slightly inhomogeneous matter distribution at recombination.

These inhomogeneities grew by the gravitational evolution and once they were large enough, first dark matter haloes were formed by the process of gravitational collapse. Subsequently these haloes merged and formed larger and larger haloes. The baryonic gas initially followed the dark matter and accreted in the dark matter potential wells. There it could reach sufficiently

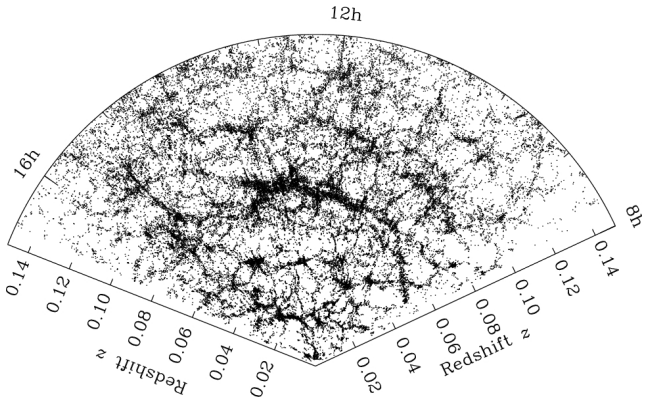

Figure 1.3.: Galaxy clustering pattern observed by the SDSS, with earth being at the center. Credit: M. Blanton and the Sloan Digital Sky Survey.

high densities to cool efficiently and to condense. The first galaxies were then created by star formation from the cold gas [4].

1.3. Our Picture of the late time Inhomogeneous Universe

The CMB provides us with a baby picture of the Universe, when it was approximately 300 000 years old and contains a wealth of cosmological information.
The local late time Universe is far from linear, featuring rich structures such as galaxies and clusters of galaxies. How do these structures relate to the linear fluctuations in the CMB? To answer this question we would like to know how the matter is distributed at late times. As we have argued in the last section, only one sixth of the matter in the Universe is luminous. One promising way to infer the late time matter clustering is to map the distribution of galaxies as a function of their properties like luminosity and color and to understand the relation between the galaxy and matter distribution based on theoretical arguments. Another approach is to measure the shape distortions of background galaxies by the mass distribution along the line of sight, a method known as weak gravitational lensing. These distortions can be analyzed by themselves or in correlation with the distribution of foreground galaxies and provide a measure of the integrated mass distribution along the line of sight. If we are interested in the four dimensional[1] distribution of matter we have to rely on galaxy surveys. While angular positions can be determined accurately, the radial distance has to be estimated from the redshift of the spectral lines and can be distorted by peculiar motions with respect to the Hubble flow. Spectroscopic Galaxy Surveys measure the spectra of galaxies to determine the redshift of spectral lines while Photometric Galaxy Surveys map the sky in a number of spectroscopic bands and use the relative intensity of the various bands to estimate the redshift of the galaxy. Both methods provide an accurate angular position but in terms of the radial distance the spectroscopic surveys have a much smaller error.
There have been several large volume galaxy redshift surveys in the past forty years, such as the CfA survey [15], the 2dF Survey [16] and the Sloan Digital Sky Survey (SDSS). Let us mention some details on the latter since it is one of the most complete and successful surveys to date. With their 9th data release the SDSS and its sucessor BOSS [17] have mapped 14 555 square degrees, measured 500 Mio. objects photometrically and 1 Mio. objects spectroscopically. The observed galaxy distribution from the SDSS is shown in Fig. 1.3 and features a sponge like pattern with nodes, filaments, walls and holes. Further observational missions that are planned

[1] As we are looking out into space we are also looking back in time.

are Euclid[2], DES[3], LSST[4] and BigBOSS[5]. Additional promising probes of LSS are the Lyman-α forest [18] or 21 cm observations [19].

1.4. Open Questions & Motivation

In the past two decades our picture of the Universe has been dramatically refined by observational campaigns that lead to the measurement of the temperature fluctuations in the CMB and the discovery of the accelerated expansion using supernovae. These new insights lead to new ideas about the origin and evolution of the Universe and raised a plethora of new questions. For instance, what are the processes that seeded the rich structures that we observe today and what is causing the Universe to accelerate?

Large scale structure, the distribution of matter and galaxies in the Universe, has been shown to have the potential to answer some of these questions. For instance, LSS is able to put an upper bound on the total neutrino mass. Furthermore, LSS can rule out modifications of gravity and constrain the properties of dark energy models, e.g., their equation of state. Finally, deviations from the simplest models of inflation can be probed on the largest scales observable in LSS [20]. Extracting these signals from galaxy surveys is a non-trivial task: galaxies are an imperfect tracer of the non-linear matter distribution and for most of the above mentioned processes, only the imprint on the linear matter distribution is understood to date. Thus, it is important to understand how the matter distribution evolves from the linear initial conditions, where galaxies form, and how fundamental physics and the initial conditions imprint themselves on the final galaxy clustering pattern. This understanding is essential for the analysis of the data collected by ongoing and proposed dark energy missions.

Galaxy formation is a complicated process involving baryonic physics, cooling, star formation etc. It has been shown [21] that these processes can only happen in the potential wells of collapsed dark matter haloes. Thus, the first step in understanding the distribution of luminous galaxies is to understand the clustering properties of their host haloes. This will be the focus of this thesis.

[2] sci.esa.int/euclid
[3] Dark Energy Survey, www.darkenergysurvey.org
[4] Large Synoptic Survey Telescope, www.lsst.org
[5] bigboss.lbl.gov

Bibliography

[1] T. Baldauf, **The Galaxy-Dark Matter Connection**, Master's thesis, University of Zurich, 2009.

[2] S. Dodelson, *Modern Cosmology: Anisotropies and Inhomogeneities in the Universe*. Academic Press, 2 ed., Mar., 2003.

[3] A. R. Liddle and D. H. Lyth, *Cosmological Inflation and Large-Scale Structure*. Cambridge Univ Pr, Apr., 2000.

[4] M. S. Longair, *Galaxy Formation*. 2008.

[5] J. A. Peacock, *Cosmological Physics*. Cambridge University Press, 1999.

[6] A. Einstein, **Die Grundlage der allgemeinen Relativitätstheorie**, *Annalen der Physik* **354** (1916) 769–822.

[7] E. Hubble, **A Relation between Distance and Radial Velocity among Extra-Galactic Nebulae**, *Proceedings of the National Academy of Science* **15** (Mar., 1929) 168–173.

[8] A. Friedmann, **Über die Krümmung des Raumes**, *Zeitschrift für Physik* **10** (1922) 377–386.

[9] S. van den Bergh, **The Curious Case of Lemaître's Equation No. 24**, *JRASC* **105** (Aug., 2011) 151, [arXiv:1106.1195].

[10] G. Lemaître, **Un Univers homogène de masse constante et de rayon croissant rendant compte de la vitesse radiale des nébuleuses extra-galactiques**, *Annales de la Societe Scietifique de Bruxelles* **47** (1927) 49–59.

[11] F. Zwicky, **Die Rotverschiebung von extragalaktischen Nebeln**, *Helvetica Physica Acta* **6** (1933) 110–127.

[12] S. Perlmutter, G. Aldering, G. Goldhaber, R. A. Knop, P. Nugent, P. G. Castro, S. Deustua, S. Fabbro, A. Goobar, D. E. Groom, I. M. Hook, A. G. Kim, M. Y. Kim, J. C. Lee, N. J. Nunes, R. Pain, C. R. Pennypacker, R. Quimby, C. Lidman, R. S. Ellis, M. Irwin, R. G. McMahon, P. Ruiz-Lapuente, N. Walton, B. Schaefer, B. J. Boyle, A. V. Filippenko, T. Matheson, A. S. Fruchter, N. Panagia, H. J. M. Newberg, W. J. Couch, and Supernova Cosmology Project, **Measurements of Omega and Lambda from 42 High-Redshift Supernovae**, *Astrophys. J.* **517** (June, 1999) 565–586, [astro-ph/9812133].

[13] A. G. Riess, A. V. Filippenko, P. Challis, A. Clocchiatti, A. Diercks, P. M. Garnavich, R. L. Gilliland, C. J. Hogan, S. Jha, R. P. Kirshner, B. Leibundgut, M. M. Phillips, D. Reiss, B. P. Schmidt, R. A. Schommer, R. C. Smith, J. Spyromilio, C. Stubbs, N. B. Suntzeff, and J. Tonry, **Observational Evidence from Supernovae for an Accelerating Universe and a Cosmological Constant**, *Astron. J.* **116** (Sept., 1998) 1009–1038, [astro-ph/9805201].

[14] J. Rich, *Fundamentals of Cosmology*. Springer, 2001.

[15] J. Huchra, M. Davis, D. Latham, and J. Tonry, **A survey of galaxy redshifts. IV - The data**, *Astrophys. J. Sup.* **52** (June, 1983) 89–119.

[16] W. J. Percival, C. M. Baugh, J. Bland-Hawthorn, T. Bridges, R. Cannon, S. Cole, M. Colless, C. Collins, W. Couch, G. Dalton, R. De Propris, S. P. Driver, G. Efstathiou, R. S. Ellis, C. S. Frenk, K. Glazebrook, C. Jackson, O. Lahav, I. Lewis, S. Lumsden, S. Maddox, S. Moody, P. Norberg, J. A. Peacock, B. A. Peterson, W. Sutherland, and K. Taylor, **The 2dF Galaxy Redshift Survey: the power spectrum and the matter content of the Universe**, *Mon. Not. Roy. Astron. Soc.* **327** (Nov., 2001) 1297–1306, [astro-ph/].

[17] C. P. Ahn, R. Alexandroff, C. Allende Prieto, S. F. Anderson, T. Anderton, B. H. Andrews, É. Aubourg, S. Bailey, E. Balbinot, R. Barnes, and et al., **The Ninth Data Release of the Sloan Digital Sky Survey: First Spectroscopic Data from the SDSS-III Baryon Oscillation Spectroscopic Survey**, *Astrophys. J. Sup.* **203** (Dec., 2012) 21, [arXiv:1207.7137].

[18] D. H. Weinberg, R. Davé, N. Katz, and J. A. Kollmeier, **The Lyman-α Forest as a Cosmological Tool**, in *The Emergence of Cosmic Structure* (S. H. Holt and C. S. Reynolds, eds.), vol. 666 of *American Institute of Physics Conference Series*, pp. 157–169, May, 2003. astro-ph/.

[19] M. Zaldarriaga, S. R. Furlanetto, and L. Hernquist, **21 Centimeter Fluctuations from Cosmic Gas at High Redshifts**, *Astrophys. J.* **608** (June, 2004) 622–635, [astro-ph/].

[20] N. Dalal, O. Doré, D. Huterer, and A. Shirokov, **Imprints of primordial non-Gaussianities on large-scale structure: Scale-dependent bias and abundance of virialized objects**, *Phys. Rev.* **77** (June, 2008) 123514, [arXiv:0710.4560].

[21] S. D. M. White and M. J. Rees, **Core condensation in heavy halos - A two-stage theory for galaxy formation and clustering**, *Mon. Not. Roy. Astron. Soc.* **183** (May, 1978) 341–358.

CHAPTER 2

The Expanding Universe[†]

It will be crucial for the understanding of the concepts used in this work to be familiar with the basic ideas of general relativity and the expanding Universe. Hence we will start with a brief introduction of general relativity. We refer the reader to standard textbooks on general relativity [2] for a more detailed treatment. We then consider the solutions of the Einstein equations, that are believed to describe our Universe. Afterwards we will devote a short section to distances and luminosity measures, we will need later on. Finally we will comment on the nature of dark matter and describe in brevity the most viable dark matter candidates.

2.1. Fundamentals of General Relativity

The basic and simple principle which underlies general relativity (GR) is the **equivalence principle**:

In small enough regions of spacetime the laws of physics reduce to those of special relativity, it is impossible to detect the existence of a gravitational field by using local experiments. In a freely falling local frame all physical processes look as if there was no gravitation.

In special relativity one is used to inertial or Minkowski frames, which are unaccelerated with respect to each other but there is no distinguished frame which could be considered as a fixed static reference. Similarly in GR we have that gravity is inescapable as there is no gravitational neutral object. So all test bodies evolve under the influence of gravity and we have no fixed object w.r.t. which we could define an acceleration due to gravity. Consequently we give up the idea of gravity acting as a force but rather consider it as curvature of spacetime and define

unaccelerated $\equiv$ freely falling.

But the property of being unaccelerated will only hold for very small (in fact infinitesimally small) regions of spacetime. Therefore we won't be able to define a large inertial frame, which would enable us to define such things as relative velocities of far away objects. We have to restrain ourselves to **local inertial frames**.

[†]The material is partially based on [1] and on standard textbooks on general relativity and cosmology [2, 3].

We come to the conclusion that we can interpret the spacetime as being a curved manifold due to the following reasons:

- In small regions of a curved manifold we can establish Riemann normal coordinates for which the metric is Minkowski and the first derivatives of the metric vanish. In this coordinates the laws of physics look like those in flat Minkowski space.
- The result of parallel transporting a vector on a curved manifold depends on the way taken. This is a representation of the inability to compare vectors at widely separated regions in general relativity.

Now that we know which mathematical background can describe the spacetime, we have to consider the objects which live on this manifold, vectors and tensors. Tensor calculus essentially states that physical laws which are valid in flat space, will be true in any coordinate system if they are written in tensorial form and partial derivatives are replaced by **covariant derivatives**. The covariant derivative is constructed to reduce to the usual partial derivative when applied to scalars and to obey Leibniz rule. Application on a vector reads as

$$\nabla_\mu V^\nu = \partial_\mu V^\nu + \Gamma^\nu_{\mu\lambda} V^\lambda. \tag{2.1}$$

Here we introduced the so called **connection** or Christoffel symbols, which can be derived from the metric $g_{\mu\nu}$ if the covariant derivative is metric compatible and the connection is torsion free.[1]

$$\Gamma^\sigma_{\mu\nu} = \frac{1}{2} g^{\sigma\rho} \left(\partial_\mu g_{\rho\nu} + \partial_\nu g_{\mu\rho} - \partial_\rho g_{\mu\nu} \right) \tag{2.2}$$

In flat space force free particles move on straight lines $\ddot{x} = 0$, which can be generalised to obtain the **geodesic equation**

$$\frac{\mathrm{d}^2 x^\nu}{\mathrm{d}\lambda^2} + \Gamma^\nu_{\sigma\rho} \frac{\mathrm{d}x^\sigma}{\mathrm{d}\lambda} \frac{\mathrm{d}x^\rho}{\mathrm{d}\lambda} = 0, \tag{2.3}$$

where λ is an arbitrary parametrisation of the path. So far we considered how a curved spacetime influences the motion of test particles and how the connection can be derived from the metric. As a next step we have to consider how the energy content of the spacetime, described by the **energy-momentum tensor** $T_{\mu\nu}$, influences the curvature. To do so it will turn out convenient to introduce Riemann tensor

$$R^\mu{}_{\nu\sigma\rho} = \partial_\sigma \Gamma^\mu_{\rho\nu} - \partial_\rho \Gamma^\mu_{\sigma\nu} + \Gamma^\mu_{\sigma\lambda} \Gamma^\lambda_{\rho\nu} - \Gamma^\mu_{\rho\lambda} \Gamma^\lambda_{\sigma\nu}, \tag{2.4}$$

as well as the Ricci tensor, Ricci scalar and Einstein tensor

$$R_{\mu\nu} = R^\gamma{}_{\mu\gamma\nu}, \qquad R = R^\mu{}_\mu, \qquad G_{\mu\nu} = R_{\mu\nu} - \frac{1}{2} R g_{\mu\nu}. \tag{2.5}$$

The field equations which determine the dynamics of the spacetime are known as **Einstein equations** and can be derived from a weak field equivalence to Newton and Poisson equations or equivalently from an action principle.

$$G_{\mu\nu} = 8\pi G T_{\mu\nu} + \Lambda g_{\mu\nu} \tag{2.6}$$

The last term on the right hand side is the so called **cosmological constant**. It was introduced by Einstein in order to find a static solution of the Universe. Lateron he called this the "Biggest blunder" of his life but, as we will see below, today there is striking evidence for a nonzero value of this constant.

[1] Here we used Einstein summation convention were equal upper and lower indices are summed over

2.2. Fundamentals of Cosmology

Assuming the validity of general relativity we have to make a further assumption in order to obtain a solution of the Einstein field equations that describes the Universe. This assumption is called the **Copernican principle** and states that our Universe is homogeneous and isotropic. Here isotropy says that the space looks the same irrespective in which direction one looks and homogeneity states that it looks the same irrespective from where one looks. The assumption implies that we are in no way special, we are sitting in an average galaxy and hence we are observing an average representation of the Universe. These statements are for sure only true if we average over local inhomogeneities, such as galaxies and clusters of galaxies, and the smoothing scale is taken to be around 100 h^{-1}Mpc.
Einstein first tried to find a static solution to his field equations but as observations implied there is a recession of far away galaxies. So we have to drop the assumption of a static spacetime and replace it by a spacetime Υ which is homogeneous and isotropic in space but not in time. Hence we decompose it into a set of maximal symmetric spacelike slices Σ and the time component $\Upsilon = \mathbb{R} \times \Sigma$. The line element of this spacetime can be expressed as

$$\mathrm{d}s^2 = -\mathrm{d}t^2 + a^2(t)\gamma_{ij}\mathrm{d}u^i\mathrm{d}u^j. \tag{2.7}$$

Here we introduced the **scale factor** a, which is by convention set to unity today $a_0 = 1$, and used **comoving coordinates**, which are free of cross terms with the time component. The maximal symmetric spatial metric γ_{ij} should obey spherical symmetry. This symmetry can be used to derive the general form of the **Friedmann-Robertson-Walker metric** (FRW metric) [4, 5, 6, 7, 8, 9]

$$\mathrm{d}s^2 = -\mathrm{d}t^2 + a^2(t)\left[\frac{\mathrm{d}r^2}{1-Kr^2} + r^2\mathrm{d}\Omega^2\right]. \tag{2.8}$$

Here K describes the spatial curvature of the Universe and the angular part of the metric is given by $\mathrm{d}\Omega = \mathrm{d}\theta^2 + \sin^2\theta\mathrm{d}\phi^2$. We have to distinguish three cases:

open Universe ($K < 0;\ \rho < \rho_{\mathrm{crit}};\ \Omega < 1$) There is constant negative curvature on Σ and we can set $r = S_K(\chi) = (-K)^{-1/2}\sinh\left[(-K)^{1/2}\chi\right]$.

$$\gamma_{ij}\mathrm{d}u^i\mathrm{d}u^j = \mathrm{d}\chi^2 + (-K)^{-1/2}\sinh^2\left[(-K)^{1/2}\chi\right]\mathrm{d}\Omega^2$$

flat Universe ($K = 0;\ \rho = \rho_{\mathrm{crit}};\ \Omega = 1$) There is no curvature on Σ yielding the Euclidean metric and $r = S_K(\chi) = \chi$.

$$\gamma_{ij}\mathrm{d}u^i\mathrm{d}u^j = \mathrm{d}\chi^2 + \chi^2\mathrm{d}\Omega^2 = \mathrm{d}x^2 + \mathrm{d}y^2 + \mathrm{d}z^2$$

closed Universe ($K > 0;\ \rho > \rho_{\mathrm{crit}};\ \Omega > 1$) There is positive curvature on Σ and we can set $r = S_K(\chi) = K^{-1/2}\sin\left[K^{1/2}\chi\right]$ to obtain the metric of a three sphere.

$$\gamma_{ij}\mathrm{d}u^i\mathrm{d}u^j = \mathrm{d}\chi^2 + K^{-1/2}\sin^2\left[K^{1/2}\chi\right]\mathrm{d}\Omega^2$$

The meaning of ρ_{crit} and Ω will be described below and is included in this overview for the sake of completeness. All these three cases can be conveniently expressed as

$$\mathrm{d}s^2 = -\mathrm{d}t^2 + a^2(t)\left[\mathrm{d}\chi^2 + S_K(\chi)^2(\chi)\mathrm{d}\Omega^2\right]. \tag{2.9}$$

So far we dealt only with the metric of the spacetime, but in fact we are interested in the effect of matter on the spacetime, especially on the time evolution of the scale factor. To examine this we will use perfect fluids to model the energy sources present in our Universe. We consider

the rest frame in which the matter is isotropic and therefore at rest in comoving coordinates and has velocity $U^\mu = (1, 0, 0, 0)$ to write the energy-momentum tensor as

$$T_{\mu\nu} = (p + \rho)U_\mu U_\nu + p g_{\mu\nu}, \tag{2.10}$$

$$T^\mu_{\ \nu} = \text{diag}(-\rho, p, p, p), \tag{2.11}$$

where ρ is the density and p the pressure. To proceed in this topic it is necessary to assume an **equation of state** in oder to close the set of equations. Most sources of energy obey the following simple equation of state

$$p = w\rho. \tag{2.12}$$

The time evolution of the energy density of the different species can be derived from the first component of the energy-momentum conservation

$$\nabla_\mu T^\mu_{\ 0} = -\partial_0 \rho - 3\frac{\dot{a}}{a}(\rho + p) \stackrel{!}{=} 0 \Rightarrow \frac{\dot{\rho}}{\rho} = -3(1 + w)\frac{\dot{a}}{a}. \tag{2.13}$$

Integrating this equation we obtain for the time dependence of a species described by the equation of state w

$$\rho \propto a^{3(1+w)} \tag{2.14}$$

Using the Einstein field equations we can now derive the **Friedmann equations** [4, 5]

$$\frac{\ddot{a}}{a} = -\frac{4\pi G}{3}(\rho + 3p) \tag{2.15}$$

$$\left(\frac{\dot{a}}{a}\right)^2 = \frac{8\pi G}{3}\rho - \frac{K}{a^2} \tag{2.16}$$

These equations describe the so called **Friedmann-Robertson-Walker Universe**. They can be rendered into a simpler functional form if we introduce the **Hubble parameter**

$$H = \frac{\dot{a}}{a}, \tag{2.17}$$

and the critical density

$$\rho_{\text{crit}} = \frac{3H^2}{8\pi G}. \tag{2.18}$$

All densities can then be rewritten in terms of this critical density using the **density parameter**

$$\Omega_i = \frac{\rho_i}{\rho_{\text{crit}}}. \tag{2.19}$$

The density parameters are usually evaluated at present time $a = 1$

$$\Omega_{i,0} = \frac{\rho_{i,0}}{\rho_{\text{crit},0}} \tag{2.20}$$

and the time dependence is then given by

$$\Omega_i(a) = \Omega_{i,0} a^{3(1+w_i)} \frac{H_0^2}{H^2}. \tag{2.21}$$

The total energy content can then be expressed as

$$\Omega_{\text{tot}} = \Omega_{\text{m}} + \Omega_{\text{r}} + \Omega_\Lambda. \tag{2.22}$$

Using above definition Equation (2.16) reads as

$$\Omega_{\text{tot}} - 1 = \frac{K}{H^2 a^2}. \tag{2.23}$$

So we see that the sign of the spatial curvature is completely determined by the total energy density.
We will now in brevity mention the different sources, which contribute to the energy density of the Universe

dust $w = 0$**:** Collisionless, non-relativistic matter. Universes whose energy density is mainly influenced by dust are called **matter dominated** and the time evolution of the matter is given by $\rho_\mathrm{m} \propto a^{-3}$.

radiation $w = 1/3$**:** The energy-momentum tensor $T_{\mu\nu}$ from electrodynamics is traceless and thus we have $\rho_\mathrm{r} = 3p_\mathrm{r}$. This model can be used for electromagnetic fields or massive particles with $v \approx 1$. A Universe whose energy density is mainly influenced by radiation is known as **radiation dominated**.
The number density of photons decreases in the same way as for massive particles, but the photon energies are suffering from an additional redshift by a^{-1} and we finally obtain $\rho_\mathrm{r} \propto a^{-4}$.

vacuum $w = -1$**:** Introducing vacuum energy is equivalent to a **cosmological constant** in Einstein equations and yields $\rho_\Lambda \propto a^0$

$$\rho = -p = \frac{\Lambda}{8\pi G}$$

curvature The curvature can be interpreted as another type of energy and yields

$$\rho_\mathrm{c} = -\frac{3K}{8\pi G a^2} \Rightarrow \Omega_\mathrm{c} = -\frac{K}{H^2 a^2}$$

In terms of the above defined quantities we can write the second Friedmann equation as

$$H(a)^2 = H_0^2 \left[\Omega_{\mathrm{m},0} a^{-3} + \Omega_{\mathrm{r},0} a^{-4} + \Omega_{\Lambda,0} + \Omega_{K,0} a^{-2}\right], \tag{2.24}$$

where H_0 is the present day value of the Hubble parameter. The uncertainty in H_0 is commonly expressed as $H_0 = h$ 100 km s^{-1} Mpc^{-1}. It is useful to consider the analytic solutions which exist for some simple cases with vanishing curvature in order to develop some intuition about the time scales involved. If we have a **radiation dominated** Universe we obtain

$$a \propto t^{1/2} \quad \Rightarrow \quad t = \sqrt{\frac{3}{32\pi G\rho}}, \tag{2.25}$$

whereas in the case of a **matter dominated** Universe, also known as the **Einstein-de-Sitter Universe**, we obtain

$$a \propto t^{2/3} \quad \Rightarrow \quad t = \sqrt{\frac{1}{6\pi G\rho}}. \tag{2.26}$$

A Universe that has an energy content dominated by vacuum-energy or a cosmological constant has

$$a \propto \exp\left[Ht\right] \quad \Rightarrow \quad H = \sqrt{\frac{8\pi G\rho}{3}} = \text{const.} \tag{2.27}$$

So we see that vacuum repulsion would cause the Universe to expand infinitely. The general case will not be analytically tractable but numerical solutions do a good job as well.

2.3. Useful Relations

This thesis will be mainly concerned with models for the late time Universe. Current constraints from the CMB indicate that our Universe is flat ($K = 0$) and that the matter content is dominated by collisionless cold dark matter. Furthermore, the accelerated expansion requires a non-zero value for the cosmological constant. Since the expansion rate and its derivatives are important ingredients for dynamical calculations in an expanding Universe, we give some of

the frequently used forms of the equations.
The Friedmann equations in ΛCDM Universe read

$$H^2 = \left(\frac{\dot{a}}{a}\right)^2 = \frac{8\pi G}{3}\rho + \frac{\Lambda}{3} = H_0^2\left(\Omega_{\mathrm{m},0}a^{-3} + \Omega_{\Lambda,0}\right), \tag{2.28}$$

$$\frac{\ddot{a}}{a} = -\frac{4\pi G}{3}(\rho + 3p) + \frac{\Lambda}{3} = H_0^2\left(\Omega_{\Lambda,0} - \frac{1}{2}\Omega_{\mathrm{m},0}a^{-3}\right). \tag{2.29}$$

Thus one has for the time derivative of the Hubble rate

$$\dot{H} = \frac{\ddot{a}}{a} - H^2 = -\frac{3}{2}H_0^2\Omega_{\mathrm{m},0}a^{-3}. \tag{2.30}$$

The **deceleration parameter** for a ΛCDM Universe is given by

$$q_0 = -\frac{\ddot{a}/a}{(\dot{a}/a)^2} = \frac{3}{2}\Omega_{\mathrm{m}} - 1 \tag{2.31}$$

and has to be negative to account for the accelerated expansion. All the above equations where presented in terms of **physical time** t. We will see that the analysis of perturbations around the homogeneous background Universe can be simplified by defining a **conformal time** $\mathrm{d}t = a\mathrm{d}\eta$. We will denote derivatives with respect to conformal time as primes and derivatives with respect to physical time as dots. The Friedmann equations can now be rewritten in terms of conformal time and the conformal Hubble rate $\mathcal{H} = aH = a'/a$

$$\mathcal{H}^2 = H_0^2\left(\Omega_{\mathrm{m},0}a^{-1} + \Omega_{\Lambda,0}a^2\right) \tag{2.32}$$

$$\mathcal{H}' = a^2\left(H^2 + \dot{H}\right) = \left(\Omega_\Lambda(a) - \frac{1}{2}\Omega_{\mathrm{m}}(a)\right)\mathcal{H}^2 = \left(1 - \frac{3}{2}\Omega_{\mathrm{m}}(a)\right)\mathcal{H}^2 \tag{2.33}$$

For the time dependence of the density parameters we have

$$\Omega_{\mathrm{m}}(a) = \frac{\Omega_{\mathrm{m},0}}{a^3}\frac{H_0^2}{H^2}, \qquad \Omega_\Lambda(a) = \Omega_{\Lambda,0}\frac{H_0^2}{H^2}. \tag{2.34}$$

2.4. The Nature of Redshift

The FRW Universe has no energy conservation but if $U^\mu = (1,0,0,0)$ is the velocity of comoving observers we can write down a conserved **Killing tensor**. Therefore we obtain for a particle with velocity V^μ

$$K_{\mu\nu} = a^2(g_{\mu\nu} + U_\mu U_\nu) \Rightarrow a^2\left[V_\mu V^\mu + (U_\mu V^\mu)^2\right] = \text{const.} = K. \tag{2.35}$$

For photons $V_\mu V^\mu = 0$ and hence

$$U_\mu V^\mu = \frac{K}{a}. \tag{2.36}$$

This is proportional to the frequency measured by an observer given by $\nu = -U_\mu V^\mu$. Hence the frequency between emission and absorption of a light ray changes by

$$\frac{\nu_{\mathrm{obs}}}{\nu_{\mathrm{em}}} = \frac{a_{\mathrm{em}}}{a_{\mathrm{obs}}}. \tag{2.37}$$

The **redshift** between two events is defined by the fractional change in wavelength

$$z = \frac{\lambda_{\mathrm{obs}} - \lambda_{\mathrm{em}}}{\lambda_{\mathrm{em}}} = \frac{a_{\mathrm{em}}}{a_{\mathrm{obs}}} - 1. \tag{2.38}$$

This redshift is different from Doppler effect as it is due to the expansion of space.

2.5. Age of the Universe

As sometimes it is more intuitive to think about times rather than redshifts we calculate the $t(z)$ relationship for a flat ΛCDM Universe with matter density $\Omega_m = 0.25$ and dark energy density $\Omega_\Lambda = 0.75$.

$$t(z) = \int_0^{t(z)} \mathrm{d}t' = \int_0^{a(z)} \frac{\mathrm{d}a'}{\dot{a}'}, \tag{2.39}$$

$$= \int_0^{a(z)} \frac{\mathrm{d}a'}{Ha'} = \frac{1}{H_0} \int_z^{\infty} \frac{\mathrm{d}z'}{(1+z)\sqrt{\Omega_m(1+z')^3 + \Omega_\Lambda}} \tag{2.40}$$

In Figure 2.1 we show $t_0 - t(z)$ where $t_0 = 14.15 \times 10^9$ a is the present age of the Universe. Another useful quantity is the relation between comoving distance and redshift which follows from the integration of a radial photon lightpath, the **geodesic distance**:

$$\chi(z) = \int_t^{t_0} \frac{\mathrm{d}t}{a} = \frac{1}{H_0} \int_z^1 \frac{\mathrm{d}z'}{\sqrt{\Omega_\mathrm{m}(1+z')^3 + \Omega_\Lambda}}. \tag{2.41}$$

For the Einstein-de-Sitter case we find the analytic expression

$$\chi(z) = \frac{2}{H_0 \Omega_\mathrm{m}} \left[1 - \frac{1}{\sqrt{1+z}}\right]. \tag{2.42}$$

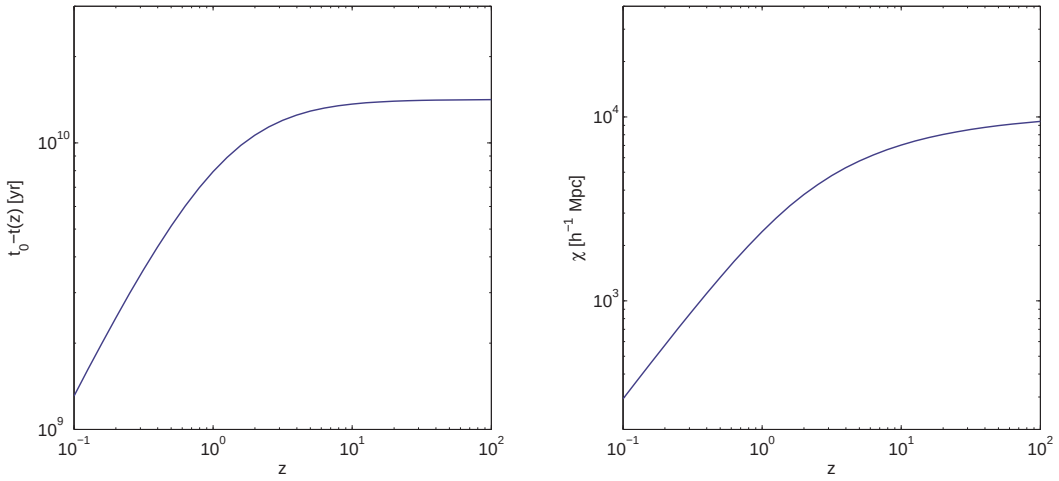

Figure 2.1.: *Left panel:* Time from redshift z to present for a ΛCDM Universe *Right panel:* Comoving radial distance to an object at redshift z.

2.6. Dark Matter

One of the main assumptions underlying this thesis is that there exists a non-luminous kind of matter, whose mass however strongly affects the gravitational evolution of the Universe. The study of galaxy dynamics revealed already in in the 1930s that there is a difference between the observed luminous matter content and the mass needed to explain the galaxy dynamics [10]. Further evidence comes from large scale flows and the flat rotation curves of galaxies. Most importantly the luminous matter present in the Universe can in no way account fro the total matter content of our flat spacetime. While there have been attempts to circumvent this missing mass problem by introducing modifications of general relativity, the most popular

explanation is that there is a non-visible or weakly interacting kind of matter.
Basicly one distinguishes baryonic and non-baryonic dark matter candidates. Often the dark matter is further classified in the categories **Hot Dark Matter** (HDM) for candidates that were relativistic at decoupling and **Cold Dark Matter** (CDM) for non-relativistic species. Hot Dark Matter suffers from free-streaming and is strongly disfavoured by structure formation, since it would damp the density contrast too much.
We will now in brevity discuss the most viable dark matter candidates:

axions The smallest mass non-baryonic cold dark matter candidate $m_A \approx 1 \times 10^{-5}$ GeV is a postulate from quantum chromodynamics. Axions would arise from a non-thermal process in the early Universe, producing a Bose condensate. They possess small electromagnetic interactions and could thus drive microwave cavities, which is the most promising approach to detect them.

WIMPs Weakly Interacting Massive Particles (WIMPs) are a standard cold dark matter candidate with $m_{WIMP} > 10$ GeV. Their existence is predicted from a supersymmetric extension of the standard model of particle physics. In this theory the role of the WIMP can be played by the neutralino, the lightest supersymmetric particle. The experimental search for WIMPs mainly focuses on the detection of energy depositions through the rare collisions of a WIMP with a nucleus. These experiments assume that a WIMP aether permeates the whole Milky Way. The DAMA experiment has reported a fluctuation of the WIMP flux during the earth's orbit around the sun [11]. This result was so far not confirmed by other experiments and is thus heavily discussed.

neutrinos The neutrino is the only yet detected candidate for non-baryonic dark matter. Neutrino oscillation experiments have shown evidence for non-zero neutrino masses and an upper bound of $\sum m_\nu < 0.17$ eV [12] is set from cosmology. Due to the upper bounds on the neutrino mass they fall into the regime of hot dark matter, which leads to some tension with structure formation. Consequently neutrinos can not account for all the required dark matter.

MACHOs Massive Astrophysical Halo Objects (MACHOs) are a baryonic dark matter candidate. They consist of ordinary matter in a non-luminous form, e. g. failed stars, stellar remnants or black holes. The search for MACHOs involves microlensing, the temporary increase of the apparent brightness of stars due to the gravitational light deflection by MACHOs passing close to the line of sight. There has been positive detection of a few objects, yielding $m_{MACHO} \approx 0.5\ M_\odot$. While the opinions about the interpretation of these detections are still divided, it is clear that the MACHOs can in no way account for all the dark matter in the Milky Way.

Bibliography

[1] T. Baldauf, **The Galaxy-Dark Matter Connection**, Master's thesis, University of Zurich, 2009.

[2] S. M. Carroll, *Spacetime and geometry. An introduction to general relativity*. Addison Wesley, San Francisco, CA, USA;, 2004.

[3] J. A. Peacock, *Cosmological Physics*. Cambridge University Press, 1999.

[4] A. Friedmann, **Über die Krümmung des Raumes**, *Zeitschrift fur Physik* **10** (1922) 377–386.

[5] A. Friedmann, **Über die Möglichkeit einer Welt mit konstanter negativer Krümmung des Raumes**, *Zeitschrift fur Physik* **1** (Dec., 1924) 326–332.

[6] H. P. Robertson, **Kinematics and World-Structure**, *Astrophys. J.* **82** (Nov., 1935) 284.

[7] H. P. Robertson, **Kinematics and World-Structure II.**, *Astrophys. J.* **83** (Apr., 1936) 187.

[8] H. P. Robertson, **Kinematics and World-Structure III.**, *Astrophys. J.* **83** (May, 1936) 257.

[9] A. G. Walker, **On Milne's theory of world structure**, *Proc. London Math. Soc.* **1** (1937) 90–127.

[10] G. Raffelt and P. Murdin, **Dark Matter: Its Nature**, .

[11] R. Bernabei, P. Belli, F. Cappella, R. Cerulli, F. Montechia, F. Nozzoli, A. Incicchitti, D. Prosperi, C. J. Dai, H. H. Kuang, J. M. Ma, and Z. P. Ye, **Dark Matter search**, *Nuovo Cimento Rivista Serie* **26** (Jan., 2003) 010000–74, [astro-ph/].

[12] U. Seljak, A. Slosar, and P. McDonald, **Cosmological parameters from combining the Lyman-alpha forest with CMB, galaxy clustering and SN constraints**, *JCAP* **0610** (2006) 014.

CHAPTER 3

Large Scale Structure of the Universe[†]

The last chapter has been concerned with the description of a homogeneous expanding Universe. We will now consider small perturbations about this background solution and study their dynamics. We will restrict ourselves to relatively small scales and velocities, where the Newtonian treatment is valid.
First we will introduce the statistics used to describe the fluctuations in the Universe. Then we will consider the dynamics of the fields and derive the fluid equations governing the evolution of the collisionless cold dark matter. We then review two of the most important techniques for a perturbative solution of the fluid equations, Standard Perturbation Theory (SPT) and Lagrangian Perturbation Theory (LPT). Finally, we describe how the dynamics are solved numerically using N-body simulations.

3.1. Statistics

The Universe we live in was seeded by quantum fluctuations, which became classical during inflation and grew by the subsequent evolution to form the highly nonlinear structures we observe today. As a consequence of this quantum mechanical origin, the structures are stochastic with random initial conditions. Due to this fact we can not hope to develop a theory that exactly reproduces the Universe we observe today. Rather, we should consider our Universe as one representation of an ensemble of possible Universes. Therefore, we need to introduce statistical quantities, which can be used to compare theoretical predictions with the observed data.

3.1.1. Overdensities

Starting from a smooth matter density field $\rho(\boldsymbol{r})$ we can define a dimensionless **overdensity** or **density contrast**

$$\delta(\boldsymbol{r}) = \frac{\rho(\boldsymbol{r}) - \bar{\rho}}{\bar{\rho}}, \tag{3.1}$$

which satisfies $\langle \delta(\boldsymbol{r}) \rangle = 0$ and should be homogeneous and isotropic in a statistical sense. Here statistical homogeneity means that all multipoint moments remain invariant under coordinate translations, whereas statistical isotropy states that the latter will be true for coordinate rotations. The brackets stand for an averaging process, which can be understood either as

[†]The material presented in this chapter is based on the extensive review on perturbation theory [1] and partially reproduced from my master's thesis [2].

an ensemble average over many possible realisations of the Universe or as a spatial average considering all $\boldsymbol{x}$ of the Universe. That these two averages are equivalent is not trivial. But we can assume that points that are far away from each other in the Universe are not causally connected and therefore we can use averages over widely separated regions as an approximation for independent realisations [3].[1]

3.1.2. Fourier Space

It will prove convenient to build up the actual density field from a superposition of modes that describe the behaviour on a certain scale.
We introduce the following Fourier convention:

$$\delta(\boldsymbol{k}) = \int \mathrm{d}^3 r \exp\left[\mathrm{i}\,\boldsymbol{k}\cdot\boldsymbol{r}\right]\delta(\boldsymbol{r}), \tag{3.2}$$

$$\delta(\boldsymbol{r}) = \int \frac{\mathrm{d}^3 k}{(2\pi)^3} \exp\left[-\mathrm{i}\,\boldsymbol{k}\cdot\boldsymbol{r}\right]\delta(\boldsymbol{k}). \tag{3.3}$$

such that the k-space representation of the nabla operator is given by $\boldsymbol{\nabla} \to -\mathrm{i}\,\boldsymbol{k}$. The Dirac Delta function is thus given by

$$\delta^{(\mathrm{D})}(\boldsymbol{x}+\boldsymbol{x}') = \int \frac{\mathrm{d}^3 q}{(2\pi)^3} \exp\left[\mathrm{i}\,(\boldsymbol{x}+\boldsymbol{x}')\boldsymbol{q}\right]. \tag{3.4}$$

An important advantage of working in Fourier space is that convolutions in real space become simple multiplications in k-space

$$f(\boldsymbol{x}) = \int \mathrm{d}^3 y\, g(\boldsymbol{y}) h(\boldsymbol{x}-\boldsymbol{y}) \Rightarrow f(\boldsymbol{k}) = g(\boldsymbol{k})h(\boldsymbol{k}). \tag{3.5}$$

This is of particular advantage, when smoothing operations are considered.
In case of spherical symmetry we can perform the angular integration in the definition of the Fourier transform

$$f(r) = \frac{1}{2\pi^2}\int \mathrm{d}k\; k^2 \frac{\sin kr}{kr} f(k) = \frac{1}{2\pi^2}\int \mathrm{d}k\; k^2 j_0(kr) f(k) \tag{3.6}$$

where j_0 is the spherical Bessel function. For the inverse transform this yields

$$f(k) = 4\pi \int \mathrm{d}r\; r^2 j_0(kr) f(r). \tag{3.7}$$

For the spherical Bessel functions we have a closure equation

$$\int_0^\infty \mathrm{d}x x^2 j_\alpha(ux) j_\alpha(vx) = \frac{\pi}{2u^2}\delta^{(\mathrm{D})}(u-v) \tag{3.8}$$

One of the most important clustering statistics in configuration space is the **two-point correlation function**, defined as

$$\xi(\boldsymbol{r}) = \langle \delta(\boldsymbol{x})\delta(\boldsymbol{x}+\boldsymbol{r})\rangle\,. \tag{3.9}$$

Due to statistical isotropy the two point correlation only depends on the magnitude of the separation $\xi(\boldsymbol{r}) = \xi(|\boldsymbol{r}|)$. The most important Fourier space statistics used in LSS are the **power spectrum** and **bispectrum** defined by

$$\langle \delta(\boldsymbol{k})\delta(\boldsymbol{k}')\rangle = (2\pi)^3 \delta^{(\mathrm{D})}(\boldsymbol{k}+\boldsymbol{k}')P(\boldsymbol{k}) \tag{3.10}$$

[1] Fields which satisfy the property that volume average is equivalent to ensemble average are termed ergodic in statistical physics.

$$\langle\delta(\boldsymbol{k})\delta(\boldsymbol{k}')\delta(\boldsymbol{k}'')\rangle = (2\pi)^3\delta^{(\mathrm{D})}(\boldsymbol{k}+\boldsymbol{k}'+\boldsymbol{k}'')B(\boldsymbol{k},\boldsymbol{k}',\boldsymbol{k}'') \tag{3.11}$$

The power spectrum has units of volume and bispectrum has units of volume squared.
Let us see how the correlation function is related to the power spectrum.

$$\xi(r) = \int\frac{\mathrm{d}^3q}{(2\pi)^3}\int\frac{\mathrm{d}^3q'}{(2\pi)^3}\langle\delta(\boldsymbol{q})\delta(\boldsymbol{q}')\rangle\exp\left[-\mathrm{i}\,\boldsymbol{q}\cdot\boldsymbol{x}\right]\exp\left[-\mathrm{i}\,\boldsymbol{q}'\cdot(\boldsymbol{x}+\boldsymbol{r})\right] \tag{3.12}$$

$$= \int\frac{\mathrm{d}^3q}{(2\pi)^3}\int\frac{\mathrm{d}^3q'}{(2\pi)^3}(2\pi)^3P(q)\delta^{(\mathrm{D})}(\boldsymbol{q}+\boldsymbol{q}')\exp\left[-\mathrm{i}\,\boldsymbol{q}\cdot\boldsymbol{x}\right]\exp\left[-\mathrm{i}\,\boldsymbol{q}'\cdot(\boldsymbol{x}+\boldsymbol{r})\right] \tag{3.13}$$

$$= \int\frac{\mathrm{d}^3q}{(2\pi)^3}P(q)\exp\left[-\mathrm{i}\,\boldsymbol{q}'\cdot\boldsymbol{r}\right] = \frac{1}{2\pi^2}\int\mathrm{d}q q^2P(q)j_0(qr) \tag{3.14}$$

In the other direction we have

$$\langle\delta(\boldsymbol{k})\delta(\boldsymbol{k}')\rangle = \int\mathrm{d}^3x\int\mathrm{d}^3x'\exp\left[\mathrm{i}\,\boldsymbol{k}\cdot\boldsymbol{x}\right]\exp\left[\mathrm{i}\,\boldsymbol{k}'\cdot\boldsymbol{x}\right]\langle\delta(\boldsymbol{x})\delta(\boldsymbol{x}')\rangle \tag{3.15}$$

$$= \int\mathrm{d}^3x\exp\left[\mathrm{i}\,\boldsymbol{x}\cdot(\boldsymbol{k}+\boldsymbol{k}')\right]\int\mathrm{d}^3r\exp\left[\mathrm{i}\,\boldsymbol{k}'\cdot\boldsymbol{r}\right]\xi(r) \tag{3.16}$$

$$= (2\pi)^3\delta^{(\mathrm{D})}(\boldsymbol{k}+\boldsymbol{k}')\int\mathrm{d}^3r\exp\left[\mathrm{i}\,\boldsymbol{k}'\cdot\boldsymbol{r}\right]\xi(r) \tag{3.17}$$

since the last line has the same form as the definition of the power spectrum in Eq. (3.10), the power spectrum is in turn related to the correlation function by

$$P(k) = \int\mathrm{d}^3r\xi(r)\exp\left[\mathrm{i}\,\boldsymbol{k}\cdot\boldsymbol{r}\right] = 4\pi\int\mathrm{d}r r^2\xi(r)j_0(kr). \tag{3.18}$$

3.1.3. Combination of Samples

Let us consider the case where a certain tracer population is split into two subsamples A and B with mean densities $\bar{\rho}_\mathrm{A} = f_\mathrm{A}\bar{\rho}_\mathrm{tot}$ and $\bar{\rho}_\mathrm{B} = f_\mathrm{B}\bar{\rho}_\mathrm{tot}$ respectively. The total density is given by $\rho_\mathrm{tot} = \rho_\mathrm{A} + \rho_\mathrm{B}$. Thus we have $\bar{\rho}_\mathrm{tot} = \bar{\rho}_\mathrm{A} + \rho_\mathrm{b} = (f_\mathrm{A} + f_\mathrm{B})\bar{\rho}_\mathrm{tot}$ and consequently $f_\mathrm{A} + f_\mathrm{B} = 1$. The respective overdensities of the tracers are given by

$$\delta_\mathrm{A} = \frac{\rho_\mathrm{A}}{\bar{\rho}_\mathrm{A}} - 1 \qquad\qquad \delta_\mathrm{B} = \frac{\rho_\mathrm{B}}{\bar{\rho}_\mathrm{B}} - 1 \tag{3.19}$$

Thus we have for the total overdensity

$$\delta_\mathrm{tot} = \frac{\rho_\mathrm{tot}}{\bar{\rho}_\mathrm{tot}} - 1 = f_\mathrm{A}(1+\delta_\mathrm{A}) + f_\mathrm{B}(1+\delta_\mathrm{B}) - 1 = f_\mathrm{A}\delta_\mathrm{A} + f_\mathrm{B}\delta_\mathrm{B}. \tag{3.20}$$

Hence we have for the correlation function

$$\langle\delta_\mathrm{tot}\delta_\mathrm{tot}\rangle = f_\mathrm{A}^2\langle\delta_\mathrm{A}\delta_\mathrm{A}\rangle + 2f_\mathrm{A}f_\mathrm{B}\langle\delta_\mathrm{A}\delta_\mathrm{B}\rangle + f_\mathrm{B}^2\langle\delta_\mathrm{B}\delta_\mathrm{B}\rangle. \tag{3.21}$$

3.1.4. Filtering of the Density Field

As we are not only interested in the local properties of perturbations, but also in averages over a certain volume, we can convolve the density field with a filter $W(R)$ of scale R. This convolution in real space translates into a simple multiplication in Fourier space.
The variance of the smoothed density field is given by

$$\sigma_R^2 = \int\frac{\mathrm{d}^3k}{(2\pi)^3}P(k)\left|W_R(k)\right|^2 = \left\langle\delta_R^2(\boldsymbol{x})\right\rangle. \tag{3.22}$$

Often one considers the Fourier transform of the **top hat filter** $W_R(r) = \theta(r-R)$ with radius R

$$W_R(k) = 3\left[\frac{\sin(kR)}{(kR)^3} - \frac{\cos(kR)}{(kR)^2}\right]. \tag{3.23}$$

This function gives notable contributions only for $|k| \leq \frac{4.5}{R}$. Note that the scale of the filter is related to a typical mass by the relation

$$M = \frac{4\pi}{3} R^3 \bar{\rho}. \tag{3.24}$$

The quantity σ_8 is the root mean square (rms) density fluctuation in spheres of radius 8 h^{-1}Mpc and is often used to normalise the power spectrum.
While the top hat filter has a wide range of applications, it leads to divergent results for derivatives of the density field. Thus one sometimes considers the **Gaussian filter**

$$W_R(r) = \exp\left[-\frac{r^2}{2R^2}\right] \tag{3.25}$$

The mass contained by the Gaussian filter is

$$M = (2\pi)^{3/2} \bar{\rho} R^3 \tag{3.26}$$

and thus Gaussian and top hat filter of the same scale contain different amounts of mass.

3.1.5. Two-Point Probability Distribution

An alternative interpretation of the correlation function defined above can be found in terms of the multi-point probability distribution functions [4]. We will consider the background density field to be traced by a certain species with number density $\bar{n}$ and consider small volumes δV, which either host or don't host one tracer particle. The one point probability for finding a particle in the small volume δV_1 is $p_{1\text{pt}}(1) = \bar{n}\delta V_1$. If we had a purely random field the joint or two point probability of finding particles both in volumes δV_1 and δV_2 separated by $r_{12} = |\boldsymbol{x}_1 - \boldsymbol{x}_2|$ would be given by the product of the independent probabilities

$$p_{2\text{pt}}(1,2) = p_{1\text{pt}}(1) p_{1\text{pt}}(2) = \bar{n}^2 \delta V_1 \delta V_2. \tag{3.27}$$

For a correlated sample the probabilities will no longer be independent and the correlation function can now be defined as the excess over random probability of finding two particles in volumes δV_1 and δV_2 separated by r_{12}

$$p_{2\text{pt}}(1,2) = \bar{n}^2 \left[1 + \xi(r_{12})\right] \delta V_1 \delta V_2. \tag{3.28}$$

Since the probability of having a particle in δV_1 is given by $\bar{n}\delta V_1$, we can write the conditional probability to find a particle in δV_2 given there is one in δV_1

$$p_{1\text{pt}}(2|1) = \frac{p_{2\text{pt}}(1,2)}{p_{1\text{pt}}(1)} = \bar{n}\left[1 + \xi(r_{12})\right] \delta V_2, \tag{3.29}$$

where we used Bayes theorem for the conditional probability. So we see that for correlated samples ($\xi(r_{12}) > 0$) the probability of finding a second particle is enhanced over random, whereas it is suppressed over random for the anti-correlated case ($\xi(r_{12}) < 0$).
Similarly, we can define a quantity which describes how much two different tracers of the cosmological density field are correlated. The **cross-correlation function** between two populations A and B is defined by

$$p_{2\text{pt}}(r) = \bar{n}_\text{A} \bar{n}_\text{B} \left[1 + \xi_\text{AB}(r)\right] \delta V_1 \delta V_2, \tag{3.30}$$

which can be calculated from the density fields as

$$\xi_\text{AB}(\boldsymbol{r}) = \langle \delta_\text{A}(\boldsymbol{x}) \delta_\text{B}(\boldsymbol{x} + \boldsymbol{r}) \rangle \,. \tag{3.31}$$

3.1.6. Bias and Cross-Correlation Coefficient

The **bias** describes the excess clustering of population A with respect to population B and can be defined from cross-correlations and auto-correlations

$$b_{\text{auto}}(r) = \sqrt{\frac{\xi_{BB}(r)}{\xi_{AA}(r)}}, \qquad b_{\text{cross}}(r) = \frac{\xi_{AB}(r)}{\xi_{AA}(r)}. \tag{3.32}$$

The bias can be scale dependent in general and only on the largest scales, the bias asymptotes to a constant. This Thesis is concerned with descriptions of scale dependent bias and an introduction to the concepts is given in Ch. 5.
The **cross-correlation coefficient** between populations A and B is defined by[2]

$$r_{\text{AB}} = \frac{\xi_{\text{AB}}}{\sqrt{\xi_{\text{AA}}\xi_{\text{BB}}}} \tag{3.33}$$

and describes the stochasticity between two density fields [5]. It was shown in N-body simulations that this quantity is close to one over a wide range of scales. Similar quantities can be defined for other clustering statistics such as projected correlation functions and power spectrum. In absence of uncorrelated noise, the cross-correlation coefficient always satisfies $-1 \leq r \leq 1$.

3.1.7. Gaussian Random Fields

The seeds for structure formation are most probably of quantum mechanical origin. Hence we can treat the density field as a noise-like random field, where the phases of the Fourier modes are independent. From **central limit theorem** we know that the superposition of a large number of independent random fields will tend to a joint normal distribution. Besides δ itself, all quantities that can be expressed by linear sums over the modes will tend to be normally distributed. Since the first moment of δ vanishes, the Gaussian random field is entirely determined by its power spectrum, the variance for a certain Fourier mode.
By **Wick theorem** the reduced correlation functions of order higher than two either vanish or are expressible in terms of two-point functions [1]

$$\langle \delta(\boldsymbol{k}_1), \ldots, \delta(k_{2n+1}) \rangle = 0, \tag{3.34}$$

$$\langle \delta(\boldsymbol{k}_1), \ldots, \delta(k_{2n}) \rangle = \sum_{\text{pairs } P\{(i,j)\}} \prod \langle \delta(\boldsymbol{k}_i), \delta(\boldsymbol{k}_j) \rangle \,. \tag{3.35}$$

The Gaussiannity of the random field is also clear from the commutation relations for the quantum field.

3.2. Dynamics in Newtonian Regime

3.2.1. Equations of Motion

Let us now consider the equations governing the cosmological fluid in the Newtonian limit, i.e., for small distances $x \ll H^{-1}$ and small velocities $v \ll 1$. The equation of motion for a particle at physical position $\boldsymbol{r}$ is

$$\ddot{\boldsymbol{r}} = -\boldsymbol{\nabla}_{\boldsymbol{r}}\Phi \tag{3.36}$$

[2] We use the common symbol r to denote the cross correlation coefficient as there should be no confusion with the radius r.

Defining **comoving coordinates** as $\boldsymbol{r} = a\boldsymbol{x}$ we have $\boldsymbol{\nabla}_{\boldsymbol{x}} = a\boldsymbol{\nabla}_{\boldsymbol{r}}$. From now on we will use the gradient with respect to comoving coordinates.[3] Let us take the derivative of the physical coordinate with respect to physical time and rewrite in terms of the comoving position

$$\dot{\boldsymbol{r}} = \mathcal{H}\boldsymbol{x} + \boldsymbol{x}'. \tag{3.37}$$

Likewise we have for the second derivative

$$\ddot{\boldsymbol{r}} = \frac{1}{a}\left(\mathcal{H}'\boldsymbol{x} + \mathcal{H}\boldsymbol{x}' + \boldsymbol{x}''\right) = -\frac{1}{a}\boldsymbol{\nabla}\Phi. \tag{3.38}$$

the term proportional to the position is peculiar, since it leads to a spatial dependence of the particle acceleration. This term arises from the comoving coordinates and accounts for the expansion of spacetime. We can thus bring it to the right hand side of the above equation and define the **peculiar potential**

$$\Phi = -\frac{1}{2}\mathcal{H}'x^2 + \phi. \tag{3.39}$$

Thus we have for the equations of motion in terms of physical and conformal time

$$\ddot{\boldsymbol{x}} + 2H\dot{\boldsymbol{x}} = -\frac{\boldsymbol{\nabla}\phi}{a^2}, \qquad \boldsymbol{x}'' + \mathcal{H}\boldsymbol{x}' = -\boldsymbol{\nabla}\phi. \tag{3.40}$$

The peculiar potential is solely seeded by the energy density fluctuations in the Universe. Since we are assuming that dark energy is homogeneous, at late times these energy density fluctuations are dominated by the fluctuations in the matter density. Hence the Poisson equation for the peculiar potential can be expressed as

$$\nabla^2_{\boldsymbol{x}}\phi = \frac{3}{2}\mathcal{H}^2\Omega_{\mathrm{m}}(a)\delta = \frac{3}{2}\Omega_{\mathrm{m},0}H_0^2\frac{\delta}{a}. \tag{3.41}$$

Defining the **canonical momentum**

$$\boldsymbol{p} = am\boldsymbol{u}, \tag{3.42}$$

where $\boldsymbol{u} = \boldsymbol{x}'$ is the **comoving velocity** we have for the equation of motion

$$\boldsymbol{p}' = -am\boldsymbol{\nabla}_{\boldsymbol{x}}\phi. \tag{3.43}$$

Let us finally stress again that these equations are only true in the Newtonian regime. We defer a more rigorous treatment to Ch. 4.

3.2.2. The Fluid Equations

The particle distribution in phase space is conveniently described by the **distribution function** $f(\boldsymbol{x}, \boldsymbol{p}, \eta)$. The number of particles in a infinitesimal phase space volume $\mathrm{d}^3x\mathrm{d}^3p$ is thus given by $\mathrm{d}N = f(\boldsymbol{x}, \boldsymbol{p}, \eta)\mathrm{d}^3x\mathrm{d}^3p$. Note that the distribution function behaves as a scalar under parameter changes $\tilde{f}\left(\boldsymbol{x}, \boldsymbol{q}, \eta\right) = f\left(\boldsymbol{x}, \boldsymbol{p}(q), \eta\right)$.
Louiville theorem asserts the conservation of the phase space density. This conservation of phase space density then yields the collisionless Boltzmann equation, also known as Vlaslov equation

$$\frac{\mathrm{d}f}{\mathrm{d}\eta} = \frac{\partial f}{\partial \eta} + \frac{\mathrm{d}\boldsymbol{x}}{\mathrm{d}\eta}\cdot\frac{\partial f}{\partial \boldsymbol{x}} + \frac{\mathrm{d}\boldsymbol{p}}{\mathrm{d}\eta}\frac{\partial f}{\partial \boldsymbol{p}} \tag{3.44}$$

$$= \frac{\partial f}{\partial \eta} + \frac{\boldsymbol{p}}{ma}\cdot\frac{\partial f}{\partial \boldsymbol{x}} - am\boldsymbol{\nabla}\phi\cdot\frac{\partial f}{\partial \boldsymbol{p}} = 0 \tag{3.45}$$

[3] For an arbitrary function $f(t)$ we have $a\dot{f} = f'$ $a^2\ddot{f} = f'' - \mathcal{H}f'$ Unless otherwise quoted we will refer to dots as derivatives with respect to coordinate time and dashes as derivatives with respect to conformal time.

where we have used the equation of motion (3.43) in the last line.
We will be rarely interested in the full phase space distribution and thus there is no need to solve this non-linear seven dimensional differential equation. Instead we will be mostly concerned with fluid properties such as density, mean streaming velocity and velocity dispersion, which are readily obtained as moments of the distribution function

$$\rho(\boldsymbol{x},\eta) = m a^{-3} \int \mathrm{d}^3 p \; f(\boldsymbol{x},\boldsymbol{p},\eta), \tag{3.46}$$

$$v_i(\boldsymbol{x},\eta) = \int \mathrm{d}^3 p \; \frac{p_i}{am} f(\boldsymbol{x},\boldsymbol{p},\eta) / \int \mathrm{d}^3 p \; f(\boldsymbol{x},\boldsymbol{p},\eta), \tag{3.47}$$

$$\sigma_{ij}(\boldsymbol{x},\eta) = \int \mathrm{d}^3 p \; \frac{p_i}{am}\frac{p_j}{am} f(\boldsymbol{x},\boldsymbol{p},\eta) / \int \mathrm{d}^3 p \; f(\boldsymbol{x},\boldsymbol{p},\eta) - v_i(\boldsymbol{x}) v_j(\boldsymbol{x}). \tag{3.48}$$

The velocity dispersion is sometimes also referred to as anisotropic stress and describes the deviation from a single coherent flow as is obvious in Eq (3.48).
The equations of motion for these quantities can now be obtained by taking moments of the Vlaslov equation (3.45). The zeroth moment of the Vlaslov equation yields the continuity equation. Upon integrating over the momentum, we have to integrate the last term by parts and use that the .

$$\delta' + \boldsymbol{\nabla} \cdot \left[\boldsymbol{v}(1+\delta)\right] = 0 \tag{3.49}$$

Taking the the first moment and using the continuity equation yields the **Euler equation**

$$v_i' + \mathcal{H} v_i + \boldsymbol{v} \cdot \boldsymbol{\nabla} v_i = -\nabla_i \phi - \frac{1}{\rho} \nabla_i (\rho \sigma_{ij}) \tag{3.50}$$

or **conservation of momentum**. In principle we could have continued to hierarchy of equations, which couples the equation of motion for n-th moment of the Vlaslov equation to the $n+1$-th moment. To close the hierarchy we will postulate that all moments beyond the velocity are vanishing, an assumption that is denoted the **pressureless perfect fluid**. This assumption is reasonable in the linear regime but needs to be validated numerically at late times, when structures collapse, virialize and shell crossing occurs.
The fluid velocity can be decomposed into a scalar and a vector part $\boldsymbol{v} = \boldsymbol{v}_\parallel + \boldsymbol{v}_\perp$, where $\boldsymbol{\nabla} \times \boldsymbol{v}_\parallel = 0$ and $\boldsymbol{\nabla} \cdot \boldsymbol{v}_\perp = 0$. The velocity field can thus be described by its vorticity $\boldsymbol{w} = \boldsymbol{\nabla} \times \boldsymbol{v}$ and its divergence $\theta = \nabla \cdot \boldsymbol{v}$.

3.2.3. Linearized Equations

Let us neglect all the quadratic terms in the continuity and Euler equation and assume that the velocity dispersion vanishes

$$\delta' + \theta = 0 \tag{3.51}$$

$$\boldsymbol{v}' + \mathcal{H} \boldsymbol{v} = -\boldsymbol{\nabla} \phi. \tag{3.52}$$

The system can be solved straightforwardly after rewriting the Euler equation in terms of velocity vorticity and divergence

$$\theta' + \mathcal{H}\theta = -\Delta\phi \tag{3.53}$$

$$\boldsymbol{w}' + \mathcal{H} \boldsymbol{w} = 0. \tag{3.54}$$

The solution of the vorticity equation is simply $\boldsymbol{w} \propto a^{-1}$, i.e., any initially present vorticity decays at linear level. To solve the scalar equation, we take the time derivative of Eq. (3.51) and replace θ' with Eq. (3.53). In the resulting equation, we can replace θ using Eq. (3.53) and $\Delta\phi$ using the Poisson Eq. (3.41). We obtain

$$\delta''(\boldsymbol{k},\eta) + \mathcal{H}(\eta)\delta'(\boldsymbol{k},\eta) - \frac{3}{2}\Omega_\mathrm{m}(\eta)\mathcal{H}^2(\eta)\delta(\boldsymbol{k},\eta) = 0. \tag{3.55}$$

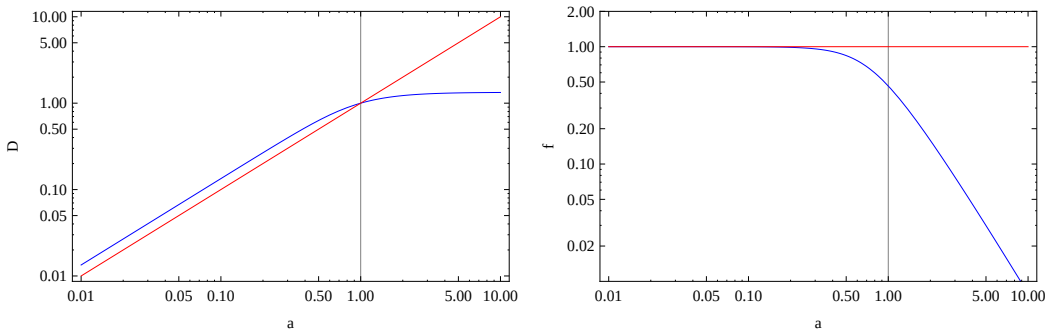

Figure 3.1.: Linear growth of structure for our fiducial ΛCDM (blue) and a matter only EdS Universe (red). *Left panel:* Linear growth factor D. *Right panel:* Logarithmic growth factor f.

As can be easily confirmed the above differential equation has a growing and a decaying mode solution $\delta(\boldsymbol{k},\eta) = D_+(\eta)\delta_{+,0}(\boldsymbol{k}) + D_-(\eta)\delta_{-,0}(\boldsymbol{k})$, where $D_-(\eta) = D_{-,0}H = \mathcal{H}/a$. The growing mode solution can then be obtained as

$$D_+(\eta) = D_{+,0}H(\eta)\int_0^{a(\eta)} \frac{\mathrm{d}a'}{\mathcal{H}^3(a')}, \tag{3.56}$$

where $D_{+,0}$ is a normalization factor used to achieve $D_+(a=1)=1$. Let us first discuss the solution in a Einstein-de-Sitter (EdS) matter only Universe. Since $a \propto t^{2/3}$ we have $H = a^{-3/2}$ and thus $D_+ = a$ and $D_- = a^{-3/2}$. This special case and the solution for our fiducial ΛCDM model are shown in the left panel of Fig. 3.1. We see that the growth in the ΛCDM Universe stalls at late times when the cosmological constant starts to dominate. In what follows we will concentrate on the growing mode solutions and use $D \equiv D_+$ unless otherwise stated.

3.2.4. Velocities

In the above subsection we have seen, that the vorticity decays at linear level in the absence of anisotropic stress. At non-linear level we have

$$\boldsymbol{w} + \mathcal{H}\boldsymbol{w} + \boldsymbol{\nabla}\times(\boldsymbol{v}\times\boldsymbol{w}) = 0. \tag{3.57}$$

This equation tells us, that even at non-linear level, if there is no initial vorticity, evolution won't generate it. Together with the knowledge that vorticity decays at early times when the fluctuations are still linear we can conclude that vorticity will be negligible throughout evolution in absence of anisotropic stress. However, there is evidence from simulations [6] that at late times velocity dispersion and thus vorticity is generated in high density regions. In the following, we will present Standard Perturbation Theory, ignoring the possible vorticity. This assumption will restrict the validity of the solutions to large scales.
In case of vanishing curl we have

$$\boldsymbol{v}(\boldsymbol{k}) = \mathrm{i}\,\frac{\boldsymbol{k}}{k^2}\theta(\boldsymbol{k}). \tag{3.58}$$

From the linearized continuity equation in Fourier space we have

$$\theta(\boldsymbol{k},\eta) = -\mathrm{i}\,\boldsymbol{k}\cdot\boldsymbol{v}(\boldsymbol{k},\eta) = -\delta'(\boldsymbol{k},\eta) = -\mathcal{H}f\delta(\boldsymbol{k},\eta), \tag{3.59}$$

where we defined the logarithmic growth factor

$$f = \frac{\mathrm{d}\ln D}{\mathrm{d}\ln a} \tag{3.60}$$

For the linear growing mode defined above in Eq. (3.56), we have

$$f(a) = \frac{\mathrm{d}\ln H}{\mathrm{d}\ln a} + \frac{a}{(aH)^3}\frac{1}{\int_0^a \mathrm{d}a' \left[a' H(a')\right]^3}, \tag{3.61}$$

which is unity for EdS. The right panel of Fig. 3.1 shows the logarithmic growth factor for a EdS and our fiducial ΛCDM cosmology. The late time dominance of the cosmological constant is even more apparent in this plot where f decays to $f(a=1) \approx 0.48$ at present time.
We can now employ this result to derive simple velocity statistics, such as the linear **velocity dispersion**

$$\kappa_{ij} = \langle v_i v_j \rangle - \langle v_i \rangle \langle v_j \rangle = \langle v_i v_j \rangle = \mathcal{H}^2 f^2 \int \frac{\mathrm{d}^3 q}{(2\pi)^3}\frac{q_i q_j}{q^4} P_{\mathrm{lin}}(q), \tag{3.62}$$

and its trace

$$\tilde{\sigma}_v^2 = \frac{1}{3}\mathrm{Tr}\left(\kappa_{ij}^2\right) = \frac{\mathcal{H}^2 f^2}{6\pi^2}\int \mathrm{d}q\; P_{\mathrm{lin}}(q). \tag{3.63}$$

In the following we will frequently consider the normalized velocity dispersion $\sigma_v = \tilde{\sigma}_v/\mathcal{H}f$, for which we obtain in our fiducial cosmology $\sigma_v \approx 6\ h^{-1}\mathrm{Mpc}$.

3.2.5. Fluid Equations in Fourier Space

After having obtained some intuition on the solutions in the linear regime, where the quadratic terms are negligible, we will now return to the full equations. To facilitate the analysis, we will work in Fourier space, where the Euler and continuity equations read as

$$\delta'(\boldsymbol{k}) + \theta(\boldsymbol{k}) = -\int \frac{\mathrm{d}^3 q}{(2\pi)^3}\frac{\mathrm{d}^3 q'}{(2\pi)^3}\delta^{(\mathrm{D})}(\boldsymbol{k}-\boldsymbol{q}-\boldsymbol{q}')\alpha(\boldsymbol{q},\boldsymbol{q}')\theta(\boldsymbol{q})\delta(\boldsymbol{q}'), \tag{3.64}$$

$$\theta'(\boldsymbol{k}) + \mathcal{H}\theta(\boldsymbol{k}) + \frac{3}{2}\Omega_{\mathrm{m}}(a)\mathcal{H}^2\delta(\boldsymbol{k}) = -\int \frac{\mathrm{d}^3 q}{(2\pi)^3}\frac{\mathrm{d}^3 q'}{(2\pi)^3}\delta^{(\mathrm{D})}(\boldsymbol{k}-\boldsymbol{q}-\boldsymbol{q}')\beta(\boldsymbol{q},\boldsymbol{q}')\theta(\boldsymbol{q})\theta(\boldsymbol{q}'). \tag{3.65}$$

The coupling kernels on the right hand side are defined as

$$\alpha(\boldsymbol{k}_1,\boldsymbol{k}_2) = \frac{\boldsymbol{k}_1\cdot(\boldsymbol{k}_1+\boldsymbol{k}_2)}{k_1^2} \tag{3.66}$$

$$\beta(\boldsymbol{k}_1,\boldsymbol{k}_2) = \frac{1}{2}(\boldsymbol{k}_1+\boldsymbol{k}_2)^2\frac{\boldsymbol{k}_1\cdot\boldsymbol{k}_2}{k_1^2 k_2^2} = \frac{1}{2}\frac{\boldsymbol{k}_1\cdot\boldsymbol{k}_2}{k_1 k_2}\left(\frac{k_2}{k_1}+\frac{k_1}{k_2}\right) + \frac{(\boldsymbol{k}_1\cdot\boldsymbol{k}_2)^2}{k_1^2 k_2^2} \tag{3.67}$$

Note that $\alpha(\boldsymbol{k}_1,\boldsymbol{k}_2)$ is not symmetric in its arguments but $\beta(\boldsymbol{k}_1,\boldsymbol{k}_2)$ is. The fluid Eqs. (3.64) and (3.65) are non-linear coupled differential equations for the density and velocity divergence. A closed form solution does in general not exist. One can however try to solve them perturbatively in the regime, where $\delta \ll 1$ and $\theta \ll 1$. We will discuss the perturbative solutions in much more detail in §6.4 below.

3.3. Perturbative Treatment of the Fluid Equations

Standard Perturbation Theory aims to solve the fluid equations perturbatively using a power law ansatz. This approach simplifies significantly in an EdS Universe, where $D = a$. Hence we will study this case first and discuss the generalization to ΛCDM later. We will furthermore neglect the decaying mode. The power law ansatz reads

$$\delta(\boldsymbol{k},\eta) = \sum_{i=1}^{\infty} a^i(\eta)^{(i)}\delta(\boldsymbol{k}) \qquad \theta(\boldsymbol{k},\eta) = -\mathcal{H}(\eta)\sum_{i=1}^{\infty} a^i(\eta)\,{}^{(i)}\theta(\boldsymbol{k}). \tag{3.68}$$

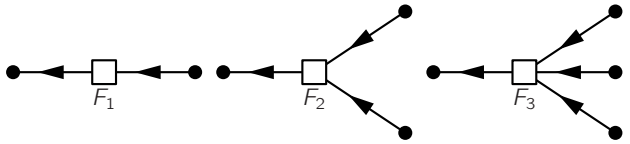

Figure 3.2.: Diagrammatic representation of the series expansion of the density field in Eq. (3.69). The points on the right side are initial density fields and the points on the left side are n-th order density fields.

The expansion is in powers of the linear density field discussed above, i.e., ${}^{(i)}\delta = \mathcal{O}({}^{(1)}\delta^i)$. We can now write the n-th order solutions as convolutions of linear density fields

$$ {}^{(n)}\delta(\boldsymbol{k}) = \prod_{m=1}^{n} \left\{ \int \frac{\mathrm{d}^3 q_m}{(2\pi)^3} {}^{(1)}\delta(\boldsymbol{q}_m) \right\} F_n(\boldsymbol{q}_1, \ldots, \boldsymbol{q}_n) \delta^{(\mathrm{D})}(\boldsymbol{k} - \boldsymbol{q}|_1^n) \tag{3.69} $$

$$ {}^{(n)}\theta(\boldsymbol{k}) = \prod_{m=1}^{n} \left\{ \int \frac{\mathrm{d}^3 q_m}{(2\pi)^3} {}^{(1)}\delta(\boldsymbol{q}_m) \right\} G_n(\boldsymbol{q}_1, \ldots, \boldsymbol{q}_n) \delta^{(\mathrm{D})}(\boldsymbol{k} - \boldsymbol{q}|_1^n) \tag{3.70} $$

A diagrammatic representation of this expansion is shown in Fig. 3.2. One can derive the following recursion relations for the convolution kernels

$$ \begin{aligned} F_n(\boldsymbol{q}_1, \ldots, \boldsymbol{q}_n) = \sum_{m=1}^{n-1} \frac{G_m(\boldsymbol{q}_1, \ldots, \boldsymbol{q}_m)}{(2n+3)(n-1)} \Big[& (2n+1)\alpha\left(\boldsymbol{q}|_1^m, \boldsymbol{q}|_{m+1}^n\right) F_{n-m}\left(\boldsymbol{q}_{m+1}, \ldots, \boldsymbol{q}_n\right) \\ & + 2\beta\left(\boldsymbol{q}|_1^m, \boldsymbol{q}|_{m+1}^n\right) G_{n-m}\left(\boldsymbol{q}_{m+1}, \ldots, \boldsymbol{q}_n\right) \Big] \end{aligned} \tag{3.71} $$

$$ \begin{aligned} G_n(\boldsymbol{q}_1, \ldots, \boldsymbol{q}_n) = \sum_{m=1}^{n-1} \frac{G_m(\boldsymbol{q}_1, \ldots, \boldsymbol{q}_m)}{(2n+3)(n-1)} \Big[& 3\alpha\left(\boldsymbol{q}|_1^m, \boldsymbol{q}|_{m+1}^n\right) F_{n-m}\left(\boldsymbol{q}_{m+1}, \ldots, \boldsymbol{q}_n\right) \\ & + 2n\beta\left(\boldsymbol{q}|_1^m, \boldsymbol{q}|_{m+1}^n\right) G_{n-m}\left(\boldsymbol{q}_{m+1}, \ldots, \boldsymbol{q}_n\right) \Big], \end{aligned} \tag{3.72} $$

where $\boldsymbol{q}|_i^j = \sum_{m=i}^{j} \boldsymbol{q}_l$. For general ΛCDM the series ansatz in Eq. (3.68) can be generalized to

$$ \delta(\boldsymbol{k}, \eta) = \sum_{i=1}^{\infty} D^i(\eta) {}^{(i)}\delta(\boldsymbol{k}) \qquad \theta(\boldsymbol{k}, \eta) = -\mathcal{H}(\eta) f(\eta) \sum_{i=1}^{\infty} D^i(\eta) \, {}^{(i)}\theta(\boldsymbol{k}). \tag{3.73} $$

The exact solution deviates from the above solution and doesn't allow for a separation of time and space dependence as in Eq. (3.73). The differences are discussed in detail in [7] and are generally at the sub-percent level. We will thus stick to the approximation Eq. (3.73), which is sufficiently accurate for our purpose.
Let us come back to the kernels and evaluate them explicitly at second and third order. The second order density kernel is given by

$$ F_2(\boldsymbol{k}_1, \boldsymbol{k}_2) = \frac{5}{7}\alpha(\boldsymbol{k}_1, \boldsymbol{k}_2) + \frac{2}{7}\beta(\boldsymbol{k}_1, \boldsymbol{k}_2) \tag{3.74} $$

$$ = \frac{5}{7} + \frac{1}{2}\frac{\boldsymbol{k}_1 \cdot \boldsymbol{k}_2}{k_1 k_2}\left(\frac{k_2}{k_1} + \frac{k_1}{k_2}\right) + \frac{2}{7}\frac{(\boldsymbol{k}_1 \cdot \boldsymbol{k}_2)^2}{k_1^2 k_2^2} \tag{3.75} $$

$$ = \frac{5}{7} + \frac{1}{2}\mu_{12}\left(\frac{k_2}{k_1} + \frac{k_1}{k_2}\right) + \frac{2}{7}\mu_{12}^2 \tag{3.76} $$

Here we defined $\boldsymbol{k}_1 \cdot \boldsymbol{k}_2 = k_1 k_2 \mu_{12}$ and symmetrized Eq. (3.69) over the momenta. The latter can be rewritten as

$$ F_2(\boldsymbol{k}_1, \boldsymbol{k}_2) = \frac{17}{21} + \frac{1}{2}\frac{\boldsymbol{k}_1 \cdot \boldsymbol{k}_2}{k_1 k_2}\left(\frac{k_2}{k_1} + \frac{k_1}{k_2}\right) + \frac{2}{7}\left[\frac{(\boldsymbol{k}_1 \cdot \boldsymbol{k}_2)^2}{k_1^2 k_2^2} - \frac{1}{3}\right] \tag{3.77} $$

where the quadratic density term, the shift term and the anisotropic stress term are more obvious. At the same time, the angular structure of monopole, dipole and quadrupole is more obvious. The second order velocity kernel reads

$$\begin{aligned} G_2(\boldsymbol{k}_1, \boldsymbol{k}_2) &= \frac{3}{7}\alpha(\boldsymbol{k}_1, \boldsymbol{k}_2) + \frac{4}{7}\beta(\boldsymbol{k}_1, \boldsymbol{k}_2) && (3.78)\\ &= \frac{3}{7} + \frac{1}{2}\frac{\boldsymbol{k}_1 \cdot \boldsymbol{k}_2}{k_1 k_2}\left(\frac{k_2}{k_1} + \frac{k_1}{k_2}\right) + \frac{4}{7}\frac{(\boldsymbol{k}_1 \cdot \boldsymbol{k}_2)^2}{k_1^2 k_2^2} && (3.79)\\ &= \frac{3}{7} + \frac{1}{2}\mu_{12}\left(\frac{k_2}{k_1} + \frac{k_1}{k_2}\right) + \frac{4}{7}\mu_{12}^2. && (3.80) \end{aligned}$$

Note that

$$F_2(\boldsymbol{q}_1, \boldsymbol{q}_2) - G_2(\boldsymbol{q}_1, \boldsymbol{q}_2) = \frac{2}{7}\big[\alpha(\boldsymbol{q}_1, \boldsymbol{q}_2) - \beta(\boldsymbol{q}_1, \boldsymbol{q}_2)\big] \tag{3.81}$$

The explicit expressions for F_3 and G_3 are

$$\begin{aligned} F_3(\boldsymbol{q}_1, \boldsymbol{q}_2, \boldsymbol{q}_3) =& \frac{1}{18}\left(7\alpha(\boldsymbol{q}_1, \boldsymbol{q}_2 + \boldsymbol{q}_3)F_2(\boldsymbol{q}_2, \boldsymbol{q}_3) + 2\beta(\boldsymbol{q}_1, \boldsymbol{q}_2 + \boldsymbol{q}_3)G_2(\boldsymbol{q}_2, \boldsymbol{q}_3)\right)\\ &+ \frac{G_2(\boldsymbol{q}_1, \boldsymbol{q}_2)}{18}\left(7\alpha(\boldsymbol{q}_1 + \boldsymbol{q}_2, \boldsymbol{q}_3) + 2\beta(\boldsymbol{q}_1 + \boldsymbol{q}_2, \boldsymbol{q}_3)\right) && (3.82)\\ G_3(\boldsymbol{q}_1, \boldsymbol{q}_2, \boldsymbol{q}_3) =& \frac{1}{18}\left(3\alpha(\boldsymbol{q}_1, \boldsymbol{q}_2 + \boldsymbol{q}_3)F_2(\boldsymbol{q}_2, \boldsymbol{q}_3) + 6\beta(\boldsymbol{q}_1, \boldsymbol{q}_2 + \boldsymbol{q}_3)G_2(\boldsymbol{q}_2, \boldsymbol{q}_3)\right)\\ &+ \frac{G_2(\boldsymbol{q}_1, \boldsymbol{q}_2)}{18}\left(3\alpha(\boldsymbol{q}_1 + \boldsymbol{q}_2, \boldsymbol{q}_3) + 6\beta(\boldsymbol{q}_1 + \boldsymbol{q}_2, \boldsymbol{q}_3)\right) && (3.83) \end{aligned}$$

The above formulae are not symmetrized over the arguments yet. Upon integration over three equivalent density fields $\delta(\boldsymbol{q}_1)\delta(\boldsymbol{q}_2)\delta(\boldsymbol{q}_3)$ we have to symmetrize, accounting both for the cyclic and odd permutations of the arguments in the kernels.

3.3.1. Power Spectrum & Bispectrum

The discussion in the previous section allowed us to express non-linear density and velocity fields as a sum of products of linear density fields. If we are interested in n-spectra of the fields, we have to correlate two of these non-linear fields with each other. This will again lead to a sum of correlators. As we have seen in Sec. 3.1.7, only even correlators of linear density fields contribute and these correlators can be expressed as products of linear power spectra, whose form is given by the process seeding the fluctuations and the subsequent linear growth. Thus we were able to reduce the problem of calculating spectra of non-linear fields to convolutions of linear power spectra.

As this calculation becomes more and more tedious order by order, we usually truncate the calculation at next-to-leading order or next-to-next-to-leading order. In this context it is also useful to introduce the notion of **loops**. The leading order contribution to the power spectrum is second order in the fields and doesn't involve any momentum integrations and is thus formally a zero-loop result. The next to leading order has to be of fourth order in the fields by Wick theorem. There are two possibilities to achieve this, by correlating two second order density fields or by correlating a linear density field with a second order density field

$$\begin{aligned} \langle\delta(\boldsymbol{k})\delta(-\boldsymbol{k})\rangle =& \left\langle {}^{(1)}\delta(\boldsymbol{k}){}^{(1)}\delta(-\boldsymbol{k})\right\rangle + 2\left\langle {}^{(1)}\delta(\boldsymbol{k}){}^{(3)}\delta(-\boldsymbol{k})\right\rangle + \left\langle {}^{(2)}\delta(\boldsymbol{k}){}^{(2)}\delta(-\boldsymbol{k})\right\rangle && (3.84)\\ P_{1\text{loop}}(k) =& P_{\text{lin}}(k) + P_{13}(k) + P_{22}(k). && (3.85) \end{aligned}$$

A diagrammatic representation of the above power spectrum is given in Fig. 3.3. As we will see in detail below, the next to leading order calculations involve one momentum integral and are thus one loop terms. Up to sixth order in the fields, i.e. two loops, we have

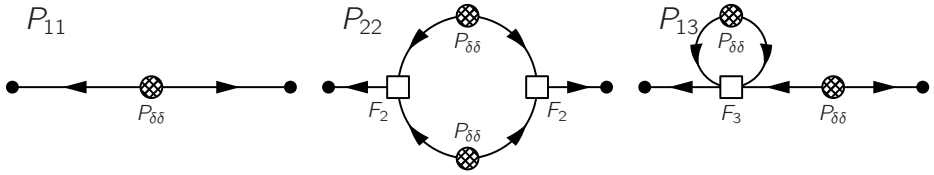

Figure 3.3.: Diagrammatic representation of the one loop matter power spectrum in Eq. (3.85) where $P_{11} = P_{\rm lin}$.

$$\begin{aligned}\langle\delta(\boldsymbol{k})\delta(-\boldsymbol{k})\rangle = &\left\langle {}^{(1)}\delta(\boldsymbol{k}){}^{(1)}\delta(-\boldsymbol{k})\right\rangle + 2\left\langle {}^{(1)}\delta(\boldsymbol{k}){}^{(3)}\delta(-\boldsymbol{k})\right\rangle + 2\left\langle {}^{(1)}\delta(\boldsymbol{k}){}^{(5)}\delta(-\boldsymbol{k})\right\rangle \\ &+ \left\langle {}^{(2)}\delta(\boldsymbol{k}){}^{(2)}\delta(-\boldsymbol{k})\right\rangle + \left\langle {}^{(3)}\delta(\boldsymbol{k}){}^{(3)}\delta(-\boldsymbol{k})\right\rangle + 2\left\langle {}^{(2)}\delta(\boldsymbol{k}){}^{(4)}\delta(-\boldsymbol{k})\right\rangle \end{aligned} \tag{3.86}$$

here we separated the terms correlating non-linear density field and linear density field (propagator terms) in the first line and the mode coupling terms in the second line.
In Sec. 3.1.7 we mentioned, that Gaussian random fields have a vanishing bispectrum and that their trispectrum can be written as a product of power spectra. The gravitational evolution changes this behaviour and leads to a non-vanishing bispectrum given by

$$B(\boldsymbol{k}_1, \boldsymbol{k}_2, \boldsymbol{k}_3) = 2F_2(\boldsymbol{k}_1, \boldsymbol{k}_2)P_{\rm lin}(k_1)P_{\rm lin}(k_2) + 2 \text{ cyc.} \tag{3.87}$$

Here cyc. stands for a cyclic permutation of the three k vectors in the arguments of the power spectra and coupling kernels. The connected trispectrum receives non-linear corrections both from the cubic coupling kernel

$$T_{F_3}(\boldsymbol{k}_1, \boldsymbol{k}_2, \boldsymbol{k}_3, \boldsymbol{k}_4) = 6F_3(\boldsymbol{k}_1, \boldsymbol{k}_2)P_{\rm lin}(\boldsymbol{k}_1)P_{\rm lin}(\boldsymbol{k}_2)P_{\rm lin}(\boldsymbol{k}_3) + 3 \text{ cyc.} \tag{3.88}$$

and the quadratic coupling kernel

$$T_{F_2}(\boldsymbol{k}_1, \boldsymbol{k}_2, \boldsymbol{k}_3, \boldsymbol{k}_4) = 4F_2(-\boldsymbol{k}_1, \boldsymbol{k}_1+\boldsymbol{k}_4)F_2(-\boldsymbol{k}_2, -\boldsymbol{k}_1-\boldsymbol{k}_4)P_{\rm lin}(k_1)P_{\rm lin}(k_2)P_{\rm lin}(|\boldsymbol{k}_1 + \boldsymbol{k}_4|)+23 \text{ cyc.} \tag{3.89}$$

3.3.2. P_{22} - the Mode Coupling

Evaluating the correlator of two second order density fields we obtain

$$P_{22}(k) = 2\int \frac{\mathrm{d}^3 q}{(2\pi)^3} P_{\rm lin}(\boldsymbol{q})P_{\rm lin}(|\boldsymbol{k}-\boldsymbol{q}|)\,|F_2(\boldsymbol{q}, \boldsymbol{k}-\boldsymbol{q})|^2 \tag{3.90}$$

$$= \frac{k^3}{2\pi^2}\int \mathrm{d}r\; r^2 \int \mathrm{d}\mu\; P_{\rm lin}(rk)P_{\rm lin}(\psi(r,\mu)k)\,|F_{2,\mathrm{d}}(q,\mu)|^2\,. \tag{3.91}$$

One realizes immediately that this term is a convolution of two power spectra with a k-dependent kernel. Thus, this term can be interpreted as a **mode coupling**. The $F_2(\boldsymbol{q}, \boldsymbol{k}-\boldsymbol{q})$ kernel of the difference vector can be simplified as ($q = rk$ and $\mu = \boldsymbol{q}\cdot\boldsymbol{k}/kq$ and $\psi(r,\mu) = \sqrt{1+r^2-2r\mu}$)

$$F_{2,\mathrm{d}}(r,\mu) = \frac{5}{7} + \frac{1}{2}\frac{r-\mu}{\psi(r,\mu)}\left(\frac{r}{\psi(r,\mu)} + \frac{\psi(r,\mu)}{r}\right) + \frac{2}{7}\left(\frac{r-\mu}{\psi(r,\mu)}\right)^2 \tag{3.92}$$

$$= \frac{7\mu + \left(3-10\mu^2\right)r}{14r\left(r^2-2\mu r+1\right)} \tag{3.93}$$

For the equivalent correlator of two second order velocity divergence fields the kernel can be simplified to the following form

$$G_{2,\mathrm{d}}(r,\mu) = \frac{(6\mu^2+1)r - 7\mu}{14r(1+r^2-2r\mu)}. \tag{3.94}$$

Evaluations of power spectra for realistic cosmologies require us to resort to numerical Boltzmann codes. Thus, the linear power spectrum is known only over a limited range of k-modes. Cutting of the loop integral at high k corresponds to setting the power spectrum to zero for $k > k_{\mathrm{max}}$ and $k < k_{\mathrm{min}}$. To do this consistently we have to make sure that $k_{\mathrm{min}} < k\psi(x,\mu) < k_{\mathrm{max}}$. This can be translated into constraints on the angular integration

$$\mu_{\mathrm{min}} = \max\left\{-1, \frac{k^2+q^2-k_{\mathrm{max}}^2}{2kq}\right\} \qquad \mu_{\mathrm{max}} = \max\left\{1, \frac{k^2+q^2-k_{\mathrm{min}}^2}{2kq}\right\}. \tag{3.95}$$

$F_{2,\mathrm{d}}(r,\mu)$ has poles at $r=0$ and $r=1, \mu=1$. Both poles are excised from the computational domain by setting the power spectrum to 0 for $0 < k < k_{\mathrm{min}}$ (see Fig. 3.4 below).
In is interesting to understand the behaviour of the mode coupling term in the limit of very small and very large external momenta. We are first considering the high-k limit $k \gg q$

$$\begin{aligned} P_{22}(k) &\xrightarrow{k\gg q} \left[\frac{569}{735}P_{\mathrm{lin}}(k) - \frac{47}{105}k\frac{\mathrm{d}P}{\mathrm{d}k} + \frac{1}{10}k^2\frac{\mathrm{d}^2P}{\mathrm{d}k^2}\right]\int\frac{\mathrm{d}^3q}{(2\pi)^3}P_{\mathrm{lin}}(q) + \frac{1}{3}k^2P_{\mathrm{lin}}(k)\int\frac{\mathrm{d}^3q}{(2\pi)^3}\frac{P_{\mathrm{lin}}(q)}{q^2} \\ &= \left[\frac{569}{735}P_{\mathrm{lin}}(k) - \frac{47}{105}k\frac{\mathrm{d}P}{\mathrm{d}k} + \frac{1}{10}k^2\frac{\mathrm{d}^2P}{\mathrm{d}k^2}\right]\sigma^2 + k^2P_{\mathrm{lin}}(k)\sigma_v^2 \end{aligned} \tag{3.96}$$

The velocity dispersion cancels with the corresponding term in P_{13} below. The low-k limit yields

$$P_{22}(k) \xrightarrow{k\ll q} \frac{9}{98}k^4\int\frac{\mathrm{d}^3q}{(2\pi)^3}\frac{P^2(q)}{q^4}. \tag{3.97}$$

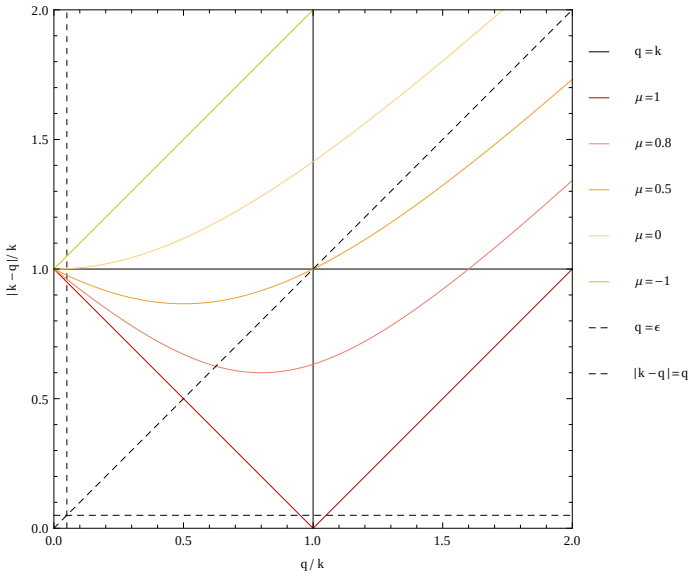

Figure 3.4.: Domains in the computation of the P_{22} term. The integrand is symmetric with respect to the diagonal dashed line and the vertical and horizontal dashed lines show an low-k cutoff in the power spectra. Since the parametrization by μ and q does not reflect the symmetry, we have to introduce cuts on the angles to implement the low-k cutoff in the power spectrum consistently.

3.3.3. P_{13} - the Propagator

The correlator of the linear and the third order density field leads to the following integral

$$P_{13}(k) = 6P_{\mathrm{lin}}(k)\int\frac{\mathrm{d}^3q}{(2\pi)^3}P_{\mathrm{lin}}(q)F_3(\boldsymbol{k},\boldsymbol{q},-\boldsymbol{q}). \tag{3.98}$$

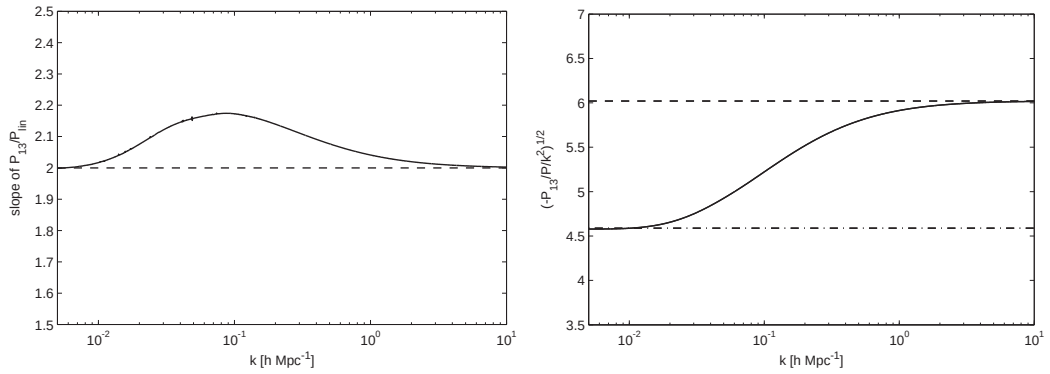

Figure 3.5.: *Left panel:* Slope of $P_{13}(k)/P_{\rm lin}(k)$. *Right panel:* Effective velocity dispersion of $P_{13}(k)$.

One realizes immediately that this term is a product of a linear density field and a k-dependent correction. Thus, this term is usually interpreted as the gravitational modification of the initial linear power spectrum and thus denoted **propagator**. The integral over the angular part can be analytically calculated leading to

$$P_{13}(k) = \frac{k^3}{252(2\pi)^2} P_{\rm lin}(k) \int \mathrm{d}r\, r^2 P_{\rm lin}(kr) \times \\ \times \left[\frac{12}{r^4} - \frac{158}{r^2} + 100 - 42r^2 + \frac{3}{r^5}\left(7r^2+2\right)\left(r^2-1\right)^3 \log\left(\frac{r+1}{r-1}\right)\right] \tag{3.99}$$

Expanding the kernel in the brackets in $1/r$ around zero we see that it asymptotes to $-488/5r^2$. The term becomes numerically unstable for large r, which is why we use the asymptotic behavior for $r \geq 100$ in the numerical evaluation.
For the equivalent term in the correlator of two velocity divergence fields we have

$$P_{\theta\theta,13}(k) = \frac{k^3}{84(2\pi)^2} P_{\rm lin}(k) \int \mathrm{d}r\, r^2 P_{\rm lin}(kr) \times \\ \times \left[\frac{12}{r^4} - \frac{82}{r^2} + 4 - 6r^2 + \frac{3}{r^5}\left(r^2+2\right)\left(r^2-1\right)^3 \log\left(\frac{r+1}{r-1}\right)\right]. \tag{3.100}$$

Expanding the brackets in $1/r$ around zero we see that it asymptotes to $-504/5r^2$.
In the high-k limit the density kernel asymptotes to

$$P_{13}(k) \xrightarrow{k\gg q} -\frac{1}{3}k^2 P_{\rm lin}(k) \int \frac{\mathrm{d}^3 q}{(2\pi)^3} \frac{P_{\rm lin}(q)}{q^2} \left(1 - \frac{116}{105}\frac{q^2}{k^2} + \frac{188}{245}\frac{q^4}{k^4} + \ldots\right) = -k^2 P_{\rm lin}(k)\sigma_v^2 \tag{3.101}$$

in the low-k limit we have instead

$$P_{13}(k) \xrightarrow{k\ll q} -\frac{1}{3}k^2 P_{\rm lin}(k) \int \frac{\mathrm{d}^3 q}{(2\pi)^3} \frac{P_{\rm lin}(q)}{q^2} \left(\frac{61}{105} - \frac{4}{35}\frac{k^2}{q^2} + \ldots\right) = -\frac{61}{105}k^2 P_{\rm lin}(k)\sigma_v^2 \tag{3.102}$$

these scalings are in fact observed in the numerical evaluation of $P_{13}(k)/P_{\rm lin}(k)/k^2$ in Fig. 3.5, where we also see the imprint of the prefactor $61/105 \approx 0.59$ for low k. The above result also suggests that P_{13}/P scales as k^2, which also had to be expected from mass and momentum conservation arguments. However, the change in amplitude between the two regimes requires a change of slope in the intermediate regime, which is shown in the left panel of Fig. 3.5. Here we defined the slope as the logarithmic derivative

$$n = \frac{\mathrm{d}\ln P}{\mathrm{d}\ln k}. \tag{3.103}$$

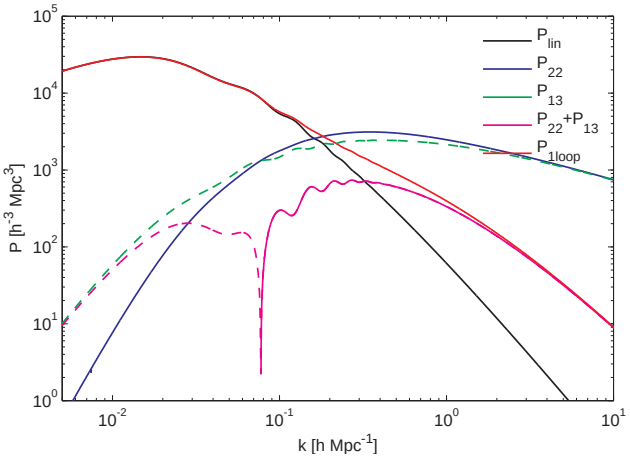

Figure 3.6.: Scale dependence of the linear power spectrum (black) in our fiducial cosmology and one-loop corrections. The mode coupling P_{22} (blue) and the propagator P_{13} (green) ad up to the one loop correction (magenta). Together with the linear power spectrum they give the one loop power spectrum $P_{1\text{loop}}$ (red). Negative parts are shown as dashed lines.

The sum of $P_{\text{lin}}(k)$ and $P_{13}(k)$ in the high-k regime can be approximated as

$$P_{\text{lin}}(k) + P_{13}(k) = P_{\text{lin}}(k)\left(1 - \sigma_v^2 k^2\right) \approx P_{\text{lin}}(k) \exp\left[-\sigma_v^2 k^2\right]. \tag{3.104}$$

A similar expansion is possible in the low-k regime using the low-k velocity dispersion

$$\sigma^2_{v,\text{low}-k} = 61/105\sigma_v^2. \tag{3.105}$$

We can conclude, that P_{13} describes an exponential damping of the linear fluctuations from the initial conditions and that σ_v can be interpreted as a smoothing scale $k_{\text{nl}} = 1/\sigma_{\text{v}} = 0.17\ h\text{Mpc}^{-1}$. One can define a scale dependent velocity dispersion via

$$\sigma_v^{-1}(k) \approx \sqrt{-\frac{P_{\text{lin}}(k)k^2}{P_{13}(k)}}. \tag{3.106}$$

3.3.4. Propagator and Mode Coupling in Numerical Simulations

The propagator is defined [8, 9] to measure the correlation between the linear initial density field δ_{i} and the evolved density field δ_{f}, i.e., the memory of the initial conditions

$$(2\pi)^3 G(\boldsymbol{k})\delta^{(\text{D})}(\boldsymbol{k} + \boldsymbol{k}') = \left\langle \frac{\partial \delta_{\text{f}}(\boldsymbol{k})}{\partial \delta_{\text{i}}(\boldsymbol{k})} \right\rangle. \tag{3.107}$$

Here the derivative is to be understood as a functional derivative. From a practical perspective it is more useful to estimate the propagator as

$$G(k) = \frac{\langle \delta_{\text{i}}(\boldsymbol{k})\delta_{\text{f}}(-\boldsymbol{k})\rangle}{\langle \delta_{\text{i}}(\boldsymbol{k})\delta_{\text{i}}(-\boldsymbol{k})\rangle} D_{\text{i}}. \tag{3.108}$$

This term does not agree with the sum of P and P_{13} considered in the last section since in P_{13} both constituent fields of the correlator can be non-linear, i.e., third order fields. Considering one of the fields to be evolved and one to be linear we obtain the term that was identified as the high-k limit of the propagator in Renormalized Perturbation Theory (RPT) [10, 9]

$$G(k) \approx \exp\left[-\frac{\sigma_v^2 k^2}{2}\right]. \tag{3.109}$$

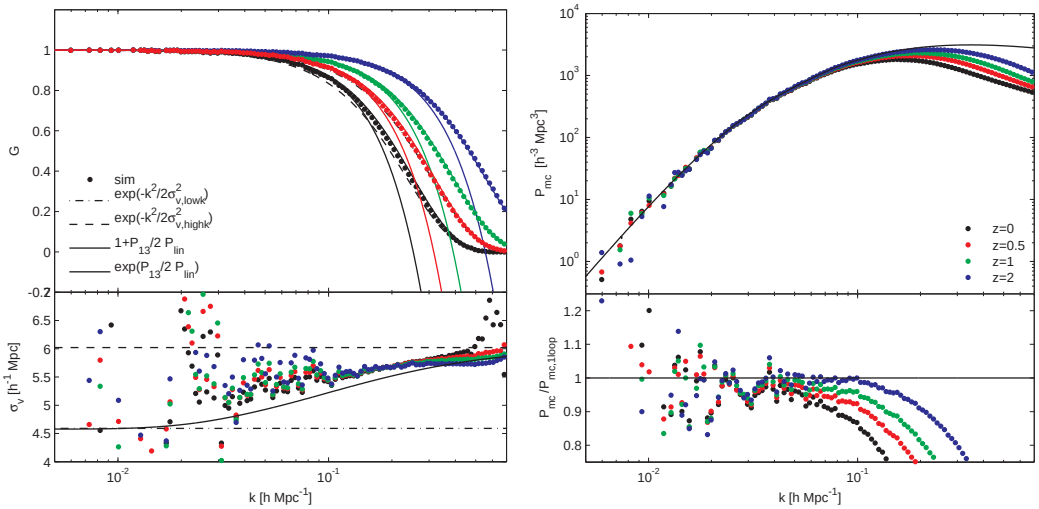

Figure 3.7.: Behaviour of the propagator and mode coupling in N-body simulations. *Left upper panel:* Propagator defined in Eq. (3.108) at redshifts $z = 0$ (black) $z = 0.5$ (red) $z = 1$ (green) and $z = 2$ (blue). *Left lower panel:* Effective velocity dispersion from the simulations *Right upper panel:* Mode coupling as defined in Eq. (3.111) at the same redshifts as the propagator in the left panel. We overplot the SPT prediction for the one loop mode coupling $P_{22}(k)$ and its low-k limit (dashed line). *Right lower panel:* Ratio of the simulation mode coupling and the SPT prediction. We see that SPT overpredicts the mode coupling for all redshifts.

Based on the form of the propagator Eq. (3.109), we can estimate the velocity dispersion from simulations as

$$\sigma_v(k) = \frac{\sqrt{-2 \ln G_{\mathrm{sim}}(k)}}{k}. \tag{3.110}$$

The propagator is shown in the left panel of Fig. 3.7. As expected the damping scale increases with redshift. When comparing the simulation propagator to the estimates based on SPT, we see that the naive estimate $1 + P_{13}/P$ fails at relatively low k and even crosses zero, whereas the true propagator asymptotes to zero at high wavenumbers. The exponential of the low-k velocity dispersion also fails to reproduce the propagator in the weakly non-linear regime $k \approx 0.2\ h\mathrm{Mpc}^{-1}$, whereas the high-$k$ limit seems to do a good job. The agreement can be checked in more detail in the lower panel, where we compare the simulation estimate of the velocity dispersion Eq. (3.110) to the SPT prediction in Eq. (3.106). We clearly see that the interpolation by $\exp[-P_{13}/P/2]$ has not enough damping. This failure could either indicate a need for two loop contributions [11] or the need for physics beyond the pressureless perfect fluid [12].

The mode coupling can then be estimated as the residual after subtracting the propagated initial conditions from the final power spectrum

$$(2\pi)^3 \delta^{(\mathrm{D})}(\boldsymbol{k} + \boldsymbol{k}') P_{\mathrm{mc,sim}}(k) = \langle \delta_{\mathrm{f}}(\boldsymbol{k}) \delta_{\mathrm{f}}(\boldsymbol{k}') \rangle - \frac{\langle \delta_{\mathrm{i}}(\boldsymbol{k}) \delta_{\mathrm{f}}(\boldsymbol{k}') \rangle^2}{\langle \delta_{\mathrm{i}}(\boldsymbol{k}) \delta_{\mathrm{i}}(\boldsymbol{k}') \rangle} \tag{3.111}$$

and is shown in the right panel of Fig. 3.7. We see that while the simulation measurement is well reproduced on the largest scales by SPT, this agreement becomes bad at relatively low wavenumbers (e.g. $k < 0.1\ h\mathrm{Mpc}^{-1}$ at $z = 0$). The overprediction of the mode coupling in SPT might be caused by the instantaneous interaction of the linear modes, whereas RPT suggests that the interacting modes are really the ones evolved using the propagator.

Finally, we show the simulation power spectra in comparison to the SPT predictions in Fig. 3.8 for redshifts $z = 0, 0.5, 1, 2$. While at high redshift SPT describes the deviations from linear theory reasonably well up to $k \approx 0.25\ h\mathrm{Mpc}^{-1}$, this agreement becomes worse for lower

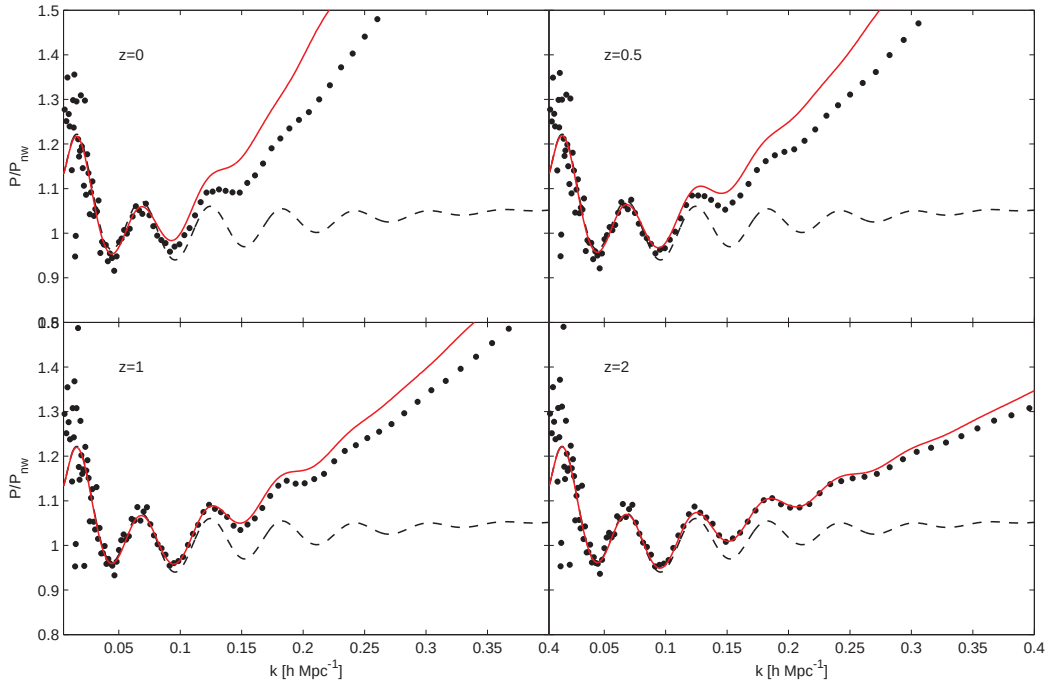

Figure 3.8.: Matter power spectra from numerical simulations at redshifts $z = 0, 0.5, 1, 2$ normalized by the BBKS no-wiggle power spectrum defined in Eq. (4.59). For reference we overplot the linear theory (black dashed) and one loop SPT (red solid) results.

redshifts.

3.4. Matrix Formulation of the Fluid Equations

As we will see in the next chapter, when considering a coupled fluid of haloes and matter, it can be quite beneficial to rewrite the equations of motion in a matrix formulation [8, 1]. One first introduces the vector $\mathbf{\Psi} = (\delta, -\theta/\mathcal{H}f)$ and the time variable $y = \ln(a)$. It is useful to re-express the time derivative of the velocity divergence in the Euler equation as

$$\theta' = \mathcal{H}f\left(\frac{\mathrm{d}}{\mathrm{d}y}\frac{\theta}{\mathcal{H}f} - \theta\frac{\mathrm{d}}{\mathrm{d}\eta}\frac{1}{\mathcal{H}f}\right) = \mathcal{H}^2 f^2 \frac{\mathrm{d}}{\mathrm{d}y}\frac{\theta}{\mathcal{H}f} + \frac{f'}{f}\theta + \frac{\mathcal{H}'}{\mathcal{H}}\theta. \tag{3.112}$$

From the linear growth equation (3.55) we know that

$$\frac{\mathrm{d}f}{\mathrm{d}\eta} = \frac{3}{2}\Omega_{\mathrm{m}}(a)\mathcal{H}(1+f) - \mathcal{H}f(2+f). \tag{3.113}$$

Using these results, the continuity and Euler equation can be written in the joint form [8]

$$\partial_y \Psi_a(\boldsymbol{k},\eta) + \Omega_{ab}\Psi_b(\boldsymbol{k},\eta) = \gamma_{abc}(\boldsymbol{k},\boldsymbol{k}_1,\boldsymbol{k}_2)\Psi_b(\boldsymbol{k}_1,\eta)\Psi_c(\boldsymbol{k}_2,\eta). \tag{3.114}$$

Equal indices are implicitly summed over and also momenta on the right hand side are integrated over. The linear coupling matrix is given by

$$\Omega_{ab} = \begin{pmatrix} 0 & -1 \\ -\frac{3}{2}\frac{\Omega_{\mathrm{m}}}{f^2} & \frac{3}{2}\frac{\Omega_{\mathrm{m}}}{f^2} - 1 \end{pmatrix} \tag{3.115}$$

and the only non-vanishing components of the non-linear coupling matrix on the right hand side are

$$\gamma_{112} = \alpha/2 \qquad \gamma_{121} = \alpha/2 \qquad \gamma_{222} = \beta. \tag{3.116}$$

To proceed we will employ the approximation $\Omega_m/f^2 \approx 1$. One can then employ the Laplace transformation[4] to obtain

$$(\lambda\delta^{(K)}_{ab} + \Omega_{ab})\Psi_b = \phi_a, \tag{3.117}$$

where $\phi_a = \Psi_a(y = 0)$ is the initial condition. Inverting the operator we get

$$(\lambda\delta^{(K)}_{ab} + \Omega_{ab})^{-1} = \frac{1}{(2\lambda+3)(\lambda-1)}\begin{pmatrix} 2\lambda+1 & 2 \\ 3 & 2\lambda \end{pmatrix} \tag{3.118}$$

$$= \frac{1}{5(\lambda-1)}\begin{pmatrix} 3 & 2 \\ 3 & 2 \end{pmatrix} + \frac{1}{5(\lambda+3/2)}\begin{pmatrix} 2 & -2 \\ -3 & 3 \end{pmatrix}. \tag{3.119}$$

Applying the inverse Laplace transform we obtain the linear propagator

$$g_{ab}(y) = \oint \frac{\mathrm{d}\lambda}{2\pi\mathrm{i}}\sigma_{ab}(\lambda)e^{\lambda y} = \frac{e^y}{5}\begin{pmatrix} 3 & 2 \\ 3 & 2 \end{pmatrix} + \frac{e^{-3/2\,y}}{5}\begin{pmatrix} 2 & -2 \\ -3 & 3 \end{pmatrix}. \tag{3.120}$$

The integration is performed via decomposition into partial fractions, identification of the poles and the using Cauchy's integral formula[5]. The first term describes the growing mode and the second term the decaying mode. Finally we obtain the following formal solution for the non-linear field vector

$$\Psi_a(\boldsymbol{k}, \eta) = g_{ab}(\eta)\phi_b(\boldsymbol{k}) + \int \mathrm{d}\eta' g_{ab}(\eta - \eta')\gamma_{abc}\Psi_c\Psi_d. \tag{3.121}$$

where ϕ describes the initial conditions. In contrast to SPT this approach integrates both the growing and decaying mode solutions. The second order solution explicitly reads as

$${}^{(1)}\Psi_a(\eta) = g_{ab}(\eta)\phi_b \tag{3.122}$$

$${}^{(2)}\Psi_a(\boldsymbol{k}, \eta) = \int \mathrm{d}\eta' g_{ab}(\eta - \eta')\gamma_{abc}(\boldsymbol{k}, \boldsymbol{q}, \boldsymbol{q}')g_{ce}(\eta')\phi_c(\boldsymbol{q})g_{df}(\eta')\phi_f(\boldsymbol{q}') \tag{3.123}$$

3.5. Zel'dovich Approximation and Lagrangian PT

3.5.1. Equation of Motion

Lagrangian Perturbation Theory (LPT) starts from the initial unperturbed Lagrangian position $\boldsymbol{q}$ of the particle and follows their trajectory to their final position $\boldsymbol{x}$. The Lagrangian and Eulerian coordinates are related via the mapping $\boldsymbol{\Psi}$

$$\boldsymbol{x}(\boldsymbol{q}, \eta) = \boldsymbol{q} + \boldsymbol{\Psi}(\boldsymbol{q}, \eta). \tag{3.124}$$

The corresponding change of the density is given by the continuity relation

$$[1 + \delta(\boldsymbol{x})]\,\mathrm{d}^3x = \mathrm{d}^3q, \tag{3.125}$$

where the volume distortion is described by the Jacobian

$$\mathcal{J} = \left|\frac{\mathrm{d}^3x}{\mathrm{d}^3q}\right| = \det\left[\delta^{(K)}_{ij} + \frac{\partial\Psi_i}{\partial q_j}\right] = \det\left[\delta^{(K)}_{ij} + \Psi_{i,j}\right]. \tag{3.126}$$

[4] The Laplace transformation and the inverse Laplace transformation are defined as

$$\tilde{f}(\lambda) = \int_0^\infty \mathrm{d}y e^{-\lambda y} f(y) \qquad\qquad f(y) = \int_{c-\mathrm{i}\infty}^{c+\mathrm{i}\infty} \frac{\mathrm{d}\lambda}{2\pi\mathrm{i}} e^{\lambda y}\tilde{f}(\lambda)$$

[5] For a disk D in the complex plane and $a \in D$ one has

$$f(a) = \oint_{\partial D} \frac{\mathrm{d}\lambda}{2\pi\mathrm{i}} \frac{f(\lambda)}{\lambda - a}$$

Thus we have $\delta(\boldsymbol{x}) = 1/\mathcal{J} - 1$. Taking the divergence of the particle equation of motion Eq. (3.40) and the Poisson equation we obtain

$$\mathcal{J}\,\boldsymbol{\nabla}_{\boldsymbol{x}} \cdot \left[\frac{\mathrm{d}^2\boldsymbol{x}}{\mathrm{d}\eta^2} + \mathcal{H}\frac{\mathrm{d}\boldsymbol{x}}{\mathrm{d}\eta}\right] = \frac{3}{2}\Omega_{\mathrm{m}}(a)\mathcal{H}^2(\mathcal{J}-1). \tag{3.127}$$

This equation is not yet completely expressed in terms of Lagrangian variables since $\nabla_{x_i} = (\delta_{ij}^{(\mathrm{K})} + \Psi_{i,j})^{-1}\nabla_{q_j}$. The equation can be solved perturbatively with the ansatz [13]

$$\boldsymbol{\Psi} = {}^{(1)}\boldsymbol{\Psi} + {}^{(2)}\boldsymbol{\Psi} + {}^{(3)}\boldsymbol{\Psi} + \dots \tag{3.128}$$

The determinant is equivalently expanded as

$$\mathcal{J} = 1 + {}^{(1)}\mathcal{J} + {}^{(2)}\mathcal{J} + {}^{(3)}\mathcal{J} + \dots \tag{3.129}$$

and the Jacobian can be expressed as [13]

$${}^{(1)}\mathcal{J} = {}^{(1)}\mathcal{L} = \sum_i {}^{(1)}\Psi_{i,i} \tag{3.130}$$

$${}^{(2)}\mathcal{J} = {}^{(2)}\mathcal{L} + {}^{(2)}\mathcal{K} = \sum_i {}^{(2)}\Psi_{i,i} + \frac{1}{2}\sum_{i\neq j}\left\{{}^{(1)}\Psi_{i,i}{}^{(1)}\Psi_{j,j} - {}^{(1)}\Psi_{i,j}\Psi^{(1)}_{j,i}\right\} \tag{3.131}$$

$${}^{(3)}\mathcal{J} = {}^{(3)}\mathcal{L} + {}^{(3)}\mathcal{K} + {}^{(3)}\mathcal{M} = \sum_i {}^{(3)}\Psi_{i,i} + \sum_{i\neq j}\left\{{}^{(2)}\Psi_{i,i}{}^{(1)}\Psi_{j,j} - {}^{(2)}\Psi_{i,j}{}^{(1)}\Psi_{j,i}\right\} + \det {}^{(1)}\Psi_{i,j} \tag{3.132}$$

where $\mathcal{L}$, $\mathcal{K}$ and $\mathcal{M}$ are invariant scalars of the deformation tensor. At first order we have for the equation of motion

$$\left[\frac{\mathrm{d}^2\Psi_{i,i}}{\mathrm{d}\eta^2} + \mathcal{H}\frac{\mathrm{d}\Psi_{i,i}}{\mathrm{d}\eta}\right] = \frac{3}{2}\Omega_{\mathrm{m}}(a)\mathcal{H}^2\Psi_{i,i}. \tag{3.133}$$

3.5.2. The Power Spectrum in the Zeldovich Approximation

The **Zeldovich approximation** [14] effectively truncates LPT after the leading order. This means that the particles move on straight lines along their Lagrangian velocity vector. Let us explicitly calculate the mapping in Eq. (3.124) at leading order. In linear theory we can integrate the velocity to obtain the displacement field in Fourier space

$$\boldsymbol{\Psi}(\boldsymbol{k},\eta) = \int \mathrm{d}\eta'\ \boldsymbol{v}(\boldsymbol{k},\eta') = -\mathrm{i}\,\frac{\boldsymbol{k}}{k^2}\delta_{\mathrm{lin}}(\boldsymbol{k},\eta), \tag{3.134}$$

where $\delta_{\mathrm{lin}}(\boldsymbol{k},\eta)$ is the evolved linear density field. The next step we want to estimate the final density field originating from the linear displacement of the particles. This is best done in Fourier space. Rewriting the Fourier transform of the density field and replacing the Eulerian volume element using Eq. (3.125) we obtain

$$\delta_{\mathrm{Z}}(\boldsymbol{k}) = \int \mathrm{d}^3x \exp\left[\mathrm{i}\,\boldsymbol{k}\cdot\boldsymbol{x}\right]\delta(\boldsymbol{x}) \tag{3.135}$$

$$= \int \mathrm{d}^3x\big[1+\delta(\boldsymbol{x})\big]\exp\left[\mathrm{i}\,\boldsymbol{k}\cdot\boldsymbol{x}\right] - \int \mathrm{d}^3q \tag{3.136}$$

$$= \int \mathrm{d}^3q \exp\left[i\boldsymbol{k}\cdot\boldsymbol{q}\right]\big\{\exp\left[\mathrm{i}\,\boldsymbol{k}\cdot\boldsymbol{\Psi}(\boldsymbol{q})\right]-1\big\}. \tag{3.137}$$

Since $\langle\delta\rangle = 0$ we have $\langle\exp\left[\mathrm{i}\,\boldsymbol{k}\cdot\boldsymbol{\Psi}(\boldsymbol{q})\right]\rangle = 1$. The power spectrum is given by

$$P_{\mathrm{Z}}(k) = \int \mathrm{d}^3r \exp\left[\mathrm{i}\,\boldsymbol{k}\cdot\boldsymbol{r}\right]\langle\exp\left[\mathrm{i}\,\boldsymbol{k}\cdot\Delta\boldsymbol{\Psi}\right]-1\rangle \tag{3.138}$$

where $\boldsymbol{r} = \boldsymbol{q} - \boldsymbol{q}'$ and $\Delta\boldsymbol{\Psi}(\boldsymbol{r}) = \boldsymbol{\Psi}(\boldsymbol{q}) - \boldsymbol{\Psi}(\boldsymbol{q}')$. Here we used that this quantity can only depend on the distance between the points by translation invariance. One can now use the cumulant expansion theorem to bring the expectation value into the exponential[6] $\langle \exp[\mathrm{i}\,\boldsymbol{k}\cdot\Delta\boldsymbol{\Psi}]\rangle = \exp\left[-1/2\left\langle(\boldsymbol{k}\cdot\Delta\boldsymbol{\Psi})^2\right\rangle\right]$. The next step consists in evaluating the argument of the exponential

$$-1/2\left\langle(\boldsymbol{k}\cdot\boldsymbol{\Psi})^2\right\rangle = \int \frac{\mathrm{d}^3k'}{(2\pi)^3}\frac{(\boldsymbol{k}\cdot\boldsymbol{k}')^2}{k'^4}\cos(\boldsymbol{k}'\cdot\boldsymbol{r})P_{\mathrm{lin}}(k') - \frac{k^2}{3}\int\frac{\mathrm{d}^3k'}{(2\pi)^3}\frac{P_{\mathrm{lin}}(k')}{k'^2} \tag{3.139}$$

$$= k_i k_j I_{ij}(\boldsymbol{r}) - k^2\sigma_v^2 \tag{3.140}$$

where σ_v was defined above in Eq. (3.63). We can evaluate the integrals in a frame where $\boldsymbol{q} \parallel \boldsymbol{e}_z$. The integration over the azimutal angle φ reduces the matrix I_{ij} to two non-vanishing components

$$I_{11}(\boldsymbol{r}) = \int\frac{\mathrm{d}^3k'}{(2\pi)^3}\sin^2(\varphi)\,\frac{1-\mu^2}{k'^2}\cos(\mu k' r)P_{\mathrm{lin}}(k') = \frac{4\pi}{(2\pi)^3}\int\mathrm{d}k'\,\frac{j_1(k'r)}{k'r}P_{\mathrm{lin}}(k') \tag{3.141}$$

$$I_{33}(\boldsymbol{r}) = \int\frac{\mathrm{d}^3k'}{(2\pi)^3}\frac{\mu^2}{k'^2}\cos(\mu k' r)P_{\mathrm{lin}}(k') = \frac{4\pi}{(2\pi)^3}\int\mathrm{d}k'\left[j_0(k'r) - 2\frac{j_1(k'r)}{k'r}\right]P_{\mathrm{lin}}(k') \tag{3.142}$$

where j_0 and j_1 are spherical Bessel functions.[7] For the multiplication with the k-vectors in $k_i I_{ij} k_j$ we have to rotate to the frame, where $\boldsymbol{k} \parallel \boldsymbol{e}_z$ using a rotation matrix R and obtain $kRIR^{\mathrm{T}}k = k^2\left[I_{11}(1-\mu^2) + I_{33}\mu^2\right]$. The rotation matrix is a product of a rotation around the y-axis by an angle $\mu = \cos(\theta)$ and a rotation around z-axis by an angle ϕ. We finally obtain for the power spectrum

$$P_{\mathrm{Z}}(k) = \exp\left[-\sigma_v^2k^2\right]\int\mathrm{d}^3r\;\exp[\mathrm{i}\,\boldsymbol{k}\cdot\boldsymbol{r}]\Big\{\exp\left[k^2I_{11}(r) + k^2\mu^2\big(I_{33}(r) - I_{11}(r)\big)\right] - 1\Big\} \tag{3.143}$$

The term $\exp\left[-\sigma_v^2k^2\right]$ can always be pulled out since, the second term in the brackets contributes only at $k = 0$, where the exponential is unity. Evaluating the above expression in its original form is numerically difficult, since the angular integration can not be done analytically. To enable a analytic calculation of the angular integral, we expand the exponential in the integral

$$P_{\mathrm{Z}}(k) = \exp\left[-\sigma_v^2k^2\right]\int\mathrm{d}^3r\;\exp[\mathrm{i}\,\boldsymbol{k}\cdot\boldsymbol{r}]\sum_{n=1}^{\infty}\frac{[k_ik_jI_{ij}(\boldsymbol{r})]^n}{n!} \tag{3.144}$$

$$= \exp\left[-\sigma_v^2k^2\right]\int\mathrm{d}^3r\;\exp[\mathrm{i}\,\mu kr]\sum_{n=1}^{\infty}\frac{k^{2n}\left[I_{11}(r) + \mu^2\big(I_{33}(r) - I_{11}(r)\big)\right]^n}{n!}. \tag{3.145}$$

This form allows for an analytic evaluation of the angular integral. In fact, the terms of the sum are all positive and contribute only over a certain range of k, with higher powers contributing at higher k. Thus the summation can be restricted to the first few terms.
There are different possibilities to evaluate the Zeldovich power spectrum, for instance [15] used an approach that seems to have a faster convergence. We first slightly reorganize Eq. (3.143)

$$P_{\mathrm{Z}}(k) = \exp\left[-\sigma_v^2k^2\right]\int\mathrm{d}^3r\;\exp[\mathrm{i}\,\boldsymbol{k}\cdot\boldsymbol{r}]\Big[\exp\left[-k^2(I_{33}(r) - I_{11}(r))(1-\mu^2) + k^2I_{33}(r)\right] - 1\Big] \tag{3.146}$$

[6] For Gaussian fields we have

$$\langle\exp[X]\rangle = \exp\left[\sum_{n=1}^{\infty}\frac{1}{n!}\left\langle X^N\right\rangle_{\mathrm{c}}\right]$$

where the $\left\langle X^N\right\rangle_{\mathrm{c}}$ are the connected moments or cumulants.

[7]

$$j_0(x) = \frac{\sin x}{x} \qquad\qquad j_1(x) = \frac{\sin x}{x^2} - \frac{\cos x}{x}$$

and then use the following identity

$$\int_0^1 \mathrm{d}\mu \cos(A\mu) \exp\left[-B(1-\mu^2)\right] = \sum_{i=0}^{\infty} \left(\frac{-2B}{A}\right)^i j_i(A). \tag{3.147}$$

This finally yields the following expansion

$$P_Z(k) = \exp\left[-\sigma_v^2 k^2\right] \int \mathrm{d}r\ r^2 \Bigg\{ \left\{\exp\left[k^2 I_{33}(r)\right] - 1\right\} j_0(kr) + \sum_{i=1}^{\infty} \exp\left[k^2 I_{33}(r)\right] \left\{2k^2 \left[I_{11}(r) - I_{33}(r)\right]\right\}^i \frac{j_i(kr)}{(kr)^i} \Bigg\}. \tag{3.148}$$

We compare the two approaches in Fig. 3.9. The approach in [15] clearly shows better convergence properties. The no-wiggle plot clearly shows that the Zeldovich power spectrum predicts a power that is even lower than the linear power in contrast to the simulation measurements shown in Fig. 3.8, which show that the non-linear power exceeds the linear power. However, [16] note that it has better correlation properties for the particles displacements and should thus be used as the background solution for perturbation theories.

3.6. N-Body Codes

Modern cosmology is highly dependent on computer simulations. Due to the lack of analytic formalisms to treat the non-linear gravitational dynamics and hydrodynamics the simulations are sometimes the only way to confront experimental data with theoretical predictions [17].
`GADGET-2` [18] is a parallel TreeSPH code, which can follow the dynamics of collisionless fluids with the *N*-**body** method and can treat ideal gases by the smoothed particle hydrodynamics method (SPH). We are not using the gas dynamics part since we are mainly interested in large scale effects that are governed by the collisionless dynamics of the dark matter distribution. For cosmological *N*-body simulations the direct calculation of the gravitational force needs $\mathcal{O}(N^2)$ operations and is hence computationally expensive and many methods have been invented to perform this task in a more efficient way. In `GADGET-2` the gravitational forces can be computed with a pure Tree code, which uses a hierarchical multipole expansion of the gravitational field. To speed the method further up `GADGET-2` offers a TreePM method, which uses the exact Tree method for small scales and high speed Fast Fourier Transforms (FFTs) to solve Poisson equation on large scales. These so called particle mesh (PM) methods are the fastest way to calculate gravitational forces, but at scales close to the FFT grid size the force is heavily suppressed.
In principle the continuous dark matter density field would be described by the collisionless Boltzmann equation coupled to Poisson equation in an expanding Friedmann-Lemaître Universe. However, to make the problem computationally treatable the phase space density is sampled by a finite number of tracer particles. We will refer to these tracers as dark-matter particles, but keep in mind that their masses are orders of magnitude above the expected masses for real dark-matter particles such as WIMPs or Axions (See 2.6 for properties of realistic candidates.). The Hamiltonian of the system is given by [18]

$$H = \sum_{i=1}^{N} \frac{\boldsymbol{p}_i^2}{2m_i a^2} + \frac{1}{2} \sum_{i,j=1}^{N} \frac{m_i m_j \varphi(\boldsymbol{x}_i - \boldsymbol{x}_j)}{a}. \tag{3.149}$$

Here we used comoving coordinates and defined canonical momenta by $\boldsymbol{p}_i = a^2 m_i \dot{\boldsymbol{x}}_i$. Periodic boundary conditions are assumed for the box. The Tree code groups distant particles into cells and allows their gravitational action to be accounted for by a single multipole force. So the

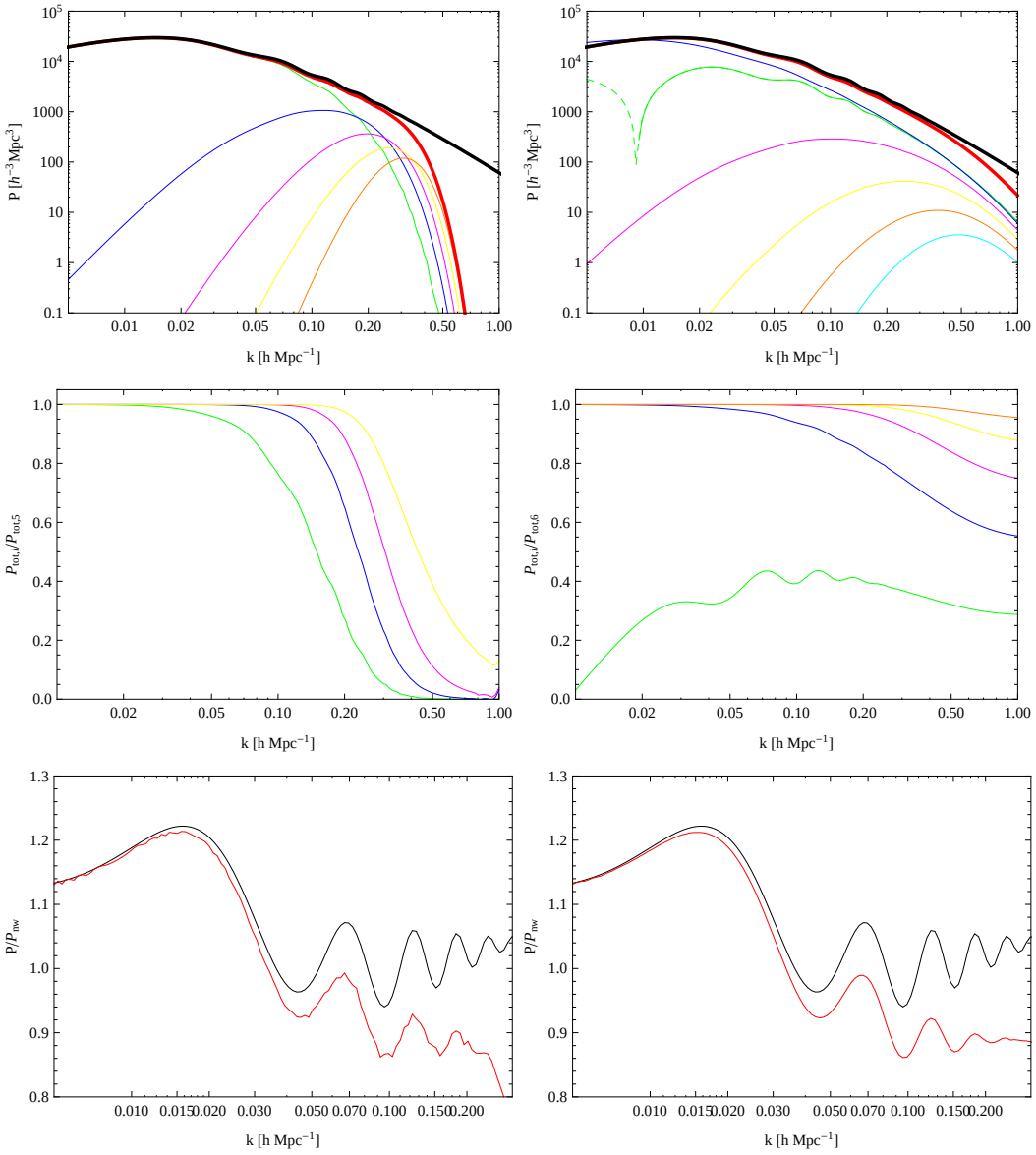

Figure 3.9.: The two approaches to the Zeldovich Power Spectrum. *Top panels:* Linear power spectrum (thick black), Zeldovich power spectrum (thick red) and contributions order by order in the respective expansion. *Middle panels:* Convergence of the Zeldovich power spectra with respect to the fifth (left) and sixth order (right) result. *Bottom panels:* Zeldovich power spectrum divided by the BBKS no-wiggle power spectrum (red) and linear power spectrum divided by no-wiggle (black). *Left panels:* Expansion according to Eq. (3.145). *Right panels:* Expansion according to Eq. (3.148).

computation of the gravitational force on a single particle reduces from $\mathcal{O}(N)$ operations to $\mathcal{O}(\log N)$ operations. The accuracy of the method can be adapted to the specific requirements by choosing an appropriate opening criterion, at which the code uses a finer subdivision of space.
Finally, time integration of the force uses a quasi-symplectic leapfrog scheme with adaptive timesteps.

Boundary Conditions

Cosmological simulations are usually carried out for a cubic domain of space. Conceptually this domain is cut from the surrounding Universe and one must somehow define the boundary conditions. The common solution to this problem is to impose **periodic boundary conditions**

$$\delta(x + iL, y + jL, z + kL) = \delta(x, y, z) \quad \forall i, j, k \in \mathbb{N}, \tag{3.150}$$

where L is the box length. With this assumption the Universe is considered as being composed of an infinite number of simulation volumes, glued at their faces.
When calculating correlation functions and power spectra from the simulation data periodic boundary conditions have to be considered as well. Owing to this fact, one has to reorganize the box before doing the radial averages for $\xi(r)$.

3.7. Identification of Gravitationally Bound Objects - The Halo Finder

When the evolution of the density field under gravity is finished, we want to investigate the clustering of the dark matter. We already noted that the haloes are a fundamental building blocks of the large scale structure and formation sites of galaxies. But how do we identify virialized objects in the dark matter density field? The results of the spherical top-hat collapse model imply that a halo should be a bound dark matter clump of overdensity $\delta \approx 180$ for the Einstein-de Sitter case. There are two main methods that are used for the identification of haloes in the N-body simulations: The so called **spherical overdensity** halo finder [19] tries to localise all peaks in the density field and associates all particles in a sphere with mean density 180 times the background density to the halo.
The **Friends-of-Friends** (FoF) halo finder [20] is based on the definition of a **linking length** h. In a first step all particles with separation less than h are identified as friends. Then a halo is defined as the equivalence class of particles that are connected by at least one friendship, i. e. particles that are friends-of-friends. The linking length has to be carefully chosen in order to identify all structures exceeding a certain threshold ρ. In a simulation with average particle mass M_p a sphere of radius

$$h = \sqrt[3]{\frac{2M_p}{4/3\pi\bar{\rho}}}, \tag{3.151}$$

which is situated in a region with density exceeding ρ contains on average two or more particles. In turn, in regions exceeding ρ, particles will be typically closer than h and will hence be linked by the `FoF` algorithm. Another important parameter for the `FoF` halo finder is the minimum number of particles N_min per halo. This number is used to reject spurious haloes that are formed by particles not belonging to a gravitationally bound object. Thus with a sufficiently high N_min, one will be able to reject all of those spurious objects.
The big advantage of the `FoF` halo finder, is that it can identify the full triaxial halo profile without imposing a spherical profile. But there are also some shortcomings of the `FoF` halo finder. The most serious ones are the junction of nearby haloes and the poor distinction of small mass haloes from the background noise.

One possibility to obtain a more robust estimate for the actual halo parameters is to iteratively remove unbound particles. This is done by calculating the particle's potential energy in the gravitational field produced by the other particles of the assumed halo. Then this energy is compared to the particle's kinetic energy. If there are particles with positive total energy then they are considered as unbound and removed.
The dark matter haloes used for this work were identified using the `B-FoF` algorithm kindly provided by Volker Springel, where the linking length was set to 0.2 times the mean interparticle spacing. The minimum particle number per halo was set to $N_{\mathrm{min}} = 20$, hence the lightest haloes have a mass of $1.65 \times 10^{13}\ h^{-1} M_{\odot}$.

Bibliography

[1] F. Bernardeau, S. Colombi, E. Gaztañaga, and R. Scoccimarro, **Large-scale structure of the Universe and cosmological perturbation theory**, *Phys. Rep.* **367** (Sept., 2002) 1–248, [astro-ph/].

[2] T. Baldauf, **The Galaxy-Dark Matter Connection**, Master's thesis, University of Zurich, 2009.

[3] J. A. Peacock, *Cosmological Physics*. Cambridge University Press, 1999.

[4] P. J. E. Peebles, *The large-Scale Structure of the Universe*. Princeton University Press, Princeton, NJ, 1980.

[5] S. Bonoli and U. Pen, **Halo stochasticity in global clustering analysis**, *ArXiv e-prints* **astro-ph:0810.0273** (2008) [arXiv:0810.0273].

[6] S. Pueblas and R. Scoccimarro, **Generation of vorticity and velocity dispersion by orbit crossing**, *Phys. Rev.* **80** (Aug., 2009) 043504, [arXiv:0809.4606].

[7] R. Takahashi, **Third-Order Density Perturbation and One-Loop Power Spectrum in Dark-Energy-Dominated Universe**, *Progress of Theoretical Physics* **120** (Sept., 2008) 549–559, [arXiv:0806.1437].

[8] R. Scoccimarro, **A New Angle on Gravitational Clustering**, in *The Onset of Nonlinearity in Cosmology* (J. N. Fry, J. R. Buchler, and H. Kandrup, eds.), vol. 927 of *Annals of the New York Academy of Sciences*, pp. 13–23, 2001. astro-ph/.

[9] M. Crocce and R. Scoccimarro, **Renormalized Cosmological Perturbation Theory**, *Phys. Rev.* **D73** (2006) 063519, [astro-ph/0509418].

[10] M. Crocce and R. Scoccimarro, **Memory of Initial Conditions in Gravitational Clustering**, *Phys. Rev.* **D73** (2006) 063520, [astro-ph/0509419].

[11] F. Bernardeau, A. Taruya, and T. Nishimichi, **Cosmic propagators at two-loop order**, *ArXiv e-prints* (Nov., 2012) [arXiv:1211.1571].

[12] J. J. M. Carrasco, M. P. Hertzberg, and L. Senatore, **The Effective Field Theory of Cosmological Large Scale Structures**, *ArXiv e-prints* (June, 2012) [arXiv:1206.2926].

[13] F. Bouchet, S. Colombi, E. Hivon, and R. Juszkiewicz, **Perturbative Lagrangian approach to gravitational instability**, *Astron.Astrophys.* **296** (1995) 575, [astro-ph/9406013].

[14] Y. B. Zel'dovich, **Gravitational instability: An approximate theory for large density perturbations.**, *A&A* **5** (Mar., 1970) 84–89.

[15] P. Schneider and M. Bartelmann, **The power spectrum of density fluctuations in the Zel'dovich approximation**, *Mon. Not. Roy. Astron. Soc.* **273** (Mar., 1995) 475–483.

[16] S. Tassev and M. Zaldarriaga, **The mildly non-linear regime of structure formation**, *JCAP* **4** (Apr., 2012) 13, [arXiv:1109.4939].

[17] E. Bertschinger, **Simulations of structure formation in the universe**, *Ann. Rev. Astron. Astrophys.* **36** (1998) 599–654.

[18] V. Springel, **The cosmological simulation code GADGET-2**, *Mon.Not.Roy.Astron.Soc.* **364** (2005) 1105–1134.

[19] C. Lacey and S. Cole, **Merger Rates in Hierarchical Models of Galaxy Formation - Part Two - Comparison with N-Body Simulations**, *Mon. Not. Roy. Astron. Soc.* **271** (1994) 676–+, [astro-ph/].

[20] M. Davis, G. Efstathiou, C. S. Frenk, and S. D. M. White, **The evolution of large-scale structure in a universe dominated by cold dark matter**, *Astrophys. J.* **292** (1985) 371–394.

CHAPTER 4

Inflation & Relativistic Perturbation Theory[†]

In this chapter we will first explain how perturbations about the homogeneous Universe can be described in a general relativistic framework. Then we will proceed to discuss inflation, the period of accelerating expansion in the early Universe. We will first describe how the simplest inflationary model can generate the seeds for structure formation and calculate the corresponding spectra. In the end, we will give a brief overview of possible extensions of this simplest model and how they can possibly be detected through primordial non-Gaussianity.

4.1. Cosmological Perturbation Theory

In the previous chapter we assumed that after recombination small density fluctuations were present in all components but did not say much about their creation. Besides the Gaussian fluctuations generated by Inflation, there are also non-Gaussian fluctuations, predicted for instance by topological defects. We will neglect the latter and assume that inflation is the valid physical model to describe the early phase of the Universe.
In order to calculate the spectrum of the density fluctuations we have to use a fully relativistic approach, where deviations from homogeneity are described by small perturbations around the flat Friedmann-Robertson-Walker background metric $\eta_{\mu\nu}$

$$g_{\mu\nu} = \eta_{\mu\nu} + h_{\mu\nu}. \tag{4.1}$$

Following the notation of [4, 5] we can write down the first order **perturbed metric** as

$$\mathrm{d}s^2 = a^2(\eta)\left\{-(1+2A)\,\mathrm{d}\eta^2 - 2B_i \mathrm{d}x^i \mathrm{d}\eta + \left[(1+2D)\delta_{ij}^{(\mathrm{K})} + 2E_{ij}\right]\mathrm{d}x^i \mathrm{d}x^j\right\}. \tag{4.2}$$

Here we decomposed the metric perturbations into time, space and mixed time space component, where E_{ij} is the traceless part of the spatial perturbation and D is its trace. We will restrict ourselves to scalar modes $B_i = BQ_i^{(0)}$ and $E_{ij} = EQ_{ij}^{(0)}$, where $Q^{(0)}$ is the scalar eigenmode of the Laplacian. Here we perform the scalar-vector-tensor decomposition in k-space, where $Q^{(0)} = \exp\left[i\boldsymbol{k}\cdot\boldsymbol{x}\right]$. We decompose the energy momentum tensor (EMT) as

$$T^{\mu\nu} = (\rho + p)u^\mu u^\nu + pg^{\mu\nu} + \Sigma^{\mu\nu}, \tag{4.3}$$

[†]The material in this Chapter is partially reproduced from my Master's thesis [1] and based on standard textbooks and reviews on cosmological perturbation theory and inflation [2, 3, 4].

where $\Sigma^{\mu\nu}$ is the anisotropic stress. There is no longer a preferred coordinate system for spatial averages if we go over to a perturbed Universe. We did not yet specify a specific **gauge** for the coordinates used in (4.2) but have rather chosen an arbitrary coordinate system applicable throughout the whole space-time.
We can furthermore define density and pressure perturbation as

$$\rho(\eta, x_i) = \bar{\rho}(\eta) + \delta\rho(\eta, x_i), \qquad p(\eta, x_i) = \bar{p}(\eta) + \delta p(\eta, x_i). \tag{4.4}$$

Gauge transformations can be described as first order (infinitesimal) changes ξ^μ in the coordinates

$$\tilde{x}^\mu = x^\mu + \xi^\mu, \tag{4.5}$$

which can be split up into time and space part

$$\tilde{x}^0 = x^0 + T(x^\mu), \qquad \tilde{x}^i = x^i + L^i(x^\mu). \tag{4.6}$$

The line element has to be conserved under this transformation and hence we can write down the transformation law of a general tensor under this change of coordinates

$$\tilde{Q}_{\mu\nu}(\tilde{x}^\gamma) = \frac{\partial x^\alpha}{\partial \tilde{x}^\mu}\frac{\partial x^\beta}{\partial \tilde{x}^\nu} Q_{\alpha\beta}(\tilde{x}^\gamma - \xi^\gamma). \tag{4.7}$$

The metric pertrubations transform as

$$\tilde{A} = A - T' - \mathcal{H}T \tag{4.8}$$
$$\tilde{B} = B + L' + kT \tag{4.9}$$
$$\tilde{D} = D - \frac{k}{3}L - \mathcal{H}T \tag{4.10}$$
$$\tilde{E} = E + kL \tag{4.11}$$

and the perturbations in the energy momentum tensor as

$$\delta\tilde{\rho} = \delta\rho - \rho' T, \tag{4.12}$$
$$\delta\tilde{p} = \delta p - p' T, \tag{4.13}$$
$$\tilde{v} = v + L'. \tag{4.14}$$

The scalar field, which will be the driving force of inflation, transforms as

$$\delta\tilde{\phi} = \delta\phi - \phi' T. \tag{4.15}$$

4.1.1. Fixing the Gauge

To proceed in our goal of deriving the spectrum of fluctuations from inflation we have to use a convenient gauge. Thus we will briefly discuss three important gauges.

Newtonian Gauge

This gauge is defined by $\tilde{B} = \tilde{E} = 0$. Renaming the remaining two scalar perturbations $A \to \Psi$ and $D \to -\Phi$, the metric then reduces to the form

$$\mathrm{d}s^2 = a^2\left\{-(1+2\Psi)\mathrm{d}\eta^2 + (1-2\Phi)\mathrm{d}x_i\mathrm{d}x_j\right\} \tag{4.16}$$

In the absence of anisotropic stress we furthermore have $\Phi = \Psi$. There is no remaining gauge ambiguity, i.e. the gauge is completely fixed by the transformation

$$L = -\frac{E}{k}, \qquad T = -\frac{B}{k} + \frac{E'}{k^2}, \tag{4.17}$$

where B and E are evaluated in an arbitrary gauge. Some important equations following from the Einstein field equations are

$$-k^2\Phi = 4\pi G a^2 \left[3\mathcal{H}(\bar{\rho}+\bar{p})\frac{v_{\rm N}}{k} + \delta\rho_{\rm N}\right], \tag{4.18}$$

$$\Phi' + \mathcal{H}\Psi = 4\pi G a^2 (\bar{\rho}+\bar{p})\,\frac{v_{\rm N}}{k}, \tag{4.19}$$

$$k^2(\Phi-\Psi) = 8\pi G a^2 \Sigma. \tag{4.20}$$

On small scales ($k \ll \mathcal{H}$) we can neglect the first term on the rhs of the first equation to obtain a Poisson equation for the expanding Universe

$$-k^2\Phi = 4\pi G a^2 \delta\rho_{\rm N}. \tag{4.21}$$

Comoving Gauge

This gauge is defined such that the momentum density T^0_i vanishes. We have one further gauge freedom, which we can use to set $\tilde{E}=0$ and get the following transformation

$$L = -\frac{E}{k}, \qquad\qquad T = \frac{v-B}{k}. \tag{4.22}$$

The two remaining scalar perturbations are renamed as $A \to \xi$ and $D \to \zeta$, where ζ is known as the **curvature perturbation**. We quote only two Einstein and one conservation equation for later use

$$k^2\left(\zeta + \mathcal{H}\frac{v_{\rm com}}{k}\right) = 4\pi G a^2 \delta\rho_{\rm com}, \tag{4.23}$$

$$\mathcal{H}\xi = \zeta', \tag{4.24}$$

$$(\bar{\rho}+\bar{p})\xi = -\delta p + \frac{2}{3}\Sigma. \tag{4.25}$$

Thus in absence of anisotropic stress and pressure perturbations we have $\xi = 0$. While being useful for the description of perturbations outside horizon, comoving gauge has the disadvantage that scalar field fluctuations vanish $\delta\phi_{\rm com} = 0$.

Spatially Flat Gauge

In spatially flat gauge, we set $\tilde{D} = \tilde{E} = 0$. We will employ spatially flat gauge only to calculate the evolution of fluctuations in the inflationary scalar field and will thus only consider the evolution equation of a scalar field in this gauge

$$\delta\phi'' + 2\mathcal{H}\delta\phi + \left(k^2 + a^2 V_{,\phi\phi}\right)\delta\phi = (A' - kB) - 2a^2 V_{,\phi} A. \tag{4.26}$$

4.2. Inflation - The Initial Conditions

4.2.1. Inflation in a Nutshell

Inflation was proposed by [6] to account for the large scale homogeneity and horizon problem present in the big bang paradigm. He argued that shortly after **big bang** the Universe must undergo an epoch of accelerated expansion $\ddot{a} > 0$ which should be over at $t \approx 10^{-34}$ s. During this expansion the comoving Hubble length $1/\mathcal{H}$ decreases with time while the metric approaches that of a flat isotropic Robertson-Walker Universe. From the first Friedmann equation (2.15) one immediately sees that the field driving inflation needs to come along with negative pressure.

The easiest model of inflation is based on a Universe dominated by a single scalar field ϕ, the **inflaton field**, whose action is given by

$$S = \int \mathrm{d}^4x\sqrt{-g}\left[\frac{M_{\mathrm{pl}}^2 R}{2} - X - V(\phi)\right] \tag{4.27}$$

where $X = -g^{\mu\nu}\partial_\mu\phi\partial_\nu\phi$ is the canonical kinetic term, V is the potential and $M_{\mathrm{pl}} = (8\pi G)^{-1/2}$ is the Planck mass. From the Lagrangian of the inflaton field one can derive pressure and density

$$p_\phi = \frac{\phi'^2}{2a^2} - V(\phi), \qquad \rho_\phi = \frac{\phi'^2}{2a^2} + V(\phi). \tag{4.28}$$

The equation of motion is the Klein-Gordon equation, that in an expanding Universe has an additional friction term

$$\phi'' + 2\mathcal{H}\phi' + V_{,\phi}(\phi) = 0. \tag{4.29}$$

Inflation stretches all lengths exponentially by a certain **number of** e**-foldings** $N = \ln(a_{\mathrm{f}}/a_{\mathrm{i}}) \approx 75$, where a_{i} and a_{f} are the expansion factors at begin and end of inflation, respectively. When a mode with comoving wavelength $1/k$ becomes comparable to the comoving Hubble length $1/\mathcal{H}$, it will cross the **horizon**[1] and will remain unchanged until it reenters the horizon after the end of inflation.
One of the simplest inflationary models, **slow-roll inflation**, states that the scalar field approaches the minimum of its potential by slowly rolling down the potential. The first slow roll parameter describes the deviations from the de Sitter case $w_\phi = p_\phi/\rho_\phi = -1$

$$\epsilon = \frac{3}{2}(1 + w_\phi) = 4\pi G\left(\frac{V_{,\phi}}{V}\right)^2. \tag{4.30}$$

The slowly rolling field has to satisfy $\dot{\phi} \ll 1$, which is described by the second slow roll parameter

$$\eta = \frac{\mathrm{d}^2\phi}{\mathrm{d}t^2} = \frac{\phi''}{\mathcal{H}\phi'} - 1 = 8\pi G\frac{V_{,\phi\phi}}{V}. \tag{4.31}$$

Successfull inflation requires $\epsilon \ll 1$ and $\eta \ll 1$. At the end of inflation the scalar field starts to oscillate and by doing so, it loses its energy and creates particles. To lowest order in the slow roll parameters we have

$$\epsilon = \frac{3\dot{\phi}^2}{2a^2V}, \qquad \dot{\phi} = -\frac{a^2V_{,\phi}}{3\mathcal{H}}. \tag{4.32}$$

The simplest model for exponential expansion would be a de Sitter Universe with $H = \text{const.}$ and $a \propto \exp[Ht]$. In this scenario we have $\epsilon = \eta = 0$, but inflation would last forever. Thus we need a quasi de Sitter expansion to allow for a graceful exit from inflation. Inflation can be ended by violation of the slow roll conditions, i.e. when $\epsilon \approx 1$. This could happen when the field comes to a point where the kinetic energy starts to dominate over the potential energy.

4.2.2. Perturbations from Inflation

We already noted that the concept of inflation can account both for the horizon and the flatness problem. Another important advantage of having inflation in the early Universe is that it can produce the seeds for structure formation in the Universe. These fluctuations arise as zero point fluctuations of a scalar field and are then stretched by the exponential expansion

[1] The horizon scale determines over which distances physical processes can be in causal contact at a given cosmological time and is usually of order $\mathcal{H}^{-1}$.

to become classical at horizon crossing. As a first step we will consider the relation between Newtonian potential Φ and curvature perturbation ζ

$$\delta\rho_{\text{com}} = \delta\rho_{\text{N}} - \rho'_{\text{N}} T_{\text{N}\to\text{com}} = \delta\rho_N + 3\mathcal{H}(\bar{\rho}+\bar{p})\frac{v_N}{k}, \tag{4.33}$$

where we used continuity equation $\bar{\rho}' = -3\mathcal{H}(\bar{\rho}+\bar{p})$.
Using the above result in Eq. (4.18) leads to

$$-k^2\Phi = 4\pi G a^2 \delta\rho_{\text{com}}. \tag{4.34}$$

With the Poisson equation in comoving gauge (4.23) we can derive

$$\zeta + \mathcal{H}\frac{v_{\text{com}}}{k} = \Phi. \tag{4.35}$$

In Newtonian gauge $E = 0$ and hence $L_{N\to\text{com}} = 0$, which implies $v_{\text{com}} = v_{\text{N}} + L'_{N\to\text{com}} = v_{\text{N}}$.

$$\zeta = -\Phi - \frac{2}{3}\frac{\mathcal{H}^{-1}\Phi' + \Psi}{1+\omega} \tag{4.36}$$

Here we used (4.18) and the Friedmann equation for the smooth background

$$\mathcal{H}^2 = \frac{8\pi G a^2}{3}\bar{\rho}. \tag{4.37}$$

If we furthermore neglect anisotropic stress $\Sigma = 0$ for a Universe dominated by ideal fluids, we obtain $\Phi = \Psi$ and thus

$$\Phi = -\frac{3+3\omega}{5+3\omega}\zeta. \tag{4.38}$$

Thus we have the well known result that in matter domination ($w = 0$) $\zeta = -5/3\Phi$. We can now use above results to show that curvature perturbation is constant outside horizon. To do so, we rewrite the evolution and conservation equations for the curvature perturbation (4.23) and (4.24) to yield

$$\zeta' = \mathcal{H}\xi = -\frac{\mathcal{H}\delta p_{\text{com}}}{\bar{\rho}+\bar{p}} \tag{4.39}$$

We will now show that this quantity is very small $|\zeta'| \ll \mathcal{H}\zeta$ outside horizon, i.e. for $k/\mathcal{H} \to 0$. Assuming vanishing entropy perturbation, we have $\delta p_{\text{com}} = c_s^2 \delta\rho_{\text{com}}$ and equation (4.34) as well as (4.39) lead to

$$\zeta' = \frac{c_s^2 k^2 \mathcal{H}\Phi}{4\pi G a^2(\bar{\rho}+\bar{p})} = -\frac{2}{5+3\omega}\left(\frac{c_s k}{\mathcal{H}}\right)^2 \mathcal{H}\zeta. \tag{4.40}$$

So we in fact see, that ζ' vanishes outside horizon and hence $\zeta = \text{const}$.
We now want to calculate the spectrum of the metric perturbation that are produced by the scalar field driving inflation. To calculate these zero point fluctuations we have to transform to spatially flat gauge, since the scalar field fluctuation vanishes in comoving gauge. This implies for any transformation to comoving gauge

$$0 = \delta\phi_{\text{com}} = \delta\phi_{\text{flat}} - T_{\text{flat}\to\text{com}}\phi' \Rightarrow T_{\text{flat}\to\text{com}} = \frac{\delta\phi_{\text{flat}}}{\phi'}. \tag{4.41}$$

The sense of using the spatially flat gauge becomes obvious when writing down the equation which relates the curvature perturbation to the scalar field

$$\zeta = D - \frac{k}{3}L - \mathcal{H}T = D + \frac{E}{3} - \mathcal{H}T_{\text{flat}\to\text{com}} = -\mathcal{H}\frac{\delta\phi_{\text{flat}}}{\phi'}. \tag{4.42}$$

Now that we know how to calculate the curvature perturbation from the scalar field we can derive the actual fluctuations. As already noted, the evolution equation for the scalar field

simplifies if we assume slow-roll inflation and neglect all terms proportional to the slow-roll parameters

$$\delta\phi'' + 2\mathcal{H}\delta\phi'' + k^2\delta\phi = 0. \tag{4.43}$$

Introducing $y = a\delta\phi$ and using $a''/a \approx 2\mathcal{H}^2$ with $\eta \approx -\mathcal{H}^{-1}$ we can simplify this to obtain the **Mukhanov-Sasaki equation**

$$y'' + \left(k^2 - \frac{2}{\eta^2}\right) y = 0. \tag{4.44}$$

On small scales the term proportional to k^2 will dominate and we obtain an harmonic oscillator equation for Minkowski space, which can be quantised using creation $\hat{a}^\dagger$ and annihilation operators $\hat{a}$ with the usual bosonic commutation relations

$$\left[a(\boldsymbol{k}), a^\dagger(\boldsymbol{k}')\right] = (2\pi)^3\delta^{(\mathrm{D})}(\boldsymbol{k} + \boldsymbol{k}'). \tag{4.45}$$

A general state is described by a superposition of both operators

$$\hat{y}(\boldsymbol{k}, \eta) = \lambda(k, \eta)\hat{a}(\boldsymbol{k}) + \lambda^\dagger(k, \eta)\hat{a}^\dagger(\boldsymbol{k}). \tag{4.46}$$

We can now calculate the variance of the ground state for the harmonic oscillator by calculating the expectation values in the vacuum

$$\left\langle 0|\hat{y}\hat{y}^\dagger|0\right\rangle - \langle 0|\hat{y}|0\rangle^2 = \left\langle 0|\hat{y}\hat{y}^\dagger|0\right\rangle = |\lambda(k)|^2 . \tag{4.47}$$

The classical solution to equation (4.46) is given by

$$\lambda(k) = \frac{1}{\sqrt{2k^3}} (\mathrm{i} - k\eta) \exp\left[-\mathrm{i}\, k\eta\right] = \frac{1}{\sqrt{2k^3}} \left(\mathrm{i} - \frac{k}{\mathcal{H}}\right) \exp\left[-\mathrm{i}\, \frac{k}{\mathcal{H}}\right]. \tag{4.48}$$

Here we picked a solution to match the vacuum at early times, i.e., in Minkowski space. This choice for the vacuum is known as **Bunch-Davies vacuum**. The small $k/\mathcal{H} \to \infty$ and large scale $k/\mathcal{H} \to 0$ limits of the mode function are

$$|\lambda(k)| = \frac{1}{\sqrt{2k}}, \qquad\qquad |\lambda(k)| = \frac{\mathcal{H}}{\sqrt{2k^3}}. \tag{4.49}$$

Here we neglected the phase factor, which cancels in expectation values. Since we are interested in the classical solution after horizon crossing, we can use the large scale limit and (4.42) to obtain

$$\zeta = \frac{-\mathrm{i}\,\mathcal{H}^2}{\sqrt{2k^3}a\phi'}. \tag{4.50}$$

From this quantity we can derive the variance or **power spectrum**[2] of the curvature fluctuation

$$\langle\zeta(\boldsymbol{k})\zeta(\boldsymbol{k}')\rangle = (2\pi)^3\delta^{(\mathrm{D})}(\boldsymbol{k} + \boldsymbol{k}')\frac{2\pi^2}{k^3}\Delta^3_\zeta(k) \tag{4.51}$$

where

$$\Delta^2_\zeta(k) = \frac{k^3\,|\zeta|^2}{2\pi^2} = \frac{G}{\pi\epsilon}\left(\frac{\mathcal{H}}{a}\right)^2, \tag{4.52}$$

where we used $4\pi G\phi'^2 = \epsilon\mathcal{H}^2$. Since the Hubble parameter $H = \mathcal{H}/a$ is approximately constant during inflation the variance is almost scale invariant. Furthermore we derived above that

[2] There are two definitions of the power spectrum in the literature. The rest of this Thesis mainly uses $P(k)$, the power per unit k-space element $\mathrm{d}^3k/(2\pi)^3$, which is related to the logarithmic power $\Delta^2(k)$ used here as

$$P(k)\frac{\mathrm{d}^3k}{(2\pi)^3} = P(k)\frac{4\pi k^3}{(2\pi)^3}\mathrm{d}\ln k = \Delta^2(k)\mathrm{d}\ln k \Rightarrow \Delta^2(k) = \frac{k^3}{2\pi^2}P(k)$$

the curvature perturbation is frozen outside the horizon. The reason for this scale independence is that the perturbations cross horizon very fast and no physical processes can imprint their scale.
Relating the logarithmic derivative of Δ_ζ^2 at horizon crossing $k/\mathcal{H} = 1$ to the slow roll parameters we can derive the slope

$$n_s - 1 = \left.\frac{\mathrm{d}\ln\Delta_\zeta^2}{\mathrm{d}\ln k}\right|_{k=\mathcal{H}} = -4\epsilon - 2\eta. \tag{4.53}$$

This guides us to make an power law ansatz for the power spectrum

$$\Delta_\zeta^2(k) \propto k^{n_s-1}. \tag{4.54}$$

The value $n_s = 1$ is predicted by slow roll inflation $\epsilon \ll 1, \eta \ll 1$ and corresponds to the Harrison-Zeldovich or **scale free spectrum**. To calculate the actual density perturbation in Newtonian gauge during matter domination $w = 0$ we simply use Poisson equation $-k^2\Phi = 4\pi G a^2 \bar{\rho}\delta_{\mathrm{com}} = \frac{3}{2}\mathcal{H}^2\delta_{\mathrm{com}}$

$$\delta_{\mathrm{com}} = -\frac{2}{3}\left(\frac{k}{\mathcal{H}}\right)^2 \Phi = \frac{2}{5}\left(\frac{k}{\mathcal{H}}\right)^2 \zeta. \tag{4.55}$$

Hence the power spectrum of the density fluctuations in comoving gauge is given by

$$\Delta_\delta^2(k) = \frac{4}{25}\left(\frac{k}{\mathcal{H}}\right)^4 \Delta_\zeta^2(k) \quad \Rightarrow \quad P_\delta(k) \propto k^{n_s}. \tag{4.56}$$

4.3. Evolution of the Primordial Spectrum

In the last section we developed an understanding of the shape of the perturbations at the moment when a mode crosses the horizon. We saw that the modes outside horizon do not grow both in matter and in radiation domination. But modes entering during radiation domination will grow as $\delta \propto \ln\eta$, whereas during matter domination the growth scales as $\delta \propto \eta^2$. So the amplitude of small scale (high k) modes entering during radiation domination will be suppressed compared to the modes entering only after matter radiation equality. A convenient way to express how the amplitude of a certain mode changes by the cosmological evolution is the **transfer function**

$$T(k,\eta) = \frac{\delta(k,\eta)}{\delta(k,\eta_e)}. \tag{4.57}$$

Here we used η_e to denote the time of horizon entry, given by $\eta_e \propto k^{-1}$. The processed power spectrum then is given by

$$P(k,\eta) = T^2(k,\eta)P(k,\eta_e). \tag{4.58}$$

The transfer function will be close to unity on large scales and suppressed for small scales. We show the transfer function calculated for the cosmology under consideration in our simulations in Figure 4.1.
The reason for the different growth rates is that the species present in the Universe are not evolving independently after horizon crossing and have to be described by the Boltzmann equations, a coupled set of differential equations describing the densities and distribution functions of the relativistic and nonrelativistic species. There are fitting functions for $T(k)$ in the literature [7, 8] and numerical codes like `CMBFAST` [9] or `CAMB` [10].
BBKS [7] proposed the following fit for the transfer function

$$T(k) = \frac{\log 1 + 2.34q}{2.34q}\left[1 + 3.89q + (16.1q)^2 + (5.46q)^3 + (6,71q)^4\right]^{1/4}, \tag{4.59}$$

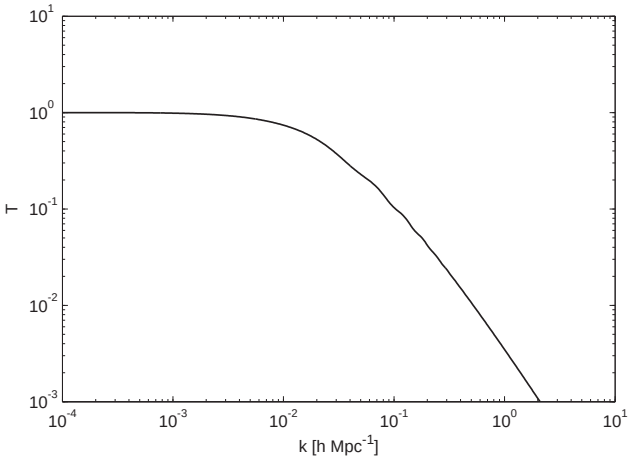

Figure 4.1.: Transfer function for our fiducial cosmology.

where $q = k/\Gamma/\ h\mathrm{Mpc}^{-1}$ and $\Gamma = \Omega_\mathrm{m} h \exp\left[-\Omega_\mathrm{b} - \sqrt{2h}\Omega_\mathrm{b}/\Omega_\mathrm{m}\right]$. It does not contain the BAO wiggles and can thus be used as a no-wiggle template to highlight the effect of the BAO wiggles in measured power spectra and perturbation theory.
We will compare measured power spectra to the matter power spectrum predicted by slow roll inflation

$$P_\mathrm{i}(k) = Ak^{n_\mathrm{s}} \tag{4.60}$$

Using the transfer function we calculate the normalisation A of the power spectrum by demanding for the right root mean square overdensity within spheres of $R = 8h^{-1}\mathrm{Mpc}$

$$\sigma_R^2 = \frac{4\pi V}{(2\pi)^3} \int dk A k^{n_\mathrm{s}+2} T^2(k) \left|W_R(k)\right|^2 . \tag{4.61}$$

Here $W_R(k)$ is the Fourier transform of the top hat window function.

4.4. Beyond Slow-Roll: Primordial non-Gaussianity

In the above section we introduced the concepts for the simplest possible inflationary model and calculated the two point function of curvature fluctuations at the end of inflation.
Primordial non-Gaussianity refers to the fact that the linear initial fluctuations might have a non-vanishing three point function or bispectrum

$$\langle \zeta(\boldsymbol{k}_1)\zeta(\boldsymbol{k}_2)\zeta(\boldsymbol{k}_3)\rangle = (2\pi)^3 B_\zeta(k_1, k_2, k_3)\delta^{(\mathrm{D})}(\boldsymbol{k}_1 + \boldsymbol{k}_2 + \boldsymbol{k}_3) \tag{4.62}$$

, where the delta function arises from translation invariance and rotational invariance enables us to write the amplitude as a function of the magnitudes of the momenta.
As shown in [11], the non-Gaussianity of single field slow-roll models is extremely small and possibly not-detectable. More generally [12] showed that general single field models obey the **consistency relation**

$$\lim_{k_1 \to 0} \langle \zeta(\boldsymbol{k}_1)\zeta(\boldsymbol{k}_2)\zeta(\boldsymbol{k}_3)\rangle = (2\pi)^3 \delta^{(\mathrm{D})}(\boldsymbol{k}_1 + \boldsymbol{k}_2 + \boldsymbol{k}_3)(n_\mathrm{s} - 1) P_\zeta(\boldsymbol{k}_1) P_\zeta(\boldsymbol{k}_3). \tag{4.63}$$

There is a multitude of inflationary models and their bispectra can be characterised by shape S and amplitude f_NL. The shape function S is defined through [2]

$$B_\zeta(k_1, k_2, k_3) = \frac{18}{5} f_\mathrm{NL} \left(2\pi^2\right)^2 \frac{\left[\Delta_\zeta^2(k^*)\right]^2}{(k_1 k_2 k_3)^2} S(k_1, k_2, k_3), \tag{4.64}$$

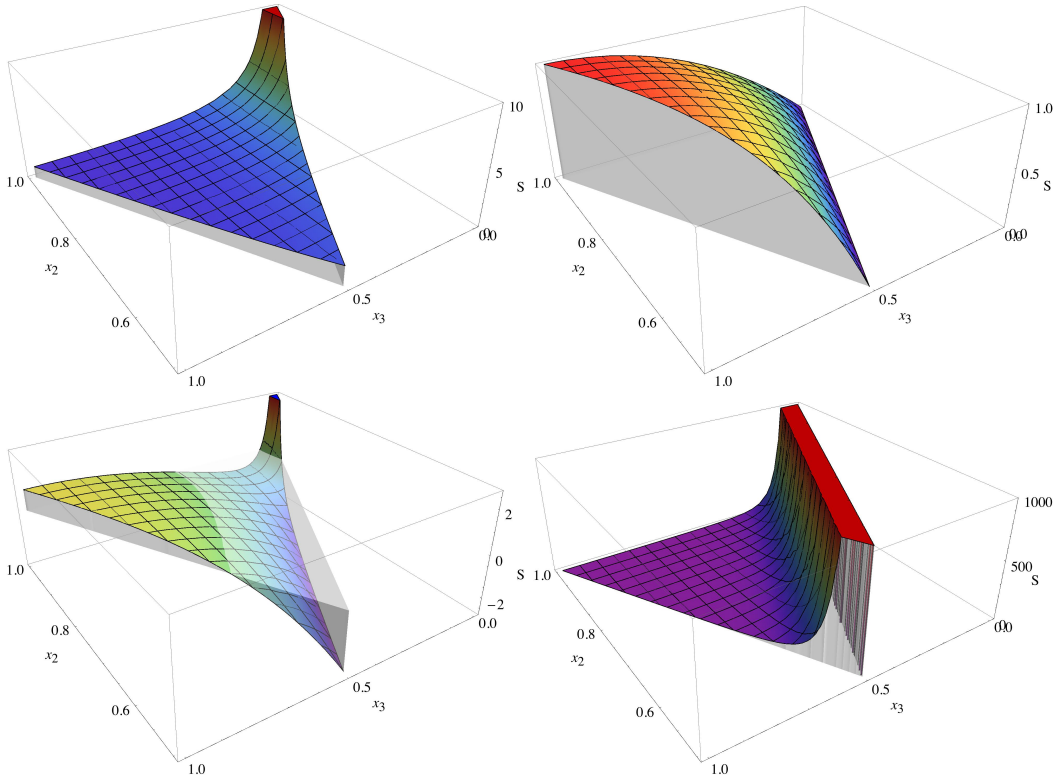

Figure 4.2.: Shape functions of the primordial bispectra. *Top left:* Local *Top right:* Equilateral *Bottom left:* Orthogonal *Bottom right:* Folded

where k^* is a fiducial momentum scale. The shape is now characterised as the behaviour of S under changes of $x_2 = k_2/k_1$ and $x_3 = k_3/k_1$ at fixed $K = 1/3(k_1 + k_2 + k_3)$. To avoid degeneracies we can set $0 < x_3 < x_2 < 1$. Then the triangle inequality furthermore restricts x_3 to $1 - x_2 < x_3 < x_2$ and x_2 to $x_2 > 0.5$. The shape function is usually normalised to the equilateral configuration $k_1 = k_2 = k_3 = K$

$$S(K, K, K) = 1. \tag{4.65}$$

Let us briefly discuss a few possible mechanisms that could lead to a detectable amount of non-Gaussianity. In Fig. 4.3 we show the triangle configurations corresponding to the shapes of primordial bispectra. In Fig. 4.2 we show the shape functions for the local, equilateral, folded and orthogonal templates.

4.4.1. Higher Order Kinetic Terms

One can imagine generalizations of the inflationary Lagrangian of the form.

$$S = \int \mathrm{d}^4x\sqrt{-g}\left[\frac{M_{\mathrm{pl}}^2 R}{2} + P(X, \phi)\right], \tag{4.66}$$

where $P(X, \phi)$ can contain higher-derivative operators such as $\partial_\mu\phi\partial^\mu\phi/\Lambda^{4n-4}$ but not higher order operators of the form ϕ^n/Λ^{n-4} in order not to spoil the inflationary background solution. The higher-derivative operators leave the background solution unaffected but can lead to strong interactions.
One expample of such a modification is Dirac-Born-Infeld (DBI) inflation arising from string

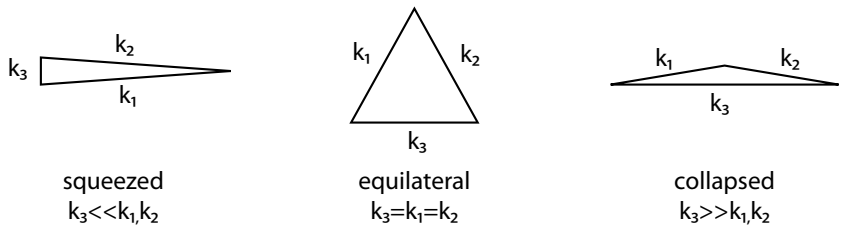

Figure 4.3.: Dominant triangle configurations of the local (squeezed), equilateral and folded non-Gaussianities.

theory, where

$$P(X,\phi) = \frac{\Lambda^4}{f(\phi)}\sqrt{1 - f(\phi)\frac{X}{\Lambda^4}} - V(\phi). \tag{4.67}$$

These models can feature small speeds of sound

$$c_s^2 = \frac{P_{,X}}{P_{,X} + 2XP_{,XX}} \ll 1 \tag{4.68}$$

and lead to large equilateral non-Gaussianity, i.e. the correlation between the modes is strong if all modes are roughly of the same order. Note that the non-Gaussianity is created inside the horizon in this case. The shape function can be approximated as

$$S^{(\text{equil.})}(k_1,k_2,k_3) = \left(\frac{k_1}{k_2} + 5 \text{ cyc.}\right) - \left(\frac{k_1^2}{k_2 k_3} + 2 \text{ cyc.}\right) - 2 \tag{4.69}$$

and $f_{\text{NL}}^{(\text{equil.})} \approx 1/c_s^2$. The current CMB limits on equilateral non-Gaussianity are [13]

$$-125 < f_{\text{NL}}^{(\text{equil.})} < 435 \tag{4.70}$$

at 95 % confidence level.

4.4.2. Multifield Inflation

In principle inflation can feature more than one field [14]. Let us consider the particular case of two fields $\delta\phi$ and $\delta\sigma$. In this case the bispectrum arises from the non-linear relation between the curvature perturbation and one of the fields which can be calculated in the δN formalism [15]. The δN formalism accounts for the fact that all the fields, even those not sourcing the Hubble parameter, can determine the end of inflation and thus the number of e-foldings. Thus we have for the curvature perturbation [16]

$$\zeta \propto \delta N = N_{,\phi}\delta\phi + N_{,\sigma}\delta\sigma + N_{,\sigma\sigma}\delta\sigma\delta\sigma. \tag{4.71}$$

where we set $N_{,\phi\phi} = N_{,\phi\sigma} = 0$. The power spectrum is thus given by

$$P_\zeta(k) = N_{,\phi}^2 P_{\delta\phi}(k) + N_{,\sigma}^2 P_{\delta\sigma}(k) \tag{4.72}$$

and the bispectrum by

$$B_\zeta(k_1,k_2,k_3) = 2N_{,\sigma\sigma}N_{,\sigma}^2\left[P_{\delta\sigma}(k_1)P_{\delta\sigma}(k_2) + 2 \text{ cyc.}\right]. \tag{4.73}$$

If we assume $P_{\delta\sigma}/P_\zeta = r_\sigma = \text{const.}$ we can write

$$B_\zeta(k_1,k_2,k_3) = 2N_{,\sigma\sigma}N_{,\sigma}^2 r_\sigma^2\left[P_\zeta(k_1)P_\zeta(k_2) + 2 \text{ cyc.}\right]. \tag{4.74}$$

and the shape function is given by

$$S^{(\mathrm{loc.})}(k_1, k_2, k_3) = \frac{1}{3}\left(\frac{k_1^2}{k_2 k_3} + 2 \text{ cyc.}\right). \tag{4.75}$$

We can conclude that the multifield model leads to local type non-Gaussianity of amplitude $f_{\mathrm{NL}}^{(\mathrm{loc.})} = 5/3 N_{,\sigma\sigma} N_{,\sigma}^2 r_\sigma^2$. If either $N_{,\sigma}$, $N_{,\sigma\sigma}$ or r_σ are k-dependent, this model can furthermore lead to scale dependent f_{NL} [16]. The shape is peaked in the squeezed limit $k_3 \ll k_1 \approx k_2$ and describes a coupling between the small scale power spectrum and a long wavelength background mode. This leads to a distinct imprint on the clustering of dark matter haloes as we will discuss in detail in Ch. 6. Note that this shape can also generated from the local quadratic model

$$\zeta(\boldsymbol{x}) = \zeta_{\mathrm{G}}(\boldsymbol{x}) + \frac{3}{5} f_{\mathrm{NL}}^{(\mathrm{loc.})} \left[\zeta_{\mathrm{G}}^2(\boldsymbol{x}) - \left\langle \zeta_{\mathrm{G}}^2 \right\rangle\right]. \tag{4.76}$$

One of the strongest constraints on local non-Gaussianity comes from LSS [17]

$$-31 < f_{\mathrm{NL}}^{(\mathrm{loc.})} < 70 \tag{4.77}$$

at 95 % confidence level.

4.4.3. Curvaton Scenario

In the curvaton scenario [18, 19] there is a light spectator field during inflation, denoted the **curvaton**. This field thus has isocurvature initial conditions. The adiabatic density perturbations are generated after inflation, for instance during radiation domination and generate an accompanying curvature fluctuation. This model allows for residual non-vanishing isocurvature perturbations but they are not mandatory. The fluctuations in the energy density are given by the curvaton potential, which we will assume to be quadratic

$$\rho_\sigma = \frac{m_\sigma^2}{2}(\sigma + \delta\sigma)^2 \Rightarrow \delta\rho_\sigma = \frac{m_\sigma^2}{2}(2\sigma\delta\sigma + \delta\sigma^2). \tag{4.78}$$

The total curvature receives contributions from both the inflaton and the curvaton, which contributes proportionally to its energy density fluctuations

$$\zeta(\boldsymbol{x}) = \zeta_\phi(\boldsymbol{x}) + \zeta_\sigma(\boldsymbol{x}) + \frac{3}{5} f_{\mathrm{NL}} \left[\zeta_\sigma(\boldsymbol{x}) - \langle \zeta_\sigma \rangle\right] \tag{4.79}$$

We see that this model also creates local type non-Gaussianities.

4.4.4. Non-standard Vacuum

The Bunch-Davies vacuum chosen in the above discussion of slow-roll inflation is not generic. In Eq. (4.48) we picked the solution that asymptotes to the lowest energy state in Minkowski space. However, any feature in the inflationary potential could lead to a new vacuum that is a mixture of the two states

$$\lambda(k) = \frac{1}{\sqrt{2k^3}}\left\{C_1 (\mathrm{i} - k\eta) \exp\left[-\mathrm{i}\, k\eta\right] + C_2 (\mathrm{i} + k\eta) \exp\left[\mathrm{i}\, k\eta\right]\right\}. \tag{4.80}$$

The shape generated by variations of the vacuum is generally related to the folded template [20]

$$S^{(\mathrm{fold.})} = \frac{1}{3}\left(\frac{1}{(k_1 + k_2 - k_3)^3} + 2 \text{ cyc.}\right) \tag{4.81}$$

4.4.5. Orthogonal Shape

Based on the effective field theory of multifield inflation [13] argued that derivative interactions can be efficiently probed by defining a shape orthogonal to the equilateral shape. Here the orthogonality is in terms of the shape scalar product

$$S_1 \cdot S_2 = \sum_k \frac{S_1(k_1, k_2, k_3) S_2(k_1, k_2, k_3)}{P(k_1)P(k_2)P(k_3)} \tag{4.82}$$

We can go even further and demand the shape to be orthogonal to both the local and the equilateral shape and obtain [2]

$$S^{(\text{orth.})}(k_1, k_2, k_3) = -3.84 \left(\frac{k_1^2}{k_2 k_3} + 2 \text{ cyc.} \right) + 3.94 \left(\frac{k_1}{k_2} + 5 \text{ cyc.} \right) - 11.1 \tag{4.83}$$

The CMB constraints on the amplitude of the orthogonal shape are [13]

$$-369 < f_{\text{NL}}^{(\text{orth.})} < 71 \tag{4.84}$$

at the 95 % confidence level.

Bibliography

[1] T. Baldauf, **The Galaxy-Dark Matter Connection**, Master's thesis, University of Zurich, 2009.

[2] D. Baumann, **TASI Lectures on Inflation**, *ArXiv e-prints* (July, 2009) [arXiv:0907.5424].

[3] W. Hu, **Covariant Linear Perturbation Formalism**, *ArXiv Astrophysics e-prints* (Feb., 2004) [astro-ph/].

[4] A. R. Liddle and D. H. Lyth, *Cosmological Inflation and Large-Scale Structure*. Cambridge Univ Pr, Apr., 2000.

[5] U. Seljak, **Lectures on Dark Matter**, 2000.

[6] A. H. Guth, **Inflationary universe: A possible solution to the horizon and flatness problems**, *Phys. Rev.* **D23** (1981) 347–356.

[7] J. M. Bardeen, J. R. Bond, N. Kaiser, and A. S. Szalay, **The Statistics of Peaks of Gaussian Random Fields**, *Astrophys. J.* **304** (1986) 15–61.

[8] D. J. Eisenstein and W. Hu, **Power Spectra for Cold Dark Matter and Its Variants**, *Astrophys. J.* **511** (Jan., 1999) 5–15, [astro-ph/].

[9] U. Seljak and M. Zaldarriaga, **A Line of Sight Approach to Cosmic Microwave Background Anisotropies**, *Astrophys. J.* **469** (1996) 437–444, [astro-ph/9603033].

[10] A. Lewis, A. Challinor, and A. Lasenby, **Efficient Computation of CMB anisotropies in closed FRW models**, *Astrophys. J.* **538** (2000) 473–476, [astro-ph/9911177].

[11] J. Maldacena, **Non-gaussian features of primordial fluctuations in single field inflationary models**, *Journal of High Energy Physics* **5** (May, 2003) 13, [astro-ph/].

[12] P. Creminelli and M. Zaldarriaga, **A single-field consistency relation for the three-point function**, *JCAP* **10** (Oct., 2004) 6, [astro-ph/].

[13] L. Senatore, K. M. Smith, and M. Zaldarriaga, **Non-Gaussianities in single field inflation and their optimal limits from the WMAP 5-year data**, *JCAP* **1** (Jan., 2010) 28, [arXiv:0905.3746].

[14] F. Vernizzi and D. Wands, **Non-Gaussianities in two-field inflation**, *JCAP* **5** (May, 2006) 19, [astro-ph/].

[15] M. Sasaki and E. D. Stewart, **A General Analytic Formula for the Spectral Index of the Density Perturbations Produced during Inflation**, *Progress of Theoretical Physics* **95** (Jan., 1996) 71–78, [astro-ph/].

[16] S. Shandera, N. Dalal, and D. Huterer, **A generalized local ansatz and its effect on halo bias**, *JCAP* **3** (Mar., 2011) 17, [arXiv:1010.3722].

[17] A. Slosar, C. Hirata, U. Seljak, S. Ho, and N. Padmanabhan, **Constraints on local primordial non-Gaussianity from large scale structure**, *JCAP* **8** (Aug., 2008) 31, [arXiv:0805.3580].

[18] D. H. Lyth, C. Ungarelli, and D. Wands, **Primordial density perturbation in the curvaton scenario**, *Phys. Rev.* **67** (Jan., 2003) 023503, [astro-ph/].

[19] D. H. Lyth and D. Wands, **Generating the curvature perturbation without an inflaton**, *Physics Letters B* **524** (Jan., 2002) 5–14, [hep-ph/01].

[20] X. Chen, **Primordial Non-Gaussianities from Inflation Models**, *Advances in Astronomy* **2010** (2010) [arXiv:1002.1416].

CHAPTER 5

Abundance and Clustering of Dark Matter Haloes

One of the major goals of observational cosmology is to extract information about fundamental physics and the composition of the Universe from the observed distribution of luminous matter in the Universe. Most of the interesting physical phenomena can be encoded in terms of modifications of the linear power spectrum of fluctuations. In Ch. 3 we saw how the non-linear matter spectra can be calculated from the linear power spectrum. Thus we are missing a theoretical model that relates the non-linear matter distribution to the luminous tracers. In the current standard paradigm for galaxy formation, galaxies form in the potential wells of virialized clumps of dark matter, because only there baryons can cool sufficiently fast [1]. Since the detailed baryonic processes governing galaxy formation are very complicated, it has become common to split the understanding of galaxy clustering into two separate steps: 1) the clustering of dark matter haloes as a function of a number of properties $\boldsymbol{P}$ 2) the occupation of haloes with galaxies as a function of galaxy type and halo properties $\boldsymbol{P}$.
In this chapter we will review the current understanding about the abundance and clustering of non-linear structures in the dark matter density field, with a focus on dark matter haloes. The phenomenological building blocks of the late time non-linear matter distribution are

- **halo** - virialized clumps of dark matter
- **filament** - streams of dark matter connecting the haloes
- **sheet** - faces spanned by the filaments
- **void** - the empty space between the haloes, filaments and sheets

The density of these building blocks is decreasing from top to bottom. In Fig. 5.1, we show the evolution of the particles associated with the most massive halo in one of our simulations from redshift $z = 20$ to its final configuration. One clearly sees how the final halo forms out of a large and fairly homogeneous Lagrangian patch and how the matter distribution collapses into the filamentary structure connecting to the halo.

5.1. Abundance of Haloes - The Mass Function

From the spherical collapse model we learned, that overdense regions in Lagrangian space will segregate from the homogeneous expansion and collapse into virialized objects. The abundance of such objects is an important prediction of the ΛCDM model and was first calculated in a

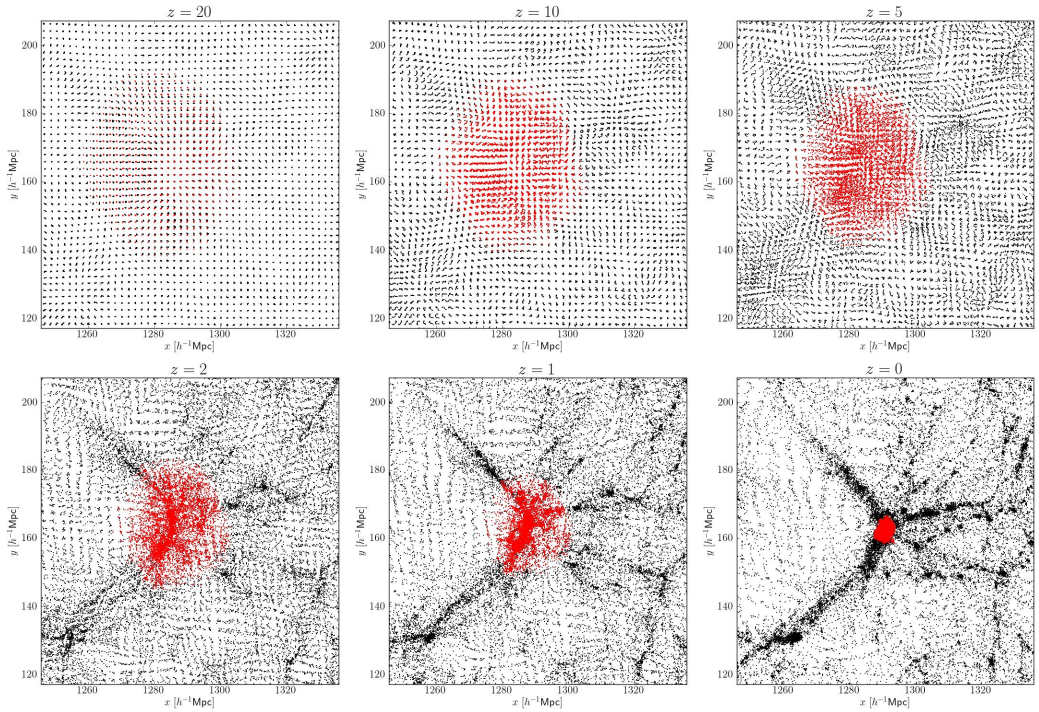

Figure 5.1.: Evolution of the particles surrounding the most massive halo in our simulation. The particles highlighted in red have been identified to belong to the halo by the FoF halo finder at redshift $z = 0$. This Figure also shows how the matter density field evolves from the fairly homogeneous distribution on the initial condition grid in Lagrangian space to the rich filamentary structure of the final Eulerian density field.

seminal paper by Press & Schechter [2]. The spherical collapse model tells us that a spherical region of size R whose present day linear overdensity is δ_c will collapse into a virialized object of mass

$$M = \frac{4\pi}{3} R^3 \bar{\rho}. \tag{5.1}$$

Here we neglected the overdensity, since it is negligible compared to the mean density in Lagrangian space. The above one-to-one relation between mass and radius will allow use the two interchangeably in the following. Let us first estimate the probability of finding a spherical region with a given density in a Gaussian random field. For this purpose we first calculate the rms amplitude of fluctuations at the scale R or mass M, smoothing the density field with a top hat window of size R

$$\sigma^2(M) = \int \frac{\mathrm{d}^3 q}{(2\pi)^3} P(q) W_{\mathrm{TH}}^2(kR) \tag{5.2}$$

Then the probability of finding a region that has an overdensity of δ_c is given by the probability density function of a Gaussian random variable

$$p(\delta|M) = \frac{1}{\sqrt{2\pi\sigma^2(M)}} \exp\left[-\frac{1}{2}\frac{\delta^2}{\sigma^2(M)}\right] \tag{5.3}$$

The probability for a region to exceed the density threshold δ_c is given by

$$P(>\delta_c|M) = \int_{\delta_c}^{\infty} \mathrm{d}\delta \; p(\delta|M) = \int_{\tilde{\nu}}^{\infty} \mathrm{d}x \; \exp\left[-\frac{x^2}{2}\right], \tag{5.4}$$

where $\tilde{\nu} = \delta_c/\sigma$ is the **peak height** or **significance**. Since $\sigma(M)$ is a decreasing function of mass for the vanilla ΛCDM model, small scale inhomogeneities have a larger rms amplitude

and are thus the first to cross the critical collapse density. Hence, structure formation happens in a **bottom up** scenario, where small scale objects collapse first and merge to form more and more massive objects as time proceeds. In Universes whose matter content is dominated by hot dark matter, structure formation follows a top down scenario, where large objects form first and subsequently disintegrate into smaller objects.
Since we are interested in the regions that form a halo of mass M, we need to account for the fact that a high overdensity of mass M might be part of a larger region containing mass $M + \mathrm{d}M$ that also exceeds the critical collapse density and could thus form a more massive halo. Thus, the fraction of regions that form haloes of mass M is given by

$$P(>\delta_\mathrm{c}|[M, M+\mathrm{d}M]) = |P(>\delta_\mathrm{c}|M+\mathrm{d}M) - P(>\delta_\mathrm{c}|M)| \approx -\frac{\mathrm{d}P}{\mathrm{d}M} \tag{5.5}$$

$$= -\frac{1}{\sqrt{2\pi}}\frac{\delta_\mathrm{c}}{\sigma^2}\exp\left[-\frac{\delta_\mathrm{c}^2}{2\sigma^2}\right]\frac{\mathrm{d}\sigma}{\mathrm{d}M} \tag{5.6}$$

The above argument accounts only for half of the mass in the Universe, since underdense regions never collapse. This can be formally seen by integrating the above formula over σ or $\tilde{\nu}$, yielding $1/2$. To correct for this problem, PS introduced an ad hoc factor of 2, that can be explained in the language of uncorrelated random walks.
To obtain the abundance of haloes of mass M,i.e. their **mass function**, we need to multiply this number by the maximum number of regions of mass M in a certain volume V containing mass M_tot, which is given by $N_\mathrm{max} = M_\mathrm{tot}/M$. Thus the maximum number density is $n_\mathrm{max} = M_\mathrm{tot}/M/V = \bar{\rho}/M$, which is independent of the norm volume.

$$n(M) = n_\mathrm{max}P(>\delta_\mathrm{c}|[M, M+\mathrm{d}M]) = -\sqrt{\frac{2}{\pi}}\frac{\bar{\rho}}{M}\frac{\delta_\mathrm{c}}{\sigma^2}\exp\left[-\frac{\delta_\mathrm{c}^2}{2\sigma^2}\right]\frac{\mathrm{d}\sigma}{\mathrm{d}M} \tag{5.7}$$

$$= \sqrt{\frac{2}{\pi}}\frac{\bar{\rho}}{M}\exp\left[-\frac{\tilde{\nu}^2}{2}\right]\frac{\mathrm{d}\tilde{\nu}}{\mathrm{d}M} \tag{5.8}$$

Sometimes the peak height is defined as $\nu = \tilde{\nu}^2$ and the corresponding PS mass function reads

$$n(M) = \sqrt{\frac{\nu}{2\pi}}\frac{\bar{\rho}}{M^2}\exp\left[-\frac{\nu}{2}\right]\frac{\mathrm{d}\ln\nu}{\mathrm{d}\ln M} \tag{5.9}$$

When compared to halo counts in N-body simulations the Press-Schechter formula underestimates the abundance of massive haloes. For this reason, Sheth & Tormen [3] (hereafter ST) devised an improved mass function

$$n(M) = A\sqrt{\frac{q\nu}{2\pi}}\left(1+\frac{1}{(q\nu)^p}\right)\frac{\bar{\rho}}{M^2}\exp\left[-\frac{q\nu}{2}\right]\frac{\mathrm{d}\ln\nu}{\mathrm{d}\ln M} \tag{5.10}$$

The parameters proposed by Sheth & Tormen are $q = 0.707$ $p = 0.3$ whereas $q = 1$ $p = 0$ gives the Press & Schechter mass function. The normalization of the mass function is given by the constraint that all mass in the universe is to be contained in haloes of some mass

$$\int \mathrm{d}M M n(M) = \bar{\rho}. \tag{5.11}$$

The condition $\nu(M_*) = \delta_\mathrm{c}^2/\sigma^2(M_*) = 1$ defines a typical halo mass $M_* \approx 5\times10^{12}\ h^{-1}M_\odot$. In Fig. 5.2 we show the mass function measured in N-body simulations in comparison to the theoretical mass function models described above. The plot clearly shows that the high mass tail of the mass function is suppressed at higher redshifts, i.e., high mass haloes form at late times. For the same reason a change in the normalization of density fluctuations σ_8 has a strong influence on the abundance of massive haloes. A detailed comparison between theoretical predictions and mass functions measured in N-body simulations is given in [4].

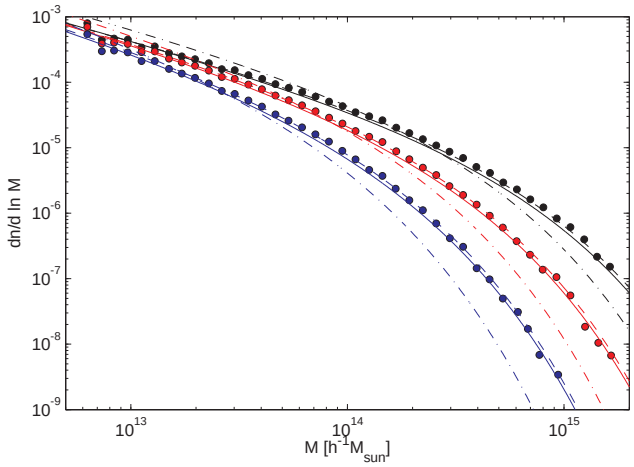

Figure 5.2.: Mass function from a N-body simulations at redshifts $z = 0, 1, 2$ from top to bottom (black, red, blue). The corresponding predictions for the ST and PS models are overplotted. The Solid line shows the fiducial parameters $p = 0.3, q = 0.707$, the dashed line shows $p = 0.1, q = 0.707$ and the dash-dotted line shows $p = 0, q = 1$ corresponding to the original PS mass function.

5.2. Local Eulerian Bias

The available bias models can be roughly classified by the evolutionary state they describe as Eulerian and Lagrangian and by their functional form as perturbative or non-perturbative. Below in Sec. 5.3, we will discuss the perturbative local Lagrangian bias model, which is a perturbative model and allows a mapping to the late time halo clustering, which we will discuss in Sec. 5.4. On top of these perturbative models there are exact models in Lagrangian space, e.g., the correlation of thresholded regions and the clustering of peaks, which we will discuss in Sec. 5.6 and Sec. 5.7, respectively. These models provide a richer phenomenology than the local models and allow for a convergence test of the expansion in Lagrangian space. Unfortunately, the link between the predictions of these models and the resulting clustering in Eulerian space has not yet been fully understood.

The final goal of any bias model is to describe the final Eulerian distribution of dark matter haloes in terms of the underlying linear or non-linear density fluctuations. The most general form of such a model is a functional, where the smoothed halo overdensity at a certain position is given in terms of the smoothed matter overdensity

$$\delta_{\mathrm{h}}(\boldsymbol{x}) = \mathcal{F}\left[\delta(\boldsymbol{x}')\right]. \tag{5.12}$$

This functional is not very instructive when one wants to make explicit predictions for the halo distribution and compare them to observations. Thus, it has become common practice to follow [5] in expanding the functional into a Taylor series which is local both in space and time

$$\delta_{\mathrm{h}}^{(\mathrm{E})}(\boldsymbol{x}) \approx \sum_{i=1}^{\infty} \frac{b_i^{(\mathrm{E})}}{i!} \left(\delta^i(\boldsymbol{x}) - \left\langle \delta^i \right\rangle\right), \tag{5.13}$$

where $b_i^{(\mathrm{E})}$ are the **Eulerian bias** parameters. Note that we are not explicitly writing the smoothing scale in the halo and matter density fields, since we have no way to deduce this smoothing scale from first principles. Furthermore the halo spectra should be independent of the smoothing scale on scales exceeding the smoothing scale.

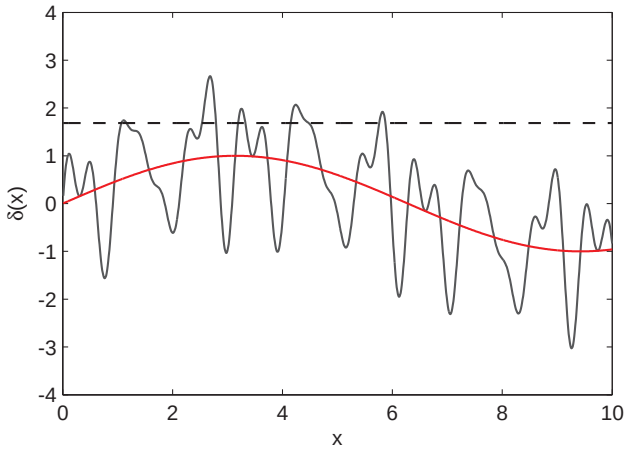

Figure 5.3.: Schematic picture of short wavelength fluctuations (black solid) in presence of a long wavelength mode (red solid). According to the spherical collapse argument, the regions exceeding the density threshold collapse to form virialized haloes.

5.3. Local Lagrangian Bias and the Peak-Background Split

Haloes form out of short wavelength fluctuations, i.e., small scale perturbations in the Lagrangian density field. The amplitude of these short wavelength fluctuations is modulated by long wavelength fluctuations as shown in Fig. 5.3. This separation into halo scale and large scale perturbations is denoted **peak-background split**. In presence of a positive long wavelength fluctuation, the collapse threshold δ_c for the short wavelength fluctuation is effectively reduced $\delta_c \to \delta_c - \delta_l$. In our above considerations on the mass function we saw the the abundance of collapsed objects depends on the peak height $\nu = \delta_c/\sigma$. In presence of a long wavelength mode the peak height is reduced. Since the mass function is a decreasing function of ν, the local abundance of objects is enhanced with respect to the background. Thus we can express the response of the protohalo number density on the presence of a long wavelength fluctuation through derivatives of the mass function with respect to the long wavelength amplitude

$$n(\boldsymbol{q}) = \bar{n} + \sum_{i=1}^{\infty} \frac{\partial^i \bar{n}}{\partial \delta_l^i} \left(\delta_l^i(\boldsymbol{q}) - \langle \delta_l^i \rangle \right) . \tag{5.14}$$

Hence we have for the overdensity

$$\delta_h^{(L)}(\boldsymbol{q}) = \frac{n(\boldsymbol{q})}{\bar{n}} - 1 = \sum_{i=1}^{\infty} \frac{b_i^{(L)}}{i!} \left(\delta_l^i(\boldsymbol{q}) - \langle \delta_l^i \rangle \right) , \tag{5.15}$$

where we identified the **Lagrangian bias** parameters as

$$b_i^{(L)} = \frac{1}{\bar{n}} \frac{\partial^i \bar{n}}{\partial \delta_l^i} = -\frac{1}{\bar{n}} \frac{\partial^i \bar{n}}{\partial \delta_c^i} . \tag{5.16}$$

In Ch. 7 we will generalize this concept to a general relativistic framework, where the long wavelength fluctuation can locally be interpreted as an effective curvature in an otherwise unperturbed Universe. If the mass function is universal, i.e., a function of peak height only, the derivative can be rewritten as a derivative with respect to ν. The above expression allows for an evaluation of the Lagrangian bias parameters in terms of any given mass function. Here we will for definiteness employ the ST mass function Eq. (5.10) and obtain for the first three bias parameters

$$b_1^{(L)} = \frac{2p}{\delta_c \left[(\nu q)^p + 1 \right]} + \frac{\nu q - 1}{\delta_c} , \tag{5.17}$$

$$b_2^{(\mathrm{L})} = \frac{2\left(2p^2 + 2\nu pq - p\right)}{\delta_c^2\left[(\nu q)^p + 1\right]} + \frac{\nu q(\nu q - 3)}{\delta_c^2}, \tag{5.18}$$

$$b_3^{(\mathrm{L})} = \frac{2\left(4p^3 + 6\nu p^2 q + 3\nu^2 pq^2 - 6\nu pq - p\right)}{\delta_c^3\left[(\nu q)^p + 1\right]} + \frac{\nu q\left(\nu^2 q^2 - 6\nu q + 3\right)}{\delta_c^3}. \tag{5.19}$$

Note that the above expansion is in terms of linearly evolved long wavelength perturbations. Had we written the bias expansion in terms of the initial Lagrangian density amplitudes, the bias parameters would have been rescaled as $\tilde{b}_i^{(\mathrm{L})} = b_i^{(\mathrm{L})}/D(z_\mathrm{i})$, where $D(z_\mathrm{i})$ is the growth factor of the Lagrangian time slice (see Ch. 8 for more details).

5.4. Relation Between Eulerian and Lagrangian Bias

The Eulerian bias model by itself is not predictive in the sense that the Eulerian bias parameters in Eq. (5.13) are free parameters that would have to be measured from the data. Under some simplifying assumptions we can however gain some insight on their amplitude by considering a mapping from the properties of the halo formation sites in Lagrangian space to the final evolved haloes. In Sec. 3.5.1 we saw that the mapping between the Lagrangian and Eulerian volume elements can be expressed as

$$[1 + \delta(\boldsymbol{x})]\,\mathrm{d}^3x = \mathrm{d}^3q. \tag{5.20}$$

Assuming that the haloes are comoving with the matter and that the number of haloes is conserved, we can write down a similar equation relating the halo overdensities in Lagrangian and Eulerian space

$$\left[1 + \delta_\mathrm{h}^{(\mathrm{E})}(\boldsymbol{x})\right]\mathrm{d}^3x = \left[1 + \delta_\mathrm{h}^{(\mathrm{L})}(\boldsymbol{q})\right]\mathrm{d}^3q. \tag{5.21}$$

Combining the two equation yields [6]

$$1 + \delta_\mathrm{h}^{(\mathrm{E})}(\boldsymbol{x}) = [1 + \delta(\boldsymbol{x})]\left[1 + \delta_\mathrm{h}^{(\mathrm{L})}(\boldsymbol{q})\right] \tag{5.22}$$

where the relation between $\boldsymbol{x}$ and $\boldsymbol{q}$ is given by the displacement field $\boldsymbol{\Psi}$ introduced in Eq. (3.124). Writing the Eulerian and Lagrangian bias models up to third order

$$\delta_\mathrm{h}^{(\mathrm{E})} = b_1^{(\mathrm{E})}\delta + \frac{b_2^{(\mathrm{E})}}{2!}\delta^2 + \frac{b_3^{(\mathrm{E})}}{3!}\delta^3 + \ldots \tag{5.23}$$

$$\delta_\mathrm{h}^{(\mathrm{L})} = b_1^{(\mathrm{E})}\delta_0 + \frac{b_2^{(\mathrm{E})}}{2!}\delta_0^2 + \frac{b_3^{(\mathrm{E})}}{3!}\delta_0^3 + \ldots \tag{5.24}$$

the problem reduces to a relation between the non-linear density perturbation δ and the linearly evolved Lagrangian density perturbation δ_0. The standard way to relate the Lagrangian and Eulerian overdensities is to employ the relation between linear and non-linear overdensity in the spherical collapse model [7], which allows to express δ_0 as a power series in the non-linear density field δ

$$\delta_0 = \sum_i a_i\delta^i = a_1\delta + a_2\delta^2 + a_3\delta^3 + \ldots, \tag{5.25}$$

where $a_1 = 1$ $a_2 = -\frac{17}{21}$ $a_3 = \frac{341}{567}$.
The resulting map for the bias parameters is (see also [8])

$$b_1^{(\mathrm{E})} = 1 + b_1^{(\mathrm{L})}, \tag{5.26}$$

$$\frac{b_2^{(\mathrm{E})}}{2} = \frac{b_2^{(\mathrm{L})}}{2} + \frac{4}{21}b_1^{(\mathrm{L})}, \tag{5.27}$$

$$\frac{b_3^{(\mathrm{E})}}{3!} = -\frac{118}{567}b_1^{(\mathrm{L})} - \frac{13}{21}\frac{b_2^{(\mathrm{L})}}{2} + \frac{b_3^{(\mathrm{L})}}{3!}. \tag{5.28}$$

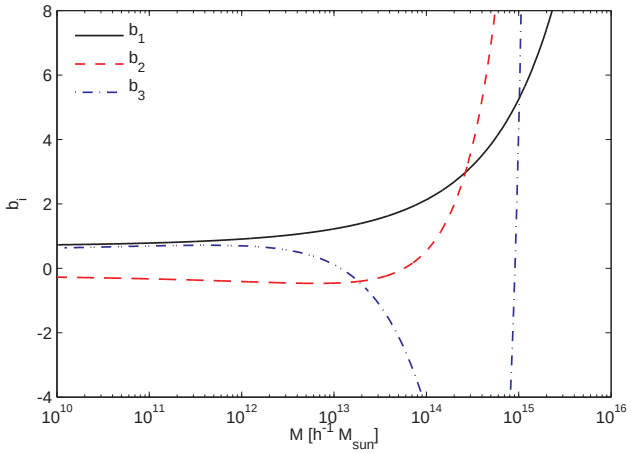

Figure 5.4.: Mass dependence of the first three Eulerian bias parameters b_1 (black solid), b_2 (red dashed) and b_3 (blue dash-dotted) at redshift $z = 0$.

The mass dependence of the Eulerian bias parameters is plotted in Fig. 5.4. As we will argue in Ch. 8, the spherical collapse relation is overly simplified, since a consistent coevolution of haloes and dark matter introduces a non-local bias term at second order (see also [9]).

5.5. Power Spectra in the Eulerian Bias Model

Let us finally employ the Eulerian bias model to calculate the halo-halo and halo-matter power spectra following [10]. We write the halo density field as a power series $\delta(\boldsymbol{r})$

$$\delta_\mathrm{h}(\boldsymbol{r}) = \mathcal{F}[\delta(\boldsymbol{r})] = \frac{b_1}{1!}\delta(\boldsymbol{r}) + \frac{b_2}{2!}\delta^2(\boldsymbol{r}) + \frac{b_3}{3!}\delta^3(\boldsymbol{r}) + \ldots = \sum_{i=1}^{\infty}\frac{b_i}{i!}\delta^i(\boldsymbol{r}). \tag{5.29}$$

This Taylor series is considered only up to third order in the following. The halo density field in Fourier space then reads as

$$\begin{aligned}\delta_\mathrm{h}(\boldsymbol{k}) =& b_1\delta(\boldsymbol{k}) + \frac{b_2}{2}\int \mathrm{d}^3r \int \frac{\mathrm{d}^3q}{(2\pi)^3}\int \frac{\mathrm{d}^3q'}{(2\pi)^3}\exp\left[-\mathrm{i}\,\boldsymbol{r}\cdot(\boldsymbol{q}+\boldsymbol{q}')\right]\delta(\boldsymbol{q})\delta(\boldsymbol{q}') \\ &+\frac{b_3}{6}\int \mathrm{d}^3r \int \frac{\mathrm{d}^3q}{(2\pi)^3}\int \frac{\mathrm{d}^3q'}{(2\pi)^3}\int \frac{\mathrm{d}^3q''}{(2\pi)^3}\exp\left[-\mathrm{i}\,\boldsymbol{r}\cdot(\boldsymbol{q}+\boldsymbol{q}'+\boldsymbol{q}'')\right]\delta(\boldsymbol{q})\delta(\boldsymbol{q}')\delta(\boldsymbol{q}'')\end{aligned} \tag{5.30}$$

$$= b_1\delta(\boldsymbol{k}) + \frac{b_2}{2}\int \frac{\mathrm{d}^3q}{(2\pi)^3}\delta(\boldsymbol{q})\delta(\boldsymbol{k}-\boldsymbol{q}) + \frac{b_3}{6}\int \frac{\mathrm{d}^3q}{(2\pi)^3}\int \frac{\mathrm{d}^3q'}{(2\pi)^3}\delta(\boldsymbol{q})\delta(\boldsymbol{q}')\delta(\boldsymbol{k}-\boldsymbol{q}-\boldsymbol{q}'). \tag{5.31}$$

We can now use the expressions for the non-linear density field in terms of the SPT mode coupling kernels

$$\begin{aligned}\delta(\boldsymbol{k}) =& {}^{(1)}\delta(\boldsymbol{k}) + \int \frac{\mathrm{d}^3q}{(2\pi)^3}{}^{(1)}\delta(\boldsymbol{q})\,{}^{(1)}\delta(\boldsymbol{k}-\boldsymbol{q})F_2(\boldsymbol{q},\boldsymbol{k}-\boldsymbol{q}) \\ &+\int \frac{\mathrm{d}^3q}{(2\pi)^3}\int \frac{\mathrm{d}^3q'}{(2\pi)^3}{}^{(1)}\delta(\boldsymbol{q})\,{}^{(1)}\delta(\boldsymbol{q}')\,{}^{(1)}\delta(\boldsymbol{k}-\boldsymbol{q}-\boldsymbol{q}')F_3(\boldsymbol{q},\boldsymbol{q}',\boldsymbol{k}-\boldsymbol{q}-\boldsymbol{q}').\end{aligned} \tag{5.32}$$

to express the halo density field consistently up to third order in the linear density field. This finally leads to the following expressions for the halo-matter and halo-halo power spectra up to

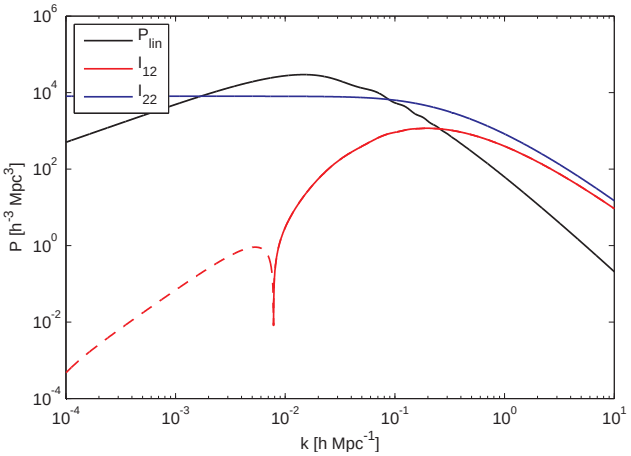

Figure 5.5.: Scale dependence of the linear power spectrum and the perturbative bias terms $I_{12}(k)$ and $I_{22}(k)$ defined in Eqs. (5.35) and (5.36). Note that the $I_{22}(k)$ term contributes even on the largest scales, where it scales as k^0.

fourth order in the density field, i.e., one-loop level

$$\begin{aligned}
P_{h\delta}(k) =& b_1 \{P(k) + P_{13}(k) + P_{22}(k)\} \\
&+ \frac{b_2}{2}\left\{2\int \frac{d^3q}{(2\pi)^3} P(q)P(\boldsymbol{k}-\boldsymbol{q})F_2(\boldsymbol{q},\boldsymbol{k}-\boldsymbol{q}) + \frac{68}{21}\sigma^2 P(k)\right\} \\
&+ \frac{1}{2} b_3 P(k)\sigma^2 \\
P_{hh}(k) =& b_1^2\{P(k) + P_{13}(k) + P_{22}(k)\} \\
&+ b_1 b_2 \left\{2\int \frac{d^3q}{(2\pi)^3} P(q)P(\boldsymbol{k}-\boldsymbol{q})F_2(\boldsymbol{q},\boldsymbol{k}-\boldsymbol{q}) + \frac{68}{21}\sigma^2 P(\boldsymbol{k})\right\} \\
&+ \frac{1}{2} b_2^2 \int \frac{d^3q}{(2\pi)^3} P(q)P(\boldsymbol{k}-\boldsymbol{q}) \\
&+ b_1 b_3 P(k)\sigma^2
\end{aligned} \tag{5.33, 5.34}$$

To simplify the above expressions we will define the recurring integrals

$$I_{12}(k) = 2\int \frac{d^3q}{(2\pi)^3} P(q)P(|\boldsymbol{k}-\boldsymbol{q}|)F_2(\boldsymbol{q},\boldsymbol{k}-\boldsymbol{q}), \tag{5.35}$$

$$I_{22}(k) = 2\int \frac{d^3q}{(2\pi)^3} P(q)P(|\boldsymbol{k}-\boldsymbol{q}|), \tag{5.36}$$

whose scale dependence of these terms is shown in Fig. 5.5. The I_{12} term is a well behaved perturbative correction that only contributes on relatively small scales. In the contrary, the I_{22} term contributes on the largest scales and is thus non-perturbative.
For the halo power spectra we finally have

$$P_{h\delta}(k) = \left(b_1 + \frac{34}{21} b_2\sigma^2 + \frac{1}{2} b_3\sigma^2\right) P(k) + b_1\big(P_{22}(k) + P_{13}(k)\big) + \frac{b_2}{2} I_{12}(k) \tag{5.37}$$

$$\begin{aligned}
P_{hh}(k) =& \left(b_1^2 + \frac{68}{21} b_1 b_2 \sigma_v^2 + b_1 b_3 \sigma_v^2\right) P(k) + b_1^2\big(P_{22}(k) + P_{13}(k)\big) \\
&+ b_1 b_2 I_{12}(k) + \frac{1}{4} b_2^2 I_{22}(k)
\end{aligned} \tag{5.38}$$

The fact that the prefactor of the linear power spectrum is different from b_1 and depending on the variance and thus the smoothing scale is somewhat disturbing. Thus [10] proposed to

understand this parameter as an effective renormalization of the linear bias

$$\tilde{b}_1 = b_1 + \frac{34}{21}\sigma^2 b_2 + \frac{1}{2}b_3\sigma^2. \tag{5.39}$$

This renormalization applies both to the halo-halo and halo-matter correlation functions if we neglect terms $\mathcal{O}(\sigma^4)$ which are not relevant up to fourth order since they are multiplied by the linear power. Up to fourth order the prefactors of the P_{22} and P_{13} terms are also given by the renormalized bias, because the difference is of sixth order

$$P_{\mathrm{h}\delta}(k) = \tilde{b}_1 P_{1loop}(k) + \frac{b_2}{2} I_{12}(k) \tag{5.40}$$

$$P_{\mathrm{hh}}(k) = \tilde{b}_1^2 P_{1loop} + \tilde{b}_1 b_2 I_{12}(k) + \frac{1}{4} b_2^2 I_{22}(k). \tag{5.41}$$

Recently, [11] proposed a reinterpretation of the peak background split that resolves the renormalization problem at least in Lagrangian space.
Let us consider the Fourier transform of the squared non-linear density field

$$\tilde{\delta}(\boldsymbol{k}) = \mathrm{FT}\left[\delta^2(\boldsymbol{x})\right] = \int \frac{\mathrm{d}^3 q}{(2\pi)^3}\delta(\boldsymbol{q})\delta(\boldsymbol{k}-\boldsymbol{q}). \tag{5.42}$$

The renormalisation of the bias parameters is tightly coupled to the following matter correlators

$$\left\langle \delta(\boldsymbol{k})\tilde{\delta}(-\boldsymbol{k})\right\rangle \propto I_{12}(k) + \frac{68}{21}P(k)\sigma^2 \tag{5.43}$$

$$\left\langle \tilde{\delta}(\boldsymbol{k})\tilde{\delta}(-\boldsymbol{k})\right\rangle \propto I_{22}(k) + \left(\frac{68}{21}\sigma^2\right)^2 P(k) + \ldots \tag{5.44}$$

where the second term in the second equation is formally a two-loop term and the dots stand for the omitted two loop contributions. In Ch. 9 we will discuss the I_{22} term and its relation to the shotnoise in more detail.

5.6. Threshold Bias

The Lagrangian matter density field is a Gaussian random field, whose statistical properties are fully described by its two-point function. This remains to be true after smoothing the density field at the mass scale of the halo sample under consideration. Hence, we can calculate the exact correlation function of regions above threshold following [12].
The one and two point Probability Density Functions (PDFs) of a Gaussian random field are given by

$$p_{1\mathrm{pt}}(\delta) = \frac{1}{\sqrt{2\pi\sigma^2}}\exp\left[-\frac{1}{2}\frac{\delta^2}{\sigma^2}\right] \qquad p_{2\mathrm{pt}}(\boldsymbol{Y}) = \frac{1}{\sqrt{(2\pi)^2\det C}}\exp\left[-\frac{1}{2}\boldsymbol{Y}C^{-1}\boldsymbol{Y}^T\right] \tag{5.45}$$

where $\boldsymbol{Y} = (\delta(\boldsymbol{x}_1), \delta(\boldsymbol{x}_2)) = (\delta_1, \delta_2)$ and C is the covariance matrix of density fluctuations at positions $\boldsymbol{x}_1$ and $\boldsymbol{x}_2$. The covariance matrix is given by

$$C = \langle \delta(\boldsymbol{x}_1)\delta(\boldsymbol{x}_2)\rangle = \begin{pmatrix} \sigma^2 & \xi(r) \\ \xi(r) & \sigma^2 \end{pmatrix}, \tag{5.46}$$

where $r = |\boldsymbol{x}_1 - \boldsymbol{x}_2|$ and ξ is the usual correlation function of the smoothed linear density field. Here we omitted the subscript R, but the density fields, correlation functions and variance should be understood as smoothed on the scale R using a top hat filter. The inverse covariance matrix is readily written as

$$C^{-1} = \frac{1}{\sigma^4 - \xi^2(r)}\begin{pmatrix} \sigma^2 & -\xi(r) \\ -\xi(r) & \sigma^2 \end{pmatrix}. \tag{5.47}$$

Introducing $\delta = \sigma\nu$ the two point PDF can be written as

$$p_{2\mathrm{pt}}(\nu_1, \nu_2) = \frac{1}{(2\pi)^3\sigma^2\sqrt{1-\xi^2(r)/\sigma^4}} \exp\left[-\frac{1}{2}\frac{\nu_1^2+\nu_2^2-2\nu_1\nu_2\xi(r)/\sigma^2}{1-\xi^2(r)/\sigma^4}\right]. \tag{5.48}$$

Integrating the two point PDF over all peak heights, we recover the underlying two-point function. If we are interested in the distribution of protohaloes, we would rather like to consider the regions above threshold in a Gaussian field smoothed on the mass scale of the halo sample under consideration. The probability for finding the overdensity in a certain regime of peak heights can be found by integrating the above PDFs between two limiting peak heights or from a threshold peak height to infinity. The latter case will select all haloes above a certain mass threshold and be dominated by peak heights close to the threshold due to the steeply decreasing mass function.
As we have seen in Ch. 3, the correlation function is defined as the excess over random probability of finding two objects separated by a distance r

$$p_{2\mathrm{pt}}(r) = p_{1\mathrm{pt}}^2\left[1+\xi_{\mathrm{tr}}(r)\right]. \tag{5.49}$$

Thus we have for the correlation function of the thresholded regions

$$1+\xi_{\mathrm{tr}}(r) = \frac{\int \mathrm{d}\nu_1 \int \mathrm{d}\nu_2 p_{2\mathrm{pt}}(\nu_1,\nu_2)}{\int \mathrm{d}\nu_1 p_{1\mathrm{pt}}(\nu_1)\int \mathrm{d}\nu_2 p_{1\mathrm{pt}}(\nu_2)} \tag{5.50}$$

The one point function or abundance in the denominator reminds us of the PS results discussed above. The difference is that we are not considering the differential abundance between masses M and $M+\mathrm{d}M$. The above equation is a non-perturbative expression for the correlation of thresholded regions in a Gaussian random field. To find the relation between the correlation function of thresholded regions and the underlying matter correlation function we can expand in the large distance, small correlation limit and obtain

$$\xi_{\mathrm{tr}}(r) = \sum_{i=1}^{\infty}\frac{b_i^2}{i!}\xi^i(r). \tag{5.51}$$

We see that at leading order in this expansion, the correlation function of thresholded regions is a linearly biased version of the smoothed correlation function. The bias is given by

$$b_1 = \frac{1}{\sigma}\frac{\int \mathrm{d}\nu\nu\exp\left[-\nu^2/2\right]}{\int \mathrm{d}\nu\exp\left[-\nu^2/2\right]} \approx \frac{\nu}{\sigma} \approx \frac{\nu^2}{\delta_{\mathrm{c}}} \tag{5.52}$$

The higher order biases are given as

$$b_i = \frac{\int \mathrm{d}\nu f_i(\nu)\exp\left[-\nu^2/2\right]}{\int \mathrm{d}\nu\exp\left[-\nu^2/2\right]} \approx \frac{\nu^i}{\sigma^i} \approx b_1^i, \tag{5.53}$$

where the integral kernels can be expressed in terms of the probabilists Hermite polynomials H_n as

$$f_2 = \frac{1}{2!\sigma^2}\left(\nu^2-1\right) = \frac{1}{2!\sigma^2}H_2(\nu) \tag{5.54}$$

$$f_3 = \frac{1}{3!\sigma^3}\nu\left(\nu^2-3\right) = \frac{1}{3!\sigma^2}H_3(\nu) \tag{5.55}$$

$$f_4 = \frac{1}{4!\sigma^4}\left(3-6\nu^2+\nu^4\right) = \frac{1}{4!\sigma^4}H_4(\nu) \tag{5.56}$$

$$f_5 = \frac{1}{5!\sigma^5}\nu\left(15-10\nu^2+\nu^4\right) = \frac{1}{5!\sigma^5}H_5(\nu). \tag{5.57}$$

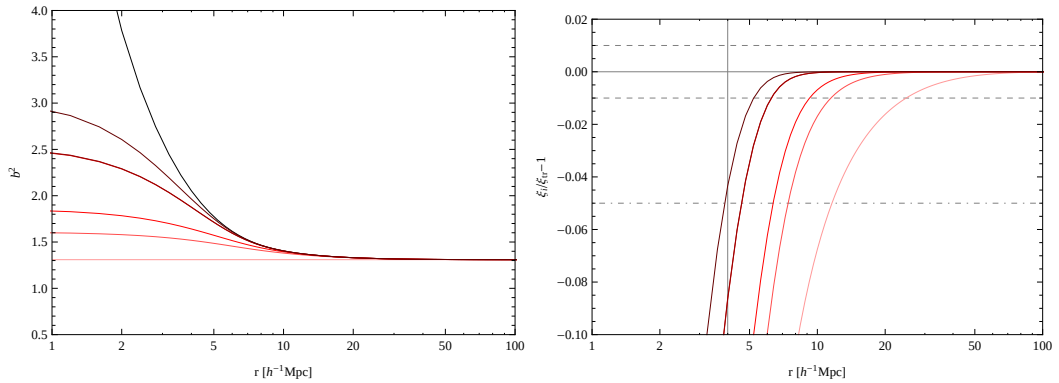

Figure 5.6.: Correlation function of thresholded regions with radius $R = 4\ h^{-1}$Mpc and corresponding mass $M = 1.84 \times 10^{13}\ h^{-1} M_\odot$. *Left panel:* Full bias $\xi_{\rm tr}/\xi$ and contributions from linear (light red) and higher order bias expansions up to sixth order (light to dark). *Right panel:* Convergence of the bias expansion to the full correlation function of thresholded regions. The vertical line shows the smoothing scale defining the regions. A 5% fit of the full correlation function requires a sixth order bias expansion.

Expanding the small scale correlation function as

$$\xi(r) = \sigma_0^2 - \frac{\sigma_1^2 r^2}{3!} + \dots \tag{5.58}$$

we have for the small scale correlation function of the thresholded regions

$$\xi_{\rm tr} = \frac{\sigma_0}{\sigma_1} \frac{\sqrt{3}}{r} \exp\left[\frac{\nu^2}{2}\right]. \tag{5.59}$$

In Fig. 5.6 we show the scale dependent bias $b^2(r) = \xi_{\rm tr}/\xi$ and the convergence of the bias expansion Eq. (5.51). The left panel shows the strong scale dependence and the right panel shows that one needs to consider bias terms up to sixth order in order to reproduce the correlation function down to the smoothing scale at the percent level.

5.7. Peak Bias

Bardeen, Bond, Kaiser and Szalay [13] (hereafter BBKS) went beyond the thresholded regions approach in considering the maxima of Gaussian random field as the formation sites for dark matter haloes. This has the advantage, that one deals with a discrete set of points and makes distinct predictions for the abundance and clustering of protohaloes. Due to the technical difficulty in deriving the results in the three dimensional case, we will restrict ourselves to the one dimensional case, where both the non-perturbative and the perturbative results can be obtained in a straightforward fashion [14].

5.7.1. The 1-D Power Spectrum and Correlation Function

Let us start from a smoothed version of the three dimensional density field and calculate the correlation function along the z-axis

$$\xi_{\rm 1D}(z) = \int \frac{{\rm d}^3 k}{(2\pi)^3} P(k) W_R^2(k) \exp\left[-{\rm i}\, k_z z\right]. \tag{5.60}$$

This one dimensional correlation function should agree with the three dimensional one since the latter obeys statistical isotropy. The one dimensional Fourier transform of the one dimensional

correlation function then yields

$$P_{1\mathrm{D}}(k_{1\mathrm{D}}) = \int_{-\infty}^{\infty} \mathrm{d}z \exp\left[\mathrm{i}\, k_{1\mathrm{D}} z\right] \xi_{1\mathrm{D}}(z) \tag{5.61}$$

$$= \int_{k_{1\mathrm{D}}}^{\infty} \frac{k\mathrm{d}k}{2\pi} P(k) W_R^2(k). \tag{5.62}$$

Note that the 1-D power spectrum goes as $k_{1\mathrm{D}}^0$ in the low-k regime.
As we will see shortly, it will become useful to write the field amplitude and its first and second derivatives in vector notation. For the two-point PDF we define $\boldsymbol{Y} = (\delta_1, \delta_1', \delta_1'', \delta_2, \delta_2', \delta_2'')$ and for the one-point PDF we define $\boldsymbol{y} = (\delta, \delta', \delta'')$. The derivatives are readily evaluated as

$$\delta(\boldsymbol{r}) = \int \frac{\mathrm{d}^3 q}{(2\pi)^3} \exp\left[-\mathrm{i}\, \boldsymbol{q}\cdot\boldsymbol{r}\right] \delta(\boldsymbol{q}) \tag{5.63}$$

$$\partial_x \delta(\boldsymbol{r}) = \int \frac{\mathrm{d}^3 q}{(2\pi)^3} (-i q_x) \exp\left[-\mathrm{i}\, \boldsymbol{q}\cdot\boldsymbol{r}\right] \delta(\boldsymbol{q}) \tag{5.64}$$

$$\partial_x^2 \delta(\boldsymbol{r}) = \int \frac{\mathrm{d}^3 q}{(2\pi)^3} (-i q_x)^2 \exp\left[-\mathrm{i}\, \boldsymbol{q}\cdot\boldsymbol{r}\right] \delta(\boldsymbol{q}) \tag{5.65}$$

The symmetric 6×6 covariance matrix of the field amplitude and derivatives can then be decomposed into block matrices as

$$M = \langle Y_i Y_j \rangle = \begin{pmatrix} m & B_u \\ B_l & m \end{pmatrix}. \tag{5.66}$$

The diagonal block matrices describe the one-point correlators and are given by

$$m = \begin{pmatrix} \sigma_0^2 & 0 & -\sigma_1^2 \\ 0 & \sigma_1^2 & 0 \\ -\sigma_1^2 & 0 & \sigma_2^2 \end{pmatrix}, \tag{5.67}$$

whereas the off-diagonal block matrices describe the correlation between two different field points

$$B_u = \begin{pmatrix} \xi_0(r) & -\xi_{1/2}(r) & -\xi_1(r) \\ \xi_{1/2}(r) & \xi_1(r) & -\xi_{3/2}(r) \\ -\xi_1(r) & \xi_{3/2}(r) & \xi_2(r) \end{pmatrix}, \quad B_l = \begin{pmatrix} \xi_0(r) & \xi_{1/2}(r) & -\xi_1(r) \\ -\xi_{1/2}(r) & \xi_1(r) & \xi_{3/2}(r) \\ -\xi_1(r) & -\xi_{3/2}(r) & \xi_2(r) \end{pmatrix}. \tag{5.68}$$

The correlators follow directly from Eqs. (5.63), (5.64) and (5.65)

$$\xi_{(n+m)/2}(r) = \left\langle \delta^{(n)}(z) \delta^{(m)}(z') \right\rangle = \int_{-\infty}^{\infty} \frac{\mathrm{d}k}{2\pi} (-1)^n (\mathrm{i}\, k)^{n+m} \left[\cos(kr) - \mathrm{i}\, \sin(kr)\right] P_{1\mathrm{D}}(k), \tag{5.69}$$

where $r = z - z'$. If $n + m$ is even the integral over the sine vanishes and if $n + m$ is odd the integral over the cosine vanishes

$$\xi_{(n+m)/2}(r) = \begin{cases} \int \mathrm{d}k k^{n+m} P_{1\mathrm{D}}(k) \cos(kr) & \text{if } \; n+m \text{ even} \\ -\int \mathrm{d}k k^{n+m} P_{1\mathrm{D}}(k) \sin(kr) & \text{if } \; n+m \text{ odd} \end{cases} \tag{5.70}$$

The variance is given by $\sigma^2_{(n+m)/2} = \xi_{n+m}(0)$.
Equivalently we could have calculated the 1-D correlators directly from the 3-D power spectrum

$$\xi_{(n+m)/2}(r) = \int \frac{\mathrm{d}^3 k}{(2\pi)^3} (-1)^n (\mathrm{i}\, \mu k)^{n+m} \exp\left[\mathrm{i}\, \mu k x\right] P_{3\mathrm{D}}(k) W_R(k) \tag{5.71}$$

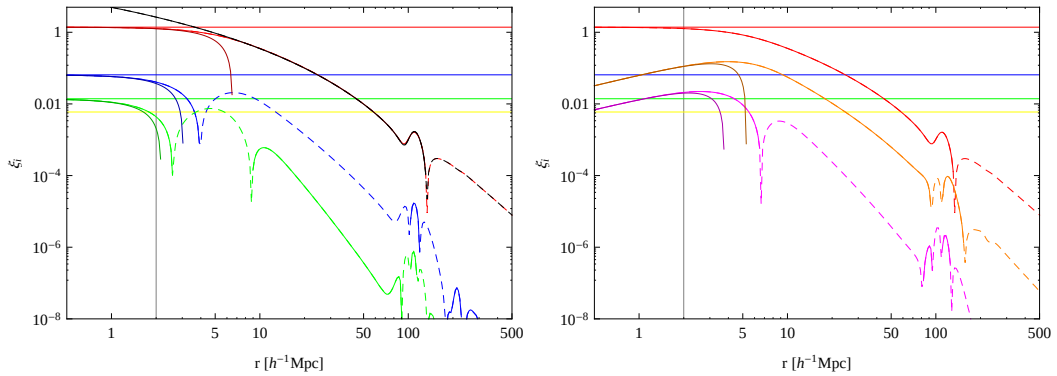

Figure 5.7.: Components of the covariance matrix of field, field derivative and field curvature: ξ_0 (red), ξ_1 (blue), ξ_2 (green), $\xi_{1/2}$ (orange) and $\xi_{3/2}$ (magenta). The horizontal lines show the corresponding rms amplitudes of the terms. Dashed lines describe negative parts.

and thus we have for the components

$$\xi_0(r) = \int \frac{\mathrm{d}^3k}{(2\pi)^3} j_0(kr) P_{3\mathrm{D}}(k) W_R(k)$$
$$\xi_1(r) = \int \frac{\mathrm{d}^3k}{(2\pi)^3} \left[-\frac{2}{3} j_2(kr) + \frac{1}{3} j_0(kr) \right] P_{3\mathrm{D}}(k) W_R(k)$$
$$\xi_2(r) = \int \frac{\mathrm{d}^3k}{(2\pi)^3} \left[\frac{24}{105} j_4(kr) - \frac{20}{35} j_2(kr) + \frac{1}{5} j_0(kr) \right] P_{3\mathrm{D}}(k) W_R(k)$$
$$\xi_{1/2}(r) = \int \frac{\mathrm{d}^3k}{(2\pi)^3} \left[-j_1(kr) \right] P_{3\mathrm{D}}(k) W_R(k)$$
$$\xi_{3/2}(r) = \int \frac{\mathrm{d}^3k}{(2\pi)^3} \left[\frac{2}{5} j_3(kr) - \frac{3}{5} j_1(kr) \right] P_{3\mathrm{D}}(k) W_R(k)$$

The scale dependence of these terms is depicted in Fig. 5.7. The three and one dimensional spectral moments are related by $\sigma^2_{j,1D} = \sigma^2_{j,3D}/(2j+1)$. It is common to define the following parameters: $\gamma = \sigma_1^2/\sigma_0\sigma_2$ and $R_* = \sigma_1/\sigma_2$.

5.7.2. Peak Statistics

After having assembled the ingredients of the PDFs for density and its derivatives in a 1-D field, let us derive the expressions for the correlation of maxima of the density field. Note that the results in this Section are not restricted to one dimensional density fields.
The number density of peaks can be written as a sum over delta function at the peak positions $\boldsymbol{x}_{\mathrm{pk}}$

$$n_{\mathrm{pk}}(\boldsymbol{x}) = \sum_{\mathrm{pk}} \delta^{(\mathrm{D})}(\boldsymbol{x} - \boldsymbol{x}_{\mathrm{pk}}). \tag{5.72}$$

Defining the Hessian

$$H_{ij}(\boldsymbol{x}) = \left. \frac{\partial^2 \delta(\boldsymbol{x}')}{\partial x_i' \partial x_j'} \right|_{\boldsymbol{x}'=\boldsymbol{x}} \tag{5.73}$$

and using that the gradient of the field vanishes at the peak position, we can expand the density field around the peak position

$$\delta(\boldsymbol{x}) = \delta(\boldsymbol{x}_{\mathrm{pk}}) + \frac{1}{2}(x_i - x_{i,\mathrm{pk}}) H_{ij}(\boldsymbol{x}_{\mathrm{pk}}) (x_j - x_{j,\mathrm{pk}}). \tag{5.74}$$

Taking the derivative we obtain

$$\partial_i \delta(\boldsymbol{x}) = H_{ij}(\boldsymbol{x}_{\rm pk})(x_j - x_{j,\rm pk}). \tag{5.75}$$

Thus with $\det H = 1/\det H^{-1}$ and using the transformation properties of the Dirac delta we have

$$\delta^{(\rm D)}(\boldsymbol{x} - \boldsymbol{x}_{\rm pk}) = \det H \delta^{(\rm D)}(\boldsymbol{\nabla}\delta). \tag{5.76}$$

The mean number density is readily obtained as an integral over the one point probability density function of the field amplitude, slope and curvature

$$\bar{n}_{\rm pk} = \langle n_{\rm pk}(\boldsymbol{x})\rangle = \int {\rm d}\boldsymbol{y}\ p_{\rm 1pt}(\boldsymbol{y}) \det H \delta^{(\rm D)}(\boldsymbol{\nabla}\delta) \tag{5.77}$$

where $\boldsymbol{y} = (\delta, \boldsymbol{\nabla}\delta, H)$. Thus, we can define a peak overdensity $\delta_{\rm pk}(\boldsymbol{x}) = n_{\rm pk}(\boldsymbol{x})/\bar{n}_{\rm pk} - 1$. The clustering of the peaks is encoded in the correlation of the peak overdensity

$$\langle \delta_{\rm pk}(\boldsymbol{x}_1)\delta_{\rm pk}(\boldsymbol{x}_2)\rangle = \int {\rm d}\boldsymbol{Y}\ p_{\rm 2pt}(|\boldsymbol{x}_1 - \boldsymbol{x}_2|; \boldsymbol{Y})\delta_{\rm pk}(\boldsymbol{x}_1)\delta_{\rm pk}(\boldsymbol{x}_2) \tag{5.78}$$

$$= \frac{1}{\bar{n}_{\rm pk}^2}\int {\rm d}\boldsymbol{Y}\ p_{\rm 2pt}(|\boldsymbol{x}_1 - \boldsymbol{x}_2|; \boldsymbol{Y}) \det H_1 \det H_2 \delta^{(\rm D)}(\boldsymbol{\nabla}\delta_1)\delta^{(\rm D)}(\boldsymbol{\nabla}\delta_2) - 1, \tag{5.79}$$

where the field amplitudes and derivatives have been summarized in a $2(1+d+d(d+1)/2)$ dimensional vector $\boldsymbol{Y} = (\delta_1, \boldsymbol{\nabla}\delta_1, H_1, \delta_2, \boldsymbol{\nabla}\delta_2, H_2)$. For the cross-correlation with the underlying field we have

$$\langle \delta_{\rm pk}(\boldsymbol{x}_1)\delta(\boldsymbol{x}_2)\rangle = \int {\rm d}\boldsymbol{Y}_4 p_{\rm 2pt}(|\boldsymbol{x}_1 - \boldsymbol{x}_2|, \boldsymbol{Y}_4)\delta_{\rm pk}(\boldsymbol{x})\delta(\boldsymbol{x}') \tag{5.80}$$

$$= \frac{1}{\bar{n}_{\rm pk}}\int {\rm d}\boldsymbol{Y}_4\ p_{\rm 2pt}(|\boldsymbol{x}_1 - \boldsymbol{x}_2|; \boldsymbol{Y}) \det H_1 \delta^{(\rm D)}(\boldsymbol{\nabla}\delta_1)\delta_2, \tag{5.81}$$

where $\boldsymbol{Y}_4 = (\delta_1, \boldsymbol{\nabla}\delta_1, H_1, \delta_2)$.

5.7.3. Correlation Function of Peaks

The one and two point PDFs are given by

$$p_{\rm 1pt}(\boldsymbol{y}) = \frac{1}{\sqrt{(2\pi)^3 \det m}} \exp\left[-\frac{1}{2}\boldsymbol{y} m^{-1} \boldsymbol{y}^T\right] \tag{5.82}$$

$$p_{\rm 2pt}(\boldsymbol{Y}) = \frac{1}{\sqrt{(2\pi)^6 \det M}} \exp\left[-\frac{1}{2}\boldsymbol{Y} M^{-1} \boldsymbol{Y}^T\right] \tag{5.83}$$

We can now calculate the number density and correlation function of maxima requiring the first derivative to vanish at the peak position and the second derivative to be negative to select maxima ($\delta'(_{\rm pk}) = 0 \wedge \delta''(x_{\rm pk}) < 0$) with a peak height in a bin $\nu_{\rm min}\sigma_0 = \delta_{\rm min} < \delta(x_{\rm pk}) < \nu_{\rm max}\sigma_0 = \delta_{\rm max}$. We will commonly replace $\nu = \delta/\sigma_0$ and $q = -\delta''/\sigma_2$. The number density is then given by Eq. (9.66)

$$\bar{n}_{\rm pk} = \int_{\delta_{\rm min}}^{\delta_{\rm max}} {\rm d}\delta \int_{-\infty}^{0} {\rm d}\delta'' \delta'' p_1(\boldsymbol{y}|\delta' = 0) \tag{5.84}$$

$$= \frac{\sigma_0 \sigma_2^2}{\sqrt{(2\pi)^3 \det m}} \int_0^\infty {\rm d}q\ q \int_{\nu_{\rm min}}^{\nu_{\rm max}} {\rm d}\nu\ \exp\left[-\frac{1}{2}\boldsymbol{y} m^{-1} \boldsymbol{y}^T\right] \tag{5.85}$$

The q integral can be performed analytically and we obtain

$$\bar{n}_{\rm pk} = \frac{\sqrt{1-\gamma^2}}{R_s} \int_{\nu_{\rm min}}^{\nu_{\rm max}} {\rm d}\nu \left\{ \exp\left[-\frac{\nu^2}{2\,(1-\gamma^2)}\right]\right.$$

$$\times \left[1+\sqrt{\frac{\pi}{2}}\sqrt{\frac{\gamma^2\nu^2}{1-\gamma^2}}\exp\left[\frac{\gamma^2\nu^2}{2(1-\gamma^2)}\right]\mathrm{erfc}\left(-\sqrt{\frac{\gamma^2\nu^2}{2(1-\gamma^2)}}\right)\right]\Bigg\}. \tag{5.86}$$

For the correlation function we have from Eq. (9.68)

$$1+\xi_{\rm pk}(r) = \frac{1}{\bar{n}^2_{\rm pk}}\prod_{i=1,2}\int_{\delta_{\rm min}}^{\delta_{\rm max}}\mathrm{d}\delta_i\int_{-\infty}^{0}\mathrm{d}\delta_i''\delta_i'' p_{\rm 2pt}(\boldsymbol{Y}|\delta'_{1,2}=0) \tag{5.87}$$

$$= \frac{1}{\bar{n}^2_{\rm pk}}\frac{\sigma_0^2\sigma_2^4}{\sqrt{(2\pi)^6\det M}}\int_{\nu_{\rm min}}^{\nu_{\rm max}}\mathrm{d}\nu_1\mathrm{d}\nu_2\int_0^\infty \mathrm{d}q_2\ q_2\mathrm{d}q_1 q_1\exp\left[-\frac{1}{2}\boldsymbol{Y}M^{-1}\boldsymbol{Y}^T\right] \tag{5.88}$$

The integral over q_1 can be done analytically and yields

$$\frac{1}{M_{33}^{-1}\sigma_2^2}\left[1-\exp\left[\frac{a^2}{2}\right]a\sqrt{\frac{\pi}{2}}\mathrm{erfc}\left(\frac{a}{\sqrt{2}}\right)\right], \tag{5.89}$$

where

$$a = -\frac{\sigma_0}{\sqrt{M_{33}^{-1}}}\left(M_{13}^{-1}\nu_1+M_{34}^{-1}\nu_2-M_{36}^{-1}q_2\frac{\sigma_2}{\sigma_0}\right). \tag{5.90}$$

The final result can be written as

$$1+\xi_{\rm pk}(r) = \frac{1}{\bar{n}^2_{\rm pk}}\frac{\sigma_0^2\sigma_2^2}{M_{33}^{-1}\sqrt{\det M}}\int_{\nu_{\rm min}}^{\nu_{\rm max}}\mathrm{d}\nu_1\int_{\nu_{\rm min}}^{\nu_{\rm max}}\mathrm{d}\nu_2$$
$$\times\int_0^\infty \mathrm{d}q_2\ q_2\exp\left[-Q_0\right]\left[1-\exp\left[\frac{a^2}{2}\right]a\sqrt{\frac{\pi}{2}}\mathrm{erfc}\left(\frac{a}{\sqrt{2}}\right)\right], \tag{5.91}$$

where

$$Q_0 = 2M_{14}^{-1}\nu_1\nu_2\sigma_0^2+M_{11}^{-1}(\nu_1^2+\nu_2^2)\sigma_0^2+q_2\sigma_2(-2M_{16}^{-1}\nu_1\sigma_0-2M_{13}^{-1}\nu_2\sigma_0+M_{33}^{-1}q_2\sigma_2) \tag{5.92}$$

We show the peak-peak correlation function for various bin widths in the left panel of Fig. 5.8. Interestingly a finite ν bin is quite important for exclusion effects. This can be seen by approximating the integrand in Eq. (5.91) $I(\nu_1,\nu_2)$ as

$$I(\nu_1,\nu_2)\approx I(\nu_{1,0},\nu_{2,0})+\partial_{\nu_i}I(\nu_1,\nu_2)(\nu_i-\nu_{i,0})+\frac{1}{2}\partial_{\nu_i}\partial_{\nu_j}I(\nu_1,\nu_2)(\nu_i-\nu_{i,0})(\nu_j-\nu_{j,0}) \tag{5.93}$$

integrating over $\nu_i\in[\nu_{i,0}-\Delta\nu_i/2,\nu_{i,0}+\Delta\nu_i/2]$ we obtain

$$\int\mathrm{d}\nu_1\int\mathrm{d}\nu_2\ I(\nu_1,\nu_2)\approx I(\nu_{1,0},\nu_{2,0})\Delta\nu_1\Delta\nu_2+\frac{1}{24}\Delta\nu_1\Delta\nu_2\left[\partial^2_{\nu_1}I(\nu_1,\nu_2)\Delta\nu_1^2+\partial^2_{\nu_2}I(\nu_1,\nu_2)\Delta\nu_2^2\right] \tag{5.94}$$

The first term leads to a basically constant correlation on small scales, whereas the second term subtracts on small scales but overcorrects and does not reproduce the asymptote to -1.

5.7.4. Linear Bias in the Peak Model

On large scales we can neglect all but $\xi_0(r)$ in $B_{\rm l}$ and $B_{\rm u}$. Thus we can expand in the small quantities $\Psi_i=\xi_i/\sigma_i^2$ and obtain

$$\xi_{\rm pk,pk}(r)\approx b_\nu^2\xi_0(r)+2b_\nu b_\zeta\xi_1(r)+b_\zeta^2\xi_2(r). \tag{5.95}$$

The cross correlation is given by

$$\xi_{\rm pk,\delta}(r)\approx b_\nu\xi_0(r)+b_\zeta\xi_1(r), \tag{5.96}$$

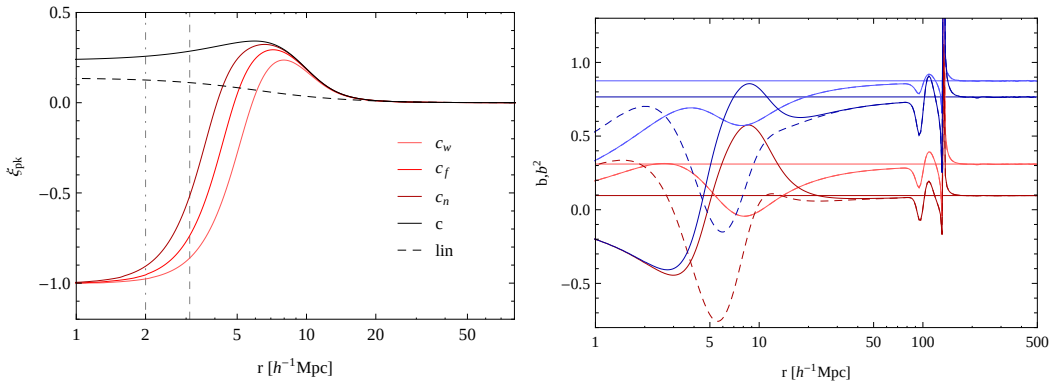

Figure 5.8.: *Left panel:* Effect of bin width on the peak correlation function. Exact peak height (black) and increasing bin width (dark to light). The dashed line shows the linear density bias. *Right panel:* Peak-matter (light lines) and peak-peak bias (dark lines) for two different central peak heights. For reference we overplot the linear peak bias (dashed lines) and the scale independent linear bias (horizontal lines).

where the bias parameters are given by

$$b_\nu = \frac{1}{\sigma_0}\int \mathrm{d}q\; q\frac{\nu-q\gamma}{1-\gamma^2}\exp\left[-\frac{q^2-2\gamma\nu+\nu^2}{2(1-\gamma^2)}\right] \Big/ \int \mathrm{d}q\; q\exp\left[-\frac{q^2-2\gamma\nu+\nu^2}{2(1-\gamma^2)}\right] \tag{5.97}$$

$$= \frac{1}{\sigma_0}\frac{\nu-\gamma\bar{q}}{1-\gamma^2} \tag{5.98}$$

$$b_\zeta = \frac{1}{\sigma_2}\int \mathrm{d}q\; q\frac{q-\gamma\nu}{1-\gamma^2}\exp\left[-\frac{q^2-2\gamma\nu+\nu^2}{2(1-\gamma^2)}\right] \Big/ \int \mathrm{d}q\; q\exp\left[-\frac{q^2-2\gamma\nu+\nu^2}{2(1-\gamma^2)}\right] \tag{5.99}$$

$$= \frac{1}{\sigma_2}\frac{\bar{q}-\gamma\nu}{1-\gamma^2} \tag{5.100}$$

The presence of scale dependent *linear* bias is the most striking result about the peak model. The one dimensional model allows for an explicit evaluation of the full peak correlation and can thus be used for convergence tests of the bias expansion. We show such a comparison in the right panel of Fig. 5.8. The bias in the realistic three dimensional case is derived in [15] and has a similar form to the result presented in Eqs. (5.95) and (5.95). In Fourier space the bias can be represented by a k-dependent linear bias function $b_{\rm pk}(k) = (b_\nu + b_\zeta k^2)W_R(k)$.
The peak model predicts a difference between the local matter velocity and the velocity of the peak. The origin of this **velocity bias** is twofold. First there is a smoothing scale associated with the peak and then the velocity statistics are also biased because the peaks live at special locations.

5.8. Coupled Fluids in the Matrix Approach

One can consider the evolution of the halo overdensity also as a coupled fluid of haloes and dark matter. In this case one can extend the matrix formulation of the fluid equations introduced in Sec. 3.4 to two fluids haloes and dark matter (see also [16, 9]). This allows to study various prescriptions for the coevolution of haloes and dark matter. In the following we will consider the standard coevolution in absence of velocity bias, initial velocity bias as predicted by the peak model and a dynamical velocity bias throughout the evolution.

5.8.1. No Velocity Bias

In the absence of velocity bias we have $\theta_{\rm h} = \theta_{\rm m}$ and consequently the coupling matrix for the vector $\mathbf{\Psi}^{\rm T} = (\delta, -\theta/\mathcal{H}, \delta_{\rm h})$ can be written as

$$\Omega_{ab} = \begin{pmatrix} 0 & -1 & 0 \\ -3/2 & 1/2 & 0 \\ 0 & 0 & -1 \end{pmatrix}. \tag{5.101}$$

Using the initial conditions $\boldsymbol{\phi}^{\rm T} = (\delta_{\rm i}(k), \delta_{\rm i}(k), b_i(k)\delta_{\rm i}(k))$ we have for the linear solution

$$\mathbf{\Psi}(\boldsymbol{k}, y) = \begin{pmatrix} 1 \\ 1 \\ 1 + (b_i - 1)e^{-y} \end{pmatrix} \delta(\boldsymbol{k}, y), \tag{5.102}$$

where $\delta = e^y \delta_{\rm i}$. We obtain the standard relation between the Eulerian and Lagrangian bias parameters after identifying $b^{(\rm L)} = (b_i - 1)e^{-y}$.

5.8.2. Initial Velocity Bias

In presence of initial velocity bias we have $\theta_{h,i} = b_{v,i}\theta_{m,i}$. To study the evolution of the halo velocity we need to add the halo velocity component to the field vector $\mathbf{\Psi}^{\rm T} = (\delta, -\theta/\mathcal{H}, \delta_{\rm h}, -\theta_{\rm h}/\mathcal{H})$. The only coupling between the halo and matter fluids is via the gravitational potential in the Euler equation for the halo fluid

$$\Omega_{ab} = \begin{pmatrix} 0 & -1 & 0 & 0 \\ -3/2 & 1/2 & 0 & 0 \\ 0 & 0 & 0 & -1 \\ -3/2 & 0 & 0 & 1/2 \end{pmatrix}. \tag{5.103}$$

The initial conditions at linear order can be chosen as ${}^{(1)}\boldsymbol{\phi} = (1, 1, b_{\delta,\rm i}, b_{v,\rm i})\delta_{\rm i}$. The linear solution reads

$$\mathbf{\Psi}(\boldsymbol{k}, y) = \begin{pmatrix} 1 \\ 1 \\ 1 + (b_{\delta,\rm i} + 2b_{v,\rm i} - 3)e^{-y} + 2(1 - b_{v,\rm i})e^{-3y/2} \\ 1 + (b_{v,\rm i} - 1)e^{-3y/2} \end{pmatrix} \delta(\boldsymbol{k}, y). \tag{5.104}$$

This result suggests that the presence of initial velocity bias is washed out immediately by gravity and that one recovers the standard result.

5.8.3. Initial Velocity Bias and Velocity Coupling Bias

Let us now consider the case where the halo fluid is coupled to the matter fields via a biased force, in the simplest case this would just be a smoothing on the Lagrangian size of the halo. The coupling matrix now contains the dynamical velocity bias b_v, which could in principle have a weak time dependence

$$\Omega_{ab} = \begin{pmatrix} 0 & -1 & 0 & 0 \\ -3/2 & 1/2 & 0 & 0 \\ 0 & 0 & 0 & -1 \\ -3/2b_v & 0 & 0 & 1/2 \end{pmatrix} \tag{5.105}$$

The initial conditions at linear order can be again chosen as ${}^{(1)}\boldsymbol{\phi} = (1, 1, b_{\delta,\rm i}, b_{v,\rm i})\delta_{\rm i}$. The linear solution is

$$\mathbf{\Psi}(\boldsymbol{k}, y) = \begin{pmatrix} 1 \\ 1 \\ b_v + 2(b_v - b_{v,i})e^{-3/2y} + (b_{\delta,\rm i} + 2b_{v,\rm i} - 3b_v)e^{-y} \\ b_v + (b_{v,\rm i} - b_v)e^{-3/2y} \end{pmatrix} \delta(\boldsymbol{k}, y) \tag{5.106}$$

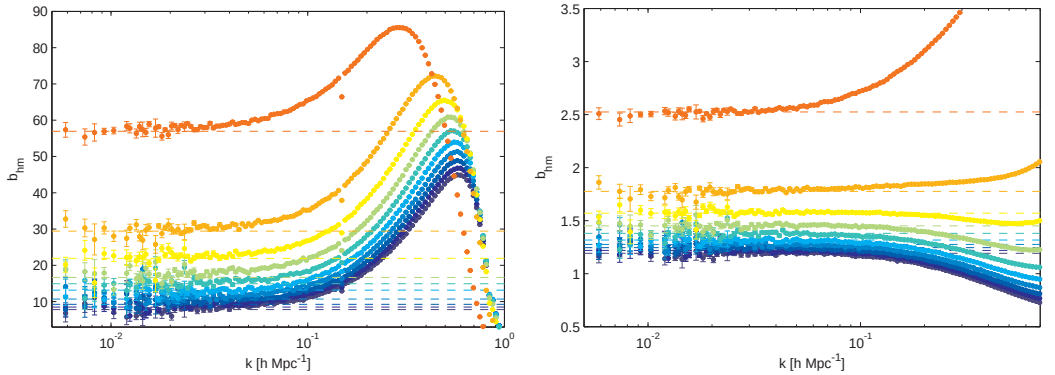

Figure 5.9.: Bias from the halo matter cross power spectrum for 10 mass bins increasing in mass from blue to orange. *Left panel:* Protohaloes in the initial conditions at $z = 49$. *Right panel:* Haloes in the final configuration at $z = 0$.

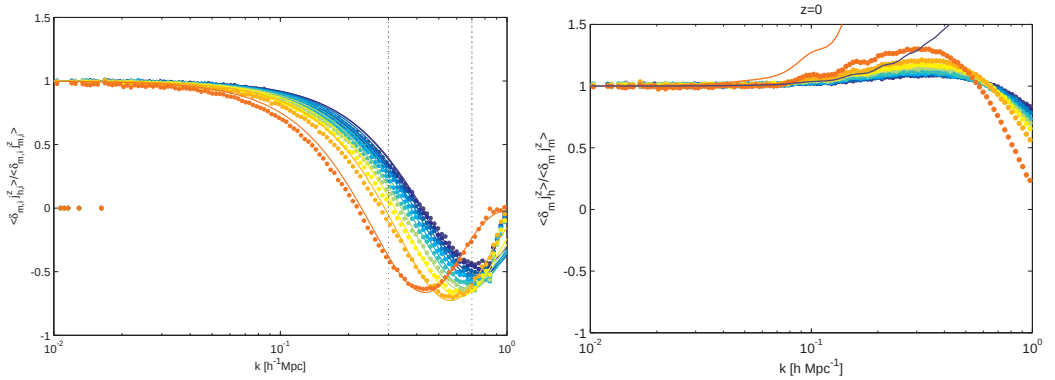

Figure 5.10.: Matter density cross-correlated with the halo momentum. Mass is increasing from blue to orange.*Left panel:* Protohaloes in the initial conditions at $z = 49$. On large scales there is no velocity bias, i.e., haloes are coherently moving with the dark matter but on small scales there is a suppression of halo momentum. *Right panel:* Haloes in the final configuration at $z = 0$. The range over which halo and matter momentum are coherent extends to much smaller scales than in the initial conditions, but on very small scales there is still a clear suppression. The orange and blue line shows a simple linear bias prediction for the momentum bias in absence of velocity bias and clearly overpredicts the signal.

The dynamical coupling bias can in principle lead to non-vanishing contributions to the late time halo density and velocity divergence fields.

5.9. Results from N-Body Simulations

All the models introduced above are approximations to the highly non-linear dynamics leading to the formation of dark matter haloes. Thus, the validity of these approximations needs to be carefully checked against N-body experiments. In Fig. 5.9 we show the halo bias for ten equal number density mass bins in the initial conditions and the final configuration. The initial haloes were obtained by tracing back the constituent particles of the final haloes to the initial conditions. We see that both cases are well reproduced by linear bias on the largest scales. Note that the Lagrangian bias is plotted with respect to the Lagrangian density field. After accounting for the linear growth factor, the relation between initial and final bias parameters is well described by Eq. (5.26). On smaller scales there is a strong scale dependence both in the initial condition bias as well as in the evolved bias. The enhancement in the initial conditions is related to the peak constraint and the corresponding scale dependent bias $b_{\rm pk}(k) =$

$(b_\nu + b_\zeta k^2)W_R(k)$ [16, 17], where the damping on small scales is due to the smoothing. Gravitational evolution tends to erase the peak bias. The scale dependent bias in Eulerian space arises from the coupling of non-linear biasing and non-linear clustering and possible remnants of the peak bias. A robust and consistent modelling of this scale dependence is subject of ongoing research.
In Fig. 5.10 we estimate velocity bias from the momentum power spectra. For this purpose we assign the halo and matter momenta in z-direction $(1+\delta)v^z$ to the grid and cross-correlate with the matter density. The estimator of velocity bias is then given by

$$\hat{b}_v = \frac{\left\langle \delta_{\rm m}(\boldsymbol{k}) j_{\rm h}^z(-\boldsymbol{k}) \right\rangle}{\left\langle \delta_{\rm m}(\boldsymbol{k}) j_{\rm m}^z(-\boldsymbol{k}) \right\rangle}. \tag{5.107}$$

Estimating velocity bias from the momentum power spectra has the disadvantage that one deals with a non-linear quantity and thus needs to account for all the possible non-linear bias and clustering contributions. This is particularly difficult in the final configuration. However, momenta are the natural measurable quantities in N-body simulations, since the velocity field is only defined at the particle positions. The initial condition velocity bias is quite robust and shows a clear damping of halo momentum with respect to the matter momentum on small scales. The lines in the left panel of Fig. 5.10 show a fit using the peak model prediction [17]

$$\theta_{\rm pk}(\boldsymbol{k}) = \left(1 - \frac{\sigma_0^2}{\sigma_1^2}k^2\right)\theta(\boldsymbol{k})W_R(k) \tag{5.108}$$

which reproduces the data very well (see also [16]). The momentum bias in the evolved halo density field is relatively flat except for a damping at very high k and a mild upturn in the intermediate regime for massive haloes. The overplotted orange and blue lines are an estimate of the non-linear contributions for the lowest and highest mass bin in absence of any velocity bias. The disagreement can be certainly attributed to the failure of SPT at low redshifts, but might be also partially due to some residual velocity bias. There is certainly no doubt about the fact that velocity bias is damped by the gravitational evolution and the shrinking size of the haloes. On the other hand the presence of velocity bias at intermediate times can have an influence on the late time matter clustering. We hope to report on this in the near future.

Bibliography

[1] S. D. M. White and M. J. Rees, **Core condensation in heavy halos - A two-stage theory for galaxy formation and clustering**, *Mon. Not. Roy. Astron. Soc.* **183** (May, 1978) 341–358.

[2] W. H. Press and P. Schechter, **Formation of galaxies and clusters of galaxies by selfsimilar gravitational condensation**, *Astrophys. J.* **187** (1974) 425–438.

[3] R. K. Sheth and G. Tormen, **Large scale bias and the peak background split**, *Mon.Not.Roy.Astron.Soc.* **308** (1999) 119, [astro-ph/9901122].

[4] J. Tinker, A. V. Kravtsov, A. Klypin, K. Abazajian, M. Warren, G. Yepes, S. Gottlöber, and D. E. Holz, **Toward a Halo Mass Function for Precision Cosmology: The Limits of Universality**, *Astrophys. J.* **688** (Dec., 2008) 709–728, [arXiv:0803.2706].

[5] J. N. Fry and E. Gaztanaga, **Biasing and hierarchical statistics in large scale structure**, *Astrophys. J.* **413** (1993) 447–452, [astro-ph/9302009].

[6] P. Catelan, F. Lucchin, S. Matarrese, and C. Porciani, **The bias field of dark matter halos**, *Mon.Not.Roy.Astron.Soc.* **297** (1998) 692–712, [astro-ph/9708067].

[7] H. J. Mo and S. D. M. White, **An analytic model for the spatial clustering of dark matter haloes**, *Mon. Not. Roy. Astron. Soc.* **282** (Sept., 1996) 347–361, [astro-ph/].

[8] R. Scoccimarro, R. K. Sheth, L. Hui, and B. Jain, **How Many Galaxies Fit in a Halo? Constraints on Galaxy Formation Efficiency from Spatial Clustering**, *Astrophys. J.* **546** (Jan., 2001) 20–34, [astro-ph/].

[9] K. C. Chan, R. Scoccimarro, and R. K. Sheth, **Gravity and large-scale nonlocal bias**, *Phys. Rev.* **85** (Apr., 2012) 083509, [arXiv:1201.3614].

[10] P. McDonald, **Clustering of dark matter tracers: Renormalizing the bias parameters**, *Phys. Rev.* **74** (Nov., 2006) 103512, [astro-ph/].

[11] F. Schmidt, D. Jeong, and V. Desjacques, **Peak-Background Split, Renormalization, and Galaxy Clustering**, *ArXiv e-prints* (Dec., 2012) [arXiv:1212.0868].

[12] N. Kaiser, **On the spatial correlations of Abell clusters**, *Astrophys. J. Let.* **284** (Sept., 1984) L9–L12.

[13] J. M. Bardeen, J. R. Bond, N. Kaiser, and A. S. Szalay, **The Statistics of Peaks of Gaussian Random Fields**, *Astrophys. J.* **304** (1986) 15–61.

[14] S. L. Lumsden, A. F. Heavens, and J. A. Peacock, **The clustering of peaks in a random Gaussian field**, *Mon. Not. Roy. Astron. Soc.* **238** (May, 1989) 293–318.

[15] V. Desjacques, **Baryon acoustic signature in the clustering of density maxima**, *Phys. Rev.* **78** (Nov., 2008) 103503, [arXiv:0806.0007].

[16] A. Elia, S. Kulkarni, C. Porciani, M. Pietroni, and S. Matarrese, **Modelling the clustering of dark matter haloes in resummed perturbation theories**, *Mon. Not. Roy. Astron. Soc.* **416** (Sept., 2011) 1703–1716, [arXiv:1012.4833].

[17] V. Desjacques and R. K. Sheth, **Redshift space correlations and scale-dependent stochastic biasing of density peaks**, *Phys. Rev.* **81** (Jan., 2010) 023526, [arXiv:0909.4544].

CHAPTER 6

Primordial non-Gaussianity in the Halo Bispectrum[†]

The bispectrum vanishes for linear Gaussian fields and is thus a sensitive probe of non-linearities and non-Gaussianities in the cosmic density field. Hence, a detection of the bispectrum in the halo density field would enable tight constraints on non-Gaussian processes in the early Universe and allow inference of the dynamics driving inflation. We present a tree level derivation of the halo bispectrum arising from non-linear clustering, non-linear biasing and primordial non-Gaussianity. A diagrammatic description is developed to provide an intuitive understanding of the contributing terms and their dependence on scale, shape and the non-Gaussianity parameter $f_{\rm NL}$. We compute the terms based on a multivariate bias expansion and the peak-background split method and show that non-Gaussian modifications to the bias parameters lead to amplifications of the tree level bispectrum that were ignored in previous studies. Our results are in a good agreement with published simulation measurements of the halo bispectrum. Finally, we estimate the expected signal to noise on $f_{\rm NL}$ and show that the constraint obtainable from the bispectrum analysis significantly exceeds the one obtainable from the power spectrum analysis.

6.1. Introduction

The question whether the inhomogeneities in our Universe have been seeded by a Gaussian initial distribution raised a lot of excitement recently (see [2, 3] for reviews). Inflation [4, 5, 6] is a theoretical paradigm that could generate the initial fluctuations, but has not yet been directly confirmed observationally. Standard slow-roll inflation predicts a very low level of non-Gaussianity. However, there is no shortage of single and multifield inflationary models with most of them predicting a fluctuation distribution distinct from the simple Gaussian case. Thus detection of a non-Gaussian signal would provide unprecedented information about the dynamics driving inflation and the interactions of the inflaton field [7].

The fluctuations in the inflaton field are imprinted in the distribution of photons and matter in the Universe. This raises the question, which observable is best suited to detect the tiny deviations from the fiducial Gaussian distribution of field amplitudes. Certainly, it is promising to look at statistics that would vanish in the Gaussian case, such as the bispectrum of the Cosmic Microwave Background (CMB) radiation that for a long time was believed to be the most promising probe of primordial non-Gaussianity [8]. In Large Scale Structure (LSS) the

[†]This chapter is based on a publication by T. Baldauf, U. Seljak and L. Senatore that appeared in the Journal of Cosmology and Astroparticle Physics, Issue 4 (2011) [1]. I am the first author of the paper, performed the perturbation theory calculations, developed the diagramatic approach and compiled the manuscript.

detection of primordial non-Gaussianity is hampered by the non-Gaussianity produced by late time non-linear clustering, a caveat not present in the linear CMB physics. Only in recent years it was realised that equally strong constraints can be obtained from the LSS [9]. One of the most promising features of primordial non-Gaussianity in the LSS is the scale dependence of the halo bias. This scale dependent bias is most prominent for non-Gaussianities with non-vanishing squeezed limit of the bispectrum, such as the local shape [10, 11] and the shapes with both equilateral and local limit recently found in the Effective Theory of Multifield Inflation [12]. It was theoretically predicted for the local type non-Gaussianity by [13] and subsequently other derivations were presented by [14, 15]. These were confirmed in simulations by [13, 16, 17, 18, 19, 20, 21]. First data analysis based on the scale dependent non-Gaussian bias lead to remarkably strong constraints on local non-Gaussianity [15].
The two point function and its Fourier transform, the power spectrum, are the most important statistics that have been used to analyze LSS surveys so far. Their drawback in terms of the detection of non-Gaussianities is that the signatures may be small and difficult to separate from non-Gaussianities generated by gravity, whereas the distinct features of alternative inflationary models will be imprinted more clearly in higher order statistics such as the three point function or the bispectrum

$$\langle \delta(\boldsymbol{k}_1)\delta(\boldsymbol{k}_2)\delta(\boldsymbol{k}_3)\rangle = (2\pi)^3\delta^{(\mathrm{D})}(\boldsymbol{k}_1+\boldsymbol{k}_2+\boldsymbol{k}_3)B(\boldsymbol{k}_1,\boldsymbol{k}_2,\boldsymbol{k}_3), \tag{6.1}$$

which vanish for Gaussian fields. Measuring the higher order statistics is more involved than the standard power spectrum analysis because these statistics show both shape and scale dependence, and both of these dependencies need to be considered in order to constrain different forms of primordial non-Gaussianity. In this paper we try to address whether the bispectrum analysis can improve on the power spectrum analysis of LSS surveys in terms of detecting primordial non-Gaussianity of the local type. Previous studies of the halo bispectrum in presence of primordial non-Gaussianity [22, 23] are based on the standard local bias model. The non-Gaussian correction to the halo bispectrum in these approaches arises mainly from loop terms and is thus dependent on the smoothing scale. We will try to improve on these calculations and present an independent and smoothing invariant approach to obtain the halo bispectrum.
In [24] it was proven that the optimal estimator of non-Gaussianity is the bispectrum. This raises the question how the power spectrum could possibly give tighter constraints than the bispectrum. In the analysis of LSS surveys it is extremely difficult to extract information from the very high-k non-linear modes. This restricts the analysis of the bispectrum to relatively low-k modes that are sufficiently linear. The situation is changed when one considers biased tracers of the density field. These can be related to bispectrum [25], hence they trace non-Gaussian information. The bias effectively allows us to extract some of the non-Gaussian information in the high-k modes from the power spectrum analysis. This effectively increases the number of modes in the survey, and allows to tighten the limits on the non-Gaussian parameters. Still, one would expect that the bispectrum analysis contains further information and the question is how it compares to the power spectrum analysis of biased tracers.
For simplicity, we will focus our attention on the local type of non-Gaussianity, where the potential shows a self coupling that is local in real space. The local shape of non-Gaussianity is for instance predicted by multi-field inflation [26, 27, 28] and in the bouncing cosmology model [29]. Recently [12] found new shapes with none vanishing squeezed limit whose LSS phenomenology is yet to be derived.
This paper breaks down as follows. We first review the basics of non-Gaussianity in Section 6.2 and then describe the multivariate biasing scheme and peak-background split approach previously introduced by [15, 30] in Section 6.3. Section 6.4 introduces the perturbative solutions for the distribution of matter and biased tracers as well as our new diagrammatic prescription for the calculation of their n-spectra. Section 6.5 is devoted to the calculation of the halo bispectrum whose constraining power is compared to the power spectrum in Section 6.6. We conclude our findings in Section 8.5.

6.2. Basics

We consider the local type of non-Gaussianity [10, 11, 31, 32]

$$\Phi_{\rm nG}(\boldsymbol{x}) = \varphi(\boldsymbol{x}) + f_{\rm NL}\left(\varphi^2(\boldsymbol{x}) - \left\langle\varphi^2\right\rangle\right) + g_{\rm NL}\varphi^3(\boldsymbol{x}), \tag{6.2}$$

where φ is an auxiliary primordial Gaussian potential.[1] Following the peak-background split approach [15] we consider the potential as a superposition of small and large scale modes $\varphi = \varphi_{\rm s} + \varphi_{\rm l}$ separated by a cut-off wavenumber Λ. Thus from Eq. (6.2) one obtains

$$\Phi_{\rm nG} = \varphi_{\rm l} + f_{\rm NL}\varphi_{\rm l}^2 + g_{\rm NL}\varphi_{\rm l}^3 + (1 + 2f_{\rm NL}\varphi_{\rm l} + 3g_{\rm NL}\varphi_{\rm l}^2)\varphi_{\rm s} + (f_{\rm NL} + 3g_{\rm NL}\varphi_{\rm l})\varphi_{\rm s}^2 + g_{\rm NL}\varphi_{\rm s}^3, \tag{6.4}$$

where all the fields are evaluated at the same spatial position $\boldsymbol{x}$. Short modes in the above expression can be easily identified since only terms containing at least one Gaussian short mode can contribute to the short wavelength power. These short wavelength modes dominate the collapse of dark matter haloes, whereas the long wavelength modes raise or lower the actual density in large patches of the sky, effectively lowering and raising the collapse threshold. In the presence of non-Gaussianity the long wavelength modes furthermore affect the variance of the short modes and thus lead to an additional dependence of the number density of collapsed objects on the amplitude of the long wavelength modes. As we will see, in the presence of local non-Gaussianities, this effect is proportional to the value of the long wavelength Newtonian potential, leading to a distinct scale dependent effect.
The actual effect of the long mode on the variance of the non-Gaussian short modes can be estimated as follows. Squaring the short part of the non-Gaussian potential we obtain

$$\Phi_{\rm nG,s}^2 = \left(1 + 4f_{\rm NL}\varphi_{\rm l} + 6g_{\rm NL}\varphi_{\rm l}^2 + 4f_{\rm NL}^2\varphi_{\rm l}^2 + 12f_{\rm NL}g_{\rm NL}\varphi_{\rm l}^3 + 9g_{\rm NL}^2\varphi_{\rm l}^4\right)\varphi_{\rm s}^2, \tag{6.5}$$

of which we can easily compute the expectation over the short modes

$$\sigma_{\rm nG,s}^2 = \left\langle\Phi_{\rm nG,s}^2\right\rangle_{\rm s} = \left(1 + 4f_{\rm NL}\varphi_{\rm l} + 6g_{\rm NL}\varphi_{\rm l}^2 + 4f_{\rm NL}^2\varphi_{\rm l}^2 + 12f_{\rm NL}g_{\rm NL}\varphi_{\rm l}^3 + 9g_{\rm NL}^2\varphi_{\rm l}^4\right)\sigma_{\rm G,s}^2, \tag{6.6}$$

where we identified $\sigma_{\rm G,s}^2 = \left\langle\varphi_{\rm s}^2\right\rangle_{\rm s}$. Here we neglect all correlators of odd number of $\varphi_{\rm s}$ as well as the $\sigma_{\rm G,s}^4 = \left\langle\varphi_{\rm s}^4\right\rangle$ term. The resulting expression agrees with the expressions previously derived by [13, 15]. In contrast to the variance, the three point function or skewness

$$\left\langle\Phi_{\rm nG,s}^3\right\rangle_{\rm s} = 6f_{\rm NL}\left\langle\varphi_s^2\right\rangle_{\rm s}^2(1 + 4f_{\rm NL}\varphi_{\rm l}) + 6g_{\rm NL}\left\langle\varphi_s^2\right\rangle_{\rm s}^2\varphi_{\rm l} \tag{6.7}$$

vanishes in the Gaussian case. Similar to the variance, the skewness is rescaled by the long wavelength potential.
Now it remains to connect the non-Gaussian effects on the gravitational potential to the distribution of matter. In the Newtonian limit, valid well inside the horizon, the Poisson equation relates the long wavelength Gaussian potential to the density perturbation,

$$\Phi(\boldsymbol{k}) = \frac{\delta_{\rm p}(\boldsymbol{k}, z)}{\alpha(k, z)}, \tag{6.8}$$

[1] The coupling of the potentials in Eq. (6.2) is naturally imposed in the early Universe during Inflation. This approach, which is followed by our study, is denoted the CMB convention. However, some authors impose the same equation in the late time evolved Universe (the LSS convention). Therefore one has to be careful when comparing quoted constraints on the non-Gaussianity parameters. Namely, the potential evolves as

$$\varphi(\boldsymbol{x}, a) = \frac{D(a)}{a}\varphi(\boldsymbol{x}, a_0 = 1) = g(a)\varphi(\boldsymbol{x}, a_0 = 1), \tag{6.3}$$

where $D(a)$ is the linear growth factor normalised to unity at $a_0 = 1$ and thus $g(a_0 = 1) = 1$. In an Einstein-de-Sitter Universe the potential is constant in time, whereas it decays as $g(a = 0)/g(a_0 = 1) = 1.34 \approx 4/3$ in the currently favoured ΛCDM model.

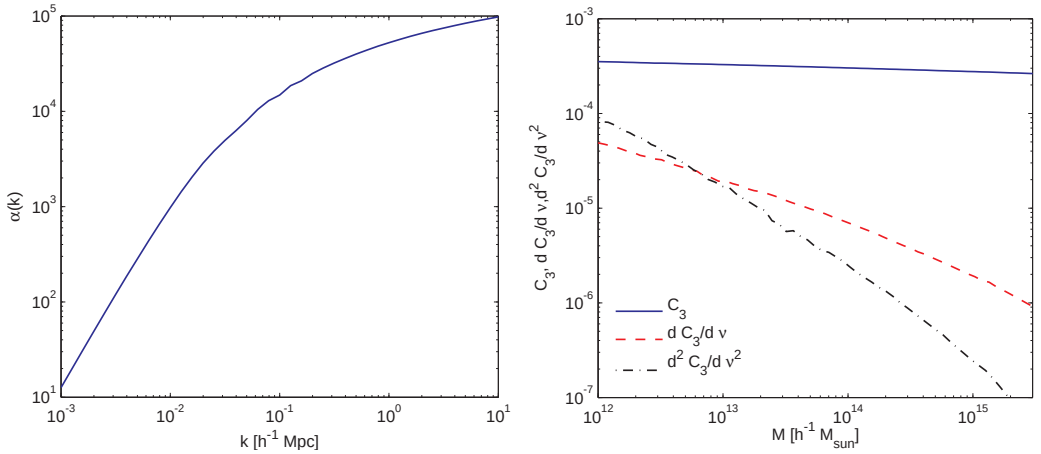

Figure 6.1.: *Left panel:* Poisson factor $\alpha(k)$ relating density and potential via $\delta(k) = \alpha(k)\Phi(k)$. On scales of $k \approx 0.1\ h\mathrm{Mpc}^{-1}$ the potential is smaller than the density by a factor of 10^5, whereas they are equal on very large scales of $k \approx 2 \times 10^{-4}\ h\mathrm{Mpc}^{-1}$. The non-Gaussian corrections generally scale as $f_{\rm NL}/\alpha(k)$ and are thus suppressed on high k's. Note that the Poisson equation in Newtonian gauge receives general relativistic corrections as $\alpha(k)$ approaches unity. *Right panel:* Skewness $C_3 = \sigma S_3$ and its first and second mass derivatives evaluated for $f_{\rm NL} = 1$ and $\varphi_{\rm I} = 0$.

where we introduced the auxiliary function[2]

$$\alpha(k,z) = \frac{2k^2c^2D(z)T(k)}{3H_0^2\Omega_{\rm m}}\frac{g(z=0)}{g(z_\infty)}, \tag{6.9}$$

which scales as k^2/H^2 on large scales where the transfer function is unity. As discussed in [33, 34, 35], on horizon scales unphysical gauge modes and relativistic corrections to the Poisson equation require a more careful analysis. Fig. 6.1 shows the Poisson factor as a function of k-mode. Note that the corrections to the Gaussian spectra are given as powers of $f_{\rm NL}/\alpha(k)$. The importance of potential and density terms is equal at $k \approx 2\times10^{-4}\ h\mathrm{Mpc}^{-1}$ for $f_{\rm NL} = \mathcal{O}(1)$ and at $k \approx 2 \times 10^{-3}\ h\mathrm{Mpc}^{-1}$ for $f_{\rm NL} = \mathcal{O}(100)$. Here and in the rest of the paper we use the transfer function for a cosmology with $\Omega_{\rm m} = 0.25,\ \Omega_\Lambda = 0.75,\ \sigma_8 = 0.8,\ n_{\rm s} = 1.0$.

6.3. Bias from the Universal Mass Function

Galaxies and their host haloes are believed to trace a smoothed version of the underlying distribution of dark matter. The relation between the local overdensity in the matter and halo fields is described by the bias function. This bias function can be related to the abundance of haloes of mass M described by the halo mass function. In this Section we will review the basic Gaussian mass functions and their non-Gaussian corrections. Finally, we will present the peak-background split and multivariate biasing scheme previously introduced by [15, 30].

6.3.1. Mass Functions

Haloes are assumed to form at the peaks of the underlying dark matter density field. Numerical simulations and analytical calculations indicate that the abundance of collapsed objects can be inferred from the distribution of points that exceed the density threshold $\delta_{\rm c} = 1.686$. Following the first studies of [36] (hereafter PS) it was found that the mass function, the number density

[2]Note that we are not writing explicitly the norm of a vector but use the notation $k = |\boldsymbol{k}|$

of collapsed objects of mass M, reduces to an universal functional form for different redshifts and cosmologies if it is expressed in terms of the peak height

$$\nu = \left(\frac{\delta_\mathrm{c}}{\sigma_\mathrm{nG}}\right)^2, \tag{6.10}$$

where $\sigma(M)$ is the variance of the density field smoothed on mass scale M. This definition of ν follows e. g. [15], while other authors define $\nu = \delta_\mathrm{c}/\sigma$. All the results presented in this paper can be written in terms of either definition by replacing the variables accordingly. Then the number of collapsed objects of mass M can be expressed as

$$n(M) = \nu f(\nu)\frac{\bar{\rho}}{M^2}\frac{\mathrm{d}\ln\nu}{\mathrm{d}\ln M}. \tag{6.11}$$

Using a random walk in a Gaussian density field PS derived

$$\nu f(\nu) = \sqrt{\frac{\nu}{2\pi}}\exp\left[-\frac{\nu}{2}\right], \tag{6.12}$$

which is however not in very good agreement with the mass function measured in numerical simulations. To improve the agreement, [37] (hereafter ST) proposed a modified version of the Press-Schechter mass function

$$\nu f(\nu) = A(p)\left(1+\frac{1}{(q\nu)^p}\right)\sqrt{\frac{q\nu}{2\pi}}\exp\left[-\frac{q\nu}{2}\right], \tag{6.13}$$

where the parameters $q = 0.707$ and $p = 0.3$ were obtained from a fit to numerical simulations and A is a normalisation factor.
Performing the random walk using non-Gaussian statistics is more involved, however using an Edgeworth expansion of the exponential [38] (hereafter LV) obtained for the mass function

$$n_\mathrm{LV}(M) = \sqrt{\frac{2}{\pi}}\frac{\bar{\rho}}{M}\exp\left[-\frac{\delta_c^2}{2\sigma^2}\right]\left[\frac{d\ln\sigma}{dM}\left(\frac{\delta_c}{\sigma}+\frac{S_3\sigma}{6}\left(\frac{\delta_c^4}{\sigma^4}-2\frac{\delta_c^2}{\sigma^2}-1\right)\right)+\frac{1}{6}\frac{dS_3}{dM}\sigma\left(\frac{\delta_c^2}{\sigma^2}-1\right)\right], \tag{6.14}$$

where the skewness is defined as

$$S_3 = \frac{\langle\delta_M^3\rangle_\mathrm{c}}{\langle\delta_M^2\rangle^2}. \tag{6.15}$$

The above derivation based on the Edgeworth expansion is expected to be satisfactory for low peaks only. As LV show in their Appendix B, higher cummulants than S_3 gain importance for high mass haloes $M \gtrsim 10^{15}\ h^{-1}M_\odot$. As we will see in the next section, bias parameters are basically derivatives of the mass function, and thus the bias parameters derived from the LV mass function should be trusted for low and intermediate mass haloes only. The full treatment of the excursion set theory using non-Markovian random walks [39] seems to be a promising alternative in the high mass limit. In the case of local type non-Gaussianity we obtain for the skewness

$$C_3 = \sigma_\mathrm{G}S_3 = \frac{6f_\mathrm{NL}}{\sigma_\mathrm{G}^3}\int\frac{\mathrm{d}^3q}{(2\pi)^3}\int\frac{\mathrm{d}^3q'}{(2\pi)^3}\alpha_M(\boldsymbol{q})\alpha_M(\boldsymbol{q}')\alpha_M(\boldsymbol{q}+\boldsymbol{q}')P_{\varphi\varphi}(\boldsymbol{q})P_{\varphi\varphi}(\boldsymbol{q}'), \tag{6.16}$$

where $\alpha_M(k) = W_M(k)\alpha(k)$ and $W_M(k)$ is the filter of mass scale M. The LV mass function in Eq. (6.14) is not in the form of an universal mass function. We can however rewrite it simply applying the chain rule to σS_3.

$$\begin{aligned} n_\mathrm{LV}(M) =& \sqrt{\frac{1}{2\pi}}\frac{\bar{\rho}}{M^2}\exp\left[-\frac{\delta_c^2}{2\sigma^2}\right]\frac{d\ln\nu}{d\ln M}\left[\frac{\delta_c}{\sigma}+\frac{S_3\sigma}{6}\left(\frac{\delta_c^4}{\sigma^4}-3\frac{\delta_c^2}{\sigma^2}\right)-\frac{1}{3}\frac{dS_3\sigma}{d\nu}\left(\frac{\delta_c^4}{\sigma^4}-\frac{\delta_c^2}{\sigma^2}\right)\right] \\ =& n_\mathrm{PS}(M)\left[1+\frac{S_3\sigma}{6}\left(\nu^{3/2}-3\nu^{1/2}\right)-\frac{1}{3}\frac{dS_3\sigma}{d\nu}\left(\nu^{3/2}-\nu^{1/2}\right)\right] \end{aligned}$$

$$= n_{\rm PS}(M) R(\nu), \tag{6.17}$$

where we introduced the auxiliary function

$$R(\nu) = 1 + \frac{S_3\sigma}{6}\left(\nu^{3/2} - 3\nu^{1/2}\right) - \frac{1}{3}\frac{dS_3\sigma}{d\nu}\left(\nu^{3/2} - \nu^{1/2}\right). \tag{6.18}$$

The presence of the σS_3 terms still spoils the universality because this term carries a mass dependence via the smoothing scale. As shown in [17] and in Fig. 6.1, σS_3 is only very weakly dependent on the smoothing radius, such that we can safely treat it as a constant in the mass function.

Thus we managed to write the non-Gaussian mass function in the form of an universal mass function and can benefit from the known results for universal mass functions. Usually the LV mass function is multiplied by a correction factor $\gamma(M) = n_{\rm ST}(M)/n_{\rm PS}(M)$ to improve the agreement with simulations, leading to $n_{\rm LV}(M) = n_{\rm ST}(M)R(\nu)$. The underlying assumption is that ST corrects PS for triaxial collapse and LV corrects PS for non-Gaussianity.[3] Alternative derivations of non-Gaussian mass functions that are valid in various, if not all, regimes have been presented by [40, 39, **?**]. For our study, the important result following from these analyses is that to a good approximation, all of the above mass functions can be treated as universal, that is as being function of $\delta_{\rm c}/\sigma$ only, and that the inferred values of the biases are not very different. While we are aware of disadvantages of both the Gaussian and non-Gaussian mass functions, it goes beyond the scope of this paper to discuss their detailed validity or to develop an improved mass function.

6.3.2. Multivariate Lagrangian Bias

The spherical top hat collapse model states that a spherical overdensity collapses to form a gravitationally bound object once it exceeds a certain overdensity threshold δ_c. Long wavelength density perturbations raise or lower the mean density in a patch of the Universe and thus effectively raise or lower the collapse threshold $\delta_{\rm c} \to \delta_{\rm c} - \delta_{\rm l}$. So far, the bias parameters were calculated by expanding the local number density in the amplitude of the long wavelength density fluctuation $\delta_{\rm l}$ only. As we saw above in Eq. (6.6), coupling between long and short modes leads to an enhancement of the variance of the short wavelength density perturbations. This enhancement is proportional to powers of the long wavelength Gaussian potential and thus suggests to calculate the distribution of collapsed objects by expanding the local number density in terms of the long wavelength modes of both density and potential [15, 41, 30]

$$n(\boldsymbol{x}) = \bar{n} + \frac{\partial n}{\partial \delta_{\rm l}}\delta_{\rm l}(\boldsymbol{x}) + \frac{\partial n}{\partial \varphi_{\rm l}}\varphi_{\rm l}(\boldsymbol{x}) + \frac{1}{2}\frac{\partial^2 n}{\partial \delta_{\rm l}^2}\delta_{\rm l}^2(\boldsymbol{x}) + \frac{2}{2!}\frac{\partial^2 n}{\partial \delta_{\rm l} d\varphi_{\rm l}}\delta_{\rm l}(\boldsymbol{x})\varphi_{\rm l}(\boldsymbol{x}) + \frac{1}{2}\frac{\partial^2 n}{\partial \varphi_{\rm l}^2}\varphi_{\rm l}^2(\boldsymbol{x}). \tag{6.19}$$

Here we write down explicitly the spatial dependence to highlight the local relation between bias, overdensity and potential. The multivariate bias expansion is not stating that density and potential are independent parameters, but rather that the different scale dependence of density and potential requires one to expand in both of them in order to keep the bias parameters scale independent. As we will stress at the end of this subsection, it is important that these fields are restricted to long-wavelengths. Notice that the fact that the overdensity depends locally only on δ and φ is a consequence of the functional dependence of the mass function on δ and φ even in the non-Gaussian case. Defining $\delta_{\rm h}(\boldsymbol{x}) = n(\boldsymbol{x})/\bar{n} - 1$ and identifying the partial derivatives with the bias parameters we obtain in Lagrangian space

$$\delta_{\rm h}^{\rm L}(\boldsymbol{x}) = b_{10}^{\rm L}\delta_0(\boldsymbol{x}) + b_{01}^{\rm L}\varphi(\boldsymbol{x}) + \frac{b_{20}^{\rm L}}{2!}\delta_0^2(\boldsymbol{x}) + b_{11}^{\rm L}\delta_0(\boldsymbol{x})\varphi(\boldsymbol{x}) + \frac{b_{02}^{\rm L}}{2!}\varphi^2(\boldsymbol{x}) + \ldots, \tag{6.20}$$

[3] It is not clear how well this statement is theoretically justified, but it is enough for us for obtaining an estimate on the non-Gaussian effects on the mass function and the induced biases.

where δ_0 is the initial Lagrangian overdensity.
We can now calculate the Lagrangian bias parameters under the assumption that the local number density can be expressed with an universal mass function as in Eq. (6.11).
The presence of a long wavelength mode can be accounted for by replacing $\delta_c \to \delta_c - \delta_l$ and $\sigma_G \to \sigma_{nG}$ in the peak height, such that that the conditional peak height in presence of a long wavelength mode can be written as

$$\tilde{\nu} = \left(\frac{\delta_c - \delta_l}{\sigma_G (1 + 2 f_{NL} \varphi_l + 3 g_{NL} \varphi_l^2 + 2 f_{NL}^2 \varphi_l^2)} \right)^2 \tag{6.21}$$

and the bias parameters are given by (see Appendix 6.8.1 for details on the calculation)

$$b_{10}^L = \frac{1}{\bar{n}} \frac{\partial n}{\partial \delta_l} = -\frac{1}{\bar{n}} \frac{2\nu}{\delta_c} \frac{\partial n}{\partial \nu} \tag{6.22}$$

$$b_{01}^L = \frac{1}{\bar{n}} \frac{\partial n}{\partial \varphi_l} = -\frac{4 f_{NL} \nu}{\bar{n}} \frac{\partial n}{\partial \nu} = 2 f_{NL} \delta_c b_{10}^L \tag{6.23}$$

$$b_{20}^L = \frac{1}{\bar{n}} \frac{\partial^2 n}{\partial \delta_l^2} = \frac{4}{\bar{n}} \frac{\nu^2}{\delta_c^2} \frac{\partial^2 n}{\partial \nu^2} + \frac{2}{\bar{n}} \frac{\nu}{\delta_c^2} \frac{\partial n}{\partial \nu} \tag{6.24}$$

$$b_{11}^L = \frac{1}{\bar{n}} \frac{\partial^2 n}{\partial \varphi_l \partial \delta_l} = \frac{8 f_{NL}}{\bar{n}} \left(\frac{\nu^2}{\delta_c} \frac{\partial^2 n}{\partial \nu^2} + \frac{\nu}{\delta_c} \frac{\partial n}{\partial \nu} \right) \tag{6.25}$$

$$= 2 f_{NL} \left(\delta_c b_{20}^L - b_{10}^L \right) \tag{6.26}$$

$$b_{02}^L = \frac{1}{\bar{n}} \frac{\partial^2 n}{\partial \varphi_l^2} = \frac{8 f_{NL}^2}{\bar{n}} \left(2\nu^2 \frac{\partial^2 n}{\partial \nu^2} + 3\nu \frac{\partial n}{\partial \nu} \right) - \frac{12 \nu g_{NL}}{\bar{n}} \frac{\partial n}{\partial \nu} \tag{6.27}$$

$$= 4 f_{NL}^2 \delta_c \left(b_{20}^L \delta_c - 2 b_{10}^L \right) + 6 \delta_c g_{NL} b_{10}^L \tag{6.28}$$

where all the derivatives are evaluated for $\delta_l = 0, \varphi_l = 0$. We left the derivatives of the mass function unevaluated and obtained expressions that are sufficiently general to enable application to different Gaussian and non-Gaussian mass functions.[4] For instance, the derivatives of the ST mass function Eq. (6.13) are given by

$$\frac{1}{n_{ST}} \frac{\partial n_{ST}}{\partial \nu} = -\frac{q\nu - 1}{2\nu} - \frac{p}{\nu \left(1 + (q\nu)^p\right)} \tag{6.29}$$

$$\frac{1}{n_{ST}} \frac{\partial^2 n_{ST}}{\partial \nu^2} = \frac{p^2 + \nu p q}{\nu^2 \left(1 + (q\nu)^p\right)} + \frac{(q\nu)^2 - 2q\nu - 1}{4\nu^2} \tag{6.30}$$

and for the LV mass function Eq. (6.17) by

$$\frac{1}{n_{LV}} \frac{\partial n_{LV}}{\partial \nu} = \frac{1}{n_{ST}} \frac{\partial n_{ST}}{\partial \nu} + \frac{1}{R} \frac{\partial R(\nu)}{\partial \nu} \tag{6.31}$$

$$\frac{1}{n_{LV}} \frac{\partial^2 n_{LV}}{\partial \nu^2} = \frac{1}{n_{ST}} \frac{\partial^2 n_{ST}}{\partial \nu^2} + 2 \frac{1}{n_{ST} R} \frac{\partial n_{ST}}{\partial \nu} \frac{\partial R(\nu)}{\partial \nu} + \frac{1}{R} \frac{\partial^2 R(\nu)}{\partial \nu^2}. \tag{6.32}$$

The amplitude of the halo power spectrum at a given wavelength must not depend on the smoothing scale, as it is an observable. Let us imagine to perform the one loop computation of the halo power spectrum with two different smoothing scales Λ_1 and Λ_2, with $\Lambda_2 > \Lambda_1$. Since the final answer must not change as we change Λ, we need to renormalize the bias accordingly. This means that the renormalized bias at scale Λ_1 is related to the renormalized bias at scale Λ_2 by a relation of the following form [42]

$$b_{10}^{\Lambda_2} = b_{10}^{\Lambda_1} + \left(b_{20}^{\Lambda_1} \frac{68}{21} + b_{30} \right) \sigma_{\Lambda_2, \Lambda_1}^2 \tag{6.33}$$

[4] Actually one only has to calculate the derivative of $\nu f(\nu)$ since the proportionality factors cancel out.

where $\sigma^2_{\Lambda_2,\Lambda_1}$ is the real space variance computed including only wavenumbers between Λ_1 and Λ_2. Notice that the term proportional to 68/21 arises from having inserted a gravitational interaction vertex F_2. This tells us how the renormalized bias parameters change as we change the smoothing scale and include loops that renormalize the bias parameters.

In the PBS method we assume that the long mode is infinitely long. This corresponds to having taken the smoothing scale Λ to be zero (or equivalently infinitely long smoothing length). In this regime, loop corrections, that always include only modes that run from zero wavenumber to the smoothing scale, are zero by construction, as we took $\Lambda = 0$. This tells us that the PBS method provides already the renormalized bias parameters at infinite smoothing length. As we change the smoothing length and we make it shorter and shorter, we should include loops and renormalize the bias parameters accordingly following formulae similar to the one above. However, the above formula is by construction such that the effective bias parameters do not change as we change the smoothing scale. Therefore, as we change the smoothing scale, we can simply avoid including the loops, like the ones above, that renormalize the bias parameters and use directly the bias parameters that we obtain at infinite smoothing length. This will lead to the same answer as if we had included all the loop corrections and changed the bias parameters accordingly. Although this statement has not been carefully verified from a theoretical point of view, the corrections are anyways quite small on large scales and the model seems to be in accord with what is inferred from simulations. In fact in [15, 13], a good agreement between peak background split predictions for the non-Gaussian bias b_{01} and simulations has been found. Although there is evidence for a weak dependence of the bias parameters on the smoothing scale, it has been shown by [43, 44] that even the second order bias b_{20} is quite well approximated by the local bias model in Fourier space. A more precise treatment of this point goes beyond the scope of the present paper as it would require calculations at loop level and comparison to numerical simulations.

However, the fact that the peak background split method leads directly to the renormalized bias parameters is independent of the assumption of Gaussian initial conditions. Thus it is not unreasonable to assume that this fact also extends to the non-Gaussian bias parameters used in our study.

The derivation presented so far assumes an universal mass function, *i. e.* that all the dependence on the long modes is implicitly encoded in the peak height ν. However, intrinsically non-Gaussian properties of the distribution enter in the non-Gaussian mass function, for example $S_3\sigma$ in the case of the LV mass function. Following an argument similar to the one we used to derive the φ_l dependence of the variance in Eq. (6.6), one can show based on Eq. (6.7) that the three point function in the presence of a long fluctuation gets rescaled as $\langle\delta_M^3\rangle \to \langle\delta_M^3\rangle\,(1 + 4f_\mathrm{NL}\varphi_\mathrm{l})$. This dependence on φ_l can not be encoded in ν and thus an additional explicit derivative with respect to the long wavelength potential arises, which leads to the following corrections to the bias parameters, for example for the LV mass function:

$$\Delta b_{01} = \frac{2}{3}\frac{f_\mathrm{NL}C_3}{R}\left(\nu^{3/2} - 3\nu^{1/2}\right) \tag{6.34}$$

$$\Delta b_{11} = -\frac{2}{3}\frac{f_\mathrm{NL}C_3\nu}{R\delta_c}\left[\frac{1}{n_\mathrm{ST}}\frac{\partial n_\mathrm{ST}}{\partial\nu}\left(\nu^{3/2} - 3\nu^{1/2}\right) + \frac{3}{2}\left(\nu^{1/2} - \nu^{-1/2}\right)\right] \tag{6.35}$$

$$\Delta b_{02} = -\frac{16}{3}\frac{f_\mathrm{NL}^2\nu C_3}{R}\left[\frac{1}{n_\mathrm{ST}}\frac{\partial n_\mathrm{ST}}{\partial\nu}\left(\nu^{3/2} - 3\nu^{1/2}\right) + \frac{3}{2}\left(\nu^{1/2} - \nu^{-1/2}\right)\right] \tag{6.36}$$

These corrections are generally of the same order as the bias corrections arising from the non-Gaussian LV mass function in Eq. (6.31) and (6.32). However, for high ν the latter dominate. For realistic values of f_NL all the bias corrections arising from the non-Gaussian mass function are on the percent level. The mass function itself can be trusted at the 10% level only and thus these corrections can be safely neglected.

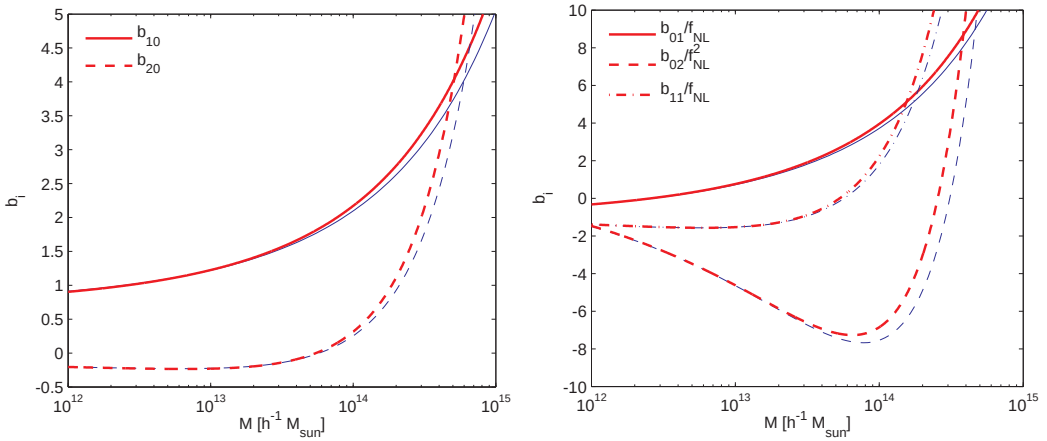

Figure 6.2.: Eulerian multivariate bias parameters for $f_{\rm NL} = 100$, $g_{\rm NL} = 0$. *Left panel:* Bias parameters for δ. *Right panel:* Bias parameters for φ. For $g_{\rm NL} = 0$ one has $b_{02} \propto f_{\rm NL}^2$, $b_{01} \propto f_{\rm NL}$, $b_{11} \propto f_{\rm NL}$ and thus the rescaled bias parameters are independent of $f_{\rm NL}$. b_{02} shown by the dashed line shows a pronounced minimum for $M \approx 1 \times 10^{14}\ h^{-1} M_\odot$ that is multiplied by $f_{\rm NL}^2$ and can thus lead to a large contribution. The red lines are derived from the ST mass function, whereas the blue thin lines are derived from the LV mass function including the explicit $\varphi_{\rm l}$ correction of Eqs. (6.34), (6.35) and (6.36).

6.3.3. Transformation to Eulerian Space

Observations are performed in the late time evolved Eulerian density field. It thus remains to translate the above result to Eulerian space. The halo density fields in Eulerian and Lagrangian space are related by [45]

$$\left(1 + \delta_{\rm h}^{\rm E}\right) = (1 + \delta)(1 + \delta_{\rm h}^{\rm L}). \tag{6.37}$$

Finally, one wants to write down the Eulerian analogue of Eq. (6.20)

$$\delta_h^{\rm E}(\boldsymbol{x}) = b_{10}^{\rm E}\delta(\boldsymbol{x}) + b_{01}^{\rm E}\varphi(\boldsymbol{x}) + \frac{b_{20}^{\rm E}}{2!}\delta^2(\boldsymbol{x}) + b_{11}^{\rm E}\delta(\boldsymbol{x})\varphi(\boldsymbol{x}) + \frac{b_{02}^{\rm E}}{2!}\varphi^2(\boldsymbol{x}) + \dots \tag{6.38}$$

In what follows we will absorb the prefactors in the bias parameters, thus $b_{20}/2! \to b_{20}$ and $b_{02}/2! \to b_{02}$. The linearly evolved Lagrangian overdensity can be expanded in powers of the final Eulerian overdensity

$$\delta_0 = \sum_i a_i \delta^i = a_1\delta + a_2\delta^2 + a_3\delta^3 + \dots \tag{6.39}$$

where the expansion parameters a_i are given by the spherical collapse dynamics $a_1 = 1$, $a_2 = -17/21$, $a_3 = 341/567$. We calculated the corresponding Eulerian bias parameters using the relations in [45, 46, 30]

$$b_{10}^{\rm E} = 1 + b_{10}^{\rm L} \tag{6.40}$$
$$b_{20}^{\rm E} = 2(a_1 + a_2)b_{10}^{\rm L} + a_1^2 b_{20}^{\rm L} \tag{6.41}$$
$$b_{01}^{\rm E} = b_{01}^{\rm L} \tag{6.42}$$
$$b_{02}^{\rm E} = b_{02}^{\rm L} \tag{6.43}$$
$$b_{11}^{\rm E} = b_{11}^{\rm L} a_1 + b_{01}^{\rm L} \tag{6.44}$$

Calculations of the evolved density field are most conveniently done in Fourier space. Thus we translate the above expansion Eq. (6.38) to k-space.

$$\delta_{\rm h}(\boldsymbol{k}) = b_{10}^{\rm E}\delta(\boldsymbol{k}) + b_{01}^{\rm E}\varphi(\boldsymbol{k}) + b_{20}^{\rm E}\,[\delta * \delta](\boldsymbol{k}) + b_{11}^{\rm E}[\delta * \varphi](\boldsymbol{k}) + b_{02}^{\rm E}[\varphi * \varphi](\boldsymbol{k}), \tag{6.45}$$

where we introduced the notation $[\delta * \delta](\boldsymbol{k})$ as a shorthand for the convolution integral. From now on we will omit the superscript E and all bias factors should be understood as the Eulerian ones.
In Fig. 6.2 we show the mass dependence of the bias parameters arising from the Gaussian ST and the non-Gaussian LV mass function. The bias factors of the potential and the density-potential cross term are scaled by their f_{NL} dependence. From this figure it is obvious that the second order biases can be negative over large parts of the interesting mass range. This can lead to subtle cancellations between terms in the resulting galaxy or halo n-point functions. Furthermore, the f_{NL}^2 dependence and the pronounced minimum in $b_{02}(M)$ around $M = 10^{14}\ h^{-1}M_\odot$ can boost the corresponding terms on large scales. As noted already by [16] and apparent in Fig. 6.2, the non-Gaussian mass function Eq. (6.17) leads to an additional scale independent offset in the bias. From Fig. 6.2 we see that the difference in the bias parameters is most apparent for high mass haloes, whereas there is only a small difference for low mass haloes. The differences between the bias from the two mass functions are very small and negligible for our purposes. The same is approximately true even for the other non-Gaussian mass functions. Thus we use the Gaussian ST mass function for our numerical predictions.

6.4. Perturbation Theory including non-Gaussianity

6.4.1. Matter Density Field

Perturbation theory (PT) aims to solve the cosmological fluid equations using an expansion about the linear overdensity $\delta_{\mathrm{m}}^{(1)}(\boldsymbol{k})$ [47]

$$\delta_{\mathrm{m}}(\boldsymbol{k}) = \delta_{\mathrm{m}}^{(1)}(\boldsymbol{k}) + \delta_{\mathrm{m}}^{(2)}(\boldsymbol{k}) + \delta_{\mathrm{m}}^{(3)}(\boldsymbol{k}) + \dots . \tag{6.46}$$

In our approach, these modes should be thought of as having wavelength longer that the cutoff Λ^{-1} that separates short and long modes. Let us define a linearly evolved primordial density field (*i.e.* evolved without taking into account the gravitational evolution), to be $\delta_{\mathrm{m,p}}$. At first order, $\alpha(k,z)\varphi(\boldsymbol{k}) = \delta_{\mathrm{m,p}}^{(1)}(\boldsymbol{k},z)$, *i. e.* the primordial Gaussian potential φ is of the same order as the primordial linear overdensity $\delta_{\mathrm{m,p}}^{(1)}$. In the following we refer to these two quantities as first order quantities and count the order of terms by counting the powers of first order terms. The non-Gaussian self-coupling of the potential introduces non-linearities in the evolved primordial density field, whereas in the Gaussian case we would have $\delta_{\mathrm{m,p}} = \delta_{\mathrm{m,p}}^{(1)}$. Transforming Eq. (6.2) to Fourier space and applying Eq. (6.8) we obtain for the linearly evolved primordial matter density up to third order

$$\begin{aligned}
\delta_{\mathrm{m,p}}(\boldsymbol{k},z) =& \alpha(k,z)\Phi(\boldsymbol{k}) && (6.47)\\
=& \alpha(k,z)\varphi(\boldsymbol{k}) + \alpha(k,z) f_{\mathrm{NL}} \int \frac{\mathrm{d}^3 q}{(2\pi)^3}\varphi(\boldsymbol{q})\varphi(\boldsymbol{k}-\boldsymbol{q}) \\
&+\alpha(k,z) g_{\mathrm{NL}} \int \frac{\mathrm{d}^3 q}{(2\pi)^3}\int \frac{\mathrm{d}^3 q'}{(2\pi)^3}\varphi(\boldsymbol{q})\varphi(\boldsymbol{q}')\varphi(\boldsymbol{k}-\boldsymbol{q}-\boldsymbol{q}'), && (6.48)\\
=& \delta_{\mathrm{m,p}}^{(1)}(\boldsymbol{k},z) + f_{\mathrm{NL}}\delta_{\mathrm{m,p}}^{(2)}(\boldsymbol{k},z) + g_{\mathrm{NL}}\delta_{\mathrm{m,p}}^{(3)}(\boldsymbol{k},z). && (6.49)
\end{aligned}$$

The resulting field is then subject to late-time non-linear gravitational clustering, which introduces further couplings. To take this effect into account we use the evolved primordial distribution as the source for the late time evolution and insert Eq. (6.49) into the known PT expressions for $\delta_{\mathrm{m}}^{(1)}$, $\delta_{\mathrm{m}}^{(2)}$ and $\delta_{\mathrm{m}}^{(3)}$ (see Ch. 3)

$$\begin{aligned}
\delta_{\mathrm{m,nG}}^{(1)}(\boldsymbol{k},z) =& \delta_{\mathrm{m,p}}^{(1)}(\boldsymbol{k},z), && (6.50)\\
\delta_{\mathrm{m,nG}}^{(2)}(\boldsymbol{k},z) =& \int \frac{\mathrm{d}^3 q}{(2\pi)^3}\delta_{\mathrm{m,p}}^{(1)}(\boldsymbol{q})\delta_{\mathrm{m,p}}^{(1)}(\boldsymbol{k}-\boldsymbol{q})F_2(\boldsymbol{q},\boldsymbol{k}-\boldsymbol{q})
\end{aligned}$$

$$+f_{\rm NL}\delta^{(2)}_{\rm m,p}(\boldsymbol{k},z), \tag{6.51}$$

$$\begin{aligned}\delta^{(3)}_{\rm m,nG}(\boldsymbol{k},z) =& \int\frac{{\rm d}^3q}{(2\pi)^3}\int\frac{{\rm d}^3q'}{(2\pi)^3}\delta^{(1)}_{\rm m,p}(\boldsymbol{q},z)\delta^{(1)}_{\rm m,p}(\boldsymbol{q}',z)\delta^{(1)}_{\rm m,p}(\boldsymbol{k}-\boldsymbol{q}-\boldsymbol{q}',z)F_3(\boldsymbol{q},\boldsymbol{q}',\boldsymbol{k}-\boldsymbol{q})\\ &+2f_{\rm NL}\int\frac{{\rm d}^3q}{(2\pi)^3}\delta^{(1)}_{\rm m,p}(\boldsymbol{q},z)\delta^{(2)}_{\rm m,p}(\boldsymbol{k}-\boldsymbol{q},z)F_2(\boldsymbol{q},\boldsymbol{k}-\boldsymbol{q})\\ &+g_{\rm NL}\delta^{(3)}_{\rm m,p}(\boldsymbol{k},z),\end{aligned} \tag{6.52}$$

where $F_2(\boldsymbol{k}_1,\boldsymbol{k}_2)$ and $F_3(\boldsymbol{k}_1,\boldsymbol{k}_2,\boldsymbol{k}_3)$ are the standard second and third order mode coupling kernels.

6.4.2. Halo Density Field

The halo density including higher order corrections from biasing, non-Gaussianity and non-linear clustering can be derived using Eq. (6.46) in Eq. (6.45)

$$\begin{aligned}\delta_{\rm h}(\boldsymbol{k}) =& b_{10}\left(\delta^{(1)}_{\rm m,nG}(\boldsymbol{k})+\delta^{(2)}_{\rm m,nG}(\boldsymbol{k})\right)+b_{01}\varphi(\boldsymbol{k})\\ &+b_{20}\big[\delta^{(1)}_{\rm m,nG}*\delta^{(1)}_{\rm m,nG}\big](\boldsymbol{k})+b_{11}\big[\delta^{(1)}_{\rm m,nG}*\varphi\big](\boldsymbol{k})+b_{02}\big[\varphi*\varphi\big](\boldsymbol{k})\\ =&b_{10}\delta^{(1)}_{\rm m,p}(\boldsymbol{k})+b_{01}\varphi(\boldsymbol{k})\\ &+b_{02}\int\frac{{\rm d}^3q}{(2\pi)^3}\varphi(\boldsymbol{q})\varphi(\boldsymbol{k}-\boldsymbol{q})+b_{20}\int\frac{{\rm d}^3q}{(2\pi)^3}\delta^{(1)}_{\rm m,p}(\boldsymbol{q})\delta^{(1)}_{\rm m,p}(\boldsymbol{k}-\boldsymbol{q})\\ &+b_{10}\int\frac{{\rm d}^3q}{(2\pi)^3}\delta^{(1)}_{\rm m,p}(\boldsymbol{q})\delta^{(1)}_{\rm m,p}(\boldsymbol{k}-\boldsymbol{q})F_2(\boldsymbol{q},\boldsymbol{k}-\boldsymbol{q})+\alpha(k)f_{\rm NL}b_{10}\int\frac{{\rm d}^3q}{(2\pi)^3}\varphi(\boldsymbol{q})\varphi(\boldsymbol{k}-\boldsymbol{q})\\ &+b_{11}\int\frac{{\rm d}^3q}{(2\pi)^3}\delta^{(1)}_{\rm m,p}(\boldsymbol{q})\varphi(\boldsymbol{k}-\boldsymbol{q}).\end{aligned} \tag{6.53, 6.54}$$

Note that at lowest order we recover the well known result of [13]

$$\delta_{\rm h}(\boldsymbol{k})=\left(b_{10}+\frac{2f_{\rm NL}\delta_{\rm c}(b_{10}-1)}{\alpha(k)}\right)\delta_{\rm m,p}(\boldsymbol{k}). \tag{6.55}$$

At this order the potential can be replaced by the density due to the linearity of the Poisson equation in k-space. Thus one finally obtains an expression that is proportional to the density, but non-local. The next to leading order, however, is not proportional to $\delta^2(\boldsymbol{k})$ since the density and the potential are convolved with each other. It is due to this effect that the bias expansion should be performed both in δ and φ.

We would like to stress an important subtlety concerning the usage of the bias parameters obtained from the peak background split in perturbation theory. Depending on the precision required for the calculation, it is possible that higher order corrections from perturbation theory need to be implemented. In the diagrammatic description, which is explained in the next subsection, there are loop diagrams (convolutions of the fields with some kernel) involving non-linear bias vertices. Unfortunately, some of these diagrams are highly dependent on the cutoff Λ (*i.e.* the smoothing scale). Clearly, physical quantities should not depend on the smoothing scale. This spurious dependence can be removed by defining effective or, more precisely, *renormalized* bias parameters that take into account both the tree level and the loop contributions and that are directly connected to observable quantities. For example, it is possible to show that loop corrections to the power spectrum originating for example from b_{20} and b_{30} terms effectively renormalize b_{10} and b_{01} [42, 48].[5]

[5] In fact, it is easy to estimate the one loop contribution due to b_{20} combined with an $f_{\rm NL}$ vertex and an F_2 vertex (see next section for these definitions). This diagram induces an effective bias b_{01} numerically equivalent to the one obtained from the peak-background split if one considers small external k's, a very high

Finally, it should be stressed that even the remaining perturbation theory should be performed in a way that ensures that the remaining contributions are independent of the smoothing length Λ^{-1}. This suggests to use a carefully defined perturbation theory, such as for example 'renormalized perturbation theory' [49], or the recently proposed effective fluid description of cosmological perturbations [50].

6.4.3. Diagrammatic Representation

In the previous section we derived the perturbative expressions for the matter and halo density fields. As a consequence of the stochastic nature of cosmological fluctuations, there is no hope to directly predict the observed distribution of galaxies and matter in the Universe. Rather, we need to calculate expectation values of products of the fields and compare them to the corresponding statistics as measured in the sky. The calculation of these statistics turns out to be an involved combinatorial task if one goes beyond second order in the fields.
To facilitate these calculations, we present a diagrammatic representation of the mode coupling terms that arise from biasing, non-linear clustering and non-Gaussianity. Similar diagrammatic representations of perturbation theory have been used in the literature [51, 52, 47, 53] but we are not aware of an intuitive inclusion of all the three effects into one prescription. These Feynman diagrams show intuitively which coupling terms arise and can be translated into the corresponding equations by straightforward application of a set of Feynman rules.
Let us start representing the fields, as the basic ingredients of the theory. What we want to calculate in the end are correlators of halo or matter density fields, thus we need symbols for the outer points, namely δ_h and δ_m. The latter two are represented by the half filled and filled circles depicted in Fig. 6.3. Note that when δ_m is used for an outer point it always includes all the possible non-Gaussian and non-linear contributions up to the considered order, whereas the density as a source field is linear. Next, we consider the primordial potential φ, represented by an open circle. Even if $\alpha(k)\varphi(\boldsymbol{k}) = \delta^{(1)}_{\mathrm{m,p}}(\boldsymbol{k})$, we introduce symbols for both the density and potential to make the $1/k^2$ behavior of the potential terms more obvious and to make sure that the potential terms arise only directly from the initial conditions. However, no difference is made between the evolved primordial and the late time non-linear matter density field in terms of the symbols, because they can be distinguished from the context. For instance, the coupling vertices for gravity are sourced by evolved primordial matter fields defined in Eq. (6.49) and lead to non-linear fields (see the discussion of the vertices below for more details). Finally, the initial conditions are known in terms of the power spectra of fluctuations. Thus we also introduce the power spectrum symbolized by the half filled big circle, where subscripts are used to distinguish the density-density, density-potential and potential-potential power spectra.

Figure 6.3.: Symbols use to represent the fields and power spectra. From left to right, the primordial Gaussian potential φ, the matter density field δ_m, the galaxy/halo density field δ_h, and the power spectrum $P(k)$ arising from two linked fields.

mass scale and most importantly sets the smoothing scale equal to the mass scale of the halo as done in [22]. This is an effect that arises from pushing the smoothing scale to very high k's, where it is unclear whether perturbative calculations can be trusted. These renormalized parameters do not depend on the smoothing scale, while the coupling constants with which we perform perturbation theory and the contributions from loop diagrams do depend on the cutoff Λ. This is a behavior familiar from quantum field theory. Actually, as mentioned in the former section, the bias parameters inferred from the peak background split method can be interpreted as the renormalized ones. Therefore, loop diagrams causing the renormalization have been already accounted for. This guarantees that the tree level calculation presented here provides the dominant contribution on very large scales. A more precise understanding of this point lies beyond the scope of the present paper, where we concentrate only on the tree-level calculation and do not deal explicitly with loop orders.

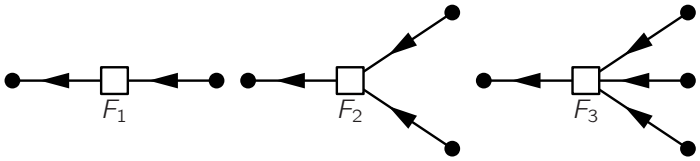

Figure 6.4.: Non-linear gravitational clustering leads to a convolution integral weighted by a F_i kernel, which we symbolize by a square shaped vertex. From left to right we show the first, second and third order mode coupling contributions to the matter density field. Note that $F_1 \equiv 1$.

The non-linear clustering vertices (we will refer to them also as gravity vertices) F_i, coupling two matter density fields, are represented by the open squares shown in Fig. 6.4. The input density field on the right hand side is an evolved primordial field $\delta_{\mathrm{m,p}}$ defined in Eq. (6.49), which receives higher order corrections from non-Gaussianity only. Fig. 6.5 shows the vertices arising from the multivariate bias expansion, where the input can be a matter density field of any order or the primordial potential. The identification of the higher order bias terms with vertices is possible, since in k-space the products of fields lead to convolution integrals, which are similar to the non-linear gravity terms, where the F_i kernels are replaced by the scale independent bias factors b_{ij}. Thus we interpret biasing as an unweighted convolution of source modes. As noted above, loop diagrams involving higher order bias vertices can thus lead to large or divergent contributions, effectively renormalising lower order bias parameters. Similarly, the non-Gaussian terms are effectively coupling potential modes to a higher order primordial matter mode $\delta^{(n)}_{\mathrm{m,p}}$. This interaction is represented by the diamond shaped open vertices depicted in Fig. 6.6, corresponding to $\alpha(k)Q_{\mathrm{NL}}$, where $Q_{\mathrm{NL}} = \{e_{\mathrm{NL}}, f_{\mathrm{NL}}, \ldots\}$. These coupling vertices are a specific property of local type non-Gaussianity, basically expanding the bispectrum in terms of the primordial potential

$$B_{\Phi\Phi\Phi}(\boldsymbol{k}_1, \boldsymbol{k}_2, \boldsymbol{k}_3) = 2 f_{\mathrm{NL}} P_{\varphi\varphi}(\boldsymbol{k}_1) P_{\varphi\varphi}(\boldsymbol{k}_2) + 2 \text{ cyc.}. \tag{6.56}$$

For other shapes of non-Gaussianity such an expansion might take a different form with a k-dependent kernel that can be easily included.
Time integration is trivially performed in standard perturbation theory since all the initial fields are linearly evolved, considering only the growing mode. Thus the lines correspond to propagators, *i. e.* linear growth factors. However, these linear growth factors can be used to transform the initial fields to linearly evolved fields such that we can totally ignore the time evolution as long as we use linearly evolved primordial matter fields as a source. We only need to ensure causality by following the time evolution of the fields. Non-Gaussian coupling happens directly after inflation, then non-linear clustering and finally biasing. The lines used to connect the primordial potential with the non-Gaussian vertices and the non-Gaussian bias vertices are dashed to highlight the fact that the coupling of primordial potentials, and thus the imprint of non-Gaussianity, happens directly after inflation. To facilitate the distinction of the density propagators, we use straight and wiggly lines for the matter and halo density field, respectively. The i-th order contribution to an evolved matter or halo field can be obtained following the time evolution step by step starting from the initial conditions and going all the way to the final field

1. Draw i initial fields $\delta^{(1)}_{\mathrm{m,p}}$ or φ.

2. Draw the non-Gaussian Q_{NL} vertices and connect them to the primordial potential using dashed lines.

3. Draw the gravity vertices and connect them to the non-Gaussian vertices or initial density fields by solid lines.

4. For biased tracers, draw the bias vertices and connect them to either initial density fields, gravity vertices, non-Gaussian vertices or primordial potentials. Use a wiggly line to connect them with the outer point.

So far we focused our attention on the fields. To compute the i-th order contribution[6] to the n-spectra we need to glue n diagrams with i source fields and n outer points in all possible ways and then pair the source fields in all possible ways. Two linked source fields lead to a power spectrum and a momentum conserving delta function $\langle\delta(\boldsymbol{k})\delta(\boldsymbol{k}')\rangle = (2\pi)^3\delta^{(D)}(\boldsymbol{k}+\boldsymbol{k}')P_{\delta\delta}(k)$. The potential-potential and density-potential power spectra are related to the density-density power spectra by the appropriate Poisson factors $\alpha(k,z)$. For the translation of the above diagrams into mathematical expressions we assign k-vectors to each of the outer fields. The different ways of performing this assignment are accounted for by the cyclic permutations of the k-vectors.

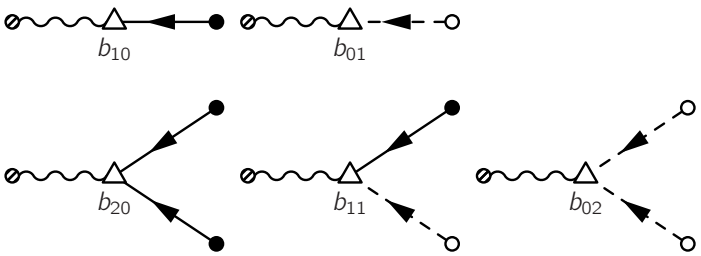

Figure 6.5.: The multivariate bias expansion can be expressed by the triangular vertices shown above. The interaction of two fields on a vertex corresponds to a convolution integral over the ingoing k-vectors without any weighting. The vertex is connected to the outer point by the wiggly halo propagator. Ingoing potentials are always primordial because the coupling of long and short modes, and thus the enhancement of the short wavelength variance, happens in the early Universe.

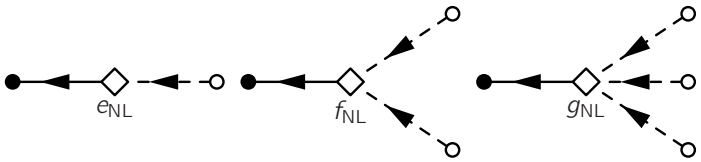

Figure 6.6.: The non-Gaussian vertices correspond to an unweighted convolution integral times one factor of α and the corresponding $Q_{\mathrm{NL}} = \{e_{\mathrm{NL}}, f_{\mathrm{NL}}, \ldots\}$. We introduce the e_{NL} vertex to represent the conversion from φ to $\delta^{(1)}_{\mathrm{m,p}}$. Note that the ingoing potentials are always primordial, which is highlighted by the dashed line.

6.4.4. Feynman Rules for the n-Spectra

Even though the diagrams can be straightforwardly translated into the corresponding mathematical expressions we write down the Feynman rules explicitly for the sake of definiteness. For the calculation of the i-th order contribution to the n-spectrum do the following

1. Draw all distinct connected diagrams with n external lines up to the desired order i in φ
   i.) For each vertex with ingoing momenta $\boldsymbol{q}_i$ and outgoing momenta $\boldsymbol{p}_j$ write a delta function $\delta^{(\mathrm{D})}\left(\sum_i \boldsymbol{q}_i - \sum_j \boldsymbol{p}_j\right)$

[6] The index i has to be even since the correlator of an odd number of Gaussian fields vanishes due to the Wick-theorem

ii.) Assign a linear power spectrum $(2\pi)^3\delta^{(D)}(\boldsymbol{q}+\boldsymbol{q}')P_{\rm lin}(q)$ to each of the big circles with outgoing momenta $\boldsymbol{q}$ and $\boldsymbol{q}'$. Divide by $\alpha(q)$ or $\alpha^2(q)$ for $P_{\delta\varphi}$ and $P_{\varphi\varphi}$, respectively.

iii.) For the outer fields with momenta $\boldsymbol{k}_i$ write a delta function $\delta^{(\rm D)}\left(\sum_i \boldsymbol{k}_i\right)$

iv.) For each square shaped vertex F_n with ingoing momenta $\boldsymbol{q}_i$ write a mode coupling kernel $F_n(\boldsymbol{q}_1,\ldots,\boldsymbol{q}_n)$

v.) For each triangular shaped vertex write a bias factor b_{ij}

vi.) For each diamond shaped vertex $Q_{\rm NL}=\{e_{\rm NL}, f_{\rm NL}, g_{\rm NL},\ldots\}$ with outgoing momentum $\boldsymbol{q}$ write $\alpha(\boldsymbol{q})Q_{\rm NL}$

vii.) Integrate over all inner momenta $\int d^3q_i/(2\pi)^3$

viii.) Multiply with the symmetry factor

ix.) Sum over all distinct labelings of the external lines

2. Add up the resulting expressions from all diagrams

6.4.5. Matter Power Spectrum

As a first application of our diagrammatic approach we write down the terms contributing to the non-Gaussian matter power spectrum and show the corresponding diagrams in Fig. 6.7

$$\begin{aligned}P_{\rm mm}(k) =& P_{11}(k)+P_{22}(k)+P_{13}(k)\\ &+\left(2\alpha^2(k)f_{\rm NL}^2\int\frac{{\rm d}^3q}{(2\pi)^3}\frac{P(q)}{\alpha^2(q)}\frac{P(\boldsymbol{k}-\boldsymbol{q})}{\alpha^2(\boldsymbol{k}-\boldsymbol{q})}\right)_{\rm A}\\ &+\left(4\alpha(k)f_{\rm NL}\int\frac{{\rm d}^3q}{(2\pi)^3}\frac{P(q)}{\alpha(q)}\frac{P(\boldsymbol{k}-\boldsymbol{q})}{\alpha(\boldsymbol{k}-\boldsymbol{q})}F_2(\boldsymbol{q},\boldsymbol{k}-\boldsymbol{q})\right)_{\rm B}\\ &+\left(8f_{\rm NL}\frac{P(k)}{\alpha(k)}\int\frac{{\rm d}^3q}{(2\pi)^3}\frac{P(q)}{\alpha(q)}F_2(\boldsymbol{q},\boldsymbol{k}-\boldsymbol{q})\alpha(\boldsymbol{k}-\boldsymbol{q})\right)_{\rm C}\\ &+\left(6\alpha(k)g_{\rm NL}\frac{P(k)}{\alpha(k)}\int\frac{{\rm d}^3q}{(2\pi)^3}\frac{P(q)}{\alpha^2(q)}\right)_{\rm D},\end{aligned} \tag{6.57}$$

where P_{13} and P_{22} are the standard one-loop corrections to the power spectrum (see [47] and Appendix A). The subscripts on the brackets in the above equation can be used to identify the corresponding terms in Fig. 6.7. The functional form agrees with previous results as presented in [54], who also performed a numerical evaluation which is thus not repeated here. The corrections arising from the $f_{\rm NL}$ terms are generally small and most prominent for high k, where the validity of perturbation theory has to be doubted.

6.4.6. Matter Bispectrum

A non-vanishing matter bispectrum beyond the non-linear gravitational contribution would be a direct sign of non-Gaussian initial conditions. From the diagrams depicted in Fig. 6.8 we can derive the following expression for the tree-level matter bispectrum

$$B_{\rm mmm}(\boldsymbol{k}_1,\boldsymbol{k}_2,\boldsymbol{k}_3)=\left(2P(k_1)P(k_2)F_2(\boldsymbol{k}_1,\boldsymbol{k}_2)+2\text{ cyc.}\right)+\left(2f_{\rm NL}\frac{P(k_1)P(k_2)\alpha(k_3)}{\alpha(k_1)\alpha(k_2)}+2\text{ cyc.}\right) \tag{6.58}$$

$$=B_{F_2}(\boldsymbol{k}_1,\boldsymbol{k}_2,\boldsymbol{k}_3)+B_{f_{\rm NL}}(\boldsymbol{k}_1,\boldsymbol{k}_2,\boldsymbol{k}_3) \tag{6.59}$$

Here cyc. is used to symbolise that the function arguments in the preceding terms have to be cyclically permuted as $\{(k_1,k_2,k_3),(k_2,k_3,k_1),(k_3,k_1,k_2)\}$. An evaluation of the latter term

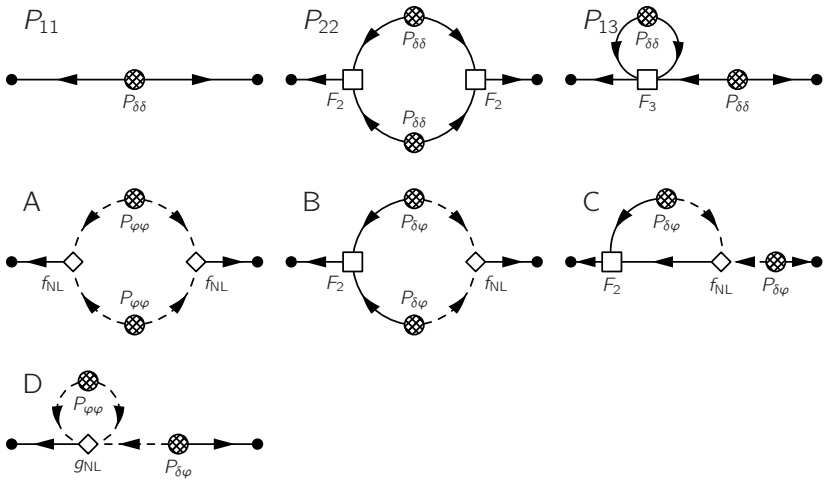

Figure 6.7.: Diagrams contributing to the matter power spectrum as calculated in Eq. (6.57). The first line shows the standard PT terms, whereas the terms in the second and third line are purely non-Gaussian.

and comparison to n-body simulations is provided in a recent study by [55]. They find that the inclusion of one-loop terms leads to a considerable improvement of the agreement between theory and simulation on scales exceeding $k = 0.1\ h\mathrm{Mpc}^{-1}$.

Estimating the bispectrum of the dark matter distribution is an involved task even for the upcoming lensing surveys. Thus we will focus our attention on the bispectra of biased tracers such as galaxies in the next section.

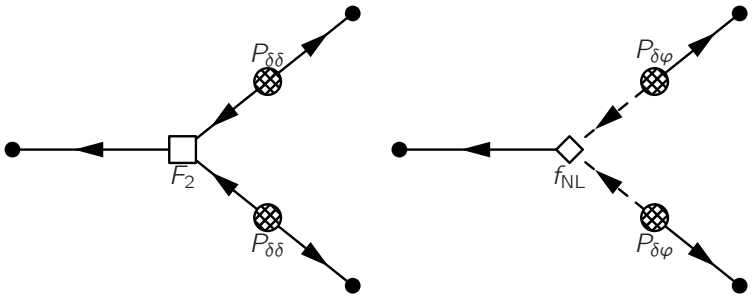

Figure 6.8.: The two diagrams contributing to the tree level matter bispectrum $B_{\rm mmm}$ in Eq. (6.59).

6.5. Bispectra of Biased Tracers

In the following section we present the main result of this paper, the derivation of the halo bispectra. The bispectrum measures the correlation between three fields and thus halo and matter fields lead to four possible combinations. The matter auto-bispectrum was already discussed in the previous section such that we can focus our attention in this section to bispectra involving at least one biased tracer.

6.5.1. Halo Bispectrum

Summing up the diagrammatic expressions shown in Fig. 6.9 we can write down the tree-level expression for the halo auto-bispectrum

$$
\begin{aligned}
B_{\mathrm{hhh}}(\boldsymbol{k}_1,\boldsymbol{k}_2,\boldsymbol{k}_3) =& b_{10}^3\left(2P(k_1)P(k_2)F_2(\boldsymbol{k}_1,\boldsymbol{k}_2)+2f_{\mathrm{NL}}\frac{P(k_1)P(k_2)\alpha(k_3)}{\alpha(k_1)\alpha(k_2)}+2\text{ cyc.}\right)_{\mathrm{A}}\\
&+b_{10}^2 b_{01}\left(2P(k_1)P(k_2)\left(\frac{1}{\alpha(k_1)}+\frac{1}{\alpha(k_2)}\right)F_2(\boldsymbol{k}_1,\boldsymbol{k}_2)\right.\\
&\left.+\,2f_{\mathrm{NL}}\frac{P(k_1)P(k_2)\alpha(k_3)}{\alpha(k_1)\alpha(k_2)}\left(\frac{1}{\alpha(k_1)}+\frac{1}{\alpha(k_2)}\right)+2\text{ cyc.}\right)_{\mathrm{B}}\\
&+b_{10}b_{01}^2\left(2\frac{P(k_1)P(k_2)}{\alpha(k_1)\alpha(k_2)}F_2(\boldsymbol{k}_1,\boldsymbol{k}_2)+2f_{\mathrm{NL}}\frac{P(k_1)P(k_2)\alpha(k_3)}{\alpha^2(k_1)\alpha^2(k_2)}+2\text{ cyc.}\right)_{\mathrm{C}}\\
&+b_{01}^2 b_{02}\left(2\frac{P(k_1)P(k_2)}{\alpha^2(k_1)\alpha^2(k_2)}+2\text{ cyc.}\right)_{\mathrm{D}}\\
&+b_{01}b_{10}b_{02}\left(2\frac{P(k_1)P(k_2)}{\alpha(k_1)\alpha(k_2)}\left(\frac{1}{\alpha(k_1)}+\frac{1}{\alpha(k_2)}\right)+2\text{ cyc.}\right)_{\mathrm{E}}\\
&+b_{10}^2 b_{02}\left(2\frac{P(k_1)P(k_2)}{\alpha(k_1)\alpha(k_2)}+2\text{ cyc.}\right)_{\mathrm{F}}\\
&+b_{01}^2 b_{11}\left(\frac{P(k_1)P(k_2)}{\alpha(k_1)\alpha(k_2)}\left(\frac{1}{\alpha(k_1)}+\frac{1}{\alpha(k_2)}\right)+2\text{ cyc.}\right)_{\mathrm{G}}\\
&+b_{01}b_{10}b_{11}\left(P(k_1)P(k_2)\left(\frac{1}{\alpha^2(k_1)}+\frac{2}{\alpha(k_1)\alpha(k_2)}+\frac{1}{\alpha^2(k_2)}\right)+2\text{ cyc.}\right)_{\mathrm{H}}\\
&+b_{10}^2 b_{11}\left(P(k_1)P(k_2)\left(\frac{1}{\alpha(k_1)}+\frac{1}{\alpha(k_2)}\right)+2\text{ cyc.}\right)_{\mathrm{I}}\\
&+b_{01}^2 b_{20}\left(2\frac{P(k_1)P(k_2)}{\alpha(k_1)\alpha(k_2)}+2\text{ cyc.}\right)_{\mathrm{J}}\\
&+b_{01}b_{10}b_{20}\left(2P(k_1)P(k_2)\left(\frac{1}{\alpha(k_1)}+\frac{1}{\alpha(k_2)}\right)+2\text{ cyc.}\right)_{\mathrm{K}}\\
&+b_{10}^2 b_{20}\left(2P(k_1)P(k_2)+2\text{ cyc.}\right)_{\mathrm{L}}
\end{aligned}
\tag{6.60}
$$

The subscripts on the brackets can be used to identify the terms with the corresponding diagrams in Fig. 6.9. In the diagrams and the above equation there are no explicit g_{NL} terms, since the g_{NL} vertices are not explicitly contributing to the tree level halo bispectrum. However, there is an implicit dependence via the second order bias parameter b_{02}. We will not further examine this dependence since it changes only a parameter of the model. Note that for $g_{\mathrm{NL}}=0$ the bias factors scale approximately as $b_{01}\propto f_{\mathrm{NL}}$, $b_{02}\propto f_{\mathrm{NL}}^2$ and $b_{11}\propto f_{\mathrm{NL}}$. Thus the exponent of f_{NL} in the terms is the same as the exponent of $\alpha(k)$ in the denominator. Hence, it is the ratio of $f_{\mathrm{NL}}/\alpha(k)$, where $k=\min\{k_1,k_2,k_3\}$ that is dominating the overall amplitude on large scales. The highest order contribution is f_{NL}^4 in the D term. This term is negative and gains importance for extremely small k and large f_{NL}.
The wave vectors are related by $\boldsymbol{k}_1+\boldsymbol{k}_2+\boldsymbol{k}_3=0$ and thus the configuration is fully determined by the magnitude of one vector k_1, one angle $\mu=\boldsymbol{k}_1\cdot\boldsymbol{k}_2/(k_1k_2)$ and the ratio of two vectors $x_2=k_2/k_1$. The magnitude of the third vector is then given by

$$
x_3=\frac{k_3}{k_1}=\sqrt{1+2\mu x_2+x_2^2}, \tag{6.61}
$$

which for the isosceles configuration $k_1=k_2$ simplifies to $x_3=\sqrt{2(1+\mu)}$. The transfer function is unity for large scale modes entering horizon after matter radiation equality and is damped on small scales, leading to an asymptotic slope of ≈ -1.75. Starting from a primordial

power spectrum $P_0(k) = Ak^n$ with $n \approx 1$ we see that the primordial Gaussian potential is scale invariant with $P_{\varphi\varphi} \propto k^{-3}$. The matter power spectrum in contrast is given by $P_{\delta\delta} = T^2(k)P_0(k)$ and thus it scales as k^1 at low k's and approximately as $k^{-2.5}$ at high k's. For the isosceles configuration and for low $k = k_1 = k_2$ the dominant contribution to terms including second order bias (terms D-L of the above equation) scales as

$$\frac{P(k_1)P(k_3)}{\alpha^i(k_1)\alpha^j(k_3)} \propto \frac{k^2 x_3}{k^{2i+2j} x_3^{2j}} = k^{2-2i-2j} x_3^{1-2j}, \tag{6.62}$$

while the dominant contribution to the A, B, C terms scales as

$$\frac{P(k_1)P(k_3)}{\alpha^{i-1}(k_1)\alpha^j(k_3)} \propto \frac{k^2 x_3}{k^{2i+2j-2} x_3^{2j}} = k^{4-2i-2j} x_3^{1-2j}. \tag{6.63}$$

The latter equation considers only the $f_{\rm NL}$ contribution, dominating at small x_3's. In Table 6.1 we quote the exponents i, j and the corresponding power of $f_{\rm NL}$. The combination $2(i+j-1)$ is the exponent of the dominating short mode in the squeezed limit and can go up to k^6. The estimation of the importance of the terms is further complicated by the different bias prefactors. We thus evaluate the expression numerically and discuss the results in Sec. 6.5.3 below.

Recent studies of the tree-level bispectrum [56] are based on the univariate bias parameters b_{10} and b_{20} only (univariate or Gaussian biasing). At tree level they thus consider only a subset of the above terms (see their Eq. (18)) leading to

$$B_{\rm hhh}(\boldsymbol{k}_1, \boldsymbol{k}_2, \boldsymbol{k}_3) = b_{10}^3 \left[B_{F_2}(\boldsymbol{k}_1, \boldsymbol{k}_2, \boldsymbol{k}_3) + B_{f_{\rm NL}}(\boldsymbol{k}_1, \boldsymbol{k}_2, \boldsymbol{k}_3)\right] + b_{10}^2 b_{20} \left[2P(k_1)P(k_2) + 2 \text{ cyc.}\right], \tag{6.64}$$

where B_{F_2} and $B_{f_{\rm NL}}$ are implicitly defined in Eq. (6.59). This approach neglects the influence of non-Gaussianity on the bias parameters, whereas it has been explicitly shown in simulations [16, 19, 30] that local non-Gaussianity introduces a scale dependent bias.

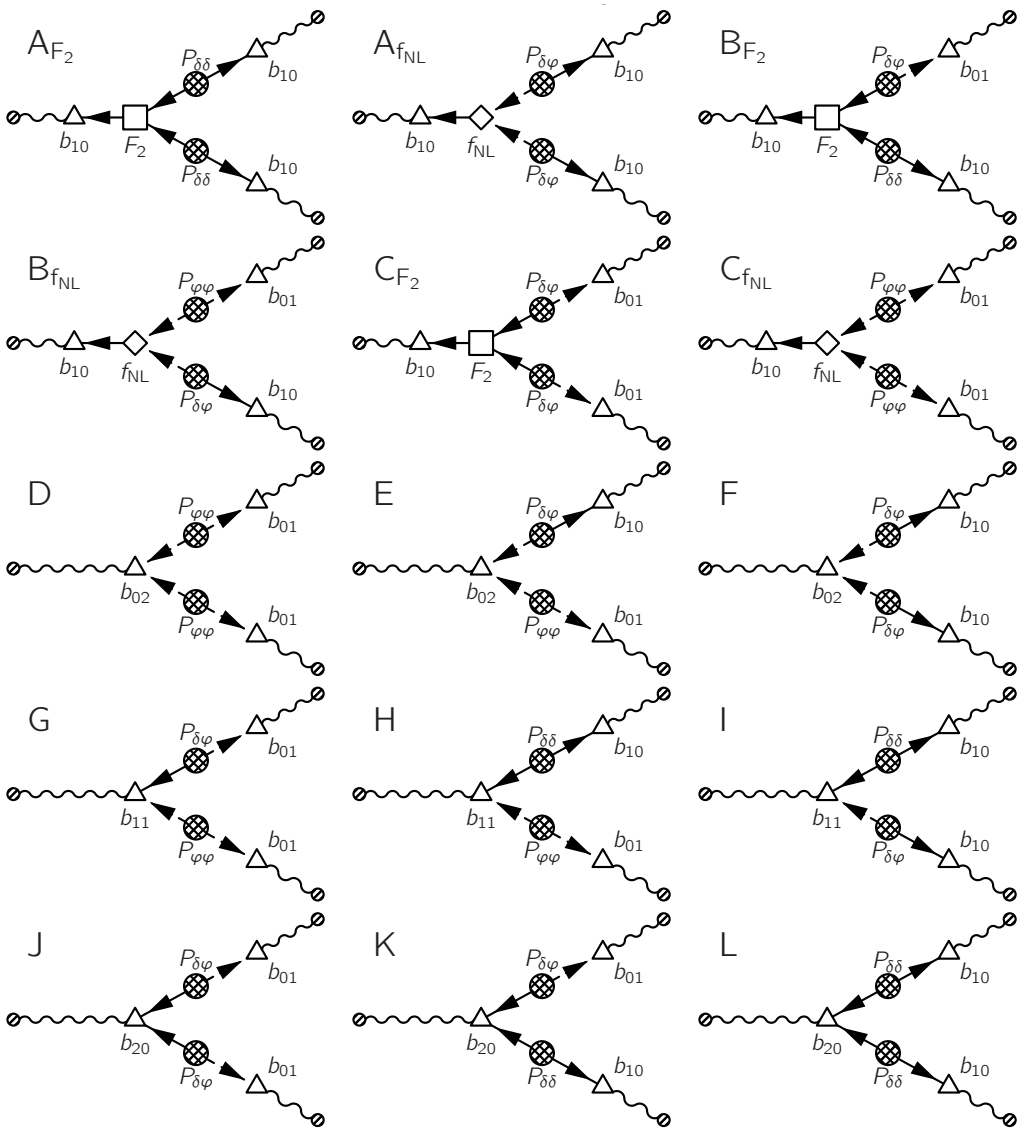

Figure 6.9.: Tree level bispectrum diagrams considered for Eq. (6.60). The scaling of the different terms with f_{NL} as well as their k dependence are described in Table 6.1.

	i	j	$2(i+j-1)$	$2j-1$	$f_{\rm NL}$
A_{F_2}	0	0	-2	-1	0
$A_{f_{\rm NL}}$	1	1	2	1	1
B_{F_2}	0	1	0	1	1
$B_{f_{\rm NL}}$	1	2	2	3	2
C_{F_2}	1	1	2	1	2
$C_{f_{\rm NL}}$	2	2	6	3	3
D	2	2	6	3	4
E	2	1	4	1	3
	1	2	4	3	3
F	1	1	2	1	2
G	2	1	4	1	3
	1	2	4	3	3
H	2	0	2	-1	2
	1	1	2	1	2
	0	2	2	3	2
I	1	0	0	-1	1
	0	1	0	1	1
J	1	1	2	1	2
K	1	0	0	-1	1
	0	1	0	1	1
L	0	0	-2	-1	0

Table 6.1.: Order of the terms contributing to the bispectrum $B_{\rm hhh}$ in Eq. (6.60) as defined via Eq. (6.62). From left to right we quote the exponents of the k-vectors, the exponent of the long k-mode, the exponent of the long-short ratio and the exponent of $f_{\rm NL}$. More than one line per diagram can arise if there are different possibilities for combining the components of the diagram.

6.5.2. Cross-Bispectra

The measurement of the halo auto-bispectrum is limited by the finite number of haloes and shotnoise. Thus it is interesting to consider also the cross spectra between matter and haloes. Weak gravitational lensing in cross-correlation with galaxies could be a possible observational probe providing measurements of these effects. Without showing the diagrams we write down the expressions for the halo-halo-matter bispectrum:

$$\begin{aligned}
B_{\rm hhm}(\boldsymbol{k}_1,\boldsymbol{k}_2,\boldsymbol{k}_3) =& b_{10}^2\left(6F_2(\boldsymbol{k}_1,\boldsymbol{k}_2)P(k_1)P(k_2)+6f_{\rm NL}\alpha(k_3)\frac{P(k_1)}{\alpha(k_1)}\frac{P(k_2)}{\alpha(k_2)}+2\text{ cyc.}\right)\\
&+b_{01}b_{10}\left(4F_2(\boldsymbol{k}_1,\boldsymbol{k}_2)P(k_1)P(k_2)\left(\frac{1}{\alpha(k_1)}+\frac{1}{\alpha(k_2)}\right)\right.\\
&\left.+4f_{\rm NL}\alpha(k_3)P(k_1)P(k_2)\left(\frac{1}{\alpha^2(k_1)\alpha(k_2)}+\frac{1}{\alpha(k_1)\alpha^2(k_2)}\right)+2\text{ cyc.}\right)\\
&+b_{01}^2\left(2F_2(\boldsymbol{k}_1,\boldsymbol{k}_2)\frac{P(k_1)P(k_2)}{\alpha(k_1)\alpha(k_2)}+2f_{\rm NL}\alpha(k_3)\frac{P(k_1)P(k_2)}{\alpha^2(k_1)\alpha^2(k_2)}+2\text{ cyc.}\right)\\
&+b_{10}b_{20}\left(4P(k_1)P(k_2)+2\text{ cyc.}\right)\\
&+b_{20}b_{01}\left(2P(k_1)P(k_2)\left(\frac{1}{\alpha(k_1)}+\frac{1}{\alpha(k_2)}\right)+2\text{ cyc.}\right)\\
&+b_{11}b_{10}\left(2P(k_1)P(k_2)\left(\frac{1}{\alpha(k_1)}+\frac{1}{\alpha(k_2)}\right)+2\text{ cyc.}\right)\\
&+b_{11}b_{01}\left(P(k_1)P(k_2)\left(\frac{1}{\alpha^2(k_1)}+\frac{2}{\alpha(k_1)\alpha(k_2)}+\frac{1}{\alpha^2(k_2)}\right)+2\text{ cyc.}\right)\\
&+b_{10}b_{02}\left(4\frac{P(k_1)P(k_2)}{\alpha^2(k_1)\alpha^2(k_2)}+2\text{ cyc.}\right)
\end{aligned} \tag{6.65}$$

$$+b_{02}b_{01}\left(2P(k_1)P(k_2)\left(\frac{1}{\alpha^2(k_1)\alpha(k_2)}+\frac{1}{\alpha(k_1)\alpha^2(k_2)}\right)+2\text{ cyc.}\right)$$

The corresponding prediction of a purely univariate bias model is given by

$$B_{\rm hhm}(\boldsymbol{k}_1,\boldsymbol{k}_2,\boldsymbol{k}_3)=3b_{10}^2\left[B_{F_2}(\boldsymbol{k}_1,\boldsymbol{k}_2,\boldsymbol{k}_3)+B_{f_{\rm NL}}(\boldsymbol{k}_1,\boldsymbol{k}_2,\boldsymbol{k}_3)\right]+2b_{10}b_{20}\left[2P(k_1)P(k_2)+2\text{ cyc.}\right]. \tag{6.66}$$

Finally, one can also correlate two matter and one halo density field:

$$\begin{aligned}B_{\rm hmm}(\boldsymbol{k}_1,\boldsymbol{k}_2,\boldsymbol{k}_3)=&b_{10}\left(6F_2(\boldsymbol{k}_1,\boldsymbol{k}_2)P(k_1)P(k_2)+6f_{\rm NL}\alpha(k_3)\frac{P(k_1)P(k_2)}{\alpha(k_1)\alpha(k_2)}+2\text{ cyc.}\right)\\&+b_{01}\left(2F_2(\boldsymbol{k}_1,\boldsymbol{k}_2)P(k_1)P(k_2)\left(\frac{1}{\alpha(k_1)}+\frac{1}{\alpha(k_2)}\right)\right.\\&\left.+2f_{\rm NL}\alpha(k_3)P(k_1)P(k_2)\left(\frac{1}{\alpha^2(k_1)\alpha(k_2)}+\frac{1}{\alpha(k_1)\alpha^2(k_2)}\right)+2\text{ cyc.}\right)\\&+b_{20}\left(2P(k_1)P(k_2)+2\text{ cyc.}\right)\\&+b_{11}\left(P(k_1)P(k_2)\left(\frac{1}{\alpha(k_1)}+\frac{1}{\alpha(k_2)}\right)+2\text{ cyc.}\right)\\&+b_{02}\left(2\frac{P(k_1)P(k_2)}{\alpha(k_1)\alpha(k_2)}+2\text{ cyc.}\right),\end{aligned} \tag{6.67}$$

where the corresponding prediction of the univariate bias model reads as

$$B_{\rm hmm}(\boldsymbol{k}_1,\boldsymbol{k}_2,\boldsymbol{k}_3)=3b_{10}\left[B_{F_2}(\boldsymbol{k}_1,\boldsymbol{k}_2,\boldsymbol{k}_3)+B_{f_{\rm NL}}(\boldsymbol{k}_1,\boldsymbol{k}_2,\boldsymbol{k}_3)\right]+b_{20}\left[2P(k_1)P(k_2)+2\text{ cyc.}\right]. \tag{6.68}$$

As for the halo auto-bispectrum, we show the results of a numerical evaluation of the above results in the next subsection.

6.5.3. Discussion of the Results

In this section we focus on the evaluation and discussion of the bispectrum expressions derived in Section 6.5 above. For the evaluation no smoothing is required since at tree level there are no integrations. The effect of smoothing at tree level breaks down to a multiplication with a smoothing function and thus suppresses the result on small scales keeping the large scales unaffected. The bias parameters are evaluated for a peak height of $\nu = 4$ corresponding to haloes of $M \approx 1\times10^{14}\ h^{-1}M_\odot$ and our fiducial cosmology introduced in Section 6.2.
In Fig. 6.10 we evaluate the terms in Eq. (6.60) separately to asses their importance. To make the comparison of the terms easier we plot the reduced bispectrum

$$Q(k_1,k_2,k_3)=\frac{B(k_1,k_2,k_3)}{P(k_1)P(k_2)+P(k_2)P(k_3)+P(k_3)P(k_1)}. \tag{6.69}$$

- We see that diagram A's contribution is constant at high-k's and grows at low-k's. This is due to the fact that at high-k's the signal from the subdiagram A_{F_2} grows (a fact that by the way Q is designed means that Q is constant), while on large scales the signal from the $A_{f_{\rm NL}}$ grows. The two subdiagrams have a different scale dependence.
- It is easy to see that diagrams B are obtained by substituting δ-bias with the one in φ. Since φ is suppressed with respect to δ for high-k's, we have that the signal in B is peaked at smaller k's. The value of $f_{\rm NL}$ used for this plot is rather large, thus the B contribution is larger than the one of A at small k's.
- In order to pass to the C diagrams, we exchange one δ leg with a φ leg and exchange a b_{10} factor with a b_{01}. Since in the B diagram one of the φ legs is already associated to

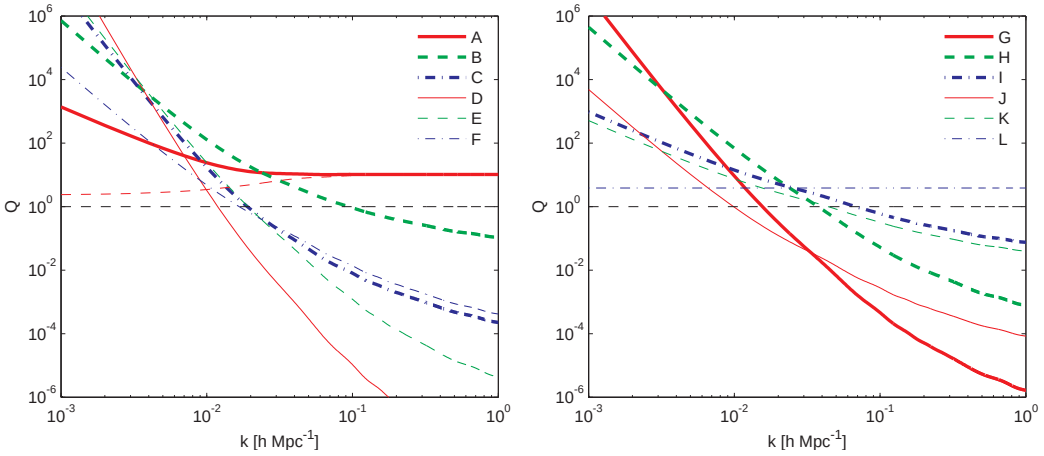

Figure 6.10.: Scale dependence of the terms contributing to the halo bispectrum $B_{\rm hhh}$ in Eq. (6.60) for $f_{\rm NL} = 100$ and $\nu = 4$ in an isosceles configuration $k = k_1 = k_2$, $\mu = -0.99$. The lines are labeled according to the corresponding diagrams in Fig. 6.9 and Table 6.1. The thin red dashed line in the left panel shows the bispectrum in the Gaussian case, which vanishes on large scales due to the shape dependence of the F_2 kernel. We show the reduced bispectrum defined in Eq. (6.69). The amplitude of the terms is determined both by the bias prefactors and the amplitude of the k-dependent factors. We see that the B and H terms are dominating on intermediate scales $k \approx 1 \times 10^{-2}\ h\mathrm{Mpc}^{-1}$, whereas D,E and G take over on smaller k's.

the low k mode, we need to associate the remaining leg to a high k mode. This means that the C diagram scales with respect to the B diagram by a factor of $b_{01}/(b_{10}\alpha(k_{\rm high}))$ that, for the values of $f_{\rm NL}$ and $k_{\rm high}$, that we are using is about a factor of 10 at the smallest k's we plot. Notice that since the terms here have additional factors of $1/k^2$, it raises more steeply at low k's. Even more than for the B diagram, this term becomes irrelevant at high k's because of the many φ factors that it involves.

- The remaining diagrams $D - L$ are constructed using the non-linear biases in all possible contractions. This means that the steepest at low k's will be the D diagram that involves b_{02} and b_{01}^2, while the most important at high k's will be the L diagram, that does not involve any φ. By construction the L diagram is scale independent when plotted in terms of its contribution to the reduced bispectrum Q.

In Fig. 6.11, we show how the various diagrams scale with the shape parameter x_3 in the isosceles configuration. For to overall size we consider $k = 0.1\ h\mathrm{Mpc}^{-1}$ and $k = 0.01\ h\mathrm{Mpc}^{-1}$. The x_3 scaling is also given in Table 6.1 and can be easily reconstructed from Eqs. (6.62) and (6.63). There is a clear correction at small k's from the φ terms. Since the signal is not scale invariant, as we move to higher k's, the contribution from terms involving $\delta_{\rm m}$ and its non-linearities, such as the A_{F_2} diagram, gain importance.
The left panel of Fig. 6.12 shows the dependence of the bispectrum amplitude on the variation of the non-Gaussianity parameter $f_{\rm NL}$. This plot shows that higher than linear powers in $f_{\rm NL}$ have to be considered to describe the full bispectrum amplitude. The plot also shows that the sensitivity to $f_{\rm NL}$ increases as one considers more squeezed configurations. While evaluated for a different halo sample and redshift, the plot shows qualitative agreement with the simulation measurements of [57]. In the right panel of Fig. 6.12 we plot the angular dependence of the bispectrum for an almost isosceles configuration $k_1 = k_2/1.2$ since the exact isosceles configuration is divergent for $\theta \to \pi$. Here $\theta = \arccos(\mu)$ refers to the angle between $\boldsymbol{k}_1$ and $\boldsymbol{k}_2$.[7] Besides an overall enhancement the most remarkable feature is the upturn of the

[7] The divergence of the isosceles case means nothing but the fact that as $\theta \to \pi$ one of the sides of the triangle goes to zero, and so the bispectrum amplitude goes formally to infinity.

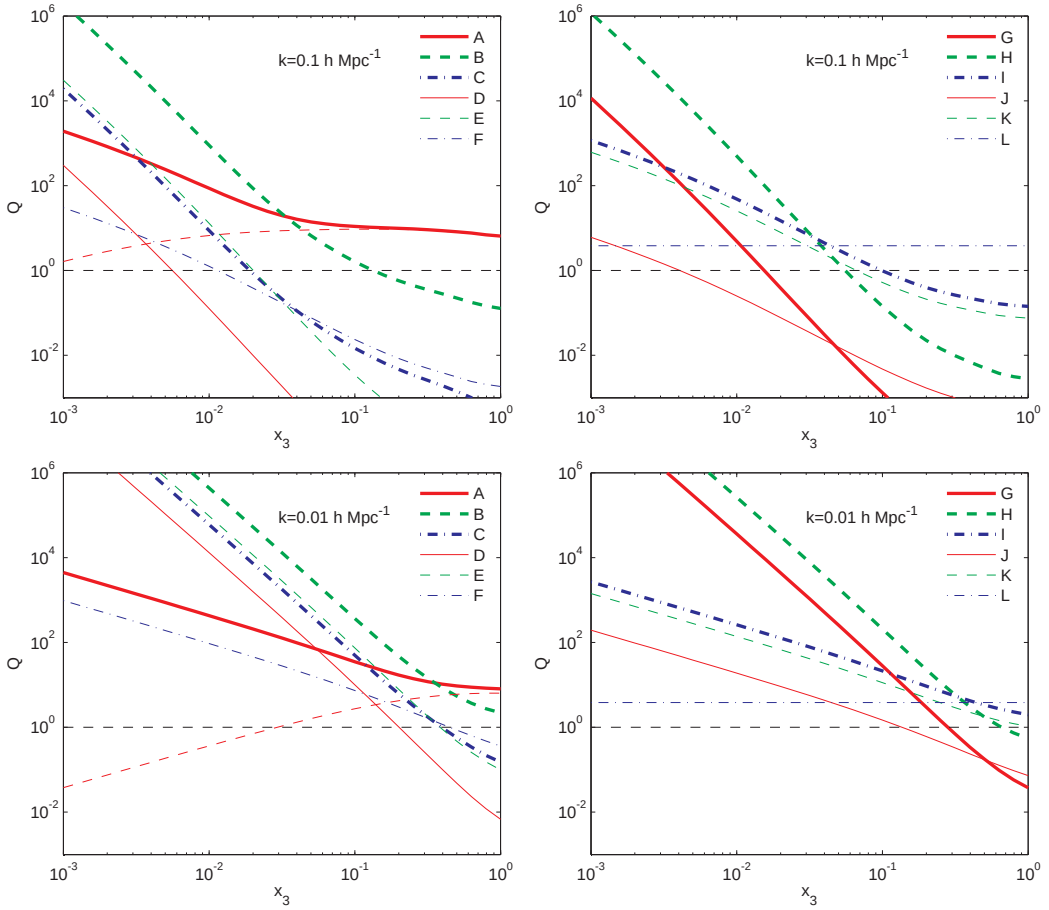

Figure 6.11.: Dependence of the terms contributing to the halo bispectrum $B_{\rm hhh}$ in Eq. (6.60) on the long-short axis ratio x_3 for an isosceles configuration with $k = k_1 = k_2$. The overall scale of the triangle is $k = 0.1\ h\mathrm{Mpc}^{-1}$ for the upper panels and $0.01\ h\mathrm{Mpc}^{-1}$ for the lower panels. This plot clearly shows the effect of the φ-bias corrections in the squeezed limit $x_3 \to 0$. As in the above plot the thin red dashed line in the left panels shows the A_{F_2} contribution.

multivariate bias prediction in the squeezed limit.

Fig. 6.13 shows the halo auto- and cross-bispectra. We show both their scale dependence as well as the ratio to the Gaussian expression for a squeezed isosceles configuration $k_1 = k_2, \mu = -0.99, x_3 \approx 1/7$ and compare to the predictions of the univariate bias model. These figures show that the non-Gaussian bispectrum asymptotes to the Gaussian one for high k's (small scales). On larger scales both the univariate bias model as well as our prediction are increased with respect to the Gaussian case due to the coupling between long and short modes. Our expression for $B_{\rm hhh}$ predicts an enhancement by a factor of 2 with respect to the existing univariate biasing calculations on scales of $k \approx 0.03\ h\mathrm{Mpc}^{-1}$. The enhancement is less pronounced for the mixed halo-matter bispectra. From the scaling with k and x_3 in Eq. (6.62) and Table 6.1 it is clear that the bispectrum amplitude is largest for squeezed configurations $\mu \to -1,\ \theta \to \pi$ and low overall scale $k \to 0$. However, the shape and scale of the triangle are limited by the fundamental mode and the sampling variance in exactly this limit. We will quantify the signal-to-noise ratio in the next section.

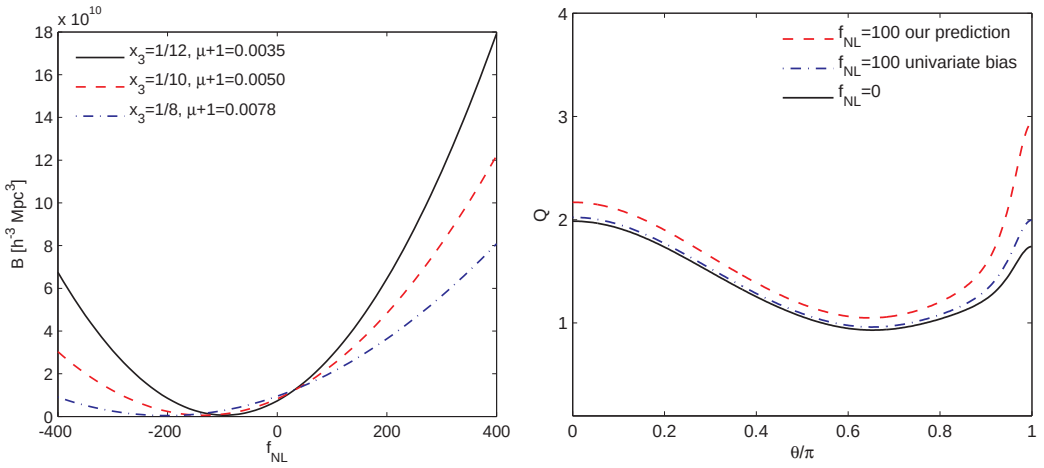

Figure 6.12.: *Left panel:* Dependence of the amplitude of the halo bispectrum $B_{\rm hhh}$ on the non-Gaussianity parameter $f_{\rm NL}$ for $g_{\rm NL} = 0$ and $k_1 = k_2 = 0.042\ h\mathrm{Mpc}^{-1}$. We show the bispectrum amplitude for three different values of the short-long ratio x_3 defined in Eq. (6.61). This plot agrees qualitatively with Fig. 4 in [57]. It is obvious from this plot that the bispectrum decreases with respect to the Gaussian non-linear clustering case for weakly negative $f_{\rm NL}$. *Right panel:* Angular dependence of the non-Gaussian and Gaussian reduced bispectra for $f_{\rm NL} = 100$ as a function of $\theta = \arccos(\boldsymbol{k}_1, \boldsymbol{k}_2) = \arccos(\mu)$ for a halo sample with $\nu = 4$ and a nearly isosceles configuration with $k_1 = k_2/1.2 = 0.03\ h\mathrm{Mpc}^{-1}$. We show our result (6.60) (red dashed) and the univariate biasing result (6.64) (blue dash-dotted). Besides the overall enhancement of the multivariate bias result with respect to the univariate bias result there is a remarkable upturn for $\theta \to \pi$.

6.5.4. Comparison to Simulations

While a full simulation based analysis of the halo bispectrum goes beyond the scope of this paper, we can nevertheless compare to published simulation measurements. The only published simulation measurement of the halo bispectrum we are aware of, was performed on a $L = 2000\ h^{-1}\mathrm{Mpc}$ cosmological simulation by [57]. They consider a cosmology with $\sigma_8 = 0.816$, $\Omega_{\rm m} = 0.28$, $\Omega_\Lambda = 0.72$ and present their results for $z = 0.5$. In Fig. 6.14 we show the comparison between our theoretical predictions and their simulation measurement for a halo sample with $M > 4.6 \times 10^{13}\ h^{-1} M_\odot$. The bias value inferred from the simulations $b_{10,\rm sim} = 2.9$ [58] points towards a halo sample with $M > 7 \times 10^{13}\ h^{-1} M_\odot$. This deviation to the low mass cutoff quoted by the authors might be due to an incomplete sampling of haloes around the cutoff. We adopt $M > 7 \times 10^{13}\ h^{-1} M_\odot$ as the lower boundary of the halo sample and calculate the average bias parameters using the LV mass function. Consistent with [57] we rescale b_{01} as $b_{01} \to 0.75\, b_{01}$, a modification motivated by ellipsoidal collapse (although this seems to apply only to Friends-of-Friends identified halos and not to spherical overdensity halos, [3]). Fig. 6.14 shows that the scale and shape dependence is quite well described by the theory, especially the upturn of the bispectrum for squeezed configurations. The terms dominating the non-Gaussian signal for $x_3 \approx 0.1$ in this comparison are A,B,H and I in Eq. (6.60). Concentrating on the dominating terms for the squeezed isosceles configuration $k_1 = k_2 = k$, $x_3 \approx 0$ the bispectrum reads as

$$B_{\rm hhh}(\boldsymbol{k}_1, \boldsymbol{k}_2, \boldsymbol{k}_3) = \left(4 b_{10}^3 f_{\rm NL} + 2 b_{10}^2 b_{11}\right) \frac{P(k)P(x_3 k)}{\alpha(x_3 k)} + \left(4 f_{\rm NL} b_{10}^2 b_{01} + 2 b_{10} b_{11} b_{01}\right) \frac{P(k)P(x_3 k)}{\alpha^2(x_3 k)} + \left(4 f_{\rm NL} b_{10}^2 b_{01} + 4 b_{10} b_{11} b_{01}\right) \frac{P(k)P(x_3 k)}{\alpha(x_3 k)\alpha(k)} + b_{10}^2 b_{01} \frac{P(k)P(x_3 k)}{\alpha(x_3 k)} \frac{13 - 5x_3^2}{7} \tag{6.70}$$

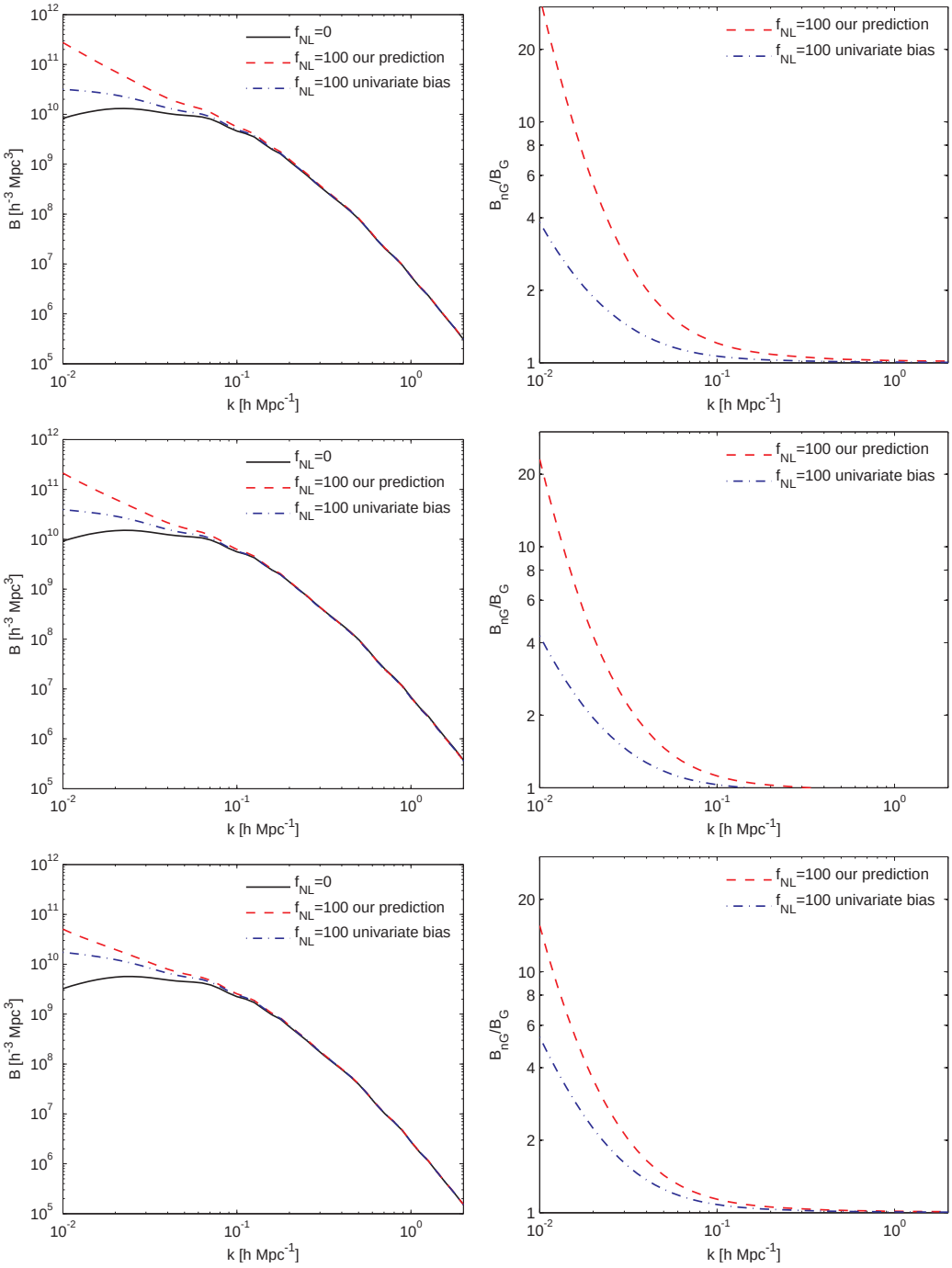

Figure 6.13.: *Upper Left Panel:* Halo auto bispectrum $B_{\rm hhh}$ according to Eq. (6.60) for $f_{\rm NL} = 100$ and $\mu = -0.99$ in the isosceles configuration $k_1 = k_2 = k$. We show the Gaussian bispectrum (black solid line), the univariate bias prediction of Eq. (6.64) (blue dash dotted) and our predictions (red dashed). *Upper Right panel:* Ratio of the non-Gaussian bispectra and the Gaussian bispectrum shown in the left panel. *Middle Panels:* Same as above, but for the halo-matter cross bispectrum $B_{\rm hhm}$ according to Eq. (6.65). *Lower Panels:* Same as above, but for the halo-matter cross bispectrum $B_{\rm hmm}$ according to Eq. (6.67).

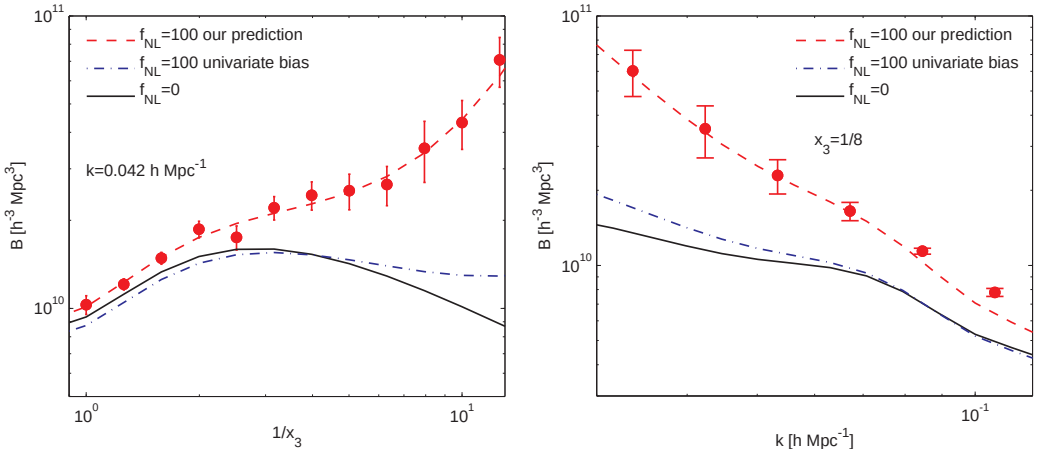

Figure 6.14.: Halo bispectrum in the isosceles configuration $k_1 = k_2$ for $z = 0.5$ and $M > 4.6 \times 10^{13}\ h^{-1}M_\odot$ in comparison to the data points in Fig. (6) of [57]. The lines show the multivariate bias (red dashed) and univariate bias (blue dash-dotted) non-Gaussian bispectrum as well as the Gaussian bispectrum (black solid). We adjust the low mass cutoff to bring the bias parameters derived from the mass function in agreement with the simulation measurement $b_{10} = 2.9$ and rescale $b_{01} \to 0.75\, b_{01}$. *Left panel:* Bispectrum as a function of the high-low-k ratio $1/x_3 = k/k_3$ and $k = 0.042\ h\mathrm{Mpc}^{-1}$. *Right panel:* Bispectrum as a function of scale k for $1/x_3 = 7.94$.

We see that for the scales and shapes considered, the bispectrum amplitude is dominated by $f_{\rm NL}$ and $f_{\rm NL}^2$ terms. The disagreement between our predictions and the simulation measurement on scales of $k \approx 0.1\ h\mathrm{Mpc}^{-1}$ is probably due to loop corrections in the matter bispectrum [55] or to the inaccuracy of the non-Gaussian mass function that we have used to extract the bias parameters.[8]

6.6. Signal-to-Noise

One goal of this work is to show the viability of the bispectrum to put constraints on primordial non-Gaussianity. The question is whether it is worth the additional effort of measuring the halo bispectrum given that the halo power spectrum can be used to put constraints on non-Gaussianity as well. The bispectrum analysis is naively more sensitive than the power spectrum to non-Gaussianities but it remains to show that this can overcome the enhanced errors. To estimate the errors we assume a survey of volume V from which the halo density field $\delta_{\rm h}(\boldsymbol{k})$ is estimated. The bispectrum and power spectrum estimators are constructed from a decomposition of k-space into spherical shells of width δk. Then the k-modes within the shell are spherically averaged to obtain the estimators [59]

$$\hat{P}(k) = \frac{V_{\rm f}}{V_{12}} \int_k \frac{{\rm d}^3 q_1}{(2\pi)^3} \int_k \frac{{\rm d}^3 q_2}{(2\pi)^3} \delta(\boldsymbol{q}_1)\delta(\boldsymbol{q}_2)\delta^{(\rm D)}(\boldsymbol{q}_1 + \boldsymbol{q}_2) \tag{6.71}$$

for the power spectrum and

$$\hat{B}(\boldsymbol{k}_1, \boldsymbol{k}_2, \boldsymbol{k}_3) = \frac{V_{\rm f}}{V_{123}} \int_{k_1} \frac{{\rm d}^3 q_1}{(2\pi)^3} \int_{k_2} \frac{{\rm d}^3 q_2}{(2\pi)^3} \int_{k_3} \frac{{\rm d}^3 q_3}{(2\pi)^3} \delta(\boldsymbol{q}_1)\delta(\boldsymbol{q}_2)\delta(\boldsymbol{q}_3)\delta^{(\rm D)}(\boldsymbol{q}_1 + \boldsymbol{q}_2 + \boldsymbol{q}_3) \tag{6.72}$$

for the bispectrum, where the integrals are over spherical shells $q_i \in [k_i - \delta k/2, k_i + \delta k/2]$. As shown in [59] the covariance of this bispectrum estimator is given by

$$(\Delta B)^2 = s_{123} \frac{V_{\rm f}}{V_{123}} \left(P_{\rm h}(k_1) + \frac{1}{\bar{n}}\right)\left(P_{\rm h}(k_2) + \frac{1}{\bar{n}}\right)\left(P_{\rm h}(k_3) + \frac{1}{\bar{n}}\right) \tag{6.73}$$

[8] It is indeed possible that other non-Gaussian mass functions might give improved results, but a more careful treatment of these effects goes beyond the scope of our paper.

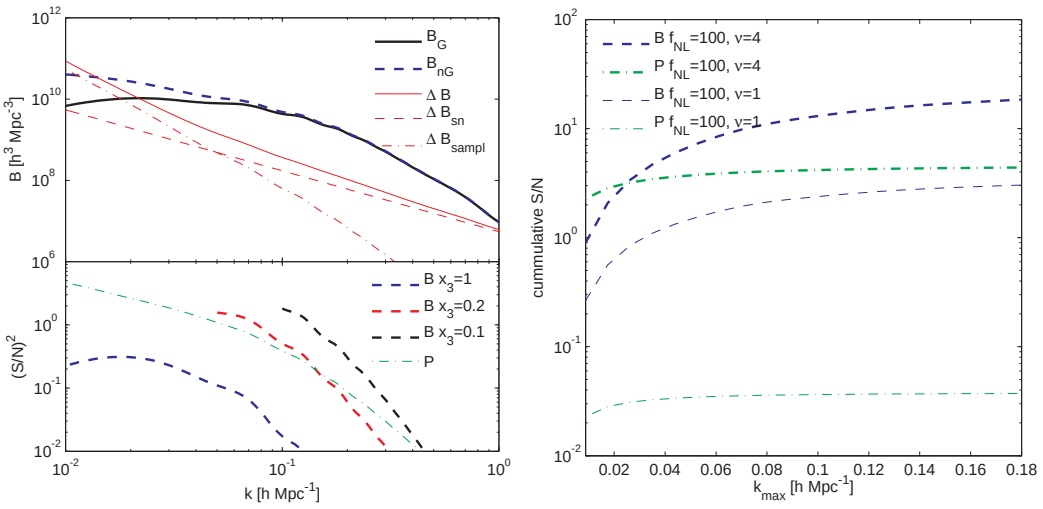

Figure 6.15.: *Left top panel:* Variance of the halo bispectrum $B_{\rm hhh}$ for $f_{\rm NL} = 100$, $x_3 = 0.1$. Gaussian (thick black) and non-Gaussian (thick blue dashed) bispectrum amplitude and error on the bispectrum for $\bar{n} = 1 \times 10^{-5} h^3$ Mpc^{-3}, $V = 10\ h^{-3}$Mpc^3 $k_{\rm f} = 2.9 \times 10^{-3}$ hMpc^{-1} and $\delta k = 3k_{\rm f} = 0.008$ hMpc^{-1}. For the biased tracer we assume a halo sample with $\nu = 4$, corresponding to $M \approx 1 \times 10^{14}\ h^{-1} M_\odot$ ($b_{10} = 2.23$, $b_{20} = 0.38$). We plot the full error $\Delta B(k)$ (red) as well as the sampling variance (red dash-dotted) and shotnoise (red dashed) contributions. *Left bottom panel:* SNR for the halo bispectrum $B_{\rm hhh}$ (blue, red and green dashed for $x_3 = 1$, 0.2 and 0.1 from bottom to top) and the halo power spectrum $P_{\rm hh}$ (green dash-dotted). The signal is defined as the difference between the non-Gaussian and Gaussian prediction. As we go to higher k more squeezed configurations gain importance. *Right panel:* Cumulative signal-to-noise for the bispectrum (blue dashed) and power spectrum (green dash-dotted). We evaluate the SNR for $\nu = 4$ (thick) and $\nu = 1$ (thin).

and the one for the power spectrum [59, 60] by

$$(\Delta P)^2 = 2\frac{V_{\rm f}}{V_{12}} \left(P_{\rm h}(k_1) + \frac{1}{\bar{n}} \right) \left(P_{\rm h}(k_2) + \frac{1}{\bar{n}} \right). \tag{6.74}$$

Here s_{123} is a symmetry factor, with $s_{123} = 6, 2, 1$ for equilateral, isosceles and general configurations, respectively. In the noise estimators we approximate the halo power spectrum by the leading contribution $P_{\rm h}(k) = (b_{10} + b_{01}/\alpha(k))\, P_{\rm lin}(k)$ for simplicity. The k-space volume of the fundamental cell is $V_{\rm f} = k_{\rm f}^3 = (2\pi)^3/L^3$ and the norm volumes are given by

$$V_{123} = \int_{k_1} \frac{{\rm d}^3 q_1}{(2\pi)^3} \int_{k_2} \frac{{\rm d}^3 q_2}{(2\pi)^3} \int_{k_3} \frac{{\rm d}^3 q_3}{(2\pi)^3} \delta^{(\rm D)}(\boldsymbol{q}_{123}) \approx 8\pi^2 k_1 k_2 k_3 \delta k^3 \tag{6.75}$$

and

$$V_{12} = \int_{k_1} \frac{{\rm d}^3 q_1}{(2\pi)^3} \int_{k_2} \frac{{\rm d}^3 q_2}{(2\pi)^3} \delta^{(\rm D)}(\boldsymbol{q}_{12}) \approx 4\pi k_1 k_2 \delta k. \tag{6.76}$$

If $P \gg 1/\bar{n}$ the cosmic variance dominates whereas shotnoise dominates when $P \ll 1/\bar{n}$. As our fiducial case we consider a survey of $V = 10\ h^{-3}$Mpc^3 and $\delta k = 3k_{\rm f} = 9 \times 10^{-3}$ hMpc^{-1} and a halo sample with overdensity $\nu = 4$ corresponding to $M \approx 1 \times 10^{14}\ h^{-1} M_\odot$ ($b_{10} = 2.23$, $b_{20} = 0.38$). The number density of the halo sample is assumed to be $\bar{n} = 1 \times 10^{-5}$ hMpc^{-1}. The left panel of Fig. 6.15 shows the errors and the signal-to-noise ratio (SNR) for the halo bispectrum $B_{\rm hhh}$ in a squeezed isosceles configuration $k = k_1 = k_2$, $x_3 = 0.1$. Here we define the signal as the signal-to-noise weighted difference between the total non-Gaussian and the fiducial Gaussian bispectrum amplitude

$${\rm SNR}_B^2(k_i, k_j, k_l) = \frac{\left(B_{\rm nG}(k_i, k_j, k_l) - B_{\rm G}(k_i, k_j, k_l)\right)^2}{(\Delta B)^2(k_i, k_j, k_l)} \tag{6.77}$$

with an equivalent expression for the power spectrum. We see that the $f_{\rm NL}$ contribution enhances the signal on a wide range of scales and most relevantly on the smallest k's. The left bottom panel of Fig. 6.15 shows the SNR for a given bin of k modes, for isosceles triangles with three different values of x_3. We see that the bispectrum signal is enhanced as we make the triangle more and more squeezed and as we take the highest k's of the triangle closer to the non-linear scale. We should stress that our tree-level calculation does not apply for k's close or larger than the non-linear scale. We finally also plot the binned SNR from the power spectrum, which is peaked at the smallest k's. So far we restricted our discussion to a particular bispectrum configuration. For the extraction of a non-Gaussian signal from a survey one would rather add up all the possible information, *i. e.* sum over all possible configurations up to a maximum wavenumber $k_{\rm max}$. The total signal-to-noise is given by a sum over all the possible combinations of shells up to the maximum wavenumber $k_{\rm max}$

$$\left(\frac{S}{N}\right)^2_{{\rm tot},B} = \sum_{i=1}^{i_{\rm max}} \sum_{j=1}^{i} \sum_{l=i-j}^{i+j} {\rm SNR}^2_B(k_i, k_j, k_l) \tag{6.78}$$

where we used $k_i = i\delta k$. In the right panel of Fig. 6.15 we plot the cumulative signal-to-noise for the bispectrum and power spectrum for $f_{\rm NL} = 100$ and tracers with peak height $\nu = 4$ and $\nu = 1$. For the high bias tracer we see that for the considered survey and going up to $k_{\rm max} = 0.18\ h{\rm Mpc}^{-1}$ we could constrain $\sigma_{f_{\rm NL}} \approx 5$ from the bispectrum analysis, whereas the power spectrum leads to constraints of $\sigma_{f_{\rm NL}} \approx 25$. Note that we are plotting the total non-Gaussian signal. To obtain the SNR on $f_{\rm NL}$, the lines in the figure have to be divided by $f_{\rm NL}$. For k higher than about $0.1\ h{\rm Mpc}^{-1}$ non-linear corrections should be implemented. The bispectrum wins over the power spectrum even if the maximum wave number is restricted to $k_{\rm max} \approx 0.03\ h{\rm Mpc}^{-1}$. Furthermore the plot shows that extraction of $f_{\rm NL} = \mathcal{O}(10)$ is possible only with the bispectrum analysis but not with the power spectrum analysis for these tracers. Note that the choice of bias, volume and number density is similar to values for luminous red galaxies expected in SDSS-III (BOSS) redshift survey [61]. The bispectrum of the low bias $\nu = 1$ tracers shows an even more remarkable improvement in SNR compared to the corresponding power spectrum.

6.7. Conclusions

In this paper we present a diagrammatic prescription for the calculation of multipoint statistics of biased tracers of the cosmological density field accounting for the effect of non-Gaussian initial fluctuations. The diagrammatic approach combines biasing, non-Gaussianity and non-linear clustering into one consistent and intuitive picture. While we focused on the bispectrum, the generalisation to higher order correlators should be straightforward. Also, non-local shapes can be implemented using their primordial bispectrum instead of the mode coupling vertices in Fig. 6.6.

We use this diagrammatic prescription to derive the halo bispectrum accounting for all tree level/zero loop contributions. Unsurprisingly, the bispectrum is largest in the squeezed limit $x_3 \to 0$, where our prediction exceeds the results obtained using univariate bias only, by about a factor of 2 on scales of $k \approx 0.03\ h{\rm Mpc}^{-1}$. Given the fact, that we see these corrections compared to the univariate bias approach already at tree level, we caution the use of the univariate bias expansion as presented in [23] and [22]. While the qualitative results are quite general, the quantitative results presented in Section 6.5.3 are somewhat dependent on the choice of the halo sample. We considered a $\nu = 4$ tracer, corresponding to haloes of mass $M \approx 1 \times 10^{14}\ h^{-1}M_\odot$ ($b_{10} = 2.23,\ b_{20} = 0.38$).

Comparing our results to the ones obtained in [22] we see that their one-loop terms proportional to b_2 are comparable to some of our tree level terms if i) the smoothing scale equals the halo mass scale, ii) high mass haloes are considered and iii) large scales are considered. But, these

terms can not be seen as a replacement to the non-Gaussian terms obtained in our approach because all the one loop terms arising in the univariate bias approach are also present in our approach. The final comparison of the terms would require a careful resummation of the bias parameters, which was not considered in [22].

Probably the most important result of this paper is that the halo bispectrum analysis offers an alternative to the power spectrum for detecting local non-Gaussianities with an even higher constraining power. For the $\nu = 4$ tracers in a $V = 10\ h^{-3}\mathrm{Mpc}^3$ survey, our signal-to-noise analysis predicts a factor of five improvement in the constraints on f_{NL} compared to the power spectrum. For lower bias tracers at the same number density the total signal-to-noise is a bit lower, but it is in fact much higher relative to the power spectrum analysis, which contains no signal for unbiased tracers.

Our results suggest that the bispectrum should be the statistic of choice for detecting primordial non-Gaussianity in current and future survey data. However, some additional work has to be done before this method can be applied to the real data. One extension is to make predictions for photometric surveys, where only projected density fluctuations are observed. Alternatively, if a redshift survey is used in the analysis then the predictions here should be generalized to include redshift space distortions [62]. In the light of ever increasing surveys and simulations one might also be concerned about general relativistic corrections on horizon scales [34].

Convergence is probably one of the most important problems for perturbative calculations. For Gaussian initial conditions, comparisons of the matter bispectrum in simulations to the theoretical predictions as presented in [55] and [63] conclude that 1-loop calculations are required to achieve a reasonable agreement on scales of $k \approx 0.1\ h^{-1}\mathrm{Mpc}$. The bispectrum in presence of local non-Gaussianity is the perfect statistic to apply perturbation theory at tree level combined with the bias from the peak-background split since the non-Gaussian effects are most prominent for low k or large smoothing scales. Still, we focus on a tree level calculation and find that the signal receives relevant contributions from scales close to the non-linear scale. For this reason, loop-corrections should be examined to fully assess the detailed amplitude of the signal. As we discuss, this will probably require to study the cutoff dependence both of the loop corrections and of the bias coefficients, such that final observables do not depend on the cutoff.[9] Some of these 1-loop terms will be renormalized and absorbed into the tree level terms discussed here. Still, a consistent calculation of the halo bispectrum at the next order would require consideration of non-linear couplings up to F_4 and biasing up to fourth order, both in δ and φ. This increases the number of terms by a large amount and goes beyond the scope of the current paper. The final decision about the validity of the perturbative calculation presented in this paper has to be based on a detailed comparison to the halo bispectrum measured in simulations. A first comparison of our results to the measurements published by [57] shows an encouraging level of agreement.

Acknowledgments

We acknowledge M. Zaldarriaga for initial collaboration on this project and for many discussions. Furthermore, we would like to thank N. Hamaus, P. McDonald, C. Porciani, F. Schmidt, R. Scoccimarro and in particular E. Sefusatti for helpful discussions. Special thanks to V. Desjacques both for fruitful discussions and comments on the manuscript. We would also like to thank T. Nishimichi for providing the data points of the simulation bispectrum measurement and the Asian Pacific Centre for Theoretical Physics in Pohang, Korea, for their kind hospitality during the workshop on "Cosmology and Fundamental Physics". This work is supported by DOE, the Swiss National Foundation under contract 200021-116696/1 and WCU grant R32-2009-000-10130-0.

[9] Previous studies [22, 23] did not stress the conceptual separation between the smoothing scale, the cutoff of the loops and the mass scale of the halos.

6.8. Appendix

6.8.1. Explicit Derivation of the Bias Parameters

As shown in Section 6.3, long wavelength modes in presence of primordial non-Gaussianity change the effective collapse threshold and variance of density fluctuations. In the mass function, the presence of a long wavelength mode can be accounted for by rescaling the peak height as

$$\nu = \left(\frac{\delta_c}{\sigma_G}\right)^2 \to \tilde{\nu} = \left(\frac{\delta_c - \delta_l}{\sigma_G(1 + 2f_{NL}\varphi_l + 3g_{NL}\varphi_l^2 + 2f_{NL}^2\varphi_l^2)}\right)^2 . \tag{6.79}$$

As we will need them for the explicit calculation of the bias parameters, we write down the partial derivatives of the peak height with respect to primordial potential and long wavelength density fluctuation

$$\frac{\partial\tilde{\nu}}{\partial\delta_l}\Big|_{\delta_l=0,\varphi_l=0} = -2\frac{\nu}{\delta_c} \qquad \frac{\partial\tilde{\nu}}{\partial\varphi_l}\Big|_{\delta_l=0,\varphi_l=0} = -4f_{NL}\nu \tag{6.80}$$

$$\frac{\partial^2\tilde{\nu}}{\partial\delta_l^2}\Big|_{\delta_l=0,\varphi_l=0} = 2\frac{\nu}{\delta_c^2} \qquad \frac{\partial^2\tilde{\nu}}{\partial\varphi_l\partial\delta_l}\Big|_{\delta_l=0,\varphi_l=0} = 8f_{NL}\frac{\nu}{\delta_c} \tag{6.81}$$

$$\frac{\partial^2\tilde{\nu}}{\partial\varphi_l^2}\Big|_{\delta_l=0,\varphi_l=0} = (24f_{NL}^2 - 12g_{NL})\nu \tag{6.82}$$

Using these expressions and the results of Section 6.3 we can first derive the Gaussian bias parameters arising from the rescaling of the collapse threshold

$$b_{10}^L = \frac{1}{\bar{n}}\frac{\partial n}{\partial\delta_l} = \frac{1}{\bar{n}}\frac{\partial n}{\partial\nu}\frac{\partial\tilde{\nu}}{\partial\delta_l} = -\frac{1}{\bar{n}}\frac{2\nu}{\delta_c}\frac{\partial n}{\partial\nu} \tag{6.83}$$

$$\begin{aligned} b_{20}^L =& \frac{1}{\bar{n}}\frac{\partial^2 n}{\partial{\delta_l}^2} = \frac{1}{\bar{n}}\frac{\partial^2 n}{\partial\nu^2}\left(\frac{\partial\tilde{\nu}}{\partial\delta_l}\right)^2 + \frac{1}{\bar{n}}\frac{\partial n}{\partial\nu}\frac{\partial^2\tilde{\nu}}{\partial{\delta_l}^2} \\ =& \frac{4}{\bar{n}}\frac{\nu^2}{\delta_c^2}\frac{\partial^2 n}{\partial\nu^2} + \frac{2}{\bar{n}}\frac{\nu}{\delta_c^2}\frac{\partial n}{\partial\nu} \end{aligned} \tag{6.84}$$

The non-Gaussian bias parameters are now arising from the rescaling of the variance in the denominator of Eq. (6.79)

$$b_{01}^L = \frac{1}{\bar{n}}\frac{\partial n}{\partial\varphi_l} = \frac{1}{\bar{n}}\frac{\partial n}{\partial\nu}\frac{\partial\tilde{\nu}}{\partial\varphi_l} = -\frac{4f_{NL}\nu}{\bar{n}}\frac{\partial n}{\partial\nu} = 2f_{NL}\delta_c b_{10}^L \tag{6.85}$$

$$\begin{aligned} b_{11}^L =& \frac{1}{\bar{n}}\frac{\partial^2 n}{\partial\varphi_l\partial\delta_l} = \frac{1}{\bar{n}}\frac{\partial^2 n}{\partial\nu^2}\frac{\partial\tilde{\nu}}{\partial\varphi_l}\frac{\partial\nu}{\partial\delta_l} + \frac{1}{\bar{n}}\frac{\partial n}{\partial\nu}\frac{\partial^2\tilde{\nu}}{\partial\varphi_l\partial\delta_l} \\ =& \frac{8f_{NL}}{\bar{n}}\left(\frac{\nu^2}{\delta_c}\frac{\partial^2 n}{\partial\nu^2} + \frac{\nu}{\delta_c}\frac{\partial n}{\partial\nu}\right) \\ =& 2f_{NL}\left(b_{20}^L\delta_c - b_{10}^L\right) \end{aligned} \tag{6.86}$$

$$\begin{aligned} b_{02}^L =& \frac{1}{\bar{n}}\frac{\partial^2 n}{\partial{\varphi_l}^2} = \frac{1}{\bar{n}}\frac{\partial^2 n}{\partial\nu^2}\left(\frac{\partial\tilde{\nu}}{\partial\varphi_l}\right)^2 + \frac{1}{\bar{n}}\frac{\partial n}{\partial\nu}\frac{\partial^2\tilde{\nu}}{\partial{\varphi_l}^2} \\ =& \frac{8f_{NL}^2}{\bar{n}}\left(2\nu^2\frac{\partial^2 n}{\partial\nu^2} + 3\nu\frac{\partial n}{\partial\nu}\right) - \frac{12\nu g_{NL}}{\bar{n}}\frac{\partial n}{\partial\nu} \\ =& 4f_{NL}^2\delta_c\left(b_{20}^L\delta_c - 2b_{10}^L\right) + 6\delta_c g_{NL} b_{10}^L \end{aligned} \tag{6.87}$$

where we used the results for b_{10}^L and b_{20}^L obtained above to replace the partial derivatives of the massfunction with respect to the peak height.

Bibliography

[1] T. Baldauf, U. Seljak, and L. Senatore, **Primordial non-Gaussianity in the bispectrum of the halo density field**, *JCAP* **4** (Apr., 2011) 6, [arXiv:1011.1513].

[2] M. Liguori, E. Sefusatti, J. R. Fergusson, and E. P. S. Shellard, **Primordial non-Gaussianity and Bispectrum Measurements in the Cosmic Microwave Background and Large-Scale Structure**, *ArXiv e-prints* (Jan., 2010) [arXiv:1001.4707].

[3] V. Desjacques and U. Seljak, **Primordial non-Gaussianity from the large scale structure**, *ArXiv e-prints* (Mar., 2010) [arXiv:1003.5020].

[4] A. H. Guth, **Inflationary universe: A possible solution to the horizon and flatness problems**, *Phys. Rev.* **23** (Jan., 1981) 347–356.

[5] A. D. Linde, **A new inflationary universe scenario: A possible solution of the horizon, flatness, homogeneity, isotropy and primordial monopole problems**, *Physics Letters B* **108** (Feb., 1982) 389–393.

[6] A. Albrecht and P. J. Steinhardt, **Cosmology for grand unified theories with radiatively induced symmetry breaking**, *Physical Review Letters* **48** (Apr., 1982) 1220–1223.

[7] C. Cheung, A. L. Fitzpatrick, J. Kaplan, L. Senatore, and P. Creminelli, **The effective field theory of inflation**, *Journal of High Energy Physics* **3** (Mar., 2008) 14–014, [arXiv:0709.0293].

[8] E. Komatsu, K. M. Smith, J. Dunkley, C. L. Bennett, B. Gold, G. Hinshaw, N. Jarosik, D. Larson, M. R. Nolta, L. Page, D. N. Spergel, M. Halpern, R. S. Hill, A. Kogut, M. Limon, S. S. Meyer, N. Odegard, G. S. Tucker, J. L. Weiland, E. Wollack, and E. L. Wright, **Seven-Year Wilkinson Microwave Anisotropy Probe (WMAP) Observations: Cosmological Interpretation**, *ArXiv e-prints* (Jan., 2010) [arXiv:1001.4538].

[9] E. Sefusatti and R. Scoccimarro, **Galaxy bias and halo-occupation numbers from large-scale clustering**, *Phys. Rev.* **71** (Mar., 2005) 063001–+, [astro-ph/0412626].

[10] D. S. Salopek and J. R. Bond, **Nonlinear evolution of long-wavelength metric fluctuations in inflationary models**, *Phys. Rev.* **42** (Dec., 1990) 3936–3962.

[11] D. S. Salopek and J. R. Bond, **Stochastic inflation and nonlinear gravity**, *Phys. Rev.* **43** (Feb., 1991) 1005–1031.

[12] L. Senatore and M. Zaldarriaga, **The Effective Field Theory of Multifield Inflation**, *ArXiv e-prints* (Sept., 2010) [arXiv:1009.2093].

[13] N. Dalal, O. Doré, D. Huterer, and A. Shirokov, **Imprints of primordial non-Gaussianities on large-scale structure: Scale-dependent bias and abundance of virialized objects**, *Phys. Rev.* **77** (June, 2008) 123514–+, [arXiv:0710.4560].

[14] S. Matarrese and L. Verde, **The Effect of Primordial Non-Gaussianity on Halo Bias**, *Astrophys. J. Let.* **677** (Apr., 2008) L77–L80, [arXiv:0801.4826].

[15] A. Slosar, C. Hirata, U. Seljak, S. Ho, and N. Padmanabhan, **Constraints on local primordial non-Gaussianity from large scale structure**, *Journal of Cosmology and Astro-Particle Physics* **8** (Aug., 2008) 31–+, [arXiv:0805.3580].

[16] V. Desjacques, U. Seljak, and I. T. Iliev, **Scale-dependent bias induced by local non-Gaussianity: a comparison to N-body simulations**, *Mon. Not. Roy. Astron. Soc.* **396** (June, 2009) 85–96, [arXiv:0811.2748].

[17] V. Desjacques and U. Seljak, **Signature of primordial non-Gaussianity of phiˆ3-type in the mass function and bias of dark matter haloes**, *ArXiv e-prints* (July, 2009) [arXiv:0907.2257].

[18] M. Grossi, K. Dolag, E. Branchini, S. Matarrese, and L. Moscardini, **Evolution of massive haloes in non-Gaussian scenarios**, *Mon. Not. Roy. Astron. Soc.* **382** (Dec., 2007) 1261–1267, [arXiv:0707.2516].

[19] M. Grossi, E. Branchini, K. Dolag, S. Matarrese, and L. Moscardini, **The mass density field in simulated non-Gaussian scenarios**, *Mon. Not. Roy. Astron. Soc.* **390** (Oct., 2008) 438–446, [arXiv:0805.0276].

[20] A. Pillepich, C. Porciani, and O. Hahn, **Halo mass function and scale-dependent bias from N-body simulations with non-Gaussian initial conditions**, *Mon. Not. Roy. Astron. Soc.* **402** (Feb., 2010) 191–206, [arXiv:0811.4176].

[21] R. E. Smith, V. Desjacques, and L. Marian, **Nonlinear clustering in models with primordial non-Gaussianity: the halo model approach**, *ArXiv e-prints* (Sept., 2010) [arXiv:1009.5085].

[22] D. Jeong and E. Komatsu, **Primordial Non-Gaussianity, Scale-dependent Bias, and the Bispectrum of Galaxies**, *Astrophys. J.* **703** (Oct., 2009) 1230–1248, [arXiv:0904.0497].

[23] E. Sefusatti, **1-loop Perturbative Corrections to the Matter and Galaxy Bispectrum with non-Gaussian Initial Conditions**, *ArXiv e-prints* (May, 2009) [arXiv:0905.0717].

[24] P. Creminelli, L. Senatore, and M. Zaldarriaga, **Estimators for local non-Gaussianities**, *JCAP* **0703** (2007) 019, [astro-ph/0606001].

[25] S. Matarrese, F. Lucchin, and S. A. Bonometto, **A path-integral approach to large-scale matter distribution originated by non-Gaussian fluctuations**, *Astrophys. J. Let.* **310** (Nov., 1986) L21–L26.

[26] D. H. Lyth, C. Ungarelli, and D. Wands, **Primordial density perturbation in the curvaton scenario**, *Phys. Rev.* **67** (Jan., 2003) 023503–+, [astro-ph/0208055].

[27] N. Bartolo, S. Matarrese, and A. Riotto, **On non-Gaussianity in the curvaton scenario**, *Phys. Rev.* **D69** (2004) 043503, [hep-ph/0309033].

[28] M. Zaldarriaga, **Non-Gaussianities in models with a varying inflaton decay rate**, *Phys. Rev.* **69** (Feb., 2004) 043508–+, [astro-ph/].

[29] P. Creminelli and L. Senatore, **A smooth bouncing cosmology with scale invariant spectrum**, *Journal of Cosmology and Astro-Particle Physics* **11** (Nov., 2007) 10–+, [hep-th/0702165].

[30] T. Giannantonio and C. Porciani, **Structure formation from non-Gaussian initial conditions: Multivariate biasing, statistics, and comparison with N-body simulations**, *Phys. Rev.* **81** (Mar., 2010) 063530–+, [arXiv:0911.0017].

[31] J. Maldacena, **Non-gaussian features of primordial fluctuations in single field inflationary models**, *Journal of High Energy Physics* **5** (May, 2003) 13–+, [astro-ph/0210603].

[32] D. Wands, **Local non-Gaussianity from inflation**, *ArXiv e-prints* (Apr., 2010) [arXiv:1004.0818].

[33] D. Wands and A. Slosar, **Scale-dependent bias from primordial non-Gaussianity in general relativity**, *Phys. Rev.* **79** (June, 2009) 123507–+, [arXiv:0902.1084].

[34] J. Yoo, A. L. Fitzpatrick, and M. Zaldarriaga, **New perspective on galaxy clustering as a cosmological probe: General relativistic effects**, *Phys. Rev.* **80** (Oct., 2009) 083514–+, [arXiv:0907.0707].

[35] J. Yoo, **General Relativistic Description of the Observed Galaxy Power Spectrum: Do We Understand What We Measure?**, *ArXiv e-prints* (Sept., 2010) [arXiv:1009.3021].

[36] W. H. Press and P. Schechter, **Formation of Galaxies and Clusters of Galaxies by Self-Similar Gravitational Condensation**, *Astrophys. J.* **187** (Feb., 1974) 425–438.

[37] R. K. Sheth and G. Tormen, **Large-scale bias and the peak background split**, *Mon. Not. Roy. Astron. Soc.* **308** (Sept., 1999) 119–126, [astro-ph/9901122].

[38] M. Lo Verde, A. Miller, S. Shandera, and L. Verde, **Effects of scale-dependent non-Gaussianity on cosmological structures**, *Journal of Cosmology and Astro-Particle Physics* **4** (Apr., 2008) 14–+, [arXiv:0711.4126].

[39] M. Maggiore and A. Riotto, **The Halo Mass Function from Excursion Set Theory. III. Non-Gaussian Fluctuations**, *ArXiv e-prints* (Mar., 2009) [arXiv:0903.1251].

[40] S. Matarrese, L. Verde, and R. Jimenez, **The Abundance of High-Redshift Objects as a Probe of Non-Gaussian Initial Conditions**, *Astrophys. J.* **541** (Sept., 2000) 10–24, [astro-ph/0001366].

[41] P. McDonald, **Primordial non-Gaussianity: Large-scale structure signature in the perturbative bias model**, *Phys. Rev.* **78** (Dec., 2008) 123519–+, [arXiv:0806.1061].

[42] P. McDonald, **Clustering of dark matter tracers: Renormalizing the bias parameters**, *Phys. Rev.* **D74** (2006), no. 10 103512, [astro-ph/0609413].

[43] N. Padmanabhan and M. White, **Calibrating the baryon oscillation ruler for matter and halos**, *Phys. Rev.* **80** (Sept., 2009) 063508–+, [arXiv:0906.1198].

[44] M. Manera and E. Gaztanaga, **The local bias model in the large scale halo distribution**, *ArXiv e-prints* (Dec., 2009) [arXiv:0912.0446].

[45] H. J. Mo and S. D. M. White, **An analytic model for the spatial clustering of dark matter haloes**, *Mon. Not. Roy. Astron. Soc.* **282** (Sept., 1996) 347–361, [astro-ph/9512127].

[46] H. J. Mo, Y. P. Jing, and S. D. M. White, **The correlation function of clusters of galaxies and the amplitude of mass fluctuations in the Universe**, *Mon. Not. Roy. Astron. Soc.* **282** (Oct., 1996) 1096–1104, [astro-ph/9602052].

[47] F. Bernardeau, S. Colombi, E. Gaztañaga, and R. Scoccimarro, **Large-scale structure of the Universe and cosmological perturbation theory**, *Phys. Rep.* **367** (Sept., 2002) 1–248, [astro-ph/0112551].

[48] P. McDonald, **Primordial non-Gaussianity: large-scale structure signature in the perturbative bias model**, *Phys. Rev.* **D78** (2008) 123519, [arXiv:0806.1061].

[49] M. Crocce and R. Scoccimarro, **Renormalized cosmological perturbation theory**, *Phys. Rev.* **73** (Mar., 2006) 063519–+, [astro-ph/].

[50] D. Baumann, A. Nicolis, L. Senatore, and M. Zaldarriaga, **Cosmological Non-Linearities as an Effective Fluid**, *ArXiv e-prints* (Apr., 2010) [arXiv:1004.2488].

[51] M. H. Goroff, B. Grinstein, S. Rey, and M. B. Wise, **Coupling of modes of cosmological mass density fluctuations**, *Astrophys. J.* **311** (Dec., 1986) 6–14.

[52] R. Scoccimarro and J. Frieman, **Loop Corrections in Nonlinear Cosmological Perturbation Theory**, *Astrophys. J. Sup.* **105** (July, 1996) 37–+, [astro-ph/].

[53] T. Matsubara, **Resumming cosmological perturbations via the Lagrangian picture: One-loop results in real space and in redshift space**, *Phys. Rev.* **77** (Mar., 2008) 063530–+, [arXiv:0711.2521].

[54] A. Taruya, K. Koyama, and T. Matsubara, **Signature of primordial non-Gaussianity on the matter power spectrum**, *Phys. Rev.* **78** (Dec., 2008) 123534–+, [arXiv:0808.4085].

[55] E. Sefusatti, M. Crocce, and V. Desjacques, **The Matter Bispectrum in N-body Simulations with non-Gaussian Initial Conditions**, *ArXiv e-prints* (Feb., 2010) [arXiv:1003.0007].

[56] E. Sefusatti and E. Komatsu, **Bispectrum of galaxies from high-redshift galaxy surveys: Primordial non-Gaussianity and nonlinear galaxy bias**, *Phys. Rev.* **76** (Oct., 2007) 083004–+, [arXiv:0705.0343].

[57] T. Nishimichi, A. Taruya, K. Koyama, and C. Sabiu, **Scale Dependence of Halo Bispectrum from Non-Gaussian Initial Conditions in Cosmological N-body Simulations**, *ArXiv e-prints* (Nov., 2009) [arXiv:0911.4768].

[58] T. Nishimichi, "private communication."

[59] R. Scoccimarro, E. Sefusatti, and M. Zaldarriaga, **Probing primordial non-Gaussianity with large-scale structure**, *Phys. Rev.* **69** (May, 2004) 103513–+, [astro-ph/0312286].

[60] R. E. Smith, **Covariance of cross-correlations: towards efficient measures for large-scale structure**, *Mon. Not. Roy. Astron. Soc.* **400** (Dec., 2009) 851–865, [arXiv:0810.1960].

[61] D. Schlegel, M. White, and D. Eisenstein, **The Baryon Oscillation Spectroscopic Survey: Precision measurement of the absolute cosmic distance scale**, in *astro2010: The Astronomy and Astrophysics Decadal Survey*, vol. 2010 of *ArXiv Astrophysics e-prints*, pp. 314–+, 2009. arXiv:0902.4680.

[62] R. E. Smith, R. K. Sheth, and R. Scoccimarro, **Analytic model for the bispectrum of galaxies in redshift space**, *Phys. Rev.* **78** (July, 2008) 023523–+, [arXiv:0712.0017].

[63] R. E. Smith, R. Scoccimarro, and R. K. Sheth, **Scale dependence of halo and galaxy bias: Effects in real space**, *Phys. Rev.* **75** (Mar., 2007) 063512–+, [astro-ph/0609547].

CHAPTER 7

Galaxy Bias in General Relativity[†]

Length scales probed by large scale structure surveys are becoming closer to the horizon scale. Further, it has been recently understood that non-Gaussianity in the initial conditions could show up in a scale dependence of the bias of galaxies at the largest distances. It is therefore important to include General Relativistic effects. Here we provide a General Relativistic generalization of the bias, valid both for Gaussian and non-Gaussian initial conditions. The collapse of objects happens on very small scales, while long-wavelength modes are always in the quasi linear regime. Around every collapsing region, it is therefore possible to find a reference frame that is valid for all times and where the space time is almost flat: the Fermi frame. Here the Newtonian approximation is applicable and the equations of motion are the ones of the N-body codes. The effects of long-wavelength modes are encoded in the mapping from the cosmological frame to the local frame. For the linear bias, the effect of the long-wavelength modes on the dynamics is encoded in the local curvature of the Universe, which allows us to define a General Relativistic generalization of the bias in the standard Newtonian setting. We show that the bias due to this effect goes to zero as the squared ratio of the physical wavenumber with the Hubble scale for modes longer than the horizon, as modes longer than the horizon have no dynamical effects. However, the bias due to non-Gaussianities does not need to vanish for modes longer than the Hubble scale, and for non-Gaussianities of the local kind it goes to a constant. As a further application, we show that it is not necessary to perform large N-body simulations to extract information on long-wavelength modes: N-body simulations can be done on small scales and long-wavelength modes are encoded simply by adding curvature to the simulation and rescaling the coordinates.

7.1. Introduction and Summary

Large Scale Structure (LSS) surveys are becoming larger and larger, and soon they will be able to probe cosmological modes whose length scale is comparable to the Hubble scale. General Relativistic effects scale as the ratio of the physical wavenumber k/a and the Hubble scale

$$\text{General Relativistic Effects} \sim \left(\frac{Ha}{k}\right)^2 , \tag{7.1}$$

[†]This chapter is based on a publication by T. Baldauf, U. Seljak, L. Senatore and M. Zaldarriaga that appeared in the Journal of Cosmology and Astroparticle Physics, Issue 10 (2011) [1]. L. Senatore and I are joint first authors, I derived major results of the paper, wrote major parts of the text and provided figures.

and it is therefore important to take these effects into account in order to be able to interpret next generation of LSS data. All the relativistic effects are basically projection effects relating what happens in one place to what we see: they include such things as lensing, redshift, distortion, gravitational redshift, etc. A consistent derivation of them for dark matter has been recently performed in [2]. Unfortunately we do not observe dark matter directly, but just luminous objects. From the observation of them we are able to reconstruct the dark matter density field by the realization that collapsed objects are biased tracers of the dark matter field. The concept of bias has so far always been defined using the Newtonian approximation that is valid for small length scales. The purpose of this paper is to provide a generalization of this concept that is valid at arbitrary long-wavelengths.
Another reason that motivates us to provide such a generalization is due to the recent observation that non-Gaussianity in the primordial density field can induce a scale dependence in the bias at large wavelengths [3, 4]. In the presence of non-Gaussianities of the local kind, the bias receives a scale dependence that in the Newtonian treatment behaves as

$$\delta_{n_g}(k) = b(k)\delta_m(k) \ , \qquad b_{f_{\rm NL}^{loc.}} \sim b_{f_{\rm NL}^{loc.}=0}\left(1 + f_{\rm NL}^{\rm loc.}\frac{H^2a^2}{k^2}\right) \ , \tag{7.2}$$

where δ_{n_g} is the perturbation to the density of objects, δ_m the perturbation to the matter density, and k is the wavenumber of the mode, and where we have neglected factors of order unity and the transfer function for simplicity. The important point of this expression is that in the presence of non-Gaussianities that have a non-vanishing squeezed limit, such as the ones of the local kind or the new ones that have been found in the Effective Field Theory of Multifield Inflation [5] with support both on equilateral and squeezed configurations, the bias receives a scale dependence at large scales proportional to $f_{\rm NL}$. This provides an ideal setup for measuring non-Gaussianities in LSS, as the signal is peaked on large scales, where theoretical predictions are under better control. Indeed current limits on $f_{\rm NL}^{\rm loc.}$ obtained from the Sloan Digital Sky Survey (SDSS) data are already competitive with the ones from WMAP [4], and analysis of the bispectrum is expected to be even more promising [6].
An odd feature of (7.2) is that

$$b_{f_{\rm NL}^{loc.}} \to \infty \quad \text{as} \quad k \to 0 \ . \tag{7.3}$$

It is equally strange that the standard Gaussian bias does not go to zero as $k \to 0$: one might indeed expect that modes longer than the Hubble scale should have no effects on the local dynamics. Of course, all of these results are due to the fact that we are trusting (7.2) way into a regime where it does not apply: as k/a becomes close to H, a proper General Relativistic treatment becomes necessary.
The main purpose of this paper is to provide such a General Relativistic generalization of the bias that is valid both in the case of primordial Gaussian and non-Gaussian initial conditions. In doing this, we will also provide a way to understand small N-body simulations in the General Relativistic setting, and to show that in order to study the effects of long-wavelength modes, it is not necessary to run large, time consuming, N-body simulations. Let us briefly summarize the logic and the main results.

- Cosmological perturbations become non-linear and lead to collapse only on very small scales, where the Newtonian approximation is valid. This suggests that if we insist on describing length scales much smaller than the Hubble scale, then the current Newtonian description is valid.

- Given a perturbed Friedman Robertson Walker (FRW) Universe with fluctuations of arbitrary length scale, it is possible to identify a coordinate frame valid on spatial distances much smaller than the horizon and for an arbitrary amount of time, where the metric appears locally as the one of Minkowski space, with small perturbations of order $(Hx)^2$,

x being the spatial distance from the origin. These coordinates represent the inertial frame of a free falling observer, and they are called Fermi coordinates [7]. In the case where the matter is non-relativistic, in this frame the Newtonian approximation is manifest, and we argue that this is the frame where results of small-box N-body simulations can be interpreted. We explicitly construct such a reference frame at linear order in the long scale fluctuations for a spherically symmetric configuration of the long-wavelength modes, as this is sufficient for the description of linear bias. Generalizations to different configurations for the long-wavelength modes or to the non-linear level should be straightforward.

- In these coordinates, all the effect of the long-wavelength mode is included in the mapping from the global frame to the Fermi frame, and in the long-wavelength curvature of the local patch. Since for the linear bias we can use spherical symmetry for the long-wavelength modes, the long-wavelength part of the Fermi metric must be equivalent to that of a curved FRW Universe, and therefore all the effect that a long-wavelength mode has on the local dynamics is indeed in the curvature of the local FRW Universe. This is given by

$$\Omega_K \sim \frac{\nabla^2 \zeta(\boldsymbol{x}_L, t_L)}{a^2 H^2} \ , \tag{7.4}$$

where ζ is the curvature perturbation in comoving gauge, and here for simplicity we have omitted numerical factors given later in the text.

- This allows us to generalize the concept of bias to the General Relativistic setting, by declaring it to be the derivative of the proper number density of objects at a fixed proper time with respect to the curvature of the local Universe:

$$b \sim \frac{1}{n_p}\frac{\partial n_p}{\partial \Omega_K} \quad \Rightarrow \quad \delta_{n_p} \sim b\frac{\nabla^2 \zeta}{a^2 H^2} + \dots \ , \tag{7.5}$$

where n_p is the proper number density of objects, δ_{n_p} their relative overdensity and the dots stand for additional terms coming from various projection effects that we will discuss in the text. Here we have neglected numerical factors. This expression makes sense physically, as for modes much longer than the Hubble scale, $\Omega_K \to 0$, making explicit the General Relativistic statement that metric modes that have no measurable gradients do not affect the local dynamics.

- In presence of primordial non-Gaussianities, the initial conditions for the fluctuations in the Fermi patch can depend on other parameters. In the case of non-Gaussianities of the local kind, initial conditions depend explicitly on ζ, a quantity that has no effect on the local dynamics. In this case, we extend the definition of the bias to include the derivative of the proper number density of objects with respect to the parameter itself. For example, in the case of non-Gaussianities of the local kind, we have

$$b_{f_{\rm NL}^{loc.}} \sim \frac{1}{n_p}\frac{\partial n_p}{\partial \zeta} \quad \Rightarrow \quad \delta_{n_p} \sim b\frac{\nabla^2 \zeta}{a^2 H^2} + b_{f_{\rm NL}^{loc.}}\zeta + \dots \ , \tag{7.6}$$

where again the ... stand for additional terms coming from various projection effects which we will discuss in the text. We see that the relative factor of k^2 between the standard bias and the one induced by $f_{\rm NL}$ is preserved in the General Relativistic limit. However, most importantly, the physical effect of long-wavelength fluctuations on the local overdensity does not blow up as $k \to 0$: it is simply the fact that the standard Gaussian effect goes to zero while the non-Gaussian one stays constant.

- Finally we point out that our construction of the local Fermi coordinates shows that it is not strictly required to run time-consuming large-box N-body simulations to study

the effect of long-wavelength fluctuations: their effect can be simply included by running small-box N-body simulations with different cosmological parameters than in the standard cosmology.

Related works on the way to include long-wavelength perturbations inside small-box N-body simulations have appeared in [8, 9, 10]. Related work on the way to derive the bias of the local form in the General Relativistic context has appeared in [11, 12, 13, 14] and a connection of the latter to primordial non-Gaussianities of the local form has been made in [15].

7.2. Fermi Coordinates for Perturbed FRW

Given a sufficiently smooth spacetime, it is possible to identify a set of coordinates centered around a timelike geodesic, known as Fermi coordinates [7]. They have two important properties: the metric is approximately that of Minkowski space, with corrections that start quadratically in the (space-like) geodesic distance from the time-like geodesic taken as the origin, and they are valid in the (spatial) vicinity of the time-like geodesic for all times.

In an FRW spacetime the Hubble expansion appears in the Fermi coordinates as a small correction to the standard dynamics in Minkowski space. This set of coordinates was found for unperturbed FRW first in [16]. Here we are going to provide such a set of coordinates for a linearly perturbed FRW Universe. We will then argue that in this set of coordinates the Newtonian approximation is valid, and that this is actually the frame in which N-body simulations are performed. Furthermore, we will provide a mapping from the local Fermi coordinates to the global coordinates of a perturbed FRW, and we will show how simulations have to be performed in order to include the effect of perturbations with wavelengths larger than the box size.

Let us therefore find these coordinates. Let us suppose we have an FRW metric with some linear long-wavelength fluctuations. We start from a perturbed FRW metric in Newtonian gauge:

$$ds^2 = -\left(1+2\Phi(\boldsymbol{x}_G, t_G)\right) dt_G^2 + a(t_G)^2 \left(1-2\Psi(\boldsymbol{x}_G, t_G)\right) d\boldsymbol{x}_G^2 \ . \tag{7.7}$$

In app. 7.5.1 we perform the same construction starting from ζ-gauge. Here the subscript $_G$ stands for Global to stress that these coordinates are valid for the entire FRW space. A great simplification comes from the fact that we wish to study the properties of the large scale structures mainly in the regime where the long-wavelength modes are linear: in other words, we are mainly interested in the two-point function of large-scale fluctuations. This has two consequences. First, the behavior of Φ and Ψ can be found by solving the linear Einstein equations and the linearized equations of motion for matter. For example, we can assume that there is no anisotropic stress at linear level, so that $\Psi = \Phi$. Second, if we wish to compute scalar quantities (as we will wish), we can use superposition principle to restrict ourselves to consider configurations where Φ is spherically symmetric around one point, let us say the point $\boldsymbol{x}_G = 0$. Generalization to the non-linear treatment of Φ is conceptually straightforward, but computationally not so, and we leave it to future work [1].

In order to find the Fermi coordinates (fig. 7.1), we can restrict ourselves to the neighborhood of a time-like geodesic. Spherical symmetry suggests to consider the geodesic $\boldsymbol{x}_G(t_G) = 0$. If we consider modes whose wavelength is much larger than the region of interest, we can Taylor expand the metric around the origin, and keep only the leading two derivatives. Notice that numerical simulations have to follow dark matter particles, and therefore their region of interest corresponds to scales corresponding to the length traveled by the particles, of the order of the

[1] Of course such a non-linear treatment would become much more pressing if we had convincing evidence that the primordial perturbation were non-Gaussian. There is some reason of possible excitement: in the CMB Gaussianity is excluded only at the 2σ level [17] through the analysis of the three-point function of the orthogonal kind parametrized by $f_{\rm NL}^{\rm orthog.}$ [18].

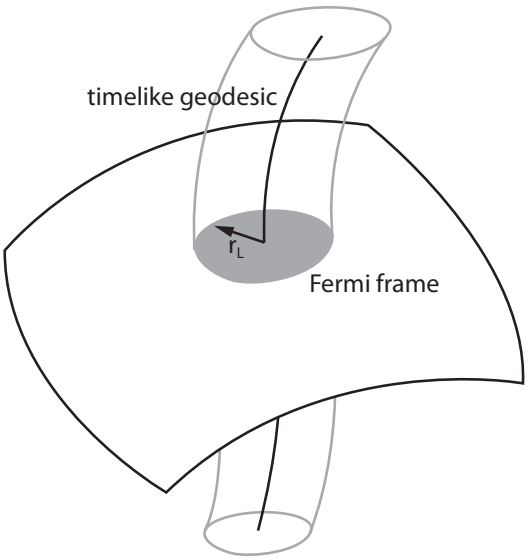

Figure 7.1.: *Fermi Coordinates.*

non-linear scale. We obtain:

$$ds^2 \simeq -\left(1+2\Phi(\mathbf{0},t_G)+\Phi(\mathbf{0},t_G)_{,r_G r_G} r_G^2\right) dt_G^2 + a(t_G)^2 \left(1-2\Phi(\mathbf{0},t_G)-\Phi(\mathbf{0},t_G)_{,r_G r_G} r_G^2\right) d\boldsymbol{x}_G^2 \,, \tag{7.8}$$

where $r_G^2 = x_{G,1}^2 + x_{G,2}^2 + x_{G,3}^2$. We can find the coordinates in which the above metric appears in the Fermi way in a simple, but brute force, way that we describe here. A more geometric derivation is presented in app. 7.5.2. Let us first warm up by considering the case of an unperturbed, curved FRW Universe, whose metric is of the form

$$ds^2 = -dt_G^2 + a(t_G)^2 \frac{d\boldsymbol{x}_G^2}{\left[1+\frac{1}{4}K\,\boldsymbol{x}_G^2\right]^2} \,. \tag{7.9}$$

We consider the curved case here because it will be useful for later purposes. It is easy to check that upon the following change of coordinates, valid at small distances [16]:

$$\begin{aligned} t_G &= t_L - \frac{1}{2}H(t_L) r_L^2 \,, \\ x_G^i &= \frac{x_L^i}{a(t_L)}\left(1+\frac{1}{4}H(t_L)^2 r_L^2\right) \,, \end{aligned} \tag{7.10}$$

where $r_L^2 = x_{L,1}^2 + x_{L,2}^2 + x_{L,3}^2$ and the subscript $_L$ reminds us that these are the Locally valid coordinates, the metric takes the form

$$ds^2 \;=\; -\left[1-\left(\dot{H}(t_L)+H(t_L)^2\right) r_L^2\right] dt_L^2 + \left[1-\frac{1}{2}\left(H(t_L)^2+\frac{K}{a(t_L)^2}\right) r_L^2\right] d\boldsymbol{x}_L^2 \tag{7.11}$$

As we had anticipated, for an indefinite amount of time, the metric near the spatial origin is approximately the Minkowski one, with corrections starting at order r_L^2 and suppressed by powers of $H\, r_L \ll 1$. So for example this metric is valid for distances smaller than Hubble, but it clearly can include cosmologically interesting length scales such as the non-linear scale where structures form.

To consider now the generic perturbed FRW flat space, let us generalize the change of coordinates as

$$t_G = t_L - \frac{1}{2}H(t_L) r_L^2 - \int_0^{t_L} \Phi(\mathbf{0},t')dt' + g_1(t_L) r_L^2 \,, \tag{7.12}$$

$$x_G^i = \frac{x_L^i}{a(t_L)}\left(1+\frac{1}{4}H(t_L)^2 r_L^2 + f_1(t_L) + f_2(t_L) r_L^2\right) ,$$

and let us determine the functions $f_{1,2}$, g_1, meant to be first order in the metric fluctuations, by imposing that the metric in the local coordinates is of the Fermi form, with the additional constraint that the spatial part be proportional to δ_{ij}. Notice that we have made the educated guess that at the origin the Local time equals the proper time. We will verify shortly that this is a good guess. After some straightforward algebra, we obtain

$$\begin{aligned}
t_G &= t_L - \int_0^{t_L} \Phi(\mathbf{0}, t_L) dt' \\
&\quad - \left(\frac{1}{2}H(t_L) - H(t_L)\Phi(\mathbf{0}, t_L) - \frac{1}{2}\Phi(\mathbf{0}, t_L)_{,t_L} - \frac{\dot{H}(t_L)}{2}\int_0^{t_L}\Phi(\mathbf{0}, t')dt'\right) r_L^2 , \\
x_G^i &= \frac{x_L^i}{a(t_f)}\left[1 + \Phi(\mathbf{0}, t_L) + H(t_L)\int_0^{t_L}\Phi(\mathbf{0}, t')dt' + \right. \\
&\left. \frac{1}{4}\left(H(t_L)^2 + H(t_L)\left(H(t_L)^2 - 2\dot{H}(t_L)\right)\int_0^{t_L}\Phi(\mathbf{0}, t')dt' - H(t_L)^2\Phi(\mathbf{0}, t_L) - 2H(t_L)\Phi(\mathbf{0}, t_L)_{,t_L}\right) r_L^2\right] .
\end{aligned} \tag{7.13}$$

Let us recall the common definition of the comoving-gauge curvature perturbation ζ

$$\zeta(\boldsymbol{x}_G, t_G) = -\Phi(\boldsymbol{x}_G, t_G) + \frac{H(t_G)^2}{\dot{H}(t_G)}\left(\Phi(\boldsymbol{x}_G, t_G) + \frac{\dot{\Phi}(\boldsymbol{x}_G, t_G)}{H(t_G)}\right) , \tag{7.14}$$

and the fact that this is constant for adiabatic fluctuations and for wavelengths longer than the sound horizon:

$$\dot{\zeta}(\boldsymbol{x}_G, t_G) = \frac{H(t)}{\dot{H}(t)}\left[\ddot{\Phi}(t) + \left(H(t) - \frac{\ddot{H}(t)}{\dot{H}(t)}\right)\dot{\Phi}(t) + \left(2\dot{H}(t) - \frac{\ddot{H}(t)H(t)}{\dot{H}(t)}\right)\Phi(t)\right] = 0 , \tag{7.15}$$

where the dot stays for derivative with respect to the time variable. This implies that we can write ζ as

$$\zeta(t) = -\Phi(t) - H(t)\int_0^t dt'\,\Phi(t') , \quad \Rightarrow \quad \dot{\Phi}(t) + H(t)\Phi(t) + \dot{H}(t)\int_0^t dt'\Phi(t') = 0 , \tag{7.16}$$

and therefore we can simplify the former expressions to get

$$\begin{aligned}
t_G &= t_L - \int_0^{t_L}\Phi(\mathbf{0}, t_L)dt' - \frac{1}{2}H(t_L)\left(1 - \Phi(\mathbf{0}, t_L)\right) r_L^2 , \\
x_G^i &= \frac{x_L^i}{a(t_f)}\left[1 + \frac{H(t_L)^2}{4} r_L^2\right]\left(1 - \zeta(\mathbf{0}, t_L)\right) .
\end{aligned} \tag{7.17}$$

The resulting metric is of the form

$$\begin{aligned}
ds^2 &= -\left[1 - \left\{\dot{H}(t_L) + H(t_L)^2 - 2\left(H(t_L)^2 + \dot{H}(t_L)\right)\Phi(\mathbf{0}, t_L) - 3H(t_L)\Phi(\mathbf{0}, t_L)_{,t_L}\right.\right. \\
&\quad \left.\left. -\Phi(\mathbf{0}, t_L)_{,t_L t_L} - \left(2H(t_L)\dot{H}(t_L) + \ddot{H}(t_L)\right)\int_0^{t_L}\Phi(\mathbf{0}, t')dt' - \frac{\Phi(\mathbf{0}, t_L)_{,r_G r_G}}{a(t_L)^2}\right\} r_L^2\right] dt_L^2 + \\
&\quad + \left[1 - \left\{\frac{H(t_L)^2}{2} - H(t_L)^2\Phi(\mathbf{0}, t_L) - H(t_L)\Phi(\mathbf{0}, t_L)_{,t_L}\right.\right. \\
&\quad \left.\left. -H(t_L)\dot{H}(t_L)\int_0^{t_L}\Phi(\mathbf{0}, t')dt' + \frac{\Phi(\mathbf{0}, t_L)_{,r_G r_G}}{a(t_L)^2}\right\} r_L^2\right] d\boldsymbol{x}_L^2 .
\end{aligned} \tag{7.18}$$

which is valid without assuming that ζ is constant. If we use that ζ is indeed constant outside of the sound horizon, the metric simplifies to

$$ds^2 = -\left[1 - \left(\dot{H}(t_L) + H(t_L)^2 - \frac{\Phi(\mathbf{0}, t_L)_{,r_G r_G}}{a(t_L)^2}\right) r_L^2\right] dt_L^2 \tag{7.19}$$

$$+\left[1-\left(\frac{H(t_L)^2}{2}+\frac{\Phi(\mathbf{0},t_L)_{,r_G r_G}}{a(t_L)^2}\right)r_L^2\right]d\boldsymbol{x}_L^2\ .$$

The above metric represents the description of a perturbed FRW Universe on scales much smaller than the typical length scale of the perturbations. For this reason, in the presence of adiabatic perturbations whose wavelength is longer than the sound horizon, it has to be equivalent to the local version of an FRW metric, as represented in the local coordinates of (7.11). This is indeed due to Birkhoff theorem. This is in fact true: upon identification of an effective local expansion rate $H_L(t_L)$ and of an effective curvature K_L given by

$$H_L(t_L)=H(t_L)+\frac{1}{H(t_L)a(t_L)^2}\left(\Phi(\mathbf{0},t_L)+\zeta(\mathbf{0},t_L)\right)_{,r_G r_G}\ , \tag{7.20}$$

$$K_L=2\left[\Phi(\mathbf{0},t_L)-\frac{H(t_L)^2}{\dot{H}(t_L)}\left(\Phi(\mathbf{0},t_L)+\frac{\Phi(\mathbf{0},t_L)_{,t_L}}{H(t_L)}\right)\right]_{,r_G r_G}=-\frac{2}{3}\nabla_G^2\zeta(\mathbf{0},t_G)\ ,$$

where $H_L(t_L)=\dot{a}_L(t_L)/a_L(t_L)$, the metric (7.18) takes the form of the curved unperturbed FRW Universe in (7.11) with the simple replacement $a\to a_L,\ K\to K_L$ [2]. In this case, the local curvature K_L is proportional to the Laplacian of the curvature perturbation usually denoted by ζ, and is thus constant in time. H_L follows the normal Friedmann equations for a curved FRW. In summary, we have been able to see that an FRW Universe with a linear adiabatic perturbation whose wavelength is longer than the sound horizon can be described, locally, by a metric that is very close to the Minkowski one, and is actually equivalent to one of a curved FRW Universe. The assumption of adiabaticity and that the wavelength of the mode is longer than the sound horizon is necessary in order for the curvature of the Universe to be constant in time: it is only in this case that there is one single local history for the Universe, which implies that the long-wavelength mode at linear level can be completely re-absorbed into the curvature of a local FRW Universe. In practice, this implies that our method of dealing with long wavelength perturbations is applicable to adiabatic long-wavelength fluctuations in the case where the speed of sound of the fluctuations is very small. This includes a Universe filled with dark matter and a cosmological constant, or with dark matter and quintessence with a very small speed of sound as the models studied in [19], while it does not apply to models with quintessence with non-vanishingly small speed of sound.
Although for some questions one can restrict to the case of spherical symmetry, this is not possible in general. The Fermi coordinates exist also in the absence of spherical symmetry. In app. 7.5.3 we present the form of the Fermi coordinates starting in Newtonian gauge with a plane wave perturbation.

7.2.1. A Simple Check

It is worth to show explicitly how our procedure works in a practical example, where the long-wavelength fluctuation is short enough to allow for a Newtonian treatment. Since we just said that the effect of a long mode can be re-absorbed in a curvature of the background (at linear level and after using superposition principle), this suggests that we should be able to re-derive the growth function at second order for short wavelength fluctuations in the presence of longer, spherically symmetric fluctuations as derived in [20] in the standard perturbation theory approach. Here instead we derive it from the growth of modes in a curved Universe. Working

[2] It might be useful to notice that the curvature perturbation $K=-\frac{2}{3}\nabla^2\zeta$ can be expressed in terms of the matter density perturbation in comoving gauge $\delta_l^{(com)}$ as

$$K=\left(\Omega_{m,0}+\frac{2}{3}f_0\right)H_0^2\delta_{l,0}^{(com)}\ , \tag{7.21}$$

where H_0 is the Hubble parameter at the present time, $\Omega_{m,0}$ is the fraction of energy in matter at present time, and $f=\frac{\partial\log D}{\partial\log a}$ with D being the growth factor such that $\delta^{(com)}(t)=D(t)\delta_0^{(com)}$.The subscript 0 is used for quantities evaluated at redshift zero.

only in the limit where all the modes are describable within the Newtonian approximation and working in Einstein-de-Sitter space, this calculation is carried out in app. 7.5.4, and here we summarize the main results.
The evolution of short modes in the effective curved Universe is related to the short modes in an flat Universe $\delta_{s,\text{flat}}$ as

$$\delta_s(\boldsymbol{x}) = \delta_{s,\text{flat}}(\boldsymbol{x}) \left(1 + \frac{34}{21}\delta_l(\boldsymbol{x})\right) , \tag{7.22}$$

where we have restricted ourselves to the matter only Einstein-de-Sitter Universe. In Fourier space we get

$$\delta_s(\boldsymbol{k}_s) = \delta_{s,\text{flat}}(\boldsymbol{k}_s) \left(1 + \frac{34}{21}\delta_l(k_l)\right) , \tag{7.23}$$

where we have assumed that the long mode is peaked at one frequency k_l.
Exactly the same expression can be computed in standard perturbation theory [20] as the coupling between an general short and a spherically symmetric long mode $\delta(k_l)$ leading to

$$\delta_s^{(2)}(\boldsymbol{k}_s) = \delta_s^{(1)}(\boldsymbol{k}_s) + \int \frac{\mathrm{d}\Omega_l}{4\pi} F_2(\boldsymbol{k}_s, \boldsymbol{k}_l)\delta_s^{(1)}(\boldsymbol{k}_s)\delta_l^{(1)}(k_l) = \delta_s^{(1)}(\boldsymbol{k}_s) \left(1 + \frac{34}{21}\delta_l^{(1)}(k_l)\right) . \tag{7.24}$$

We see that for long modes sufficiently far within the horizon so that a Newtonian treatment is possible, the two expressions agree.

7.3. The Coordinate Frame of N-body Simulations

Usually, N-body simulations are performed on very small scales compared to the Hubble scale, and no hint is usually given onto in what gauge the calculation is actually performed. Further, the equations that are solved in the simulations are not even the General Relativistic equations, but the Newton's equations, where all the General Relativistic effects are neglected [3].
Of course, there is a good reason for this. Usually simulations are performed in boxes which are much smaller than the Hubble scale. Since all General Relativistic effects, from the corrections to Newton's equation to the specification of the coordinate frame, scale proportionally to $(Ha)/k$, these effects are usually negligible. We begin to need to worry when the box size of the simulations becomes larger and larger, and reaches the Hubble scale. At this point, at least naively, we have to modify our codes to include the General Relativistic equations, choose some gauge in which to perform the calculation, take care of what is actually the observable quantity that needs to be computed. This is in fact different from $\delta\rho_m/\rho_m$, ρ_m being the matter density, as recently stressed in [2], due to lensing and redshift distortion effects. But doing all of this may seem a bit too much: at the end of day, we know that large scales evolve linearly, and it is only scales much smaller than the horizon that become non-linear and require N-body simulations. Further, if the sound horizon is much smaller than the Hubble scale, local *dynamics* does not really probe long distances, but it only probes distances of the order of the mean free path of the particles, which is the non-linear scale, and so it should not be affected by General Relativistic effects. On small scales, we should be able to apply the Newtonian approximation, and so our way of doing simulations should be fine to describe the small scale non-linearities. There seems to be a tension between including long wavelength fluctuations in the simulations, and the fact that the non-linearities occur just on small scales.
This tension has been solved in a recent paper [21], where it was shown how, exploiting the above facts, it is possible to re-interpret the results of current Newtonian N-body simulations directly in the General Relativistic context, by providing a mapping between the results of N-body simulations and the fluctuations in a specific gauge valid at arbitrary length scales. The

[3] The fact that usually the spatial coordinates are rescaled by a time-dependent factor equal to the scale factor, using the so-called comoving coordinates, should not be misleading: that is just a convenient change of variables for the same equations, which are still just the Newtonian ones.

only mistakes in this procedure are suppressed by powers of $(v/c) \ll 1$, with no corrections of the form $(Ha)/k$.

We are now going to argue that this same tension between N-body simulations and General Relativistic effects can be resolved in yet another way, by simply stating that in order to include long wavelength modes into the simulations, it is not necessary to make large-box simulations, but it is simply necessary to perform small-box simulations, in slightly curved backgrounds. The results obtained from the small scale simulations can then be reinterpreted as results obtained in local patches of the whole Universe. We will provide such a mapping [4].

Let us see how this works by showing that simulations can be interpreted in the General Relativistic context as nothing but solving the Einstein equations in the frame defined by the local coordinates (7.13), where the metric has the form (7.11) with the scale factor, the Hubble rate and the curvature as given by (7.20). If we now add short scale perturbations $\delta\Phi$ to the metric we have:

$$\begin{aligned} ds^2 &= -\left[1-\left(\dot{H}_L(t_L)+H_L(t_L)^2\right) r_L^2 + 2\delta\Phi(\boldsymbol{x}_L,t_L)\right] dt_L^2 \\ &\quad + \left[1-\frac{1}{2}\left(H_L(t_L)^2+\frac{K}{a_L(t_L)^2}\right) r_L^2 - 2\delta\Phi(\boldsymbol{x}_L,t_L)\right] d\boldsymbol{x}_L^2 \ . \end{aligned} \tag{7.25}$$

As we write down the Einstein equations for a Universe of dark matter particles plus a cosmological constant, where the perturbations are non-relativistic, we immediately realize that in the above metric the Newtonian approximation is valid: the metric looks like Minkowski with just small corrections, and the system is non-relativistic. Straightforward algebra then shows that the Einstein equations take the form of the simple Poisson equation

$$\nabla^2\delta\Phi(\boldsymbol{x}_L,t_L) = 4\pi G\delta\rho(\boldsymbol{x}_L,t_L) \ , \tag{7.26}$$

while the geodesic equation for the dark matter particles takes the form

$$\ddot{\delta\boldsymbol{x}}(t_L) + 2H_L(t_L)\dot{\delta\boldsymbol{x}}(t_L) = -\boldsymbol{\nabla}\delta\Phi(\boldsymbol{x}(t_L),t_L) \ . \tag{7.27}$$

In obtaining the above two equations, we have done several approximations and definitions that require explanation. We have defined

$$\delta\rho(\boldsymbol{x}_L,t_L) = \rho(\boldsymbol{x}_L,t_L) - \frac{3}{8\pi G}\left(H_L(t_L)^2+\frac{K}{a_L(t_L)^2}-\frac{\Lambda}{3}\right) \ , \qquad \dot{\boldsymbol{x}}(t_L) = H_L(t_L)\boldsymbol{x} + \dot{\delta\boldsymbol{x}}(t_L) \ , \tag{7.28}$$

where here we decided to focus on a ΛCDM Universe, thought we stress that trivial generalization of our formulas apply to the case of clustering dark energy [19]. Notice that the unperturbed velocity is nothing but the Hubble flow as seen at small distances from the origin. Then, we have expanded in perturbations by applying the Newtonian approximation: i.e., we have counted the perturbations in powers of $\delta\Phi \sim v^2$, where $\boldsymbol{v} = \dot{\boldsymbol{x}}(t_L)$, and taken the linear equations in these perturbations. Notice that this amounts to taking the leading terms also in r_L^2 in the Einstein equations, while we have not expanded in $\delta\rho/\rho$. The fact that these approximations are justified can be checked a-posteriori, but will become clear in the next paragraph.

In fact, eqs. (7.26) and (7.27) are *exactly the same equations* that are solved in N-body numerical simulations. This tells us two important things. First, that the Newtonian approximation is indeed justified. Second, most importantly, we *now know* how to interpret the above equations in a General Relativistic setting: they are the equations for a local patch described by the local frame. Thanks to the change of coordinates in (7.13), we can interpret the results of the

[4] The statement that in order to include large scale modes into small-box simulations one should include curvature and a rescaling of the coordinates has been already given in [8] and then more properly in [9]. However, a mapping from the frame of the simulations to the global frame had not been given, nor, it seems to us, a clear derivation has been presented. Further, all the statements in [8, 9] are not in the General Relativistic context. All of this becomes important if we are dealing with modes comparable to Hubble size.

N-body simulations as points in the full manifold of the spacetime (let us say for example as described in standard Newtonian gauge).
The presence of a long-wavelength mode affects the result of the N-body simulations in two different ways: first it affects the mapping from the global to the local coordinates in (7.13), second it affects the evolution of the short modes by adding a small curvature (7.20) to the effective local FRW Universe.
In summary, what we found can be synthesized by stating the following simple procedure for performing N-body simulations that include large scale fluctuations. Simulations are to be thought of as computing the gravitational structures in the local frame defined by the change of coordinates (7.13). In the presence of a long-wavelength mode, simulations should be performed in a curved (background) Universe where the curvature is given by (7.20) [5]. Any scalar quantity measured in the simulations, let us say the proper number density of halos of a given mass, should be intepreted as given at this time:

$$N-\text{body Simulations} \qquad \rightarrow \qquad n_p^L(\boldsymbol{x}_L, t_L; \Omega_K(\zeta)) \ , \tag{7.29}$$

where the explicit dependence on ζ comes from the curvature, and the superscript ^{L} reminds us that the output of the N-body simulations is to be interpreted as given in Local coordinates. From the mapping (7.13), we then finally get the value in the set of coordinates that are globally valid, for example in Newtonian gauge:

$$n_p^G(\boldsymbol{x}_G, t_G; \zeta) = n_p^L\left(\boldsymbol{x}_L(\boldsymbol{x}_G, t_G), t_L(\boldsymbol{x}_G, t_G); \Omega_K(\zeta)\right) \ , \tag{7.30}$$

where the superscript ^{G} reminds us that this quantity is defined in global coordinates valid everywhere, and we have used that the proper number density is a scalar.
Finally, we should comment on the initial conditions for the patches corresponding to the regions of space simulated in the N-body simulations. In the case of Gaussian initial conditions (we will comment on non-Gaussian initial conditions in the next section), it will turn out that to a very good approximation the initial power spectrum, expressed in terms of the local coordinates, should be the same as it would be in the absence of the long-wavelength mode. In order to understand the reason of this, it is useful to express the global metric in the comoving (ζ) gauge which is comoving with the density perturbations (see appendix 7.5.7). In this gauge, for adiabatic initial conditions, and for modes that are far outside of the sound horizon, the metric takes the form

$$ds^2 = -dt^2 + a^2 e^{2\zeta} d\boldsymbol{x}^2 \ . \tag{7.31}$$

Let us decompose the fluctuation ζ in a long-wavelength and a short-wavelength component $\zeta_l + \zeta_s$, where $_l$ stays for long, and $_s$ stays for short. Let us assume for the moment that the long-component is on scales longer than the sound-horizon. This means that it entered the Hubble scale after matter-radiation equality. In this case, ζ_l is constant in time. The property of the exponential is such that $\mathrm{Exp}(\zeta) = \mathrm{Exp}(\zeta_l) + \mathrm{Exp}(\zeta_s)$, which implies that in the limit in which we can neglect completely the gradients of ζ_l, ζ_l can be re-absorbed in a constant rescaling of the scale factor, and is therefore unobservable. This implies that the local physics (from matter radiation equality to recombination and so on) happens in exactly the same way as if the long mode was absent. As we learned in the former section, when we consider gradients of ζ_l, the leading effect of the long mode is to induce a curvature for the local Universe, which clearly affects the local evolution. So, the initial power spectrum of the short scales modes is the one that is obtained in a curved FRW Universe where the curvature is given by the Laplacian of ζ_l as in eq. (7.20). In practice, this means that we should run numerical codes as CMBFAST [22] or CAMB [23], run them with the relevant curvature of the Universe, and, after a rescaling by the scale factor, simply interpret the output as in local coordinates. In reality, it is not even necessary to obtain the power spectrum in such a curved

[5] As we stressed, the same approach can be generalized to include perturbations at non-linear level and to compute non-scalar quantities: in this case the local patch will not evolve as a curved FRW.

Universe as it is easy to realize that the initial curvature is negligible. The relevance of the curvature scales as $\nabla^2_G\zeta_l/(a^2_G H^2_L) \propto 1/\dot{a}^2_L$, and therefore it becomes irrelevant in the past. In practice, neglecting the effect of the initial curvature amounts to neglecting terms of order $\nabla^2_G\zeta_l(t_{L,in})$, where $t_{L,in}$ is the initial time of the N-body simulation. When we later define the bias we will define it as the coefficient of proportionality between the local number density and $\nabla^2_G\zeta_l(t_{L,obs})$, where $t_{L,obs}$ is the time of observation. The effect of the initial term scales as $\dot{a}_L(t_{L,obs})^2/\dot{a}_L(t_{L,in})^2$ and gives a negligible contribution to the bias if the initial time of the N-body simulation is early enough. In practice, this is the simple fact that the curvature is irrelevant at early times. This implies that, for long modes that entered the horizon during matter domination, the initial conditions for the simulations are equivalent to the ones in an unperturbed Universe.

The situation becomes slightly more complicated for long wavelength modes that enter the horizon during radiation domination. In this case, there is a window of time from horizon re-entry to matter-radiation equality during which ζ_l depends on time. This means that the mode in this case can not simply be interpreted as a rescaling of a and an additional curvature term. In this case gradients of the long fluctuation are relevant, as the mode travels approximately an Hubble horizon in an Hubble time. In order to evaluate the effect of the long mode on the short scale power, one should then solve the non-linear equations that couple ζ_s and ζ_l, along the line of what done in [24]. However, we can argue that this effect is negligible. The biasing of structures as due to a long wavelength mode is an intrinsically non-linear effect, and it therefore receives most of its contribution from late times, as density perturbations become closer and closer to being non-linear. In perturbation theory, it is straightforward to realize that neglecting the non-Gaussianities of the initial conditions set up at a time parameterized by a_{in} amounts to neglecting a non-Guassianity of the matter fields at a late time parametrized by a_{obs} that is of the order of a_{in}/a_{obs}. This is equivalent to the order of the relative error in the bias we have if we neglect the non-Gaussianity in the initial conditions. By taking the initial conditions to be early enough, we can make this error small enough. Given the fact that it is quite hard to measure the bias to great precision, the initial condition can be set up at a reasonably late time.

Let us summarize the discussion about the initial conditions. Concerning modes that entered the horizon during matter domination, one can simply take the power spectrum in local coordinates as in an unperturbed FRW Universe. Concerning modes that entered the horizon during radiation domination, one should take non-Gaussian initial conditions that can be estimated in perturbation theory as for example in [24]; however, their effect is likely to be negligible. The procedure we have outlined in this section enables to extract information about very long wavelength modes without practically modifying the N-body codes, and without having to run very large and time-consuming simulations. This should give a valid description for certain questions, such as the halo mass function, where spherical symmetry that we assumed to derive Fermi coordinates is likely to be valid (see app. 7.5.3 for a plane wave case). In app. 7.5.2 and 7.5.2 we give a detailed recipe for how to run a N-body simulation given the cosmological parameters and the amplitude of the long-wavelength mode.

7.4. Bias in General Relativity and its Scale Dependence

As an application of our technique we will derive an expression for the bias that is valid in the General Relativistic setting. As it has been recently noted in [3, 4] in the case of the local kind of non-Gaussianities parametrized by the parameter $f^{\rm loc.}_{\rm NL}$, the bias on large scales (as usually measured with respect to to the local matter overdensity) receives a contribution that is scale dependent, proportional to $1/k^2$, where k is the wavenumber of the long-wavelength mode, proportional to $f^{\rm loc.}_{\rm NL}$. The same is expected to be true for the new non-Gaussian shapes that have been found in the Effective Theory of Multifield Inflation [5] (a generalization of the

Effective Field Theory of inflation [25]) that have support both in the equilateral and in the squeezed limit. These results were derived in the Newtonian approximation, and here we will derive their generalization for wavelengths comparable or longer than the horizon.

7.4.1. Gaussian Bias

If we consider surveys that are comparable to the horizon scale, then relativistic effects become important and one needs to be very careful in defining observables. We do not directly observe the proper number of galaxies at a given point $n_p(t_G, \boldsymbol{x}_G)$ because the photons are deflected and redshifted on their way from the source galaxy to the observer.
What we can do, is count the number of galaxies in bins of angle and redshift. We will refer to the observed number density of galaxies, i.e., the number of galaxies divided by the observed volume, as $n_{obs}(z, \theta, \phi)$. Here z is the observed redshift of the bin, and the tuple (θ, ϕ) represents the observed angular position.
The observed position (z, θ, ϕ) corresponds to a set of global coordinates $(t_G, \boldsymbol{x}_G)$. Here we make use of the fact that a spacetime point can be described in in different coordinate systems and that global, local and observed coordinates are just three choices of such a coordinate frame that describe the same point. Thus the global coordinates are a function of the observed coordinates

$$(t_G, \boldsymbol{x}_G) = (t_G(z, \theta, \phi), \boldsymbol{x}_G(z, \theta, \phi)) \ , \tag{7.32}$$

and since the proper number density n_p is a scalar, i.e., a function of the point rather than its coordinates, we have

$$n_p(z, \theta, \phi) = n_p\big(t_G(z, \theta, \phi), \boldsymbol{x}_G(z, \theta, \phi)\big) \ . \tag{7.33}$$

To compute the observed number density $n_{obs}(z, \theta, \phi)$ we need to model both the proper density of objects n_p and the mapping between proper and observed coordinates. Let us start with the proper number density.

Proper and Observed Number Density

We have argued that in presence of long wavelength modes, the local inertial frame corresponds to a homogeneous curved FRW Universe. As a result the proper number density of galaxies at the spacetime point is given by the number density in the effective curved Universe. We will denote this number $n_p(t_L; \Omega_K)$. The time argument t_L stresses the fact that the proper time of the free falling observer is in general different from the global coordinate time.
We have:

$$n_p(z, \theta, \phi) = n_p\big(t_L\big(t_G(z, \theta, \phi), \boldsymbol{x}_G(z, \theta, \phi)\big); \Omega_K\big) \ , \tag{7.34}$$

where $t_L(t_G, \boldsymbol{x}_G)$ denotes the time in the Fermi frame centered at $(t_G, \boldsymbol{x}_G)$ and Ω_K is the curvature associated with the long wavelength mode. To evaluate this expression we need to compute the relation between (z, θ, ϕ) and t_L. We can split this relation in two parts.
First we can relate (z, θ, ϕ) to the global coordinates. As shown in [2] there is a lapse between the coordinate redshift $1 + z_G = 1/a_G(t_G)$ and the observed redshift z

$$z - z_G = (1 + z_G)\delta z_{G\to z} \tag{7.35}$$

where $\delta z_{G\to z}$ is given in app. 7.5.7. We also need to relate the global time coordinate to the time in the Fermi frame at the origin (see eq. 7.13),

$$t_L(t_G, \boldsymbol{x}_G) = t_G + \delta t_{G\to L}(t_G, \boldsymbol{x}_G). \tag{7.36}$$

The time shift between the global and the local coordinates is the difference between the global coordinate-time and the proper-time. In Newtonian gauge we have

$$\delta t_{G\to L}(z, \theta, \phi) = t_L\big(t_G(z, \theta, \phi)\big) - t_G(z, \theta, \phi) = \int_0^{t_G(z,\theta,\phi)} \Phi(t'_G(z, \theta, \phi), \boldsymbol{x}_G(z, \theta, \phi)) dt'_G \ , \tag{7.37}$$

$$= -\frac{1}{H(z)}\left[\zeta\big(t_G(z,\theta,\phi),\boldsymbol{x}_G(z,\theta,\phi)\big) + \Phi\big(t_G(z,\theta,\phi),\boldsymbol{x}_G(z,\theta,\phi)\big)\right] \ .$$

We can now expand eq. (7.34) to first order in the perturbations to obtain,

$$n_p(t_L;\Omega_K) = n_p(t_L,\Omega_K=0)\left[1+\frac{1}{\bar{n}_p}\frac{\partial n_p}{\partial\Omega_K}\Omega_K\right] \ , \tag{7.38}$$

where $\bar{n}_p$ is the unperturbed number density at the redshift of observation. Doing so, we have performed a split into background and perturbation such that $n_p(t_L,\Omega_K=0)$ is not a scalar but a function of its time argument. Thus

$$n_p(z,\theta,\phi) = n_p(t_G,\Omega_K=0)\left[1+\frac{1}{\bar{n}_p}\frac{\partial n_p}{\partial\Omega_K}\Omega_K + \frac{\partial\log\bar{n}_p}{\partial t}\delta t_{G\to L}\right] \tag{7.39}$$

$$= n_p(z_G,\Omega_K=0)\left[1+\frac{1}{\bar{n}_p}\frac{\partial n_p}{\partial\Omega_K}\Omega_K + \frac{\partial\log\bar{n}_p}{\partial\log(1+z)}\delta z_{G\to L}\right] \ , \tag{7.40}$$

where we have rewritten the prefactor and the time shift in terms of the global redshift z_G, which is possible since there is a one-to-one relationship between redshift and time in the auxiliary background Universe that can be translated into a relation between $\delta t_{G\to L}$ and $\delta z_{G\to L}$

$$\delta t_{G\to L}(z,\theta,\phi) = -\frac{z_G(t_L)-z_G(t_G)}{H(z)(1+z)} = -\frac{\delta z_{G\to L}}{H(z)} \ . \tag{7.41}$$

When calculating spherical averages, the observed redshift z is fixed while coordinate redshift z_G and global time t_G vary. As we will see shortly, it is beneficial to evaluate the prefactor at $z = z_G + \delta z_{G\to z}$

$$n_p(z,\theta,\phi) = n_p(z,\Omega_K=0)\left[1+\frac{1}{\bar{n}_p}\frac{\partial n_p}{\partial\Omega_K}\Omega_K + \frac{\partial\log\bar{n}_p}{\partial\ln(1+z)}\left(\delta z_{G\to L}-\delta z_{G\to z}\right)\right] \ . \tag{7.42}$$

We can now define the bias as

$$b_{\Omega_K}(t) = -\frac{1}{\bar{n}_p}\frac{\partial n_p}{\partial\Omega_K}, \tag{7.43}$$

and use that $\Omega_K(t) = 2\nabla_G^2\zeta/(3a^2H^2)$ in eq. (7.39). We discuss the relation between this definition of the bias and the standard one in the Newtonian approximation in the next section.

Volume Distortion

Finally, to compute $n_{obs}(z,\theta,\phi)$ we need to take into account the distortions in the volume induced by the mapping between (z,θ,ϕ) and the local frame. These geometric factors were recently derived at linear level in [2]. We denote V_p the proper volume corresponding to a bin in (z,θ,ϕ) and define

$$V_p = \bar{V}_p(1+\mathcal{J}), \tag{7.44}$$

where $\bar{V}_p$ is the corresponding volume in an unperturbed Universe and[6]

$$\mathcal{J} = -\Phi - (1+z)\frac{d}{dz}\delta z_{G\to z} - 2\frac{1+z}{Hr}\delta z_{G\to z} - \delta z_{G\to z} - 2\kappa + \frac{1+z}{H}\frac{dH}{dz}\delta z_{G\to z} + 2\frac{\delta r}{r} \ , \tag{7.46}$$

gives the geometrical projection effects computed in [2]. Finally, we have

$$n_{obs}(z,\theta,\phi) = n_p(z,\Omega_K=0)\left[1 - b_{\Omega_K}\Omega_K + \frac{\partial\log\bar{n}_p}{\partial\ln(1+z)}\left(\delta z_{G\to L}-\delta z_{G\to z}\right) + \mathcal{J}\right] \ . \tag{7.47}$$

Note that all the terms in the bracket are first order, i.e., they can be evaluated at z, z_G or t_G equivalently, since these agree at zeroth order.

[6] Our expression for $\mathcal{J}$ assumes that the survey is volume limited. If instead the survey is flux limited, we have to add the corrections due to the change in the apparent luminosity. In this case we have to replace $\mathcal{J}$ with

$$\mathcal{J} \quad\to\quad \mathcal{J} - 5p\,\delta\mathcal{D}_L \ . \tag{7.45}$$

See app. 7.5.7 for details.

Observed Overdensity & Averaging

The observed overdensity is the fractional difference between the overdensity in a certain direction and the angular average over the survey area

$$\delta_{obs}(z,\theta,\phi) = \frac{n_{obs}(z,\theta,\phi) - \bar{n}_{obs}(z)}{\bar{n}_{obs}(z)} \ . \tag{7.48}$$

When evaluating the observed mean number density we can use that all the terms in the bracket in eq. (7.47) vanish, when averaged over a sufficiently big survey area. Hence we obtain for the angular average

$$\bar{n}_{obs}(z) = \int_{\Omega_{survey}} \frac{\sin\theta \mathrm{d}\theta \mathrm{d}\phi}{\Omega_{survey}} n_{obs}(z,\theta,\phi) = n_p(z;\Omega_K = 0) \ . \tag{7.49}$$

Now, the benefit of evaluating prefactor in eq. (7.47) at the observed redshift becomes obvious. Since the observed redshift is fixed, $n_p(z,\Omega_K = 0)$ agrees with the survey average and we have for the observed overdensity (we will ignore the additional effects on monopole and dipole, which are influenced by the contributions at the observer's position),

$$\delta_{obs}(z,\theta,\phi) = -b_{\Omega_K}\Omega_K + \frac{\partial \log \bar{n}_p}{\partial \ln(1+z)} \left(\delta z_{G\to L} - \delta z_{G\to z}\right) + \mathcal{J} \ . \tag{7.50}$$

The volume distortion is in principle observable and thus has to be gauge invariant by itself. The first term $-b_{\Omega_K}\Omega_K$ is the number of collapsed objects in the inertial frame and thus totally independent of the choice of coordinates on the global manifold. The remaining redshift lapse is gauge invariant as we show in app. 7.5.7. Together with the first term it forms another observable. With the above results the observed number density can be written as

$$n_{obs}(z,\theta,\phi) = \bar{n}_{obs}(z)\left[1 + \delta_{obs}(z,\theta,\phi)\right] \ . \tag{7.51}$$

We can also relate the expression in (7.47) to the overdensity in the global coordinates, $\delta_G(t_G,\boldsymbol{x}_G) = (n_p(t_G,\boldsymbol{x}_G) - \bar{n}_p(t_G))/\bar{n}_p(t_G)$, where the averaging is done over hypersurfaces of constant coordinate time. We obtain

$$n_{obs}(z,\theta,\phi) = \bar{n}_{obs}(z)\left[1 + \delta_G - \frac{\partial \log \bar{n}_p}{\partial \log(1+z)}\delta z_{G\to z} + \mathcal{J}\right] . \tag{7.52}$$

Note that in the case where the tracer has a number density that scales like $(1+z)^3$ the combination $\delta_G - (\partial \log \bar{n}_p/\partial \log(1+z))\ \delta z_{G\to z}$ becomes $\delta_G - 3\delta z_{G\to z}$ in agreement with [2]. In our formalism it was natural to define the bias directly in terms of the Laplacian of the ζ perturbation at the point of interest, which in turn is proportional to the curvature of the local FRW Universe. Because of the Friedmann equation, the curvature turns out to be proportional to the overdensity of the Universe at the source galaxy position, as shown next. This offers us a procedure to extract the bias from N-body simulations: run simulations with varying Ω_K, and then take the derivative with respect to this parameter.

7.4.2. Comparison with Standard Newtonian Treatment of Bias

Our bias definition tells us that we should take the derivative of the number density with respect to the curvature of the local Universe. While our receipe is well defined in the full General Relativistic setup, it still should agree in the limit in which the long mode is well inside the horizon, so that the Newtonian approximation is valid for the long mode itself. However, in this case a naive look at the expression might make us think that the two procedures do not agree. Indeed, in the classical Newtonian treatment, the bias is defined as the derivative of the number density with respect to the local long-wavelength overdensity. In this section we will first relate the above bias definition to an overdensity and then consider the subhorizon limit.

The curvature energy density of the local Universe scales as $\Omega_K = \Omega_{K,0} H_0^2/(a_G H_G)^2$ and is thus fully specified by its value at redshift 0. The latter can be related to the matter density in (synchronous) comoving gauge as

$$\Omega_{K,0} = -\frac{K}{H_0^2} = \frac{2}{3}\frac{\nabla^2\zeta}{H_0^2} = -\left(1 - \frac{f_0 H_0^2}{\dot{H}_0}\right)(1-\Omega_{DE,0})\delta_{l,0}^{(com)} \tag{7.53}$$

$$= -\left(\Omega_{m,0} + \frac{2}{3} f_0\right)\delta_{l,0}^{(com)} \tag{7.54}$$

where the last two equalities are valid for a Universe with time varying dark energy and a ΛCDM Universe, respectively. Hence the bias term in eq. (7.47) can be written as

$$-b_{\Omega_K}(t)\Omega_K(t) = b_{\Omega_K}(t)\left(1 - \frac{f_0 H_0^2}{\dot{H}_0}\right)\frac{(1-\Omega_{DE,0})H_0^2}{D(t)H(t)^2 a(t)^2}\delta_l^{(com)}(t) \equiv b(t)\delta_l^{(com)}(t) \tag{7.55}$$

We restored the time dependence of the long wavelength density perturbation, dividing by the linear growth factor $D(t)$. Our new bias b_{Ω_K} is related to the standard bias parameter by a time dependent but scale independent factor. From the above equation we can see that the density perturbation in the comoving gauge is equally suited, at an algebraical level, as an expansion parameter for the galaxy bias, but the justification of this statement relies simply on the proportionality of b to b_{Ω_K}. Further, the bias expressed in terms of Ω_K makes manifest its gauge-invariant physical origin and the fact that the biasing vanishes for modes longer than the Hubble scale.

Well inside the horizon ($k \gg aH$) the velocity term in the relation between comoving and Newtonian gauge matter overdensity (see eq. (7.156) in app. 7.5.7) becomes negligible and thus both density perturbations reduce to the Newtonian density perturbation $\delta_l^N \approx \delta_l^{com} \approx \delta_l$. Furthermore, inside the horizon the volume distortion as well as the lapse between the global, local and observed redshift are negligible. Thus eq. (7.50) reduces to

$$\delta_{obs}(z,\theta,\phi) = -b_{\Omega_K}(t)\Omega_K(t) = b(t)\delta_l(t)\ , \tag{7.56}$$

which is the standard relation between observed tracer overdensity and underlying matter overdensity in the Newtonian approximation.

Finally, we point out that another way to understand the connection between our bias b_{Ω_K} and the standard one is by referring to the peak background split method. There, in the Newtonian context, it is usually assumed that the presence of a long scale mode can be interpreted as a shift of δ_c: $\delta_c \to \delta_c - \delta_l$, and after Taylor expansion we obtain the expression for the linear bias. In our context, the presence of a long mode is instead interpreted as a curvature of the background Universe, and therefore we have to rescale δ_c accordingly to $\delta_c(\Omega_K = 0) \to \delta_c(\Omega_K \neq 0)$ and then Taylor expand. In app. 7.5.5, we show that indeed the two approaches are equivalent on short scales.

7.4.3. Bias in Presence of non-Gaussianities of the Local Kind

So far we have assumed that the only way a long-wavelength mode affects the local structure formation is through its dynamical effects: that is by changing the local geometry and by introducing curvature in the resulting local FRW Universe. If the initial conditions are Gaussian, this accounts for all the effects of the long mode on local processes: in the linear regime the statistical properties of the short wavelength modes are decoupled from long wavelength modes, and the non-linearities kick in only at late times on small scales, where all the effect of the long mode can be absorbed by a redefinition of the local expansion history. If the initial conditions are non-Gaussian, then the statistical properties of the initial short scale fluctuations are in general affected by the presence of a long mode and this has to be taken into account. The scales that become non-linear are very small compared to the horizon, and the scales that we

are interested in are much larger than the non-linear scale. Thus, in order for the properties of the short scale fluctuations to be affected by the long mode, the non-Gaussian initial conditions need to be such that they correlate very long and very short modes.
In general the description of the statistical distribution of modes in the initial conditions requires knowledge of all the moments of their distribution. For special cases a limited set of parameters **p** is sufficient. For instance, if the initial conditions are Gaussian, they are fully quantified by their variance. If the parameters **p** depend on the long wavelength amplitude, then the proper number density of objects has an additional explicit dependence on the long wavelength amplitude. Thus we can generalize eq. (7.30) to:

$$n_p(\boldsymbol{x}_G, t_G; \zeta) = n_p\big(\boldsymbol{x}_L(\boldsymbol{x}_G, t_G), t_L(\boldsymbol{x}_G, t_G); \Omega_K, \mathbf{p}(\zeta)\big) \ . \tag{7.57}$$

These parameters **p** represent all the relevant information needed to describe the initial conditions on small scales. The abundance of objects of a given mass M is mainly sensitive to the amplitude of fluctuations smoothed on a scale enclosing the mass, given in terms of the variance σ_M. There is also a weak dependence on the slope of the power spectrum at the scale M and possibly on parameters describing deviations from a Gaussian distribution of the small scale modes, e.g. skewness. For definiteness we will consider only the dependence on σ_M.
The so-called local kind of non-Gaussianities [26] that can be produced in multifield inflationary models [27, 28] or in the new bouncing cosmology [29] provides an example where σ_M depends explicitly on the long wavelength amplitude ζ [7]. In these models the initial conditions are such that the curvature perturbation is a non-linear function (local-in-space) of an auxiliary Gaussian random variable ζ_g:

$$\zeta(\boldsymbol{x}_G) = \zeta_g(\boldsymbol{x}_G) - \frac{3}{5} f_{\rm NL}^{\rm loc.} \left(\zeta_g(\boldsymbol{x}_G)^2 - \langle \zeta_g^2 \rangle\right) \ . \tag{7.58}$$

If we decompose ζ into long and a short modes as we did before, we can see that the short mode takes the form

$$\zeta_s \simeq \left(1 - \frac{6}{5} f_{\rm NL}^{\rm loc.} \zeta_{g,l}\right) \zeta_{g,s} \ , \tag{7.59}$$

where we have neglected a term in ζ_s^2 which is irrelevant for our discussion of the bias. From this equation we see that the variance of the short scale power is modulated by the long mode. This implies that in the case of local non-Gaussianities there is an additional source of bias. If we set up the initial conditions for the simulation in the presence of non-Gaussianities of the local kind, the resulting proper number density of halos n_p will depend on the long-mode not only through its explicit dependence on the curvature of the local Universe, but also through the dependence on the initial power spectrum of the modes [8]. Eq. (7.47) is generalized to

$$\begin{aligned} n_{obs}(z,\theta,\phi) \ &\simeq \ n_p(z; \Omega_K = 0, \bar{\mathbf{p}}) \times \\ &\quad \left[1 - b_{\Omega_K} \frac{2\nabla_G^2 \zeta}{3a^2 H^2} + \frac{1}{\bar{n}_p} \frac{\partial n_p}{\partial \sigma_M^2} \frac{\partial \sigma_M^2}{\partial \zeta} \zeta + \frac{\partial \log \bar{n}_p}{\partial \log(1+z)} \left(\delta z_{G\to L} - \delta z_{G\to z}\right) + \mathcal{J}\right] \\ &= \ \bar{n}_p(z) \left[1 - b_{\Omega_K} \Omega_K + b_\zeta \zeta + \frac{\partial \log \bar{n}_p}{\partial \log(1+z)} \left(\delta z_{G\to L} - \delta z_{G\to z}\right) + \mathcal{J}\right] \ , \end{aligned} \tag{7.60}$$

where $\partial \sigma_M^2 / \partial \zeta = -12 f_{\rm NL}^{\rm loc.}/5$ is independent of M and $\bar{\mathbf{p}}$ describes the initial conditions in absence of long perturbations. We see that in presence of non-Gaussianities of the local kind the bias receives an additional contribution proportional to ζ, while the standard Gaussian contribution is proportional to $\nabla^2 \zeta$. There is a relative scale dependence proportional to k^2 between the two. But this does not imply the very unphysical result that the bias blows up as $k \to 0$. It is rather the fact that the bias for large scales should be interpreted as a different

[7] The same is expected to be true for the new non-Gaussian shapes that have been found in the Effective Theory of Multifield Inflation that have support both in the equilateral and in the squeezed limit [5].
[8] Though we are now talking about non-Gaussian effects, notice that we are consistently treating the long mode at linear level.

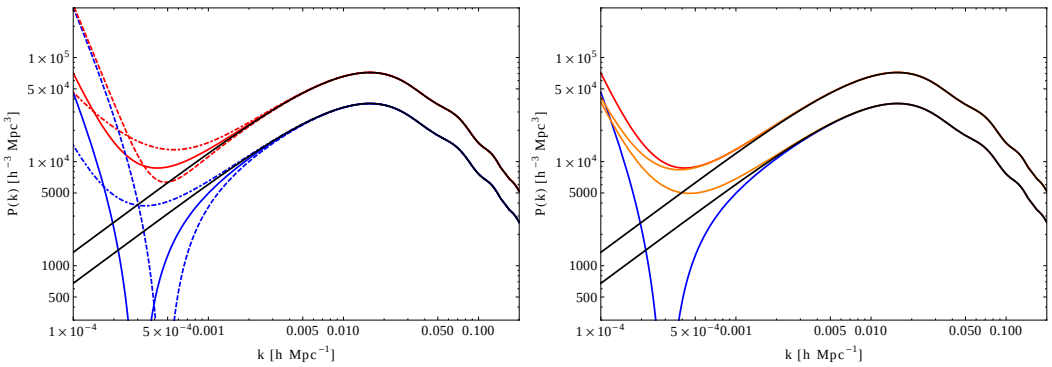

Figure 7.2.: Observed galaxy power spectrum for $z = 1$, $b_{\Omega_K} = 1.5$ ($b = 2$) and $\partial \log n_p / \partial \log(1+z) = 3$. We choose the following cosmological parameters: $\Omega_m = 0.28$, $\sigma_8 = 0.84$, $H_0 = 0.70$. *Left panel:* We show the spectra parallel to the line of sight (red) and transverse to the line of sight (blue). The solid line is for Gaussian initial conditions, whereas dot-dashed is $f_{\rm NL}^{loc.} = +0.5$ and dashed is $f_{\rm NL}^{loc.} = -0.5$. The lower black line is just the power spectrum of density in comoving gauge, the upper is multiplied by the redshift space distortion factor $(1 + f/b)^2$ to give the power parallel to the line of sight. We see that the effects of non-Gaussianity and GR-effects on the power spectrum differ, because the latter depend also on the line of sight parameter μ through the peculiar velocity effects. *Right panel:* Same as left, but orange lines show non -Gaussian power spectrum without the GR-effects (just redshift space distortions).

bias: as the coefficient of proportionality between the local number density and ζ and $\nabla^2\zeta$ [9]. The final expression for the observed overdensity in presence of local non-Gaussianities is thus

$$\delta_{obs}(z,\theta,\phi) = -b_{\Omega_K}\Omega_K + b_\zeta \zeta + \frac{\partial \log \bar{n}_p}{\partial \ln(1+z)} \left(\delta z_{G\to L} - \delta z_{G\to z}\right) + \mathcal{J} \ . \tag{7.61}$$

The presence of Φ terms in the redshift lapse terms and the volume distortion term mimicks $f_{\rm NL}^{loc.}$ of order unity. But this should not bias any measurement of non-Gaussianity since the General Relativistic effects are calculable and can thus be removed from the measurement.
As in the case of Gaussian initial conditions our formula can be applied directly to the results of N-body simulations, but for illustrative purposes we can also calculate the effect analytically assuming that the number density of collapsed objects is described by a universal mass function

$$n_p \propto f\left(\frac{\delta_c}{\sigma_M}\right) \ , \tag{7.62}$$

i.e., it is a function of the peak height, the ratio of collapse threshold and fluctuation amplitude. In this case the derivatives of n_p with respect to σ_M^2 and with respect to the curvature $\nabla^2\zeta$ are related:

$$\begin{aligned} \frac{\partial n_p}{\partial \zeta} &= \frac{\partial n_p}{\partial \sigma_M^2}\frac{\partial \sigma_M^2}{\partial \zeta} = -\frac{1}{2}\frac{\partial n_p}{\partial \delta_c}\frac{\delta_c}{\sigma_M^2}\frac{\partial \sigma_M^2}{\partial \zeta} \ , \\ \frac{\partial n_p}{\partial(-\Omega_K)} &= \frac{\partial n_p}{\partial \delta_c}\frac{\partial \delta_c}{\partial(-\Omega_K)} \ , \end{aligned} \tag{7.63}$$

which means that the Gaussian and the non-Gaussian bias are analytically related.
For general initial distributions, the additional contribution to the fluctuations in the proper number density arise from $\partial \mathbf{p}/\partial\zeta$. In the case of σ_M considered above, this is nothing but the

[9] Our conclusions about the bias as due to local non-Gaussianities are in general agreement with the ones of [13], though they differ in the way the results are derived and in parts of their interpretation. We stress that our derivation does not crucially rely on the assumption of spherical symmetry. It should allow for a straightforward generalization to the non-linear case where spherical symmetry can not be used.

squeezed limit of the three point function, because this measures the coupling between small and large scale modes. Squeezed in this context refers to the fact that we are talking about a correlation between short and long wavelengths so two of the momenta in the relevant three point function are very large compared to the other one and thus the three momenta form a squeezed triangle. In the local model that we use as an illustration, the derivative

$$\frac{\partial \sigma_M^2}{\partial \zeta(k)} \tag{7.64}$$

is independent of both k and of M (we have explicitly pointed out that the derivative might be different as a function of the wavenumber of the long momenta). Relatively simple models can and have been constructed where this derivative depends on both M and/or k [30]. Even when this derivative is not constant our formulas remain valid.
As an illustration, in fig. 7.2 we show an example for the the observed galaxy power spectrum for $b_{\Omega_K} \approx 1.5$ ($b = 2$) at $z = 1$ assuming a volume limited survey. The plots show the power parallel and orthogonal to the line of sight for a sample with evolution slope of $\partial \log \bar{n}_p / \partial \log(1+z) = 3$. We are adding local non-Gaussianity of $f_{\rm NL}^{loc.} = \pm 1$. The right panel shows that ignoring the GR-effects could lead to a fake detection of $f_{\rm NL} = \mathcal{O}(1)$, but this degeneracy is broken if modes both transverse and along the line of sight are considered. This is because GR-effects have a peculiar velocity contribution that has a μ dependence, where $\mu = \cos\theta$ and θ is the angle between the Fourier mode angle and the line of sight. For a related study on distinguishing GR effects from primordial non-Gaussianity see [31]. Note that the magnitude of the GR-effects depends on the redshift distribution of the sample. The non-Gaussian bias parameter b_ζ is calculated from the Gaussian bias using eq. (7.63). For the evaluation we are neglecting all the line of sight integrals (convergence, Shapiro-delay, integrated Sachs-Wolfe effect), which contribute power mainly to transverse modes. For the details of the evaluation of the observed power spectrum, we refer the reader to eq. (7.174) in app. 7.5.7.
It is also important to note that the relevant quantity is the change in the amplitude of fluctuations at a given physical scale M not of course a comoving scale. In single field inflationary models this derivative goes to zero in the squeezed limit, when k corresponds to a much larger scale than M. In fact it goes to zero as the square of k just because the long wavelength mode affects the production of the short modes during inflation only through tidal type effects. In a sense it goes to zero in this way for reasons identical to the ones that lead to the $\nabla_G^2\zeta$ dependence in the bias formulas. Thus, in single field inflationary models there is no modulation of the proper number density that scales with lower powers of k than $\nabla_G^2\zeta$ [10]. The reader familiar with the standard calculation of the single-field inflationary three point function might recall that in the squeezed limit they do not seem to vanish but that they satisfy a consistency condition where the shape of the three point function looks like that of a local model with an amplitude given by the tilt of the fluctuations usually called $(n_s - 1)$. But this dependence arises entirely from the fact that what is being calculated is a three point function in terms of comoving momenta. If expressed in terms of physical momenta, the $(n_s - 1)$ is exactly the amplitude required to make the relevant derivative vanish.

7.4.4. Observing Local-type non-Gaussianities in the Presence of GR Corrections

The salient fact about the local-type non-Gaussianities is that they induce a dependence of the proper number density of objects on the long wavelength modes that is much stronger than what the dynamical effects can produce, proportional to ζ rather than $\nabla_G^2\zeta$. Unfortunately when we count objects in our Universe there are projection type effects that make the observed densities depend directly on ζ even if the proper density does not. The volume corresponding

[10] One can construct examples were there is an intermediate "squeezed regime" over which the scaling is different than k^2 but for sufficiently large ratio the scaling needs to be k^2 [32, 33, 34, 35, 36, 37].

to a given observed range of angles and redshifts varies as a result of the long wavelength modes and results in the factor of $\mathcal{J}$ in eq. (7.47). Furthermore a given observed redshift corresponds to a different proper time in different directions resulting in the terms proportional to $\partial \log \bar{n}_p / \partial \log(1+z)$. Both of these terms lead to contributions proportional to ζ, contributions that have the same form as that coming from the local-type of non-Gaussianities. Failing to correct for them would bias the results for $f_{\rm NL}^{\rm loc.}$ by a number of order one which depends on the details of the population of objects surveyed.

Of course the various terms have different dependences on the properties of the objects as they depend on different derivatives of n_p^L. The effects will also depend differently on redshift and furthermore, because the GR effects are projection effects induced by the intervening matter, it may be possible to distinguish them using observations of the distribution of matter at the intervening redshifts. It is beyond the scope of this paper to quantify the extent to which these different effects may be isolated in practice or what it is required of the observations to distinguish them.

It is clear however that the GR effects are just projection effects, so if we were able to construct observables that were directly sensitive to quantities in the local frame we could side track those difficulties. In this section we just want to point out that this is in principle possible. We will not address wether this can be done in practice given our current tools or wether this route is better than just trying to correct for the projection distortions in a realistic situation.

To be able to ignore the projection effects we would need to be able to measure the proper density of some object at a given proper time. Thus we would need a ruler that would allow us to measure distances independently of the observed angles and redshifts and we would need a clock that would allow us to compare regions of the Universe at the same proper time independently of the observed redshift. If we managed to find such local clocks and rulers the observed density should only depend on $\nabla^2_G \zeta$ in the absence of primordial non-Gaussianity. In fact there should only be a $\nabla^2_G \zeta$ dependence in any single field model of inflation.

There are many such rulers that one could imagine using. One option is to use the acoustic scale. This could be used for example by measuring the the number of objects in regions of a given size in units of the acoustic scale. The acoustic scale can be determined by measuring the correlation function of these or other objects. Another option is to measure the ratio of the densities of two tracers. Then the volume projection effects would cancel, in a sense we are using the density of one of the objects to define the ruler for the other.

We still need a clock to make sure that one is comparing the number densities at a fixed proper time rather than observed redshift. This difference is responsible for the terms proportional to $(\partial \log \bar{n}_p / \partial \log(1+z))$ in eq. (7.47). This appears a bit more tricky but not a problem of principle. One needs to date the object observed independently of their redshift, something that happens automatically for tracers that appear only at a characteristic time in the history of the Universe. Examples of such things might one day be the first stars or perhaps quasars could be used as their abundance has a peak in redshift. In other words, the ratio of densities of tracers that come from a given proper time and could be identified without using the observed redshift would only depend of the long wavelength modes through the $\nabla^2_G \zeta$.

A similar construction for measuring the three point function in the squeezed limit could be accomplished using the CMB. The CMB comes already from a defined proper time, the recombination of hydrogen provides the clock. So one could use the dependence of the small scale power on large modes as a test of the squeezed three point function. One should use a local definition for fluctuations and power, meaning normalizing the fluctuations to the mean fluctuation level in the region of interest to eliminate the equivalent of the $\delta z_{G\to z}$ term in our equations for the densities of haloes. There is still the projection effect related to the mapping between angles and physical distances at recombination. This however can be avoided by comparing the amplitude of fluctuations at a fixed scale measured in units of the acoustic scale, thus at a fixed physical scale. For example the amplitude of the power spectrum at the N-th peak should only depend on the long modes through the $\nabla^2_G \zeta$ in the absence of primordial

non-Gaussianities. One could also use the anisotropies in the small scale power to de-lense the CMB along the lines considered in [38, 39].

Acknowledgments

While this paper was being written, very recently Ref. [40, 41, 42, 31] appeared which treat problems similar to ours and reach similar conclusions where there is overlap with our study. We would also like to thank the Asian Pacific Centre for Theoretical Physics in Pohang, Korea, for their kind hospitality during the workshop on "Cosmology and Fundamental Physics". TB thanks the Lawrence Berkeley National Laboratory, the Berkeley Center for Cosmological Physics, and EWHA Womans University for kind hospitality while parts of this project have been carried out. We thank Jaiyul Yoo for helpful discussions. This work is supported by DOE, the Swiss National Foundation under contract 200021-116696/1 and WCU grant R32-2009-000-10130-0.

7.5. Appendix

7.5.1. Fermi Coordinates from ζ-gauge

Here we give the change of coordinates necessary to go from ζ-gauge to the Fermi coordinates in the case of a spherically symmetric perturbation.
In ζ-gauge the metric takes the form

$$ds^2 = -N^2 dt^2 + \delta_{ij} e^{2\zeta} a^2 \left(dx^i + N^i dt\right)\left(dx^j + N^j dt\right) \ , \tag{7.65}$$

where we have used the ADM parametrization. In this gauge time diffeomorphisms are fixed by requiring $T_i^0 = 0$. The lapse N and shift N^i are constrained variables, whose solutions in terms of ζ are [43]

$$N = 1 + \frac{\dot\zeta}{H} \ , \qquad N_i = -\frac{\nabla_{G,i}\zeta}{H} - \frac{\dot H}{H^2}\frac{a^2}{c_s^2}\frac{\nabla_{G,i}}{\nabla_G^2}\dot\zeta \ . \tag{7.66}$$

The equation of motion for ζ reads [43]

$$\frac{1}{a^3}\partial_t\left(\frac{a^3}{c_s^2}\frac{\dot H}{H^2}\dot\zeta\right) + \frac{\dot H}{H^2}\frac{\nabla_G^2\zeta}{a^2} = 0 \ . \tag{7.67}$$

Outside the sound horizon and assuming c_s constant, we can simplify it to

$$\dot\zeta = \frac{\dot H}{H^2}\frac{c_s^2}{\left(\partial_t\left(\frac{\dot H}{H^2}\right) + 3\frac{\dot H}{H}\right)}\frac{\nabla_G^2\zeta}{a^2} \ . \tag{7.68}$$

Plugging back in (7.66), we can simplify the expression for N and N_i to be

$$N \simeq 1 \ , \qquad N_i = -\left(\frac{1}{H} + \frac{\dot H}{H^2}\frac{1}{3H - \partial_t\left(\dot H/H^2\right)}\right)\nabla_{G,i}\zeta \ . \tag{7.69}$$

At this point we proceed as in the main text. We Taylor expand ζ around the origin assuming spherical symmetry, we make an ansatz for the change of coordinates, and we impose the resulting metric to be in the Fermi form. After some straightforward algebra, we obtain for the change of coordinates

$$t_G \ = \ t_L - \frac{1}{2}\left[H(t_L) + \frac{\zeta_{,r_G r_G}}{a^2}\left(1 - \frac{H\dot H}{-3H^4 - 2\dot H^2 + H\ddot H}\right)\right] r_L^2 \ ,$$

$$x_G^i = \frac{x_L^i}{a(t_L)}\left[1+\frac{H(t_L)^2}{4}r_L^2\right](1-\zeta(\mathbf{0})) \ , \tag{7.70}$$

and for the metric

$$\begin{aligned} ds^2 = & \\ -\Bigg\{1-\Bigg[&\dot{H}(t_L)+H(t_L)^2-\frac{\zeta_{,r_G r_G}}{a^2}\frac{1}{H^2\left(3H^4+2\dot{H}^2-H\ddot{H}\right)^2}\left(9H^8\dot{H}+9H^6\dot{H}^2+4\dot{H}^5-3H^7\ddot{H}\right.\\ &\left.-6H^5\dot{H}\ddot{H}+2H^3\dot{H}^2\ddot{H}-4H\dot{H}^3\ddot{H}+H^2\dot{H}\left(-2\dot{H}^3+\ddot{H}^2\right)+H^4\left(12\dot{H}^3+\ddot{H}^2-\dot{H}\dddot{H}\right)\right)\Bigg]r_L^2\Bigg\}dt_L^2\\ &+\left\{1-\left(\frac{H(t_L)^2}{2}-\frac{\zeta_{,r_G r_G}}{a(t_L)^2}\cdot\frac{H^2\dot{H}}{-3H^4-2\dot{H}^2+H\ddot{H}}\right)r_L^2\right\}d\boldsymbol{x}_L^2 \ . \end{aligned} \tag{7.71}$$

As expected, this metric has the same form as the Fermi patch of a closed FRW Universe with

$$\begin{aligned} H_L(t_L) &= H(t_L)+\frac{\zeta_{,r_G r_G}}{a(t_L)^2}\left(\frac{1}{H}+\frac{H\dot{H}}{3H^4+2\dot{H}^2-H\ddot{H}}\right) \ , \\ K_L &= -\frac{2}{3}\nabla_G^2\zeta(\mathbf{0},t_G) \ , \end{aligned} \tag{7.72}$$

in agreement with what found in the Newtonian-gauge case.

7.5.2. A Geometric Derivation of the Fermi Coordinates

In this section we will describe how the Fermi coordinates can be constructed from a geometric point of view.

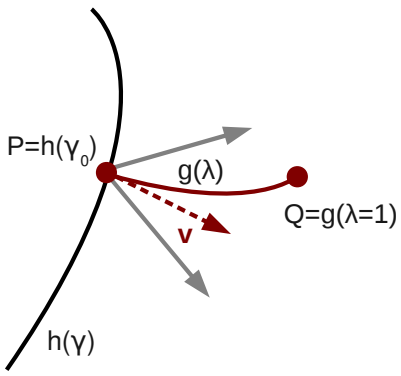

Figure 7.3.: Geometrical Construction of the Fermi Coordinates.

The starting point for the derivation will be a free falling observer moving along a timelike geodesic $h(\gamma)$ in the background Universe (fig. 7.3). His coordinate axes are described by an orthonormal set $(\boldsymbol{e}_0, \boldsymbol{e}_1, \boldsymbol{e}_2, \boldsymbol{e}_3)$ which is parallely transported along h. Thus if $\boldsymbol{e}_0$ is tangent to the geodesic $h(\gamma)$ at its origin it will remain so for all values of the affine parameter γ. Without loss of generality we can assume $\boldsymbol{e}_0$ to be timelike and the $\boldsymbol{e}_i$, $i=1,2,3$ to be spacelike, and the geodesic to be the origin of the global coordinate frame $x_G^i = 0$.
Now we consider a point $P = h(\gamma_0)$ on this geodesic. Our goal is to describe the spacetime in a neighborhood $\mathcal{U}$ of P starting from the global metric at P. Any point Q in the vicinity of P can be connected to P with a geodesic $g(\lambda)$ that is perpendicular to the tangent vector of h at P, i.e., its tangent vector $\boldsymbol{v}$ at P is a linear combination of the $\boldsymbol{e}_i$. The coefficients of this linear combination are the Fermi coordinates and the time component of the Fermi coordinates

is chosen to be the proper time of the observer moving along h. The point Q can thus be fully described by the proper time τ of the observer at P, the direction cosines x^i and the length of the geodesic λ joining Q with P. For simplicity we will normalize the direction cosines such that the point Q corresponds to $\lambda = 1$. This prescription is the natural extension of the flat space polar coordinates to curved space. The observer points in a certain direction defined by the direction cosines x_L^i and then follows the geodesic defined by the direction.
The initial conditions for the geodesic connecting P and Q can thus be summarized as

$$\begin{aligned} x^i(\lambda = 0) &= 0 \ , & \tau(\lambda = 0) &= t_L \ , \\ \left.\frac{dt_G}{d\lambda}\right|_{\lambda=0} &= 0 \ , & \left.\frac{dx_G^i}{d\lambda}\right|_{\lambda=0} &= x_L^i \boldsymbol{e}_i(t_0) \ . \end{aligned} \tag{7.73}$$

The point $Q \in \mathcal{U}$ with Fermi coordinates x_L^μ is then found by propagating along $g(\lambda)$ until $\lambda = 1$. We now have to find the mapping between arbitrary coordinates x^μ and the Fermi coordinates defining the geodesic $g(\lambda)$. This can be done by solving the geodesic equation for $g(\lambda)$

$$\frac{d^2x^\mu}{d\lambda^2} + \Gamma^\mu_{\alpha\beta}\frac{dx^\alpha}{d\lambda}\frac{dx^\beta}{d\lambda} = 0 \ , \tag{7.74}$$

perturbatively using the power law ansatz

$$x^\mu(\lambda) = \alpha_0^\mu + \alpha_1^\mu\lambda + \alpha_2^\mu\lambda^2 + \alpha_3^\mu\lambda^3 + \dots . \tag{7.75}$$

The validity of this series is clearly limited as is the validity of the Fermi coordinates themselves, which is obviously related to the curvature of the spacetime. The four vector formulation for the initial conditions stated above is

$$\begin{aligned} \alpha_0^\mu &= (t_0, 0, 0, 0), \\ \alpha_1^\mu &= \left.\frac{\mathrm{d}x^\mu}{\mathrm{d}\lambda}\right|_{\lambda=0} = x_L^i[\boldsymbol{e}_i]^\mu. \end{aligned} \tag{7.76}$$

where t_0 is the coordinate time corresponding to γ_0. The coefficients of the second and third order terms in the Taylor series follow straightforwardly from the geodesic equation evaluated at P

$$\begin{aligned} \alpha_2^\mu &= \left.\frac{1}{2!}\frac{\mathrm{d}^2x^\mu}{\mathrm{d}\lambda^2}\right|_{\lambda=0} = -\frac{1}{2}\Gamma^\mu_{\gamma\nu}\alpha_1^\gamma\alpha_1^\nu, \\ \alpha_3^\mu &= \left.\frac{1}{6!}\frac{\mathrm{d}^3x^\mu}{\mathrm{d}\lambda^3}\right|_{\lambda=0} = -\frac{1}{6}\left(\frac{\partial\Gamma^\mu_{\gamma\nu}}{\partial x^\kappa}\alpha_1^\gamma\alpha_1^\nu\alpha_1^\kappa + 4\Gamma^\mu_{\gamma\nu}\alpha_1^\gamma\alpha_2^\nu\right), \end{aligned} \tag{7.77}$$

where we already simplified using the initial conditions. In the following two subsections we will describe the mapping for two specific cases: perturbed and unperturbed FRW Universes.

FRW

We will now follow the above procedure for the homogeneous Friedmann-Robertson-Walker metric

$$\mathrm{d}s^2 = -\mathrm{d}t_G^2 + a(t_G)^2\frac{\mathrm{d}\boldsymbol{x}_G^2}{\left[1 + \frac{1}{4}K\boldsymbol{x}_G^2\right]}, \tag{7.78}$$

The vierbein associated to a comoving geodesic is

$$\begin{aligned} [\boldsymbol{e}_0]^\mu &= (1, 0, 0, 0) \ , & [\boldsymbol{e}_1]^\mu &= a^{-1}(0, 1, 0, 0) \ , \\ [\boldsymbol{e}_2]^\mu &= a^{-1}(0, 0, 1, 0) \ , & [\boldsymbol{e}_3]^\mu &= a^{-1}(0, 0, 0, 1) \ . \end{aligned} \tag{7.79}$$

The linear coefficients in the geodesic expansion read

$$\alpha_1^\mu = a(t_0)^{-1}(0, x_L, y_L, z_L) \ . \tag{7.80}$$

Hence, the first order spatial separation is $x_G^i \simeq x_L^i/a(t_0)$ and thus x_L^i is nothing but the physical separation of Q from P. Up to third order in the affine parameter we obtain

$$\begin{aligned} t_G =& t_L - \frac{H\boldsymbol{x}_L^2}{2} \ , \\ x_G^i =& \frac{x_L^i}{a(t_L)}\left(1 + \frac{H^2\boldsymbol{x}_L^2}{3}\right) \ . \end{aligned} \tag{7.81}$$

This leads to the following metric in Fermi Normal coordinates

$$\begin{aligned} \mathrm{d}s^2 =& -\left[1 - \left(\dot{H}(t_L) + H^2(t_L)\right)\boldsymbol{x}_L^2\right] dt_L^2 \\ &+ \left[\delta_{ij} - \left(H^2(t_L) + \frac{K}{a^2}\right)\frac{\boldsymbol{x}_L^2\delta_{ij} - x_L^i x_L^j}{3}\right]\mathrm{d}x_L^i\,\mathrm{d}x_L^j \end{aligned} \tag{7.82}$$

The above metric has non-zero off-diagonal contributions. The general transformation to remove off diagonal terms can be derived considering the metric in the old coordinates $\tilde{x}$

$$\mathrm{d}s^2 = \tilde{A}\,\delta_{ij}\,\mathrm{d}\tilde{x}^i\,\mathrm{d}\tilde{x}^j + \tilde{B}\,\tilde{x}_i\tilde{x}_j\ \mathrm{d}\tilde{x}^i\,\mathrm{d}\tilde{x}^j \ , \tag{7.83}$$

and new coordinates $x(\tilde{x})$

$$\mathrm{d}s^2 = A\,\delta_{ij}\,\mathrm{d}x^i\,\mathrm{d}x^j \ . \tag{7.84}$$

Using the ansatz $\tilde{x}^i = x^i(1 + \gamma x^2)$ we obtain the condition valid at second order in x:

$$\begin{aligned} \gamma =& -\frac{\tilde{B}}{4\tilde{A}} \\ A =& \tilde{A}(1 + 2\gamma x^2) \ . \end{aligned} \tag{7.85}$$

For the FRW case we have $\gamma = -H^2/12 - K/(12a^2)$ and the time component up to second order is unaffected

$$\begin{aligned} t_G =& t_L - \frac{H(t_L)}{2}\boldsymbol{x}_L^2 \ , \\ x_G^i =& \frac{x_L^i}{a(t_L)}\left(1 + \frac{H(t_L)^2}{4}\boldsymbol{x}_L^2\right) \ , \end{aligned} \tag{7.86}$$

finally leading to the following metric

$$\mathrm{d}s^2 = -\left[1 - \left(\dot{H}(t_L) + H(t_L)^2\right)\boldsymbol{x}_L^2\right]\mathrm{d}t_L^2 + \left[1 - \left(H(t_L)^2 + \frac{K}{a(t_L)^2}\right)\frac{\boldsymbol{x}_L^2}{2}\right]\mathrm{d}\boldsymbol{x}_L^2 \ , \tag{7.87}$$

which has the desired form.

Perturbed FRW

Let us now consider a perturbed FRW Universe in Newtonian gauge

$$\mathrm{d}s^2 = -\Big(1 + 2\Phi(t)\Big)\mathrm{d}t^2 + a^2(t)\Big(1 - 2\Psi(t)\Big)\mathrm{d}\boldsymbol{x}^2 \ . \tag{7.88}$$

We assume vanishing anisotropic stress leading to $\Phi = \Psi$. The vierbein associated to the coordinate frame is

$$[\boldsymbol{e}_0]^\mu = (1 - \Phi, 0, 0, 0) \ , \qquad [\boldsymbol{e}_1]^\mu = a^{-1}(0, 1 + \Phi, 0, 0) \ , \tag{7.89}$$

$$[\boldsymbol{e}_2]^\mu = a^{-1}(0,0,1+\Phi,0)\ , \qquad [\boldsymbol{e}_3]^\mu = a^{-1}(0,0,0,1+\Phi)\ .$$

We can now for simplicity expand the potentials around P

$$\Phi(\boldsymbol{x},t) = \Phi(\mathbf{0},t) + \frac{1}{2}\frac{\partial^2\Phi}{\partial r_G^2}\bigg|_0 r_G^2 = \Phi(\mathbf{0},t) + \frac{1}{2}\Phi(\mathbf{0},t)_{,r_G r_G} r_G^2\ , \tag{7.90}$$

where we asumed spherical symmetry [11] leading to

$$\mathrm{d}s^2 = -\Big(1+2\Phi(\mathbf{0},t)+\Phi(\mathbf{0},t)_{,r_G r_G} r_G^2\Big)\mathrm{d}t_G^2 + a^2(t)\Big(1-2\Phi(\mathbf{0},t)-\Phi(\mathbf{0},t)_{,r_G r_G} r_G^2\Big)\mathrm{d}\boldsymbol{x}_G^2,\ . \tag{7.91}$$

There is no linear term in this expansion, because we require the potential to be differentiable at $r = 0$. Let us proceed to find the Fermi coordinates. As noted above, the Fermi time is the proper time of the observer following the central geodesic h

$$t_L = \int_0^t \sqrt{-g_{00}}\,\mathrm{d}t' = t + \int_0^t \Phi(\mathbf{0},t')\,\mathrm{d}t'\ . \tag{7.92}$$

The coordinate time at P thus is $t_0 = t_L - \int_0^{t_L}\Phi(\mathbf{0},t')\ \mathrm{d}t'$, where in the integral boundary $t_L = t_0$ at leading order in Φ. This leads to the following expansion factors

$$\begin{aligned}\alpha_0^\mu =& (t_0,0,0,0)\ , \\ \alpha_1^\mu =& \frac{1+\Phi(\mathbf{0},t_0)}{a(t_0)}\big(0,x_L,y_L,z_L\big)\ .\end{aligned} \tag{7.93}$$

At this point, simple algebra as shown in the former section leads to the same relationship among the coordinates as in (7.17) and to the same Fermi metric as in (7.19).

Local Expansion Factor

With the aim of giving very specific recipe for running simulations given a certain long wavelength fluctuation, we provide some more specific relations. Some expressions can be simplified by noticing that the potential in Newtonian gauge and the density perturbation in the comoving gauge are related by (see Appendix 7.5.7)

$$\nabla^2\Phi(\boldsymbol{x},t) = 4\pi G a^2\bar{\rho}\,\delta_l^{(com)}(\boldsymbol{x},t)\ . \tag{7.94}$$

Note that this equation is exact, even on horizon scales. We define the growth factor in comoving synchronous gauge as $\delta_l^{(com)}(t) = D(t)\delta_{l,0}^{(com)}$, which is normalised to unity at present time. We also define the logarithmic growth factor $f(a) = \mathrm{d}\ln D/\mathrm{d}\ln a$. From eq. (7.94), we define the growth factor of the Newtonian potential D as follows $\Phi(t) = D(t)\Phi_0/a(t)$, where Φ_0 is the present day value. From the linear growth and eq. (7.94) it follows

$$\Phi(\mathbf{0},t)_{,t\,r_G r_G} = H\Phi(\mathbf{0},t)_{,r_G r_G}(f-1)\ . \tag{7.95}$$

Using the constancy of ζ we have shown that the value of the metric perturbation at the origin is irrelevant for the local expansion. Thus it only remains to derive the rescaling of the expansion factor corresponding to the effective local Hubble rate. Starting from (7.20), which, by defining $H_L(t) = H_G(t) + \delta H(t)$, gives

$$\delta H = \frac{1}{a_G^2(t)}\frac{H_G(t)}{\dot{H}_G(t)}\left(\Phi(\mathbf{0},t) + \frac{\Phi(\mathbf{0},t)_{,t}}{H}\right)_{,r_G r_G}\ , \tag{7.96}$$

[11] Note that

$$\nabla^2\Phi = \frac{2}{r}\frac{\partial\Phi}{\partial r} + \frac{\partial^2\Phi}{\partial r^2} = 3\frac{\partial^2\Phi}{\partial r^2}$$

where the last equality is true for a power law in r assuming no linear dependence in r.

we can find the corresponding rescaling for the expansion factor using the ansatz

$$a_L(t) = a_G(t)\,(1 + \delta a(t)_{rel}) \ , \tag{7.97}$$

where δa_{rel} has to satisfy the following:

$$\begin{aligned} \dot{\delta a}_{rel}(t) &= \frac{1}{3a_G^2(t)H_G(t)}\nabla_G^2\left(\Phi(\mathbf{0},t)+\zeta(\mathbf{0},t)\right) \ , \\ \Rightarrow \qquad \delta a_{rel}(t) &= \int_0^t dt' \frac{1}{3a_G^2(t')H_G(t')}\nabla_G^2\left(\Phi(\mathbf{0},t')+\zeta(\mathbf{0},t')\right) \ , \end{aligned} \tag{7.98}$$

where we have chosen the constant so that the two scale factors agree at early times. $\delta a(t)_{rel}$ can be numerically integrated from the transfer functions for any given cosmology. Finally, the Friedmann equations in the Fermi frame read as

$$H_L^2 = \frac{8\pi G}{3}\bar{\rho}_L + \frac{8\pi G}{3}\bar{\rho}_{DE} - \frac{K}{a_L^2} \ , \tag{7.99}$$

and

$$\frac{\ddot{a}_L}{a_L} = -\frac{4\pi G}{3}\bar{\rho}_L + \frac{8\pi G}{3}\bar{\rho}_{DE} \ , \tag{7.100}$$

where $\bar{\rho}_L$ is the local mean matter density. From the rescaling between the global and local Hubble rate we can derive the rescaling of the local mean density

$$\frac{H_L(t)^2 + \frac{K}{a(t)^2} - \frac{8\pi G}{3}\bar{\rho}_{DE}(t)}{H_G(t)^2 - \frac{8\pi G}{3}\bar{\rho}_{DE}(t)} = \frac{\bar{\rho}_L(t)}{\bar{\rho}_G(t)} \ , \tag{7.101}$$

leading to

$$\bar{\rho}_L(t) = \bar{\rho}_G(t) + \frac{3\Phi(\mathbf{0},t)_{,r_G r_G}}{4\pi G a^2(t)} = \bar{\rho}_G(t)\big(1+\delta_l^{(com)}(t)\big) \ . \tag{7.102}$$

This relation can be intuitively understood in the Newtonian context: the long wavelength density just rescales the local mean density. This relationship gets upgraded to the relativistic setup by using the comoving gauge overdensity.
For definiteness we give also the closed form expressions for the expansion and Hubble rate in a ΛCDM background

$$\begin{aligned} H_L(t) =& H_G(t)\left(1 - \frac{f(t)\Phi(\mathbf{0},t)_{,r_G r_G}}{4\pi G a^2(t)\bar{\rho}_G(t)}\right) = H_G(t)\left(1 - \frac{1}{3}f(t)\delta_l^{(com)}(t)\right) \ , \\ a_L(t) =& a_G(t)\left(1 - \frac{\Phi(\mathbf{0},t)_{,r_G r_G}}{4\pi G a^2(t)\bar{\rho}_G(t)}\right) = a_G(t)\left(1 - \frac{1}{3}\delta_l^{(com)}(t)\right) . \end{aligned} \tag{7.103}$$

Local Density Parameters

The time evolution of the local patch is determined by the local Friedmann eqns. (7.99) and (7.100), which are parametrized by the effective local density parameters. We will now provide the explicit mapping from the global to the local cosmological parameters that are needed for simulations. We specialize to ΛCDM for simplicity, though, as we stressed, our approach applies also to clustering dark energy. From the relationship between H_G and H_L and from the definition of of K given in (7.20), we have

$$\begin{aligned} \Omega_{K,L}(t_L) &= -\frac{K}{a_L(t_L)^2 H_L(t_L)^2} = \frac{2}{3}\frac{1}{a_L(t_L)^2 H_L(t_L)^2}\nabla_G^2\zeta(\boldsymbol{x}_G) \ , \\ \Omega_{\Lambda,L}(t_L) &= \frac{\Lambda}{3H_L^2} \ , \qquad \Omega_{m,L}(t_L) = 1 - \Omega_K(t_L) - \Omega_\Lambda(t_L) \ . \end{aligned} \tag{7.104}$$

It is convenient to normalize the cosmological parameters at $a = 1$ (for us $a_L = 1$), which leads to

$$\Omega_{K,L,0} = -\frac{K}{H_{L,0}^2} = \frac{2}{3}\frac{1}{H_{L,0}^2}\nabla_G^2\zeta(\boldsymbol{x}_G) \ , \tag{7.105}$$
$$\Omega_{\Lambda,L,0} = \frac{\Lambda}{3H_{L,0}^2} \ , \qquad \Omega_{m,L,0} = 1 - \Omega_{K,0} - \Omega_{\Lambda,0} \ ,$$

where the subscript $_0$ stays for evaluating the quantity when $a_L = 1$. In order to be able to use the above formulas, we simply need to find the time t_L at which $a_L = 1$. This can be found by solving eq. (7.97) with $a_L = 1$ to identify $t_{L,0}$. From there, by plugging into (7.20) we get $H_{L,0}$. The former expressions can be further simplified to give

$$\Omega_{m,L,0} = \frac{8\pi G\bar{\rho}_L}{3H_{L,0}^2} = \Omega_{m,0}\left[1 - \frac{2}{3}\frac{\nabla_G^2\zeta(\mathbf{0})}{H_{G,0}^2}\right] = \Omega_{m,0}\left[1 + \left(\Omega_{m,0} + \frac{2}{3}f_0\right)\delta_{l,0}^{(com)}\right] \tag{7.106}$$
$$\Omega_{K,L,0} = -\frac{K}{H_{L,0}^2} = \frac{2}{3}\frac{\nabla_G^2\zeta(\mathbf{0})}{H_{G,0}^2} = -\left(\Omega_{m,0} + \frac{2}{3}f_0\right)\delta_{l,0}^{(com)}$$
$$\Omega_{\Lambda,L,0} = \frac{\Lambda}{3H_{L,0}^2} = (1 - \Omega_{m,0})\left[1 - \frac{2}{3}\frac{\nabla_G^2\zeta(\mathbf{0})}{H_{G,0}^2}\right] = (1 - \Omega_{m,0})\left[1 + \left(\Omega_{m,0} + \frac{2}{3}f_0\right)\delta_{l,0}^{(com)}\right] \ .$$

The local Hubble rate at $a_L = 1$ is given by

$$H_{L,0} = H_{G,0}\left(1 + \frac{1}{3}\frac{\nabla_G^2\zeta(\mathbf{0})}{H_{G,0}^2}\right) = H_{G,0}\left[1 - \frac{1}{2}\left(\Omega_{m,0} + \frac{2}{3}f_0\right)\delta_{l,0}^{(com)}\right] \ . \tag{7.107}$$

As an example we consider the WMAP5 Flat ΛCDM cosmology with matter density parameter $\Omega_{m,0} = 0.28$ and Hubble constant $H_{G,0} = 70\,\mathrm{km\,s^{-1}\,Mpc^{-1}}$. For a long wavelength amplitude of $\delta_{l,0}^{(com)} = 0.1$ corresponding to $\nabla_G^2\zeta/H_{G,0}^2 = 0.89$ we obtain

$$\Omega_{m,L,0} = 0.30 \ , \qquad \Omega_{K,L,0} = -0.06 \ , \qquad \Omega_{\Lambda,L,0} = 0.76 \qquad h_{L,0} = 0.68 \ , \tag{7.108}$$

where we wrote the Hubble constant in terms of h_L as $H_{L,0} = 100h_L\,\mathrm{km\,s^{-1}\,Mpc^{-1}}$.
In fig. 7.4 we show the time dependence of the effective local expansion history. At early times the curvature is negligible and the effective local Universe approaches the flat background Universe. At late times, the cosmological constant dominates and thus the contribution of matter and curvature to the energy budget becomes irrelevant.

7.5.3. Fermi Coordinates for Plane-Wave Perturbed FRW Universe

Let us assume we start in Newtonian gauge with $\Phi(\boldsymbol{x}_G, t_g)$ being a plane wave with wavenumber that we can take without loss of generality in the x-direction

$$\Phi(\boldsymbol{x}_G, t_G) = \Phi_0\, e^{ikx_G} \ . \tag{7.109}$$

We can find the Fermi coordinates around the origin by working as in the main text and assume a change of coordinates valid at cubic order in the spatial distance of the form:

$$t_G = t_L - \frac{1}{2}H(t_L)r_L^2 - \int_0^{t_L}\Phi(\mathbf{0}, t')dt' + g_1(t_L)r_L^2 + \tag{7.110}$$
$$+ g_{a,1;j}(t_L)x_L^j + g_{a,2;j,k}(t_L)x_L^j x_L^k \ ,$$
$$x_G^i = \frac{x_L^i}{a(t_L)}\left(1 + \frac{1}{4}H(t_L)^2 r_L^2 + f_1(t_L) + f_2(t_L)r_L^2\right)$$
$$+ f_{a,tr}^i(t_L) + f_{a,0;j}^i(t_L)x_L^j + f_{a,1;j,k}^i(t_L)x_L^j x_L^k + f_{a,2;j,k,l}^i(t_L)x_L^j x_L^k x_L^l \ .$$

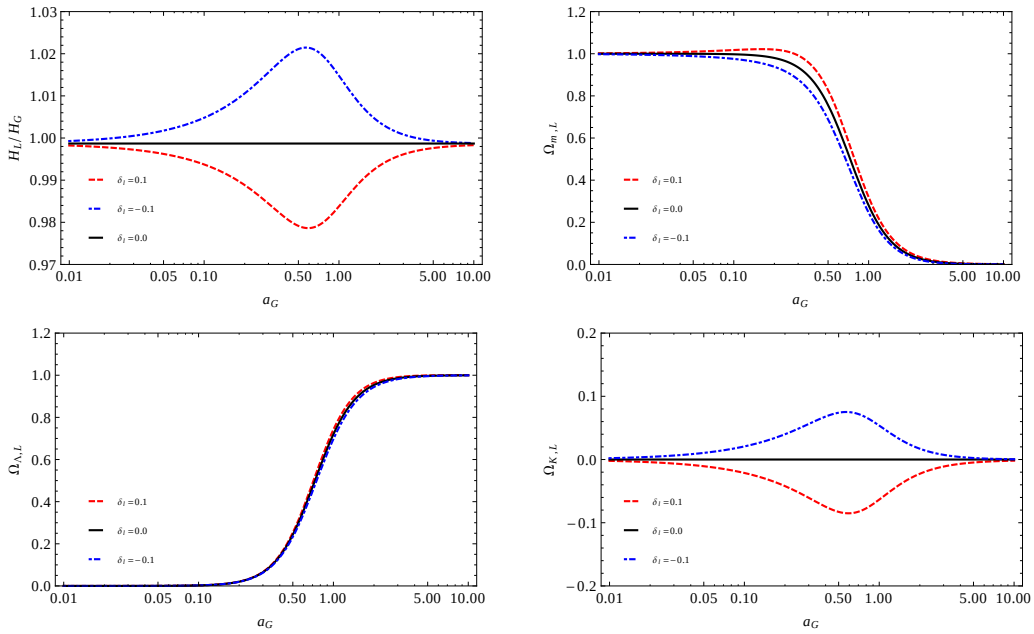

Figure 7.4.: Time dependence of the local expansion history as a function of the global expansion factor. In all panels the solid black line represents the flat background model, whereas the red dashed and blue dash-dotted lines represent an over- or underdense region. *Top left:* Ratio of the local and global Hubble rate. *Top right:* Local matter density parameter. *Bottom left:* Local cosmological constant density parameter. *Bottom right:* Local curvature density parameter.

This represents the most general change of coordinates around $\boldsymbol{x}_G = \mathbf{0}$ at cubic order in the distance from the origin, and it is a straightforward generalization of (7.12). The subscript a represents the fact that those functions are zero in the limit of isotropic perturbations. By imposing the metric in the new local coordinates to be of the Fermi form, we can proceed and identify the unknown functions. We skip the details associated to straightforward algebra, and just quote the final result. In order to limit the size of the expressions, we simply quote the simple expressions that are obtained after we restrict to the case of constant ζ.
Under the following change of coordinates

$$
\begin{aligned}
t_G &= t_L - \int_0^{t_L} \Phi(\mathbf{0}, t_L) dt' - \frac{1}{2} H(t_L) \left(1 - \Phi(\mathbf{0}, t_L)\right) r_L^2 \\
&\quad + \frac{x_L^1}{a(t_L) H(t_L)} \nabla_{G,1} \left[\Phi(\boldsymbol{x}_G, t_L) + \zeta(\boldsymbol{x}_G, t_L)\right]\big|_{\boldsymbol{x}_G=0} \ , \\
x_G^i &= \frac{x_L^i}{a(t_L)} \left\{ \left[1 + \frac{H(t_L)^2}{4} r_L^2\right] \left(1 - \zeta(\mathbf{0}, t_L)\right) - \frac{x_L^1}{a(t_L)} \nabla_{G,1} \zeta(\boldsymbol{x}_G, t_L) \right\} \\
&\quad + \delta_{i,1} \left[\nabla_{G,1} \int_0^{t_L} dt' \frac{\Phi(\boldsymbol{x}_G, t'_L) + \zeta(\boldsymbol{x}_G, t'_L)}{H(t'_L) a(t'_L)^2} \bigg|_{\boldsymbol{x}_G=0} - \frac{1}{2} \frac{r_L^2}{a(t_L)^2} \nabla_{G,1} \Phi(\boldsymbol{x}_G, t_L) \right. \\
&\quad \left. + \frac{(x_L^1)^3}{6 a(t_L)^3} \nabla^2_{G,11} \Phi(\boldsymbol{x}_G, t_L)\big|_{\boldsymbol{x}_G=0} \right] \ ,
\end{aligned}
\tag{7.111}
$$

we obtain the following metric components:

$$
\begin{aligned}
g_{00} &= -1 + \left(H(t_L)^2 + \dot{H}(t_L)\right) r_L^2 - \frac{(x_L^1)^2}{a(t_L)^2} \nabla^2_{G,11} \Phi(\boldsymbol{x}_G, t_L)\big|_{\boldsymbol{x}_G=0} \ , \\
g_{0i} &= \frac{H(t_L)}{4 a(t_L)} \left(2 x_L^i x_L^1 + \delta_{i1} r_L^2\right) \nabla_{G,1} \left[\zeta(\boldsymbol{x}_G, t_L) + 3\Phi(\boldsymbol{x}_G, t_L)\right]\big|_{\boldsymbol{x}_G} \ ,
\end{aligned}
\tag{7.112}
$$

$$g_{ij} = \delta_{ij}\left(1 - \frac{r_L^2}{2}H(t_L)^2 - \frac{(x_L^1)^2}{a(t_L)^2}\,\nabla_{G,11}\Phi(\boldsymbol{x}_G, t_L)|_{\boldsymbol{x}_G}\right) + \delta_{i1}\delta_{j1}\frac{(x_L^1)^2}{a(t_L)^2}\,\nabla^2_{G,11}\Phi(\boldsymbol{x}_G, t_L)\big|_{\boldsymbol{x}_G}\ ,$$

We see that in the anisotropic case, the metric has non-vanishing $0i$ components at order r_L^2. This form of the metric is important if we are interested in evaluating the bias for a non-scalar quantity, for which case the problem can not be reduced to the spherically symmetric case.

7.5.4. Growth in Presence of a Long Mode

In the main text, we derived a change of coordinates that is valid in a small region around a given time-like geodesic and that allowed us to describe the effect of a long wavelength fluctuation effectively as a local closed FRW Universe. This change of coordinates is valid at linear order in the long mode and at any order in the short wavelength perturbations. In the main text we focus on collapsed objects, as our main interest is extracting information about halo bias. Therefore we follow the short scale power well into the non-linear regime. On the other hand, the mapping can also be used to analytically examine the coupling of linear short wavelength modes to long wavelength modes while the short modes are still in the quasi-linear regime. In this regime, we are now going to explicitly compare results derived in our formalism to the ones obtained in standard perturbation theory. Since standard perturbation theory is performed in the Newtonian limit ($k/aH \gg 1$), we will adopt the simplifying assumption that the long mode is sufficiently far inside the horizon that the Newtonian approximation holds also for the long mode. In this limit we can for example neglect $\Phi \ll \nabla^2\Phi/(a^2H^2)$ [12]. We will also restrict ourselves to the Einstein de-Sitter (EDS) Universe for simplicity.
As shown in the main text, the effect of a long wavelength mode on the local dynamics can be ascribed to a non-vanishing spatial curvature K in a fictious closed global FRW Universe. The curvature parameter Ω_K and the curvature K are related by

$$\Omega_K = -\frac{K}{a^2H^2}. \tag{7.113}$$

Let us begin to investigate the growth of short scale fluctuations in a closed FRW Universe. The linear growth equation for the short wavelength matter density perturbations reads as

$$\ddot{\delta}_s + 2H\dot{\delta}_s - 4\pi G\bar{\rho}\delta_s = 0\ . \tag{7.114}$$

This equation is solved by the linearly growing modes $\delta_s(t) = D(t)\delta_{s,0}$:

$$D(t) = \frac{5}{2}\Omega_m H_0^2 H(t)\int_0^{a(t)}\frac{d\tilde{a}}{[\tilde{a}H(\tilde{a})]^3}\ , \tag{7.115}$$

which in EDS simplifies to $D(t) = a(t)$, where we use the subscript $_0$ to indicate present time and where we have normalized $a_0 = 1$. We will now look at the relation between the linear growth in a globally flat Universe and the effective local curved Universe. Using $\dot{H}(t) = -3H^2(t)/2$ in EDS, we obtain for the local effective curvature in terms of the long wavelength density perturbation

$$K = 2\left[\Phi(\mathbf{0}, t_L) - \frac{H_G^2(t_L)}{\dot{H}_G(t_L)}\left(\Phi(\mathbf{0}, t_L) + \frac{\Phi(\mathbf{0}, t_L)_{,t_L}}{H_G(t_L)}\right)\right]_{,r_G r_G} = \frac{5}{3}H_G^2 a_G^3\delta_{l,0}\ . \tag{7.116}$$

Here we have inserted a subscript $_l$ to δ to make it more explicit that it represents a long wavelength fluctuation. The growth now depends on the effective curvature in two ways. First, the growth in overdense regions is enhanced by a factor of $20\delta_l/21$. Furthermore, from (7.97) we obtain for the relation between local and global expansion $a_L(t_L) = (1 - \delta_l/3)a_G(t_L)$, and,

[12] We stress that we perform this approximation just in this appendix to make contact with former literature, but we do not do this same approximation in the main text, where the derivation is performed in full GR.

at a given fixed proper time, thus we have to evaluate the local growth at an earlier (later) scale-factor for overdense (underdense) regions. This partially cancels the first dependence. Adding both contributions, the derivative of the growth rate with respect to the long wavelength density reads as

$$\left.\frac{\partial D}{\partial \delta_{l,0}}\right|_{a_G} = \left.\frac{\partial D}{\partial \Omega_K}\right|_{a_L} \left.\frac{\partial \Omega_K}{\partial \delta_{l,0}}\right|_{a_G} + \left.\frac{\partial D}{\partial a_L}\right|_{\Omega_K} \left.\frac{\partial a_L}{\partial \delta_{l,0}}\right|_{a_G} = \frac{20}{21}a_G^2 - \frac{1}{3}a_G^2 = \frac{13}{21}a_G^2 \ , \tag{7.117}$$

Thus, we finally have with $\delta_l(t) = a_G \delta_{l,0}$:

$$D(\delta_l \neq 0) = D_0 + \left.\frac{\partial D}{\partial \delta_{l,0}}\right|_0 \delta_{l,0} = a_G \left(1 + \frac{13}{21}\delta_l\right) \tag{7.118}$$

It turns out that the coupling strength of 13/21 is a particlular property of the Einstein-de-Sitter Universe. In a more general ΛCDM Universe the coupling is less strong. Thus we will write the enhanced growth generally as $D = D_0(1 + \beta\delta_l)$ in the following. From the rescaling between the global and local Hubble rate we can derive the rescaling of the local mean density

$$\frac{H_L^2 + K/a^2}{H_G^2} = \frac{\bar{\rho}_L}{\bar{\rho}_G} \tag{7.119}$$

leading to

$$\bar{\rho}_L = \bar{\rho}_G(1 + \delta_l) \tag{7.120}$$

Since ρ is a scalar, local and global density agree $\rho_G(x) = \rho_L(x)$ when evaluated at the same physical point. Given that in this approximation we are neglecting the difference between t_L and t_G,we have

$$\delta_L(\boldsymbol{x}) = \frac{\rho(\boldsymbol{x})}{\bar{\rho}_L} - 1 \ , \quad \delta_G(\boldsymbol{x}) = \frac{\rho(\boldsymbol{x})}{\bar{\rho}_G} - 1 \quad \Rightarrow \quad \delta_G = (1 - \delta_l)(1 + \delta_L) - 1 \ . \tag{7.121}$$

Manipulating the last expression, we obtain

$$\delta_G(x) = \delta_{L,0}(1+\beta\delta_l)(1+\delta_l) + \delta_l = \delta_{L,0}[1 + (1+\beta)\delta_l] + \delta_l = \delta_{L,0}\left(1 + \frac{34}{21}\delta_l\right) + \delta_l \ , \tag{7.122}$$

where in the last step we have assumed EDS Universe. Here, we accounted both for the excess growth in the local frame and for the rescaling of the local mean density, with respect to which the local overdensity is defined. The three point function between long and short modes thus reads

$$\langle \delta_{\mathrm{G,s}}(\boldsymbol{x})\delta_{\mathrm{G,s}}(\boldsymbol{x})\delta_l(\boldsymbol{x})\rangle = 2 \times \frac{34}{21}\sigma_s^2 P_l(k) \ . \tag{7.123}$$

Correlators between Long and Short Modes

The coupling between long and short modes in the Newtonian regime can also be examined using perturbation theory (for a review see [20]). Standard perturbation theory solves the Newtonian fluid equations using a perturbative expansion in matter density and velocity divergence. In an Einstein de Sitter Universe, the second order contribution to the matter density field can be calculated as

$$\delta^{(2)}(\boldsymbol{k}) = \int \frac{d^3q}{(2\pi)^3} F_2(\boldsymbol{q}, \boldsymbol{k} - \boldsymbol{q})\ \delta^{(1)}(\boldsymbol{q})\ \delta^{(1)}(\boldsymbol{k} - \boldsymbol{q}) \tag{7.124}$$

where $\delta^{(1)}$ is the linearly evolved primordial density field and the second order mode coupling kernel is defined as

$$F_2(\boldsymbol{k}_1, \boldsymbol{k}_2) = \frac{5}{7} + \frac{1}{2}\frac{\boldsymbol{k}_1 \cdot \boldsymbol{k}_2}{k_1 k_2}\left(\frac{k_2}{k_1} + \frac{k_1}{k_2}\right) + \frac{2}{7}\frac{(\boldsymbol{k}_1 \cdot \boldsymbol{k}_2)^2}{k_1^2 k_2^2} \ . \tag{7.125}$$

We can now apply (7.124) to the case where we have a Universe with short modes $\delta_s(\boldsymbol{k}_s)$ and a spherical symmetric monochromatic long mode $\delta_l(k_l)$. In this case we get for the matter field up to second order

$$\delta_s^{(2)}(\boldsymbol{k}_s) = \int \frac{\mathrm{d}\Omega_l}{4\pi} F_2(\boldsymbol{k}_s, \boldsymbol{k}_l)\delta_s^{(1)}(\boldsymbol{k}_s)\delta_l^{(1)}(k_l) = \delta_s^{(1)}(\boldsymbol{k}_s)\left(1 + \frac{34}{21}\delta_l^{(1)}(k_l)\right) \ , \tag{7.126}$$

where we neglected the coupling of the short and long modes with themselves.
The skewness of the density field at second order is

$$\left\langle \delta(\boldsymbol{x})^3 \right\rangle = 6 \int \frac{\mathrm{d}^3 q}{(2\pi)^3} \int \frac{\mathrm{d}^3 q'}{(2\pi)^3} P(q)P(q')F_2(\boldsymbol{q}, \boldsymbol{q}') = 3 \times \frac{34}{21}\sigma^4 \ . \tag{7.127}$$

The prefactor 3 arises from the fact that all three density fields in $\left\langle \delta^3 \right\rangle$ can be expanded to second order. For the correlator between short and long modes we obtain

$$\langle \delta_s(\boldsymbol{x})\delta_s(\boldsymbol{x})\delta_l(\boldsymbol{x}) \rangle = 4 \int \frac{\mathrm{d}^3 q}{(2\pi)^3} \int \frac{\mathrm{d}^3 q'}{(2\pi)^3} P_s(q)P_l(q')F_2(\boldsymbol{q}, \boldsymbol{q}') = 2 \times \frac{34}{21}\sigma_s^2 P(k_l) \ , \tag{7.128}$$

where we assumed $P_l(\boldsymbol{q}) = (2\pi)^3\delta^{(\mathrm{D})}(\boldsymbol{q} - \boldsymbol{k})P(\boldsymbol{k})$, k_l is the long wavelength and the prefactor 2 arises from the fact that now only two of the three fields can be expanded to second order. This is in perfect agreement with our result in (7.123).

7.5.5. Spherical Collapse Dynamics

The collapse of a dark matter halo can be calculated considering a spherical overdensity within an otherwise homogeneous background Universe. In the standard calculation the background is assumed to be a flat matter-only Universe (aka Einstein-de-Sitter Universe). After reviewing the standard spherical collapse dynamics we extend the calculation to the case where the background Universe is curved. As we argued in the main text, this corresponds to the collapse in the presence of a long-wavelength mode. This procedure will offer us a way to match our General Relativistic definition of the bias with the standard Newtonian definition.

Collapse in Flat FRW

According to Birkhoff's theorem, a spherically symmetric overdense region evolves as a closed FRW Universe, whose Friedmann equation reads as

$$H_C^2 = \left(\frac{\dot{a}_C}{a_C}\right)^2 = \frac{8\pi G\rho_C}{3a_C^3} - \frac{K_C}{a_C^2} \ , \tag{7.129}$$

where the subscript C is used to refer to the collapsing region. This collapsing region typically has the size of a dark matter halo and should not be mistaken for the local patch described in the main part of this paper, which can contain many of these collapsing regions. The time evolution of the scale factor of the closed patch can be parametrized by the cycloid solution

$$a_C = A_C\,(1 - \cos\theta) \ , \qquad t = B_C\,(\theta - \sin\theta) \ , \quad \text{with} \quad \theta \in [0, 2\pi] \ , \tag{7.130}$$

where we defined

$$A_C = \frac{4\pi G\rho_C}{3K_C} \ , \quad \text{and} \quad B_C = \frac{4\pi G\rho_C}{3K_C^{3/2}} \ . \tag{7.131}$$

The spherical overdense region described by this parametrization expands until $\theta = \pi$, then it turns around to collapse at $\theta = 2\pi$, corresponding to the collapse time $t_{coll} = 2\pi B_C$. Formally the expansion at the collapse time is zero, but physically one expects the region to form a

virialized object at some time between turnaround and collapse. At early times $\theta \ll 1$ the parametric solution can be expanded as

$$a_C = A_C \frac{\theta^2}{2}\left(1 - \frac{\theta^2}{12} + \frac{\theta^4}{360} - \frac{\theta^6}{20160} + \dots\right) , \tag{7.132}$$

$$t = B_C \frac{\theta^3}{6}\left(1 - \frac{\theta^2}{20} + \frac{\theta^4}{840} - \frac{\theta^6}{60480} + \dots\right) . \tag{7.133}$$

Solving the above equations consistently up to order $\mathcal{O}(\theta^4)$ one obtains

$$a_C = A_C \frac{6^{2/3}}{2}\left(\frac{t}{B_C}\right)^{2/3}\left[1 - \frac{6^{2/3}}{20}\left(\frac{t}{B_C}\right)^{2/3}\right] . \tag{7.134}$$

The linear overdensity of the closed Universe collapsing at t_{coll} is then given by the fractional deviation between the local and the background volume (described here by the respective expansion factors)

$$\delta(t; t_{coll}) = \frac{a_B^3}{a_C^3} - 1 = \frac{3}{5}\left(\frac{3\pi}{2}\right)^{2/3}\left(\frac{t}{t_{coll}}\right)^{2/3} = \frac{3}{5}\left(\frac{3\pi}{2}\right)^{2/3}\frac{1+z_{coll}}{1+z(t)} , \tag{7.135}$$

where we have used that the matter-only background Universe evolves according to $a_B \propto t^{2/3}$. Finally, one obtains the critical density for collapse at z_{coll}, linearly extrapolated to the present time $z(t_0) = 0$

$$\delta_c(z_{coll}) = \frac{3}{5}\left(\frac{3\pi}{2}\right)^{2/3}(1 + z_{coll}) \approx 1.686\,(1 + z_{coll}) . \tag{7.136}$$

7.5.6. Closed Background

We will now extend the above calculation to the case, where the collapsing region resides in a curved background Universe following [44] and [45]. We will consider the case of an overdense, closed background Universe and note that the open background can be treated analogously. Furthermore, we will restrict ourselves to a background Universe without a dark energy component, such that only matter and curvature contribute to the energy budget. This closed background Universe is parametrized as

$$a_B = A_B\,(1 - \cos\eta) \qquad\qquad t = B_B\,(\eta - \sin\eta) \tag{7.137}$$

with $\eta \in [0, 2\pi]$ and the parameters

$$A_B = \frac{4\pi G\rho_B}{3K_B} , \quad \text{and} \quad B_B = \frac{4\pi G\rho_B}{3K_B^{3/2}} . \tag{7.138}$$

This curved background can now be identified with the effective curved patch describing a long wavelength fluctuation. We study the evolution of a collapsing spherical overdensity, expanding the parametric solutions for both the background (7.137) and the collapsing region (7.130) at early times. This means that we restrict ourselves to treat the curvature of the background at linear order. The linear density contrast then scales as

$$\delta = \frac{a_C^3}{a_B^3} - 1 = \frac{3}{5}\left(\frac{3\pi}{2}\right)^{2/3}\left[\left(\frac{1}{t_{\rm coll}}\right)^{2/3} - \left(\frac{1}{t_\Omega}\right)^{2/3}\right] t^{2/3} , \tag{7.139}$$

where $t_\Omega = 2\pi B$. For $K \to 0$ we have $t_\Omega \to \infty$ and thus we recover the EDS result shown above. The overdensity for an object that collapses at $t_{\rm coll}$, linearly extrapolated to present time thus reads as

$$\frac{\delta_{\rm c}(z_{coll})}{1 + z_{\rm coll}} = \frac{3}{5}\left(\frac{3\pi}{2}\right)^{2/3}\left[1 - \left(\frac{t_0}{t_\Omega}\right)^{2/3}\left(\frac{t_{coll}}{t_0}\right)^{2/3}\right] . \tag{7.140}$$

We can now write down the collapse time for the background Universe.

$$t_\Omega = 2\pi B_B = \frac{\pi\Omega_{m,B}}{H_0(\Omega_{m,B}-1)^{3/2}} = \frac{\pi\,(1-\Omega_{K,B})}{H_0(-\Omega_{K,B})^{3/2}} \tag{7.141}$$

Using $(t_0/t_{\rm coll})^{2/3} = 1 + z_{coll}$ and $t_0 \approx 2/(3H_0)$ the overdensity of the collapsing region can be rewritten as

$$\frac{\delta_{\rm c}(z_{coll})}{1+z_{\rm coll}} = \frac{3}{5}\left(\frac{3\pi}{2}\right)^{2/3}\left[1+\left(\frac{2}{3\pi}\right)^{2/3}\frac{\Omega_{K,B}}{(1-\Omega_{K,B})^{2/3}}\frac{1}{1+z_{coll}}\right] \ . \tag{7.142}$$

We are now going to consider the case where the curvature of the background Universe can be described by a long wavelength fluctuation with present day amplitude $\delta_{l,B}$. In this case we obtain for the density parameters of the background Universe

$$\Omega_{m,B} = \frac{1+\delta_{l,B}}{(1-\delta_{l,B}/3)^2} = 1+\frac{5}{3}\delta_{l,B} \quad \Rightarrow \quad \Omega_{K,B} = -\frac{5}{3}\delta_{l,B} \ . \tag{7.143}$$

For the overdensity of a perturbation that collapses at $z_{\rm coll}$ linearly extrapolated to the present day we obtain

$$\delta_c(z_{coll}) \approx 1.686\,(1+z_{coll}) - \delta_{l,0} = \delta_c(\Omega_{K,B}=0) - \delta_{l,B} \ . \tag{7.144}$$

This result is of course very intuitive and it allows us to explicitly verify that our General Relativistic definition of the bias agrees with the standard Newtonian one.

7.5.7. Perturbed Geodesic Parameters

In this appendix we will provide the essence of cosmological perturbation theory and expalain the gauge choices used in this paper. Then we will quickly review the most important formulae required for the mapping to observables before we conclude by specialising our result for the observed overdensity to the case where the matter distribution itself is the tracer.

7.5.8. Gauge Transformations

The most general perturbed metric for a flat Universe reads as [46]

$$\mathrm{d}s^2 = -(1+2A)\mathrm{d}t^2 - 2aB_i\mathrm{d}x^i\mathrm{d}t + a^2\left[(1+2D)\delta_{ij} + E_{ij}\right]\mathrm{d}x^i\mathrm{d}x^j \ . \tag{7.145}$$

We will restrict ourselves to scalar modes $B_i = BQ_i^{(0)}$ and $E_{ij} = EQ_{ij}^{(0)}$, where $Q^{(0)}$ is the scalar eigenmode of the Laplacian. Here we perform the scalar-vector-tensor decomposition in k-space, where $Q^{(0)} = \exp\left[i\boldsymbol{k}\cdot\boldsymbol{x}\right]$. We consider a Universe filled with dark matter plus dark energy and neglect anisotropic stress and pressure perturbations.
A gauge transformation corresponds to a change in spatial position x^i and comoving time $a\mathrm{d}\tau = \mathrm{d}t$

$$\tilde{x}^i = x^i + L^i \qquad\qquad \tilde{\tau} = \tau + T \tag{7.146}$$

under such a transformation the metric perturbations transform as

$$\begin{aligned} \tilde{A} &= A - a\dot{T} - aHT & \tilde{D} &= D - \frac{k}{3}L - aHT \\ \tilde{B} &= B + a\dot{L} + kT & \tilde{E}_{ij} &= E_{ij} + kT \end{aligned} \tag{7.147}$$

and the components of the energy momentum tensor transform as

$$\tilde{\delta} = \delta + 3aHT \qquad\qquad \tilde{v} = v + a\dot{L} \ , \tag{7.148}$$

where $v_i = vQ_i^{(0)}$. Gauge invariance refers to the fact that certain combinations of metric and energy momentum perturbations are invariant under a change of coordinates (7.146), i.e., the numerical value of a quantity does not change. Gauge invariance is necessary, but not sufficient, for observability.
We will consider two gauges

1. Newtonian Gauge
   Newtonian gauge is defined by $B = E = 0$ setting $A = \Phi$ and $D = -\Psi$.

$$\mathrm{d}s^2 = -(1+2\Phi)\mathrm{d}t^2 + a^2(1-2\Psi)\mathrm{d}\boldsymbol{x}^2 \tag{7.149}$$

   Neglecting anisotropic stress we have $\Phi = \Psi$. For the Einstein equations we have

$$-k^2\Phi - 3a^2H^2\left(\Phi + \frac{\dot{\Phi}}{H}\right) = 4\pi G a^2 \bar{\rho}\delta^{(N)} \tag{7.150}$$

$$aH\left(\Phi + \frac{\dot{\Phi}}{H}\right) = 4\pi G a^2 \left(\bar{\rho} + \bar{p}\right)\frac{v^{(N)}}{k} = -a^2\dot{H}\frac{v^{(N)}}{k} \tag{7.151}$$

2. Comoving Gauge
   In comoving gauge we set $E = 0$ and $\delta T_i^0 = 0$ corresponding to $v_i = B_i$. Setting $A = \xi$ and $D = \zeta$ leads to the metric

$$\mathrm{d}s^2 = -(1+2\xi)\mathrm{d}t^2 + a v_i \mathrm{d}x^i \mathrm{d}t + a^2(t)(1+2\zeta)\mathrm{d}\boldsymbol{x}^2 \tag{7.152}$$

   then the Einstein equations read as

$$k^2\left(\zeta + aH\frac{v^{(com)}}{k}\right) = 4\pi G a^2 \bar{\rho}_m \delta^{(com)} \tag{7.153}$$

$$H\xi - \dot{\zeta} = 0\ , \tag{7.154}$$

   where $v^{(com)} = v^{(N)}$. One can show that on scales larger than the sound horizon ζ is constant. Using $\dot{\zeta} = 0$ we see that the lapse function ξ vanishes in pressureless media and thus the comoving gauge is also synchronous, i.e., proper time agrees with the coordinate time. Using

$$T_{N\to com} = \frac{v^{(N)} - B^{(N)}}{k} = \frac{v^{(N)}}{k} \tag{7.155}$$

   the overdensities in the Newtonian and comoving gauge are related by

$$\delta^{(com)} = \delta^{(N)} - a\dot{\bar{\rho}}T_{N\to com} = \delta^{(N)} + 3aH\frac{v^{(N)}}{k} \tag{7.156}$$

   For the spatial metric perturbations we have

$$\zeta = -\Phi - aHT_{N\to com} = -\Phi - aH\frac{v^{(N)}}{k} = -\Phi + \frac{H^2}{\dot{H}}\left(\Phi + \frac{\dot{\Phi}}{H}\right) \tag{7.157}$$

   In synchronous gauge $A = B = 0$ there are no sources in the equation of motion for the velocity of stress free matter, i.e., if it was at rest initially it will remain so for all times [47]. In this case the density perturbation in comoving and synchronous gauge agree $\delta^{(com)} = \delta^{(syn)}$. The CMBFAST Boltzmann code [22] is providing the synchronous gauge transfer function and can thus be used to infer the transfer function for the comoving gauge density perturbation.

Combining the Einstein equations in comoving and Newtonian gauge we have

$$-k^2\Phi = 4\pi G a^2 \delta^{(com)}\ , \tag{7.158}$$

which is valid on *all* scales.

7.5.9. Volume Distortion & Observed Redshifts

Here we explain the symbols used in eq. (7.50) for the reader's convenience (see [2] for a detailed explanation and derivation):

$$\begin{aligned}\mathcal{J} = \delta V/V =& -\Phi + v^i e_i - (1+z)\frac{d}{dz}\delta z_{G\to z} - 2\frac{1+z}{Hr}\delta z_{G\to z} - \delta z_{G\to z} \\ & -2\kappa + \frac{1+z}{H}\frac{dH}{dz}\delta z_{G\to z} + 2\frac{\delta r}{r} \\ =& -\Phi + \left[\frac{\mathrm{d}\ln H}{\mathrm{d}\ln(1+z)} - 1 - 2\frac{1+z}{Hr_s}\right]\left[v^i e_i - \Phi - 2\int_0^{r_s}\mathrm{d}r\, a\dot{\Phi}\right] \\ & +\frac{4}{r_s}\int_0^{r_s}\mathrm{d}r\,\Phi - 2\int_0^{r_s}\mathrm{d}r\,\frac{r_s - r}{r r_s}\hat{\nabla}\Phi + \frac{1}{H}\left[\dot{\Phi} - \frac{1}{a}\frac{\partial v_i e^i}{\partial r}\right] .\end{aligned} \tag{7.159}$$

In the evaluation of the above expression we used that the total derivative is given by $d/dz = H^{-1}d/dr = -(\partial_o - e^i\partial_i) = -(\partial_0 - \partial_r)$ and that the velocity follows the evolution equation

$$\dot{v}_i + Hv_i = -\frac{\Phi_{,i}}{a} . \tag{7.160}$$

The perturbation to the redshift of the source $\delta z_{G\to z}$, is given by the relationship

$$\delta z_{G\to z} = aH\delta\tau_o + \left[v_i e^i - \Phi\right]_0^s - 2\int_0^{r_s} a\dot{\Phi}\, dr . \tag{7.161}$$

Here the four velocity of the source is given by $u^\alpha = a^{-1}\big((1+\Phi), v^i\big)$ and e^i is the photon propagation direction as seen from the observer, r is the comoving line-of-sight distance, r_s is the comoving line-of-sight distance of the source. $\delta\tau_o$ is the perturbation to the conformal time at the time of observation, and it is just a monopole term that cancels when measuring fluctuations. δr is the radial displacement, given by

$$\delta r = \delta\tau_0 + 2\int_0^{r_s} dr\ \Phi . \tag{7.162}$$

The deflection of the photons on their way form the source galaxy to the observer can be quantified as

$$\begin{aligned}\delta\theta &= 2\int_0^{r_s} dr\left(\frac{r_s - r}{r\, r_s}\right)\Phi_{,\theta} , \\ \delta\phi &= 2\int_0^{r_s} dr\left(\frac{r_s - r}{r\, r_s \sin\theta}\right)\Phi_{,\phi} .\end{aligned} \tag{7.163}$$

The latter can be combined to calculate the distortion of the solid angle as quantified by the convergence κ

$$\kappa = 2\int_0^{r_s} dr\ \left(\frac{r_s - r}{r\, r_s}\right)\hat{\nabla}^2\Phi , \tag{7.164}$$

where $\hat{\nabla}$ is the differential operator on the two dimensional unit sphere. In case the survey is not volume limited but rather flux limited, we need to replace $\mathcal{J}$ with

$$\mathcal{J} \quad\to\quad \mathcal{J} - 5p\,\delta\mathcal{D}_L , \tag{7.165}$$

where $\delta\mathcal{D}_L$ is the perturbation to the luminosity distance, which is given by

$$\begin{aligned}\frac{\delta\mathcal{D}_L(z)}{D_L(z)} &= 1 + v_i e^i - \Phi_s - \frac{1+z_s}{H_s r_s}\delta z_{G\to z} + \left(\mathcal{H}_o + \frac{1}{r_s}\right)\delta\tau_o \\ & +2\int_0^{r_s} dr\left[\frac{\Phi}{r_s} - \frac{r}{r_s}a\dot{\Phi} + \frac{(r_s - r)r}{2r_s}\left(\nabla^2\Phi - a\frac{d(a\dot{\Phi})}{dt} + 2a\dot{\Phi}_{,i}\, e^i\right)\right]\end{aligned} \tag{7.166}$$

where $D_L(z) = (1+z)r(z)$ is the unperturbed luminosity distance and p is the slope of the luminosity function.
Using $dz = -H(1+z)dt$ we can write in a general and in Newtonian gauge

$$\begin{aligned}\delta z_{G\to L} =& \frac{z_G(t_L) - z_G(t_G)}{1+z_G(t_G)} = -H(t_G)(t_L - t_G) = -H\int_0^{t_G} dt A \\ =& -H\int_0^{t_G} dt\ \Phi = -aH\frac{v^{(N)}}{k}\ , \end{aligned} \tag{7.167}$$

$$\begin{aligned}\delta z_{G\to z} =& \frac{z - z_G(t_G)}{1+z_G} = \left[(v_i - B_i)\, e^i - A\right]_o^s - \int_0^{r_s} dr\ \left[a\left(\dot{A} - \dot{D}\right) - \left(B_{i,j} + a\dot{E}_{ij}\right) e^i e^j\right] \\ =& \left[v_i e^i - \Phi\right]_o^s - 2\int_0^{r_s} dr\, a\dot{\Phi}\ . \end{aligned} \tag{7.168}$$

Under a gauge transformation (7.146) we have

$$\widetilde{\delta z}_{G\to L} = \delta z_{G\to L} + aHT\ , \qquad \widetilde{\delta z}_{G\to z} = \delta z_{G\to z} + aHT\ . \tag{7.169}$$

Thus $\delta z_{G\to L} - \delta z_{G\to z}$ does not change under the gauge transformation and is gauge invariant. For the evaluation of the full expression in eq. (7.61) we first transform all the quantities to k-space. First, we consider the line of sight projection of the velocity

$$v_i e^i = \int \frac{\mathrm{d}^3k}{(2\pi)^3}\ \left(-i\mu v^{(N)}(\boldsymbol{k})\right)\ Q^{(0)}(\boldsymbol{k})\ , \tag{7.170}$$

where $\mu = \boldsymbol{x}\cdot\boldsymbol{k}/(xk)$ is the cosine between the k-mode and the line of sight. For the redshift space distortion term we have then

$$\partial_r v_i e^i = n^j \partial_j e^i v_i = \int \frac{\mathrm{d}^3k}{(2\pi)^3}\ \left(\mu^2 v^{(N)}(\boldsymbol{k})\right)\ Q^{(0)}(\boldsymbol{k})\ . \tag{7.171}$$

Thus the volume distortion term reads as

$$\mathcal{J}(\boldsymbol{k}) = -\Phi(\boldsymbol{k}) + \mathcal{A}(z)\big(-i\mu v^{(N)}(\boldsymbol{k}) - \Phi(\boldsymbol{k})\big) + \big(f(z) - 1\big)\Phi(\boldsymbol{k}) - \mu^2\frac{k}{aH}v^{(N)}(\boldsymbol{k})\ . \tag{7.172}$$

The full observed density perturbation is the sum of the latter and the perturbation in the proper number density of tracers

$$\delta_p(\boldsymbol{k}) = b\,\delta^{(com)}(\boldsymbol{k}) + b_\zeta\zeta(\boldsymbol{k}) + \mathcal{B}(z)\left(-\frac{aH}{k}v^{(N)}(\boldsymbol{k}) - i\mu v^{(N)}(\boldsymbol{k}) - \Phi(\boldsymbol{k})\right)\ , \tag{7.173}$$

$$\begin{aligned}\delta_{obs}(\boldsymbol{k}) =& \Bigg\{\Bigg[-2 - \mathcal{A}(z) + f(z) + f(z)\frac{\mathcal{B}(z)}{\beta(z)} + B(z) - b_\zeta\left(1 - \frac{f(z)}{\beta(z)}\right) \\ &+ \left(\mu^2\frac{f(z)}{\beta(z)} - \frac{b}{\alpha(z)}\right)\left(\frac{k}{aH}\right)^2\Bigg] + i\left[\big(\mathcal{A}(z) - \mathcal{B}(z)\big)\mu\frac{f(z)}{\beta(z)}\frac{k}{aH}\right]\Bigg\}\Phi(\boldsymbol{k})\ , \end{aligned} \tag{7.174}$$

where we related the density and velocity perturbations to the Newtonian gauge metric perturbation

$$\delta^{(com)}(\boldsymbol{k}) = -\left(\frac{k}{aH}\right)^2\frac{H^2}{4\pi G\bar{\rho}}\Phi(\boldsymbol{k})\ , \qquad v(\boldsymbol{k}) = f\frac{k}{aH}\frac{H^2}{\dot{H}}\Phi(\boldsymbol{k})\ , \tag{7.175}$$

and introduced the auxiliary functions

$$\mathcal{A}(z) = \frac{\mathrm{d}\log H}{\mathrm{d}\log(1+z)} - 1 - 2\frac{1+z}{Hr_s} = \frac{3}{2}\frac{(1+z)^2}{\Omega_{m,0}(1+z)^3 + \Omega_{\Lambda,0}} - 1 - 2\frac{(1+z)c}{r_s H}\ , \tag{7.176}$$

$$\beta = \frac{\dot{H}}{H^2}\ , \qquad \alpha = \frac{4\pi G\bar{\rho}}{H^2}\ , \qquad \mathcal{B}(z) = \frac{\partial\log\bar{n}_p}{\partial\log(1+z)}\ .$$

The power spectrum is then given by $(2\pi)^3\delta^{(D)}(\boldsymbol{k}+\boldsymbol{k}')P_{obs}(k) = \left\langle\delta_{obs}(\boldsymbol{k})\delta^*_{obs}(\boldsymbol{k}')\right\rangle$.

Matter as Tracer

For matter we have $n_p(t_L;\Omega_K) = \bar{\rho}(t_L)\big(1 + D(t_L)\delta_0^{(com)}\big)$. This can be seen in two ways: firstly, in synchronous slicings the proper time and the coordinate time agree, thus the matter overdensity in the local frame must agree with the matter overdensity in comoving gauge. Also, we saw above in eq. (7.102), that the local matter density is related to the global one by $\bar{\rho}_L = \bar{\rho}_G(1 + D(t_L)\delta_{com,0})$. Using that $\Omega_{K,0} \propto \delta_{com,0}$ and that $\partial \log \bar{\rho}/\partial \log(1+z) = 3$ we have

$$\delta_{obs}(z,\theta,\phi) = \delta^{(com)}(z_G) + 3\delta z_{G\to L} - 3\delta z_{G\to z} + \mathcal{J} \ , \tag{7.177}$$

where the δz's are in a general, yet unspecified gauge.
For the transformation from a comoving to general gauge we have for the densities

$$\delta^{(gen)} = \delta^{(com)} + 3aHT_{com\to gen} \ . \tag{7.178}$$

The integral entering into $\delta z_{G\to L}$ transforms as

$$3\delta z_{G\to L}^{(gen)} = -3H\int dt A^{(gen)} = -3H\int dt A^{(com)} + 3aHT_{com\to gen} = 3aHT_{com\to gen} = \delta^{(gen)} - \delta^{(com)} \ , \tag{7.179}$$

where we used that $A^{(com)} = 0$ and solved eq. (7.178) for $T_{com\to gen}$. Evaluating δ_{obs} in the general gauge we obtain

$$\delta_{obs}(z,\theta,\phi) = \delta^{(com)} - 3H\int dt A^{(gen)} - 3\delta z_{G\to z}^{(gen)} + \mathcal{J} = \delta^{(gen)} - 3\delta z_{G\to z}^{(gen)} + \mathcal{J}, \tag{7.180}$$

where $\delta^{(gen)}$ and $\delta z_{G\to L}^{(gen)}$ are the matter overdensity and the redshift lapse in a general gauge. This expression agrees with $\delta_{n_p} = \delta^{(gen)} - 3\delta z_{G\to z}^{(gen)}$ in [2]. In the follow up paper, [14] used a local bias in the matter density at the observed redshift $\delta^{(gen)} - 3\delta z_{G\to z}^{(gen)}$. This means that in contrast to our approach the bias factor b is also multplying the redshift lapse terms between global, local and observed redshift, i.e. the evolution of the sample is fixed to be $\partial \log \bar{n}_p/\partial \log(1+z) = 3b$, while for a typical quasar sample this number can vary in a much wider range depending on the redshift distribution of the sample.

Bibliography

[1] T. Baldauf, U. Seljak, L. Senatore, and M. Zaldarriaga, **Galaxy bias and non-linear structure formation in general relativity**, *JCAP* **10** (Oct., 2011) 31, [arXiv:1106.5507].

[2] J. Yoo, A. L. Fitzpatrick, and M. Zaldarriaga, **A New Perspective on Galaxy Clustering as a Cosmological Probe: General Relativistic Effects**, *Phys. Rev.* **D80** (2009) 083514, [arXiv:0907.0707].

[3] N. Dalal, O. Dore, D. Huterer, and A. Shirokov, **The imprints of primordial non-gaussianities on large- scale structure: scale dependent bias and abundance of virialized objects**, *Phys. Rev.* **D77** (2008) 123514, [arXiv:0710.4560].

[4] A. Slosar, C. Hirata, U. Seljak, S. Ho, and N. Padmanabhan, **Constraints on local primordial non-Gaussianity from large scale structure**, *JCAP* **0808** (2008) 031, [arXiv:0805.3580].

[5] L. Senatore and M. Zaldarriaga, **The Effective Field Theory of Multifield Inflation**, arXiv:1009.2093.

[6] T. Baldauf, U. Seljak, and L. Senatore, **Primordial non-Gaussianity in the Bispectrum of the Halo Density Field**, *JCAP* **1104** (2011) 006, [arXiv:1011.1513].

[7] F. K. Manasse and C. W. Misner, **Fermi Normal Coordinates and Some Basic Concepts in Differential Geometry**, *Journal of Mathematical Physics* **4** (June, 1963) 735–745.

[8] G. Tormen and E. Bertschinger, **Adding Long Wavelength Modes to an *N*-Body Simulation**, astro-ph/9512131.

[9] S. Cole, **Adding Long-Wavelength Power to N-body Simulations**, astro-ph/9604046.

[10] M. D. Schneider, S. Cole, C. S. Frenk, and I. Szapudi, **Fast generation of ensembles of cosmological N-body simulations via mode-resampling**, *Astrophys. J.* **737** (2011) 11, [arXiv:1103.2767].

[11] M. Sasaki, **The magnitude-redshift relation in a perturbed Friedmann universe**, *Mon. Not. Roy. Astron. Soc.* **228** (Oct., 1987) 653–669.

[12] S. Dodelson, F. Schmidt, and A. Vallinotto, **Universal weak lensing distortion of cosmological correlation functions**, *Phys. Rev.* **78** (Aug., 2008) 043508, [arXiv:0806.0331].

[13] D. Wands and A. Slosar, **Scale-dependent bias from primordial non-Gaussianity in general relativity**, *Phys. Rev.* **D79** (2009) 123507, [arXiv:0902.1084].

[14] J. Yoo, **General relativistic description of the observed galaxy power spectrum: Do we understand what we measure?**, *Phys. Rev.* **82** (Oct., 2010) 083508, [arXiv:1009.3021].

[15] N. Bartolo, S. Matarrese, and A. Riotto, **Relativistic effects and primordial non-Gaussianity in the galaxy bias**, *JCAP* **4** (Apr., 2011) 11, [arXiv:1011.4374].

[16] F. I. Cooperstock, V. Faraoni, and D. N. Vollick, **The influence of the cosmological expansion on local systems**, *Astrophys. J.* **503** (1998) 61, [astro-ph/9803097].

[17] **WMAP** Collaboration, E. Komatsu et al., **Seven-Year Wilkinson Microwave Anisotropy Probe (WMAP) Observations: Cosmological Interpretation**, *Astrophys. J. Suppl.* **192** (2011) 18, [arXiv:1001.4538].

[18] L. Senatore, K. M. Smith, and M. Zaldarriaga, **Non-Gaussianities in Single Field Inflation and their Optimal Limits from the WMAP 5-year Data**, *JCAP* **1001** (2010) 028, [arXiv:0905.3746].

[19] P. Creminelli, M. A. Luty, A. Nicolis, and L. Senatore, **Starting the universe: Stable violation of the null energy condition and non-standard cosmologies**, *JHEP* **12** (2006) 080, [hep-th/0606090].

[20] F. Bernardeau, S. Colombi, E. Gaztanaga, and R. Scoccimarro, **Large-scale structure of the universe and cosmological perturbation theory**, *Phys. Rept.* **367** (2002) 1–248, [astro-ph/0112551].

[21] N. E. Chisari and M. Zaldarriaga, **Connection between Newtonian simulations and general relativity**, *Phys. Rev.* **D83** (2011) 123505, [arXiv:1101.3555].

[22] U. Seljak and M. Zaldarriaga, **A Line of Sight Approach to Cosmic Microwave Background Anisotropies**, *Astrophys. J.* **469** (1996) 437–444, [astro-ph/9603033].

[23] A. Lewis, A. Challinor, and A. Lasenby, **Efficient Computation of CMB anisotropies in closed FRW models**, *Astrophys. J.* **538** (2000) 473–476, [astro-ph/9911177].

[24] A. L. Fitzpatrick, L. Senatore, and M. Zaldarriaga, **Contributions to the Dark Matter 3-Pt Function from the Radiation Era**, *JCAP* **1005** (2010) 004, [arXiv:0902.2814].

[25] C. Cheung, P. Creminelli, A. L. Fitzpatrick, J. Kaplan, and L. Senatore, **The Effective Field Theory of Inflation**, *JHEP* **03** (2008) 014, [arXiv:0709.0293].

[26] A. Gangui, F. Lucchin, S. Matarrese, and S. Mollerach, **The Three point correlation function of the cosmic microwave background in inflationary models**, *Astrophys. J.* **430** (1994) 447–457, [astro-ph/9312033].

[27] D. H. Lyth, C. Ungarelli, and D. Wands, **The primordial density perturbation in the curvaton scenario**, *Phys. Rev.* **D67** (2003) 023503, [astro-ph/0208055].

[28] M. Zaldarriaga, **Non-Gaussianities in models with a varying inflaton decay rate**, *Phys. Rev.* **D69** (2004) 043508, [astro-ph/0306006].

[29] P. Creminelli and L. Senatore, **A smooth bouncing cosmology with scale invariant spectrum**, *JCAP* **0711** (2007) 010, [hep-th/0702165].

[30] X. Chen and Y. Wang, **Quasi-Single Field Inflation and Non-Gaussianities**, *JCAP* **1004** (2010) 027, [arXiv:0911.3380].

[31] M. Bruni, R. Crittenden, K. Koyama, R. Maartens, C. Pitrou, and D. Wands, **Disentangling non-Gaussianity, bias, and general relativistic effects in the galaxy distribution**, *Phys. Rev.* **85** (Feb., 2012) 041301, [arXiv:1106.3999].

[32] E. Silverstein and A. Westphal, **Monodromy in the CMB: Gravity Waves and String Inflation**, *Phys. Rev.* **D78** (2008) 106003, [arXiv:0803.3085].

[33] L. McAllister, E. Silverstein, and A. Westphal, **Gravity Waves and Linear Inflation from Axion Monodromy**, *Phys. Rev.* **D82** (2010) 046003, [arXiv:0808.0706].

[34] D. Green, B. Horn, L. Senatore, and E. Silverstein, **Trapped Inflation**, *Phys. Rev.* **D80** (2009) 063533, [arXiv:0902.1006].

[35] N. Barnaby, Z. Huang, L. Kofman, and D. Pogosyan, **Cosmological Fluctuations from Infra-Red Cascading During Inflation**, *Phys. Rev.* **D80** (2009) 043501, [arXiv:0902.0615].

[36] R. Flauger, L. McAllister, E. Pajer, A. Westphal, and G. Xu, **Oscillations in the CMB from Axion Monodromy Inflation**, *JCAP* **1006** (2010) 009, [arXiv:0907.2916].

[37] X. Chen, R. Easther, and E. A. Lim, **Large non-Gaussianities in single field inflation**, *JCAP* **0706** (2007) 023, [astro-ph/0611645].

[38] C. M. Hirata and U. Seljak, **Analyzing weak lensing of the cosmic microwave background using the likelihood function**, *Phys. Rev.* **D67** (2003) 043001, [astro-ph/0209489].

[39] C. M. Hirata and U. Seljak, **Reconstruction of lensing from the cosmic microwave background polarization**, *Phys. Rev.* **D68** (2003) 083002, [astro-ph/0306354].

[40] A. Challinor and A. Lewis, **The linear power spectrum of observed source number counts**, *Phys. Rev.* **D84** (2011) 043516, [arXiv:1105.5292].

[41] C. Bonvin and R. Durrer, **What galaxy surveys really measure**, *Phys. Rev.* **D84** (2011) 063505, [arXiv:1105.5280].

[42] D. Jeong, F. Schmidt, and C. M. Hirata, **Large-scale clustering of galaxies in general relativity**, *Phys. Rev.* **85** (Jan., 2012) 023504, [arXiv:1107.5427].

[43] D. Seery and J. E. Lidsey, **Primordial non-gaussianities in single field inflation**, *JCAP* **0506** (2005) 003, [astro-ph/0503692].

[44] P. J. E. Peebles, *The large-Scale Structure of the Universe*. Princeton University Press, Princeton, NJ, 1980.

[45] C. G. Lacey and S. Cole, **Merger rates in hierarchical models of galaxy formation**, *Mon. Not. Roy. Astron. Soc.* **262** (1993) 627–649.

[46] W. Hu, **Covariant Linear Perturbation Formalism**, *ArXiv Astrophysics e-prints* (Feb., 2004) [astro-ph/].

[47] C.-P. Ma and E. Bertschinger, **Cosmological perturbation theory in the synchronous and conformal Newtonian gauges**, *Astrophys. J.* **455** (1995) 7–25, [astro-ph/9506072].

CHAPTER 8

Evidence for Tidal Tensor Bias from the Halo Bispectrum[†]

The relation between the clustering properties of luminous matter in the form of galaxies and the underlying dark matter distribution is of fundamental importance for the interpretation of ongoing and upcoming galaxy surveys. The so called local bias model, where galaxy density is a function of local matter density, is frequently used to infer the matter power spectrum or correlation function from the measured galaxy correlation. We argue that the local bias cannot be a complete model based on the coevolution of the halo and dark matter fluids both in Lagrangian and Eulerian space. We show that these models generally introduce both bias quadratic in density and an additional non-local term quadratic in the tidal tensor, which is generated in Eulerian space even if absent in initial conditions (Lagrangian space). We measure the corresponding coupling strengths from the matter-matter-halo bispectrum in numerical simulations and find non-vanishing coefficients for the tidal tensor term. We find no scale dependence of the bias parameters up to $k \sim 0.1\ h\mathrm{Mpc}^{-1}$. The mass dependence of the inferred bias coefficients are qualitatively well described by the spherical collapse model and suggest there is little evidence of tidal tensor bias in the initial conditions, although the coefficient of the quadratic term deviates from the theoretical prediction. Both local and non-local bias terms must be included in the modeling of galaxy clustering of current and future surveys if we want to achieve the high precision cosmology promise of these datasets.

8.1. Introduction

Large Scale Structure (LSS), the distribution of matter in the Universe contains a wealth of information about the history and composition of the Universe as well as fundamental physics. For instance, LSS has the potential to constrain neutrino masses or modifications of gravity, which however requires percent level accuracy for the theory and observations. Besides gravitational lensing, which is sensitive to the total matter distribution, the positions of galaxies are the main observable and tool to infer the underlying matter distribution. They have the advantage of higher statistical power relative to weak lensing surveys. Ongoing and upcoming LSS surveys such as BOSS, BigBOSS, EUCLID, DES will provide an unprecedented quality of galaxy clustering data, which needs to be properly analyzed.

[†]This chapter is based on a publication by T. Baldauf, U. Seljak, P. McDonald and V. Desjacques that appeared in the Physical Review D, Vol. 86, Issue 8, Id. 083540 [1]. I am the first author of this paper, compiled the manuscript, carried out the analysis of the simulations kindly provided by V. Desjacques and performed the perturbation theory calculations.

A crucial step in the analysis of galaxy surveys is to connect the distribution of the tracer to the underlying distribution of matter. The first step in this logical chain is the realization that galaxies form preferentially in the potential wells of collapsed dark matter haloes, where the hot gas can cool sufficiently fast. This leads to the question of how the clustering properties of dark matter haloes relate to the clustering of matter in general. The answer to this question is usually phrased in terms of a relation between the overdensities in these two fields and is dubbed a halo biasing scheme. With the ever increasing computing power it is in principle possible to generate templates for the survey analysis for standard ΛCDM and even modified gravity models using *N*-body simulations. This approach becomes very expensive when it is to be used in Markov-Chain-Monte-Carlo parameter inference methods and does not provide insight into the underlying clustering properties. We thus consider it important to understand the properties of halo clustering by testing theoretical prescriptions on simulations with the final goal of devising *analytical* and thus easily evaluable models for the survey analysis.
The so called local biasing model [2, 3], where galaxy and halo density is a function of local matter density, has been the most popular model used in previous work. In the simplest version one adds another contribution that scales quadratically with density, the quadratic density bias term. Recent work has argued, based on symmetry and analyticity arguments, that there are additional terms not included in the local bias model that appear in the power spectrum and are formally at the same order as that of quadratic bias [4]. One of these terms is quadratic in density but non-local and can be written as the square of the tidal tensor. The first goal of this paper is to provide additional theoretical motivation for inclusion of this term in the analysis of galaxy clustering.
The working horses in LSS analysis are the two-point functions, the correlation function and the power spectrum. Purely Gaussian, linear fields are completely characterized by their two point function. However, non-linear phenomena in galaxy and halo formation as well as non-linear gravitational clustering can generate the full hierarchy of *n*-point functions. These higher order statistics might be difficult to measure in the sky due to non-trivial survey windows and redshift space distortions, but they can be easily extracted from *N*-body simulations. The simplest statistic beyond the power spectrum is the bispectrum

$$\langle \delta(\boldsymbol{k}_1)\delta(\boldsymbol{k}_2)\delta(\boldsymbol{k}_3)\rangle = B\left(\boldsymbol{k}_1, \boldsymbol{k}_2, \boldsymbol{k}_3\right)\ (2\pi)^3\delta^{(\mathrm{D})}(\boldsymbol{k}_1+\boldsymbol{k}_2+\boldsymbol{k}_3), \tag{8.1}$$

which is well suited for the study of next-to-leading order effects in cosmic density fields. While these contribute only loop terms to the power spectrum they are the leading order terms for the bispectrum, which vanishes for purely linear Gaussian fields.
The second aim of this study is to probe the halo bispectrum for Gaussian initial conditions in the low-*k* regime, in order to extract the two terms that lead to a quadratic coupling between the number density of collapsed objects and the long wavelength matter fluctuations, quadratic density bias and quadratic tidal tensor bias. We present a study of their scale and mass dependence using *N*-body simulations and we compare the numerical results to the theoretical expectations based on simple halo bias models.
This paper is organized as follows. In §9.4.1 we review the standard formulation of the bias model and discuss possible extensions. §8.3 describes the simulations, the bispectrum measurement and data reduction as well as the parameter estimation. The results are presented in §8.4. Finally, in §8.5 we discuss our findings and their implications as well as possible directions for future investigation.

8.2. The Bias Model: Local and non-Local Forms

8.2.1. Standard Formulation: Local Bias

The formation of galaxies and their host dark matter haloes is a complicated highly non-perturbative process. It is, however, reasonable to assume that certain properties of collapsed

objects, for instance their number density, are related to the coarse grained underlying matter density field in the same region of space. Neglecting complications arising from gas physics, the number density of collapsed objects can be written as a functional of the underlying matter density perturbation [3]

$$\delta_{\mathrm{h}}\left(\boldsymbol{x},\eta\right)=\mathcal{F}\left[\delta(\boldsymbol{x}',\eta)\right]. \tag{8.2}$$

On large scales, this functional is commonly approximated by a *local* and *linear* bias model $\delta_{\mathrm{h}}\left(\boldsymbol{x},\eta\right)=b_1\delta\left(\boldsymbol{x},\eta\right)$. The next step is to give up on linearity and to introduce the second order *local* bias model $\delta_{\mathrm{h}}\left(\boldsymbol{x},\eta\right)=b_1\delta\left(\boldsymbol{x},\eta\right)+b_2\delta^2\left(\boldsymbol{x},\eta\right)$. This model has been well studied in the literature in combination with Standard Perturbation Theory (SPT) and leads to non-trivial renormalizations of the leading order bias parameter [5]. Measurements of the quadratic bias parameters of this model in the bispectrum have lead to contradictory results, which raises doubts about the completeness of the model [6].

8.2.2. Tidal Terms

The power series expansion of the functional presented above is certainly overly simplified and one should consider whether other terms could influence the number density of collapsed objects. As proposed in [4], the environmental dependence of halo formation could lead to a dependence on the tidal field, as quantified by the tidal tensor

$$s_{ij}(\boldsymbol{x},\eta)=\partial_i\partial_j\Phi(\boldsymbol{x},\eta)-\frac{1}{3}\delta_{ij}^{(\mathrm{K})}\delta(\boldsymbol{x},\eta). \tag{8.3}$$

Note that we absorbed the constants in the Poisson equation into the gravitational potential $\boldsymbol{\nabla}^2\Phi(\boldsymbol{x},\eta)=\delta(\boldsymbol{x},\eta)$ and subtract out the trace from the tidal tensor because it is degenerate with the density field. The corresponding expression in Fourier space is given by

$$s_{ij}(\boldsymbol{k},\eta)=\left(\frac{k_ik_j}{k^2}-\frac{1}{3}\delta_{ij}^{(\mathrm{K})}\right)\delta(\boldsymbol{k},\eta). \tag{8.4}$$

The halo overdensity is a scalar quantity and can thus only depend on scalars. The simplest scalar that can be constructed from the tidal tensor is given by $s^2(\boldsymbol{x})=s_{ij}(\boldsymbol{x})s_{ij}(\boldsymbol{x})$ which in Fourier space is expressed by the convolution

$$s^2(\boldsymbol{k},\eta)=\int\frac{\mathrm{d}^3k'}{(2\pi)^3}S_2(\boldsymbol{k}',\boldsymbol{k}-\boldsymbol{k}')\delta(\boldsymbol{k}',\eta)\delta(\boldsymbol{k}-\boldsymbol{k}',\eta)\ , \tag{8.5}$$

where we have implicitly defined the kernel

$$S_2(\boldsymbol{q}_1,\boldsymbol{q}_2)=\frac{(\boldsymbol{q}_1\cdot\boldsymbol{q}_2)^2}{\boldsymbol{q}_1^2\boldsymbol{q}_2^2}-\frac{1}{3}\ . \tag{8.6}$$

As shown in [4], the halo density field up to second order can be written as

$$\delta_{\mathrm{h}}(\boldsymbol{x},\eta)=b_1\delta(\boldsymbol{x},\eta)+b_2\delta^2(\boldsymbol{x},\eta)+b_{s^2}s^2(\boldsymbol{x},\eta), \tag{8.7}$$

where we are omitting prefactors of $1/2$ since they can always be absorbed into the bias parameters. We truncated the series at second order, since higher order terms influence the bispectrum only through loop corrections, which are believed to be subdominant on large scales.

8.2.3. Lagrangian Bias

In the Lagrangian bias picture, the galaxy formation sites are identified in the primordial density field, and it is assumed that the primordial halo density field at initial time η_{i} can be written as a

power series in the primordial matter fluctuations. For calculational convenience, the expansion can be rewritten in terms of the linearly extrapolated density field $\delta(\boldsymbol{q},\eta) = D(\eta)/D(\eta_i)\delta(\boldsymbol{q})$

$$\delta_{\rm h}(\boldsymbol{q}) = \sum_l \frac{b_l^{(\rm L)}(\eta_{\rm i})}{l!}\delta^l(\boldsymbol{q}) = \sum_l \frac{b_l^{(\rm L)}(\eta)}{l!}\delta^l(\boldsymbol{q},\eta), \tag{8.8}$$

where $b_l^{(\rm L)}(\eta) = \big(D(\eta_i)/D(\eta)\big)^l\, b_l^{(\rm L)}(\eta_i)$ and $\boldsymbol{q}$ is the Lagrangian position. Here, we introduced the conformal time $a{\rm d}\eta = {\rm d}t$ and the linear growth factor $D(\eta)$, normalized to unity at present time. In contrast to this, the Eulerian bias model expands the halo density field at a certain point in time in the non-linear matter density field at the same time. Motivation for a Lagrangian nature of halo bias comes from the peak model [7, 8, 9], where the peaks of the primordial density field are associated with the formation sites of protohaloes.
It now remains to connect the Lagrangian density fields to the observable Eulerian ones. The continuity equation for haloes requires

$$[1+\delta_{\rm h}(\boldsymbol{x},\eta)]\,{\rm d}^3x = [1+\delta_{\rm h}(\boldsymbol{q})]\,{\rm d}^3q, \tag{8.9}$$

where

$$[1+\delta(\boldsymbol{x},\eta)]\,{\rm d}^3x = {\rm d}^3q \tag{8.10}$$

is the continuity equation for the underlying dark matter field. Note that the Lagrangian density is always a linear quantity.
The Lagrangian and Eulerian positions are related by $\boldsymbol{x}(\boldsymbol{q},\eta) = \boldsymbol{q} + \boldsymbol{\Psi}(\boldsymbol{q},\eta)$, thus up to third order in the density field we have

$$\delta(\boldsymbol{q}) = \delta(\boldsymbol{x},\eta) - \Psi_i(\boldsymbol{q},\eta)\partial_i\delta(\boldsymbol{q}) + \frac{1}{2}\Psi_i(\boldsymbol{q},\eta)\Psi_j(\boldsymbol{q},\eta)\partial_i\partial_j\delta(\boldsymbol{q}). \tag{8.11}$$

In contrast to Eulerian perturbation theory, where the density is the central quantity, Lagrangian Perturbation Theory (LPT) has the displacement field $\boldsymbol{\Psi}$ as the central dynamic quantity and the density fields are only derived quantities (for the basics of LPT and its relation to SPT see Appendix 8.6.1). For simplicity, we will focus on the matter-only Einstein-de-Sitter Universe. Using the Lagrangian bias expansion (8.8) in (8.9) and expressing the Lagrangian position field in terms of the Eulerian position, we have (see also [10])

$$\begin{aligned}\delta_{\rm h}(\boldsymbol{x},\eta) =& b_0^{(\rm L)}(\eta) + \Big(1 + b_0^{(\rm L)}(\eta) + b_1^{(\rm L)}(\eta)\Big)\,{}^{(1)}\delta(\boldsymbol{x},\eta)\\ &+ \left(b_1^{(\rm L)}(\eta) + \frac{1}{2}b_2^{(\rm L)}(\eta)\right){}^{(1)}\delta^2(\boldsymbol{x},\eta) - b_1^{(\rm L)}(\eta)\boldsymbol{\Psi}(\boldsymbol{q},\eta)\cdot\boldsymbol{\nabla}\delta(\boldsymbol{x},\eta) + \Big(1 + b_0^{(\rm L)}(\eta)\Big)\,{}^{(2)}\delta(\boldsymbol{x},\eta).\end{aligned} \tag{8.12}$$

Reorganising the terms in order to have the first order bias multiply the full second order matter density field we obtain

$$\begin{aligned}\delta_{\rm h}(\boldsymbol{x},\eta) =& b_0^{(\rm L)}(\eta) + \Big(1 + b_0^{(\rm L)}(\eta) + b_1^{(\rm L)}(\eta)\Big)\Big({}^{(1)}\delta(\boldsymbol{x},\eta) + {}^{(2)}\delta(\boldsymbol{x},\eta)\Big)\\ &+ \left(\frac{4}{21}b_1^{(\rm L)} + \frac{1}{2}b_2^{(\rm L)}(\eta)\right){}^{(1)}\delta^2(\boldsymbol{x},\eta) - \frac{2}{7}b_1^{(\rm L)}(\eta)s^2(\boldsymbol{x},\eta),\end{aligned} \tag{8.13}$$

where we used that the second order mass density (in SPT and LPT) can be written in configuration space as

$${}^{(2)}\delta(\boldsymbol{x},\eta) = \frac{17}{21}{}^{(1)}\delta^2(\boldsymbol{x},\eta) - \boldsymbol{\Psi}(\boldsymbol{x},\eta)\cdot\boldsymbol{\nabla}\delta(\boldsymbol{x},\eta) + \frac{2}{7}s^2(\boldsymbol{x},\eta). \tag{8.14}$$

We see that the functional form of the above result agrees with Eq. (8.7), but complements it with a dynamical perspective. In particular, we see that even in the absence of a tidal tensor bias in the initial conditions, such a term will be generated by subsequent gravitational evolution.

8.2.4. Coevolution of Haloes and Dark Matter

In this subsection we will consider an Eulerian approach to halo clustering and consider the coevolution of the coupled halo-dark matter fluid (For a similar approach in combination with resummed perturbation theory see [11]). Asuming vanishing velocity bias $\boldsymbol{v}_\mathrm{h} = \boldsymbol{v}$ and *conservation of halo number*, we can write down a coupled system of differential equations for the matter and halo fluid [1], namely the continuity equation for haloes, the continuity equation for the matter and the combined Euler and Poisson equations for matter

$$\delta_\mathrm{h}'(\boldsymbol{k},\eta) + \theta(\boldsymbol{k},\eta) = -\int \frac{\mathrm{d}^3k'}{(2\pi)^3}\alpha(\boldsymbol{k}',\boldsymbol{k}-\boldsymbol{k}')\theta(\boldsymbol{k}',\eta)\delta_\mathrm{h}(\boldsymbol{k}-\boldsymbol{k}',\eta) \tag{8.15}$$

$$\delta'(\boldsymbol{k},\eta) + \theta(\boldsymbol{k},\eta) = -\int \frac{\mathrm{d}^3k'}{(2\pi)^3}\alpha(\boldsymbol{k}',\boldsymbol{k}-\boldsymbol{k}')\theta(\boldsymbol{k}',\eta)\delta(\boldsymbol{k}-\boldsymbol{k}',\eta) \tag{8.16}$$

$$\theta'(\boldsymbol{k},\eta) + \mathcal{H}(\eta)\theta(\boldsymbol{k},\eta) + \frac{3}{2}\Omega_\mathrm{m}(\eta)\mathcal{H}^2(\eta)\delta(\boldsymbol{k},\eta) = -\int \frac{\mathrm{d}^3k'}{(2\pi)^3}\beta(\boldsymbol{k}',\boldsymbol{k}-\boldsymbol{k}')\theta(\boldsymbol{k}',\eta)\theta(\boldsymbol{k}-\boldsymbol{k}',\eta) \tag{8.17}$$

Here we introduced the velocity divergence $\theta(\boldsymbol{x}) = \boldsymbol{\nabla}\cdot\boldsymbol{v}(\boldsymbol{x})$. The matter equations at first order are solved by ${}^{(1)}\theta(\boldsymbol{k},\eta) = -\mathcal{H}(\eta){}^{(1)}\delta(\boldsymbol{k},\eta)$ and ${}^{(1)}\delta(\boldsymbol{k},\eta) = D(\eta){}^{(1)}\delta_0(\boldsymbol{k})$. The second order solution for the matter yields

$${}^{(2)}\delta(\boldsymbol{k},\eta) = \int \frac{\mathrm{d}^3k'}{(2\pi)^3}F_2(\boldsymbol{k}',\boldsymbol{k}-\boldsymbol{k}'){}^{(1)}\delta(\boldsymbol{k}',\eta){}^{(1)}\delta(\boldsymbol{k}-\boldsymbol{k}',\eta) \tag{8.18}$$

$${}^{(2)}\theta(\boldsymbol{k},\eta) = -\mathcal{H}(\eta)\int \frac{\mathrm{d}^3k'}{(2\pi)^3}G_2(\boldsymbol{k}',\boldsymbol{k}-\boldsymbol{k}'){}^{(1)}\delta(\boldsymbol{k}',\eta){}^{(1)}\delta(\boldsymbol{k}-\boldsymbol{k}',\eta) \tag{8.19}$$

where the second order SPT mode coupling kernel are defined as [12]

$$F_2(\boldsymbol{q}_1,\boldsymbol{q}_2) = \frac{5}{7}\alpha(\boldsymbol{q}_1,\boldsymbol{q}_2) + \frac{2}{7}\beta(\boldsymbol{q}_1,\boldsymbol{q}_2) \tag{8.20}$$

$$G_2(\boldsymbol{q}_1,\boldsymbol{q}_2) = \frac{3}{7}\alpha(\boldsymbol{q}_1,\boldsymbol{q}_2) + \frac{4}{7}\beta(\boldsymbol{q}_1,\boldsymbol{q}_2) \tag{8.21}$$

with

$$\alpha(\boldsymbol{q}_1,\boldsymbol{q}_2) = \frac{(\boldsymbol{q}_1+\boldsymbol{q}_2)\cdot\boldsymbol{q}_1}{q_1^2} \qquad \beta(\boldsymbol{q}_1,\boldsymbol{q}_2) = \frac{1}{2}(\boldsymbol{q}_1+\boldsymbol{q}_2)^2\,\frac{\boldsymbol{q}_1\cdot\boldsymbol{q}_2}{q_1^2 q_2^2} \tag{8.22}$$

The first order equation for the haloes can be solved using the local bias ansatz ${}^{(1)}\delta_\mathrm{h}(\boldsymbol{k},\eta) = b_1^{(\mathrm{E})}(\eta){}^{(1)}\delta(\boldsymbol{k},\eta)$, which then gives the time evolution of the first order bias as

$$\frac{b_1^{(\mathrm{E})}(\eta)-1}{b_1^{(\mathrm{E})}(\eta_\mathrm{i})-1} = \frac{D(\eta_\mathrm{i})}{D(\eta)}. \tag{8.23}$$

This relation known as **debiasing**, i.e., at late times the bias converges to unity and halo and matter density field agree [13].
Solving Eq. (8.15) at second order using the second order matter solutions, we obtain

$$\begin{aligned}{}^{(2)}\delta_\mathrm{h}(\boldsymbol{k},\eta) = {}^{(2)}\delta_\mathrm{h}(\boldsymbol{k},\eta_\mathrm{i}) + b_1^{(\mathrm{E})}(\eta)\int \frac{\mathrm{d}^3k'}{(2\pi)^3}F_2(\boldsymbol{k}',\boldsymbol{k}-\boldsymbol{k}')\delta(\boldsymbol{k}',\eta)\delta(\boldsymbol{k}-\boldsymbol{k}',\eta)\\ + \frac{4}{21}\left(b_1^{(\mathrm{E})}(\eta)-1\right)\int \frac{\mathrm{d}^3k'}{(2\pi)^3}\delta(\boldsymbol{k}',\eta)\delta(\boldsymbol{k}-\boldsymbol{k}',\eta)\end{aligned} \tag{8.24}$$

[1] A similar approach was presented by R. Scoccimarro at the PTchat workshop in Saclay.

$$-\frac{2}{7}\left(b_1^{(\mathrm{E})}(\eta)-1\right)\int\frac{\mathrm{d}^3k'}{(2\pi)^3}S_2(\boldsymbol{k}',\boldsymbol{k}-\boldsymbol{k}')\delta(\boldsymbol{k}',\eta)\delta(\boldsymbol{k}-\boldsymbol{k}',\eta),$$

where we assumed $D(\eta_i)\ll D(\eta)$. Here, we have isolated the part proportional to the second order matter field in the first line. Thus, the dynamical evolution naturally introduces a $\delta^2(\boldsymbol{x})$ and a $s^2(\boldsymbol{x})$ term, even in the absence thereof at some initial time η_i. Translating back to real space, we see that this has the same functional form as (8.7) and agrees with the Lagrangian bias picture. The equivalence is even more obvious if we have ${}^{(2)}\delta_\mathrm{h}(\boldsymbol{x},\eta_\mathrm{i})=b_2^{(\mathrm{L})}(\eta_\mathrm{i})^{(1)}\delta^2(\boldsymbol{x},\eta_\mathrm{i})/2=b_2^{(\mathrm{L})}(\eta)^{(1)}\delta^2(\boldsymbol{x},\eta)/2$ in correspondence to the Lagrangian bias picture discussed above (see next subsection for a relation between the parameters of the models discussed here).

8.2.5. Relation between Eulerian and Lagrangian Bias Parameters

As we have seen above, the Lagrangian bias model, the coevolution model and the educated guess of [4] all lead to the same functional form for the halo density field if one identifies the parameters of the model as

$$b_1=b_1^{(\mathrm{E})}(\eta)=1+b_1^{(\mathrm{L})}(\eta) \tag{8.25}$$

$$b_2=\frac{1}{2}b_2^{(\mathrm{E})}(\eta)=\frac{4}{21}b_1^{(\mathrm{L})}(\eta)+\frac{1}{2}b_2^{(\mathrm{L})}(\eta) \tag{8.26}$$

where we set $b_0^{(\mathrm{L})}=0$. This identification agrees with the one of the spherical collapse picture [14]. Note however that our results are *not* relying on the spherical collapse dynamics. For the prefactor of the tidal field scalar we have

$$b_{s^2}=-\frac{2}{7}\left(b_1^{(\mathrm{E})}(\eta)-1\right)=-\frac{2}{7}b_1^{(\mathrm{L})}(\eta). \tag{8.27}$$

In this model there is no tidal field bias in Lagrangian space, consistent with the spherical collapse model, although in ellipsoidal collapse model [15, 16] such a term would be allowed. When comparing our measurements to theoretical bias models, we consider the bias derived from the Sheth-Tormen [17] mass function with parameters $p=0.15$ and $q=0.75$ that were shown to be in good agreement with first order bias in N-body simulations [18].

The Lagrangian bias parameters are then given by the first and second derivative of the mass function $n(M)$ with respect to a long wavelength background fluctuation δ_l. For universal mass functions these can be rewritten as derivatives with respect to the peak height $\nu(M)=\delta_\mathrm{c}^2/\sigma^2(M,\eta)$

$$b_1^{(\mathrm{L})}=\frac{1}{\bar{n}}\frac{\partial n}{\partial\delta_\mathrm{l}}=-\frac{1}{\bar{n}}\frac{2\nu}{\delta_\mathrm{c}}\frac{\partial n}{\partial\nu} \tag{8.28}$$

$$b_2^{(\mathrm{L})}=\frac{1}{\bar{n}}\frac{\partial^2 n}{\partial\delta_\mathrm{l}^2}=\frac{4}{\bar{n}}\frac{\nu^2}{\delta_c^2}\frac{\partial^2 n}{\partial\nu^2}+\frac{2}{\bar{n}}\frac{\nu}{\delta_\mathrm{c}^2}\frac{\partial n}{\partial\nu}, \tag{8.29}$$

where $\delta_\mathrm{c}=1.686$ is the critical density for spherical collapse. The derivatives of the Sheth-Tormen mass function read

$$\frac{1}{n}\frac{\partial n}{\partial\nu}=-\frac{q\nu-1}{2\nu}-\frac{p}{\nu\left(1+(q\nu)^p\right)} \tag{8.30}$$

$$\frac{1}{n}\frac{\partial^2 n}{\partial\nu^2}=\frac{p^2+\nu pq}{\nu^2\left(1+(q\nu)^p\right)}+\frac{(q\nu)^2-2q\nu-1}{4\nu^2}. \tag{8.31}$$

The mass dependence of the bias function is presented in Figure 8.4 and discussed in §8.4.

8.2.6. Bispectra

The leading order contribution to the bispectrum arises from quadratic terms in the fields. Higher order couplings enter only through loop corrections, which gain importance for high momenta. This is equivalent to the situation in the power spectrum, where linear terms in the field are dominant on large scales and loop corrections from quadratic and higher order terms gain importance for high momenta.
The tree-level matter bispectrum in SPT is given by

$$B_{\rm mmm}(\boldsymbol{k}_1, \boldsymbol{k}_2, \boldsymbol{k}_3) = 2P(k_1)P(k_2)F_2(\boldsymbol{k}_1, \boldsymbol{k}_2) + 2\,\text{cyc.}\,, \tag{8.32}$$

where cyc. symbolizes the two cyclic permutations of the k-vectors in the power spectrum and mode coupling kernel. From an observational point of view the halo auto bispectrum $B_{\rm hhh}$ is probably the most appealing statistic. Unfortunately it is suffering from shotnoise, which might deviate from its fiducial Poisson form $1/\bar{n}$ [19]. Besides the halo auto power spectrum, there are two halo-matter cross bispectra $B_{\rm mhh}$ and $B_{\rm mmh}$, where either one or two matter fields are correlated with two or one halo fields, respectively. One further needs to state whether the cross bispectra are symmetrized over the $\boldsymbol{k}$ modes or not.
Our focus is not on observability but on understanding the clustering properties of dark matter haloes in N-body simulations and devising a theoretical framework that can later be used to analyze real data. Thus, we will consider the un-symmetrized matter-matter-halo cross bispectrum defined as

$$B^{\rm (unsym)}_{\rm mmh}(\boldsymbol{k}_1, \boldsymbol{k}_2, \boldsymbol{k}_3)\ (2\pi)^3\delta^{\rm (D)}(\boldsymbol{k}_1 + \boldsymbol{k}_2 + \boldsymbol{k}_3) = \langle \delta(\boldsymbol{k}_1)\delta(\boldsymbol{k}_2)\delta_{\rm h}(\boldsymbol{k}_3)\rangle\,, \tag{8.33}$$

where the halo density field is always on the $\boldsymbol{k}_3$-mode. This particular configuration might not be the one with the highest signal to noise ratio but it has a couple of quite useful properties for our study: a) The cross-bispecrum does not suffer from a spurious shotnoise contamination and is thus a clean probe of the clustering of haloes b) the functional simplicity of the second order bias contributions in terms of k_1, k_2 and the enclosed angle μ where the b_2 and b_{s^2} contributions are basically orthogonal (see below). The latter should allow for a clear distinction between the standard second order bias picture or its possible extensions discussed above.
As noted above, all of the models under consideration share the same functional form (8.7) for the second order halo density field. Only the standard quadratic bias model has $b_{s^2} = 0$. Therefore, we can write down the bispectrum as

$$B^{\rm (unsym)}_{\rm mmh}(\boldsymbol{k}_1, \boldsymbol{k}_2, \boldsymbol{k}_3) - b_1 B_{\rm mmm}(\boldsymbol{k}_1, \boldsymbol{k}_2, \boldsymbol{k}_3) = 2P(k_1)P(k_2)\left[b_2 + b_{s^2}\left(\mu^2 - \frac{1}{3}\right)\right]. \tag{8.34}$$

Note that we again omitted factors of 1/2 for simplicity. We will restore these prefactors only at the very end, when we are comparing our bias measurements to the theoretical bias functions. A non-vanishing b_{s^2} in the above equation would be a clear evidence for a dynamical biasing picture. After dividing by the two matter power spectra, the remaining quantity is a function of the angle μ only, which simplifies the combination of information from several scales k_1 and k_2.

8.3. Simulations & Bispectrum Estimation

8.3.1. The Simulations

We are studying the cosmic density field in a suite of 11 dark matter only simulations with box size of $L = 1600\ h^{-1}$Mpc, which are an extension of the simulations described in [20]. The ΛCDM model is based on best-fit parameters inferred from the WMAP 5-year data release [21]. Thus, we adopt a mass density parameter $\Omega_{\rm m} = 0.279$, a baryon density parameter

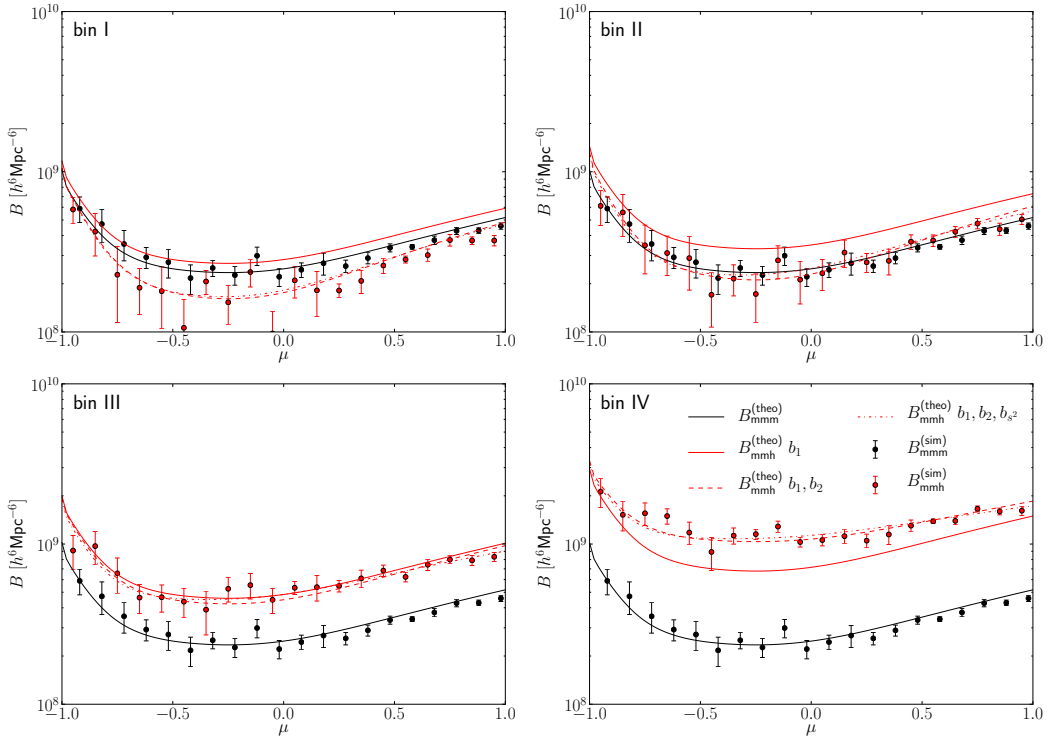

Figure 8.1.: Matter (black points) and halo-matter-matter (red points) bispectra as a function of triangle shape for configuration $k_1 = 0.052\ h\mathrm{Mpc}^{-1}$ $k_2 = 0.06\ h\mathrm{Mpc}^{-1}$. The black solid line shows the tree level prediction for the matter bispectrum, the red solid line has b_1 only and dashed and dashed-dotted lines are adding b_2 and b_{s^2}. The list of bias parameters listed behind the theoretical cross bispectra in the legend indicates the parameters that were considered for the corresponding curve. The error bars are estimated from the box-to-box variance of the bispectrum measurement.

$\Omega_\mathrm{b} = 0.0462$, a Hubble constant $h = 0.701$, a spectral index $n_\mathrm{s} = 0.96$, and a normalization of the curvature perturbations of $\Delta^2_\mathcal{R} = 2.21 \times 10^{-9}$ at the pivot point $k = 0.02\ \mathrm{Mpc}^{-1}$. This normalization leads to a present day fluctuation amplitude of $\sigma_8 \approx 0.81$. The initial conditions are set up a redshift $z_\mathrm{i} = 99$. The gravitational evolution of the $N_\mathrm{p} = 1024^3$ particles is integrated using the publicly available `Gadget2` code [22]. Simulations size, particle number and matter density parameter yield a particle mass of $3 \times 10^{11}\ h^{-1}M_\odot$. Dark matter haloes are identified using a Friends-of-Friends halo finder with a linking length of 0.2 times the mean inter particle spacing. Only haloes exceeding 20 particles are considered for our analysis, corresponding to a minimum halo mass of approximately $6 \times 10^{12}\ h^{-1}M_\odot$. We consider four mass bins, each spanning a factor of three in mass. For the estimation of the statistics,

	b_1	Δb_1	b_2	Δb_2	b_{s^2}	Δb_{s^2}	$M[h^{-1}M_\odot]$
I	1.138	0.002	−0.74	0.01	−0.06	0.03	9.68×10^{12}
II	1.407	0.004	−0.83	0.02	−0.21	0.03	2.90×10^{13}
III	1.941	0.006	−0.21	0.03	−0.37	0.04	8.58×10^{13}
IV	2.856	0.020	2.57	0.10	−0.60	0.11	2.48×10^{14}

Table 8.1.: Best fit bias parameters, their errors and mean mass for our four mass bins. The bias parameters are compared to the theoretical bias functions in Figure 8.4. The first order bias b_1 is extracted from the halo-matter cross power spectrum and the second order bias parameters are inferred from the cross bispectrum.

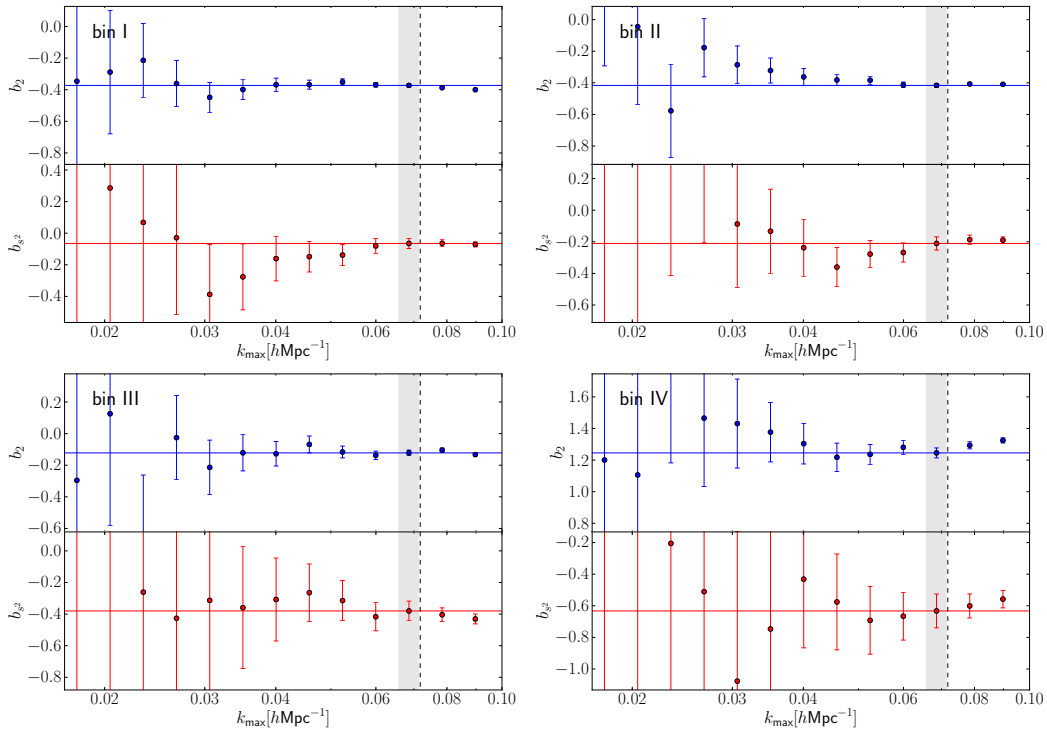

Figure 8.2.: Convergence of the measured b_2 and b_{s^2} parameters with increasing maximum k-mode for the four mass bins. The horizontal red and blue lines show the constraints obtained for pivot $k_{\rm max} = 0.07\ h{\rm Mpc}^{-1}$. The pivot data point is highlighted by the gray shaded region. The b_{s^2} constraints are slightly offset on the k-axis for better visibility of the errorbars. Note the different y-axis scale for mass bin IV.

particles are interpolated on a $N_{\rm c} = 512$ grid using the Cloud-in-Cell (CIC) algorithm and the gridded density field is corrected for the window of the grid. The matter-matter-halo and matter bispectrum are measured for low k-modes $k < 0.12\ h{\rm Mpc}^{-1}$ in the simulation output at redshift $z = 0$. This restriction is motivated by the non-linear scale $k_{\rm NL} = 1/\sigma_{\rm v} \approx 0.17\ h{\rm Mpc}^{-1}$, which is a rough measure for the scale, where loop corrections become dominant.

8.3.2. Bispectrum Estimation and Data Reduction

The bispectrum modes must satisfy the triangle condition $\boldsymbol{k}_1 + \boldsymbol{k}_2 + \boldsymbol{k}_3 = 0$, thus the shape of the bispectrum is fully specified by two lengths and one angle, which we choose as k_1, k_2 and $\mu = \boldsymbol{k}_1 \cdot \boldsymbol{k}_2 / k_1 k_2$. Since $\delta(\boldsymbol{x})$ is a real valued field, the Fourier modes have to satisfy $\delta^*(\boldsymbol{k}) = \delta(-\boldsymbol{k})$. Consequently, the imaginary part of the bispectrum cancels when we add $\delta(\boldsymbol{k}_1)\delta(\boldsymbol{k}_2)\delta(\boldsymbol{k}_3)$ and $\delta(-\boldsymbol{k}_1)\delta(-\boldsymbol{k}_2)\delta(-\boldsymbol{k}_3)$. We consider bins that are logarithmically spaced in k_1 and k_2 and linearly in μ. We add all the bispectrum amplitudes that fall into the bin centered at (k_1, k_2, μ).
As a first step in our analysis we subtract out the b_1 contribution proportional to the matter bispectrum and divide by the power spectrum measured in the same simulation and k-bins to cancel part of the cosmic variance

$$\hat{M}(k_1, k_2, \mu) = \frac{\hat{B}^{(\rm unsym)}_{\rm mmh}(k_1, k_2, \mu) - \hat{b}_1 \hat{B}_{\rm mmm}(k_1, k_2, \mu)}{2\hat{P}_{\rm mm}(k_1)\hat{P}_{\rm mm}(k_2)}. \tag{8.35}$$

Comparing to Eq. (8.34), the resulting statistic should be a function of μ only. The hat is used to mark quantities estimated from the simulations. This quantity is distinct from the the

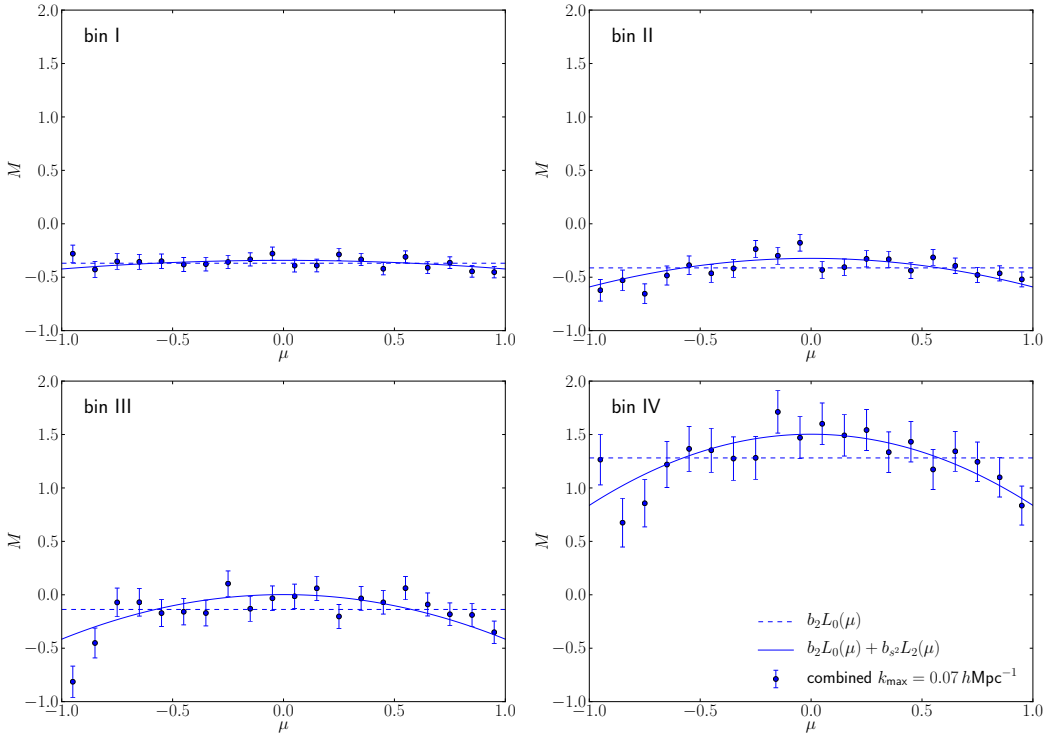

Figure 8.3.: Residual shape dependence of the halo bispectrum for our reduced bispectrum defined in Eq. (8.35). The blue data points with error bars show the result of the combined reduced bispectrum defined in Eq. (8.37) including all the configurations up to $k_{\max} = 0.07\ h\mathrm{Mpc}^{-1}$. The horizontal dashed line shows the model including b_2 only, the solid blue line shows the model including both b_2 and b_{s^2}.

usual definition of the reduced bispectrum since the power spectra in the denominator do not depend on k_3 and can thus be controlled by limiting k_1 and k_2. The first order bias parameter $\hat{b}_1$ is estimated from the halo-matter cross power spectrum on large scales $k < 0.03\ h\mathrm{Mpc}^{-1}$, where the linear bias model is believed to be accurate.
Note that the resulting statistic depends only on the magnitude of the k_1 and k_2 modes, so that we can ensure the validity of the perturbative expansion by limiting these modes accordingly.
When showing the reduced data as a function of μ only, we reduce them as follows

$$\chi^2_M = \sum_{k_1,k_2} \left(\frac{\hat{M}(k_1,k_2,\mu) - \overline{M}(\mu)}{\Delta M(k_1,k_2,\mu)} \right)^2 \tag{8.36}$$

$$\overline{M}(\mu) = \sum_{k_1,k_2} \frac{\hat{M}(k_1,k_2,\mu)}{\Delta M^2(k_1,k_2,\mu)} \left(\sum_{k_1,k_2} \frac{1}{\Delta M^2(k_1,k_2,\mu)} \right)^{-1} \tag{8.37}$$

$$\Delta\overline{M}(\mu) = \left(\sum_{k_1,k_2} \frac{1}{\Delta M^2(k_1,k_2,\mu)} \right)^{-1/2} \tag{8.38}$$

for each μ.
The cosmic variance of the bispectrum estimates could in principle be measured from the standard deviation between our simulation boxes. Given the small number of boxes this approach is bound to give a very noisy estimate. Since we are using the error for the weighting of the modes, we would like to avoid a spurious upweighting of modes which by chance have a low simulation to simulation variance. For this purpose we prefer a smooth error estimate. As

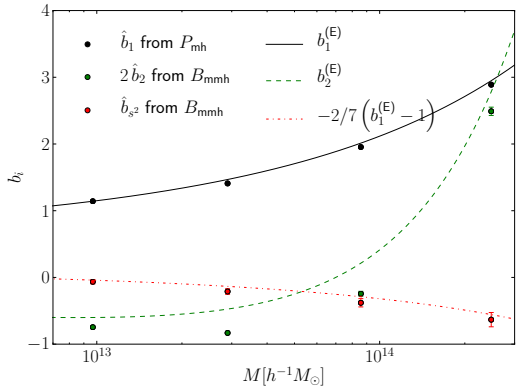

Figure 8.4.: Mass dependence of the bias parameters and theoretical predictions. The points with error bars are our best fit parameters for $\hat{b}_1$, $2\hat{b}_2$ and $\hat{b}_{s^2}$. The numerical values of the data points are given in Table 8.1. The curves show the corresponding theoretical bias functions as calculated using the relations in §8.2.5. While the measurements for $\hat{b}_1$ and $\hat{b}_{s^2}$ are in very good agreement with the theory, there is a clear deviation for the b_2 measurement for the two central mass bins.

shown in [23] the variance of the bispectrum is given by

$$\Delta B^2_{\rm mmh}(k_1,k_2,\mu) = s_{123}\frac{(2\pi)^3 V_{\rm f}}{V_{123}} P_{\rm mm}(k_1)P_{\rm mm}(k_2)\left(P_{\rm hh}(k_3)+\frac{1}{\bar{n}_{\rm h}}\right), \tag{8.39}$$

where $V_{\rm f} = (2\pi)^3/L^3$ is the volume of the fundamental cell, $\bar{n}_{\rm h}$ is the number density of the tracer and s_{123} takes on values of 1, 2 and 6 for general, isosceles and equilateral triangles, respectively. The norm volume is given by

$$V_{123} = 8\pi^2 k_1^3 k_2^3 \,(\mathrm{d}\ln k)^2\,\mathrm{d}\mu \tag{8.40}$$

for our bins, which are logarithmically spaced in k_1, k_2 and linearly spaced in μ. The above just quantifies the diagonals of the covariance matrix between the different triangle shapes and scales, but the correlations between different triangles are believed to be small [23]. When calculating the error on the reduced bispectrum, we focus on the error contribution from the matter-matter-halo bispectrum described above and thus have

$$\Delta M(k_1,k_2,\mu) \approx \frac{\Delta B(k_1,k_2,\mu)}{2P(k_1)P(k_2)} \tag{8.41}$$

This procedure could be clearly improved by modeling or measuring the full covariance matrix.

8.3.3. Bias Estimation

We can now estimate b_2 and b_{s^2} minimizing

$$\chi^2 = \sum_{k_1,k_2}\sum_{\mu}\left(\frac{\hat{M}(k_1,k_2,\mu) - b_2 L_0(\mu) - b_{s^2}L_2(\mu)}{\Delta M(k_1,k_2,\mu)}\right)^2 \tag{8.42}$$

where $L_0(\mu)=1$ and $L_2(\mu)=\left(\mu^2-1/3\right)$ are the zeroth and second order Legendre polynomials, which form an orthogonal set on $[-1,1]$. The k-sums are performed over $k_{\rm min} < k_1 < k_{\rm max}$, $k_{\rm min} < k_2 < \kappa k_1$ such that $(1-\kappa)k_1 < k_3 < (1+\kappa)k_1$ and we use $\kappa = 3/4$ for definiteness. Defining the cosine

$$\langle a(k_1,k_2,\mu), b(k_1,k_2,\mu)\rangle := \sum_{k_1,k_2}\sum_{\mu}\frac{a(k_1,k_2,\mu)b(k_1,k_2,\mu)}{\Delta M^2(k_1,k_2,\mu)} \tag{8.43}$$

we obtain for the best fit parameters

$$\hat{b}_2 = \frac{\langle L_2, L_2\rangle \langle L_0, \hat{M}\rangle}{\Delta} - \frac{\langle L_0, L_2\rangle \langle L_2, \hat{M}\rangle}{\Delta} \tag{8.44}$$

$$\hat{b}_{s^2} = -\frac{\langle L_0, L_2\rangle \langle L_0, \hat{M}\rangle}{\Delta} + \frac{\langle L_0, L_0\rangle \langle L_2, \hat{M}\rangle}{\Delta}, \tag{8.45}$$

where $\Delta = \langle L_0, L_0\rangle \langle L_2, L_2\rangle - \langle L_0, L_2\rangle^2$. Note an equivalent expression holds for the cosine of the reduced data

$$\langle a, b\rangle_\mu := \sum_\mu \frac{a(\mu)b(\mu)}{\Delta\overline{M}^2(\mu)}, \tag{8.46}$$

where for $a(\mu)$, $b(\mu)$ we have $\langle a(\mu), M(k_1, k_2, \mu)\rangle = \langle a(\mu), \overline{M}(\mu)\rangle_\mu$ and $\langle a(\mu), b(\mu)\rangle = \langle a(\mu), b(\mu)\rangle_\mu$. The bias parameter b_1 is estimated from the halo-matter cross power spectrum on large scales/low k, where loop corrections are believed to be unimportant. Furthermore there is no shotnoise contamination in the cross power spectrum. An important issue beyond the scope of this paper is whether b_1 from the power spectrum is expected to be identical to that from the bispectrum. The renormalization issues discussed in [5] suggest this issue is not entirely trivial. We will not address this question here: we simply define b_1 to be the one from the power spectrum, since ultimately the goal of these studies is to connect bispectrum to power spectrum.

The errors on the estimated parameters are calculated from the expected deviation in the χ^2. For a n-component parameter vector $\boldsymbol{a}$ the χ^2 in the vicinity of the best fit parameter set $\hat{\boldsymbol{a}}$ can be described as

$$\chi^2(\boldsymbol{a}) = \chi^2(\hat{\boldsymbol{a}}) + \frac{1}{2}\sum_{i,j}(a_i - \hat{a}_i)\frac{\partial^2\chi^2}{\partial a_i \partial a_j}(a_j - \hat{a}_j), \tag{8.47}$$

where $\Delta\chi^2 = \left|\chi^2(\boldsymbol{a}) - \chi^2(\hat{\boldsymbol{a}})\right| = 1$ corresponds to one sigma errors on the parameters. Thus

$$\Delta b_2 = \sqrt{1/\langle L_0, L_0\rangle} \qquad\qquad \Delta b_2 = \sqrt{1/\langle L_2, L_2\rangle} \tag{8.48}$$

We compared these errors with the standard deviation of the bias constraints obtained from the single realizations and found good in general good agreement.

8.4. Results

Figure 8.1 shows the matter bispectrum and matter-matter-halo bispectra for our four mass bins for one configuration of ($k_1 = 0.052\ h\mathrm{Mpc}^{-1}, k_2 = 0.06\ h\mathrm{Mpc}^{-1}$) as a function of the opening angle μ. The matter bispectrum is in quite good agreement with the theoretical prediction in Eq. (8.32). There is some small tension for positive μ, but this should not be a problem for our study since our bias constraints are not relying on this theoretical modeling since we are subtracting out the matter bispectrum.

We also plot the matter-matter-halo cross bispectrum and the theoretical model of Eq. (8.7). To visualize the effect of the contributions of the bias parameters, we plot the model with vanishing b_2 and b_{s^2}, with vanishing b_{s^2} and the full model. The non-vanishing bias parameters for the theory lines were chosen according to our best fit model discussed below. While the k-values were chosen quite high to reduce the errors, there is still too much scatter in the data points to decide whether the model with and without b_{s^2} gives a better description of the data. This motivated the careful combination of all the information available by weighting the modes accordingly, as described above.

Our main reason to study lowest order non-linear biasing in the bispectrum was that these terms are the leading order terms on large scales. As one includes higher momenta, loop corrections

gain importance and need to be modeled accordingly. To asses the importance of higher order corrections and to show the convergence of our fitting procedure, we perform our parameter estimation as a function of the maximum wavenumber and show the results in Figure 8.2. The error bars clearly shrink as we go to higher momenta and the inferred bias parameters are always consistent with our fiducial result shown by the horizontal lines. In these plots we also show the scale up to which we have a complete measurement of all the modes by the vertical dashed line and highlight our pivot $k_{\rm max}$ by the vertical shaded region.

Figure 8.3 shows our reduced bispectrum $\overline{M}(\mu)$ defined in Eq. (8.37) as a function of opening angle μ and the combined errors according to Eq. (8.38). We overplot the b_2 only model and the model including both b_2 and b_{s^2}. These plots show clear evidence for the presence of the tidal term except for the lowest mass bin, for which the b_2 only model gives an acceptable description of the angular dependence.

In Table 8.1 we give the best fit values of the first and second order bias parameters for our four halo mass bins obtained considering all the modes up to $k_{\rm max} = 0.07\ h{\rm Mpc}^{-1}$. Figure 8.4 shows the bias parameters as a function of mass together with the corresponding predictions of the spherical collapse model. Note that we are plotting $2\hat{b}_2$, which agrees with the second order Eulerian bias. The $\hat{b}_1$ measurements from the halo-matter cross power spectrum are in good agreement with the theoretical predictions. The measured $\hat{b}_{s^2}$ are slightly lower than the theoretical predictions, but the trend with mass is well reproduced by the theory. The $\hat{b}_2$ measurements are less well reproduced by the theoretical bias function, especially mass bins II and III are well below the theory. We can only speculate about the reason for this disagreement. It certainly could be a measurement error and an underestimation of the error bars. On the other hand, the theoretical predictions for b_1 and b_{s^2} are given by first derivatives of the mass function and even they don't reproduce the data perfectly. Thus one would naturally expect some corrections for the second derivatives. The disagreement could also be an indication for a failure of the spherical collapse picture at second order.

As in the power spectrum analysis, the bispectrum is increasingly affected by loop corrections as one increases the maximum momentum in the problem. The relevant quantity here is the largest external momentum involved and thus one should make sure that all the k's are in the perturbative regime and can be well described by the order of perturbation theory considered. Our study focuses on the large scale bispectrum, where a tree level treatment should be sufficiently accurate and we have shown that the constraints are both stable and consistent as we increase $k_{\rm max}$ up to $0.1\ h{\rm Mpc}^{-1}$.

8.5. Discussion & Outlook

In this paper we presented a dynamical motivation for the second order non-local bias term proposed in [4]. Furthermore we performed a measurement of the tidal tensor bias showing clear evidence for this tidal tensor bias, increasing with the halo mass. Our results are consistent with the Lagrangian bias (or a dynamical coevolution of haloes and dark matter) picture in which there is no tidal tensor bias in the initial conditions, but it is generated by the subsequent gravitational evolution. While the functional form of the additional terms agrees with the discussion in [4] the dynamical derivation can supplement it by a prediction of the time dependence and gives at least qualitative understanding about the mass dependence of the bias parameters.

The disagreement between the theoretical and measured b_2 parameters calls for a reinvestigation and improvement of the theoretical bias function or measurement of the second order bias parameters in the initial conditions, where the Lagrangian bias parameters are postulated to describe the density field of the protohaloes. The deviation between the theoretical and measured b_2 parameters does not necessarily mean that the Lagrangian picture is wrong, but rather that the bias functions derived from the spherical collapse model and the mass function

might not be sufficiently accurate.
A consistent calculation of the halo correlation function or power spectrum at one loop level requires a model of the halo density field up to third order, including all the non-local terms [4]. This gives rise to several terms that contribute to the power spectrum at the same order, each with a prefactor that may depend on the halo mass. A clean extraction of these non-linear bias coefficients from the power spectrum alone is not possible and instead higher order correlations are needed to separate these terms. This paper is a first step in extracting the quadratic coupling terms from the bispectrum. The next step in this program is to extract the cubic order terms from the trispectrum: such an analysis will be presented elsewhere. For this reason a discussion of the implications on the two point function based on our results for the quadratic couplings cannot be complete. Still, there are some obvious implications of our results. One is that the non-local tidal tensor bias contributions must be included in the analysis of galaxy power spectrum and ignoring them will lead to incorrect conclusions. One consequence of this is that a presence of such a term will shift the baryonic acoustic oscillations (BAO), just like the quadratic density term does if $b_2 \neq 0$ [24]. Our calculation in Appendix 8.6.2 shows that this effect is subdominant, with about a factor of 4 lower prefactor in front of b_{s^2} relative to the b_2 term, suggesting it will not strongly affect the measurement of the true BAO scale.

Acknowledgments

During the submission phase of this draft the draft by [25] appeared, some of which is based on a similar analysis with some similar conclusions. This work is supported by the DOE, the Swiss National Foundation under contract 200021-116696/1 and WCU grant R32-10130. The authors would like to thank Teppei Okumura, Ravi Sheth, Zvonimir Vlah and Matias Zaldarriaga for discussions. TB would like to thank the Berkeley Center for Cosmological Physics and the Lawrence Berkeley Labratory for the kind hospitality. The simulations were performed on the ZBOX3 supercomputer of the Institute for Theoretical Physics at the University of Zurich.

8.6. Appendix

8.6.1. Matter density in LPT up to Second Order

In the above derivation of the final halo density field arising from a local bias in Lagrangian space we used the Lagrangian displacement field and the second order matter density in SPT. In [26] it is shown that after expanding the exponential damping pre factor, the one loop power spectra in LPT and SPT are identical. This appendix shows that this equivalence is true also in terms of the fields *if* one expands the LPT expressions up to the desired order in the density field. Without these expansions, LPT was shown to contain a non-trivial resummation of SPT terms.
For n-th order displacement field one has [26]

$$ {}^{(n)}\boldsymbol{\Psi}(\boldsymbol{k},\eta) = -\frac{\mathrm{i}}{n!}\int \frac{\mathrm{d}^3p_1}{(2\pi)^3}\cdots\int \frac{\mathrm{d}^3p_n}{(2\pi)^3}\,{}^{(n)}\boldsymbol{L}(\boldsymbol{p}_1,\ldots,\boldsymbol{p}_n)\,\delta(\boldsymbol{p}_1,\eta)\ldots\delta(\boldsymbol{p}_n,\eta)\,(2\pi)^3\delta^{(\mathrm{D})}\left(\boldsymbol{k}-\sum\boldsymbol{p}_i\right), \tag{8.49} $$

with the kernels

$$ {}^{(1)}\boldsymbol{L}(\boldsymbol{p}) = \frac{\boldsymbol{p}}{p^2}, \qquad {}^{(2)}\boldsymbol{L}(\boldsymbol{p}_1,\boldsymbol{p}_2) = \frac{3}{7}\frac{\boldsymbol{p}_1+\boldsymbol{p}_2}{|\boldsymbol{p}_1+\boldsymbol{p}_2|^2}\left[1-\left(\frac{\boldsymbol{p}_1\cdot\boldsymbol{p}_2}{p_1p_2}\right)^2\right]. \tag{8.50} $$

The density field in k-space can be obtained upon Fourier transforming the Eulerian field in configuration space and using the Jacobian mapping $\left[1+\delta(\boldsymbol{x},\eta)\right]\mathrm{d}^3x = \mathrm{d}^3q$

$$ \delta(\boldsymbol{k},\eta) = \int \mathrm{d}^3q\,\exp\left[\mathrm{i}\,\boldsymbol{k}\cdot\boldsymbol{q}\right]\left\{\exp\left[\mathrm{i}\,\boldsymbol{k}\cdot\boldsymbol{\Psi}(\boldsymbol{q},\eta)\right]-1\right\} \tag{8.51} $$

We can now expand the exponential up to second order in the displacement field

$$\delta(\boldsymbol{k},\eta) \approx \int \mathrm{d}^3q \exp\left[\mathrm{i}\,\boldsymbol{k}\cdot\boldsymbol{q}\right]\left\{\mathrm{i}\,\boldsymbol{k}\cdot\boldsymbol{\Psi}(\boldsymbol{q},\eta) - \frac{1}{2}(\boldsymbol{k}\cdot\boldsymbol{\Psi}(\boldsymbol{q},\eta))^2\right\} \tag{8.52}$$

$$= \mathrm{i}\,\boldsymbol{k}\cdot{}^{(1)}\boldsymbol{\Psi}(\boldsymbol{k},\eta) + \mathrm{i}\,\boldsymbol{k}\cdot{}^{(2)}\boldsymbol{\Psi}(\boldsymbol{k},\eta) + \frac{1}{2}\int\frac{\mathrm{d}^3k'}{(2\pi)^3}\frac{\boldsymbol{k}\cdot\boldsymbol{k}'}{(\boldsymbol{k}')^2}\frac{\boldsymbol{k}\cdot(\boldsymbol{k}-\boldsymbol{k}')}{|\boldsymbol{k}-\boldsymbol{k}'|^2}{}^{(1)}\delta(\boldsymbol{k}',\eta)^{(1)}\delta(\boldsymbol{k}-\boldsymbol{k}',\eta) \tag{8.53}$$

$$= {}^{(1)}\delta(\boldsymbol{k},\eta) + \int\frac{\mathrm{d}^3k'}{(2\pi)^3}F_2(\boldsymbol{k}',\boldsymbol{k}-\boldsymbol{k}'){}^{(1)}\delta(\boldsymbol{k}',\eta)^{(1)}\delta(\boldsymbol{k}-\boldsymbol{k}',\eta) \tag{8.54}$$

Thus, expanding the exponential we see that LPT and SPT agree at second order in the density field.

8.6.2. On Shifts in the BAO

As shown recently in [27] and discussed before in [28], second order bias terms lead to a distinct shift in the position of the BAO feature. In this Appendix we generalize their calculation to account also for the shift due to the tidal tensor bias. Let us start by generalizing the mode coupling kernel to biased tracers. The structure of the quadratic and tidal tensor terms in the second order halo density field in Eq. (8.25) suggests the following functional form

$$F_{2,\mathrm{h}}(\boldsymbol{q}_1,\boldsymbol{q}_2) = b_1F_2(\boldsymbol{q}_1,\boldsymbol{q}_2) + b_2 + b_{s^2}S_2(\boldsymbol{q}_1,\boldsymbol{q}_2). \tag{8.55}$$

With this definition, the second order halo density field can be written as

$${}^{(2)}\delta_{\mathrm{h}}(\boldsymbol{k}) = \int\frac{\mathrm{d}^3q_1}{(2\pi)^3}\int\frac{\mathrm{d}^3q_2}{(2\pi)^3}F_{2,\mathrm{h}}(\boldsymbol{q}_1,\boldsymbol{q}_2){}^{(1)}\delta(\boldsymbol{q}_1){}^{(1)}\delta(\boldsymbol{q}_2)\delta^{(\mathrm{D})}(\boldsymbol{k}-\boldsymbol{q}_1-\boldsymbol{q}_2) \tag{8.56}$$

and the mode coupling power spectrum is given by

$$P_{\mathrm{hh},22}(\boldsymbol{k}) = \int\frac{\mathrm{d}^3q_1}{(2\pi)^3}\int\frac{\mathrm{d}^3q_2}{(2\pi)^3}F_{2,\mathrm{h}}^2(\boldsymbol{q}_1,\boldsymbol{q}_2)P(\boldsymbol{q}_1)P(\boldsymbol{q}_2)\delta^{(\mathrm{D})}(\boldsymbol{k}-\boldsymbol{q}_1-\boldsymbol{q}_2). \tag{8.57}$$

When considering the full one loop halo power spectrum, there is also a contribution from the coupling between linear and cubic halo density field, the term corresponding to the propagator $P_{13}(k)$ in the matter power spectrum. This term does not contribute to the shift of the BAO and can thus be neglected for our arguments here, except for a cancelation to be discussed below.

For the BAO shift, we are interested in the effect of long wavelength modes ($q \ll \Lambda$) on the correlation function around the BAO scale. Thus, we need to consider the high-k limit of the above integral, corresponding to $q_1 \ll k$ and $q_2 \ll k$

$$\begin{aligned}P_{\mathrm{hh},22}(\boldsymbol{k}) \overset{k\gg\Lambda}{\approx} &\left[\frac{569}{735}b_1^2 + \frac{52}{21}b_1b_2 + 4b_2^2 - \frac{272}{315}b_1b_{s^2} + \frac{16}{45}b_{s^2}^2\right]P(k)\sigma_{\mathrm{l}}^2 + k^2P(k)\sigma_{v,\mathrm{l}}^2\\ &+\left[\frac{47}{105}b_1^2 + \frac{4}{3}b_1b_2 + \frac{16}{45}b_1b_{s^2}\right]kP'(k)\sigma_{\mathrm{l}}^2 + \frac{1}{10}b_1^2k^2P''(k)\sigma_{\mathrm{l}}^2,\end{aligned} \tag{8.58}$$

where $\sigma_{\mathrm{l}}^2 = \int_0^\Lambda\frac{\mathrm{d}^3q}{(2\pi)^3}P(q)$ is the variance of the long wavelength modes and $\sigma_{v,\mathrm{l}}^2 = \int_0^\Lambda\frac{\mathrm{d}^3q}{(2\pi)^3}P(q)/3q^2$ is the velocity dispersion of the long wavelength displacement field. The $k^2P(k)\sigma_{v,\mathrm{l}}^2$ term is cancelled by the propagator $P_{\mathrm{hh},13}$ in the high-k regime and can thus be neglected in the following. Using the following two Fourier Transform (FT) relations between the correlation function and power spectrum, $\mathrm{FT}\left[kP'(k)\right] = -r\xi'(r) - 3\xi(r)$ and $\mathrm{FT}\left[k^2P''(k)\right] = r^2\xi''(r) + 8r\xi'(r) + 12\xi(r)$, we obtain for the correlation function in presence of a long wavelength mode

$$\xi_{\mathrm{hh,s}}(r) \approx b_1^2\xi(r) + \left[\frac{356}{147}b_1^2 + \frac{80}{21}b_1b_2 - \frac{32}{63}b_1b_{s^2} + 4b_2^2 + \frac{16}{45}b_{s^2}^2\right]\xi(r)\sigma_{\mathrm{l}}^2$$

$$+\left[\frac{131}{105}b_1^2+\frac{4}{3}b_1b_2+\frac{16}{45}b_1b_{s^2}\right]r\xi'(r)\sigma_{\rm l}^2+\frac{1}{10}b_1^2r^2\xi''(r). \tag{8.59}$$

Here we have added in the linear correlation function of the haloes, $b_1^2\xi(r)$.
Finally, we have for the shift term proportional to $r\xi'(r)$

$$\frac{131}{105}b_1^2\sigma_{\rm l}^2\left(1+\frac{140}{131}\frac{b_2}{b_1}+\frac{112}{393}\frac{b_{s^2}}{b_1}\right)r\xi'(r). \tag{8.60}$$

Let us discuss the relevance of the shift terms based on the mass dependence of the bias parameters depicted in Fig. 8.4. For haloes with $M < 10^{14}\ h^{-1}M_\odot$ the b_{s^2} effect has the same sign as the b_2 effect, whereas they cancel partially for higher mass objects. On the other hand b_{s^2} is parametrically smaller than b_2 for most of the considered mass range and even if the bias parameters were of the same magnitude, the prefactors in Eq. (8.60) lead to a factor four stronger contribution from the quadratic bias term. Thus, we conclude that the tidal tensor term only leads to a small shift correction on top of the already small correction due to quadratic bias.

Bibliography

[1] T. Baldauf, U. Seljak, V. Desjacques, and P. McDonald, **Evidence for quadratic tidal tensor bias from the halo bispectrum**, *Phys. Rev.* **86** (Oct., 2012) 083540, [arXiv:1201.4827].

[2] N. Kaiser, **On the Spatial correlations of Abell clusters**, *Astrophys. J.* **284** (1984) L9–L12.

[3] J. N. Fry and E. Gaztanaga, **Biasing and hierarchical statistics in large scale structure**, *Astrophys. J.* **413** (1993) 447–452, [astro-ph/9302009].

[4] P. McDonald and A. Roy, **Clustering of dark matter tracers: generalizing bias for the coming era of precision LSS**, *JCAP* **0908** (2009) 020, [arXiv:0902.0991].

[5] P. McDonald, **Clustering of dark matter tracers: renormalizing the bias parameters**, *Phys. Rev.* **D74** (2006) 103512, [astro-ph/0609413].

[6] J. E. Pollack, R. E. Smith, and C. Porciani, **Modelling large-scale halo bias using the bispectrum**, arXiv:1109.3458.

[7] J. M. Bardeen, J. R. Bond, N. Kaiser, and A. S. Szalay, **The Statistics of Peaks of Gaussian Random Fields**, *Astrophys. J.* **304** (1986) 15–61.

[8] V. Desjacques, M. Crocce, R. Scoccimarro, and R. K. Sheth, **Modeling scale-dependent bias on the baryonic acoustic scale with the statistics of peaks of Gaussian random fields**, *Phys.Rev.* **D82** (2010) 103529, [arXiv:1009.3449].

[9] A. Elia, A. D. Ludlow, and C. Porciani, **The spatial and velocity bias of linear density peaks and proto-haloes in the LCDM cosmology**, arXiv:1111.4211.

[10] P. Catelan, C. Porciani, and M. Kamionkowski, **Two Ways of Biasing Galaxy Formation**, *Mon. Not. Roy. Astron. Soc.* **318** (2000) 39, [astro-ph/0005544].

[11] A. Elia, S. Kulkarni, C. Porciani, M. Pietroni, and S. Matarrese, **Modeling the clustering of dark-matter haloes in resummed perturbation theories**, arXiv:1012.4833.

[12] F. Bernardeau, S. Colombi, E. Gaztanaga, and R. Scoccimarro, **Large-scale structure of the universe and cosmological perturbation theory**, *Phys. Rept.* **367** (2002) 1–248, [astro-ph/0112551].

[13] J. N. Fry, **The Evolution of Bias**, *Astrophys.J.* **461** (1996) L65.

[14] R. Scoccimarro, R. K. Sheth, L. Hui, and B. Jain, **How many galaxies fit in a halo? Constraints on galaxy formation efficiency from spatial clustering**, *Astrophys.J.* **546** (2001) 20–34, [astro-ph/0006319].

[15] R. K. Sheth, H. J. Mo, and G. Tormen, **Ellipsoidal collapse and an improved model for the number and spatial distribution of dark matter haloes**, *Mon.Not.Roy.Astron.Soc.* **323** (May, 2001) 1–12, [astro-ph/].

[16] V. Desjacques, **Environmental dependence in the ellipsoidal collapse model**, *Mon. Not. Roy. Astron. Soc.* **388** (2008) 638, [arXiv:0707.4670].

[17] R. K. Sheth and G. Tormen, **Large scale bias and the peak background split**, *Mon.Not.Roy.Astron.Soc.* **308** (1999) 119, [astro-ph/9901122].

[18] U. Seljak and M. S. Warren, **Large-scale bias and stochasticity of haloes and dark matter**, *Mon. Not. Roy. Astron. Soc.* **355** (Nov., 2004) 129–136, [astro-ph/].

[19] N. Hamaus, U. Seljak, V. Desjacques, R. E. Smith, and T. Baldauf, **Minimizing the stochasticity of halos in large-scale structure surveys**, *Phys. Rev.* **D82** (2010) 043515, [arXiv:1004.5377].

[20] V. Desjacques, U. Seljak, and I. T. Iliev, **Scale-dependent bias induced by local non-Gaussianity: a comparison to N-body simulations**, *Mon. Not. Roy. Astron. Soc.* **396** (June, 2009) 85–96, [arXiv:0811.2748].

[21] **W**MAP Collaboration, E. Komatsu et al., **Five-Year Wilkinson Microwave Anisotropy Probe (WMAP 1) Observations:Cosmological Interpretation**, *Astrophys. J. Suppl.* **180** (2009) 330–376, [arXiv:0803.0547].

[22] V. Springel, **The cosmological simulation code GADGET-2**, *Mon. Not. Roy. Astron. Soc.* **364** (2005) 1105–1134, [astro-ph/0505010].

[23] R. Scoccimarro, E. Sefusatti, and M. Zaldarriaga, **Probing Primordial Non-Gaussianity with Large-Scale Structure**, *Phys. Rev.* **D69** (2004) 103513, [astro-ph/0312286].

[24] N. Padmanabhan and M. White, **Calibrating the baryon oscillation ruler for matter and halos**, *Phys. Rev. D* **80** (Sept., 2009) 063508, [arXiv:0906.1198].

[25] K. Chuen Chan, R. Scoccimarro, and R. K. Sheth, **Gravity and Large-Scale Non-local Bias**, *ArXiv e-prints* (Jan., 2012) [arXiv:1201.3614].

[26] T. Matsubara, **Resumming Cosmological Perturbations via the Lagrangian Picture: One-loop Results in Real Space and in Redshift Space**, *Phys. Rev.* **D77** (2008) 063530, [arXiv:0711.2521].

[27] B. D. Sherwin and M. Zaldarriaga, **Shift of the baryon acoustic oscillation scale: A simple physical picture**, *Phys. Rev.* **85** (May, 2012) 103523, [arXiv:1202.3998].

[28] N. Padmanabhan and M. White, **Calibrating the Baryon Oscillation Ruler for Matter and Halos**, *Phys. Rev.* **D80** (2009) 063508, [arXiv:0906.1198].

CHAPTER 9

Halo Stochasticity from Exclusion and non-linear Clustering[†]

The clustering of galaxies in ongoing and upcoming galaxy surveys contains a wealth of cosmological information, but extracting this information is a non-trivial task since galaxies and their host haloes are stochastic tracers of the non-linear matter density field. This stochasticity is usually modeled as the Poisson shot noise, which is constant as a function of wavenumber with amplitude given by $1/\bar{n}$, where $\bar{n}$ is the number density of galaxies. Here we use dark matter haloes in N-body simulations to show evidence for deviations from this simple behaviour and develop models that explain the behaviour of the stochasticity on large scales. First, haloes are extended, non-overlapping objects, i.e., their correlation function needs to go to -1 on small scales. This leads to a negative correction to the stochasticity relative to the Poisson value at low wavenumber k, decreasing to zero for wavenumbers large compared to the inverse exclusion scale. Second, haloes show a non-linear enhancement of clustering outside the exclusion scale, leading to a positive stochasticity correction. Both of these effects go to zero for high-k, making the stochasticity scale dependent even for $k < 0.1\ h\mathrm{Mpc}^{-1}$. We show that the corrections in the low-k regime are the same in Eulerian and Lagrangian space, but that the transition scale is pushed to smaller scales for haloes observed at present time (Eulerian space), relative to the initial conditions (Lagrangian space). These corrections vary with halo mass and we present approximate scalings with halo mass and redshift. We also discuss simple applications of these effects to galaxy samples with non-vanishing satellite fraction, where the stochasticity can again deviate strongly from the fiducial Poisson expectation. Overall these effects affect the clustering of galaxies at a level of a few percent even on very large scales and need to be modelled properly if we want to extract high precision cosmological information from the upcoming galaxy redshift surveys.

9.1. Introduction

The three dimensional distribution of galaxies has the potential to tell us a lot about the physics governing our Universe. However, the imprint of the composition and history of our Universe on its structure is usually quantified in terms of the linear power spectrum. From there it is a fair way to go to connect to the distribution of luminous objects. Due to the stochastic nature of the initial conditions the comparison between theory and observation has to be made at a statistical level. Thus, it has become common practice to reduce the data to n-spectra

[†]This chapter is based on a preprint [1] by T. Baldauf, U. Seljak, R. E. Smith, N. Hamaus and V. Desjacques. I am the first author, analyzed the simulations, performed the calculations and compiled the manuscript.

and to find a way to push the theory as far as possible in order to make predictions for the observed spectra. This means that the theoretical prediction needs to account for the fact that galaxies are only sampling the underlying matter distribution. While their distribution is clearly related to the matter distribution, there are a number of distinct features present in the galaxy distribution that are related to their discrete nature and the fact that galaxies form preferentially in high density regions.
Due to the complicated nature of galaxy formation, cosmological constraints from galaxy surveys are usually obtained using a bias model [2]. The simplest local bias models [3] assume a proportionality between the galaxy and matter overdensities. As we will review in detail below in §9.2.1, the auto power spectrum of a sample of N particles in a volume V is expected to have an additional *scale independent* shot noise component V/N. We will refer to this Poisson prediction as fiducial stochasticity. On top of the fiducial Poisson shot noise there are further contributions to the halo power spectrum that are white only over a limited range of wavenumbers and lead to modifications in the $k \to 0$ limit. The latter will be referred to as stochasticity corrections. For instance, the studies of [4, 5] found evidence for a sub-Poissonian noise in the halo distribution in N-body simulations (see also [6, 7]) and used this concept to increase the information content extractable from surveys by weighting haloes accordingly. Subsequently, this approach was used to improve constraints on primordial non-Gaussianity [8] and redshift space distortions [9].
Thus far, the origin of these stochasticity corrections has not been understood consistently. However, some authors noted that realistic bias models would at some point need to account for the finite size of haloes and the resulting exclusion effects [10]. The effect of halo exclusion on the power spectrum was previously discussed in [11] in a an Eulerian setting. Here, we will argue that the exclusion effect can not be seen in isolation but has to be combined with the non-linear clustering, which can lead to positive corrections on large scales. This approach partially alleviates the longstanding problem of non-vanishing contributions of the perturbative bias model on the largest scales, where perturbative corrections are considered unphysical. This paper aims at shedding light at the stochasticity properties of halo and galaxy samples and tries to quantify them where possible.
The paper breaks down as follows: We begin in §9.2 with a short review of the standard Poisson shot noise for a sample of discrete tracers. Then, in §9.3 we consider some simple toy models to understand the effects of exclusion on the power spectrum, before we go on to discuss more realistic models for the clustering of dark matter haloes in §9.4. In §9.5 we study the stochasticity and correlation function for a sample of dark matter haloes and a HOD galaxy sample in N-body simulations. Finally, we summarize our findings in §9.6.

9.2. Discrete Tracers

9.2.1. Correlation and Power Spectrum

The overdensity of discrete tracer particles (dark matter haloes, galaxies etc.) can generically be written as

$$\delta^{(\mathrm{d})}(\boldsymbol{r}) = \frac{n(\boldsymbol{r})}{\bar{n}} - 1 = \frac{1}{\bar{n}} \sum_i \delta^{(\mathrm{D})}(\boldsymbol{r} - \boldsymbol{r}_i) - 1, \tag{9.1}$$

where $\bar{n}$ is the mean number density of the point-like objects whereas $n(\boldsymbol{r})$ is their local number density. The two-point correlation of this fluctuation field is the expectation value

$$\begin{aligned}\left\langle \delta^{(\mathrm{d})}(\boldsymbol{r}) \delta^{(\mathrm{d})}(\boldsymbol{0}) \right\rangle = \frac{1}{\bar{n}^2} \left\langle \sum_{i,j} \delta^{(\mathrm{D})}\left(\boldsymbol{r} - \boldsymbol{r}_i\right) \delta^{(\mathrm{D})}\left(\boldsymbol{r}_j\right) \right\rangle \\ - \frac{1}{\bar{n}} \left\langle \sum_i \delta^{(\mathrm{D})}\left(\boldsymbol{r} - \boldsymbol{r}_i\right) \right\rangle - \frac{1}{\bar{n}} \left\langle \sum_j \delta^{(\mathrm{D})}\left(\boldsymbol{r}_j\right) \right\rangle + 1\end{aligned} \tag{9.2}$$

$$
\begin{aligned}
&= \frac{1}{\bar{n}^2}\delta^{(\mathrm{D})}(\boldsymbol{r})\left\langle\sum_i \delta^{(\mathrm{D})}(\boldsymbol{r}-\boldsymbol{r}_i)\right\rangle + \frac{1}{\bar{n}^2}\left\langle\sum_{i\neq j}\delta^{(\mathrm{D})}(\boldsymbol{r}-\boldsymbol{r}_i)\,\delta^{(\mathrm{D})}(\boldsymbol{r}_j)\right\rangle - 1 \\
&= \frac{1}{\bar{n}}\delta^{(\mathrm{D})}(\boldsymbol{r}) + \frac{1}{\bar{n}^2}\left\langle\sum_{i\neq j}\delta^{(\mathrm{D})}(\boldsymbol{r}-\boldsymbol{r}_i)\,\delta^{(\mathrm{D})}(\boldsymbol{r}_j)\right\rangle - 1 \\
&= \frac{1}{\bar{n}}\delta^{(\mathrm{D})}(\boldsymbol{r}) + \xi^{(\mathrm{d})}(r)\ .
\end{aligned}
$$

We split the sum into an $i = j$ and and $i \neq j$ part, corresponding to the correlation of the discrete particles with themselves and the correlation between different particles, respectively. The second term in the last equality is the reduced two-point correlation function of the tracers. The first term arises owing to "self-pairs", which are usually ignored in the calculation of real space correlations. Taking the Fourier transform of the last expression, the power spectrum of the discrete tracers is

$$
P^{(\mathrm{d})}(k) = \frac{1}{\bar{n}} + \int \mathrm{d}^3 r\,\xi^{(\mathrm{d})}(r)\exp\left[\mathrm{i}\,\boldsymbol{k}\cdot\boldsymbol{r}\right]\ . \tag{9.3}
$$

Self-pairs contribute the usual Poisson white noise $1/\bar{n}$. The only requirement is that the power spectrum be positive definite. This implies that the Fourier transform of the two-point correlation $\xi^{(\mathrm{d})}(r)$ can be anything equal or greater than $-1/\bar{n}$. In the limit $k \to 0$ in particular, the power spectrum tends towards

$$
P^{(\mathrm{d})}(k) \xrightarrow{k\to 0} \frac{1}{\bar{n}} + \int \mathrm{d}^3 r\,\xi^{(\mathrm{d})}(r)\ , \tag{9.4}
$$

where the intregal of $\xi^{(\mathrm{d})}(r)$ over the whole space can be positive, zero or negative (but greater than $-1/\bar{n}$) depending on the nature of the discrete tracers. This can lead to super-poisson or sub-poisson white noise in the low-k limit.
At $k = 0$, the power spectrum is $P^{(\mathrm{d})}(0) = 0$ because the fluctuation field $\delta^{(\mathrm{d})}(\boldsymbol{r})$ is defined relative to the mean number density, hence $\langle\delta^{(\mathrm{d})}\rangle = 0$. This implies that $P^{(\mathrm{d})}(k)$ drops precipitously on very large scales (so it must be discontinuous at $k = 0$) regardless the value of $\int \mathrm{d}^3 r\,\xi^{(\mathrm{d})}(r)$. To convince ourselves that this is indeed the case, we can write the Fourier modes of the tracer fluctuation field as

$$
\delta^{(\mathrm{d})}(\boldsymbol{k}) = \frac{1}{\bar{n}}\sum_i \exp\left[\mathrm{i}\,\boldsymbol{k}\cdot\boldsymbol{r}_i\right] - \int \mathrm{d}^3 r\,\exp\left[\mathrm{i}\,\boldsymbol{k}\cdot\boldsymbol{r}\right]\ . \tag{9.5}
$$

To calculate $\delta^{(\mathrm{d})}(k = 0)$ (which is formally the difference between two infinite quantities), we first assume $N, V \gg 1$ at fixed average number density $\bar{n} \equiv N/V$, and then take the limit $N, V \to \infty$. We thus have for the Fourier transform of the density field

$$
\delta^{(\mathrm{d})}(\boldsymbol{k}) = \frac{1}{\bar{n}}\sum_i \exp\left[\mathrm{i}\,\boldsymbol{k}\cdot\boldsymbol{r}_i\right] - V\delta^{(\mathrm{K})}_{\boldsymbol{k},\boldsymbol{0}}\ , \tag{9.6}
$$

which for $\boldsymbol{k} = 0$ yields

$$
\delta^{(\mathrm{d})}(\boldsymbol{0}) = \frac{V}{N}N - V = 0\ . \tag{9.7}
$$

This obviously holds also for a finite number N of tracers in a finite volume V. Therefore, the fact that $\int \mathrm{d}^3 r\,\xi^{(\mathrm{d})}(r)$ can be different from zero has nothing to do with the fact that $\langle\delta^{(\mathrm{d})}\rangle = 0$, nor with the so-called "integral constraint" that appears when measuring an excess of pairs relative to a random distribution in a finite volume [12, 13].

9.2.2. The Effect of Exclusion with Clustering

Let us now account for the fact that haloes are the centre of an ensemble of particles, which by definition can not overlap, and that these are clustered. Exclusion means it is forbidden to

have two haloes closer than the sum of their radii R. This fact can be accounted for by writing the correlation function of the discrete tracers as

$$\xi_{\rm hh}^{\rm (d)}(r) = \begin{cases} -1 & \text{for } r < R \\ \xi_{\rm hh}^{\rm (c)}(r) & \text{for } r \geq R, \end{cases} \tag{9.8}$$

where the fictitious continuous correlation function $\xi_{\rm hh}^{\rm (c)}(r)$ is defined for $r \in [0, \infty]$ and would for instance be related to the matter correlation function by the local bias model (see §9.4.1 below). Enforcing this step at the exclusion radius is certainly overly simplistic, since any triaxiality or variation of radius within the sample will smooth this step out. We will come back to this issue later.
For generic continuous clustering models, we can write the Fourier transform of the correlation function as

$$\begin{aligned} \int_0^\infty {\rm d}^3 r \xi_{\rm hh}^{\rm (d)}(r) j_0(kr) =& -\int_0^R {\rm d}^3 r j_0(kr) + \int_R^\infty {\rm d}^3 r \xi_{\rm hh}^{\rm (c)}(r) j_0(kr) \\ =& -V_{\rm excl} W_R(k) - \int_0^R {\rm d}^3 r \xi_{\rm hh}^{\rm (c)}(r) j_0(kr) + \int_0^\infty {\rm d}^3 r \xi_{\rm hh}^{\rm (c)}(r) j_0(kr) \\ =& -V_{\rm excl} W_R(k) - V_{\rm excl} \left[W_R * P_{\rm hh}^{\rm (c)} \right](k) + P_{\rm hh}^{\rm (c)}(k), \end{aligned} \tag{9.9}$$

where the exclusion volume is $V_{\rm excl} = 4\pi R^3/3$, j_0 is the zeroth order spherical Bessel function and the Fourier transform of the top-hat window is given by

$$W_R(k) = 3 \frac{\sin(kR) - kR\cos(kR)}{(kR)^3} \tag{9.10}$$

and where the notation $[A * B](k)$ describes a convolution integral

$$[A * B](k) = \int \frac{{\rm d}^3 q}{(2\pi)^3} A(q) B(|\boldsymbol{k} - \boldsymbol{q}|). \tag{9.11}$$

We also defined the continuous power spectrum as the full Fourier transform of the continuous correlation function

$$P_{\rm hh}^{\rm (c)}(k) = \int_0^\infty {\rm d}^3 r \xi_{\rm hh}^{\rm (c)}(r) j_0(kr). \tag{9.12}$$

Combining the above results with the fiducial stochasticity contribution we finally have for the power spectrum of the discrete tracers

$$P_{\rm hh}^{\rm (d)}(k) = \frac{1}{\bar{n}} + P_{\rm hh}^{\rm (c)}(k) - V_{\rm excl} W_R(k) - V_{\rm excl} \left[W_R * P_{\rm hh}^{\rm (c)} \right](k). \tag{9.13}$$

This equation is the basis of our paper and we will thus explore it in detail.
It is common practice to ignore the exclusion window and to approximate the continuous power spectrum by the linear local bias model, which yields for the power spectrum of the discrete tracers in the Poisson model

$$P_{\rm hh}^{\rm (d)}(k) = \frac{1}{\bar{n}} + b_1^2 P_{\rm lin}(k). \tag{9.14}$$

This needs to be modified because of exclusion and non-linear effects. In practice, for $k > 0$, it is difficult to separate the effects. Here we will formally define the stochasticity effects discussed in this paper as a stochasticity power spectrum [5]

$$\begin{aligned} (2\pi)^3 \delta^{\rm (D)}(\boldsymbol{k} + \boldsymbol{k}') C(k) =& \left\langle \left[\delta_{\rm h}(\boldsymbol{k}) - b_1 \delta_{\rm m}(\boldsymbol{k}) \right] \left[\delta_{\rm h}(\boldsymbol{k}') - b_1 \delta_{\rm m}(\boldsymbol{k}') \right] \right\rangle \\ =& (2\pi)^3 \delta^{\rm (D)}(\boldsymbol{k} + \boldsymbol{k}') \left[P_{\rm hh}(k) - 2 b_1 P_{\rm hm}(k) + b_1^2 P_{\rm mm}(k) \right], \end{aligned} \tag{9.15}$$

where $b_1 = P_{\rm hm}(k)/P_{\rm mm}(k)$ is the first order bias from the cross-correlation in the low-k limit. We then have in the low-k limit

$$P_{\rm hh}^{\rm (d)}(k) = C(k) + b_1^2 P_{\rm lin}(k). \tag{9.16}$$

One could make this generally valid at all k by defining $b(k) = P_{\rm hm}(k)/P_{\rm mm}(k)$, but we will not do this here, and instead explore physically motivated models of non-linear bias. In this paper we are interested in the stochasticity power spectrum $C(k)$ and in particular its limit as $k \to 0$.

What are the corrections arising from the exclusion and deviations from the local bias model? In the low k-limit, the window function scales as $W_R(k) \xrightarrow{k\to 0} 1 - k^2R^2/10$. Hence, the convolution integral leads to a constant term plus corrections scaling as k^2R^2 times moments of the continuous power spectrum

$$\left[W_R * P_{\rm hh}^{\rm (c)}\right](k) \xrightarrow{k\to 0} \int \frac{{\rm d}^3q}{(2\pi)^3} P_{\rm hh}^{\rm (c)}(q) W_R(q) + k^2R^2 \int \frac{{\rm d}^3q}{(2\pi)^3} P_{\rm hh}^{\rm (c)}(q) \left[W_R(q)\left(\frac{1}{(qR)^2} - \frac{1}{6}\right) - \frac{\sin(qR)}{(qR)^3}\right]. \tag{9.17}$$

Thus, irrespective of the shape of the continuous power spectrum on large scales, exclusion always introduces a white (k^0) correction on large scales.

Fig. 9.1 illustrates the behaviour of the correlation function of discrete tracers. In the very popular local bias model, the clustering of dark matter haloes is modeled at leading order as $P_{\rm hh}^{\rm (c)}(k) = b_1^2 P_{\rm lin}(k)$. In configuration space this leads to $\xi_{\rm hh}^{\rm (c)}(r) = b_1^2 \xi_{\rm lin}(r)$, shown by the black dashed line. We will consider this linear bias model as the fiducial model on top of which we define corrections. Non-linear halo clustering suggests an enhancement proportional to higher powers of the linear correlation function as exemplified by the red dashed line. Our above arguments suggest that this clustering model, if at all, can only be true outside the exclusion radius. Inside this radius the probability to find another halo is zero, leading to $\xi_{\rm hh}^{\rm (d)}(r < R) = -1$.

An intuitive understanding of the corrections can be obtained in the $k \to 0$ limit, where the halo power spectrum is given by an integral over the correlation function and can thus be written as

$$P_{\rm hh}^{\rm (d)}(k) \xrightarrow{k\to 0} \frac{1}{\bar{n}} - V_{\rm excl} - b_1^2 \int_0^R {\rm d}^3r\, \xi_{\rm lin}(r) + \int_R^\infty {\rm d}^3r \left[\xi_{\rm hh,NL}^{\rm (c)}(r) - b_1^2 \xi_{\rm lin}(r)\right], \tag{9.18}$$

where we introduced $\xi_{\rm hh,NL}^{\rm (c)}(r)$ to account for generic non-linear continuous models of the halo clustering. The red and blue shaded regions in Fig. 9.1 show the negative and positive corrections with respect to the linear bias model for which we would have in absence of exclusion $P_{\rm hh}^{\rm (d)}(k) \xrightarrow{k\to 0} 1/\bar{n}$. Note that the non-linear halo-halo correlation function could in principle be smaller than the linear bias prediction. Our above notion of a positive correction arising from the non-linear correction outside the exclusion radius is solely based on local bias arguments. In general this statement should be relaxed (for an example see App. 9.7.1) and the blue region could have either sign.

9.3. Toy Models

To show that the exclusion can indeed lower the stochasticity we perform a simple numerical experiment. We consider a set of hard sphere haloes of radius $R/2$. For this purpose, we distribute N particles randomly in a cubic box ensuring that $|\boldsymbol{x}_i - \boldsymbol{x}_j| > R$ for all pairs of particles (i, j). The corresponding correlation function is expected to be zero except for scales $r < R$, where $\xi = -1$ due to exclusion. Thus we expect the fiducial stochasticity to be lowered by $4\pi R^3/3$ in the $k \to 0$ limit. For an intuitive derivation of the corrections to the power

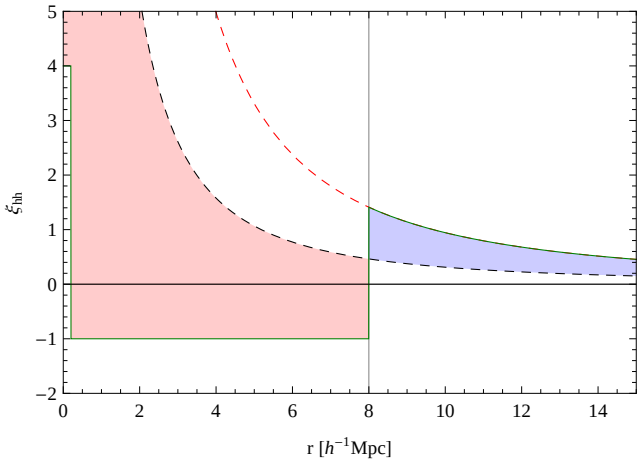

Figure 9.1.: Cartoon version of the correlation function of discrete tracers. Continuous linear correlation function (black dashed) and non-linear correlation function (red dashed). The true correlation function of discrete tracers (green solid line) agrees with the non-linear continuous correlation function outside the exclusion scale and is -1 below, except for the delta function at the origin arising from discreteness. Thus, there are two corrections compared to the continuous linear bias model, a negative correction inside the exclusion radius (red shaded) and a positive one outside the exclusion radius due to non-linear clustering (blue shaded).

spectrum we will consider a fixed number of particles N in a finite volume V. Using Eq. (9.6) the auto-power spectrum of the tracer particles can be written as [1]

$$\begin{aligned} P^{(\mathrm{d})}(k) =& \frac{1}{V}\left\langle \delta^{(\mathrm{d})}(\boldsymbol{k})\delta^{(\mathrm{d})}(-\boldsymbol{k})\right\rangle \\ =& \frac{V}{N^2}\sum_{i=j}\left\langle \exp\left[\mathrm{i}\,\boldsymbol{k}\cdot(\boldsymbol{r}_i-\boldsymbol{r}_j)\right]\right\rangle + \frac{V}{N^2}\sum_{i\neq j}\left\langle \exp\left[\mathrm{i}\,\boldsymbol{k}\cdot(\boldsymbol{r}_i-\boldsymbol{r}_j)\right]\right\rangle - V\delta^{(\mathrm{K})}_{\boldsymbol{k},\boldsymbol{0}} \\ =& \frac{1}{\bar{n}} + \frac{V}{N^2}\sum_{\mathrm{i}\neq j}\langle \exp\left[\mathrm{i}\,\boldsymbol{k}\cdot(\boldsymbol{r}_i-\boldsymbol{r}_j)\right]\rangle - V\delta^{(\mathrm{K})}_{\boldsymbol{k},\boldsymbol{0}}. \end{aligned} \tag{9.19}$$

This yields for the hard sphere sample, which we consider as a proxy for excluded haloes

$$P^{(\mathrm{d})}_{\mathrm{hh}}(k) = \frac{1}{\bar{n}_{\mathrm{h}}} - \frac{4\pi R^3}{3}W_R(k). \tag{9.20}$$

In Fig. 9.2 we show the power spectrum of this toy halo sample for $R = 8\ h^{-1}$Mpc, $N = 800$ and $V = 300^3\ h^{-3}\mathrm{Mpc}^3$. We clearly see that the measured power follows the exclusion corrected stochasticity. The window is close to unity on large scales and decays at $k \approx 1/R$, i.e., the fiducial shot noise is recovered for high k. This is a first indication for stochasticity not being scale independent. Note that the above derivations are only true in the limit, where the total exclusion volume is small compared to the total volume and thus allows for a quasi random distribution (about 0.8% volume coverage in our case).

9.3.1. Satellite Galaxies

Galaxies are believed to populate dark matter haloes. Let us consider the simple case that each of the dark matter haloes under consideration hosts a central galaxy that, as the name suggests, coincides with the halo centre plus a fixed number $N_{\mathrm{s,h}}$ of satellite galaxies, such that the total number of satellite galaxies is given by $N_{\mathrm{s}} = N_{\mathrm{s,h}}N_{\mathrm{h}}$. For simplicity, we will assume

[1] The finite grid leads to $\delta^{(\mathrm{D})}(\boldsymbol{k}-\boldsymbol{k}') = \frac{V}{(2\pi)^3}\delta^{(\mathrm{K})}_{\boldsymbol{k},\boldsymbol{k}'}$ and consequently $V\delta^{(\mathrm{K})}_{\boldsymbol{k},\boldsymbol{k}'}P(k) = \langle\delta(\boldsymbol{k})\delta(-\boldsymbol{k}')\rangle$.

that the galaxies are distributed according to a profile $\rho_s(r)$ with typical scale R_s around the centers of the host halo centers. For long wavelength modes $k < 1/R_s$ the $N_{s,h}$ galaxies within one halo are effectively one particle, which is why on large scales we expect the stochasticity of the satellite galaxy sample to be equal to the one of the host haloes and only for scales $k > 1/R_s$ the modes can probe the distinct nature of the particles and the stochasticity goes to $1/\bar{n}_s$.
We can evaluate our model Eq. (9.19) to obtain the satellite-satellite power spectrum

$$\begin{aligned} P_{ss}^{(d)}(k) =& \frac{V}{N_s} + \frac{V}{N_s^2} \sum_{h_i} \sum_{s_j \in h_i} \sum_{s_l \neq s_j \in h_i} \langle \exp\left[i\, \boldsymbol{k} \cdot (\boldsymbol{r}_j - \boldsymbol{r}_l)\right] \rangle \\ &+ \frac{V}{N_s^2} \sum_{h_i} \sum_{s_j \in h_i} \sum_{h_m \neq h_i} \sum_{s_l \in h_m} \langle \exp\left[i\, \boldsymbol{k} \cdot (\boldsymbol{r}_j - \boldsymbol{r}_l)\right] \rangle \\ =& \frac{V}{N_s} + \frac{V}{N_s} (N_{s,h} - 1) \langle \exp\left[i\, k R_s \mu\right] \rangle^2 - \frac{4\pi R^3}{3} u_s^2(k) W_R(k) \\ =& \frac{1}{\bar{n}_s} \left[1 + (N_{s,h} - 1) u_s^2(k)\right] - \frac{4\pi R^3}{3} u_s^2(k) W_R(k) \end{aligned} \tag{9.21}$$

Here μ is the cosine of the angle between $\boldsymbol{k}$ and $\Delta \boldsymbol{r}_{ij} = \boldsymbol{r}_i - \boldsymbol{r}_j$ that is averaged over, $u_s(k)$ is the normalized Fourier transform of the galaxy profile $\rho_s(r)$. For definiteness we will assume a delta function profile $\rho(r) = \delta^{(D)}(r - R_s)/r^2$ corresponding to $u_s(k) = j_0(kR_s)$, where j_0 is the zeroth order spherical Bessel function. The two terms in the above equation correspond to the one and two halo terms in the halo model [14, 15], the profile and the fiducial shot noise arise from correlations between particles in the same halo, whereas the exclusion term is dominated by the correlation between distinct haloes. The results of the numerical experiment are shown in Fig. 9.2 as the green points. The model prediction is shown as the green solid line and describes the simulation measurement very well. On small scales the power is dominated by the fiducial galaxy shot noise and on large scales the host halo stochasticity dominates

$$P_{ss}^{(d)}(k \ll 1/R_s, 1/R) = \frac{1}{\bar{n}_h} - \frac{4\pi R^3}{3}, \qquad P_{ss}^{(d)}(k \gg 1/R_s, 1/R) = \frac{1}{\bar{n}_s}. \tag{9.22}$$

While the distribution of satellite galaxies on a sphere of fixed radius around the halo centre is very peculiar and unrealistic, the qualitative behaviour is the same for all profiles with finite support. In the case studied above, the corrections to the fiducial galaxy shot noise $1/\bar{n}_h$ are always positive. This is due to the high satellite fraction. As we will discuss below, this behaviour might be completely different for galaxy samples with small satellite fraction, where the exclusion effect can be more important than the enhancement due to the satellites.

9.3.2. Central and Satellite Galaxies

We can also consider the cross power spectrum between halo centers (central galaxies) and the satellite galaxies. In this case there is no Poisson shot noise, since the samples are non-overlapping and the power is dominated by a one-halo term describing the radial distribution of the satellites around the halo centre

$$\begin{aligned} P_{cs}^{(d)}(k) =& \frac{V}{N_h N_s} \sum_{h_i} \sum_{s_j \in h_i} \langle \exp\left[i\, \boldsymbol{k} \cdot (\boldsymbol{r}_j - \boldsymbol{r}_i)\right] \rangle + \frac{V}{N_h N_s} \sum_{h_i} \sum_{h_j \neq h_i} \sum_{s_l \in h_j} \langle \exp\left[i\, \boldsymbol{k} \cdot (\boldsymbol{r}_l - \boldsymbol{r}_i)\right] \rangle \\ =& \frac{1}{\bar{n}_h} u_s(k) - \frac{4\pi R^3}{3} u_s(k) W_R(k). \end{aligned} \tag{9.23}$$

Here we have again a one halo term arising from correlations of the halo center with satellites in the same halo and a two halo term arising from the correlation of satellite galaxies in one halo with the center of another halo. The comparison with the result of the numerical experiment

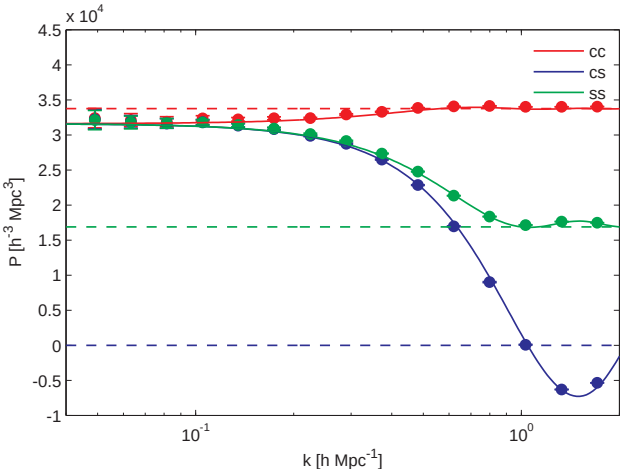

Figure 9.2.: Power spectrum of a randomly distributed halo sample obeying exclusion (red points) and corresponding model with (red solid line) and without (red dashed line) exclusion. In a second step we populate these haloes with $N_{\rm gal} = 2$ satellite galaxies, and calculate the auto power spectrum of the satellite galaxies (green points) and their cross power spectrum with the halo centers (blue points). The blue and green solid lines show our model predictions, whereas the dashed lines show the naive expectation of Poisson shot noise.

in Fig. 9.2 shows very good agreement.

The above discussion is overly simplified as we assume all haloes to be of the same mass and to host the same number of galaxies. Any realistic galaxy sample will be hosted by a range of halo masses (i.e. a range of exclusion radii) and the number of galaxies per halo will also be a function of mass.

The total galaxy power spectrum of the combined central and satellite samples can be obtained as a combination of the central-central, central-satellite and satellite-satellite contributions

$$P_{\rm gg}(k) = (1 - f_{\rm s})^2 P_{\rm cc}(k) + 2 f_{\rm s}(1 - f_{\rm s}) P_{\rm cs}(k) + f_{\rm s}^2 P_{\rm ss}(k), \tag{9.24}$$

where $f_{\rm s} = N_{\rm s}/(N_{\rm c} + N_{\rm s})$ is the satellite fraction. For realistic satellite fractions for SDSS LRGs [16] $f_{\rm s} \approx 0.1$, the weighting of the central-central power spectrum dominates over the contributions from the central-satellite and satellite-satellite power spectra by factors of 9 and 81, respectively. A more realistic galaxy sample based on a HOD population of dark matter haloes in a N-body simulation will be discussed in Sec. 9.5.6.

9.3.3. Toy Model with Clustering

Haloes are clustered, i.e., there is an enhanced probability to find two collapsed objects in the vicinity of each other to finding them widely separated. Let us discuss the influence of this phenomenological result on our toy model. For the sake of simplicity let us assume that haloes always come in pairs, i.e., that there is a second halo outside the exclusion scale at typical separation $R_{\rm clust}$. This will similarly to satellite galaxies residing in one halo, lead to a *positive* k^0 term on large scales, that decays for $k > 1/R_{\rm clust}$. In a more realistic setting, not all haloes will come in pairs, some of them will be single objects, others will come in clusters of n-haloes. Furthermore not all of them will be separated by exactly the clustering scale.

Some authors argued that any large scale k^0-behavior in the perturbation theory description of biasing is unphysical and should be suppressed by constant but aggressive smoothing [17] or by a k-dependent smoothing [18]. Based on the above considerations, we argue that such terms are just a result of the clustering of haloes and thus *not* unphysical. Whether the magnitude of these effects can be covered by a perturbative treatment such as second order bias combined

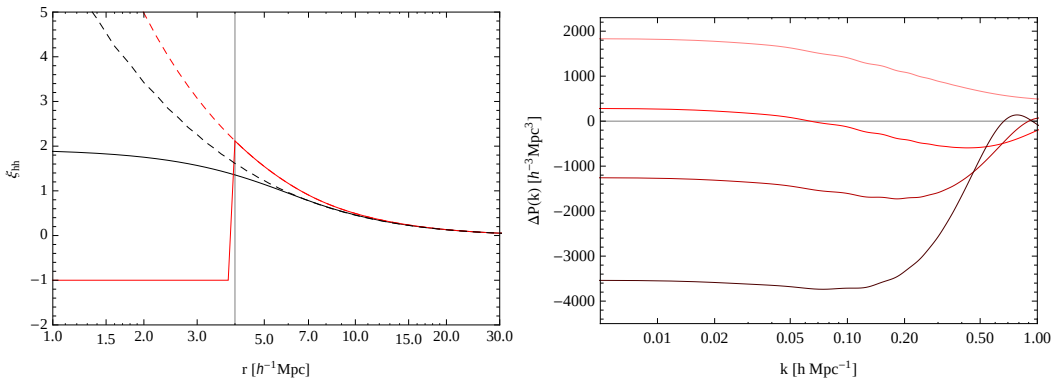

Figure 9.3.: Kaiser bias [2] in configuration and Fourier space. *Left panel:* Un-smoothed (black dashed) and $R = 4\ h^{-1}$Mpc smoothed (black solid) linearly biased matter correlation functions $b^2_{1,\mathrm{tr}}\xi(r)$ and continuous correlation function of the thresholded regions $\xi_{\mathrm{tr}}(r)$ (red dashed). The red solid line shows a simple implementation of exclusion imposed on the correlation function of the thresholded regions. *Right panel:* Power spectrum correction arising from the non-linear biasing (top line) and effect of increasing exclusion for $R = 0, 4, 6, 8\ h^{-1}$Mpc from top to bottom.

with perturbation theory, is a different question, which we will pick up later in §9.4.2. For now, let us note that such a k^0 term is also predicted by biasing models that go beyond the local bias model as for instance the correlation of thresholded regions as discussed briefly in the next subsection and for instance in [19]. Generally the clustering scale exceeds the exclusion scale and thus one should expect that the enhancement due to clustering decays at lower k than the suppression due to exclusion. This is actually what happens in the simulations as we will show in §9.5.

9.3.4. Density Threshold Bias

The spherical collapse model suggests that spherical Lagrangian regions exceeding the critical collapse density $\delta_{\mathrm{c}} \approx 1.686$ segregate from the background expansion and form gravitationally bound objects. Hence, the clustering statistics of regions above threshold can tell us something about the clustering of dark matter haloes and galaxies. The study of [2] considered the correlation function of regions whose density exceeds a certain value in a Gaussian random field, smoothed with a top-hat window of scale R. At the same time this paper pioneered bias models, which are nothing but a large scale expansion of the full correlation function of thresholded regions. Let us see how non-linear or non-perturbative clustering can affect the power spectrum on the largest scales in the full model.
The root mean square overdensity within the smoothed regions is given by

$$\sigma^2_R = \frac{1}{2\pi^2}\int \mathrm{d}k\, k^2 W^2_R(k) P_{\mathrm{lin}}(k). \tag{9.25}$$

The correlation of thresholded regions can be calculated exactly employing the two point probability density function of Gaussian random fields. For simplicity, we will consider regions of a fixed overdensity rather than regions above threshold. The peak height $\nu = \delta_{\mathrm{c}}/\sigma_R$ can be chosen based on the spherical collapse argument. For the correlation function of regions of fixed overdensity one obtains [19, 2]

$$1 + \xi_{\mathrm{tr}}(r) = \frac{1}{\bar{n}^2_{\mathrm{tr}}}\frac{1}{(2\pi)\sqrt{1-\xi^2_R(r)/\sigma^4_R}}\exp\left[-\nu^2\frac{1-\xi_R(r)/\sigma^2_R}{1-\xi^2_R(r)/\sigma^4_R}\right], \tag{9.26}$$

where $\bar{n}_{\mathrm{tr}} = 1/\sqrt{(2\pi)\sigma^2_R}\exp\left[-\nu^2/2\right]$. Here $\xi_R(r)$ is the linear correlation function smoothed on scale R. In the large distance, small correlation limit, the correlation function of the

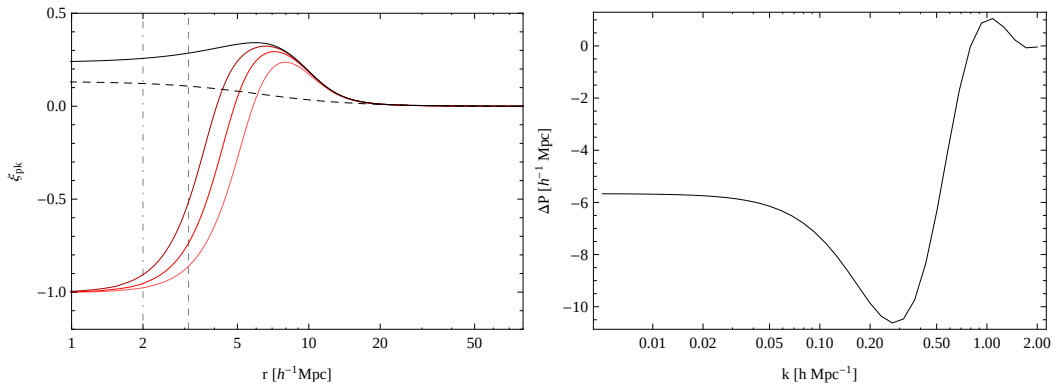

Figure 9.4.: Clustering of peaks in a one dimensional skewer through a density field smoothed with a Gaussian filter of scale $R = 2\ h^{-1}$Mpc ($M \approx 8.6 \times 10^{12}\ h^{-1} M_\odot$). *Left panel:* For fixed peak height the correlation function flattens out on small scales (black), but with increasing bin width the exclusion becomes stronger. The width of the bin in peak height increases from dark to light red. The linear local bias expansion is the same for all of these models and is shown by the dashed line. For reference we overplot the Gaussian smoothing (dash-dotted) and the top-hat smoothing scale containing the same mass (dashed). *Right panel:* Corresponding stochasticity correction $\Delta P_{\rm pk}(k) = {\rm FT}[\xi_{\rm pk}](k) - b_{1,\rm pk}^2 P_{\rm lin}(k)$ for the fiducial bin width.

thresholded regions can be approximated by a linearly biased version of the linear correlation function $\xi_{\rm tr}(r) = b_{1,\rm tr}^2 \xi_R(r)$ with $b_{1,\rm tr} \approx \nu/\sigma_R$. If one is interested in an accurate description of the non-perturbative correlation function on smaller scales, higher orders in the expansion need to be considered. Comparing the expansion of the correlation of thresholded regions in powers of the smoothed correlation to the full non-perturbative result in Eq. (9.26), we can investigate the convergence properties of the linear bias model. The left panel of Fig. 9.3 shows the correlation function of thresholded regions for a Gaussian random field smoothed on $R = 4\ h^{-1}$Mpc and the linearly biased versions of the smoothed and un-smoothed linear correlation functions.

We can now Fourier transform the correlation function of thresholded regions and subtract out the linearly biased power spectrum to obtain the correction introduced by the non-linear clustering

$$\Delta P_{\rm tr}(k) = {\rm FT}[\xi_{\rm tr}](k) - b_{1,\rm tr}^2 P_{\rm lin}(k). \tag{9.27}$$

As we show in Fig. 9.3, there is a non-vanishing correction in the $k \to 0$ limit that is approximately constant on large scales and goes to zero on small scales. The presence of such a correction was discussed in a slightly different context in [19].

In its original form, the thresholded regions are a continuous field and thus do not include any exclusion. One could however imagine that the patches defining the smoothing scale do not overlap. In this case the correlation function of thresholded regions should go to -1 for $r < 2R$. To show how the exclusion scale affects the correction in the power spectrum we consider a few exclusion radii smaller than two smoothing radii. As obvious in Fig. 9.3, increasing the smoothing scale first reduces the scale independent correction on large scales, compensates it completely and eventually leads to a negative scale independent correction for $r = 2R$.

9.3.5. Peak Bias Model

While the thresholded regions provide a continuous bias model, the peak model [20, 21] goes beyond in identifying a discrete set of points and providing the correlation function of these points. Most studies of the peak model to date have focused on the large separation limit [22, 23, 24], where closed form expressions for the peak correlation in terms of the underlying linear correlation function and its derivatives are possible. However, [25] calculated the one

dimensional peak correlation function for a set of power law power spectra and [26] computed the two dimensional peak correlation function for peaks in the CMB. The reason for the restriction to one or two dimensions owes to the dimensionality of the covariance matrix that needs to be inverted for the calculation of the peak correlation. In a one dimensional field the covariance matrix is a six by six matrix (field amplitude, first and second derivative at two points).
Here we consider realistic ΛCDM power spectra in three dimensions, smooth them on a realistic Lagrangian scale $R = 2\ h^{-1}$Mpc and evaluate the exact non-perturbative one dimensional correlation of peaks following the approach of [25] (see App. 9.7.2 for a brief review). Note that the correlation of field derivatives diverges for top-hat smoothing, which is why we follow common praxis and employ a Gaussian smoothing. The Gaussian smoothing makes the correlators of field derivatives well behaved but beyond that there is no physical motivation to employ this filter. We study a range of peak heights ν and also a range of bin widths in ν. The peak correlation function for four different bin widths is shown in the left panel of Fig. 9.4.
The first remarkable observation is that peaks of a fixed height don't seem to obey exclusion, only after considering a finite width in peak height, we can observe that the correlation function goes to -1 on small scales. The transition scale to the fixed peak height case increases with bin with, i.e., wider bins have a larger exclusion region. As above for the thresholded regions we can expand the peak correlation function in the large distance limit and obtain a bias expansion that has contributions from the underlying matter correlation function *and* correlation functions of the derivatives. Doing that, it becomes obvious, that the linear matter bias is only assumed outside of the BAO scale and that there is a distinct scale dependent bias that is partially described by the derivative terms in the bias expansion. Fourier transforming the full peak correlation function and subtracting out the linear biased power spectrum we obtain the correction shown in the right panel of Fig. 9.4. The qualitative behaviour agrees with the result obtained above for the thresholded sample with an ad hoc exclusion scale. On large scales there is a combination of clustering and exclusion effects, the clustering decays first and then also the exclusion correction goes to zero. Note that the projected one dimensional matter power spectrum scales as k^0 one large scales and thus doesn't vanish in the $k \to 0$ limit. This fact makes the distinction between clustering and stochasticity terms in the one dimensional peak model very difficult. We hope to report on results for the full three dimensional peak model in the near future.

9.4. Quantifying the Corrections

Let us now try to quantify the stochasticity corrections for a realistic halo sample. We expect the effect to be time independent in the $k \to 0$ limit if the same sample of particles is evolved under gravity. Thus, to minimize the influence of non-linearities, we will consider the protohaloes in Lagrangian space. In numerical studies of the effect, we will later define the protohalo as the initial ensemble of particles that form the Friends-of-Friends (FoF) haloes in our final output at redshift $z_\mathrm{f} = 0$.

9.4.1. Continuous Halo Power Spectrum from Local Bias

The local Lagrangian bias model assumes that the initial halo density field can be written as a Taylor series in the matter fluctuations at the same Lagrangian position $\boldsymbol{q}$

$$\delta_\mathrm{h}(\boldsymbol{q}, \eta_\mathrm{i}) = b_1^{(\mathrm{L})}(\eta_\mathrm{i})\delta(\boldsymbol{q}, \eta_\mathrm{i}) + \frac{b_2^{(\mathrm{L})}(\eta_\mathrm{i})}{2!}\delta^2(\boldsymbol{q}, \eta_\mathrm{i}) + \frac{b_3^{(\mathrm{L})}(\eta_\mathrm{i})}{3!}\delta^3(\boldsymbol{q}, \eta_\mathrm{i}) + \dots\ , \tag{9.28}$$

here η_i is the conformal time of the initial conditions and $\boldsymbol{q}$ is the Lagrangian coordinate. We will follow the approach of [27] where the smoothing scale is an unobservable scale, which should

not affect n-point clustering statistics on scales exceeding the smoothing scale. The above model can be used as the starting point for a coevolution of haloes and dark matter, which finally leads to a Eulerian bias prescription. Recently, such a calculation was shown to correctly predict non-local Eulerian bias terms [28, 29]. The peak-background-split (PBS) [30] makes predictions for the Lagrangian bias parameters in the above equation, and the corresponding late time Eulerian local bias parameters can then be obtained based on the spherical collapse model. There is some evidence that the peak model yields a better description of some aspects of the initial halo clustering than the local Lagrangian bias model. While we will briefly discuss these effects in App. 9.7.1, we refrain from using this model for the modelling of the stochasticity corrections, since the the peak bias expansion beyond leading order has not been studied in great detail and its implementation goes beyond the scope of this study.

For the continuous power spectrum in the initial conditions the local Lagrangian bias model predicts

$$P_{\mathrm{hh}}^{(\mathrm{c})}(k,\eta_{\mathrm{i}}) = \left(b_1^{(\mathrm{L})}\right)^2 D^2(\eta_{\mathrm{i}}) P_{\mathrm{lin},0}(k) + \frac{1}{2}\left(b_2^{(\mathrm{L})}\right)^2 D^4(\eta_{\mathrm{i}}) I_{22}(k), \tag{9.29}$$

where $D(\eta)$ is the linear growth factor and the scale dependent bias correction is described by

$$I_{22}(k) = \int \frac{\mathrm{d}^3 q}{(2\pi)^3} P_{\mathrm{lin},0}(q) P_{\mathrm{lin},0}(|\boldsymbol{k}-\boldsymbol{q}|). \tag{9.30}$$

This term leads to a positive k^0 contribution in the low-k regime. In this sense it deviates from typical perturbative contributions to the power spectrum, which start to dominate on small scales. For this reason, this term was partially absorbed into the shot noise by [27]. We will explicitly consider the term, since it describes the effect of non-linear clustering and is responsible for super-Poissonian stochasticity. The cross power spectrum between haloes and matter is given by

$$P_{\mathrm{hm}}^{(\mathrm{c})}(k,\eta_{\mathrm{i}}) = b_1^{(\mathrm{L})}(\eta_{\mathrm{i}}) D^2(\eta_{\mathrm{i}}) P_{\mathrm{lin},0}(k) \tag{9.31}$$

and does obviously not contain any second order bias corrections. This statement remains true if higher order biasing schemes are considered, since higher order biases only renormalise the bare bias parameters [27].

Truncating the bias expansion is only valid if $\left\langle \delta^2 \right\rangle \ll 1$, which is certainly satisfied on large scales in the initial conditions, but not necessarily on the scales relevant for halo clustering outside the exclusion radius. On these scales one might have to consider all the higher order local bias parameters. It is beneficial to calculate this effect in configuration space where the local bias model leads to a power series in the linear correlation function

$$\xi^{(\mathrm{c})}(r) = \sum \frac{\left(b_i^{(\mathrm{L})}\right)^2}{i!} D^{2i}(\eta_{\mathrm{i}}) \xi_{\mathrm{lin}}^i(r) \xrightarrow{\nu\to\infty} \exp\left[\frac{\nu}{\delta_{\mathrm{c}}}\xi_{\mathrm{lin}}(r)\right]. \tag{9.32}$$

The limit applies only in the high peak limit and Press-Schechter bias parameters [31]. We will restrict ourselves to the quadratic bias model since it can account for the main effects and since using higher order biasing schemes also requires more parameters to be determined. The Press-Schechter and Sheth-Tormen prescriptions provide a rough guideline for the scaling of bias with mass and redshift, but fail to provide correct predictions for the bias amplitude. Thus we obtain the bias parameters from fits to observables not affected by stochasticity (such as the halo-matter cross power spectrum) and obtaining higher order biases would require higher order spectra such as the bispectrum. Since our discussion is mostly in Lagrangian space we will drop the superscripts E and L from now on and absorb the growth factors into the linear power spectra and correlation functions.

bin	M	$R_{\rm excl}^{\rm (L)}$	$b_1^{\rm (L)}$	b_2	$b_1^{\rm (E)}$
I	1.14×10^{13}	2.6	7.80	1174.5	1.19
II	1.27×10^{13}	2.8	8.49	1206.0	1.22
III	1.42×10^{13}	2.8	9.24	1287.3	1.25
IV	1.62×10^{13}	3.0	10.70	1342.9	1.27
V	1.89×10^{13}	3.6	13.17	1357.7	1.31
VI	2.25×10^{13}	3.9	14.94	1404.2	1.38
VII	2.80×10^{13}	4.2	16.65	1635.7	1.45
VIII	3.72×10^{13}	4.9	21.92	1587.5	1.58
IX	5.65×10^{13}	5.8	29.42	1439.8	1.78
X	1.66×10^{14}	8.7	56.94	1346.5i	2.54

Table 9.1.: Mean masses, exclusion radii, first and second order Lagrangian and Eulerian bias parameters for our $z = 0$ halo sample. Masses are in units of $h^{-1}M_\odot$ and radii in units of h^{-1}Mpc. The mass dependence of these parameters is also plotted in Fig. 9.6. Note that the second order bias parameter is just a phenomenological fitting parameter used to get a reasonable representation of the correlation function. We do not claim that our fitting procedure yields an accurate second order bias parameter for the sample. For this purpose on has to employ the bispectrum, which yields second order bias parameters that are in much better agreement with the peak-background split expectation but fail to describe the correlation function.

9.4.2. Theory Including Clustering and Exclusion

We can now use the bias model introduced above to evaluate the discrete power spectrum Eq. (9.13). We have

$$P^{\rm (d)}(k) = \frac{1}{\bar{n}} + b_1^2 P_{\rm lin}(k) + \frac{1}{2} b_2^2 I_{22}(k) - b_1^2 V_{\rm excl}[W_R * P_{\rm lin}](k) - \frac{1}{2} b_2^2 V_{\rm excl}[W_R * I_{22}](k) - V_{\rm excl} W_R(k). \tag{9.33}$$

The splitting of I_{22}, the non-linear clustering term arising from b_2, is somewhat counterintuitive, since we expect this term to be active only outside the exclusion scale. Furthermore, there is no corresponding term in the halo-matter or matter-matter power spectra that would cancel the continuous I_{22}. Thus we combine the continuous part and the exclusion correction for the non-linear clustering term into a positive correction whose small scale contributions have been removed.

$$P^{\rm (d)}(k) = \frac{1}{\bar{n}} + b_1^2 P_{\rm lin}(k) + \frac{1}{2} b_2^2 I_{22}(k, R) - b_1^2 V_{\rm excl}[W_R * P_{\rm lin}](k) - V_{\rm excl} W_R(k). \tag{9.34}$$

Here we defined the correction term

$$I_{22}(k, R) = \int_R^\infty {\rm d}^3 r \; \xi^2(r) j_0(kr). \tag{9.35}$$

A simpler version of Eq. (9.34) has been presented in [11], where the non-linear clustering is neglected and the results are presented in Eulerian rather than Lagrangian space.
In the $k \to 0$ limit the Fourier transform simplifies to a spatial average over the correlation function

$$P^{\rm (d)}(k) \xrightarrow{k \to 0} \frac{1}{\bar{n}} + \frac{1}{2} b_2^2 \int_R^\infty {\rm d}^3 r \; \xi^2(r) - b_1^2 \int_0^R {\rm d}^3 r \; \xi(r) - V_{\rm excl}, \tag{9.36}$$

where the linear bias term vanishes due to $P_{\rm lin}(k) \xrightarrow{k \to 0} 0$. The fact that the integral over ξ^2 runs only from the exclusion scale to infinity mitigates the smoothing dependence of the correction, since smoothing on the scale of the halo affects the correlation function only on the halo scale, which is by definition smaller than the exclusion scale.

9.4.3. Stochasticity Matrix

We will now consider the power spectrum for a set of non-overlapping halo mass bins. We will consider their auto-power spectra and cross power spectra between different halo mass bins i and j and denote this quantity P_{ij}, whereas the cross power between a certain mass bin and the matter is denoted $P_{i\delta}$. The sum over equal pairs in Equation (9.19) is only present for the auto power spectra and thus the $1/\bar{n}$ shot noise affects only the diagonal entries of the power spectrum matrix $P_{ij}(k)$. On the other hand, exclusion affects also the off-diagonal matrix entries, since by definition also haloes of different mass are distinct objects and can thus not overlap. Furthermore, different mass haloes are affected by non-linear clustering, since the probability to find any sort of massive object ($M > M_*$) in the vicinity of a massive object is enhanced. For simplicity we will employ equal number density mass bins, which all have the same fiducial shot noise $1/\bar{n}$.
When trying to extract the amplitude and scale dependence of the noise, we need to remove all the contributions due to linear bias from the halo power spectra. For this purpose, we will employ the stochasticity matrix as defined in [5] (see also Eq. (9.15) for the definition of the diagonal)

$$(2\pi)^3\delta^{(\mathrm{D})}(\boldsymbol{k}+\boldsymbol{k}')C_{ij}(k) = \langle[\delta_i(\boldsymbol{k}) - b_{1,i}\delta(\boldsymbol{k})]\,[\delta_j(\boldsymbol{k}') - b_{1,j}\delta(\boldsymbol{k}')]\rangle\,, \tag{9.37}$$

such that we have in terms of the power spectra

$$C_{ij}(k) = P_{ij}(k) - b_{1,i}P_{\delta j}(k) - b_{1,j}P_{\delta i}(k) + b_{1,i}b_{1,j}P_{\delta\delta}(k). \tag{9.38}$$

The model introduced above can be straightforwardly generalized to multiple mass bins and their respective cross power spectra by the following replacements $b_1^2 \to b_{1,i}b_{1,j}$, $b_2^2 \to b_{2,i}b_{2,j}$ and $R \to R_{ij} = (R_i + R_j)/2$. The exact form of the combined exclusion radius is somewhat debatable, but for now we will employ the arithmetic mean. The resulting correction to the linear local bias model is given by

$$C_{ij}(k) = \frac{1}{\bar{n}}\delta_{ij}^{(\mathrm{K})} + \frac{1}{2}b_{2,i}b_{2,j}I_{22}(k, R_{ij}) - V_{\mathrm{excl},ij}W_{R_{ij}}(k) - b_{1,i}b_{1,j}V_{\mathrm{excl},ij}[W_{R_{ij}} * P_{\mathrm{lin}}](k), \tag{9.39}$$

where $V_{ij} = 4\pi/3R_{ij}^3$. We see that the definition of the stochasticity matrix removes all occurrences of the linearly biased power spectrum. In Eulerian space both P_{hm} and P_{hh} would have an additional contribution from $b_2 I_{12}$, where I_{12} describes the cross correlation between non-linear bias and non-linear matter clustering. The term is defined as

$$I_{12}(k) = \int \frac{\mathrm{d}^3q}{(2\pi)^3}P_{\mathrm{lin},0}(q)P_{\mathrm{lin},0}(|\boldsymbol{k}-\boldsymbol{q}|)F_2(\boldsymbol{q}, \boldsymbol{k}-\boldsymbol{q}), \tag{9.40}$$

where $F_2(\boldsymbol{q}_1, \boldsymbol{q}_2)$ is the standard perturbation mode coupling kernel [32]. The definition of the stochasticity matrix also removes all occurrences of I_{12}.

9.5. Evaluations and Comparison to Simulations

9.5.1. The Simulations & Halo Sample

Our numerical results are based on the Zürich horizon zHORIZON simulations, a suite of 30 pure dissipationless dark matter simulations of the ΛCDM cosmology in which the matter density field is sampled by $N_{\mathrm{p}} = 750^3$ dark matter particles. The box length of 1500 h^{-1}Mpc, together with the WMAP3 [33] inspired cosmological parameters ($\Omega_{\mathrm{m}} = 0.25, \Omega_\Lambda = 0.75$, $n_{\mathrm{s}} = 1, \sigma_8 = 0.8$), then implies a particle mass of $M_{\mathrm{p}} = 5.55 \times 10^{11}\ h^{-1}M_\odot$. The total simulation volume is $V \approx 100\ h^{-3}\mathrm{Mpc}^3$ and enables precision studies of the clustering statistics on scales up to a few hundred comoving megaparsecs.

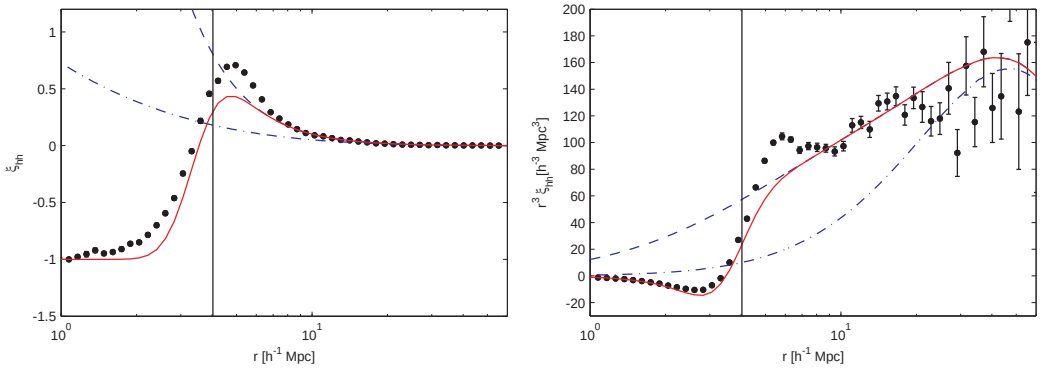

Figure 9.5.: Example of the halo-halo correlation function of the traced back haloes for mass bin V. The vertical solid line is the fitted exclusion radius. The dot-dashed line shows the linear bias contribution, whereas the dashed line shows linear plus quadratic bias. Note that the second order bias parameter was fitted to the correlation function and does deviate quite strongly from the PBS prediction. The red solid line shows a simple model for halo exclusion Eq. (9.43). In the right panel we show the integrand of the Fourier transform $r^3\xi_{\rm hh}(r)$, which is of essential importance for the stochasticity modelling.

The simulations were carried out on the ZBOX2 and ZBOX3 computer-clusters of the Institute for Theoretical Physics at the University of Zurich using the publicly available GADGET-II code [34]. The force softening length of the simulations used for this work was set to 60 h^{-1}kpc, consequently limiting our considerations to larger scales. The transfer function at redshift $z_{\rm f} = 0$ was calculated using the CMBFAST code of [35] and then rescaled to the initial redshift $z_{\rm i} = 49$ using the linear growth factor. For each simulation, a realization of the power spectrum and the corresponding gravitational potential were calculated. Particles were then placed on a Cartesian grid of spacing $\Delta x = 2\ h^{-1}$Mpc and displaced according to a second order Lagrangian perturbation theory. The displacements and initial conditions were computed with the 2LPT code of [36], which leads to slightly non-Gaussian initial conditions.

Gravitationally bound structures are identified at redshift $z_{\rm f} = 0$ using the B-FoF algorithm kindly provided by Volker Springel with a linking length of 0.2 mean inter-particle spacings. Haloes with less than 20 particles were rejected such that we resolve haloes with $M > 1.2 \times 10^{13}\ h^{-1}M_\odot$. The halo particles are then traced back to the initial conditions at $z_{\rm i} = 49$ and the corresponding centre of mass is identified. We split the halo sample into 10 equal number density bins with a number density of $\bar{n} = 3.72 \times 10^{-5} h^3{\rm Mpc}^{-3}$ leading to a shot noise contribution to the power at the level of $P_{\rm SN} \approx 2.7 \times 10^4\ h^{-3}{\rm Mpc}^3$.

9.5.2. The Correlation Function in Lagrangian Space

The corrections to the halo power spectrum in our model are motivated by certain features in the halo-halo correlation function. While the fiducial stochasticity affects the correlation function only at the origin, the two other effects, exclusion and non-linear clustering, should be clearly visible in the correlation function at finite distances. For this purpose we measure the correlation function of the traced back haloes for our 10 halo mass bins using direct pair counting.

In Fig. 9.5 we show the correlation function for mass bin V. The log-linear plot clearly shows that the correlation function is -1 on small scales and shows a smooth transition to positive values around the exclusion scale visualized by the vertical black line. The exclusion scale is fitted both in the initial and final conditions as 0.8 times the maximum in the correlation function and is shown in Fig. 9.6. The ratio between the initial and final exclusion radii is roughly 3 for all mass bins. The spherical collapse model suggests that haloes collapse by a factor 5, but

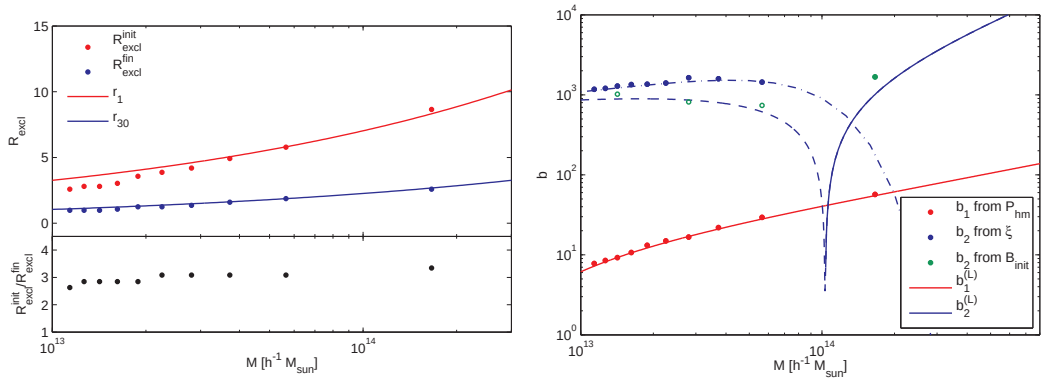

Figure 9.6.: *Upper left panel:* Exclusion radii measured in the initial and final halo-halo correlation functions. The exclusion radius is defined as a fixed fraction of the maximum in the halo-halo correlation function (see Fig. 9.5). The red line shows the naïve estimate of the exclusion radius $R = (3M/4\pi\bar{\rho})^{1/3}$, whereas the blue line shows $R = (3M/4\pi\bar{\rho}(1+\delta))^{1/3}$ with $\delta \approx 30$. This fitted overdensity is clearly distinct from the spherical collapse prediction of $\delta = 180$. *Lower left panel:* Ratio of the initial and final exclusion radii. *Right panel:* Bias parameters fitted from the halo-matter cross power spectrum (b_1), the halo-matter bispectrum and the correlation function (b_2). Note that b_2 fitted from the correlation function deviates strongly from the value predicted by the peak-background split (blue solid and dashed for positive and negative) and the value inferred from the bispectrum. The dash-dotted lines show a fit used for extrapolation purposes.

there is no reason to believe that protohaloes that are in direct contact in Lagrangian space are still touching each other in Eulerian space. Thus it is reasonable to expect a somewhat smaller reduction in the exclusion scale. On large scales 30 h^{-1}Mpc $< r <$ 90 h^{-1}Mpc the correlation function is reasonably well described by linear bias shown in the Figure as a dot-dashed line. We infer the linear bias parameter from the ratio of halo-matter cross power spectrum and matter power spectrum on scales $k < 1.5 \times 10^{-2}$ hMpc^{-1}

$$\hat{b}_{1,\mathrm{hm}} = \frac{\hat{P}_{\mathrm{hm}}}{\hat{P}_{\mathrm{mm}}}. \tag{9.41}$$

See Fig. 9.14 and App. 9.7.1 for why we have to restrict the linear bias fitting to large scales even in the initial conditions. The advantage of the cross power spectrum is that it should be free of stochasticity contributions and fully described by linear bias [37] on large scales.
There is a clear enhancement of the data in Fig. 9.5 compared to the linear bias model on small scales. Thus we consider the quadratic bias model

$$\xi^{(\mathrm{c})}_{\mathrm{hh}}(r) = b_1^2 \xi_{\mathrm{mm,lin}}(r) + \frac{1}{2} b_2^2 \xi^2_{\mathrm{mm,lin}}(r) \tag{9.42}$$

and fit for the quadratic bias parameter on scales exceeding the maximum. The resulting continuous correlation function is shown as the dashed line in Fig. 9.5. It does not fully account for the enhanced clustering outside the exclusion scale. The inferred bias parameters are shown in Fig. 9.6 and will be discussed in more detail below. Note that the above fit is performed using an un-smoothed version of the linear correlation function, whereas the local bias model relies on an explicit smoothing scale. Here, we argue that the smoothing scale for the local bias model should be related to the Lagrangian scale of the haloes and thus be smaller than the exclusion scale. In this case, the smoothing scale does typically not affect the scale dependence of the correlation function (except for around the BAO scale).
In our above discussion we have assumed a sharp transition between the exclusion regime and the clustering regime. This is certainly unphysical as is obvious in Fig. 9.5. The smoothness is probably caused by a number of phenomena, for instance mass variation within the mass bins

(should be quite small $< 1.3\ h^{-1}$Mpc for the highest mass bin which has $R \approx 8\ h^{-1}$Mpc and even smaller for the lower mass bins) or alignment of triaxial haloes. The lack of a physically motivated, working model for the transition forces us to employ a somewhat ad hoc functional form for the step, which is based on a lognormal distribution of halo distances (see App. 9.7.3)

$$\xi_{\rm hh}^{\rm (d)}(r) = \frac{1}{2}\left[1 + {\rm erf}\left(\frac{\log_{10}(r/R)}{\sqrt{2}\sigma}\right)\right]\left[\xi_{\rm hh}^{\rm (c)}(r) + 1\right] - 1. \tag{9.43}$$

For alternative implementations of exclusion windows in the context of the halo model see [38, 39]. The resulting shape of the correlation function is shown as the red solid line, where the smoothing was chosen to be $\sigma \approx 0.09$ and seems to be quite independent of halo mass. The model clearly underestimates the peak in the data in the log-linear plot. Our final goal is to construct an accurate model for the effect of exclusion and non-linear clustering on the power spectrum. Thus, we should not only check the validity of our model on plots of the correlation function itself but also on the integrand in the Fourier integrals $r^3\xi_{\rm hh}(r){\rm d}\ln r$. We do so in the right panel of Fig. 9.5, where it is obvious that the model does not reproduce the exact shape of the correlation function outside of the exclusion scale. However, we certainly improved over the naive linear biasing on all scales and obtained a reasonable parametrization of exclusion and non-linear clustering effects.

Let us now come back to the mass dependence of the inferred bias and exclusion parameters. As we show in Fig. 9.6, the linear bias b_1 is in very good agreement with the bias parameters inferred from a Sheth-Tormen mass function [40] rescaled to the initial conditions at $z_{\rm i} = 49$. For the second order bias we compare the measurement from the correlation function to measurements from the bispectrum of the protohaloes and the second order bias inferred from the Sheth-Tormen mass function. The latter agrees reasonably well with the bispectrum measurement reproducing the zero crossing in the theoretical bias function. Note that the bispectrum measurement (for details of the approach see [28]) uses only large scale information and is thus a clean probe for second order bias. Isolating second order bias effects in the correlation function is less straightforward. With decreasing scale higher and higher bias parameters become important, and to our knowledge there is no established scale down to which a certain order of bias can be trusted to a given precision. Our fitting procedure was led by the goal of obtaining a good parametrization of the correlation function, which could subsequently be used to calculate the corresponding power spectra and the corrections to the linear bias model. Note that due to the functional form of Eq. (9.42) this fitting approach allows inference of the magnitude of b_2, but not its sign. The second order bias parameters obtained in this way deviate significantly from the theoretical bias function and the bispectrum measurement. The most severe failure of the model is the imaginary b_2 for the highest mass bin. In this case the deviation is connected to corrections arising from the peak constraint, as we explain in App. 9.7.1. We find that the initial Lagrangian second order bias parameter in Fig. 9.6 can be roughly fitted as follows

$$b_2 = 1100\left(\frac{M}{10^{13}\ h^{-1}M_\odot}\right)^{0.35}\exp\left[-\left(\frac{M}{10^{14}\ h^{-1}M_\odot}\right)^2\right]. \tag{9.44}$$

We will use this fitting function for extrapolation in mass and redshift in §9.5.4. The initial second order bias parameters for halo samples identified at higher redshifts ($z = 0.5$ and $z = 1$) are roughly the same as for the $z = 0$ halo sample.

Although we will use this b_2 fit to predict the resulting stochasticity corrections, we do not believe that the observed scale dependence of the correlation function is solely a second order bias effect. We checked an expansion of Eq. (9.42) to higher orders in the correlation function using peak-background split bias parameters. Even up to tenth order there is no considerable improvement in the fit. Thus we argue that the enhancement is a non-perturbative effect (e.g. peak bias) and consider the ξ^2 scale dependence as a reasonably well working phenomenological

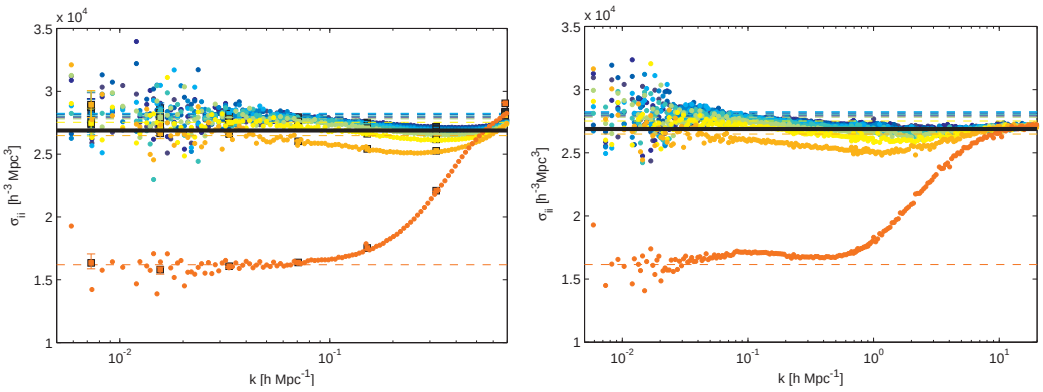

Figure 9.7.: Diagonals of the stochasticity matrix σ_{ij}. *Left panel:* Initial conditions $z_\mathrm{i} = 49$ *Right panel:* Final field $z_\mathrm{f} = 0$. There is remarkable agreement in the large scale amplitude between initial conditions and final field besides the strong difference in the bias parameters and growth factors. We highlight this fact by the horizontal dashed lines that have the same amplitude in both panels and are matched to the large scale stochasticity matrix in the initial conditions. For both panels, there is clear evidence for stochasticity going to fiducial $1/\bar{n}$ for high wavenumbers, and a modification due to exclusion and clustering for $k \leq 1/R$, where R is the scale of the halo at the corresponding redshift. Note the different scaling of the k-scale in the two plots. The mass increases from blue to orange, i.e., top to bottom.

parametrization rather than a physical truth. We hope to shed more light on this issue in a forthcoming paper.

9.5.3. Stochasticity Matrix

In Fig. 9.7 we show the diagonals of the stochasticity matrix measured in our simulations in Lagrangian space ($z_\mathrm{i} = 49$) and Eulerian space ($z_\mathrm{f} = 0$). The most remarkable observation in this plot is the agreement between the results, given the different amplitude of the growth factors and the linear bias parameters at these two times. This is a result of the fact, that gravity can not introduce or alter k^0 dependencies [41] due to mass and momentum conservation. This can for instance be seen in the low k-limit of standard perturbation theory [32]: The mode coupling term P_{22} is a gravity-gravity correlator and thus scales as k^4, whereas the propagator term P_{13} is a gravity-initial condition correlator and scales as $k^2 P_\mathrm{lin}$.
For the highest mass bin there is a clear suppression of the noise level on the largest scales which then asymptotes to the fiducial value $1/\bar{n}_\mathrm{h}$ at a scale $k \approx 1/R \approx 0.3\ h\mathrm{Mpc}^{-1}$. Since the radius of the halo shrinks during collapse, this scale is found at a higher wavenumber in Eulerian space. For the less massive haloes the behavior is not completely monotonic. On large scales we find a noise level slightly exceeding the fiducial value. Going to higher wavenumbers the fiducial value is crossed, the residual reaches a minimum and finally asymptotes to $1/\bar{n}$. This behavior can be explained as follows: the clustering scale exceeds the exclusion scale and as we have argued in §9.3.3, the enhanced correlation on the clustering scale leads to a positive contribution on the largest scales that decays for lower wavenumbers than the negative exclusion correction.
The wavenumber at which the stochasticity asymptotes to its fiducial value in the final field is at fairly high wavenumbers, exceeding the Nyquist frequencies of both $N_\mathrm{c} = 512$ and $N_\mathrm{c} = 1024$ grids. To probe smaller scales we employ a mapping technique [42, 43] that allows us to resolve small scales without having to increase the grid size beyond $N_\mathrm{c} = 512$. The technique consists of splitting the box into n parts per dimension and adding these parts to the same grid. This allows inference of each l-th mode but also increases the Nyquist frequency by a factor l. We use several different mapping factors $l = 4, 6, 12, 20, 50$ to probe all the scales up

to $k \approx 20\ h\mathrm{Mpc}^{-1}$.
In Fig. 9.8 we show the diagonals of the stochasticity matrix for one and two mass bins respectively. For the one bin case we select all the haloes in our simulation, effectively combining all the ten mass bins resulting in $M_{1\mathrm{bin}} = 3.84 \times 10^{13}\ h^{-1} M_{\odot}$. For the two bin case we combine the five lightest and the five heaviest mass bins resulting in masses $M_{2\mathrm{bin,I}} = 1.47 \times 10^{13}\ h^{-1} M_{\odot}$ and $M_{2\mathrm{bin,II}} = 6.21 \times 10^{13}\ h^{-1} M_{\odot}$. The plot shows both the initial condition and the final stochasticity and the two agree very well in the low-k limit. The stochasticity correction does not depend on the fiducial stochasticity and thus the scale dependence of the total stochasticity is more pronounced in the wider mass bins due to their lower fiducial shot noise. Interestingly the stochasticity correction for the 1-bin case vanishes in the low-k limit, but is negative in the intermediate regime. This is a sign of a perfect cancellation between exclusion and non-linear clustering. The final stochasticity seems to be a k-rescaled version of the initial stochasticity. Finally, let us stress that the power spectrum of the wide bins can not be obtained by a summation of the contributing bin-power spectra from the ten bin case since one has to account for the off-diagonal components of the stochasticity matrix.
In the left panel of Fig. 9.10 we compare our model Eq. (9.39) to the measured stochasticity matrix of the ten bins in the initial conditions. The only modification to the model is that we replace the hard cutoff by the smoothed transition Eq. (9.43). We employ the parameters obtained in the fit to the corresponding halo correlation functions in §9.5.2. The data points in the plot are copied from Fig. 9.7. Given the differences between the model and the correlation functions in Fig. 9.5, there is a reasonably good agreement both in large scale amplitude and scale dependence of the stochasticity correction. We can conclude that while being a relatively crude fit to the correlation function, our model can account for the major effects, exclusion and non-linear clustering. The drawback is that this model lives in Lagrangian space and can not be straightforwardly applied to the halo power spectrum in Eulerian space.
In Fig. 9.15 we show the off-diagonal terms of the stochasticity matrix in the initial conditions and our corresponding model predictions. As for the diagonals discussed above, the corrections can be either positive or negative, depending on whether exclusion or nonlinear clustering dominates The model predictions are in reasonable agreement with the measurements except for the highest mass bin. This failure is connected to the fact that the b_2 parameter for the highest mass bin is imaginary, i.e., we have to set the second order bias term in the cross correlations to zero. This is a severe problem of our overly simplistic model, which is related to the importance of the peak effects for the correlation function of the highest mass bin (see App. 9.7.1).
Let us try to gain some more insight on where the stochasticity corrections arise in Lagrangian and Eulerian space. For this purpose we consider the configuration space version of the diagonal of the stochasticity matrix defined in Eq. (9.38)

$$C_{ii}(r) = \xi_{ii}(r) - 2b_{1,i}\xi_{i\delta}(r) + b_{1,i}^2 \xi_{\delta\delta}(r). \tag{9.45}$$

The stochasticity level in the $k \to 0$ limit is then given by

$$C_{ij}(k) \xrightarrow{k\to 0} \int_0^\infty \mathrm{d}\ln r\ r^3 \sigma_{ij}(r). \tag{9.46}$$

In Fig. 9.9, we show the above integral as a function of the upper integration boundary where the full large scale stochasticity correction would be obtained by taking this boundary to infinity. Comparing the contributions in the initial conditions and the final configuration, we clearly see that the large scale stochasticity arises on different scales at the two times. We clearly see that the negative stochasticity corrections are dominated at much smaller scales in the final configuration as compared to the initial conditions. At these scales the halo-matter and matter-matter correlation functions are dominated by the one halo term, i.e., the halo profile, which complicates quantitative predictions of the exclusion effect in the final configuration and motivates our Lagrangian approach.

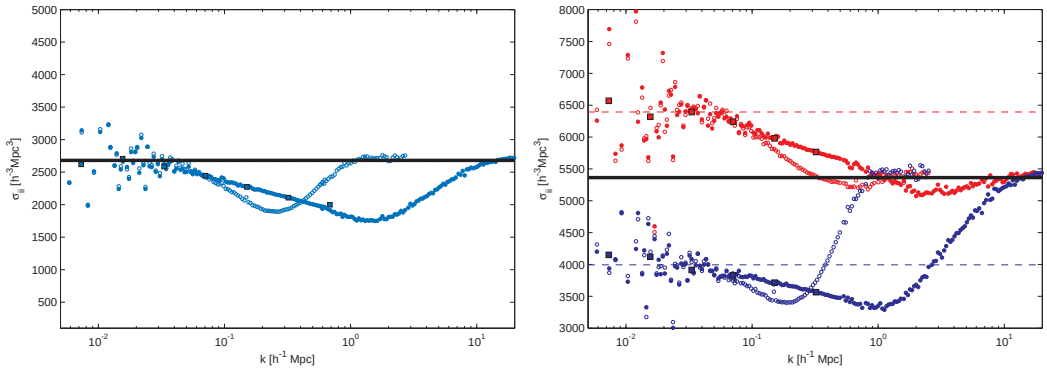

Figure 9.8.: *Left panel:* Diagonals of the stochasticity matrix for one mass bin containing all the haloes in our simulation. Open points show the initial condition measurement, whereas the filled points show the final value. The horizontal thick solid line shows the fiducial shot noise $1/\bar{n} = 2680\ h^{-1}$Mpc. The Eulerian bias is $b_1^{(\mathrm{E})} = 1.49$. On the largest scales there seems to be a cancellation between the exclusion and non-linear clustering contributions resulting in no net correction to the fiducial shot noise. *Right panel:* Same as left panel but for splitting our haloes into two mass bins with equal number density. The upper red points are the measurement for the lighter, lower bias bin $b_1^{(\mathrm{E})} = 1.25$ and the lower blue points are for the more massive, higher bias bin $b_1^{(\mathrm{E})} = 1.74$. The fiducial shot noise is $1/\bar{n} = 5362\ h^{-1}$Mpc. Note that both mass bins show a significant scale dependence of the stochasticity.

9.5.4. Redshift and Mass Dependence of the Correction

The subtraction of the fiducial $1/\bar{n}$ shot noise from the power spectrum will lead to a biased estimate of the continuous halo power spectrum. Thus, estimating the bias as

$$\hat{b}_{1,\mathrm{hh}} = \sqrt{\frac{\hat{P}_{\mathrm{hh}} - 1/\bar{n}}{\hat{P}_{\mathrm{mm}}}} \tag{9.47}$$

will lead to a flawed estimate of the bias. Indeed, it has been found in simulations that the biases estimated from the auto- and cross-power spectra are generally not in agreement [44, 45]. Studying for instance Table I in [45] we see that $\hat{b}_{1,\mathrm{hh}}$ exceeds $\hat{b}_{1,\mathrm{hm}}$ for low mass haloes at redshift 0 indicating that the fiducial shot noise subtraction underestimates the true noise level. For high mass objects the opposite happens, the bias from the cross-power exceeds the bias from the auto power indicating that the employed $1/\bar{n}$ shot noise subtraction overestimates the true noise level.

Let us try to understand this effect in more detail. Based on our model, subtraction of the fiducial shot noise on large scales leaves us with the linear bias term plus the stochasticity correction

$$\hat{P}_{\mathrm{hh}}(k) - \frac{1}{\bar{n}} = \Delta P_{\mathrm{hh}}(k) + b_1^2 P_{\mathrm{lin}}(k) = \hat{b}_{1,\mathrm{hh}}^2 \hat{P}_{\mathrm{mm}}(k), \tag{9.48}$$

where in absence of shot noise in the cross-power spectrum $b_1 = \hat{b}_{1,\mathrm{hm}}$. Thus we have for systematic error on the linear bias parameter

$$\frac{\Delta b_1}{b_1} = \frac{\hat{b}_{1,\mathrm{hh}}}{b_1} - 1 \approx \frac{1}{2}\frac{\Delta P_{\mathrm{hh}}}{b_1^2 P_{\mathrm{mm}}} \tag{9.49}$$

Consequently the ratio $\hat{b}_{1,\mathrm{hh}}/\hat{b}_{1,\mathrm{hm}}$ is a function of mass and redshift due to the mass and redshift dependence of the parameters of the model. We show the k-dependence of the bias correction in Fig. 9.10. Since we don't have a reliable model to relate the scale dependent stochasticity matrix from Lagrangian space to the one in Eulerian space we employ the scale dependent stochasticity model from Lagrangian space but divide by the present day linear power

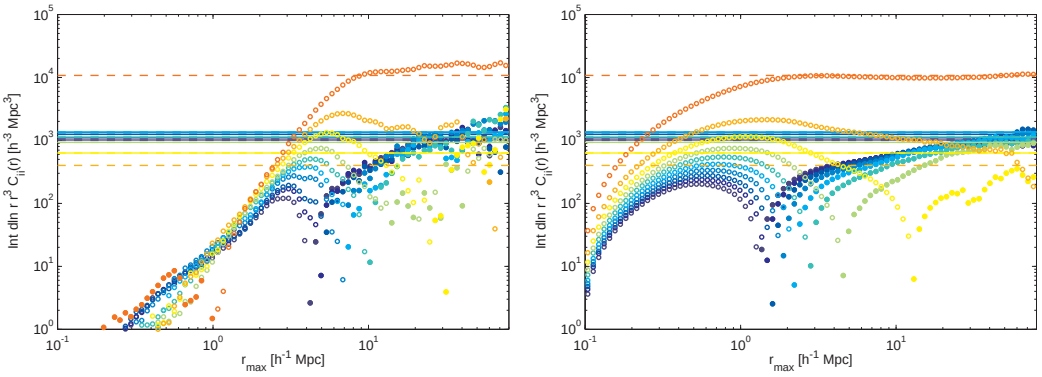

Figure 9.9.: Cumulative contributions to the stochasticity correction up to scale r (see Eq. 9.46) in configuration space for our 10 mass bin sample. Open symbols show negative contributions and filled symbols positive contributions. *Left panel:* Initial conditions. *Right panel:* Final configuration at $z = 0$. We clearly see, that the corrections in the initial conditions are dominated on larger scales than in the final configuration, where the negative corrections are clearly in the one halo regime, where both the halo-matter and matter-matter correlation functions are highly non-linear. This gives further motivation for the modelling of the effect in Lagrangian space. The horizontal solid (dashed) lines show the positive (negative) stochasticity corrections inferred from Fig. 9.7.

spectrum. This procedure should provide a reasonable estimate for the bias corrections on large scales. The linear bias is usually estimated close to the peak of the linear power spectrum, where it is approximately flat and where non-linear corrections are believed to be negligible. As a result, the bias correction is also fairly flat and would lead to a 1% overestimation of bias for low mass objects and a $3-4\%$ underestimation for clusters. This behaviour can qualitatively explain the deviations found in [45].

In Fig. 9.11 we show the amplitude of the low-k limit of the stochasticity correction for ten equal halo mass bins at redshifts $z = 0, 0.5, 1$. We overplot the theoretical expectation based on our model, linear bias parameters from the peak background split and second order bias parameters obtained from our phenomenological b_2 relation in Eq. (9.44). In particular, we calculate the Lagrangian bias parameters and exclusion radii corresponding to the halo samples at $z = 0, 0.5, 1$ and use them to predict the stochasticity correction. As a general result we can see that there is a negative correction for high masses and a positive correction for low masses with a zero crossing scale that decreases with increasing redshift. The model captures the trends in the measurements relatively well. We are also overplotting the low-k amplitude of the SN for the one and two bin samples at $z = 0$ as the squares and diamonds. Besides the fact that these bins are much wider and thus have lower fiducial shot noise, the low-k amplitude is in accordance with the model and also narrower mass bins of the same mass. This fact supports our conjecture, that the stochasticity correction does not depend on the fiducial shot noise, but rather on mass (via the exclusion scale and the linear and non-linear bias parameters). The negative correction for high masses is dominated by the exclusion term, whose amplitude depends on the linear bias parameter and the exclusion scale. The latter is a function of mass but not a function of redshift, whereas the bias increases with redshift and thus the negative correction at high masses also increases with redshift. The positive correction at the low mass end depends on the second order bias parameter. In our fits to the correlation function we found that this parameter is roughly constant for the three different redshifts under consideration.

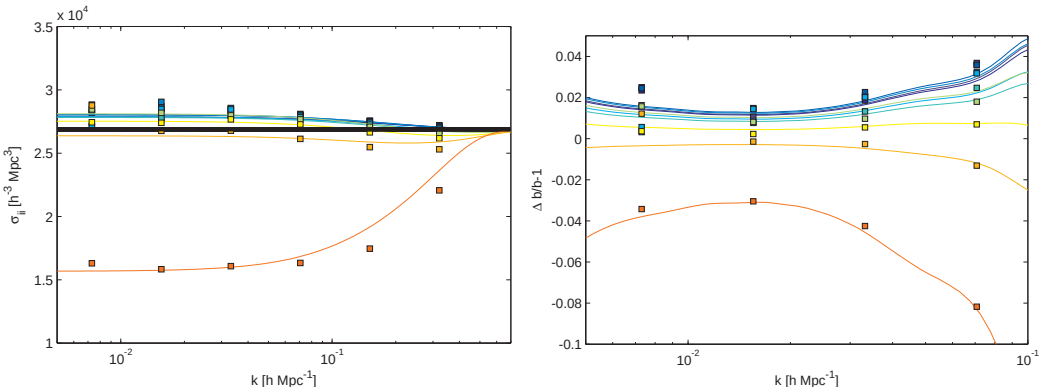

Figure 9.10.: *Left panel:* Theoretical prediction for the diagonals of the stochasticity matrix for the ten mass bins. The parameters b_2 and R are measured from the correlation function. The points are the coarsly binned simulation measurement taken from the left panel of Fig. 9.7. *Right panel:* Bias correction as defined in Eq. (9.49). While there is clear scale dependence for weakly non-linear wavenumbers $k > 0.1\ h\mathrm{Mpc}^{-1}$ the correction is fairly flat on large scales, where the cosmic variance errors are largest. It could thus be easily interpreted as a higher or lower bias value. The points show the relative deviation of the bias inferred from the halo-halo power spectrum in the final configuration from the bias inferred from the halo-matter cross power spectrum.

9.5.5. Eigensystem and Combination of Mass Bins

The stochasticity matrix can be diagonalized as

$$\sum_j \sigma_{ij} V_j^{(l)} = \lambda^{(l)} V_i^{(l)} \tag{9.50}$$

where $V_i^{(l)}$ are the eigenvectors and $\lambda^{(l)}$ the corresponding eigenvalues. The eigenvector corresponding to a low eigenvalue can be used as a weighting function in order to construct a halo sample that has the lowest possible stochasticity contamination [5]. Furthermore, the eigenvalues allow for a clean separation of the exclusion and clustering contributions to the total noise correction. We show the measurement and comparison to our model in Fig. 9.12. The data show pronounced low and high eigenvalues with most of the eigenvalues identical to the fiducial shot noise. The high eigenvalue is probably related to the non-linear clustering and the low eigenvalue to exclusion. The model also predicts eight of the ten eigenvalues to agree with the fiducial shot noise as well as one high and one low eigenvalue. The exact agreement is not perfect, which is probably due to an imperfect representation of the off-diagonal stochasticity terms. The main problem with the off-diagonals is to estimate the exclusion radii. The right panel of Fig. 9.12 shows the eigenvectors corresponding to the eigenvalues. The eigenvector corresponding to the low eigenvalue is clearly connected to the mass, i.e., the exclusion volume, whereas the eigenvector corresponding to the high eigenvalue is clearly connected to the second order bias.

So far we have concentrated on the stochasticity correction for narrow mass bins and quantified them in terms of the corresponding stochasticity matrix. If all the corrections were linear in the parameters of the model, all we needed to do is to calculate the corresponding mean parameters of the sample and use them to calculate the stochasticity correction for the combined sample. However, the corrections are in general a non-linear function of the parameters. The wider the mass bins the less exact is a bulk description by a set of mean parameters. It should be more exact to consider subbins and combine them. Thus we need to calculate the stochasticity correction for narrow mass bins $M \in [\underline{M}_i, \overline{M}_i]$ $i = 1, \ldots, h$. Then, when considering samples that span a wide range of halo masses or realistic galaxy samples, we need to weight the

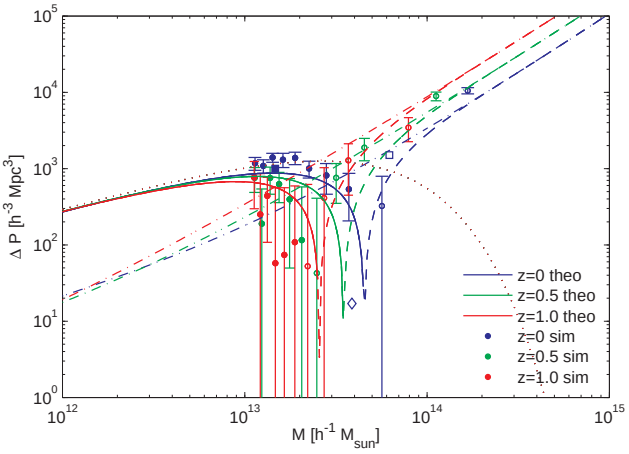

Figure 9.11.: Dependence of the stochasticity correction on halo mass and redshift. The lines are based on linear bias parameters from the peak-background split and a fitting function modelling b_2. The dashed lines and open points describe negative values. We also include the low-k limits of the one and two bin splitting as the diamond and squares, respectively. The dotted line shows the positive low mass correction arising from non-linear biasing whereas the dash-dotted blue, green and red lines show the negative high mass exclusion corrections for the three different redshifts.

prediction for the stochasticity correction accordingly. The weighted density field is then

$$\tilde{\delta} = \frac{\sum_i w_i \delta_i}{\sum_i w_i} \tag{9.51}$$

and the corresponding noise level of the combined sample is given by

$$\tilde{\sigma} = \frac{\sum_{ij} w_i \sigma_{ij} w_j}{\left(\sum_i w_i\right)^2}. \tag{9.52}$$

For halo samples the weighting is given by the mean number density in a mass bin

$$w_i = \int_{\underline{M}}^{\overline{M}} \mathrm{d}M n(M). \tag{9.53}$$

A similar weighting scheme can be derived for galaxies for the two-halo term in the context of the halo model.

9.5.6. A realistic Galaxy Sample

Let us now see how the stochasticity matrix behaves for a realistic galaxy sample. In Halo Occupation Distribution (HOD) models [48, 49] the occupation number $N_\mathrm{g}(M)$ is usually split into a central and a satellite component $N_\mathrm{g} = N_\mathrm{c} + N_\mathrm{s}$. In Fig. 9.13 we show the stochasticity of the Luminous Red Galaxy (LRG) sample described in [46, 47]. The total number density of the LRGs is $\bar{n}_\mathrm{g} = 7.97 \times 10^{-5}\ h^{-3}\mathrm{Mpc}^3$ corresponding to a fiducial shot noise of $1/\bar{n}_\mathrm{g} \approx 1.25 \times 10^4\ h^{-3}\mathrm{Mpc}^3$. The effective stochasticity level for the full sample is $\mathrm{SN}_\mathrm{eff} = 1.09 \times 10^4\ h^{-3}\mathrm{Mpc}^3$, corresponding to a correction of $\Delta P_\mathrm{gg} = -1.8 \times 10^3\ h^{-3}\mathrm{Mpc}^3$. The satellite fraction of the galaxy sample is 4.9%.
Let us try to understand the total correction based on the constituent central, satellite and central-satellite cross-power spectra. The sum of these three components weighted according to Eq. (9.24) agrees with the measured stochasticity of the full sample. The central-central power spectrum dominates the negative stochasticity correction on large scales with a weighted

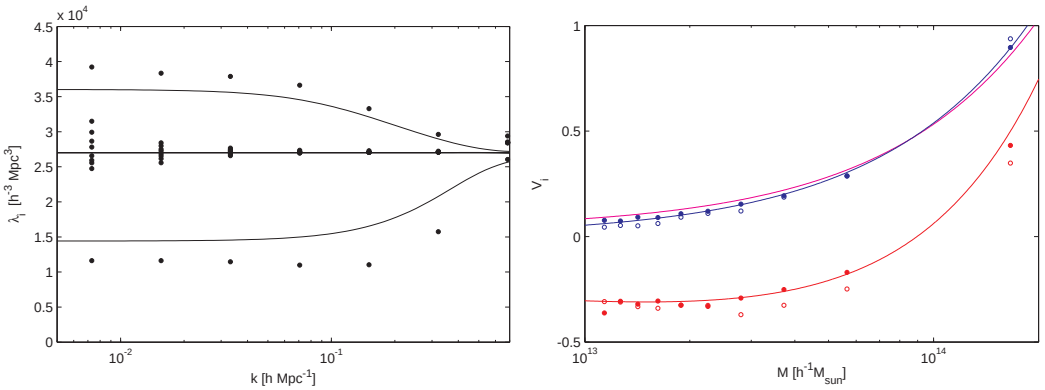

Figure 9.12.: *Left panel:* Eigenvalues of the stochasticity matrix for the traced back $z = 0$ haloes. The lines show our prediction based on the modelling of the initial correlation function whereas the points are based on the diagonalization of the measured stochasticity matrix of the traced back haloes. *Right panel:* Eigenvectors in the $k \to 0$ limit. The black and red filled points show the measured eigenvectors for the lowest and highest eigenvalue in the initial conditions, whereas the open points show the respective prediction of our model. The blue line shows mass weighting, the red line b_2-weighting and the magenta line shows the modified mass weighting proposed by [5].

correction of $(1 - f_\mathrm{s})^2 \Delta P_\mathrm{cc} = -2100\ h^{-3}\mathrm{Mpc}^3$ The satellite-satellite power spectrum has a positive one halo contribution on large scales that contributes a weighted correction of $f_\mathrm{s}^2 \Delta P_\mathrm{ss} = +570\ h^{-3}\mathrm{Mpc}^3$ The central-satellite cross power spectrum changes sign but contributes about $\Delta P_\mathrm{cs} = -370\ h^{-3}\mathrm{Mpc}^3$ at $k = 0.03\ h\mathrm{Mpc}^{-1}$. The amplitude of these corrections could in principle be understood based on a accurate model for the stochasticity correction of the host haloes and the halo model. In this context the corrections are given as [14, 15]

$$P_\mathrm{cc}^{(1\mathrm{h})}(k) = \frac{1}{\bar{n}_\mathrm{c}} \tag{9.54}$$

$$P_\mathrm{ss}^{(1\mathrm{h})}(k) = \frac{1}{\bar{n}_\mathrm{s}} + \frac{1}{\bar{n}_\mathrm{s}^2} \int \mathrm{d}M n(M) N_\mathrm{s,h}(M) \left[N_\mathrm{s,h}(M) - 1\right] u^2(k|M) \Theta(N_\mathrm{s,h} - 1) \tag{9.55}$$

$$P_\mathrm{cs}^{(1\mathrm{h})}(k) = \frac{1}{\bar{n}_\mathrm{c} \bar{n}_\mathrm{s}} \int \mathrm{d}M n(M) N_\mathrm{c,h}(M) N_\mathrm{s,h}(M) u(k|M) \Theta(N_\mathrm{s,h} - 1) \tag{9.56}$$

$$P_\mathrm{cc}^{(2\mathrm{h})}(k) = \frac{1}{\bar{n}_\mathrm{c}^2} \int \mathrm{d}M n(M) N_\mathrm{c,h}(M) \int \mathrm{d}M' n(M') N_\mathrm{c,h}(M') P_\mathrm{hh}(k|M, M') \tag{9.57}$$

$$P_\mathrm{ss}^{(2\mathrm{h})}(k) = \frac{1}{\bar{n}_\mathrm{s}^2} \int \mathrm{d}M n(M) N_\mathrm{s,h}(M) u(k|M) \int \mathrm{d}M' n(M') N_\mathrm{s,h}(M') u(k|M') P_\mathrm{hh}(k|M, M') \tag{9.58}$$

$$P_\mathrm{cs}^{(2\mathrm{h})}(k) = \frac{1}{\bar{n}_\mathrm{s} \bar{n}_\mathrm{c}} \int \mathrm{d}M n(M) N_\mathrm{c,h}(M) \int \mathrm{d}M' n(M') N_\mathrm{s,h}(M') u(k|M') P_\mathrm{hh}(k|M, M') \tag{9.59}$$

On large scales we have $u(k|M) \to 1$. Furthermore the halo-halo power spectra can be again split into a linear bias part $b(M)b(M')P(k)$ and a correction term accounting for the discreteness of the host haloes. For the central galaxy sample our model yields a correction of $\Delta P_\mathrm{cc} \approx -1000\ h^{-3}\mathrm{Mpc}^3$. More accurate predictions would require a better model of the stochasticity corrections, which in turn requires a better model of exclusion and non-linear biasing.

We also consider a slightly modified galaxy sample with a larger satellite fraction $f_\mathrm{s} = 8.47\%$. For this purpose we create a copy of each satellite galaxy at twice its separation from the host halo centre. The resulting stochasticity properties are shown in the right panel of Fig. 9.13. In contrast to the previous case the actual stochasticity now exceeds the fiducial shot noise due to the strong positive contribution of the satellite-satellite one halo term.

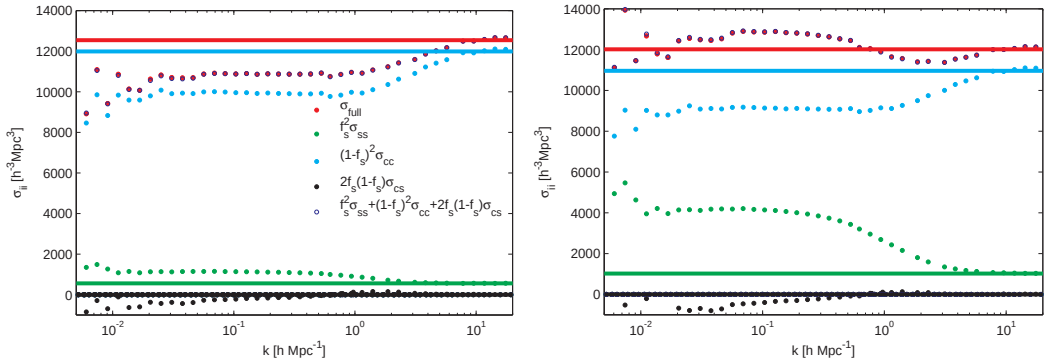

Figure 9.13.: Stochasticity of an HOD implementation of a Luminous Red Galaxy sample. We split the sample into the central-central (cyan), satellite-satellite (green) and central-satellite (black) contributions. The constituent stochasticity levels are weighted according to their contribution to the full galaxy power spectrum (see Eq. 9.24). The horizontal thick lines show the correspondingly weighted fiducial stochasticity. *Left panel:* Halo occupation distribution model with a satellite fraction of $f_s = 4.9\%$ ([46, 47]). *Right panel:* Same as left panel, but for a satellite fraction of $f_s = 8.5\%$.

9.6. Conclusions

In this paper we discuss effects of the discreteness and non-linear clustering of haloes on their stochasticity in the power spectrum. The standard model for stochasticity is the Poisson shot noise model with stochasticity given as the inverse of the number density of galaxies, $1/\bar{n}$. Motivated by the results in [5], we study the distribution of haloes in Lagrangian space and estimate the effect of exclusion and non-linear clustering of protohaloes on the stochasticity. These induce corrections relative to $1/\bar{n}$ in the low-k limit. Exclusion lowers and non-linear clustering enhances the large scale stochasticity. The total value of the large scale stochasticity depends on which of the two effects is stronger but the amplitude of the correction does not directly depend on the abundance of the sample. These stochasticity corrections must decay to zero for high-k, implying they are scale dependent in the intermediate regime. The transition scale is related to either the exclusion scale of the halo sample under consideration or to the non-linear clustering scale. At the final time (Eulerian space) these transition scales shrink due to the non-linear collapse, but the low-k amplitude of the stochasticity agrees with Lagrangian space, as expected from mass and momentum conservation.

While the presented model can explain the observed trend of modified stochasticity at a qualitative level, the quantitative agreement is not perfect. This is related to our imperfect modelling of the Lagrangian halo correlation function with a local bias ansatz. A more realistic modelling might be possible in the full framework of peak biasing in three dimensions, as the one dimensional results in §9.3.5 indicate.

We also discuss the effects of satellite galaxies, when a galaxy sample with a non-vanishing satellite fraction is considered. In this case the stochasticity can dramatically deviate from the auxiliary $1/\bar{n}$ value on large scales. In this case one has to identify the number density of host haloes to infer the stochasticity on large scales and account for the fact that on scales below the typical scale of the satellite profile there is a transition to the fiducial Poisson shot noise of the galaxy sample.

Finally, we consider the stochasticity matrix of haloes of different mass. We show that diagoalization of this matrix gives rise to one eigenvaue with a low amplitude, with the eigenvector that aproximately scales with the halo mass. This provides an explanation to the stochasticity suppression with mass weighting explored in [4, 5]. It would be interesting to explore, how the stochasticity corrections imprint themselves in the halo bispectrum, which is a promising probe of inflationary physics [50] and whose measurement becomes realistic in present and upcoming surveys [51].

Acknowledgements

The authors would like to thank Niayesh Afshordi, Kwan Chuen Chan, Donghui Jeong, Patrick McDonald, Teppei Okumura, Fabian Schmidt, Ravi Sheth, Zvonimir Vlah and Jaiyul Yoo for useful discussions. The simulations were carried out on the ZBOX3 supercomputer at the Institute for Theoretical Physics of the University of Zurich. This work is supported in part by NASA ATP Grant number NNX12AG71G, Swiss National Foundation (SNF) under contract 200021-116696/1, WCU grant R32-10130, National Science Foundation Grant No. 1066293. T.B. acknowledges the hospitality of the Aspen Center for Physics. R.E.S. acknowledges support from the ERC under advanced grant 246797 "GALFORMOD" from the European Research Council. V.D. acknowledges support from the Swiss National Sciences Foundation.

9.7. Appendix

9.7.1. Perturbative Peak Effects in the Initial Correlation Function

As pointed out by [44], there is strong numerical evidence for the presence of k^2-terms in the linear bias of protohalo. Such terms in fact appear in all the Lagrangian bias factors predicted by the peak model, as can be seen from a large scale expansion of the peak correlation function [23, 22]. In the particular case of the peak-matter cross-correlation, the linear bias expansion is exact on all scales [24] and agrees with the average density profile derived in [20]. Under the assumption that haloes are represented by peaks, we thus have for the halo-matter power spectrum in the initial conditions

$$P_{\rm hm}(k) = b_1 \left(1 + \kappa_\delta k^2\right) W_{{\rm G},R_{\rm pk}}(k) P(k), \tag{9.60}$$

where $W_{{\rm G},R_{\rm pk}}$ is the Gaussian filter of scale $R_{\rm pk}$. Note that the peak smoothing scale is not necessarily related to the exclusion scale. Similarly one can expand the peak-peak correlation function on large scales and obtain a scale dependent linear bias relation that would relate to the halo-halo power spectrum of the form

$$P_{\rm hh}(k) \approx b_1^2 \left(1 + \kappa_\delta k^2\right)^2 W^2_{{\rm G},R_{\rm pk}}(k) P(k). \tag{9.61}$$

One has to be careful when considering the correspondence between large scales in the correlation function and small wavenumbers in the power spectrum. As we stressed above, the amplitude of the low-k power spectrum is tightly coupled to the small scale correlation function. Thus, there is no reason to believe that the large scale expansion of the correlation function will yield a correct description of the low-k power spectrum. As we will discuss in more detail below, a correct description of the low-k power spectrum in the peak model requires higher order bias expansions or a non-perturbative evaluation of the full peak correlation function.

Given the functional form of the halo-matter power spectrum in the initial conditions we can fit for the linear bias b_1, the relative peak bias κ_δ and the smoothing scale $R_{\rm pk}$. We show the corresponding scale dependent bias in the left panel of Fig. 9.14. This plot also shows the linear local (i.e. scale independent) bias parameter used in the main text as the horizontal dashed line.

We can use the inferred bias parameters and peak smoothing scale to calculate the corresponding imprint on the halo-halo correlation function. As we show in the right panel of Fig. 9.14, the correlation function deviates significantly from the naïve linear scale independent bias prediction shown as the horizontal dash-dotted line. On scales exceeding $r \approx 25\ h^{-1}$Mpc, the measured correlation function is in much better correspondence with the linear peak bias shown as the solid red line. Below 25 h^{-1}Mpc the peak correlation fails to predict the scale dependence and does actually worse than the linear scale independent bias. This had to be expected, since the linear peak bias is only accurate on large scales and on smaller scales higher order

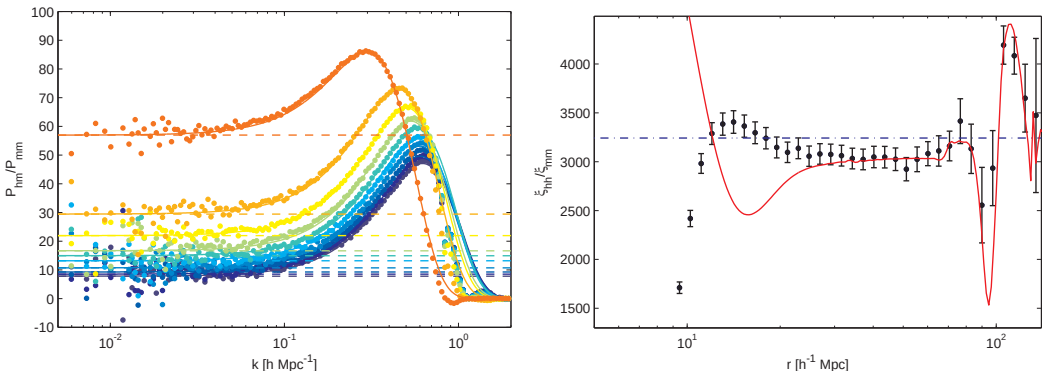

Figure 9.14.: *Left panel:* Protohalo-matter cross power spectrum. Horizontal dashed lines show the linear bias and solid lines a fit using the functional form suggested by the peak model. *Right panel:* Initial condition halo-halo correlation function divided by linear initial condition correlation function for mass bin X with linear scale independent bias (horizontal dash-dotted) and linear peak bias (red solid). Around the BAO scale and down to $r = 30\ h^{-1}$Mpc the peak model describes the ratio of halo and matter correlation functions much better, but then it fails miserably.

bias corrections need to be taken into consideration. In fact, comparison between the linear peak bias and the full numerical evaluation of the one dimensional peak model, suggests that $20 - 30\ h^{-1}$Mpc is a typical breakdown scale for the linear peak bias. We will explore the convergence properties of the perturbative peak model in more detail in a forthcoming paper. While accurately predicting the functional form of the scale dependent bias, the mass dependence of the coefficients deviates from the predictions of the peak model. The main reason for discussing the peak corrections here, is that the presence of the peak corrections invalidates the simple b_2 fitting procedure following Eq. (9.42). In this simple approach we consider the linear bias from the low-k limit of the cross power spectrum and consider the positive correction $b_2^2\xi^2$ on top of it. The right panel of Fig. 9.14 rather suggests that the quadratic bias corrections need to be considered on top of the linear peak bias. Furthermore the peak model predicts several second order bias contributions in contrast to the one bias contribution arising from the local model. Fitting the second order peak bias parameters would require higher order spectra, such as the protohalo bispectrum and even the second order biasing might not be sufficient to explain the upturn in the halo-halo correlation function. We thus restrict ourselves to the simple local model and stress that the quadratic bias parameters are a phenomenological fit rather than a true quadratic bias and we thus don't expect them to be in accordance with the peak-background split prediction.

9.7.2. The One Dimensional Peak Model

Here we review the major steps in the derivation of the one-dimensional peak model following [25]. As mentioned before, the peak model associates maxima of the density fields with the formation sites of dark matter haloes. Thus, we are interested in the clustering statistics of these points. For simplicity we will only consider a one dimensional field, which would be for a example a skewer through the full three dimensional cosmological density field. The number density of peaks can be written as a sum over delta functions at the peak positions $x_{\rm pk}$

$$n_{\rm pk}(x) = \sum_{\rm pk} \delta^{(\rm D)}(x - x_{\rm pk}) \tag{9.62}$$

and $\delta_{\rm pk}(x) = n_{\rm pk}(x)/\bar{n}_{\rm pk} - 1$. Using that the first derivative of the field vanishes at the peak position, we can expand the density field around the peak position

$$\delta(x) \approx \delta(x_{\rm pk}) + \frac{1}{2}\delta''(x_{\rm pk})(x - x_{\rm pk})^2. \tag{9.63}$$

Taking the derivative, we obtain

$$\delta'(x) \approx \delta''(x_{\rm pk})(x - x_{\rm pk}). \tag{9.64}$$

Using the transformation properties of the Dirac delta we have

$$\delta^{(\rm D)}(x - x_{\rm pk}) = \delta''(x_{\rm pk})\delta^{(\rm D)}(\delta'). \tag{9.65}$$

This expression is known as the Kac-Rice formula [23, 52]. The mean number density is readily obtained as an integral over the one point probability density function of the field amplitude, slope and curvature

$$\bar{n}_{\rm pk} = \langle n_{\rm pk}(x)\rangle = \int {\rm d}\boldsymbol{y}\ \mathbb{P}_{\rm 1pt}(\boldsymbol{y})\delta''\delta^{(\rm D)}(\delta') \tag{9.66}$$

where $\boldsymbol{y} = (\delta, \delta', \delta'')$. The two point correlation function is then given by

$$\langle \delta_{\rm pk}(x_1)\delta_{\rm pk}(x_2)\rangle = \int {\rm d}\boldsymbol{Y}\ \mathbb{P}_{\rm 2pt}(|x_1 - x_2|; \boldsymbol{Y})\delta_{\rm pk}(x_1)\delta_{\rm pk}(x_2) \tag{9.67}$$

$$= \frac{1}{\bar{n}_{\rm pk}^2}\int {\rm d}\boldsymbol{Y}\ \mathbb{P}_{\rm 2pt}(|x_1 - x_2|; \boldsymbol{Y})\delta_1''\delta_2''\delta^{(\rm D)}(\delta_1')\delta^{(\rm D)}(\delta_2') - 1, \tag{9.68}$$

where $\boldsymbol{Y} = (\delta_1, \delta_1', \delta_1'', \delta_2, \delta_2', \delta_2'')$. The one and two point PDFs are given by

$$\mathbb{P}_{\rm 1pt}(\boldsymbol{y}) = \frac{1}{\sqrt{(2\pi)^3 \det m}} \exp\left[-\frac{1}{2} y m^{-1} y^T\right], \quad \mathbb{P}_{\rm 2pt}(\boldsymbol{Y}) = \frac{1}{\sqrt{(2\pi)^6 \det M}} \exp\left[-\frac{1}{2} Y M^{-1} Y^T\right]. \tag{9.69}$$

The symmetric 6×6 covariance matrix of the field amplitude and derivatives $M_{ij} = \langle Y_i Y_j\rangle$ can then be written as

$$M = \begin{pmatrix} m & B(r) \\ B^{\rm T}(r) & m \end{pmatrix}, \tag{9.70}$$

where the constituent block matrices are given by

$$m = \begin{pmatrix} \sigma_0^2 & 0 & -\sigma_1^2 \\ 0 & \sigma_1^2 & 0 \\ -\sigma_1^2 & 0 & \sigma_2^2 \end{pmatrix}, \qquad B(r) = \begin{pmatrix} \xi_0(r) & -\xi_{1/2}(r) & -\xi_1(r) \\ \xi_{1/2}(r) & \xi_1(r) & -\xi_{3/2}(r) \\ -\xi_1(r) & \xi_{3/2}(r) & \xi_2(r) \end{pmatrix}. \tag{9.71}$$

The only remaining ingredient for the evaluation of Eq. (9.68) are the correlators of field amplitudes and derivatives, which we obtain by smoothing the three dimensional density field with a Gaussian filter and considering its values and derivatives along one coordinate axis, which we choose to be the z-direction without loss of generality

$$\xi_{(n+m)/2}(r) = \int \frac{{\rm d}^3 k}{(2\pi)^3}(-1)^n({\rm i}\,\mu k)^{n+m} \exp\left[{\rm i}\,\mu k r\right] P(k) W_{{\rm G},R_{\rm pk}}(k), \tag{9.72}$$

where $\mu = \hat{\boldsymbol{k}}\cdot\hat{\boldsymbol{z}}$. The moments of field amplitudes and derivatives are then given as $\sigma^2_{(n+m)/2} = \xi_{(n+m)/2}(0)$.

9.7.3. The Exclusion Kernel

Let us assume, that there is some scatter around the mean exclusion radius R of some sample due to triaxiality and a finite width of the mass bin. Let us furthermore assume that this scatter is lognormally distributed such that the PDF is given by

$$f(r) = \frac{1}{x\sigma\sqrt{2\pi}} \exp\left[-\frac{\ln^2(r/R)}{2\sigma^2}\right]. \tag{9.73}$$

Let us now calculate the probability of finding a pair with an actual separation that is smaller than the scale under consideration

$$F(r) = \int_0^r \mathrm{d}r' f(r') = \frac{1}{2}\left(1 + \mathrm{erf}\left[\frac{\ln(r/R)}{\sqrt{2}\sigma}\right]\right). \tag{9.74}$$

To find a pair at separation r its exclusion scale needs to be smaller than the actual separation and the total probability is given as a product of the fiducial probability of finding a pair in a non-excluded sample and the probability that the actual exclusion scale is smaller than r

$$\delta\tilde{\mathbb{P}}(r) = F(r)\delta\mathbb{P}(r) = \bar{n}\left[1 + \xi^{(\mathrm{d})}(r)\right]\delta V = F(r)\bar{n}\left[1 + \xi^{(\mathrm{c})}(r)\right]\delta V. \tag{9.75}$$

We can now infer the correlation of the discrete tracers

$$\xi^{(\mathrm{d})}(r) = F(r)\left[1 + \xi^{(\mathrm{c})}(r)\right] - 1 \tag{9.76}$$

In the main text we use the logarithm to base 10 for convenience rather than the natural logarithm. The corresponding scatters are related by a simple rescaling by a factor of $\log_{10} e \approx 0.43$.

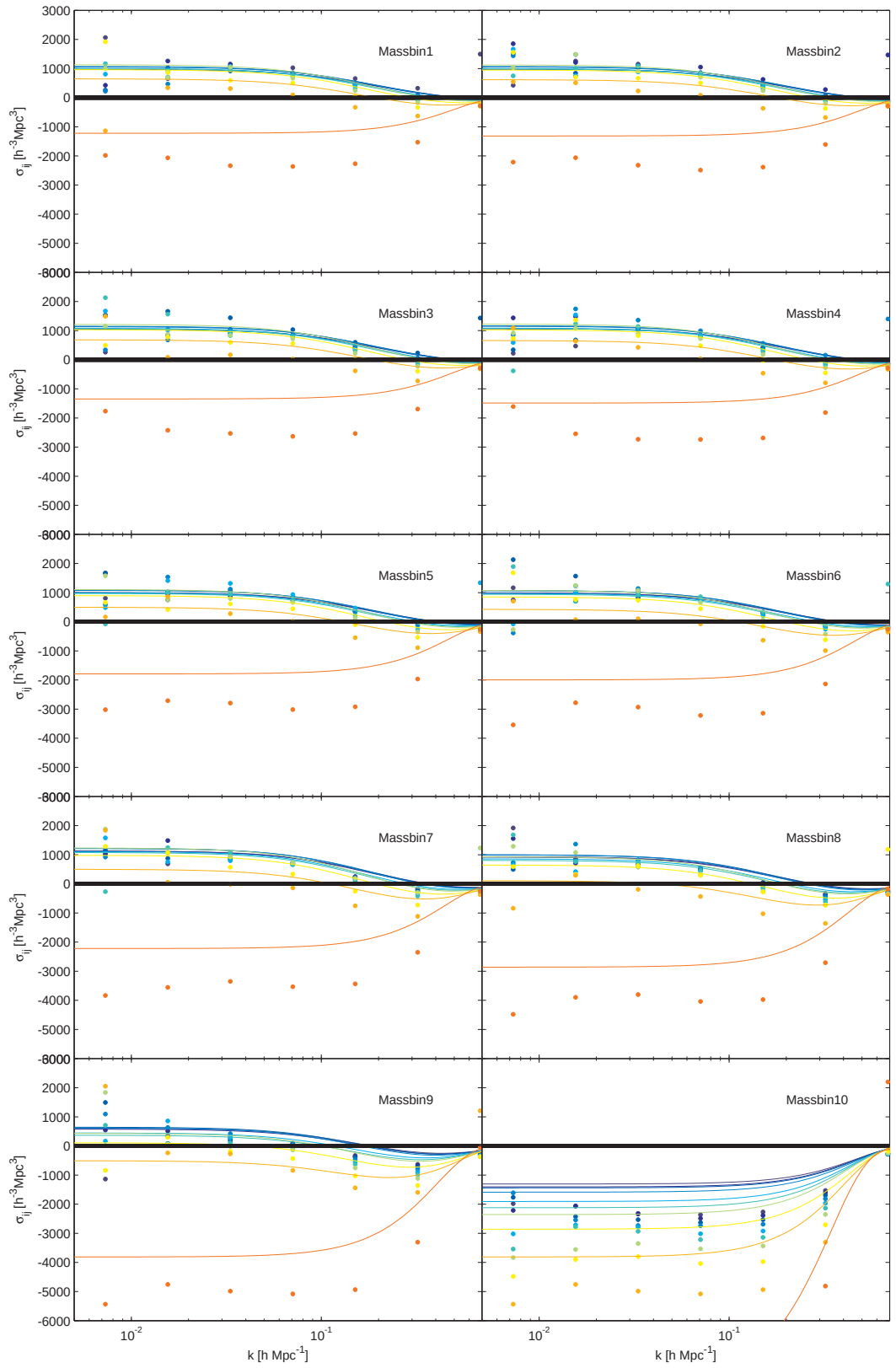

Figure 9.15.: Cross-terms of the stochasticity matrix of the $z = 0$ haloes traced back to the initial conditions. The text in the panel refers to the mass bin with which we cross correlate all the other bins. Note that for reference we also include the diagonals of the matrix with the fiducial shot noise subtracted out. Mass increases from top to bottom, i.e., blue to orange.

Bibliography

[1] T. Baldauf, U. Seljak, R. E. Smith, N. Hamaus, and V. Desjacques, **Halo Stochasticity from Exclusion and non-linear Clustering**, *ArXiv e-prints* (May, 2013) [arXiv:1305.2917].

[2] N. Kaiser, **On the spatial correlations of Abell clusters**, *Astrophys. J. Let.* **284** (Sept., 1984) L9–L12.

[3] J. N. Fry and E. Gaztanaga, **Biasing and hierarchical statistics in large scale structure**, *Astrophys. J.* **413** (1993) 447–452, [astro-ph/9302009].

[4] U. Seljak, N. Hamaus, and V. Desjacques, **How to suppress the shot noise in galaxy surveys**, *ArXiv e-prints* (Apr., 2009) [arXiv:0904.2963].

[5] N. Hamaus, U. Seljak, V. Desjacques, R. E. Smith, and T. Baldauf, **Minimizing the stochasticity of halos in large-scale structure surveys**, *Phys. Rev.* **82** (Aug., 2010) 043515, [arXiv:1004.5377].

[6] R. Casas-Miranda, H. J. Mo, R. K. Sheth, and G. Boerner, **On the distribution of haloes, galaxies and mass**, *Mon. Not. Roy. Astron. Soc.* **333** (July, 2002) 730–738, [astro-ph/].

[7] M. Manera and E. Gaztañaga, **The local bias model in the large-scale halo distribution**, *Mon. Not. Roy. Astron. Soc.* **415** (July, 2011) 383–398, [arXiv:0912.0446].

[8] N. Hamaus, U. Seljak, and V. Desjacques, **Optimal constraints on local primordial non-Gaussianity from the two-point statistics of large-scale structure**, *Phys. Rev.* **84** (Oct., 2011) 083509, [arXiv:1104.2321].

[9] N. Hamaus, U. Seljak, and V. Desjacques, **Optimal weighting in galaxy surveys: Application to redshift-space distortions**, *Phys. Rev.* **86** (Nov., 2012) 103513, [arXiv:1207.1102].

[10] R. K. Sheth and G. Lemson, **Biasing and the distribution of dark matter haloes**, *Mon. Not. Roy. Astron. Soc.* **304** (Apr., 1999) 767–792, [astro-ph/].

[11] R. E. Smith, R. Scoccimarro, and R. K. Sheth, **Scale dependence of halo and galaxy bias: Effects in real space**, *Phys. Rev.* **75** (2007), no. 6 063512, [astro-ph/].

[12] A. Labatie, J.-L. Starck, M. Lachièze-Rey, and P. Arnalte-Mur, **Uncertainty in 2-point correlation function estimators and BAO detection in SDSS DR7**, *ArXiv e-prints* (Sept., 2010) [arXiv:1009.1232].

[13] J. A. Peacock and D. Nicholson, **The large-scale clustering of radio galaxies**, *Mon. Not. Roy. Astron. Soc.* **253** (Nov., 1991) 307–319.

[14] U. Seljak, **Analytic model for galaxy and dark matter clustering**, *Mon. Not. Roy. Astron. Soc.* **318** (2000) 203–213, [astro-ph/].

[15] A. Cooray and R. Sheth, **Halo models of large scale structure**, *Phys. Rep.* **372** (Dec., 2002) 1–129, [astro-ph/].

[16] D. J. Eisenstein, J. Annis, J. E. Gunn, A. S. Szalay, A. J. Connolly, R. C. Nichol, N. A. Bahcall, M. Bernardi, S. Burles, F. J. Castander, M. Fukugita, D. W. Hogg, Ž. Ivezić, G. R. Knapp, R. H. Lupton, V. Narayanan, M. Postman, D. E. Reichart, M. Richmond, D. P. Schneider, D. J. Schlegel, M. A. Strauss, M. SubbaRao, D. L. Tucker, D. Vanden Berk, M. S. Vogeley, D. H. Weinberg, and B. Yanny, **Spectroscopic Target Selection for the Sloan Digital Sky Survey: The Luminous Red Galaxy Sample**, *Astron. J.* **122** (Nov., 2001) 2267–2280, [astro-ph/].

[17] N. Roth and C. Porciani, **Testing standard perturbation theory and the Eulerian local biasing scheme against N-body simulations**, *Mon. Not. Roy. Astron. Soc.* **415** (July, 2011) 829–844, [arXiv:1101.1520].

[18] K. Chuen Chan and R. Scoccimarro, **Halo Sampling, Local Bias and Loop Corrections**, *ArXiv e-prints* (Apr., 2012) [arXiv:1204.5770].

[19] J. Beltrán Jiménez and R. Durrer, **Effects of biasing on the galaxy power spectrum at large scales**, *Phys. Rev.* **83** (May, 2011) 103509, [arXiv:1006.2343].

[20] J. M. Bardeen, J. R. Bond, N. Kaiser, and A. S. Szalay, **The Statistics of Peaks of Gaussian Random Fields**, *Astrophys. J.* **304** (1986) 15–61.

[21] J. A. Peacock and A. F. Heavens, **The statistics of maxima in primordial density perturbations**, *Mon. Not. Roy. Astron. Soc.* **217** (Dec., 1985) 805–820.

[22] V. Desjacques, M. Crocce, R. Scoccimarro, and R. K. Sheth, **Modeling scale-dependent bias on the baryonic acoustic scale with the statistics of peaks of Gaussian random fields**, arXiv:1009.3449.

[23] V. Desjacques, **Baryon acoustic signature in the clustering of density maxima**, *Phys. Rev.* **78** (Nov., 2008) 103503, [arXiv:0806.0007].

[24] V. Desjacques and R. K. Sheth, **Redshift space correlations and scale-dependent stochastic biasing of density peaks**, *Phys. Rev.* **81** (Jan., 2010) 023526, [arXiv:0909.4544].

[25] S. L. Lumsden, A. F. Heavens, and J. A. Peacock, **The clustering of peaks in a random Gaussian field**, *Mon. Not. Roy. Astron. Soc.* **238** (May, 1989) 293–318.

[26] A. F. Heavens and R. K. Sheth, **The correlation of peaks in the microwave background**, *Mon. Not. Roy. Astron. Soc.* **310** (Dec., 1999) 1062–1070, [astro-ph/].

[27] P. McDonald, **Clustering of dark matter tracers: Renormalizing the bias parameters**, *Phys. Rev.* **74** (Nov., 2006) 103512–+, [astro-ph/].

[28] T. Baldauf, U. Seljak, V. Desjacques, and P. McDonald, **Evidence for quadratic tidal tensor bias from the halo bispectrum**, *Phys. Rev.* **86** (Oct., 2012) 083540, [arXiv:1201.4827].

[29] K. C. Chan, R. Scoccimarro, and R. K. Sheth, **Gravity and large-scale nonlocal bias**, *Phys. Rev.* **85** (Apr., 2012) 083509, [arXiv:1201.3614].

[30] H. J. Mo and S. D. M. White, **An analytic model for the spatial clustering of dark matter haloes**, *Mon. Not. Roy. Astron. Soc.* **282** (Sept., 1996) 347–361, [astro-ph/].

[31] W. H. Press and P. Schechter, **Formation of Galaxies and Clusters of Galaxies by Self-Similar Gravitational Condensation**, *Astrophys. J.* **187** (Feb., 1974) 425–438.

[32] F. Bernardeau, S. Colombi, E. Gaztanaga, and R. Scoccimarro, **Large-scale structure of the universe and cosmological perturbation theory**, *Phys. Rep.* **367** (2002) 1–248, [astro-ph/0112551].

[33] D. N. Spergel, R. Bean, O. Doré, M. R. Nolta, C. L. Bennett, J. Dunkley, G. Hinshaw, N. Jarosik, E. Komatsu, L. Page, H. V. Peiris, L. Verde, M. Halpern, R. S. Hill, A. Kogut, M. Limon, S. S. Meyer, N. Odegard, G. S. Tucker, J. L. Weiland, E. Wollack, and E. L. Wright, **Three-Year Wilkinson Microwave Anisotropy Probe (WMAP) Observations: Implications for Cosmology**, *Astrophys. J. Sup.* **170** (June, 2007) 377–408, [astro-ph/].

[34] V. Springel, **The cosmological simulation code GADGET-2**, *Mon. Not. Roy. Astron. Soc.* **364** (2005) 1105–1134, [astro-ph/0505010].

[35] U. Seljak and M. Zaldarriaga, **A Line-of-Sight Integration Approach to Cosmic Microwave Background Anisotropies**, *Astrophys. J.* **469** (Oct., 1996) 437, [astro-ph/].

[36] M. Crocce, S. Pueblas, and R. Scoccimarro, **Transients from initial conditions in cosmological simulations**, *Mon. Not. Roy. Astron. Soc.* **373** (Nov., 2006) 369–381, [astro-ph/].

[37] N. Frusciante and R. K. Sheth, **Lagrangian bias in the local bias model**, *ArXiv e-prints* (Aug., 2012) [arXiv:1208.0229].

[38] J. L. Tinker, D. H. Weinberg, Z. Zheng, and I. Zehavi, **On the Mass-to-Light Ratio of Large-Scale Structure**, *Astrophys. J.* **631** (Sept., 2005) 41–58, [astro-ph/].

[39] P. Valageas and T. Nishimichi, **Combining perturbation theories with halo models**, *A&A* **527** (Mar., 2011) A87, [arXiv:1009.0597].

[40] R. Scoccimarro, R. K. Sheth, L. Hui, and B. Jain, **How Many Galaxies Fit in a Halo? Constraints on Galaxy Formation Efficiency from Spatial Clustering**, *Astrophys. J.* **546** (Jan., 2001) 20–34, [astro-ph/].

[41] P. J. E. Peebles, *The large-scale structure of the universe*. Princeton University Press, 1980.

[42] A. Jenkins, C. S. Frenk, F. R. Pearce, P. A. Thomas, J. M. Colberg, S. D. M. White, H. M. P. Couchman, J. A. Peacock, G. Efstathiou, and A. H. Nelson, **Evolution of Structure in Cold Dark Matter Universes**, *Astrophys. J.* **499** (May, 1998) 20, [astro-ph/].

[43] R. E. Smith, J. A. Peacock, A. Jenkins, S. D. M. White, C. S. Frenk, F. R. Pearce, P. A. Thomas, G. Efstathiou, and H. M. P. Couchman, **Stable clustering, the halo model and non-linear cosmological power spectra**, *Mon. Not. Roy. Astron. Soc.* **341** (June, 2003) 1311–1332, [astro-ph/].

[44] A. Elia, A. D. Ludlow, and C. Porciani, **The spatial and velocity bias of linear density peaks and protohaloes in the Λ cold dark matter cosmology**, *Mon. Not. Roy. Astron. Soc.* **421** (Apr., 2012) 3472–3480, [arXiv:1111.4211].

[45] T. Okumura, U. Seljak, and V. Desjacques, **Distribution function approach to redshift space distortions, Part III: halos and galaxies**, *ArXiv e-prints* (June, 2012) [arXiv:1206.4070].

[46] T. Baldauf, R. E. Smith, U. Seljak, and R. Mandelbaum, **Algorithm for the direct reconstruction of the dark matter correlation function from weak lensing and galaxy clustering**, *Phys. Rev.* **81** (Mar., 2010) 063531, [arXiv:0911.4973].

[47] R. Reyes, R. Mandelbaum, U. Seljak, T. Baldauf, J. E. Gunn, L. Lombriser, and R. E. Smith, **Confirmation of general relativity on large scales from weak lensing and galaxy velocities**, *Nature* **464** (Mar., 2010) 256–258, [arXiv:1003.2185].

[48] A. A. Berlind and D. H. Weinberg, **The Halo Occupation Distribution: Toward an Empirical Determination of the Relation between Galaxies and Mass**, *Astrophys. J.* **575** (Aug., 2002) 587–616, [astro-ph/].

[49] Z. Zheng, A. A. Berlind, D. H. Weinberg, A. J. Benson, C. M. Baugh, S. Cole, R. Davé, C. S. Frenk, N. Katz, and C. G. Lacey, **Theoretical Models of the Halo Occupation Distribution: Separating Central and Satellite Galaxies**, *Astrophys. J.* **633** (Nov., 2005) 791–809, [astro-ph/].

[50] T. Baldauf, U. Seljak, and L. Senatore, **Primordial non-Gaussianity in the bispectrum of the halo density field**, *JCAP* **4** (Apr., 2011) 6–+, [arXiv:1011.1513].

[51] F. Marin, C. Blake, G. Poole, C. McBride, S. Brough, M. Colless, W. Couch, S. Croom, D. Croton, T. M. Davis, M. J. Drinkwater, K. Forster, D. Gilbank, M. Gladders, K. Glazebrook, B. Jelliffe, R. J. Jurek, I. Li, B. Madore, D. C. Martin, K. Pimbblet, M. Pracy, R. Sharp, E. Wisnioski, D. Woods, T. K. Wyder, and H. K. C. Yee, **The WiggleZ Dark Energy Survey: constraining galaxy bias and cosmic growth with 3-point correlation functions**, *ArXiv e-prints* (Mar., 2013) [arXiv:1303.6644].

[52] J. Adler, R. J. Taylor, *Random Fields and Geometry*. Springer, 2007.

CHAPTER 10

Summary & Discussion

This Thesis discussed various aspects of the clustering of dark matter haloes in the large scale structure of the Universe. In this Chapter we summarize the main results and discuss their implications and possible directions for extensions.

10.1. What have we Learned?

In Ch. 6 we studied the imprint of primordial non-Gaussianity on the halo bispectrum. The coupling between long and short wavelength fluctuations in presence of primordial non-Gaussianity of the local form leads to a distinct feature in the distribution of haloes. Modelling this feature in halo clustering statistics requires a consistent treatment of non-linear clustering, non-linear bias and the non-Gaussian distribution of the initial fluctuations. Our consistent treatment of all the contributing effects at tree level shows good agreement with simulations and allowed us to show that a full bispectrum analysis can tighten the constraint on the local non-Gaussianity amplitude $f_{\rm NL}$ by a factor of five compared to the power spectrum analysis. For this project we developed a diagrammatic scheme for the calculation of the perturbation theory, implementing standard perturbation theory, biasing and non-Gaussianity.
The prominence of the non-Gaussian signatures on large scales motivated us to consider galaxy biasing in a fully General Relativistic framework. In Ch. 7 we were able to show that the linear galaxy bias is related to the effective curvature in the local inertial frame of the galaxy under consideration. Following previous studies by [1] and using a consistent mapping between the inertial frame and the observed redshift slice, we were able to calculate the observed galaxy power spectrum, which is inherently gauge invariant. Finally, we were able to show that a long wavelength mode can be fully implemented into a Newtonian N-body simulation by adding curvature to the energy budget and mapping the coordinates appropriately. This technique provides an independent check of the consistency between peak-background-split and power spectrum bias parameters.
In Ch. 8 we investigated the presence of biasing terms beyond the Eulerian local bias model using the halo bispectrum in N-body simulations to probe quadratic interactions. We were able to show that at second order there is a tidal tensor contribution on top of the standard quadratic term in the matter overdensity. Our study also showed that both shape and amplitude of such a term are in agreement with a coevolution model, describing the joint evolution of haloes and dark matter under gravity, starting from local Lagrangian bias.
One of the major contaminants in the galaxy power spectrum on large, linear scales is the

so called shotnoise. It contributes power on top of the continuous power spectra due to the discrete nature of the tracers. There is evidence from numerical simulations that the scale independent contribution to the power spectrum is different from the Poisson value [2, 3]. In Ch. 9 we showed how this effect can be understood based on small scale halo exclusion and non-linear biasing in Lagrangian space. We furthermore found that the amplitude of the shot noise correction is approximately constant throughout evolution and goes to zero on small scales, where the fiducial shot noise $1/\bar{n}$ is recovered.

10.2. Outlook

While this thesis answers several open questions in LSS clustering, it raises new ones and leaves many existing problems unsolved. In the following we will consider a few possible directions for extending this work.

10.2.1. Non-linear Matter Clustering

Besides the relation between matter and haloes, also the matter clustering itself requires a careful modelling. As we have noted in Ch. 3, the validity of most perturbative techniques is confined to scales $k \lesssim 0.1\ h\mathrm{Mpc}^{-1}$ at redshift $z = 0$. One plausible reason for this might be that the amplitude of the density field approaches the non-perturbative regime. But it is also interesting to examine the validity of other assumptions of the standard perturbative treatment, for instance the single stream approximation and the assumption of vanishing vorticity and negligible anisotropic stress. Indeed, some recent work [4] has shown that vorticity might play an important role in the breakdown of standard perturbation theory. It would be interesting to revisit this question, especially in light of the recent developments in effective field theory treatments of LSS clustering [5, 6].

10.2.2. Halo Biasing

The bias considerations in Ch. 8 and Ch. 9 focused on very large scales. However, as we discussed in Ch. 5, physically motivated models for the distribution of protohaloes, such as the peak model [7], predict distinct features in the initial conditions that might influence the observable late time clustering. While the non-perturbative features might be damped by gravity, they can still have a non-negligible influence on the scale dependent bias at late times. Unfortunately, there is no one-to-one correspondence between haloes and peaks and the peak model has thus far only be considered in the perturbative large distance regime. For these reasons, both the initial distribution and the evolution of halo positions and velocities deserve further analytic and numeric investigation and might help to construct physically motivated and consistent galaxy clustering models.
The peak model also predicts a stochastic velocity bias [8], damping the halo velocity compared to the matter velocity on small scales and thus affecting the coevolution. Standard gravitational evolution predicts that this velocity bias is completely washed out by gravity [9], whereas the peak model predicts a constant velocity bias [8]. To date, most models assume a vanishing velocity bias, although its presence might have a strong influence on observables, especially redshift space distortions, and inferred parameters. One should clarify this issue using N-body simulations, and if necessary, implement velocity bias into existing redshift space distortion and biasing formalisms.

10.2.3. Primordial Non-Gaussianity

In Ch. 6 we discussed the influence of local quadratic non-Gaussianity on the observable galaxy or halo bispectrum and found that statistics beyond the two point function have the potential

to provide tight constraints on primordial non-Gaussianity. For other forms of primordial non-Gaussianity, such as cubic g_{NL} type interactions, scale dependent non-Gaussianity or features in the inflationary potential, the bi- and trispectrum might provide equally tight constraints. Thus it seems promising to derive the imprint of these forms of non-Gaussianity on the bi- and trispectrum and compare the results to numerical simulations. Finally, it would be interesting to investigate how well these models perform on observational data and try to constrain shape and amplitude of primordial non-Gaussianities.

10.2.4. Relativistic Effects

Following the treatment in Ch. 7 it would be interesting to develop a better understanding of the influence of GR corrections on horizon scales on statistics beyond the two point function. As mentioned above, these statistics are promising probes of the initial conditions of the Universe and thus need to be well understood. For this purpose, one needs to study the general relativistic generalization of second order bias. There are two possible approaches to do so. First, one can extend the relations between the global coordinates and the local inertial frame presented in Ch. 7 to second order. Second, one could generalize the Lagrangian framework of [10] to the largest scales. The final goal is a covariant expression for the observable galaxy bispectrum.

Bibliography

[1] J. Yoo, A. L. Fitzpatrick, and M. Zaldarriaga, **New perspective on galaxy clustering as a cosmological probe: General relativistic effects**, *Phys. Rev.* **80** (Oct., 2009) 083514–+, [arXiv:0907.0707].

[2] N. Hamaus, U. Seljak, V. Desjacques, R. E. Smith, and T. Baldauf, **Minimizing the stochasticity of halos in large-scale structure surveys**, *Phys. Rev.* **82** (Aug., 2010) 043515, [arXiv:1004.5377].

[3] U. Seljak, N. Hamaus, and V. Desjacques, **How to Suppress the Shot Noise in Galaxy Surveys**, *Physical Review Letters* **103** (Aug., 2009) 091303, [arXiv:0904.2963].

[4] S. Pueblas and R. Scoccimarro, **Generation of vorticity and velocity dispersion by orbit crossing**, *Phys. Rev.* **80** (Aug., 2009) 043504–+, [arXiv:0809.4606].

[5] M. Pietroni, G. Mangano, N. Saviano, and M. Viel, **Coarse-grained cosmological perturbation theory**, *JCAP* **1** (Jan., 2012) 19, [arXiv:1108.5203].

[6] J. J. M. Carrasco, M. P. Hertzberg, and L. Senatore, **The Effective Field Theory of Cosmological Large Scale Structures**, *ArXiv e-prints* (June, 2012) [arXiv:1206.2926].

[7] J. M. Bardeen, J. R. Bond, N. Kaiser, and A. S. Szalay, **The Statistics of Peaks of Gaussian Random Fields**, *Astrophys. J.* **304** (1986) 15–61.

[8] V. Desjacques, M. Crocce, R. Scoccimarro, and R. K. Sheth, **Modeling scale-dependent bias on the baryonic acoustic scale with the statistics of peaks of Gaussian random fields**, *Phys. Rev.* **82** (Nov., 2010) 103529, [arXiv:1009.3449].

[9] K. C. Chan, R. Scoccimarro, and R. K. Sheth, **Gravity and large-scale nonlocal bias**, *Phys. Rev.* **85** (Apr., 2012) 083509, [arXiv:1201.3614].

[10] T. Matsubara, **Nonlinear perturbation theory with halo bias and redshift-space distortions via the Lagrangian picture**, *Phys. Rev.* **78** (Oct., 2008) 083519, [arXiv:0807.1733].

APPENDIX A

Simulation Analysis

A.1. Fourier Analysis on a Grid

In numerical simulations the volume is limited, which leaves us with finite Fourier modes, the smallest of them given by the fundamental mode $k_\mathrm{f} = 2\pi/L$ and the corresponding volume of the fundamental cell is $V_\mathrm{f} = (2\pi)^3/V$. The Fourier modes are thus given by

$$\delta(\boldsymbol{k_i}) = \frac{V}{N_\mathrm{c}^3} \sum_{\boldsymbol{j}} \delta(\boldsymbol{x_j}) \exp\left[\mathrm{i}\, \boldsymbol{k_i} \cdot \boldsymbol{x_j}\right], \tag{A.1}$$

where $\boldsymbol{k_i} = k_\mathrm{f}\boldsymbol{i}$. When Fourier transforming the grid with the implemented `FFTW` algorithms, the Fourier Transform is not normalized, i.e., the subsequent FFT and inverse FFT yields a factor of N_c^3. Thus we divide by N_c^3 in the real to Fourier space transformation. Comparing to the above formula we then still need to multiply by a factor of V. Consequently the relation between discrete and FFTW Fourier modes is given by $\delta(\boldsymbol{k_i}) = V/N_\mathrm{c}^3\ \delta(\boldsymbol{k_i})^{(\mathrm{FFTW})}$. The Dirac Delta function rewritten for discrete k as

$$\delta^{(\mathrm{D})}(\boldsymbol{k_i} + \boldsymbol{k_j}) = \delta^{(\mathrm{D})}\left((\boldsymbol{i} + \boldsymbol{j})k_\mathrm{f}\right) = \frac{1}{k_\mathrm{f}}\delta^{(\mathrm{D})}(\boldsymbol{i} - \boldsymbol{j}) = \frac{V}{(2\pi)^3}\delta^{(\mathrm{K})}_{\boldsymbol{i},\boldsymbol{j}} \tag{A.2}$$

The power spectrum for discrete cells is thus given by

$$P\left(|\boldsymbol{i}|k_\mathrm{f}\right) = \frac{1}{V}\left\langle \delta(\boldsymbol{i}k_\mathrm{f})\delta(-\boldsymbol{i}k_\mathrm{f})\right\rangle \tag{A.3}$$

In simulations we estimate the power spectrum in logarithmic bins $[k\pm]$ centered at k

$$\hat{P}(k) = \frac{1}{N_k V} \sum_{\boldsymbol{i}k_\mathrm{f}\in[k\pm]} \delta(\boldsymbol{k_i})\delta(-\boldsymbol{k_i}) = \frac{V}{N_k N_\mathrm{c}^6} \sum_{\boldsymbol{i}k_\mathrm{f}\in[k\pm]} \delta^{(\mathrm{FFTW})}(\boldsymbol{k_i})\delta^{(\mathrm{FFTW})}(-\boldsymbol{k_i}), \tag{A.4}$$

where N_k is the number of cells in the k-bin. Note that the estimator is unbiased since $\left\langle \hat{P}\right\rangle = P$. The number of grid cells in the bin is given by the shell volume divided by the volume of the fundamental cell

$$N_k = \frac{V_k}{V_\mathrm{f}} = \frac{4\pi k^3 \mathrm{d}\ln k}{V_\mathrm{f}} \tag{A.5}$$

The bispectrum estimator for a fixed configuration $\{k_1, k_2, \mu = \boldsymbol{k}_1 \cdot \boldsymbol{k}_2\}$ can be estimated as

$$\hat{B}(k_1, k_2, \mu) = \frac{1}{N_\mathrm{tr} V} \sum_{\boldsymbol{i}k_\mathrm{f}\in[k\pm]} \sum_{\boldsymbol{j}k_\mathrm{f}\in[k\pm,\mu\pm]} \delta(\boldsymbol{k_i})\delta(\boldsymbol{k_j})\delta(-\boldsymbol{k_i} - \boldsymbol{k_i}) \tag{A.6}$$

$$= \frac{V^2}{N_{\rm tr} N_{\rm c}^9} \sum_{\boldsymbol{i} k_{\rm f} \in [k\pm]} \sum_{\boldsymbol{j} k_{\rm f} \in [k\pm, \mu\pm]} \delta^{(\rm FFTW)}(\boldsymbol{k_i}) \delta^{(\rm FFTW)}(\boldsymbol{k_i}) \delta^{(\rm FFTW)}(-\boldsymbol{k_i} - \boldsymbol{k_j}) \quad \text{(A.7)}$$

the estimator is unbiased since $\left\langle \hat{B} \right\rangle = B$. The number of triangles in the bin is given by the shell volume divided by the volume of the fundamental cell squared

$$N_{\rm tr} = \frac{V_{123}}{V_{\rm f}^2} = \frac{8\pi^2 k_1^3 k_2^3 (\mathrm{d} \ln k)^2 \mathrm{d}\mu}{V_{\rm f}^2} \quad \text{(A.8)}$$

Let us now calculate the variance of the power spectrum

$$\left\langle \hat{P}^2(k) \right\rangle - \left\langle \hat{P}(k) \right\rangle^2 = \frac{1}{N_k^2 V^2} \sum_{\boldsymbol{i} k_{\rm f}, \boldsymbol{j} k_{\rm f} \in [k\pm]} \left\langle \delta(\boldsymbol{k_i}) \delta(-\boldsymbol{k_i}) \delta(\boldsymbol{k_j}) \delta(-\boldsymbol{k_j}) \right\rangle - P^2(k) \quad \text{(A.9)}$$

$$= \frac{1}{N_k^2} \sum_{\boldsymbol{i} k_{\rm f}, \boldsymbol{j} k_{\rm f} \in [k\pm]} P(\boldsymbol{k_i}) P(\boldsymbol{k_j}) + \frac{2}{N_k^2} \sum_{\boldsymbol{i} k_{\rm f} \in [k\pm]} P^2(\boldsymbol{k_i}) - P^2(k) \quad \text{(A.10)}$$

$$= \frac{2}{N_k} P^2(k) = \frac{2 V_f}{4\pi k^3 \mathrm{d} \ln k} P^2(k) \quad \text{(A.11)}$$

Here we assumed Gaussianity and used the fact that due the reality condition in real space only half of the complex plane is independent. For the variance of the bispectrum estimator we have

$$\begin{aligned} \left\langle \hat{B}^2(k_1, k_2, \mu) \right\rangle - \left\langle \hat{B}(k_1, k_2, \mu) \right\rangle^2 =& \frac{1}{N_{\rm tr}^2 V^2} \sum_{\boldsymbol{i},\boldsymbol{j},\boldsymbol{l},\boldsymbol{m}} \left\langle \delta(\boldsymbol{k_i}) \delta(\boldsymbol{k_j}) \delta(-\boldsymbol{k_i} - \boldsymbol{k_j}) \delta(\boldsymbol{k_l}) \delta(\boldsymbol{k_m}) \delta(-\boldsymbol{k_l} - \boldsymbol{k_m}) \right\rangle \\ & - B^2(k_1, k_2, \mu) \\ =& s_{123} \frac{V}{N_{\rm tr}^2} \sum_{\boldsymbol{i},\boldsymbol{j}} P(\boldsymbol{k_i}) P(\boldsymbol{k_j}) P(-\boldsymbol{k_i} - \boldsymbol{k_j}) \\ =& s_{123} \frac{V}{N_{\rm tr}} P(k_1) P(k_2) P(k_3) \\ =& s_{123} \frac{(2\pi)^3 V_{\rm f}}{8\pi^2 k_1^3 k_2^3 (\mathrm{d} \ln k)^2 \mathrm{d}\mu} P(k_1) P(k_2) P(k_3) \end{aligned} \quad \text{(A.12)}$$

The factor s_{123} takes on values of $6, 2, 1$ for general, isosceles and equilateral triangles. This is a simple consequence of the fact, that for equilateral triangles the k-modes are indistinguishable. We again assumed Gaussianity, for which $B = 0$.

A.2. Mass Assignment and Estimation of the Power Spectrum

The analysis of cosmological fluctuations in Fourier space has several advantages over an analysis in configuration space. First, in linear theory, the modes evolve independetly and the power spectrum is thus less correlated than the correlation function. Furthermore, the k-space analysis allows for a clearer separation of scales. For an efficient analysis in Fourier space it is beneficial to employ the well developed Fast Fourier Transform (FFT) libraries, for instance the publically available library `FFTW`[1]. In a N-body simulation we have a distribution of particles sampling the dark matter or halo density fields. Thus we have to estimate the density in cells of a rectangular grid.

As a first step the $N_{\rm p}$ particles under consideration[2] are assigned to the cubical mesh. The

[1] www.fftw.org

[2] Here particles refers to DM particles, galaxies and haloes equivalently.

density at the mesh position $\boldsymbol{x}_i$ can be expressed as a convolution of the assignment filter with the particle field $n(\boldsymbol{r}) = \sum_{j=1}^{N_p} \delta^{\mathrm{D}}(\boldsymbol{r} - \boldsymbol{r}_j)$

$$n(\boldsymbol{x}_i) = \int \mathrm{d}^3 r n(\boldsymbol{r}) W(\boldsymbol{r} - \boldsymbol{x}_i) = \sum_{j=1}^{N_p} W(\boldsymbol{r}_j - \boldsymbol{x}_i). \tag{A.13}$$

We use the **nearest gridpoint** (NGP) or **cloud-in-cell** (CIC) mass assignment schemes [1] with window functions

$$W_{\mathrm{CIC}}(x - x_i) = \begin{cases} 1 - \frac{|x - x_i|}{\Delta r}, & \text{if } |x - x_i| \leq \Delta r \\ 0, & \text{otherwise} \end{cases} \tag{A.14}$$

$$W_{\mathrm{NGP}}(x - x_i) = \begin{cases} 1, & \text{if } |x - x_i| \leq \frac{\Delta r}{2} \\ 0, & \text{otherwise} \end{cases} \tag{A.15}$$

The assignment schemes are visualized in Fig. A.1. The Nearest Grid Point (NGP) scheme

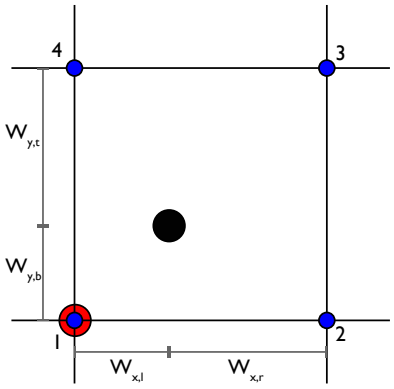

Figure A.1.: Cell in a two-dimensional grid and weightings for the NGP and CIC assignment schemes. In the NGP scheme, all the mass of the black particle is assigned to gridpoint 1 (red), whereas the CIC scheme splits the mass over all the four vertices (blue). For instance, the fraction $W_{x,r}W_{y,t}$ is assigned to gridpoint 1, where $W_{x,l} + W_{x,r} = 1$ and $W_{y,t} + W_{y,b} = 1$.

assigns all the mass to the nearest grid point, or equivalently, the density at each gridpoint receives contributions from particles within one gridcell centered on the gridpoint. The Cloud in Cell (CIC) scheme distributes the mass to the nearest eight gridpoints, i.e., the vertices of the cell in which the particle is contained. Equivalently, the density at a gridpoint receives contributions from all particles situated within the eight adjacent grid cells.
The next step consists in calculating the mean of the assigned mass and defining the overdensity

$$\delta(\boldsymbol{x}_i) = \frac{n(\boldsymbol{x}_i)}{\langle n \rangle} - 1 \tag{A.16}$$

The Fourier transform of the overdensity field can then be computed using the publicly available `FFTW` routines. The convolution with the window function of the NGP or CIC assignment in real space, leads to a multiplication with the Fourier transformed window in Fourier space. We could thus correct for the convolution by dividing out the Fourier transform of the NGP or CIC window function respectively

$$\delta_{\mathrm{corr}}(\boldsymbol{k}) = \frac{\delta(\boldsymbol{k})}{W(\boldsymbol{k})}, \tag{A.17}$$

where

$$W_{\mathrm{CIC}}(\boldsymbol{k}) = \prod_{i=1,2,3} \left[\frac{\sin\left(\frac{\pi k_i}{2k_{\mathrm{Ny}}}\right)}{\left(\frac{\pi k_i}{2k_{\mathrm{Ny}}}\right)} \right]^2, \qquad W_{\mathrm{NGP}}(\boldsymbol{k}) = \prod_{i=1,2,3} \left[\frac{\sin\left(\frac{\pi k_i}{2k_{\mathrm{Ny}}}\right)}{\left(\frac{\pi k_i}{2k_{\mathrm{Ny}}}\right)} \right]. \tag{A.18}$$

A more carefull analysis of [2] reveals that this simple correction scheme is not valid for a field sampled by discrete tracers. In this case the real power spectrum is convolved with the assignment window and iterative schemes have to be used for the recovery of the power spectrum. These corrections are not yet implemented.
The power spectrum or bispectrum can then be estimated using the methods presented in the last section.
The estimation of k-space statistics on the grid can thus be summarized as follows:

1. CIC assignment
2. normalization
3. FFT
4. CIC correction
5. n-spectra

The finite size of the cells limits the k-mode up to which (scale down to which) we can probe the density fluctuations. In Fig. A.2 we show the convergence of the power spectrum estimates with respect to the $N_c = 2048^3$, CIC-corrected case. As had to be expected, the power spectra are trustworthy roughly up to the Nyquist-frequency $k_{\mathrm{Ny}} = N_c\pi/L$. The figure also shows that the uncorrected power spectra underestimate the true power by a significant amount.

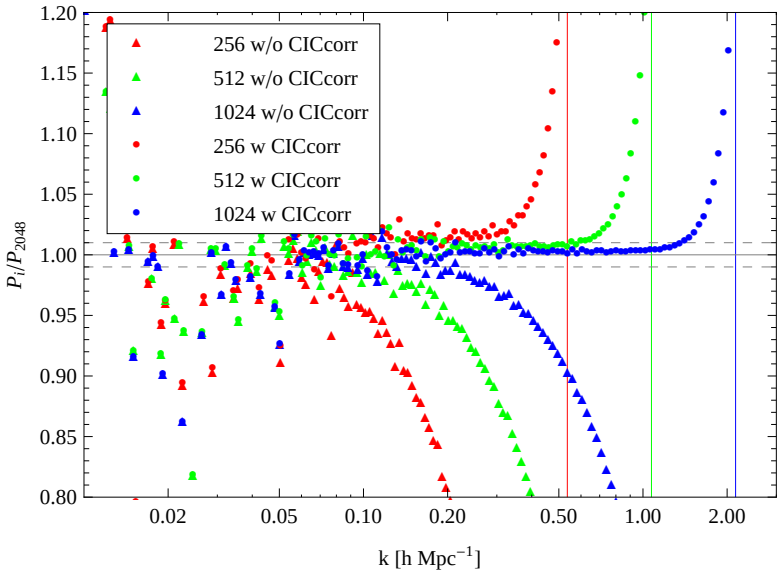

Figure A.2.: Ratio of the power spectrum computed for different grid sizes and the $N_c = 2048$ grid result with CIC correction. While all of our measurements in this Thesis employ the CIC correction (circles), we show for reference also the power spectra without CIC correction (triangles).

A.2.1. Increased resolution from subsampling

The grid based clustering analysis described in the above section has the problem that its resolution is limited to two grid spacings. Increasing the number of cells per dimension helps to obtain a higher resolution, but with the cost of grid sizes growing by the third power of the refinement. Since it is our goal to resolve the clustering down to $r_{\mathrm{min}} \approx 0.1\ h^{-1}$Mpc this would require a FFT with $N_c = 15000^3$. In the following we will describe a technique to estimate small scale power spectra and correlation functions from cosmological simulations using Fourier transforms. This technique was first introduced by [3, 4].
To become familiar with the method we consider a one dimensional grid $\mathcal{G}$ with N cells and length L. Furthermore, we assume that a density field on $x \in (0, L)$ has been assigned to the grid points using one of the mentioned assignment schemes. We now partition the fine grid $\mathcal{G}$ using a coarse grid $\tilde{\mathcal{G}}$ with M grid cells as shown in Figure A.3.

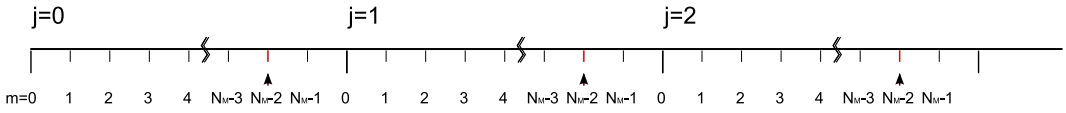

Figure A.3.: One dimensional grid partitioned into M coarse grid cells indexed by j.

The density at an arbitrary point x_l of $\mathcal{G}$ can then be written as

$$\delta(x_l) = \delta\left(x_m + j\frac{L}{M}\right), \tag{A.19}$$

where x_m is the position of the particle within the j-th coarse mesh cell. Inspired by our previous notes on the grid based analysis, we will now perform a FT of the density on above introduced mesh

$$\hat{\delta}(k_s) = \frac{1}{N}\sum_{l=0}^{N-1} \exp\left[ik_s x_l\right]\delta(x_l). \tag{A.20}$$

We may now split the sum into one over all the coarse-mesh-cells $j \in [0, M-1]$ and one over the cell positions within the first coarse-mesh-cell $x_m \in [0, L/M]$.

$$\hat{\delta}(k_s) = \frac{1}{N}\sum_{m=0}^{N_M-1}\sum_{j=0}^{M-1} \exp\left[ik_s\left(x_m + j\frac{L}{M}\right)\right]\delta\left(x_m + j\frac{L}{M}\right) \tag{A.21}$$

$$= \frac{1}{N}\sum_{m=0}^{N_M-1} \exp\left[ik_s x_m\right]\sum_{j=0}^{M-1} \exp\left[ik_s j\frac{L}{M}\right]\delta\left(x_m + j\frac{L}{M}\right). \tag{A.22}$$

Here we introduced $N_M := N/M$ to denote the number of fine mesh cells within one coarse mesh cell. If we now choose our fundamental mode for the FT as

$$k_0 = M\frac{2\pi}{L} \Rightarrow k_s = sk_0, \tag{A.23}$$

the exponential $\exp\left[ikjL/M\right]$ in (A.22) vanishes, and by defining $\tilde{\delta}(x_l) := \sum_j \delta(x_l + jL/M)$ we can write

$$\hat{\delta}(k_s) = \frac{1}{N}\sum_{m=0}^{N_M-1} \exp\left[ik_s x_m\right]\tilde{\delta}(x_m). \tag{A.24}$$

This means that we have to perform a FT for the N_M cells of the first coarse grid cell and obtain the correct density field for the modes $\hat{\delta}(k_s)$.
If we wanted to increase the range of correlation functions or power spectra obtained using the FFT techniques described above, we would have to increase the number of cells per dimension

by a factor M, which consequently would increase the size of the arrays by a factor M^3 in the 3-d case. This can easily lead to large arrays and FFTs. Instead of performing a N^3 FFT we could take the box, partition it using a coarse grid with M cells per dimension and then put a reasonable Fourier grid of dimension $N_M = N/M$ on each of the coarse grid cells. By summing up the contributions of all corresponding points in the coarse grid cells and performing the FFT for the summed subgrid (A.24), we obtain an estimate for the high k, small scale modes with a reasonable amount of operations. Compared to a M times larger grid we loose the modes

$$k_s = sR\frac{2\pi}{L} \quad R = 1 \dots M-1, s = 0 \dots N_M - 1, \tag{A.25}$$

equivalently we are considering only each M-th mode.

A.3. Velocities

The `Gadget` velocity output is

$$v_{\mathrm{G}} = \frac{v}{\sqrt{a}} \tag{A.26}$$

where $v = x'$ is the peculiar velocity. Hence we can get the peculiar velocity as $v = \sqrt{a}v_{\mathrm{G}}$ and the comoving velocity $\dot{x} = v/a = v_{\mathrm{G}}/\sqrt{a}$.

A.4. Generating Gaussian Random Fields

For the initial conditions of simulations and calculations in the peak model we need to generate realizations of Gaussian random fields. The real and imaginary parts of the mode are independent Gaussian distributed random variables. If we rewrite the complex Fourier modes as magnitude and phase

$$\delta(\boldsymbol{k}) = a(\boldsymbol{k}) + \mathrm{i}\, b(\boldsymbol{k}) = m(\boldsymbol{k}) \exp\left[\mathrm{i}\, \phi(\boldsymbol{k})\right] \tag{A.27}$$

then the phase is uniform distributed and the magnitude is Rayleigh distributed

$$p(x|\sigma) = \begin{cases} \frac{x}{\sigma^2} \exp\left[-\frac{x^2}{2\sigma^2}\right] & x > 0 \\ 0 & \text{otherwise} \end{cases} \tag{A.28}$$

This results from the following theorem. If a and b are independently, identically distributed Gaussian ($a, b \sim \mathcal{N}(0.\sigma^2)$), then $m = \sqrt{a^2 + b^2} \sim p_{\mathrm{Ray}}(x|\sigma)$. The proof can be conducted in four steps

1. If $a \sim p_a(x)$, then $a^2 \sim p_{a^2}(x)$ with

$$p_{a^2}(x) = \frac{1}{2\sqrt{x}} p_a(\sqrt{x}) \tag{A.29}$$

2. If $a \sim p_a(x)$ and $b \sim p_b(x)$ then $c = a + b \sim p_c(x)$ with

$$p_c(x) = \int \mathrm{d}y p_a(y) p_b(x - y) \tag{A.30}$$

and thus we have for the sum of the squares of Normal distributed variables

$$p_{a^2+b^2}(x) = \frac{1}{8\sigma^2} \exp\left[-\frac{x}{2\sigma^2}\right] \tag{A.31}$$

3. If $a \sim p_a(x)$, then $\sqrt{a} \sim p_{\sqrt{a}}(x)$ with

$$p_{\sqrt{a}}(x) = 2x p_a(x^2) \tag{A.32}$$

Thus we finally have

$$p_{\sqrt{a^2+b^2}}(x) = \frac{x}{4\sigma^2} \exp\left[-\frac{x^2}{2\sigma^2}\right]. \tag{A.33}$$

When setting up the modes in k-space, we have to account for the fact that field is real in configuration space and we thus have $\delta(\boldsymbol{k}) = \delta^*(-\boldsymbol{k})$. Furthermore the Nyquist theorem limits the maximum wavenumber that can be probed to $k_{\rm Ny} = N_{\rm c}\pi/L$. If one of the k-components exceeds the Nyquist wavenumber, then the corresponding mode component is remapped to the corresponding mode with a negative k-component. In Fig. A.4, we show an expample of a two-dimensional Gaussian random field.

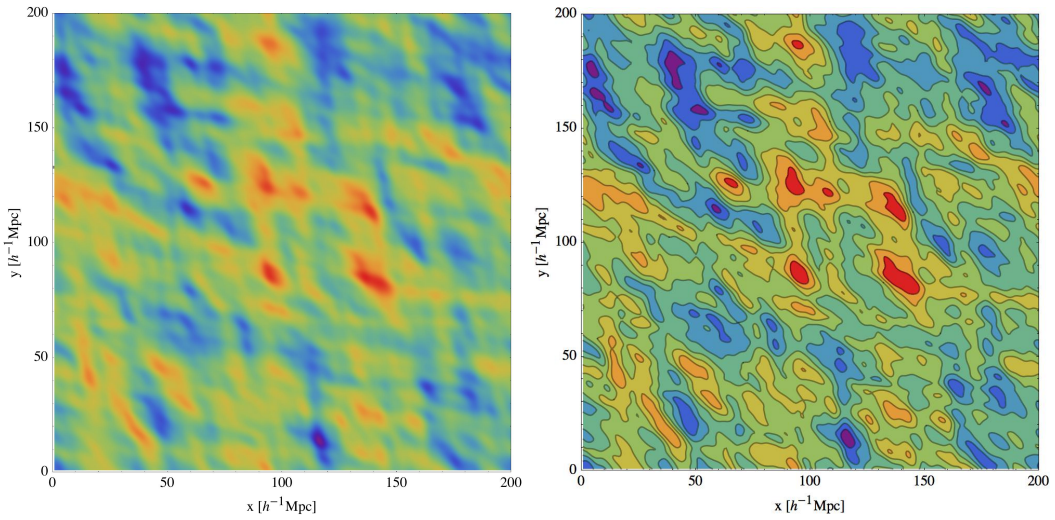

Figure A.4.: Examples of a two dimensional density field in density and contour plot. The density fluctuations correspond to a slice through a three dimensional density field smoothed on $R = 2\ h^{-1}$Mpc.

Bibliography

[1] R. W. Hockney and J. W. Eastwood, *Computer Simulation Using Particles*. Institute of Physics Publishing, 1988.

[2] Y. P. Jing, **Correcting for the alias effect when measuring the power spectrum using FFT**, *Astrophys. J.* **620** (2005) 559–563, [astro-ph/0409240].

[3] **The Virgo Consortium** Collaboration, A. Jenkins, C. S. Frenk, F. R. Pearce, P. A. Thomas, J. M. Colberg, S. D. M. White, H. M. P. Couchman, J. A. Peacock, G. Efstathiou, and A. H. Nelson, **Evolution of structure in cold dark matter universes**, *Astrophys. J.* **499** (1998) 20, [astro-ph/9709010].

[4] **The Virgo Consortium** Collaboration, R. E. Smith, J. A. Peacock, A. Jenkins, S. D. M. White, C. S. Frenk, F. R. Pearce, P. A. Thomas, G. Efstathiou, and H. M. P. Couchman, **Stable clustering, the halo model and nonlinear cosmological power spectra**, *Mon. Not. Roy. Astron. Soc.* **341** (2003) 1311, [astro-ph/0207664].

Index